# A MULTI-COIL MAGNETOSTRICTIVE ACTUATOR: DESIGN, ANALYSIS, AND EXPERIMENT

A Dissertation
Presented to
The Academic Faculty

by

Thomas Lawler Wilson, Jr.

In Partial Fulfillment
of the Requirements for the Degree
Doctor of Philosophy in the
School of Mechanical Engineering

Georgia Institute of Technology
May 2009

# A MULTI-COIL MAGNETOSTRICTIVE ACTUATOR: DESIGN AND ANALYSIS

Approved by:


Dr. Ben T. Zinn, Advisor
Schools of Mechanical and Aerospace Engineering
*Georgia Institute of Technology*

Dr. Wayne J. Book
School of Mechanical Engineering
*Georgia Institute of Technology*

Dr. Ari Glezer
School of Mechanical Engineering
*Georgia Institute of Technology*

Dr. Jerry M. Seitzman
School of Aerospace Engineering
*Georgia Institute of Technology*

Dr. Yedidia Neumeier
School of Aerospace Engineering
*Georgia Institute of Technology*


Date Approved: March 30, 2009

*To my long-suffering wife who has always wanted to be married to a doctor.*

# ACKNOWLEDGEMENTS

I wish to thank my thesis advisor, Professor Zinn, for his friendship and long support of this project. He has allowed me the freedom to pursue my idea until I declared the project complete. This is the first and perhaps only time I will be able to say I have solved a problem fully.

To my reading committee, Professors Wayne Book, Ari Glazer, Jerry Seitzman,, and Yedidia Neumeier, I would like to award a medal of commendation for service above and beyond the call of duty. As Professor Zinn has said, this is really three dissertations. To have read it and provided good and thoughtful review is testament to their dedication to education at Georgia Tech. I especially want to thank Dr. Neumeier for his many discussions throughout this research project.

I wish to thank my wife, Janice, for her contributions to the preparation of the manuscript. In addition to supporting me in every possible way on this long journey, she proofread every page. To my daughters, Julia, Katie and Sarah, I appreciate the interest, support, and patient listening that they have provided over many years. I wish to thank . my mothe, who plaintively asked, “Will I see it [the dissertation] before I die?”, for good genes and a dry sense of humor.

A number of students collaborated with me on this research. These individuals include David Butz who assisted in real-time programming of the control system, Matt Christopher for information on the input and output system hardware, Paul Rios for assistance in running experiments and checking equations. Sean Feng prepared the inputs for the FEMM modeling and performed much of the wiring on the experimental setup. Their efforts are much appreciated.

Toby Hansen and Rachel Dudley of ETREMA Products were helpful in the design and manufacture of the prototype actuator. The prototype actuator was created because they took the time to support research on their product.

My friends and colleagues on the staff at Oak Ridge National Laboratory provided both tolerance of my limited work schedule at the laboratory and genuine interest in my dissertation research, especially Gary Mays, Sacit Cetiner, Mike Muhlheim, Richard Wood, Ray Brittain, and David Holcomb.

Despite being a non-traditional student, many great young friends from Georgia Tech made me feel like I was truly a student and part of Georgia Tech again. Without their friendship and acceptance, this middle-aged quest would not have been possible. There are many people I want to thank. All of the students who worked in the Combustion Lab have been good friends. The Combustion Lab is a good and lively place to learn and to work. In the Georgia Tech student community, I want to single out Becky Brown, Jason Brown, Cliff Johnson, Akiva Sklar, Lynnanne George, Young Park, and Byungki Kim for their friendship over many years.

# TABLE OF CONTENTS

# LIST OF TABLES

# LIST OF FIGURES

# NOMENCLATURE

| *Variable* | *Dimensions* | *Description* |
|---|---|---|
| A, B, C, D | *(-)* | State space matrices for $\dot{\mathbf{x}} = \mathbf{Ax} + \mathbf{Bu}$; $\mathbf{y} = \mathbf{Cx} + \mathbf{Du}$ |
| $A$ | $m^2$ | Cross-sectional area of a rod. Used briefly in vibration model development |
| $\mathbf{A}$ | *tesla·m* | Magnetic vector potential in vector form |
| $A_r$, $A_\phi$, $A_z$ | *tesla·m* | Radial, azimuthal and axial components of magnetic vector potential |
| $A_j^{FEMM}(r,\phi,z)$ | *tesla·m* | Steady-state, magnetic vector potential due to 1 amp in the *j*-th coil as calculated by FEMM |
| $\mathbf{B}$ | *tesla* | Magnetic induction vector. Magnetic flux density. |
| $B_r$, $B_\phi$, $B_z$ | *tesla* | Radial, azimuthal and axial components of magnetic induction |
| $\Delta B$, $B_{min}$ | *tesla* | Range and offset for dimensionless magnetic field |
| $b$ | *(-)* | Dimensionless magnetic induction |
| $C_x(t)$ | *Varies* | Underdetermined function in partial integrations |
| $c$ | *m/s* | Speed of sound |
| $d_{mi}$ | *m/A* | Magnetostrictive constant $d_{mi} = \left.\frac{\partial S_i}{\partial H_m}\right\|_T = \left.\frac{\partial B_m}{\partial T_i}\right\|_H$ |
| $\boldsymbol{d}$ | *m/A* | Magnetostrictive constants in matrix form |
| $\mathbf{D}$ | *(-)* | Derivative matrix in MPC |
| $\mathbf{E}$ | *V/m* | Electric field |
| **E, F, G** | *E (-), F and G ($s^{-1}$)* | Derivative coupled matrices for state space system in $\mathbf{E}\dot{\mathbf{x}} = \mathbf{Fx} + \mathbf{Gu}$ |
| $\mathbf{E}^{xy}$, $\mathbf{F}^{xy}$, $\mathbf{G}^{x}$ | *E (-), F and G ($s^{-1}$)* | Submatrices of **E**, **F**, **G**; $x$=1-5, $y$=1-5 |
| $\mathscr{J}$ | | Performance index for MPC |
| $E_{i_0}$ | *s* | Integral error in MPC |
| $f$ | *N·s/m* | Friction coefficient in vibration model |
| $\mathbf{f}_{k,m,p}^{M}(r,\phi,z)$ | $A/m^2$ | Current density distribution function for the k,m,p-th eddy current mode |
| $G$ | $J$ | Gibbs free energy in derivation of constitutive properties of magnetostriction. |
| $h$ | *(-)* | Dimensionless variable corresponding to $\breve{H}(z,t)$ |

| *Variable* | *Dimensions* | *Description* |
|---|---|---|
| $h^{FEMM}(\xi,t)$ | | Dimensionless variable corresponding to $\breve{H}^{FEMM}(z,t)$ |
| $h^{H}(\xi,t)$ | | Transverse average of dimensionless magnetic field due to eddy current. $x_M^H(\rho,\phi,\xi,t)$ |
| $\boldsymbol{H}$ | *A/m* | Magnetic field vector |
| $\mathbf{H}$ | *(-)* | Predictor system matrix |
| $H_R^{FEMM}(r,z,\mathbf{I}_C(t))$ | *A/m* | Steady state magnetic field in the rod with currents in coils of $\mathbf{I}_C(t)$ |
| $H_{R,j}^{FEMM}(r,z)$ | *A/m* | Steady state magnetic field in the rod with *j*-coil energized at 1 amp. |
| $H_{R,z}(r,\phi,z,t)$ | *A/m* | Axial magnetic field in the rod region. |
| $H_r$, $H_\phi$, $H_z$ | *A/m* | Radial, azimuthal and axial components of magnetic field |
| $\breve{H}(z,t)$ | *A/m* | Average magnetic field in transverse plane of rod |
| $\Delta H$, $H_{min}$ | *A/m* | Range and offset for dimensionless magnetic field transformation |
| $\mathcal{H}_{R,k,m,p}^{FEMM}(t)$ | *A/m* | Integral transform of $H_R^{FEMM}(r,z,\mathbf{I}_C(t))$ |
| $I$ | *A* | Current |
| $\mathbf{I}$ | *(-)* | Identity matrix |
| $I_{C,j}$ | *A* | Current in *j*-th coil circuit |
| $\mathbf{I}_C(t)$ | *A* | Vector of currents in the coils |
| $\Delta I$, $I_{min}$ | *A* | Range and offset for dimensionless current transformation |
| $i_0$ | *(-)* | Time index for current time step in MPC |
| $i_H$ | *(-)* | Time index for time horizon in MPC. |
| $\mathrm{J}_y(x)$ | | Bessel function of first kind of order y |
| $\mathcal{J}_{r,k,m,p}(t)$, $\mathcal{J}_{\phi,k,m,p}(t)$ | | Integral transforms of $j_r$, $j_\phi$ |
| $\mathbf{J}$ | $A/m^2$ | Current density in vector form |
| $J_r$, $J_\phi$, $J_z$ | $A/m^2$ | Radial, azimuthal and axial components of current density |
| $j$ | *(-)* | Index for the coils |
| *jmax* | | Number of coils |
| $K^N(z,t)$ | *A/m* | Equivalent surface current on rod due to vibration strain. |
| $\mathcal{K}_n^N$ | *A/m* | Integral transform of $K^N(z,t)$ for *n*-th vibrational mode |
| $\Delta K$ | *A/m* | Scaling factor for converting surface current to dimensionless units |

| *Variable* | *Dimensions* | *Description* |
|---|---|---|
| $\mathbf{K}_{\Delta u}, \mathbf{K}_{Exact}, \mathbf{K}_{P}, \mathbf{K}_{P+I}$ | *(-)* | Proportional gain control matrices for conventional, exact, proportional, and proportional-integral MPC. |
| $k$ | *(-)* | Index for the radial mode of magnetic field and eddy currents |
| *kmax* | *(-)* | Maxium index for the radial modes of magnetic field and eddy currents |
| $G$ | *ohm/s* | Amplifier lumped gain |
| $l$ | *(-)* | Index for rearranging the four dimensional modal magnetic model to a one dimensional. $l = k + kmax\left[ m - 1 + mmax\left( p - 1 \right) \right]$ |
| *lmax* | *(-)* | Maximum index of $l$ |
| $L_C$ | *m* | Length of wire in one coil |
| $L^K_{j,j'}$, $L_{j,k,m,p}$, $L^N_{j,n}$ | | Dimensionless inductance coefficient between coil and coil, coil and eddy current mode, coil and vibration mode |
| $\mathscr{L}^K_{j,j'}$, $\mathscr{L}^{N,K}_{j,j'}$, $\mathscr{L}^M_{j,k,m,p}$, $\mathscr{L}^{N,N}_{j,n}$ | *V·s* | Inductance in mixed units corresponds to the coil-to-coil, coil to equivalent surface current and coil to eddy current. |
| $\mathscr{L}^K_{\sim j',j}$, $\mathscr{L}^M_{\sim k,m,p,j}$, $\mathscr{L}^N_{\sim n,j}$ | *henry* | Inductance between coil and other coils, eddy current modes and vibration modes |
| $m$ | *(-)* | Index for the azimuthal mode of magnetic field and eddy currents |
| *mmax* | *(-)* | Maximum index for the aximuthal modes of magnetic field and eddy currents |
| $\Delta M$ | *kg* | Element of mass in vibration model |
| $\boldsymbol{M}$ | *A/m* | Magnetization |
| $n$ | *(-)* | Index for the vibration modes |
| *nmax* | *(-)* | Maximum index for the vibration modes |
| *nk* | *(-)* | Number time steps experimental system's output is delayed with respect to input (latency). |
| $N\left(\beta_n\right)$ | *(-)* | Normalization constant for n-the axial vibration mode |
| $N\left(\varepsilon_{k,m}\right)$ | *(-)* | Normalization constant for *k,m*-th radial mode magnetics mode |
| $N\left(\eta_p\right)$ | *(-)* | Normalization constant for *p*-the axial magnetics mode |
| $N\left(\gamma_m\right)$ | *(-)* | Normalization constant for m-the azimuthal magnetics |
| $p$ | *(-)* | Index for the axial mode of magnetic |

| *Variable* | *Dimensions* | *Description* |
|---|---|---|
| | | field and eddy currents |
| *pmax* | *(-)* | Maxium index for the axial modes of magnetic field and eddy currents |
| $P_{k,m}$ | *(-)* | Coefficient used in averaging magnetic field over transverse plane in vibration model |
| **P** | *(-)* | Predictor system matrix |
| $q^2$ | *(-)* | Scalar weight factor on control error in conventional and proportional MPC |
| $q_P^2$ | *(-)* | Scalar weight factor on proportional control error in MPC |
| $q_I^2$ | *(-)* | Scalar weight factor on integral control error in MPC |
| $Q_{n,j}$ | *(-)* | Coefficient in coupling coil to vibration |
| **Q** | *(-)* | Weight matrix on control error in MPC |
| $\mathscr{R}_C$ | *ohm* | Resistance of the coil |
| $\mathscr{R}_L$ | *ohm* | Resistance of load resistor |
| $R_{\gamma_m}\left(\varepsilon_{k,m},\rho\right)$ | *(-)* | Radial mode function |
| **R** | *(-)* | Weight matrix for control input in MPC |
| *r* | *m* | Radial position |
| $r_g$ | *m* | Radius of rod. Inner radius of coil. Parameter of the actuator design |
| $r_c$ | *m* | Outer radius of coil. Parameter of the actuator design |
| $S_R$ | $m^2$ | Surface area of rod |
| ***S*** | *(-)* | Strain tensor |
| **S** | *(-)* | Integration matrix in MPC |
| $s_{ij}^H$ | $Pa^{-1}$ | Elastic compliance at constant H. $\left.\frac{\partial S_i}{\partial T_j}\right\|_H \equiv s_{ij}^H$, |
| $\mathbf{s}^{\mathbf{H}}$ | $Pa^{-1}$ | Elastic compliance at constant H in matrix form |
| **T** | | Stress tensor |
| **T** | *(-)* | Combined model transfer function |
| *T* | *turns/meter* | Turns per unit length. Parameter of the actuator design |
| $T_s$ | *s* | Time step |
| $T_c$ | *turns/coil* | Turns in one coil. Parameter of the actuator design |
| *t* | *s* | time |
| $U_j$ | *A* | Current demand |

| *Variable* | *Dimensions* | *Description* |
|---|---|---|
| $\mathbf{u}_{i_0+1:i_0+i_H}$ | | Predicted demands (i.e., coil current demand) from first predicted time, $i_0+1$ to prediction horizon, $i_0+i_H$ |
| $\Delta\mathbf{u}_{i_0+1:i_0+i_H}$ | | Predicted change in demands from first predicted time, $i_0+1$ to prediction horizon, $i_0+i_H$ |
| $V_{C,j}$ | $m^3$ | Volume of *j*-th coil region. |
| $\mathrm{V_R}$ | $m^3$ | Volume of rod |
| $\mathscr{V}$ | $V$ | External voltage |
| $\mathscr{V}_{C,j}$ | $V$ | Voltage across *j*-th Coil |
| $\mathscr{V}_{Inductive,j}$ | $V$ | Inductive component of voltage across j-th Coil |
| $\mathscr{V}_{Amp,j}$ | $V$ | Voltage rise across *j*-th amplifier |
| $v_{Amp,j}(t)$ | *(-)* | Dimensionless variable corresponding to $\mathscr{V}_{Amp,j}$ |
| $v_{Inductive,j}$ | *(-)* | Dimensionless variable corresponding to $\mathscr{V}_{Inductive,j}$ |
| $W_j$ | | Coefficient used in end effect (magnetostrictive boundary condition) in vibration model |
| $\mathbf{x}^K$, $\dot{\mathbf{x}}^K$, $\ddot{\mathbf{x}}^K$ | *(-), $s^{-1}$, $s^{-2}$* | Vector of coil current states. Amplitudes of modes |
| $\mathbf{x}^M$, $\dot{\mathbf{x}}^M$ | *(-), $s^{-1}$* | Vector of magnetic field states and derivatives. Dimensionless units. |
| $\mathbf{x}^\mathbf{N}$, $\dot{\mathbf{x}}^\mathbf{N}$, $\ddot{\mathbf{x}}^\mathbf{N}$ | *(-), $s^{-1}$, $s^{-2}$* | Vector of vibration states, first derivatives and second derivatives. Amplitudes of modes |
| $x_H^M(\rho,\phi,\xi,t)$ | | Dimensionless magnetic field for homogeneous equation. Field due to eddy current alone. |
| $x_H^N(\xi,t)$ | *(-)* | Homogeneous component of dimensionless displacement |
| $x_O^N(\xi,t)$ | *(-)* | Quasi-steady component of dimensionless displacement |
| $x_N(\xi,t)$ | *(-)* | Dimensionless displacement |
| $x^{FEMM}(\rho,\xi,t)$ | | Dimensionless function corresponding to $H^{FEMM}(r,z,t)$ |
| $\hat{\mathbf{x}}(i\mid i)$ | *(-)* | Kalman estimate of **x**(i) given y(i). |
| $\hat{\hat{\mathbf{x}}}_{i_0}$ | *(-)* | Kalman estimate and Smith prediction at time $i_0$ |

| *Variable* | *Dimensions* | *Description* |
|---|---|---|
| $\chi_n^N(t)$ | *(-)* | Amplitude of the n-th vibrational model. Integral transform of $x^N(\xi,t)$ |
| $\dot{\chi}_{k,m,p}^M$ | *(-)* | Amplitude of the k,m,p-th magnetics model. Integral transform of $x_M^H(\rho,\phi,\xi,t)$ |
| $x_j^K$ | *(-)* | Dimensionless coil current |
| $\mathbf{x}_{i_0}$ | *(-)* | Current state in model predictive control |
| $Y_{eff}^H$ | *Pa* | Effective Young's modulus holding magnetic field constant. Modulus of elasticity |
| $\mathbf{y}_{i_0+1:i_0+i_H}$ | *(-)* | Predicted outputs (i.e displacement) from first predicted time, $i_0+1$ to prediction horizon, $i_0+i_H$ |
| $Z(\beta_n,\xi)$ | *(-)* | Axial mode for vibration model |
| $Z(\eta_p,\xi)$ | | Axial mode for magnetic model |
| z | *m* | Axial position |
| $z_L$ | *m* | Length of actuator rod |
| $\Delta z_C$ | *m* | Axial length of one coil region |
| $\alpha_{k,m,p}$ | $s^{-1}$ | Frequency coefficient in magnetics model |
| $\beta_n$ | | Eigenvalue of the axial vibration modes. |
| $\Gamma_{k,m}$ | *(-)* | Parameter in integral average of strain component of magnetization |
| $\varepsilon_{k,m}$, $\gamma_m$, $\eta_p$ | | Eigenvalues of the radial, azimuthal, and axial magnetic modes |
| $\boldsymbol{\kappa}$ | *Pa/(A/m)=Tesla* | Matrix of magnetostrictive constants $\boldsymbol{\kappa}=\left.\frac{\partial \mathbf{B}}{\partial \mathbf{S}}\right\|_{\mathbf{H}}=\left.\frac{\partial \mathbf{T}}{\partial \mathbf{H}}\right\|_{\mathbf{S}}$ |
| $\kappa_{eff,z}$ | *Pa/(A/m)=Tesla* | Effective axial magnetostriction constant for magnetic model |
| $\kappa_{eff}$ | *Pa/(A/m)=Tesla* | Effective magnetostriction constant for vibration model |
| $\lambda$ | *(-)* | Vibration damping coefficient |
| $\boldsymbol{\mu}^{\mathbf{S}}$ | *henry/m* | Tensor of magnetic permeability at constant strain |
| $\boldsymbol{\mu}^{\mathbf{T}}$ | *henry/m* | Tensor of magnetic permeability at constant stress |
| $\mu_0$ | *henry/m* | Magnetic permeability of a vacuum. $\mu_0=4\pi\times10^{-7}$ |
| $\mu_{11}^S$, $\mu_{33}^S$ | *henry/m* | Permeability at constant strain in |

| *Variable* | *Dimensions* | *Description* |
|---|---|---|
| | | transverse and axial directions $\mu_{xx}^{S} = \left.\frac{\partial B_x}{\partial H_x}\right\|_{S}$ |
| $\mu_{11}^{T}$, $\mu_{33}^{T}$ | *henry/m* | Permeability at constant stress in transverse and axial directions $\mu_{xx}^{T} = \left.\frac{\partial B_x}{\partial H_x}\right\|_{T}$ |
| $\mu_{33}^{S}$ | *henry/m* | Permeability at constant strain in axial direction |
| $\mu_R$ | *henry/m* | Permeability at constant strain in axial direction. R designating the rod region. $\mu_R = \mu_{33}^{S}$ |
| $\phi$ | *radians* | Azimuthal angle. |
| $\phi_0$ | *radians* | Angular dimension of the segmented actuator rod. Azimuthal angle. |
| $\Phi(\gamma_m, \phi)$ | | Azimuthal modal function for magnetics |
| $\mathbf{\Theta}$ | *(-)* | Predictive form state matrix |
| $\omega_1$ | *radian/s* | Frequency of first acoustic resonance in the rod |
| $\omega_{Amp}$ | *radian/s* | Cut-off frequency of amplifier. |
| $\rho$ | *(-)* | Dimensionless radial position |
| $\rho$ | *kg/m$^3$* | Density of the rod. Used briefly in the vibration model development. |
| $\sigma$ | *(ohm·m)$^{-1}$* | Conductivity |
| $\sigma_R$ | *(ohm·m)$^{-1}$* | Conductivity or actuator rod |
| $\Theta_{k,m,p,j}$ | *(-)* | Coupling coefficient between magnetic mode and coil current |
| $\Upsilon_{k,m,p,n}$ | *(-)* | Coupling coefficient between magnetic mode and vibration mode |
| $\Xi_{k,m,p,j}$ | *(-)* | Coupling coefficient between magnetic mode and coil current pass-through term in the vibration mode |
| $\chi_R$ | *(-)* | Ratio of axial to transverse permeability of rod. $\chi_R = \frac{\mu_{33}^{S}}{\mu_{11}^{S}}$ |
| $\xi$ | *(-)* | Dimensionless axial position |
| $\zeta$ | *m* | Displacement from neutral position in the rod. |
| $\zeta_r$, $\zeta_z$ | *m* | Radial and axial components of displacement from neutral. |

# SUMMARY

This dissertation investigates a new design for a magnetostrictive actuator that employs individually controlled coils distributed axially along the magnetostrictive rod. As a quantitative goal, the objective is to show that the multi-coil actuator can operate effectively at frequencies as high as 10,000 Hz with 900 N force and 50 microns of displacement. Conventional, single coil actuators with the same parameters for force and displacement develop significant attenuation in their response at frequencies above the first longitudinal vibration resonance at about 2750 Hz. The goal of the research is to investigate whether multiple coils can effectively increase the frequency range a least four times the range of conventional magnetostrictive actuators. This document derives a new mathematical model of the actuator that represents the spatial distributions of magnetic field and vibration, devises a control design that takes advantage of the multiple inputs to control the displacement of the actuator while consuming minimum electrical power, and describes a prototype multi-coil actuator and experimental system developed to test the idea. The simulations of the multi-coil actuator and control design demonstrate successful transient operation of the actuator over the targeted frequency range with feasible levels of input power and current. Experimental tests of the design, although limited by a computer sampling rate less than 10,000 Hz, are able to validate the predictions of the developed model of the actuator and reproduce the simulated control performance within the constraints of the experimental system.

# A MULTI-COIL MAGNETOSTRICTIVE ACTUATOR: DESIGN, ANALYSIS, AND EXPERIMENT

## VOLUME I

by

Thomas L. Wilson, Jr.

# CHAPTER 1

# INTRODUCTION

The subject of this research is a novel multi-coil magnetostrictive actuator. A magnetostrictive actuator is a linear motor which converts electrical current into linear motion. The difference between a conventional magnetostrictive actuator and the actuator of this study is that a conventional actuator has a single uniform coil along the full length of the actuator rod, whereas the proposed design divides the coil into axial segments which are controlled separately. The advantage of the multi-coil design for the actuator is the opportunity to use the individually controlled coils to improve the speed of actuator response. Possible applications of this type of device include: high speed valves for diesel fuel injection, active control of combustion instability, active cancellation of noise or vibration, sonar, and public address loudspeakers. The research presented here develops a dynamic model for the rod motion, magnetic fields, and electrical circuits and develops a predictive control algorithm that provides the optimum control input to the individual coils. The multi-coil actuator is then implemented in a prototype design to measure the actuator performance, test the control design, and uncover the practical realities and limitations of real-time control.

A fast actuator with a large linear displacement is a difficult, technical challenge. In this research, the goal, predicated on the potential application to diesel fuel injection, is to achieve frequency response up to 10 kHz with 50 μm displacement and maximum force of 900 N. The problem with the conventional magnetostrictive actuator is that the design parameters work against each other, preventing all the performance parameters

from being achieved at the same time. For example, the maximum displacement of the rod is proportional to its length. The maximum force that can be generated is proportional to the transverse area. Unfortunately, increasing the length and diameter to increase displacement and force decrease the frequency response. Moreover, increasing the length of the actuator causes the resonant frequency of the rod to decrease. Similarly, increasing the diameter to achieve the force requirement causes the frequency at which eddy currents begin to act against the drive coil to be too low to achieve the desired frequency response.

To put these problems into numerical context, consider some preliminary rule-of-thumb calculations. The limiting resonant frequency for longitudinal vibration for an actuator with a uniform coil can be determined by the quarter wave formula[1],

$$\Omega_A = \frac{1}{4z_L}\sqrt{\frac{Y}{\rho}}, \tag{1.1}$$

where $Y$ is the Young's modulus, $\rho$ is the density, and $z_L$ is the length of the rod. $\Omega_A$ is frequency in Hertz. Increasing the length of the actuator rod increases its static displacement but lowers the resonant frequency. A magnetostrictive actuator with the desired 50 μm displacement must be about 0.152 m (6 inches) in length. The resulting resonant frequency is about 2700 Hz, too low for applications like diesel injection. Above the resonant frequency, the acceleration loads dominate the force balance within the actuation rod. For a harmonic signal, the coil current needed for constant amplitude of displacement increases approximately as the square of the driving frequency.

[1] The quarter wave formula comes from the fundamental vibration mode for the rod. This formula is appropriate for a rod with one fixed and one free end. With a load attached, for example with the actuator connected to the valve stem, the resonant frequency is lower. The resonant frequency equation is derived in Chapter 3.

A similar conflict in performance can be found between the required force and frequency at which eddy current becomes significant. The eddy current dynamic equation reduces to a diffusion equation analogous to the equation for conduction of heat in solids. The magnetic diffusivity analogous to thermal diffusivity is given by $(\sigma\mu)^{-1}$. Based on this analogy, a frequency constant associated with the magnetic diffusion in a cylindrical rod[2] can be defined which represents the frequency at which eddy current becomes significant.

$$\Omega_M = \frac{2.408}{2\pi\sigma\mu r^2}, \tag{1.2}$$

where 2.408 is a geometric constant based on a solid cylindrical shape, $\sigma$ is the rod's conductivity, $\mu$ is the rod's permeability, *r* is the rod's radius, and $\Omega_M$ is the magnetic diffusion frequency constant in Hertz. The dynamic force that a rod can produce is proportional to its transverse area; whereas the frequency at which eddy current becomes significant is inversely proportional to the area. For an actuator producing 900 N, the actuator rod has to be approximately 1.27 cm (0.5 inch) in diameter. The frequency from Eq. (1.2) for this diameter rod is 2400 Hz. Above this frequency, the current of the coil must increase proportionally with drive frequency to overcome the effects of eddy current. Operating beyond the limiting frequencies for acoustic resonance or eddy current with a conventional magnetostrictive requires the coil's driver amplifier to produce impractically high voltage and current.

The limitations of the conventional actuator can be overcome by the design changes introduced by the multi-coil actuator. The main design features of a

[2] The eddy current diffusion constant represents the lowest mode of radial diffusion for a solid cylinder. The formula is derived in Chapter 4.

conventional magnetostrictive actuator are shown in Figure 1.1. The key elements of the device are the magnetostrictive rod at the center, the drive coil (or coils) wound around the rod, the push rod for attaching the actuator to the load, a magnetic return path of highly magnetically permeable material to turn the magnetic field at the ends of the rod, a bias magnet formed as a cylindrical shell that provides a steady bias field to the magnetostrictive rod and a high permeability path to close the magnetic circuit efficiently, a spring (Belleville washer) to preload the actuator rod, and a case to enclose the device and provide a structural mount for the preload spring.

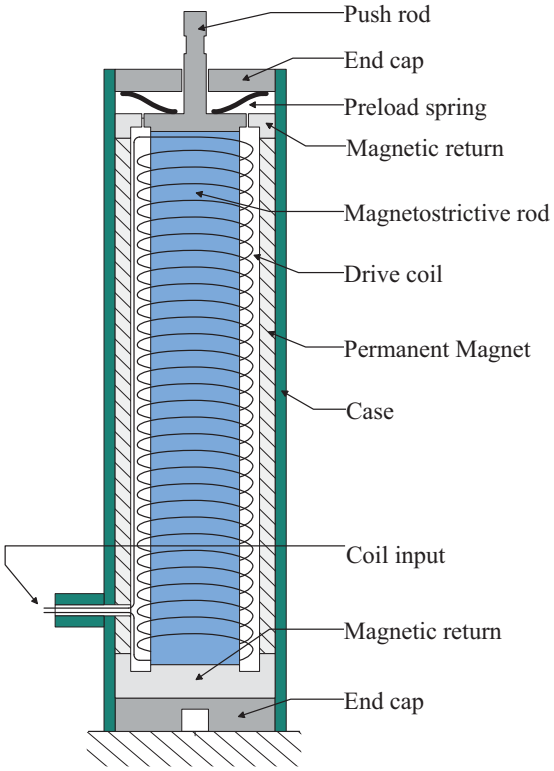


Figure 1.1: A typical arrangement of a commercial magnetostrictive actuator

The proposed actuator offers a potential technical breakthrough in speed. To extend the bandwidth, the coil in the prototype actuator investigated in this research project (see Figure 1.2) is divided axially into individually controlled coils. When current is applied to the coil in the conventional actuator, the resulting magnetic field is uniform and causes all points along the rod to elongate simultaneously. In the new approach, each coil's field acts on the adjacent the rod distributing the stress along the length. The benefit of the concept comes from the spatial distribution of the actuating force. The distribution of force allows electrical input to be timed along the rod to account for the wave propagation of stress and strain in the material and to account for resonance effects. In the schematic, four coil circuits are shown. The ellipsis, "…", between coil circuits suggests that the number of coils can be adjusted to suit the application. The prototype actuator has ten coils.

The eddy current limitation on frequency is reduced to an acceptable level in the prototype actuator by laminating the actuator rod. In the prototype actuator design, the Terfenol rod is cut into quadrants and rejoined with an insulating adhesive. The purpose of the radial cuts is to reduce eddy currents in the same way that conventional plate laminations reduce eddy current in transformer cores. Figure 1.3 illustrates the laminated actuator geometry. A pie-shaped cylinder is the descriptive name of the geometry of the magnetostrictive actuator rod.

Slicing the Terfenol actuator rod is a standard manufacturing technique for reducing eddy current in magnetostrictive actuators. The standard model of the high-frequency actuator rod manufactured by Etrema has a single, diametral slice to reduce

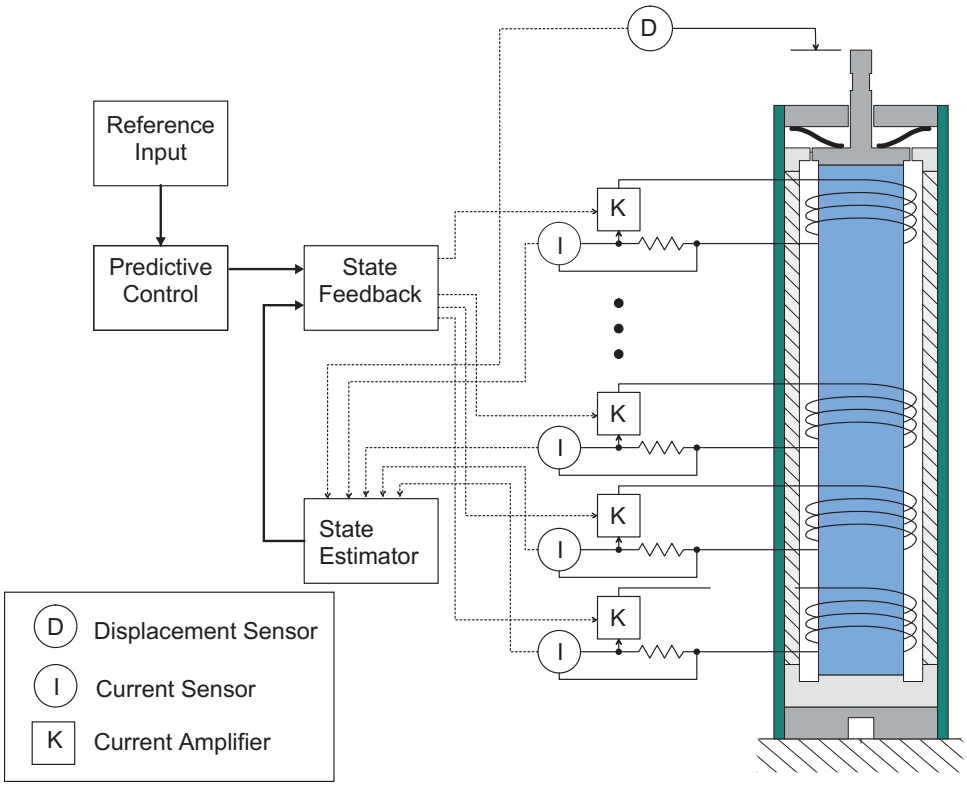


Figure 1.2: Concept of the multi-coil actuator and state space controls

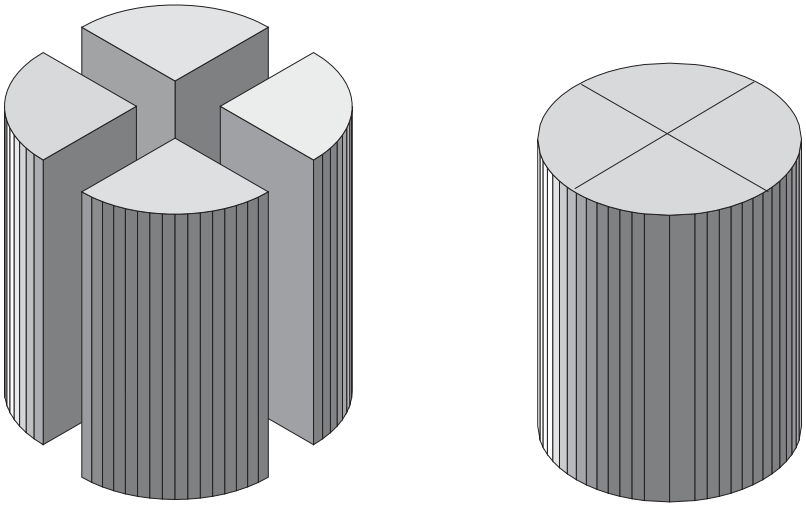

Figure 1.3: Pie-shaped cylindrical segments

eddy current. The prototype actuator, which was also fabricated by Etrema, has an additional cut, as shown in Figure 1.3, to further reduce eddy current. While the four quadrant lamination reduces eddy current significantly, the reduction does not sufficiently reduce eddy current to the point that it may be neglected. The effect of eddy current in the rod is one of the technical challenges that is addressed in the magnetic model.

The control problem for the multi-coil actuator is not as simple as controlling multiple independent actuators because each rod segment is coupled to its neighbors mechanically and magnetically. The coupled system requires modern multivariate control techniques to compute feedforward and feedback gains that realize the improved dynamic response. The primary research problem is to develop a suitable mathematical model of the system and to apply model-based control techniques that take advantage of the additional degrees of freedom that the multi-coil actuator provides.

While the particular linear motor in the prototype device employs a magnetostrictive rod, the distributed control concept can be applied to other linear actuator devices in which the control can be spatially distributed, such as a stacked piezoelectric actuator in which regions of the stack are individually controlled or a stacked voice coil actuator with individual controls on each coil and magnet.

The remainder of this chapter is devoted to introducing the ideas and plan for modeling and control of the multi-coil actuator and for the experimental evaluation of the prototype actuator. The survey of literature related specifically to the modeling, controls, or experimental development is included at the start of each chapter.

## Physics of Magnetostriction

Magnetostriction is the property of deformation in a material in response to a magnetic field. James Joule is credited with the first observation of magnetostriction [1]. The term, magnetostriction, applies to all types of deformation: elongation, bending, and volume change. Material that elongates along a preferred axis is the type of deformation that is used for the linear motion actuator in this study.

All magnetic materials exhibit a certain amount of magnetostriction, but the magnitude of deformation in most materials is so small that it is unsuitable for actuation. In 1970's, certain alloys of iron and terbium were discovered by Clark and his research team at the Naval Ordnance Laboratory which produced strains ($\Delta l/l$) on the order of $10^{-3}$. The alloys were named TERFENOL for terbium (TER), iron (FE) and the Naval Ordinance Laboratory (NOL). Adding dysprosium was found to stabilize the anisotropies of the crystal alloy without greatly reducing the achievable strains. The current generation of magnetostrictive devices uses TERFENOL-D with a composition of $Tb_{0.30}Fe_{0.70}Dy_{1.92}$.

Research into room temperature giant magnetostrictive materials began in the 1970's with the discovery of the Terfenol-D alloy by A. E. Clark and H. S. Belson[2]. In the 1980's, activity focused on the physics of the material and on developing manufacturing techniques [3]. When large scale industrial production of the material by ETREMA Products[3] began in 1988, research into developing applications of the material as actuators [4-7] and transducers began [8]. Considerable work has been conducted at the Naval Ordinance Laboratory, Iowa State, the University of Hull in the United

[3] ETREMA Products, Inc.; 2500 North Loop Drive; Ames, IA 50010. ETREMA is the sole supplier of TERFENOL-D products in the United States

Kingdom, the Royal Institute of Technology in Stockholm, Sweden, and other places. Today, literally thousands of articles are available on all aspects of magnetostrictive materials and their applications. The current state of the art is compiled in a monograph, *Handbook of Giant Magnetostrictive Materials*, edited by Engdahl [9].

The material properties have been measured and tabulated by Clark[10] and others. Figure 1.4 shows the strain and magnetization versus magnetic field intensity for a typical giant magnetostrictive alloy. The elongation effect is symmetric about the $H = 0$ axis; that is, the length of the actuator rod increases for both positive and negative magnetic fields. The magnetic and magnetostrictive properties exhibit considerable hysteresis and nonlinearity.

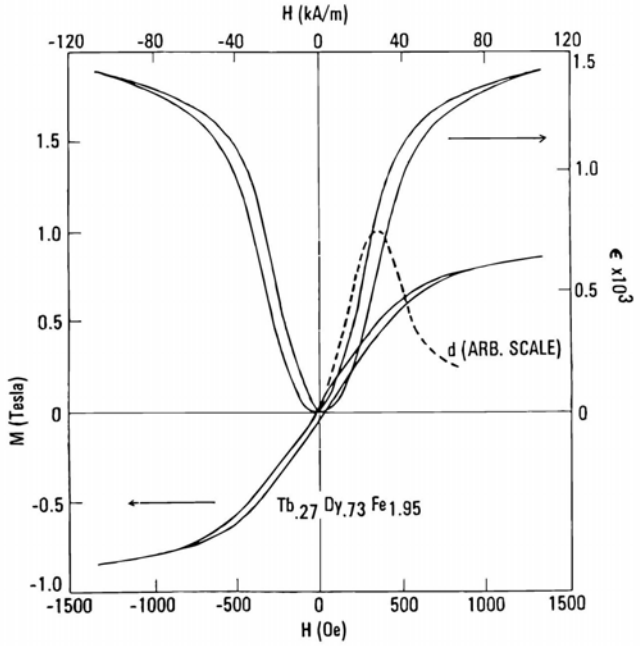


Figure 1.4: Magnetostriction and magnetization for $Te_{0.27}Dy_{0.73}Fe_{1.95}$ at room temperature.[9]

The TERFENOL-D material has excellent material properties for a low displacement actuator. Strains as high as $2\times10^{-3}$ are achieved. Fatigue is negligible and speed of response takes place at 1640-1940 m/s which is two to three times faster than a solenoid actuator [1].

The modeling of magnetostriction requires developing simplified relationships to represent the behavior. The approach is to develop linearized constitutive equations based on the behavior observed in Figure 1.4 and adapt them to the specific actuator rod application. These constitutive relationships are derived in the form needed for the actuator model in Chapter 2. Since the normalization of variables depends primarily on the magnetostrictive properties, the general rules for converting to dimensionless variables are described in Chapter 2 as well.

## Modeling Approach

A fundamental step in the process of designing the multi-coil actuator is to develop an understanding of the dynamics of the magnetostrictive actuator and to derive a suitable mathematical model for model-based control. The modeling involves simulation of the mechanics of vibration of the rod, the magnetic coupling between the magnetostrictive material and the coils, and the power electronics involved in driving the coils. The research involves understanding the dynamics in detail, assessing the magnitude of different effects, and simplifying the modeling to an appropriate and minimal level necessary for the high-speed control application. The key step is to simplify the model and cast it as a state space model. The state space model for the device is a useful byproduct of the research as a pedagogical example for control

problems. One of the more useful additions to the knowledge of modeling of magnetic materials is a low order model of eddy currents in the laminated actuator rod. Existing models of magnetostrictive materials, which are used for low frequency applications, neglect the eddy current effect. The targeted frequency response for the multi-coil actuator is sufficiently high that eddy current effects are not negligible.

**Derivation of the model**

The derivation of the mathematical model is divided into three main parts: longitudinal vibration model, the magnetic model, and the electronic circuit model which are derived in Chapters 3, 4, and 5 respectively. The longitudinal vibration model represents the mechanical motion of the rod and the effects associated with elasticity, inertia, and the magnetostrictive forces acting on the rod. The magnetic model calculates the inductive coupling, eddy currents, and magnetic effects of the magnetostrictive rod. The circuit model includes the dynamics of the electronic circuits that power the actuator and the voltage induced in each coil by itself, by other coils, by the eddy currents, and by the magnetostrictive field in the actuator rod due to strain.

Figure 1.5 shows the three main submodels and illustrates the coupling effects between them. Each subsystem affects the other two. The interactions mean that the system of equations involving the three models must be solved simultaneously. This fact has to be accounted for in the modeling plan so that the equations can be combined and solved in a convenient way. The discussion of the state space modeling later in this chapter shows how this is done.

Moreover, the interactions create a problem in the presentation of the models. One cannot proceed serially from a starting point to an ending point in the derivation

deriving every term as it is needed. For example, we start with the vibration model, but that model necessarily includes effects from the eddy current and coil models that have not been presented yet. The problem is addressed by liberal cross-references between the modeling chapters even when those references are in later chapters.

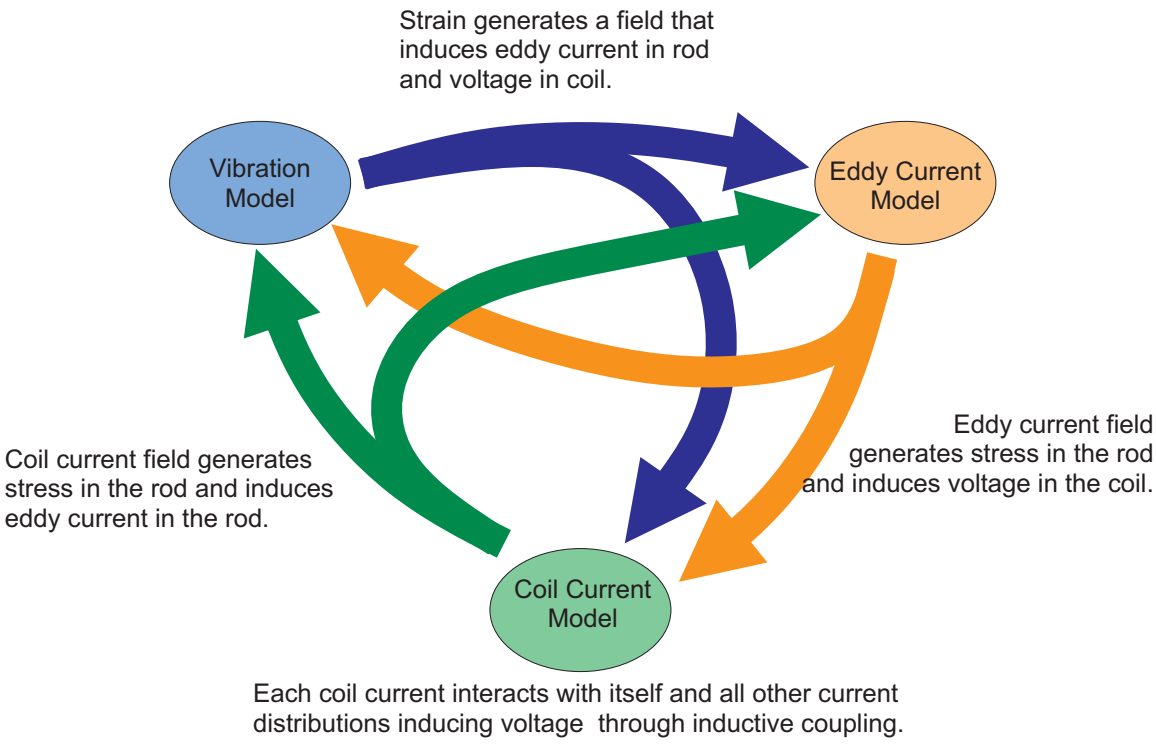


Figure 1.5: Interactions between vibration, coil current, and eddy current in the actuator model

The dynamic model of the actuator system rests on three of the most basic laws of classical physics; that is,

- Newton's second law of motion,
- Maxwell's equations, and
- Kirchhoff's loop equation for circuits.

The process of transforming the fundamental laws of physics into a set of modeling equations for the actuator involves both algebraic manipulation and approximation. The algebraic manipulation combines all the information known about the problem into a system of the fewest equations with the fewest unknowns. The model derivation includes a number of approximations. The main approximation techniques are to drop small terms, linearize relationships, make fast terms quasi-steady, and truncate infinite series. In each case, the approximations are justified by test calculations to evaluate the magnitude of the error introduced.

The vibration and magnetic models are each described by a partial differential equation that represents the process in space and time. The mathematical approach for converting the partial differential equations into ordinary differential equations involves an integral transformation using an orthogonal series of mode functions to represent the spatial dependence of the process. The spatial transformation converts the partial differential equations into a series of ordinary differential equations that are suited for state space representation and the control design application. The state variables represent the amplitudes of the spatial modes of the vibration and magnetic fields.

**The state space model**

To apply modern control techniques to the multi-coil actuator problem, the mathematical model must be written in state space form. The state space model consists of a set of constant-coefficient, ordinary differential equations of the form.

$$\dot{\mathbf{x}} = \mathbf{A}\mathbf{x} + \mathbf{B}\mathbf{u}\,, \tag{1.3}$$

where $\mathbf{x}$ and $\dot{\mathbf{x}}$ are the state vector and state derivative vector, respectively, and $\mathbf{u}$ is the control input vector. The terms **A** and **B** are constant matrices that contain the coupling

coefficients derived from the governing equations that represent the physical model. A significant fraction of the research focused on the reduction of the continuous differential equations for vibration, magnetic, and coil circuit modeling into this form.

A linear relationship in terms of the state variables and control inputs can also be defined to compute variables which are measured in the system that do not correspond to the state variables of the model. In multi-coil actuator, the measurements consist of the displacement of the actuator tip and the currents in the coils. It is customary to write the measured variables in the following form.

$$\mathbf{y} = \mathbf{C}\mathbf{x} + \mathbf{D}\mathbf{u} \,. \tag{1.4}$$

The set of state variables in Eq. (1.3) are not unique quantities. The same physical device may be modeled with state space systems that are very different in both the size of the vectors and numerical properties of the matrices. The choice of which model is best is based on a number of factors. Since the model is ultimately used for real time control, it is essential that the order of the model be low so that the control calculations can be completed within the scan rate of the control. Also the order needs to be reasonably low for numerical accuracy in the control design calculations. Due to the finite word length of digital computations, matrix operations tend to break down eventually as the order of the system increases. Solving for the normal modes of vibration and magnetism is beneficial both for numerical properties and for understanding. The orthogonality property of normal modes means that each mode does not interact with other terms in the same series. The orthogonality property results in a diagonally dominant state matrix that is beneficial to the numerical accuracy in matrix

calculations. The modes also enhance understanding because of the connection between the spatial shapes of the normal modes and their associated frequencies.

The state space model is an abstract mathematical form that overwrites the meaning associated with the original nomenclature of the physical equations with generic matrix names for the constants, state variables and control inputs. To maintain some connection to the process models and to facilitate combining the three subsystem models in a logical manner, it is convenient to subdivide the problem along the lines of the underlying physical processes from which the equations are derived. The state vectors and the subsystem models are grouped together in submatrices of the full model. In this way, the location of the variable or matrix constant in the full array is indicative of its physical meaning.

In the model development that follows, the governing equations for the vibration model results in a system of second order ordinary differential equations. The magnetic and the circuit models each yield a system of first order equations. Hence, we will write the state derivative and state vectors as the following.

$$\dot{\mathbf{x}} = \begin{bmatrix} \ddot{\mathbf{x}}^{\mathbf{N}} \\ \dot{\mathbf{x}}^{\mathbf{N}} \\ \dot{\mathbf{x}}^{\mathbf{K}} \\ \dot{\mathbf{x}}^{\mathbf{M}} \end{bmatrix}, \ \mathbf{x} = \begin{bmatrix} \dot{\mathbf{x}}^{\mathbf{N}} \\ \mathbf{x}^{\mathbf{N}} \\ \mathbf{x}^{\mathbf{K}} \\ \mathbf{x}^{\mathbf{M}} \end{bmatrix}, \tag{1.5}$$

where **N**, **M**, and **K** are mnemonics for Newton, Maxwell and Kirchhoff to identify the origins of the state variables. The state vector contains both the state and the derivatives of the vibration state, $\mathbf{x}^{\mathbf{N}}$ and $\dot{\mathbf{x}}^{\mathbf{N}}$. The two elements are used together in the state model to integrate the second order part of the model twice.

An additional problem that needs to be anticipated by the model design is that the derivation of the state equation from the governing equation does not result directly in the standard state space form given in Eq. (1.3). Instead, the equations yield a system in which the derivative side of the equation is coupled. In other words, instead of the form of Eq. (1.3), the individual governing equations yield a form that is represented by

$$\mathbf{E}\dot{\mathbf{x}} = \mathbf{F}\mathbf{x} + \mathbf{G}\mathbf{u} \,. \tag{1.6}$$

This special form of the state space equation is termed the descriptor form by Luenberger [11]. In the actuator model, each individual subsystem has more unknowns than equations. Only after the three subsystems are determined and assembled in the form of Eq. (1.6) can the system be solved algebraically for the standard state space form, $\dot{\mathbf{x}} = \mathbf{A}\mathbf{x} + \mathbf{B}\mathbf{u}$. The solution can be formally represented as

$$\dot{\mathbf{x}} = \mathbf{E}^{-1}\mathbf{F}\mathbf{x} + \mathbf{E}^{-1}\mathbf{G}\mathbf{u} \,, \tag{1.7}$$

so that the conventional state space matrices are given by $\mathbf{A} = \mathbf{E}^{-1}\mathbf{F}$ and $\mathbf{B} = \mathbf{E}^{-1}\mathbf{G}$.

To facilitate the derivation, the **E**, **F** and **G** matrices can be subdivided along the same lines as the state vector in Eq. (1.5). The subsystem matrices are numbered 1 through 4 corresponding with the elements of the state vector.

$$\begin{bmatrix} \mathbf{E}^{11} & \mathbf{E}^{12} & \mathbf{E}^{13} & \mathbf{E}^{14} \\ \mathbf{E}^{21} & \mathbf{E}^{22} & \mathbf{E}^{23} & \mathbf{E}^{24} \\ \mathbf{E}^{31} & \mathbf{E}^{32} & \mathbf{E}^{33} & \mathbf{E}^{34} \\ \mathbf{E}^{41} & \mathbf{E}^{42} & \mathbf{E}^{43} & \mathbf{E}^{44} \end{bmatrix} \begin{bmatrix} \ddot{\mathbf{x}}^{\mathbf{N}} \\ \dot{\mathbf{x}}^{\mathbf{N}} \\ \dot{\mathbf{x}}^{\mathbf{K}} \\ \dot{\mathbf{x}}^{\mathbf{M}} \end{bmatrix} = \begin{bmatrix} \mathbf{F}^{11} & \mathbf{F}^{12} & \mathbf{F}^{13} & \mathbf{F}^{14} \\ \mathbf{F}^{21} & \mathbf{F}^{22} & \mathbf{F}^{23} & \mathbf{F}^{24} \\ \mathbf{F}^{31} & \mathbf{F}^{32} & \mathbf{F}^{33} & \mathbf{F}^{34} \\ \mathbf{F}^{41} & \mathbf{F}^{42} & \mathbf{F}^{43} & \mathbf{F}^{44} \end{bmatrix} \begin{bmatrix} \dot{\mathbf{x}}^{\mathbf{N}} \\ \mathbf{x}^{\mathbf{N}} \\ \mathbf{x}^{\mathbf{K}} \\ \mathbf{x}^{\mathbf{M}} \end{bmatrix} + \begin{bmatrix} \mathbf{G}^{1} \\ \mathbf{G}^{2} \\ \mathbf{G}^{3} \\ \mathbf{G}^{4} \end{bmatrix} \mathbf{u} \,. \tag{1.8}$$

Even before deriving the submodels, some of the elements of the matrices can be evaluated. First, since the vibration model is specified to be second order, the second row is already determined. The integration of the first derivative can be represented as identity matrices.

$$\begin{bmatrix} \mathbf{E}^{11} & \mathbf{E}^{12} & \mathbf{E}^{13} & \mathbf{E}^{14} \\ \mathbf{0} & \mathbf{I} & \mathbf{0} & \mathbf{0} \\ \mathbf{E}^{31} & \mathbf{E}^{32} & \mathbf{E}^{33} & \mathbf{E}^{34} \\ \mathbf{E}^{41} & \mathbf{E}^{42} & \mathbf{E}^{43} & \mathbf{E}^{44} \end{bmatrix} \begin{bmatrix} \ddot{\mathbf{x}}^{\mathbf{N}} \\ \dot{\mathbf{x}}^{\mathbf{N}} \\ \dot{\mathbf{x}}^{\mathbf{K}} \\ \dot{\mathbf{x}}^{\mathbf{M}} \end{bmatrix} = \begin{bmatrix} \mathbf{F}^{11} & \mathbf{F}^{12} & \mathbf{F}^{13} & \mathbf{F}^{14} \\ \mathbf{I} & \mathbf{0} & \mathbf{0} & \mathbf{0} \\ \mathbf{F}^{31} & \mathbf{F}^{32} & \mathbf{F}^{33} & \mathbf{F}^{34} \\ \mathbf{F}^{41} & \mathbf{F}^{42} & \mathbf{F}^{43} & \mathbf{F}^{44} \end{bmatrix} \begin{bmatrix} \dot{\mathbf{x}}^{\mathbf{N}} \\ \mathbf{x}^{\mathbf{N}} \\ \mathbf{x}^{\mathbf{K}} \\ \mathbf{x}^{\mathbf{M}} \end{bmatrix} + \begin{bmatrix} \mathbf{G}^{1} \\ \mathbf{0} \\ \mathbf{G}^{3} \\ \mathbf{G}^{4} \end{bmatrix} \mathbf{u} . \qquad (1.9)$$

Next, we note that both $\mathbf{E}^{12}$ and $\mathbf{F}^{11}$ multiply $\dot{\mathbf{x}}^{\mathbf{N}}$ in the first row. Only one or the other is needed but not both. To make the matrix inversion operation more accurate numerically, the **E** matrix should be as sparse as possible so it is better to put the term on the right hand side. We can set the matrix, $\mathbf{E}^{12} = 0$, and put all the terms multiplying $\dot{\mathbf{x}}^{\mathbf{N}}$ on the right hand side. By similar logic, the corresponding terms in the third and forth lines are also zero, $\mathbf{E}^{32} = \mathbf{E}^{42} = 0$. Making these substitutions yields the following.

$$\begin{bmatrix} \mathbf{E}^{11} & \mathbf{0} & \mathbf{E}^{13} & \mathbf{E}^{14} \\ \mathbf{0} & \mathbf{I} & \mathbf{0} & \mathbf{0} \\ \mathbf{E}^{31} & \mathbf{0} & \mathbf{E}^{33} & \mathbf{E}^{34} \\ \mathbf{E}^{41} & \mathbf{0} & \mathbf{E}^{43} & \mathbf{E}^{44} \end{bmatrix} \begin{bmatrix} \ddot{\mathbf{x}}^{\mathbf{N}} \\ \dot{\mathbf{x}}^{\mathbf{N}} \\ \dot{\mathbf{x}}^{\mathbf{K}} \\ \dot{\mathbf{x}}^{\mathbf{M}} \end{bmatrix} = \begin{bmatrix} \mathbf{F}^{11} & \mathbf{F}^{12} & \mathbf{F}^{13} & \mathbf{F}^{14} \\ \mathbf{I} & \mathbf{0} & \mathbf{0} & \mathbf{0} \\ \mathbf{F}^{31} & \mathbf{F}^{32} & \mathbf{F}^{33} & \mathbf{F}^{34} \\ \mathbf{F}^{41} & \mathbf{F}^{42} & \mathbf{F}^{43} & \mathbf{F}^{44} \end{bmatrix} \begin{bmatrix} \dot{\mathbf{x}}^{\mathbf{N}} \\ \mathbf{x}^{\mathbf{N}} \\ \mathbf{x}^{\mathbf{K}} \\ \mathbf{x}^{\mathbf{M}} \end{bmatrix} + \begin{bmatrix} \mathbf{G}^{1} \\ \mathbf{0} \\ \mathbf{G}^{3} \\ \mathbf{G}^{4} \end{bmatrix} \mathbf{u} . \qquad (1.10)$$

Other terms in the matrix are also zero but those facts emerge from the governing equations.

The format and organization of the above equation describes the system that is needed for the model. Using this format, the physical modeling from the three separate systems can be derived separately, then combined and simulated. The first and second rows come from the vibration model. The third row comes from the circuit equation. The fourth row comes from the magnetic diffusion problem. The main objective of the model derivation in the following chapters is to manipulate the physical laws and other equations into the descriptor state space form. The subdivided matrix explicitly identifies the coupling terms between different aspects of the model. The coupling terms show how one system affects another, how various coupling terms arise from the physical laws

and how different parts of the model are connected together. If the states are normalized properly, the magnitudes of the coefficients give physical insight into the strength of the coupling of one part of the system with another and suggest how the system can be simplified without affecting the validity of the results.

## Control Design Approach

The control design for the multi-coil actuator has several problems to solve. First and foremost, the control design has to focus on making the actuator fast, but this is not the only problem. In solving the multi-coil actuator problem, it has to deal with the special control situation in which the device has more inputs than outputs and use this design feature to achieve a higher speed of response than a single coil actuator. This is a new problem in control theory that requires an innovative solution and is part of the research reported in Chapter 6 on the control design. In addition to the theoretical problem of making the actuator fast, the algorithm itself needs to be fast. The computation must be compact and efficient enough to run in real time on the control computer for the actuator experiment. Moreover, the control design system must deal with the real-world problems of a limited number of measurements and time delay in the analog to digital conversion and the computer processing. The limited number of measurements means that the control algorithm must include a full state estimator so that full state feedback from the control design can be used. In the experiment, the time delay in the digital part of the experimental system is significant compared to the speed of response of the actuator. The estimation algorithm must project the delayed measurements forward to the current time so that feedback calculations can be based on the estimated state at the current time. The solution to the problem of model estimation

with time delay and the task of performing that calculation in real time does not require an innovative solution, but it does add significant complication to the software in the experimental system. These topics are also covered in Appendices I, J, and K.

The main innovation in the actuator design is that multiple coils are distributed along the length of the rod. All are used to control a single output, the displacement of the actuator drive tip. Control theory is lacking in tools that quantify the performance advantages that can be attained from this arrangement with more inputs than outputs to the system being controlled. Controllability only tells the minimum number of inputs to control the output. Control theory emphasizes methods for square systems in which the number of control inputs and variable being controlled are equal. For the actuator problem, one coil is obviously sufficient to control one displacement. The question is what performance advantage can be achieved with the additional inputs or spare degrees of freedom. The answer is found under the general heading of Model Predictive Control [12, 13] but with modifications to address the special problem of extra degrees of freedom. The optimum control response is obtained by minimizing a quadratic performance index that combines the sums of squares of control error and control inputs. The predictive aspect of the control is that the optimization is taken over a time horizon into the future. This scheme results in a feedforward as well as a feedback component to the control and allows the algorithm to anticipate the future changes in the demand input. The application of model predictive control is the key control design feature that makes the high speed response of the actuator possible.

The control scheme with spare degrees of freedom is a new idea and has potentially a large number of applications beyond the multi-coil actuator. The scheme

can be used for any system in which multiple, distributed actuators act on a single control objective. Other applications for this control method could also be quite different from the magnetostrictive actuator problem. For example, vibration dampening in an orbiting space platform with multiple actuators acting on the frame or a combustion chamber with multiple burners is conceptually the same problem.

## Experimental Approach

In addition to the theoretical development of the model and controls in this research, the prototype, multi-coil actuator was developed and tested in the laboratory. The experimental efforts mainly consisted of the following:

- Design and development of the actuator,
- A series of open loop tests to measure the performance, characteristics of the device and to provide data for the modeling,
- Development of software for the control program to acquire data and perform the predictive control algorithm, and
- A series of closed loop experiments that demonstrate performance of the actuator in a laboratory setting.

The prototype multi-coil actuator's design is based on an existing commercial model of magnetostrictive actuator with a number of new features that include the multiple individually controlled coils and the additional lamination of the actuator rod described earlier in this chapter. To implement the multi-coil design, the case and return path are slit axially to route the leads from the coils to the outside. The slit has an additional benefit in reducing eddy currents in the case and return path by breaking the circumferential path for current. Also, materials that are used in the return path and case

of the prototype actuator have lower conductivity than the components of the standard actuator to reduce eddy current.

To power the individual coils, the prototype actuator was connected to a bank of five, modified, dual-channel audio amplifiers. The model predictive control system is implemented using a computer equipped with general purpose, input and output boards to receive measured analog signals, convert them to digital data for processing, and then convert computed demand signals back to analog form to be sent to the amplifiers. The computations of the control algorithm were performed in real time by a C program on the control computer. The control program also logs the input and output data for documentation and presentation of results.

The experimental system and the test program are described in Chapter 7. The results of open loop and closed loop tests that studied the performance of the actuator are presented. Some experimental results are included the modeling chapters where they are needed for the derivation of model input data.

# CHAPTER 2

# CONSTITUTIVE EQUATIONS OF MAGNETOSTRICTION

The unique property of magnetostrictive materials is that an externally applied magnetic field causes elongation, and conversely, an externally applied stress causes magnetization. This magnetomechanical coupling is embodied in the constitutive equations for magnetostriction. The constitutive equations for magnetostrictive materials extend and generalize the conventional linear constitutive equations for elastic and magnetic materials. For example, Hooke's law is the linearized constitutive equation relating stress and strain that is commonly used to represent the elastic properties of the material.

$$\mathbf{S} = \mathbf{s}\mathbf{T}\,, \tag{2.1}$$

where **T** is the stress tensor in the material, **S** the strain tensor and **s** is a matrix representing the elastic compliance. Similarly, it is common for magnetic materials to be represented by a linear permeability relationship,

$$\mathbf{B} = \boldsymbol{\mu}\mathbf{H}\,, \tag{2.2}$$

where **B** is the magnetic induction, **H** is the magnetic field and $\boldsymbol{\mu}$ is the magnetic permeability. The subject of this chapter is to define linearized constitutive equations of the form,

$$\mathbf{S} = \mathbf{s}^{\mathbf{H}}\mathbf{T} + \mathbf{d}\mathbf{H}\,, \tag{2.3}$$

$$\mathbf{B} = \mathbf{d}'\mathbf{T} + \boldsymbol{\mu}^{\mathbf{T}}\mathbf{H}\,, \tag{2.4}$$

where the additional terms involving the magnetostrictive constant matrix, **d,** characterize the magnetomechanical coupling. The linearized constitutive equations are then manipulated algebraically to put them in the form needed for the modeling the magnetostrictive actuator.

One of the simplifications in the actuator modeling which is worked out in this section is finding effective properties in terms of the full, three-dimensional linear constitutive equations for the case in which the vibration is a one-dimensional equation while the magnetic model is three-dimensional. The reduction in dimensionality is obtained by applying the constraint that the volume of the magnetostrictive material is constant. The constant volume property is an experimentally observed result for Terfenol-D.

### Literature Survey on Characterization of Magnetostrictive Properties

The literature on the characterization of magnetostrictive properties of Terfenol goes back to the first reports on giant magnetostrictive materials. The early papers did not characterize the full tensor and vector components of the constitutive equation but they almost always measured the dependence of such properties as strain and magnetization upon field so that the nonlinearities were clearly evident. Clark's 1972 paper [2] plots strain versus field and magnetization versus field in a format analogous to Figure 1.4. This type of plot became the standard format for presenting experimental magnetostrictive results. Clark and Crowder plotted coefficients of permeability and magnetomechanical coupling (the $\mu_{33}$ the $d_{33}$ components of the coefficient matrices in Eq. (2.3)) rather than the strain and field thus moving closer to a linear model [10]. Clark

describes much of his experimental data and his theoretical work on the properties of magnetostrictive materials in a chapter in *Handbook for Ferromagnetic Materials* [14].

The three-dimensional linear form and experimental techniques for measuring the individual three-dimensional coefficients originate with Claeyssen's paper of 1989 [15]. The technique involved a three-dimensional model of the actuator in which orthotropic symmetry is assumed. A Terfenol-D actuator in blocked (clamped in a nearly immovable frame) and free (unloaded) experimental setups were subjected to low-frequency, low amplitude coil current signals. The measured data were used to fit the three-dimensional coefficients of the constitutive relations in the actuator model. Claeyssen credits Du Tremolet de Lacheisserie's analysis and experiment [16] as the basis for the orthotropic symmetry assumption used in the model. Claeyssen's research was carried out to provide modeling data for a three-dimensional finite element code called ATILA [17] that was developed by the French navy for the design of magnetostrictive and piezoelectric transducers for sonar. The typical magnetostrictive data used in the actuator model for this research were obtained in part from the database of material properties in ATILA by Engdahl [9]. The three-dimensional construction of the constitutive data with orthotropic symmetry is the starting point for the effective linearized constitutive equations in this dissertation.

## The General Constitutive Equations for Magnetostriction

The derivation of the linear constitutive equations for the model starts with the most general, formal version of the equations for a magnetostrictive material and works through the simplifications to obtain the form needed for the vibration, magnetics and coil circuit models.

A general notation that accounts for all the mathematical coupling and dynamic mechanisms between the magnetics equation and the equation of motion can be written as the following:

$$\begin{aligned} \mathbf{S}(t) &= \mathbf{S}[\mathbf{T}(t' \mid t' \le t), \mathbf{H}(t' \mid t' \le t)], \\ \mathbf{B}(t) &= \mathbf{B}[\mathbf{T}(t' \mid t' \le t), \mathbf{H}(t' \mid t' \le t)], \end{aligned} \tag{2.5}$$

where $\mathbf{S}$ is the strain tensor, $\mathbf{B}$ is the magnetic flux density vector (or magnetic induction), $\mathbf{T}$ is stress tensor, and $\mathbf{H}$ is the magnetic field intensity vector.

The notation in Eq. (2.5) is chosen to indicate symbolically that the constitutive relationships are nonlinear and depend on the time history, $(t' \mid t' \le t)$, of $\mathbf{T}$ and $\mathbf{H}$.

Figure 1.4 shows the steady-state, nonlinear dependence of the strain and magnetization on the magnetic field for a typical Terfenol-D sample. The experiment measured the response of a long, thin rod of Terfenol-D to a steady, axially uniform magnetic field produced by a solenoid along the full length of the rod. The ordinate is the magnetic field. The strain and stress are in equilibrium in this experiment with no applied external load. The saturation of the magnetization and the magnetostriction occurs when all the magnetic moments of the iron atoms in the rod become fully aligned with the applied field. At that point, any further increase in the field strength does not produce any additional alignment. Both the strain and magnetization saturate at the maximum alignment. In Figure 1.4, saturation occurs for both the magnetization and magnetostriction at about 60 kiloamperes per meter. The magnetostrictive curve is a symmetric, U-shaped curve implying that the material elongates for either positive or negative magnetic field. The trace forms a thin loop rather than a single line. The loop indicates the path taken by increasing and decreasing the field. The width of the loop is the magnitude of hysteresis in the magnetostrictive properties. The curves in Figure 1.4

demonstrate that magnetostriction is a nonlinear phenomenon. To apply linearization, a small, approximately linear range must be selected. The dotted line shown on the figure is the slope of the magnetostriction line. To linearize the properties, the operating point for the actuator must be offset from the origin to coincide with the peak of the dotted line and the magnitude of the peak used for the linear coefficient. The actuator can then be operated in a small region about the peak where the slope is nearly constant. Thus, the linearized model is both offset from zero and the slope of the line, which is the coefficient in the constitutive equation, is approximated as a constant.

The linearized constitutive relations can obtained formally by a chain rule expansion of Eq. (2.5). In the following equation, the short-hand notation implies that repeated indices in a factor represent a summation over all elements of that index. The full three-dimensional, linear constitutive equations are expressed as follows:

$$\begin{aligned} dS_i &= \left.\frac{\partial S_i}{\partial T_j}\right|_H dT_j + \left.\frac{\partial S_i}{\partial H_k}\right|_T dH_k, \\ dB_m &= \left.\frac{\partial B_m}{\partial T_j}\right|_H dT_j + \left.\frac{\partial B_m}{\partial H_k}\right|_T dH_k, \end{aligned} \tag{2.6}$$

where $i$ is the index representing the six elements of the strain tensor, $j$ represents the six elements of the stress tensor, $m$ represents the three elements of the magnetic flux density vector, and $k$ represents the three elements of the magnetic field intensity vector.

In the six element vector notation, the elements of the vector correspond to the six unique terms of the strain tensor. The stress tensor can be written as

$$\mathbf{T} = \begin{bmatrix} T_{xx} & T_{xy} & T_{xz} \\ T_{xy} & T_{yy} & T_{yz} \\ T_{zx} & T_{zy} & T_{zz} \end{bmatrix}. \tag{2.7}$$

Since the shear terms are all symmetric, i.e., $T_{xy} = T_{yx}$, $T_{xz} = T_{zx}$, $T_{yz} = T_{yz}$, the tensor contains six unique elements. Instead of a three-by-three matrix, these elements can be arranged as a six element column vector with the following correspondence to the Cartesian tensor notation. The same six element vector numbering scheme is applied to the strain terms as well. The six element vector notation is sometimes called engineering strain.

Table 2.1: Correspondence between Tensor and Vector Nomenclature for Stress and Strain Variables

| Tensor | $T_{xx}$ | $T_{yy}$ | $T_{zz}$ | $T_{yz}, T_{zy}$ | $T_{xz}, T_{zx}$ | $T_{xy}, T_{yx}$ |
|---|---|---|---|---|---|---|
| Vector | $T_1$ | $T_2$ | $T_3$ | $T_4$ | $T_5$ | $T_6$ |

The partial derivatives in Eq. (2.6) are the linearized material properties. In the fields of mechanics of materials and electromagnetics, the coefficients are typically named as follows:

$\left.\frac{\partial S_i}{\partial T_j}\right|_H \equiv s_{ij}^H$, elastic compliance at constant H,

$\left.\frac{\partial B_m}{\partial H_k}\right|_T \equiv \mu_{mk}^T$, magnetic permeability at constant stress.

The other partial derivatives, $\left.\frac{\partial S_i}{\partial H_k}\right|_T$ and $\left.\frac{\partial B_m}{\partial T_j}\right|_H$, are cross terms due to magnetostriction. They represent the strain per unit magnetic field and the magnetic induction per unit stress. Engdahl [9, p. 130] shows by a thermodynamic symmetry argument that for a reversible, adiabatic process the two cross term coefficients must be equal; i.e.,

$$\left.\frac{\partial S_i}{\partial H_m}\right|_T = \left.\frac{\partial B_m}{\partial T_i}\right|_H \equiv d_{mi}, \tag{2.8}$$

The coefficients, $d_{mi}$ ,characterize both the strain due to magnetic field and the magnetic induction due to tension. The factor is termed the magnetostriction constant. In the three-dimensional linearized case, $d_{mi}$ is a three by six constant matrix. The presence of the magnetostrictive term, $d_{mi}$ , in the constitutive relations couples the magnetic field equation to the stress and strain equation and vice versa and results in the special coupled forms of the governing equations for vibration and magnetics.

The linearized constitutive equations for the magnetostrictive material can be rewritten in terms of the linearized parameters.

$$\begin{aligned} S_i &= s_{ij}^H T_j + d_{ik} H_k \\ B_m &= d_{mj} T_j + \mu_{mk}^T H_k \end{aligned} \tag{2.9}$$

In this indicial notation, the superscripts *H* and *T* indicate the independent variable that is held constant and the repeated subscripts in each term indicate summation. The Terfenol-D magnetostrictive material is found experimentally to be orthotropic and thus many of the coefficients are zero or equal to other coefficients. The unique, non-zero coefficients with orthotropic symmetry defined by Claeyssen [18] and Engdahl [9, p. 132] are shown in Eq. (2.10) and Eq. (2.11).

$$\begin{bmatrix} S_1 \\ S_2 \\ S_3 \\ S_4 \\ S_5 \\ S_6 \end{bmatrix} = \begin{bmatrix} s_{11}^H & s_{12}^H & s_{13}^H & 0 & 0 & 0 \\ s_{12}^H & s_{11}^H & s_{13}^H & 0 & 0 & 0 \\ s_{13}^H & s_{13}^H & s_{33}^H & 0 & 0 & 0 \\ 0 & 0 & 0 & s_{44}^H & 0 & 0 \\ 0 & 0 & 0 & 0 & s_{44}^H & 0 \\ 0 & 0 & 0 & 0 & 0 & s_{66}^H \end{bmatrix} \begin{bmatrix} T_1 \\ T_2 \\ T_3 \\ T_4 \\ T_5 \\ T_6 \end{bmatrix} + \begin{bmatrix} 0 & 0 & d_{31} \\ 0 & 0 & d_{31} \\ 0 & 0 & d_{33} \\ 0 & d_{15} & 0 \\ d_{15} & 0 & 0 \\ 0 & 0 & 0 \end{bmatrix} \begin{bmatrix} H_1 \\ H_2 \\ H_3 \end{bmatrix} \tag{2.10}$$

and

$$\begin{bmatrix} B_1 \\ B_2 \\ B_3 \end{bmatrix} = \begin{bmatrix} 0 & 0 & 0 & 0 & d_{15} & 0 \\ 0 & 0 & 0 & d_{15} & 0 & 0 \\ d_{31} & d_{31} & d_{33} & 0 & 0 & 0 \end{bmatrix} \begin{bmatrix} T_1 \\ T_2 \\ T_3 \\ T_4 \\ T_5 \\ T_6 \end{bmatrix} + \begin{bmatrix} \mu_{11}^T & 0 & 0 \\ 0 & \mu_{11}^T & 0 \\ 0 & 0 & \mu_{33}^T \end{bmatrix} \begin{bmatrix} H_1 \\ H_2 \\ H_3 \end{bmatrix} \tag{2.11}$$

Writing the constitutive relations as matrices gives the form that we sought in Eqs. (2.3) and (2.4).

$$\mathbf{S} = \mathbf{s}^{\mathbf{H}}\mathbf{T} + \mathbf{d}\mathbf{H} \tag{2.12}$$

$$\mathbf{B} = \mathbf{d}'\mathbf{T} + \boldsymbol{\mu}^{\mathbf{T}}\mathbf{H} \tag{2.13}$$

In this matrix notation, the prime in $\mathbf{d}'$ indicates the transpose of the matrix. Also, $\boldsymbol{\mu}^{\mathbf{T}}$ is the permeability holding stress constant and not the transpose of $\boldsymbol{\mu}$.

Example values for the coefficients for the three-dimensional case are listed by Engdahl [9. p. 175]. Engdahl credits the material database for ATILA as the source for some of the data. The terms which are needed for calculations in this chapter are given in Table 2.2.

Table 2.2: Linear coefficients for Terfenol-D[9]

| *Constant* | *Value* | *Units* |
|---|---|---|
| $s_{11}^H$ | $12.5\times10^{-11}$ | $Pa^{-1}$ |
| $s_{12}^H$ | $-1.8\times10^{-12}$ | $Pa^{-1}$ |
| $s_{13}^H$ | $-1.7\times10^{-11}$ | $Pa^{-1}$ |
| $s_{33}^H$ | $4.0\times10^{-11}$ | $Pa^{-1}$ |
| $s_{44}^H$ | $1.8\times10^{-10}$ | $Pa^{-1}$ |
| $s_{66}^H$ | $5.4\times10^{-11}$ | $Pa^{-1}$ |
| $d_{31}$ | $-5.3\times10^{-9}$ | m/A |
| $d_{15}$ | $2.8\times10^{-8}$ | m/A |
| $d_{33}$ | $1.1\times10^{-8}$ | m/A |
| $\mu_{11}^T$ | $1.3\times10^{-5}$ | (m·Tesla)/A |
| $\mu_{33}^T$ | $5.3\times10^{-6}$ | (m·Tesla)/A |

In the chapters that follow, the state equations for the magnetic model and vibration model are formulated with strain and magnetic field as the state variables. Hence, we wish to manipulate Eqs. (2.12) and (2.13) to solve for **T** and **B** as functions of **S** and **H**. The result of the algebraic manipulation is given by

$$\mathbf{T} = \left(\mathbf{s}^{\mathbf{H}}\right)^{-1}\mathbf{S} - \left(\mathbf{s}^{\mathbf{H}}\right)^{-1}\mathbf{dH} \tag{2.14}$$

$$\mathbf{B} = \mathbf{d}'\left(\mathbf{s}^{\mathbf{H}}\right)^{-1}\mathbf{S} + \left(\boldsymbol{\mu}^{\mathbf{T}} - \mathbf{d}'\left(\mathbf{s}^{\mathbf{H}}\right)^{-1}\mathbf{d}\right)\mathbf{H} \tag{2.15}$$

The coefficient matrices in the form given by Eqs. (2.14) and (2.15) are used frequently in the following sections. Consequently, we adopt the names for the matrices given by Engdahl [9, p. 134] to facilitate the modeling derivations that follow.

$$\mathbf{T} = \mathbf{Y}^{\mathbf{H}}\mathbf{S} - \boldsymbol{\kappa}\mathbf{H} \tag{2.16}$$

$$\mathbf{B} = \boldsymbol{\kappa}'\mathbf{S} + \boldsymbol{\mu}^{\mathbf{S}}\mathbf{H} \tag{2.17}$$

The magnetostriction coefficients in this form of the equation are defined as

$$\boldsymbol{\kappa} = \left.\frac{\partial \mathbf{B}}{\partial \mathbf{S}}\right|_{\mathbf{H}} = \left.\frac{\partial \mathbf{T}}{\partial \mathbf{H}}\right|_{\mathbf{S}} \tag{2.18}$$

where $\mathbf{Y}^{\mathbf{H}} = \left(\mathbf{s}^{\mathbf{H}}\right)^{-1}$ is the Young's modulus at constant magnetic field, $\boldsymbol{\kappa} = \left(\mathbf{s}^{\mathbf{H}}\right)^{-1}\mathbf{d} = \mathbf{Y}^{\mathbf{H}}\mathbf{d}$ is the magnetostriction coefficient which represents either the tension per unit magnetic field at constant stress or the magnetic induction per unit stress at constant magnetic field. Similarly, $\boldsymbol{\mu}^{\mathbf{S}} = \boldsymbol{\mu}^{\mathbf{T}} - \mathbf{d}'\left(\mathbf{s}^{\mathbf{H}}\right)^{-1}\mathbf{d}$ is the magnetic permeability at constant strain.

The matrices in Eqs. (2.16) and (2.17) can be evaluated numerically using the data in Table 2.2. The results are shown in the full matrix form in Table 2.3 through Table 2.5 to illustrate the zero elements and the orthotropic symmetry.

Table 2.3: Modulus of elasticity at constant magnetic induction, $Y^H$, [Pa]

| | *1* | *2* | *3* | *4* | *5* | *6* |
|---|---|---|---|---|---|---|
| *1* | $0.8541\times10^{10}$ | $0.0654\times10^{10}$ | $0.3908\times10^{10}$ | 0 | 0 | 0 |
| *2* | $0.0654\times10^{10}$ | $0.8541\times10^{10}$ | $0.3908\times10^{10}$ | 0 | 0 | 0 |
| *3* | $0.3908\times10^{10}$ | $0.3908\times10^{10}$ | $2.8322\times10^{10}$ | 0 | 0 | 0 |
| *4* | 0 | 0 | 0 | $0.5556\times10^{10}$ | 0 | 0 |
| *5* | 0 | 0 | 0 | 0 | $0.5556\times10^{10}$ | 0 |
| *6* | 0 | 0 | 0 | 0 | 0 | $1.8519\times10^{10}$ |

Table 2.4: Magnetostrictive constant, $\boldsymbol{\kappa}$ ,[Pa/(A/m) = Tesla]

| | *1* | *2* | *3* |
|---|---|---|---|
| *1* | 0 | 0 | -5.7471 |
| *2* | 0 | 0 | -5.7471 |
| *3* | 0 | 0 | 270.11 |
| *4* | 0 | 155.56 | 0 |
| *5* | 155.56 | 0 | 0 |
| *6* | 0 | 0 | 0 |

Table 2.5: Magnetic permeability at constant strain, $\boldsymbol{\mu}^S$, [(m·Tesla)/A]

| | *1* | *2* | *3* |
|---|---|---|---|
| *1* | $0.8644 \times 10^{-5}$ | 0 | 0 |
| *2* | 0 | $0.8644 \times 10^{-5}$ | 0 |
| *3* | 0 | 0 | $0.2268 \times 10^{-5}$ |

The order reduction transformation can be performed more easily if the two-by-two constitutive relations are written as a single matrix relation. This form of the equations takes **S** and **H** as inputs and gives **T** and **B** as outputs.

$$\begin{bmatrix} \mathbf{T} \\ \mathbf{B} \end{bmatrix} = \begin{bmatrix} \mathbf{Y}^{\mathbf{H}} & -\boldsymbol{\kappa} \\ \boldsymbol{\kappa}' & \boldsymbol{\mu}^{\mathbf{S}} \end{bmatrix} \begin{bmatrix} \mathbf{S} \\ \mathbf{H} \end{bmatrix} \tag{2.19}$$

The grouped matrices are described by the following notation:

$$\boldsymbol{\Sigma} = \boldsymbol{\mathcal{S}} \boldsymbol{\Psi} \tag{2.20}$$

where

$$\boldsymbol{\Psi} = \begin{bmatrix} \mathbf{T} \\ \mathbf{B} \end{bmatrix}, \ \boldsymbol{\Sigma} = \begin{bmatrix} \mathbf{S} \\ \mathbf{H} \end{bmatrix}, \boldsymbol{\mathcal{S}} = \begin{bmatrix} \mathbf{Y}^{\mathbf{H}} & -\boldsymbol{\kappa} \\ \boldsymbol{\kappa}' & \boldsymbol{\mu}^{S} \end{bmatrix} \tag{2.21}$$

**Reduction of the dimensionality of the constitutive equations by application of symmetry**

The actuator's dynamics, when fully described, is a three-dimensional wave problem. The three-dimensional wave equation could account for the radial and azimuthal components of stress induced by the field due to the eddy currents. The three-dimensional wave equation could also include the effects of the dissimilar mechanical properties of the adhesive and the magnetostrictive rod which form the laminated rod. However, the azimuthal component of wave motion is arguably small and may be neglected by performing an average of the stresses across the transverse area. This step converts the coordinate system from Cartesian coordinates to cylindrical and reduces the

wave equation from three dimensions to two representing the radial and axial components of stress and strain and eliminating the azimuthal dependence. The magnetic field and flux density retain their three-dimensional form. Because of orthotropic symmetry, the Cartesian and cylindrical components have a one-to-one correspondence. To see the correspondence, consider coincident planes in the two coordinate system, $y = 0$ and $\phi = 0$. The basis vectors of the two coordinate systems are aligned and have the following correspondences.

$$\hat{e}_x = \hat{e}_r,\ \hat{e}_y = \hat{e}_\phi,\ \hat{e}_z = \hat{e}_z. \tag{2.22}$$

The tension variables likewise have the following corresponding values. The corresponding values are arranged in columns.

Table 2.6: Correspondence between strain elements in Cartesian and cylindrical tensor notation and six-element engineering vector nomenclature

| | | | | | | |
|---|---|---|---|---|---|---|
| *Cartesian* | $T_{xx}$ | $T_{yy}$ | $T_{zz}$ | $T_{yz}, T_{zy}$ | $T_{xz}, T_{zx}$ | $T_{xy}, T_{yx}$ |
| *Cylindrical* | $T_{rr}$ | $T_{\phi\phi}$ | $T_{zz}$ | $T_{\phi z}, T_{z\phi}$ | $T_{rz}, T_{zr}$ | $T_{r\phi}, T_{\phi r}$ |
| *Engineering* | $T_1$ | $T_2$ | $T_3$ | $T_4$ | $T_5$ | $T_6$ |

Within this specified plane, the same coefficient matrices apply to both the cylindrical coordinates and the Cartesian system because the systems are both orthonormal coordinate systems and are identically oriented. Because of the cylindrical symmetry of the material properties, the same coefficients apply in the cylindrical system for any rotation about the *z* axis. Thus, there is a one-for-one correspondence of the three-dimensional properties in Cartesian and the cylindrical coordinates.

The next step in the derivation of the constitutive relations in cylindrical coordinate is to convert the stress and strain variables from Cartesian to cylindrical

coordinate variables. In this conversion, the symmetry of the stress and strain about the central axis of the rod can be used to reduce the dimensionality of the constitutive equations. Consider an axisymmetric axial load and assume that differences between the elastic properties of magnetostrictive rod and adhesive do not affect the distribution of stress and strain. (This assumption is equivalent to saying that the bond does not slip and the adhesive layer is vanishingly thin.) Under these assumptions, the resulting stress and strain are axisymmetric as well. Axisymmetric stress and strain does not mean that stress and strain are zero in the azimuthal direction. It means that the stress and strain do not vary along the circular path in the plane. Hence, the gradients in the azimuthal direction are zero and an element of volume on the circular path maintains a rectangular shape despite the deformation due to an axial load. Since the angles of the volume do not change, the shear stress terms, $T_{\phi r}$ and $T_{\phi z}$, must be zero. Applying the uniform stress and strain distribution to the terms in the six element vectors reduces the vector to four independent elements. The transformation in dimensionality can be expressed as 6×4 matrix.

$$\begin{bmatrix} T_{rr} \\ T_{\phi\phi} \\ T_{zz} \\ T_{zr} \end{bmatrix} = \begin{bmatrix} 1 & 0 & 0 & 0 & 0 & 0 \\ 0 & 1 & 0 & 0 & 0 & 0 \\ 0 & 0 & 1 & 0 & 0 & 0 \\ 0 & 0 & 0 & 0 & 1 & 0 \end{bmatrix} \begin{bmatrix} T_1 \\ T_2 \\ T_3 \\ T_4 \\ T_5 \\ T_6 \end{bmatrix}. \tag{2.23}$$

Applying matrix variables to this equation makes it more compact; i.e,

$$\mathbf{T}_4 = \mathfrak{M}_{6\to 4}\, \mathbf{T}_6 \tag{2.24}$$

where the subscripts on the vectors are used to indicate the order of the matrix. The transformation matrix, $\mathfrak{M}_{6\to4}$, is so named to indicate the transformation from the six element vector to four element. The same transformation matrix applies to the strain vector. The transformation for strains using the same notation can be written as the following.

$$\mathbf{S}_4 = \mathfrak{M}_{6\to4}\,\mathbf{S}_6 \tag{2.25}$$

The inverse relationship to transform from four to six elements is simply the transpose.

$$\begin{aligned}\mathbf{T}_6 &= \left(\mathfrak{M}_{6\to4}\right)'\mathbf{T}_4\\ \mathbf{S}_6 &= \left(\mathfrak{M}_{6\to4}\right)'\mathbf{S}_4\end{aligned} \tag{2.26}$$

The transformation of the magnetic induction does not change the dimensionality or values of the magnetic induction in the component directions. The transformation is represented by the identity matrix.

$$\begin{bmatrix}B_r\\ B_\phi\\ B_z\end{bmatrix} = \begin{bmatrix}1 & 0 & 0\\ 0 & 1 & 0\\ 0 & 0 & 1\end{bmatrix}\begin{bmatrix}B_1\\ B_2\\ B_3\end{bmatrix} \tag{2.27}$$

Equations (2.25) and(2.27) can be consolidated into a single matrix operation.

$$\begin{bmatrix}\mathbf{T}_4\\ \mathbf{B}_3\end{bmatrix} = \begin{bmatrix}\mathfrak{M}_{6\to4} & \mathbf{0}\\ \mathbf{0} & \mathbf{I}\end{bmatrix}\begin{bmatrix}\mathbf{T}_6\\ \mathbf{B}_3\end{bmatrix} \tag{2.28}$$

Using the nomenclature for the joint vector for stress and magnetic induction, $\mathbf{\Psi}$, from Eq. (2.21)and a subscript to indicate the number of independent elements of the vector, we can express Eq. (2.28) in the following form:

$$\mathbf{\Psi}_7 = \mathfrak{M}_{9\to7}\mathbf{\Psi}_9 \tag{2.29}$$

where

$$\mathfrak{M}_{9\to 7} = \begin{bmatrix} \mathfrak{M}_{6\to 4} & 0 \\ 0 & \mathbf{I} \end{bmatrix} \tag{2.30}$$

$$\boldsymbol{\Psi}_9 = \begin{bmatrix} \mathbf{T}_6 \\ \mathbf{B}_3 \end{bmatrix} \tag{2.31}$$

$$\boldsymbol{\Psi}_7 = \begin{bmatrix} \mathbf{T}_4 \\ \mathbf{B}_3 \end{bmatrix} \tag{2.32}$$

An analogous transformation holds for a vector composed of the strain and magnetic field; i.e.,

$$\boldsymbol{\Sigma}_7 = \mathfrak{M}_{9\to 7}\boldsymbol{\Sigma}_9 \tag{2.33}$$

where

$$\boldsymbol{\Sigma}_9 = \begin{bmatrix} \mathbf{S}_6 \\ \mathbf{H}_3 \end{bmatrix} \tag{2.34}$$

$$\boldsymbol{\Sigma}_7 = \begin{bmatrix} \mathbf{S}_4 \\ \mathbf{H}_3 \end{bmatrix} \tag{2.35}$$

The transformation from seven elements to nine is the transpose of the above matrix

$$\boldsymbol{\Psi}_9 = \mathfrak{M}_{7\to 9}\boldsymbol{\Psi}_7 = \mathfrak{M}'_{9\to 7}\boldsymbol{\Psi}_7 \tag{2.36}$$

The subscript indicating the number of terms in the vectors can be added to the constitutive relationship given by Eq. (2.20).

$$\boldsymbol{\Sigma}_9 = \mathfrak{S}_9\boldsymbol{\Psi}_9 \tag{2.37}$$

The constitutive relation for the seventh order vector in the axisymmetric system is given by substituting Eq. (2.36) on the right hand side and multiplying both sides by $\mathbf{M}_{9\to 7}$

$$\boldsymbol{\Sigma}_7 = \mathfrak{M}_{9\to 7}\boldsymbol{\Sigma}_9 = \mathfrak{M}_{9\to 7}\mathfrak{S}_9\mathfrak{M}'_{9\to 7}\boldsymbol{\Psi}_7 \tag{2.38}$$

By comparison to the constitutive relationship for the seventh order axisymmetric case, $\boldsymbol{\Sigma}_7 = \mathfrak{S}_7\boldsymbol{\Psi}_7$, the seventh order matrix must be the following.

$$\mathfrak{S}_7 = \mathfrak{M}_{9\to 7}\mathfrak{S}_9\mathfrak{M}'_{9\to 7} \tag{2.39}$$

The matrices representing the Young's modulus, the magnetostrictive constant, and the permeability can be obtained by subdividing $\mathfrak{S}_7$ into four individual matrices as in Eq. (2.21). The coefficient terms inside the matrices in the following equation are numbered using the indices for the six element matrices to illustrate that the values of the coefficients themselves are not changed by the reduction in order.

$$\begin{bmatrix} T_{rr} \\ T_{\phi\phi} \\ T_{zz} \\ T_{zr} \end{bmatrix} = \begin{bmatrix} Y_{11}^H & Y_{12}^H & Y_{13}^H & 0 \\ Y_{12}^H & Y_{11}^H & Y_{13}^H & 0 \\ Y_{13}^H & Y_{13}^H & Y_{33}^H & 0 \\ 0 & 0 & 0 & Y_{55}^B \end{bmatrix} \begin{bmatrix} S_{rr} \\ S_{\phi\phi} \\ S_{zz} \\ S_{zr} \end{bmatrix} - \begin{bmatrix} 0 & 0 & \kappa_{13} \\ 0 & 0 & \kappa_{13} \\ 0 & 0 & \kappa_{33} \\ \kappa_{51} & 0 & 0 \end{bmatrix} \begin{bmatrix} H_r \\ H_\phi \\ H_z \end{bmatrix} \tag{2.40}$$

$$\begin{bmatrix} B_r \\ B_\phi \\ B_z \end{bmatrix} = \begin{bmatrix} 0 & 0 & 0 & \kappa_{15} \\ 0 & 0 & 0 & 0 \\ \kappa_{31} & \kappa_{31} & \kappa_{33} & 0 \end{bmatrix} \begin{bmatrix} S_{rr} \\ S_{\phi\phi} \\ S_{zz} \\ S_{zr} \end{bmatrix} + \begin{bmatrix} \mu_{11}^S & 0 & 0 \\ 0 & \mu_{11}^S & 0 \\ 0 & 0 & \mu_{33}^S \end{bmatrix} \begin{bmatrix} H_r \\ H_\phi \\ H_z \end{bmatrix} \tag{2.41}$$

This form of the constitutive relations describes the full coupling between the magnetic and vibration models, accounting for axisymmetry and orthotropic properties. The constitutive equations in Eqs. (2.40) and (2.41) invoke the symmetry of the vibration problem without imposing any additional approximation beyond the linearization given

by Eq. (2.6). The numerical values of the coefficients are unchanged from the values in Table 2.3 through Table 2.5. The matrix of coefficients is just rearranged and reduced in size. The shear terms, which are always zero under the assumption of axisymmetry, are the only terms that have been eliminated.

The next step is to introduce an approximation that reduces the constitutive relation for the vibration to a one-dimensional stress-strain relationship while retaining the three-dimensional magnetic flux and magnetic field relationship. This means that the four component vectors for stress and strain have to collapse into single axial component in the vibration model. The radial and tangential strains must be algebraic functions of the axial strain.

**The constant volume approximation for magnetostrictive materials**

The radial and azimuthal components of stress and strain are not necessarily small, but for a long thin rod, the radial motion dynamics are significantly faster than the axial dynamics. This difference in frequency response suggests that the radial motion can be approximated as a quasi-steady process, making the radial motion an algebraic function of the slower axial motion. This approximation reduces the complexity and system order of a two-dimensional wave model to a much more manageable one-dimensional longitudinal vibration problem. The same reduction in dimensionality is not appropriate for the radial and azimuthal components in the magnetics equation because the magnetic flux density is conserved $\left(\text{i.e., } \nabla \cdot \mathbf{B} = 0\right)$ and diminishes axially only because it diffuses out of the rod in the radial direction. The radial and azimuthal components for the eddy current flow are likewise three-dimensional. Hence, the magnetic problem must retain the three-dimensional components of magnetic flux;

whereas the vibration problem can be modeled as a one dimensional problem. An approach to account for the difference in dimensionality of the various phenomena is proposed in this section to reduce the mechanical motion to an effective one-dimensional vibration model while retaining three-dimensional magnetics in the model. The approach assumes that the actuator rod's volume is constant. This assumption of constant volume under magnetostriction is mentioned by both Savage and Jiles, [15, 19, p. 127]. The constant volume approximation means that an axial elongation is accompanied by a radial contraction to maintain a constant average density in the magnetostrictive material. Jiles indicates that the constant volume approximation is in good agreement with experimental observations. Moreover, the constant volume conjecture can be tested using the material property data in Table 2.2 (see APPENDIX A). A second part of the approximation is an assumption that, in a differentially thin axial segment of the actuator rod, the mechanical stress and strain in the radial dimension are in quasi-equilibrium. This assumption implies that the stresses and strains in the *r* and $\phi$ directions come to equilibrium and balance one another instantaneously. This approximation neglects the inertia of the radial motion. The approximation of applying constant volume as a constraint causes the radial displacement and strain to become algebraic functions of the axial displacement rather than the solution of a differential equation representing wave motion in the radial direction. The final result is a set of effective constitutive equations involving the one-dimensional vibration and three-dimensional magnetics. The effective constitutive equations can be expressed as follows:

$$T_{zz} = Y_{eff}^{H} S_{zz} - \kappa_{eff} H_z \tag{2.42}$$

$$\begin{bmatrix} B_r \\ B_\phi \\ B_z \end{bmatrix} = \begin{bmatrix} \kappa_{eff,r} \\ 0 \\ \kappa_{eff,z} \end{bmatrix} S_{zz} + \begin{bmatrix} \mu_{11}^S & 0 & 0 \\ 0 & \mu_{11}^S & 0 \\ 0 & 0 & \mu_{33}^S \end{bmatrix} \begin{bmatrix} H_r \\ H_\phi \\ H_z \end{bmatrix} \tag{2.43}$$

where $Y_{eff}^H$, $\kappa_{eff}$, $\kappa_{eff,r}$, and $\kappa_{eff,z}$ are effective scalar constants that are functions of the original linearized material properties. The anisotropic permeability coefficients, $\mu_{11}^S$ and $\mu_{33}^S$, are unchanged from the original constitutive equations to retain the three-dimensional anisotropic effects in the magnetic model. The goal is to find formulae that define $\kappa_{eff}$, $\kappa_{eff,r}$, and $\kappa_{eff,z}$ in terms of the original six element data.

The constant volume relationship in terms of the radial and axial strains can be derived from the equation for a differential volume. Consider an axial segment of rod between $z$ and $z+\Delta z$. The volume of the segment under no stress is

$$\Delta V = \pi r^2 \Delta z \tag{2.44}$$

If an axial load is applied to the volume, the volume is strained in both axial and radial directions. The volume of the element in terms of the radial and axial displacement is,

$$\Delta V' = \pi \left( r + \zeta_r \right)^2 \left( \Delta z + \frac{\partial \zeta_z}{\partial z} \Delta z \right). \tag{2.45}$$

In the constant volume approximation, the volumes in Eqs. (2.44) and (2.45) must be equal, $\Delta V = \Delta V'$. Therefore,

$$\pi \left( r + \zeta_r \right)^2 \left( \Delta z + \frac{\partial \zeta_z}{\partial z} \Delta z \right) = \pi r^2 \Delta z \,. \tag{2.46}$$

Expanding the product on the left hand side and simplifying the expression yields

$$\begin{aligned} \left(r+\zeta_r\right)^2\left(1+\frac{\partial\zeta_z}{\partial z}\right)&=r^2,\\ 2r\zeta_r+\zeta_r{}^2+r^2\frac{\partial\zeta_z}{\partial z}+2r\zeta_r\frac{\partial\zeta_z}{\partial z}+\zeta_r{}^2\frac{\partial\zeta_z}{\partial z}&=0. \end{aligned} \tag{2.47}$$

Since the second, fourth and fifth terms in Eq. (2.47) are second order or higher, they may be neglected. This yields the following equation for the radial strain.

$$\frac{\zeta_r}{r}=-\frac{1}{2}\frac{\partial\zeta_z}{\partial z}. \tag{2.48}$$

The axial strain is assumed to be uniform in the radial direction. This amounts to a constant density throughout the actuator rod. This is obviously true on average for the constant volume approximation, but defining the density at every point as equal to the average is an additional assumption. If only constant volume is required, the density could be distributed in any way that keeps the volume the same. The approximation that the density is uniform throughout the rod requires the least motion by the actuator to maintain constant volume which seems plausible; however, it should be recognized that other reasonable approximations of the density distribution can be made.

If the density is uniform in the transverse direction, then the ratio on the left of Eq. (2.48) must be a function of *z* alone. This observation leads to the following relationship between the radial displacement and the axial strain.

$$\frac{\zeta_r}{r}=-\frac{1}{2}\frac{\partial\zeta_z(z)}{\partial z}. \tag{2.49}$$

Differentiating with respect to *r* gives the radial strain in terms of the axial strain:

$$\frac{\partial\zeta_r}{\partial r}=-\frac{1}{2}\frac{\partial\zeta_z(z)}{\partial z}. \tag{2.50}$$

The four components of strain in terms of the radial and axial displacements in axisymmetric cylindrical geometry are given by Engdahl [9, p. 201]. Restating Engdahl's definition of the strain components and incorporating the constant volume expressions from Eqs. (2.48) and (2.49) into these expressions yields the algebraic expressions for all the strains in terms of axial displacement under the constant volume constraint.

$$\begin{aligned} S_{rr} &= \frac{\partial \zeta_r}{\partial r} \approx -\frac{1}{2}\frac{\partial \zeta_z}{\partial z}. \\ S_{\phi\phi} &= \frac{\zeta_r}{r} \approx -\frac{1}{2}\frac{\partial \zeta_z}{\partial z}. \\ S_{zz} &= \frac{\partial \zeta_z}{\partial z}. \\ S_{rz} &= \frac{1}{2}\left(\frac{\partial \zeta_r}{\partial z} + \frac{\partial \zeta_z}{\partial r}\right) \approx \frac{1}{2}\left(\frac{\partial}{\partial z}\left(-\frac{r}{2}\frac{\partial \zeta_z}{\partial z}\right)\right), \\ &= \frac{1}{2}\left(\frac{\partial \zeta_r}{\partial z} + \frac{\partial \zeta_z}{\partial r}\right) \approx -\frac{r}{4}\frac{\partial^2 \zeta_z}{\partial z^2}. \end{aligned} \tag{2.51}$$

These four components of strain can be expressed as an operator matrix times the axial strain.

$$\begin{bmatrix} S_r \\ S_\phi \\ S_z \\ S_{rz} \end{bmatrix} = \begin{bmatrix} -\frac{1}{2} \\ -\frac{1}{2} \\ 1 \\ -\frac{r}{4}\frac{\partial}{\partial z} \end{bmatrix} \frac{\partial \zeta_z}{\partial z}. \tag{2.52}$$

Next, substituting the strain equations into the first constitutive equation in Eq. (2.40) to reduce its dimensionality yields the following expression:

$$\begin{bmatrix} T_{rr} \\ T_{\phi\phi} \\ T_{zz} \\ T_{zr} \end{bmatrix} = \begin{bmatrix} Y_{11}^H & Y_{12}^H & Y_{13}^H & 0 \\ Y_{12}^H & Y_{11}^H & Y_{13}^H & 0 \\ Y_{13}^H & Y_{13}^H & Y_{33}^H & 0 \\ 0 & 0 & 0 & Y_{55}^B \end{bmatrix} \begin{bmatrix} -\frac{1}{2} \\ -\frac{1}{2} \\ 1 \\ -\frac{r}{4}\frac{\partial}{\partial z} \end{bmatrix} \frac{\partial \zeta_z}{\partial z} - \begin{bmatrix} 0 & 0 & \kappa_{31} \\ 0 & 0 & \kappa_{31} \\ 0 & 0 & \kappa_{33} \\ \kappa_{15} & 0 & 0 \end{bmatrix} \begin{bmatrix} H_r \\ H_\phi \\ H_z \end{bmatrix}. \tag{2.53}$$

Only the third row of this equation is needed for the one-dimensional vibration model in Eq. (2.42), which is given by

$$T_{zz} = \left(Y_{33}^H - Y_{13}^H\right)\frac{\partial \zeta_z}{\partial z} - \kappa_{33} H_z . \tag{2.54}$$

The second constitutive equation is obtained after substituting Eq. (2.52) into Eq. (2.41). This yields:

$$\begin{aligned} \begin{bmatrix} B_r \\ B_\phi \\ B_z \end{bmatrix} &= \begin{bmatrix} 0 & 0 & 0 & \kappa_{15} \\ 0 & 0 & 0 & 0 \\ \kappa_{31} & \kappa_{31} & \kappa_{33} & 0 \end{bmatrix} \begin{bmatrix} -\frac{1}{2} \\ -\frac{1}{2} \\ 1 \\ -\frac{r}{4}\frac{\partial}{\partial z} \end{bmatrix} \frac{\partial \zeta_z}{\partial z} + \begin{bmatrix} \mu_{11}^S & 0 & 0 \\ 0 & \mu_{11}^S & 0 \\ 0 & 0 & \mu_{33}^S \end{bmatrix} \begin{bmatrix} H_r \\ H_\phi \\ H_z \end{bmatrix}, \\ &= \begin{bmatrix} -\frac{\kappa_{15} r}{4}\frac{\partial}{\partial z} \\ 0 \\ \kappa_{33} - \kappa_{31} \end{bmatrix} \frac{\partial \zeta_z}{\partial z} + \begin{bmatrix} \mu_{11}^S & 0 & 0 \\ 0 & \mu_{11}^S & 0 \\ 0 & 0 & \mu_{33}^S \end{bmatrix} \begin{bmatrix} H_r \\ H_\phi \\ H_z \end{bmatrix}. \end{aligned} \tag{2.55}$$

It follows that the effective constants that are needed for the reduced order system described by Eqs. (2.42) and (2.43) can be calculated in terms of the three-dimensional constants as the following:

$$Y_{eff}^H = Y_{33}^H - Y_{13}^H . \tag{2.56}$$

$$\kappa_{eff,r} = -\frac{\kappa_{15} r}{4} \frac{\partial}{\partial z}. \tag{2.57}$$

$$\kappa_{eff,z} = \kappa_{33} - \kappa_{31}. \tag{2.58}$$

$$\kappa_{eff} = \kappa_{33}. \tag{2.59}$$

Note that the coefficient, $Y_{12}^{H}$, does not appear in the formula for the effective Young's modulus constant.

The only component that is troublesome in this derivation is the radial component of magnetostriction in Eq. (2.57). Instead of resulting in a constant coefficient as might be expected, this term depends upon the radial position, *r*, and the differential operator. The term is the consequence of the approximation that the density is uniform in the transverse direction. In other words, the radial distribution of magnetization due to strain given by Eq. (2.57) is consistent with the uniform density assumption. Alternate forms for the radial component would be obtained with other assumptions about the density distribution. As stated previously, the uniform density in the transverse direction is an approximation that results in the least motion and the simplest model. However, it results in the term in question. For the time being, this term is carried in the derivation. The magnitude of this term can be estimated in comparison with the rest of the terms in the magnetics equation when those equations are derived in Chapter 4.

The final results of this section are the numerical values for the effective coefficients in the constant volume approximation. These are the forms of the constitutive relations that are used in the derivations and applications of the vibration and magnetics models that follow. The coefficients are calculated from the data in Table 2.2.

Table 2.7: Effective magnetostrictive properties for one-dimensional vibration and three-dimensional magnetics

| *Effective Linear Property* | *Value* | *Units* |
|---|---|---|
| $Y_{eff}^{H}$ | $2.441\times10^{10}$ | Pa |
| $\kappa_{eff,r}$ | 0 | Pa/(A/m)=T |
| $\kappa_{eff,z}$ | 275.86 | Pa/(A/m)=T |
| $\kappa_{eff}$ | 270.11 | Pa/(A/m)=T |
| $\mu_{11}^{S}$ | $0.8644\times10^{-5}$ | T/(A/m) |
| $\mu_{33}^{S}$ | $0.2268\times10^{-5}$ | T/(A/m) |

**Linear range and offset for the linear model.**

The nonlinear constitutive relations depicted in Figure 1.4 are the basis for the linear range and offset for the actuator operating conditions. The limits of the linear range and offset of the actuator's operating point are needed in addition to the linearized coefficients for the actuator experiment in the control design and in the experimental setup to avoid the nonlinearity associated with saturation. The basis for the limit can come from either the manufacturer's specifications for maximum current or from the observed current at which saturation occurs.

The offset is needed to set the operating point of the experiment. The linearized control problem is written in terms of perturbations about the operating point. In the perturbation form of the modeling equations, the operating point itself disappears from the normalized differential equation. This is a convenient simplification, and in many cases, the actual operating point is not even derived with the understanding that it cancels out in the final form. In the experimental setup, the operating point does have to be added to the perturbation to convert the variables from their perturbation form back to their actual offset values.

The DC offset in the current signal is needed in the prototype but is not usually applied in the commercial models of magnetostrictive actuators. In a commercial magnetostrictive actuator, offset in the magnetic field is supplied by an annular permanent magnet called the bias magnet as shown in Figure 1.1 located in a cylindrical shell just outside the drive coils. This bias magnet provides a steady field along the rod to shift the operating point from the null response at zero inductance to the steep linear region. The multi-segmented actuator designed for this experiment does not use a bias magnet because the permanent magnet materials have a high conductivity that produce eddy currents that consume too much power for the actuator to operate at high frequency. Instead, a low conductivity but unmagnetized silicon iron sleeve is used in the same annular region of the case to provide a high permeability path from the north to the south poles of the actuator. The return path reduces the magnetic losses from the end of the actuator rod; however, without a permanent magnet supplying bias, the offset in the magnetic field has to be supplied by a steady (DC) current in the coils.

A first estimate of the field needed for offset can be obtained from the Terfenol-D constitutive properties diagram in Figure 1.4. The magnetic field at the operating point can be estimated from the peak of the dotted curve representing the slope. An approximate value of $H_{OP} = 28$ kiloamperes per meter can be estimated from the figure. The current per turn of the coil can be extracted from this field using this formula for magnetic field in an infinite solenoid. In SI units, the formula is $H = T \cdot I$ where $T$ is the turns per meter and $I$ is the current per turn. The actuator design data can be used to obtain $T$. From design data, we obtain: the length of one coil of the actuator, $\Delta z$=0.0156 m (0.625 inches) and the number of turns per coil, $T_c = 105$. The value of $T$ is then

$$T = \frac{T_c}{\Delta z} = \frac{105}{0.0159} = 6614 \text{ turns/m} \tag{2.60}$$

The current at the maximum slope is a preliminary estimate for the operating point current.

$$I_{OP} = \frac{H}{T} = \frac{28,000}{6614} \approx 4 \text{ amps/turn} \tag{2.61}$$

A linear range based on Figure 1.4 about the operating point is approximately $\Delta H = \pm 6700$ ampere per meter . Converting this to a current range for the coil gives

$$\Delta I = \frac{\Delta H}{T} = \frac{6700}{6614} \approx 1 \text{ ampere/turn} \tag{2.62}$$

Thus, the range for current based on Figure 1.4 is 4±1 amperes or 3 to 5 amperes. This range turns out to be too high for the prototype actuator based on the manufacturer's specification for current. The maximum coil current specified by the manufacturer is 3 amperes. The manufacturer's limit is based partly on magnetostrictive saturation but also on the ohmic heating in the coil. Since the bias current is present at all times, the ohmic losses in the coil can cause significant heating. Also, the Terfenol alloy used in the prototype is more efficient than that shown in the figure so that the same maximum elongation is produced by a smaller applied magnetic field. The peak strain rate (maximum slope) for the prototype actuator occurs at a correspondingly lower field. The actual limits used for the prototype experiment are from 0.75 to 2.25 amperes. This range is well within the operational limits specified by the manufacturer and the actuator remains cool to the touch while operating.

## Dimensionless Variables

After the governing equations for vibration, magnetism and coil current are derived in dimensioned form in Chapter 3, 4, and 5, the variables in the system models are normalized into dimensionless variables. The dimensionless variables are all scaled by the physics of the process to be on the order of unity using the constitutive equations derived in this chapter. The conversion to dimensionless variables accomplishes several things. First, the scaling is important because the numerical properties of the control computations rely, in some cases, on proper scaling for numerical error control and stability in the calculations. A second argument for dimensionless variables is that it leads to groups of factors that combine all the parametric dependence into the fewest terms. The factors, usually called the dimensionless groups, provide a very condensed and revealing understanding of how the process scales. All cases that have the same values for dimensionless groups have exactly the same dimensionless solution. The similarity relationship can reduce a family of simulation cases into a single case that solves all the cases when the appropriate scaling factors are applied. The final reason for normalization is to facilitate the control system tuning. In control system design, adjusting the weighting factors in the quadratic error index is the main tool for tuning control response. The weight factors are more easily interpreted when the states are scaled for unit range (unitary gain). When variables are dimensioned, the weight factor must serve the dual role of converting the units and weighting the error.

One valid choice for scaling factors can be defined in terms of the steady, no-load cases at the maximum and minimum currents from the preceding section. These two points define a normalized range for each of the dimensionless variables. The steady

state case means that the current is held at the indicated limiting value until transient effects die out. No load means that no external mechanical load is applied. At steady state with no external load, the elastic stress balances the magnetostrictive stress resulting in zero net stress is in all directions.

The relationships needed for the scaling calculation are the constitutive relations and the infinite solenoid equation. The field for an infinite solenoid is given by

$$H_z = T \cdot I \,. \tag{2.63}$$

In this case, the parameter, $T$, is the number of turns per unit length, not tension, **T,** as in the earlier part of the discussion. The variable, $I$, is the current in the coil. The constitutive relations provide equations relating stress, strain, magnetic field, and magnetic induction. The infinite solenoid equation is an approximation that relates magnetic field to coil current for the case in which all coils are equally energized. Since the actuator solenoid is long and thin, the infinite solenoid formula gives a good estimate of the field through the actuator. The linear constitutive relations for the no-load steady state case can be evaluated by substituting the tension, $\mathbf{T} = 0$ and $H_z = T \cdot I$ into Eq. (2.12) and Eq. (2.13) and solving for the axial components.

$$\mathbf{S} = \mathbf{s}^{\mathbf{H}} \begin{bmatrix} 0 \\ 0 \\ 0 \end{bmatrix} + \mathbf{d} \begin{bmatrix} 0 \\ 0 \\ T \cdot I \end{bmatrix} \tag{2.64}$$

$$S_{zz} = d_{33} TI$$

$$\mathbf{B} = \mathbf{d}' \begin{bmatrix} 0 \\ 0 \\ 0 \end{bmatrix} + \boldsymbol{\mu}^{\mathbf{T}} \begin{bmatrix} 0 \\ 0 \\ TI \end{bmatrix} \tag{2.65}$$

$$B_z = \mu_{33}^{T} TI$$

The strain in Eq. (2.64) can be converted into displacement by the replacement:

$$S_{zz} = \frac{\partial \zeta}{\partial z} \tag{2.66}$$

Since the strain in the equilibrium case is uniform axially, the strain in Eq. (2.64) can be written in terms of displacement as follows.

$$S_{zz} = \frac{\zeta_z(z_L)}{z_L}. \tag{2.67}$$

Thus, the no-load, steady state displacement can be written as the following:

$$\zeta_z(z_L) = d_{33} T z_L I. \tag{2.68}$$

From the derivation of the Young's modulus and magnetostrictive constants, it can be shown that

$$d_{33} = \frac{\kappa_{eff}}{Y_{eff}^H}. \tag{2.69}$$

The displacement can be written as

$$\zeta_z(z_L) = \frac{\kappa_{eff} T z_L}{Y_{eff}^H} I. \tag{2.70}$$

Although somewhat less compact, $\mu_{33}^T$ can also be written in terms of the parameters in Table 2.7,

$$\mu_{33}^T = \left[ \frac{\kappa_{eff} \kappa_{eff,z}}{Y_{eff}^H} + \mu_{33}^S \right]. \tag{2.71}$$

Table 2.8 gives the data for evaluating the dimensionless variables. For convenient reference, all the data for the model are collected in the table.

Table 2.8: Modeling Data for Prototype Actuator

| *Parameter* | *Value* | *Units* | *Description* |
|---|---|---|---|
| $r_g$ | 0.0063 | m | Radius of actuator rod |
| $r_c$ | 0.0111 | m | Outer radius of coil |
| $z_L$ | 0.1492 | m | Length of actuator rod |
| $T_c$ | 105 | - | Turns per coil |
| $\Delta z_c$ | 0.0159 | m | Length per coil |
| $T$ | 6614 | $m^{-1}$ | Turns per unit length |
| $\phi_0$ | $\frac{\pi}{2}$ | - | Angular dimension of cylindrical lamination |
| $\omega_1$ | $1.7261\times10^{4}$ | $s^{-1}$ | Natural frequency of longitudinal vibration |
| $\lambda$ | 0.1008 | - | Damping coefficient of longitudinal vibration |
| $I_{min}$ | 0.75 | amp | Minimum current for linear range |
| $\Delta I$ | 1.5 | amp | Linear range for current |
| $\mathscr{R}_L$ | 4 | ohm | Resistance of load resistor |
| $\mathscr{R}_C$ | 9.6682e-008 | ohm | Resistance of actuator coil |
| $\mathscr{G}$ | 4.4182 | ohm | Gain of current controlled amplifier |
| $\mu_0$ | $4\pi\cdot10^{-7}$ | T/(A/m) | Permeability of free space |
| $\sigma_C$ | $5.958\times10^{7}$ | m/ohm | Conductivity of copper (coil) |
| $\sigma_R$ | $1.7241\times10^{6}$ | m/ohm | Conductivity of actuator rod (Terfenol-D) |
| $Y_{eff}^{H}$ | $2.441\times10^{10}$ | Pa | Effective Young's modulus of Terfenol-D |
| $\kappa_{eff,r}$ | 0 | Pa/(A/m)=T | Effective magnetostriction constant, transverse direction |
| $\kappa_{eff,z}$ | 275.86 | Pa/(A/m)=T | Effective magnetostriction constant, axial direction |
| $\kappa_{eff}$ | 270.11 | Pa/(A/m)=T | Effective magnetostriction constant, unidirection |
| $\mu_{11}^{S}$ | $0.8644\times10^{-5}$ | T/(A/m) | Permeability of Terfenol-D in transverse direction |
| $\mu_{33}^{S}$ | $0.2268\times10^{-5}$ | T/(A/m) | Permeability of Terfenol-D in axial direction |
| $\rho$ | 9250 | $Kg/m^3$ | Density of Terfenol-D |

Table 2.9 evaluates Eq. (2.68) for the displacement, Eq. (2.63) for magnetic field, and Eq. (2.65) for the induction at the steady-state, no-load cases for the minimum and maximum current, 0.75 and 2.25 amperes.

Table 2.9: Minimum and maximum values of actuator variables over the linearized range using steady state, no load case

| *Parameter* | *Symbol* | *Minimum* | *Symbol* | *Maximum* | *Units* |
|---|---|---|---|---|---|
| Coil Current | $I_{min}$ | 0.75 | $I_{max}$ | 2.25 | Ampére |
| Magnetic field | $H_{min}$ | 4960.6 | $H_{max}$ | $1.4882\times10^{4}$ | Ampére/meter |
| Displacement | $\zeta_{min}$ | 8.1427 | $\zeta_{max}$ | 24.4283 | μm ($10^{-6}$ m) |
| Magnetic induction | $B_{min}$ | 0.0263 | $B_{max}$ | 0.0789 | Tesla |

The corresponding normalized variables for coil current, displacement, and magnetic induction are all valued at zero for the minimum current case and unity for the maximum. The range variables, $\Delta H$ , $\Delta\zeta$ , and $\Delta B$ , in Eqs. (2.76), (2.77) and (2.78) can be written in terms of the current range by substituting $\Delta I$ into the infinite solenoid equation, Eq. (2.63), the equations for displacement and induction at no-load, Eq. (2.68) and Eq. (2.65).

$$\Delta H = T \cdot \Delta I \,, \tag{2.72}$$

$$\Delta\zeta = \frac{\kappa_{eff} T z_L}{Y_{eff}^H} \Delta I \,, \tag{2.73}$$

$$\Delta B = \mu^T T \Delta I \,. \tag{2.74}$$

The formulae for converting the dimensioned variables to normalized variables using these data are the obvious linear relationships including the offset and range.

$$x^K = \frac{I - I_{min}}{I_{max} - I_{min}} = \frac{I - I_{min}}{\Delta I} \,. \tag{2.75}$$

$$x^N = \frac{\zeta_z - \zeta_{min}}{\zeta_{max} - \zeta_{min}} = \frac{\zeta_z - \zeta_{min}}{\Delta\zeta} = \frac{\zeta_z - \zeta_{min}}{d_{33} T z_L \Delta I}, \tag{2.76}$$

$$x^M = \frac{H - H_{min}}{H_{max} - H_{min}} = \frac{H - H_{min}}{\Delta H} = \frac{H - H_{min}}{T \Delta I}, \tag{2.77}$$

$$b = \frac{B - B_{min}}{B_{max} - B_{min}} = \frac{B - B_{min}}{\Delta B} = \frac{B - B_{min}}{\mu^T T \Delta I}. \tag{2.78}$$

The voltage scaling for the coil circuit equation is based on the same current range as in Eq. (2.75). In this case, the scaling is set so that the steady state voltage rise across the amplifier (or voltage drop across the coil and load resistor) is scaled to vary from zero to one for the current range from $I_{min}$ to $I_{max}$. The scaling can be written as the following.

$$v = \frac{\mathscr{V} - \mathscr{V}_{min}}{\Delta\mathscr{V}}, \tag{2.79}$$

where

$$\begin{aligned} \Delta\mathscr{V} &= \Delta I \left( \mathscr{R}_L + \mathscr{R}_C \right), \\ \mathscr{V}_{min} &= I_{min} \left( \mathscr{R}_L + \mathscr{R}_C \right). \end{aligned} \tag{2.80}$$

The parameters, $\mathscr{R}_C$ and $\mathscr{R}_L$, are the ohmic resistances of the coil and load resistor in the coil circuit. At steady state, the inductive component does not affect the voltage. At high frequency, the inductive component dominates the loop equation. The lack of an inductive component means that the dimensionless voltage goes well outside the range of zero to one in transients.

The geometrical scaling for the problem requires a normalization of the lengths in radial and axial directions. The dimensions of the rod may be chosen as the scaling factors.

$$\xi = \frac{z}{z_L}. \tag{2.81}$$

$$\rho = \frac{r}{r_g}. \tag{2.82}$$

A dimensionless time variable could also be defined either in terms of the period of the acoustic resonance or the radial magnetic diffusion time. However, a great deal of the physical understanding of the scaling of results is rooted in the frequency range of interest in units of Hertz. Therefore, the formulation retains time as a dimensioned variable.

The relationships in Eqs. (2.75) through (2.82) and the steady-state, no load relationships given by Eqs. (2.65) and (2.68) provide the equations needed to convert the vibration model, magnetic diffusion model and the amplifier circuit model into dimensionless variables.

**Effect of Neglecting Hysteresis**

The most significant approximation in the actuator model is to neglect the nonlinear behavior of the magnetostrictive material with linear constitutive properties as in Eqs. (2.3) and (2.4). Hysteresis complicates the modeling of almost any magnetic material, including the Terfenol-D. The effect is a non-linear, time-dependent process. The mathematical difficulty of modeling the hysteresis effect using, for example, the Preisach operator as proposed by Hughes and Wen is significant [20]. In this section, the

measured hysteresis of the prototype actuator is shown and the argument is made that the effect can be neglected if the amplitude of the transients is greater than a certain minimum value. Hence, the combination of saturation and hysteresis means that the amplitude of transient cases should cover nearly the full range of current defined in Table 2.9 for results that minimize the impact of saturation and hysteresis nonlinearities on the results.

The results of an experiment devised to show the effect of amplitude on the response is shown in Figure 2.1. In this experiment, a slowly varying sinusoidal current (20 Hz) is applied to all the actuator coils simultaneously. The average current is offset from zero so that the actuator is operating in the linear range of motion. The figure shows the traces of displacement versus current for a range of amplitudes for the time-varying component of the signal. As time advances, the hysteresis produces a counterclockwise loop in displacement and current. The degree of hysteresis manifests as the width of the loop. The amplitude dependence is indicated by a change in slope. For the largest amplitude signals, the path for increasing current is roughly parallel to and offset by approximately 0.3 amps to the right of the path for decreasing current. For the smallest amplitude signal, 0.14 amps, the actuator displacement hardly changes as the current changes. In the scale of this figure, the hysteresis is not evident for the smallest amplitude loop. However, if the scale is expanded, the hysteresis for this trace is also evident.

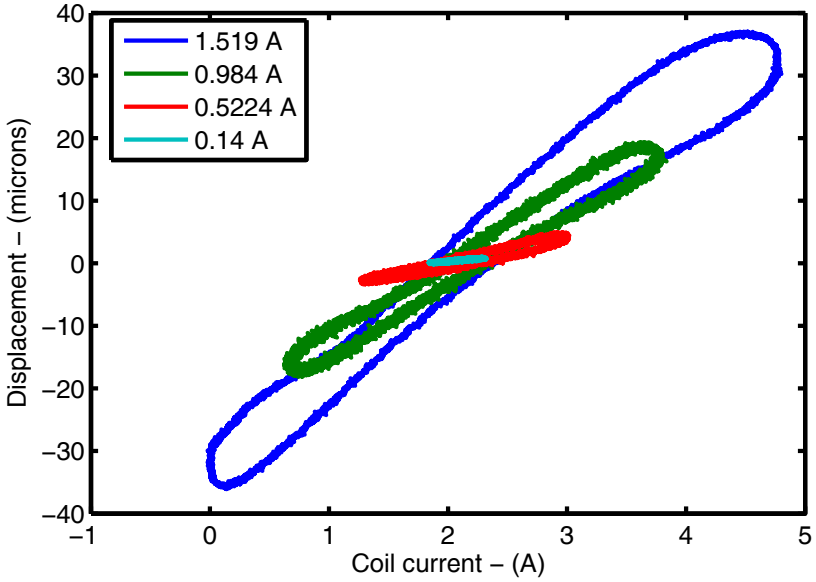


Figure 2.1: Actuator hysteresis obtained experimental data

The results in the figure suggest that hysteresis can be neglected with less impact for transients involving greater amplitude of coil current and displacement. For small amplitude signals which change less than 0.3 amps peak-to-peak, the slope of displacement versus current is quite small. However, for large amplitude signals on the order of 2 amps or more, the slope is steeper and the hysteresis is a smaller fraction of the total response. The larger amplitude current signals give a smaller hysteresis error in the position, on a relative basis, compared to the total position change. The slope of displacement to current is much larger giving a more detectable transient. This behavior suggests that neglecting hysteresis is a better approximation for larger amplitude transients. This observation suggests that the amplitude of experimental transients should be greater than a certain minimum value because of hysteresis and less than a maximum value because of saturation. With this in mind, the control test transients are designed to operate over the full current range of current in Table 2.9, 0.75 amps to 2.25 amps. This range corresponds to the second largest loop (green trace) in Figure 2.1.

## Summary of the Modeling of Magnetostrictive Materials

This section derives the form of linearized constitutive relations that are needed for modeling the multi-coil actuator. The general constitutive equations for magnetostrictive materials involve six element tensors for stress and strain and three dimensional vectors for magnetic field and magnetic induction. The relationship in terms of nine inputs and nine outputs is reduced by symmetry of the problem and the constant volume approximation to a system of four inputs and four outputs.

The approximations to neglect saturation and hysteresis are introduced and the effects of those approximations are discussed. The nonlinearity due to saturation limits the maximum amplitude transients that can be approximated with the linearized model, and hysteresis limits the smallest amplitude. The recommendation is made to formulate test cases to operate across the full scale of the normalized range of variables.

The normalization of variables in magnetics and vibration models depends on the magnetostrictive properties so the linear transformations defining the dimensionless variables are introduced in this section. This chapter collects the data which are used for the transformations in a single table. These data are used throughout the modeling chapters.

Identities which test the matrix manipulations and constant volume approximation are developed in APPENDIX A. The tests provide an independent confirmation of the formulation of the coefficients in the linearized magnetostrictive constitutive relationships.

# CHAPTER 3

# LONGITUDINAL VIBRATION MODEL

The physics of vibration is the aspect of the actuator dynamics that is exploited in the control of the multi-coil actuator to make it faster than a single coil actuator. The vibration can be modeled by a one-dimensional, longitudinal wave equation by applying the constant volume approximation introduced in Chapter 2. This chapter covers the derivation of the governing equation and boundary conditions for the vibration model, the conversion to dimensionless variables, the solution of the equation, and the representation of vibration dynamics as a state space system in descriptor form. The spatial part of the solution to the vibration problem is composed of orthogonal modal functions. The corresponding amplitude functions for the modes are obtained by applying the integral transform method to the vibration equation. The vibration equation solution is found by the superposition of the longitudinal wave modes and amplitude functions. The primary contribution of this derivation to the field of modeling of magnetostrictive actuators is the formulation for the coupling coefficients that interface the vibration modes to the individual coil currents in the circuit model and to the eddy current amplitude functions from the magnetics model. Sample calculations are presented for the vibration model as a stand alone system showing the step and impulse response in the time domain and amplitude and phase in the frequency domain for each of the coil inputs. Plots of these results and the discussion of their significance are given. The final result of the chapter is a fit of model parameters for fundamental frequency and damping coefficient to experimental data measured for the actuator.

APPENDIX B describes the integral transform solution and evaluation of the coupling coefficients for the vibration model. Test calculations for checking the derivation and programming are also described in the appendix.

## Literature Survey of Vibration Modeling

The wave equation represents a great many physical processes such as sound in air, a vibrating string, water waves, light, radio waves, and many others. The derivation of the longitudinal vibration equation representing sound waves in materials is found in almost every elementary physics or acoustics book. Standard texts [21-24] include derivations of the equation for longitudinal wave motion using much the same approach as taken in this report. The approach in this report differs from the standard textbook only because of the introduction of the magnetostrictive stress into the differential equation and the boundary conditions.

A one-dimensional, damped wave equation accounting for the distributed nature of the stress due to magnetostriction that is similar to the one presented here can be found in an early paper by Smith [25]. In Smith's paper, the one-dimensional wave equation is given as the model for vibration in a thin iron ring whose motion is stimulated by a magnetostrictive force. The magnetic field is generated by a toroidal coil. A derivation of the equation is not given but apparently comes from Joule. The subject of the paper is the experimental determination of the magnetostriction constant in the equation using measured data to fit the coefficient in the vibration model. Engdahl and many others give one-dimensional wave equations for magnetostrictive actuators and transducers. In the oft-cited handbook [9], Engdahl's distributed wave equation is slightly different than the

wave equation derived in this work. His wave equation lacks the damping term and he solves the spatial dependence with only the first mode of the trigonometric series.

The solutions available for the wave equation include the solution by the method of characteristics, Fourier's solution for a resonant cavity, and any number of finite difference or finite element methods. Since the method of characteristics does not readily convert into a state space approach, the research has to choose between the modal approach using Fourier's method and the finite difference (or finite element) approach. Both the modal method and the finite difference approach result in linear, time-invariant systems of ordinary differential equations that can be written as state space equations. The Fourier's modal solution has the advantage of giving a better match with frequency response than the finite difference method when both are evaluated with the same order of solution. The finite difference approach gives better steady state accuracy. Since frequency response is the main subject of the report, the modal approach is chosen for this research. The modal method is commonly described in textbooks on mathematical physics such as Courant and Hilbert [26, p. 288-290]. The procedure for the integral transform method for one-dimensional problems on a finite region is given by Özişik, [27, p. 508-518]

The literature available for modeling the magnetostrictive actuator or transducer which combine the effects of wave motion and magnetics range from models that represent the device as a single, spring-mass oscillator and single coil to much more detailed finite element model of magnetics and mechanical motion solved jointly. These models fall on both sides of the level of detail needed for control design and analysis of

the multi-coil device, either too simple to capture the essential physics or too complex and large in terms of matrix size to be useful in control analysis.

The simplest physical model represents the mechanical motion as a single spring-mass oscillator acted on by a single coil. The model is termed a gyrator model by Engdahl [9] because of a mathematical analogy with an electronic device of that name described by Tellegren[28]. The mechanical portion of the gyrator model is a single degree of freedom problem which produces the first resonance of the actuator. It does not include the dynamics of higher modes of vibration of the actuator rod. Nor does the gyrator model readily extend to account for the distributed nature of the coupling of multiple-coils to the actuator in which each coil provides a forcing function that is distributed along the rod length. The physics of the underlying continuum problem and the potential for interactions between different parts of the actuator have been eliminated by the lumped parameter approach, so that it not possible to handle the multiple coils and their interactions.

At the other extreme from the gyrator model of the actuator are models which represent distributed fields and vibration in too great detail to be useful for control modeling [17]. The vibration of a cylindrical piezoelectric transducer has been modeled with finite element analysis by Decarpigny [29]. The referenced paper develops a finite element model of a Tonpilz sonar transducer and determines if the vibration modes in the cylindrical actuator portion are primarily plane longitudinal waves. The finite element model is compared to a modal model to verify that the plane wave assumption is valid. The reference is primarily about the vibration model. Figures in the reference show a very fine mesh of elements in three dimensions to model the vibration. It is not clear how

the magnetic field is modeled and coupled to the vibration model. The same finite element code is apparently modified to represent magnetostrictive materials by Claeyssen. Decarpigny's finite element code is the ancestor of the commercial ATILA code [17].

Numerical stability of the control design calculations and computational time for real-time control calculations restrict practical system models to a maximum of forty to fifty state variables. This limitation means that finite element or finite difference models with thousands of nodes or elements do not translate into a system model that can be used in state space control without a considerable effort in model reduction. Moreover, the computer codes which offer detailed models of continuum mechanical modeling and magnetism are commercial products that are not available to the research.

A small number of models in the literature of magnetostrictive modeling involve an intermediate level of detail that is close to the needs of the multi-coil actuator problem. Engdahl and Svensson [30] solve the longitudinal vibration problem with lumped spring and mass approach. Kvarnsjö and Engdahl [31] present a two-dimensional, finite difference model of the vibration dynamics. The vibration model is coupled to a two dimensional magnetic field model that accounts for eddy current. These distributed models are based on a very coarse mesh, finite difference approximation. As indicated in this section, this research has taken the alternative approach of modeling spatial distribution using modal functions to obtain a more accurate response at high frequency.

### Governing Equation for Longitudinal Vibration

The original concept for the wave equation in continuous media was first constructed by Fourier as the limiting case for a system of discrete masses and springs as

the number of springs and masses approaches infinity. The lumped parameter model in which masses acted on by the forces of elasticity, magnetostrictive force and friction is a useful starting point to illustrate model. Figure 3.1 shows the lumped mass approach to modeling the actuator. The parameter, *max*, is an arbitrary number of spring-mass-coil elements.

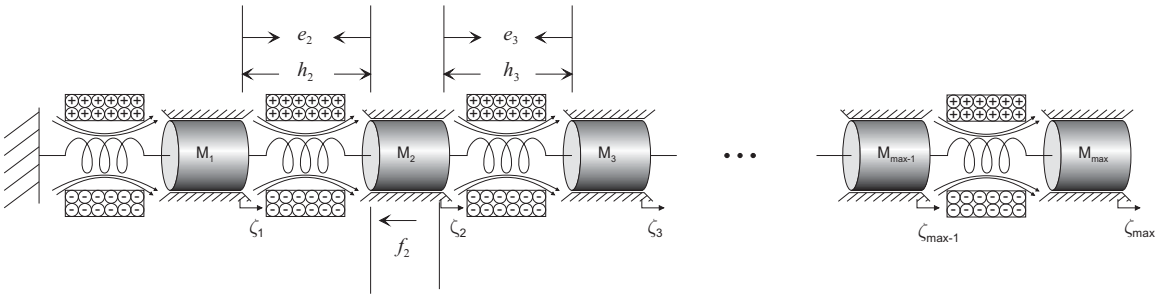


Figure 3.1: Elasticity and density of actuator rod represented as lumped springs and masses

In this illustration, the cylinders represent rigid masses, the coil-like structures represent the elastic properties of the rod, the box of circles with plus and minus symbols and associated curved lines represents the coils and their magnetic fields, and the fixed structures touching each mass represent a frictional surface that resists motion. The displacement of each mass from the unstressed position is indicated by the variable, $\zeta_j$. At rest with no magnetostrictive stress applied, each of the displacements is zero, $\zeta_i = 0$. The forces acting on the masses are labeled *e*, *h*, and *f*, in the figure representing the elastic and magnetostrictive stress and the friction force. Collectively, $T_2 = e_2 + h_2$ represents the total stress applied to the left face of $M_2$. In this idealization, the spring is massless, so by Newton's law, an equal and opposites stress of $-T_2$ must be applied to

the right face of $M_1$. Similar logic yields the stress, $T_3$, applied to the right face of $M_2$. The frictional force is idealized as a force proportional to velocity, $f_2 = -fA\Delta z \frac{d\zeta_2}{dt}$.

As the number of elements (*max*) in Figure 3.1 approaches infinity, the masses, springs, and coils are each reduced to a differential element. Deriving the wave equation for the rod starting with a differential element of mass illustrates how the magnetostrictive and elastic terms originate in Newton's equation of motion through the inclusion of the constitutive relations for magnetostriction. The term for magnetostrictive stress is distributed along the length of the rod. This feature for distributing the applied stress is the characteristic of the multi-coil actuator that is used to distribute the energy input to the actuator in space and time which results in the increase in the frequency response of the actuator.

Figure 3.2 shows a cross-sectional differential element of the rod as a free body with tension and frictional forces acting on it.

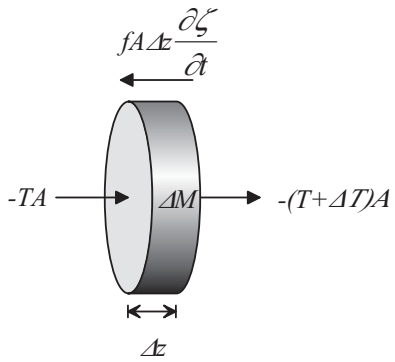


Figure 3.2: Free body diagram of a differential element of the actuator rod

In the figure, $T$ is the stress at the left face of the element, $A$ is the cross-sectional area, $\Delta z$ is a small length of rod, $\Delta T$ is the change in the stress along the length of the element,

and $f$ is the friction coefficient. The stress term, $T$, includes both magnetostrictive and elastic stresses.

Applying Newton's second law, we get

$$\underbrace{-TA+\left(T+\Delta T\right)A}_{\substack{\text{Forces applied to}\\ \text{left and right faces}}}-\underbrace{fA\Delta z\frac{\partial\zeta}{\partial t}}_{\text{Friction}}=\underbrace{\Delta M\frac{\partial^2\zeta}{\partial t^2}}_{\text{Acceleration}}. \tag{3.1}$$

Simplifying the equation and using $\Delta M=\rho A\Delta z$ gives the relation.

$$\frac{\Delta T}{\Delta z}-f\frac{\partial\zeta}{\partial t}=\rho\frac{\partial^2\zeta}{\partial t^2}. \tag{3.2}$$

Taking the limit as $\Delta z\to 0$ gives the expected partial derivative.

$$\lim_{\Delta z\to 0}\frac{\Delta T}{\Delta z}=\frac{\partial T}{\partial z}. \tag{3.3}$$

$$\frac{\partial T}{\partial z}-f\frac{\partial\zeta}{\partial t}=\rho\frac{\partial^2\zeta}{\partial t^2}. \tag{3.4}$$

The constitutive relationship for the magnetostrictive material relates the stress to the strain and magnetic flux. In Chapter 2, the three-dimensional relationships for strain and magnetostriction are reduced to an effective constitutive relationship in a single axial dimension. Equation (2.43) describes this relationship; i.e.,

$$T=Y_{eff}^{H}S-\kappa_{eff}\breve{H}. \tag{3.5}$$

In the magnetic model derivation, the magnetic field is a function of all spatial dimensions. To reduce that result to a one-dimensional vibration variable, the magnetic field is averaged over the cross-sectional area of the rod to give an effective average field in the transverse plane.

$$\breve{H}(z,t) = \frac{1}{\pi r_g^2} \int_{\phi=0}^{2\pi} \int_{r=0}^{r_g} H_z(r,\phi,z,t) r d\phi dr \,. \tag{3.6}$$

Taking the partial derivative of the linearized strain relation in Eq. (3.5) gives an expression containing the stress gradient needed in Eq. (3.4).

$$\frac{\partial T}{\partial z} = Y_{eff}^{H} \frac{\partial S}{\partial z} - \kappa_{eff} \frac{\partial \breve{H}}{\partial z} \,. \tag{3.7}$$

Recognizing that strain, *S*, is defined as

$$S = \frac{\partial \zeta}{\partial z}, \tag{3.8}$$

suggests that that the strain can be eliminated in favor of displacement by substituting Eq. (3.8) into Eq. (3.7).

$$\frac{\partial T}{\partial z} = Y_{eff}^{H} \frac{\partial^2 \zeta}{\partial z^2} - \kappa_{eff} \frac{\partial \breve{H}}{\partial z} \,. \tag{3.9}$$

Substituting Eq. (3.9) into Eq. (3.4) and rearranging terms gives the final form of the partial differential equation in dimensioned variables. The equation is easily recognized as the damped wave equation.

$$Y_{eff}^{H} \frac{\partial^2 \zeta}{\partial z^2} - \rho \frac{\partial^2 \zeta}{\partial t^2} - f \frac{\partial \zeta}{\partial t} = \kappa_{eff} \frac{\partial \breve{H}}{\partial z} \,. \tag{3.10}$$

To complete the vibration model, boundary conditions and initial conditions must be specified. The boundary condition at the free end represents the load on the actuator. We will choose an unloaded actuator for this model recognizing that this is one particular choice rather than a general solution for all possible loading conditions. A mass and a damper could be used as a simple model of a passive load such as a valve. Boundary conditions for the unloaded actuator rod are zero strain at the fixed end of the rod (e.g.

the displacement is zero) and zero stress at the free end. These conditions are expressed mathematically as

$$\begin{aligned} &\zeta = 0 \text{ at } z = 0 \text{ and} \\ &T = 0 \text{ at } z = z_L. \end{aligned} \tag{3.11}$$

For the stress at the free end of the actuator to be zero, the magnetic force must balance the elastic force; i.e.,

$$T = 0 = Y_{eff}^{H} S - \kappa_{eff} \breve{H} \text{ at } z=z_L. \tag{3.12}$$

Hence,

$$\frac{\partial \zeta}{\partial z} = \frac{\kappa_{eff} \breve{H}}{Y_{eff}^{H}} \text{ at } z = z_L. \tag{3.13}$$

**Dimensionless variables**

The governing equations for vibration in the rod can be rewritten in terms of dimensionless variables to reduce the number of physical parameters in the model to a minimum. The linear transformations described in Chapter 2 are based on unitary gain for the steady state, no-load condition. The following variable transformations in Chapter 2, define a new set of dimensionless, dependent and independent variables for the vibration model.

$$\xi = \frac{z}{z_L}. \tag{3.14}$$

$$x^N = \frac{\zeta_z - \zeta_{min}}{d_{33} T z_L \Delta I}. \tag{3.15}$$

$$h = \frac{\breve{H} - H_{min}}{T \Delta I}. \tag{3.16}$$

Regrettably, the symbol, *T*, that represents the turns per unit length in Eqs. **(2.76)** and **(2.77)** has been previously used to represent the stress. The overlap is tolerated since an explicit variable for stress is not needed for the remainder of the derivation.

Replacing the variables in the differential equation and boundary conditions gives the following differential equation.

$$\frac{\partial^2 x^N}{\partial \xi^2} - \frac{z_L^2 \rho}{Y_{eff}^H}\left(\frac{\partial^2 x^N}{\partial t^2} - \frac{f}{\rho}\frac{\partial x^N}{\partial t}\right) = \frac{\kappa_{eff}}{Y_{eff}^H d_{33}}\frac{\partial h}{\partial \xi}. \tag{3.17}$$

Equation (2.70) gives an identity for $d_{33}$ in terms of $Y_{eff}^H$ and $\kappa_{eff}$; i.e.,

$$\frac{\kappa_{eff}}{Y_{eff}^H d_{33}} = 1. \tag{3.18}$$

With this simplification, the dimensionless equation for vibration is the following.

$$\frac{\partial^2 x^N}{\partial \xi^2} - \frac{\rho z_L^2}{Y_{eff}^H}\left(\frac{\partial^2 x^N}{\partial t^2} - \frac{f}{\rho}\frac{\partial x^N}{\partial t}\right) = \frac{\partial h}{\partial \xi}. \tag{3.19}$$

Two dimensionless groups of parameters appear in the equation. Hence, only two parameters are needed to define the dimensionless damped wave problem uniquely. This is the main benefit of dimensionless variables. The two parameters can be defined freely. The most familiar dynamic characteristics are the fundamental frequency and the damping ratio of the rod. The actuator's longitudinal vibration dynamics are analogous to the resonance in a pipe which is closed at one end. The "quarter wave" resonant frequency of the pipe is usually written as a function of sound speed, *c*, and pipe length, *l*. The organ pipe formula applies to the actuator's longitudinal vibration when the end is not loaded. Written in cycles per second, the natural or undamped frequency is,

$$\upsilon = \frac{c}{4l}. \tag{3.20}$$

The general formula in radians per unit time is the following

$$\omega_1 = \frac{\pi}{2}\frac{c}{l}. \tag{3.21}$$

The parameter, $\omega_1$, is the frequency of the first resonance of the undamped oscillator in radians per second. Higher harmonics are obtained as multiples of 3, 5, 7, and so on times the base frequency.

The sound speed in the actuator material in terms of the properties of Terfenol-D is given by

$$c = \sqrt{\frac{Y_{eff}^H}{\rho}}. \tag{3.22}$$

The length of the actuator rod in this derivation is denoted by $z_L$. Hence, the group of parameters can be written in terms of the fundamental frequency where $\omega_1$ is in units of radians per second.

$$\left(\frac{\pi}{2\omega_1}\right)^2 = \frac{\rho z_L^2}{Y_{eff}^H}. \tag{3.23}$$

The damping ratio gives the ratio of one peak to the next in the decaying oscillation. In terms of the parameters of the system, each successive peak at the fundamental frequency drops by a factor of $e^{-2\pi\lambda}$. The damping ratio can be written in terms of the original parameters of the system as

$$2\lambda\omega_1 = \frac{f}{\rho}. \tag{3.24}$$

Writing the final version of the damped wave equation in terms of dimensionless variables, the resonant frequency, and the damping ratio gives the following.

$$\frac{\partial^2 x^N}{\partial \xi^2} - \left(\frac{\pi}{2\omega_1}\right)^2 \left(\frac{\partial^2 x^N}{\partial t^2} + 2\lambda\omega_1 \frac{\partial x^N}{\partial t}\right) = \frac{\partial h}{\partial \xi}. \tag{3.25}$$

The boundary conditions and initial conditions can be obtained from the same substitutions.

Boundary conditions

$$\begin{aligned} x^N(0,t) &= 0. \\ \frac{\partial x^N(1,t)}{\partial \xi} &= h(1,t). \end{aligned} \tag{3.26}$$

Initial conditions

$$\begin{aligned} x^N(\xi,0) &= 0. \\ \frac{\partial x^N(\xi,0)}{\partial t} &= 0. \end{aligned} \tag{3.27}$$

**Discussion of the governing equation and its solutions**

Equation (3.10) is the damped wave equation in one spatial dimension. The magnetostrictive effect appears both as a non-homogeneous forcing term in the differential equation and in the boundary condition for the free end. The part of the magnetostrictive force that is a distributed stress term in the differential equation is the point of departure in this modeling compared to other models used for designing control of magnetostrictive actuators [30, 32, 33]. The simplest models represent the motion of the actuator as a single spring and mass system acted on by a single coil which yield an ordinary differential equation for a harmonic oscillator to describe the dynamics of the actuator. The equation for induction in the coil gives a first-order system relating voltage

and current in the coil. The simple model is not general enough to model the multi-coil actuator. The single harmonic oscillator equation does not yield the higher harmonics that are needed to represent the high frequency behavior of the actuator vibration. The single coil does not model the interactions between multiple coils with each other or with the motion of the rod. The single lump can be thought of as a zero dimensional model.

A one-dimensional model of longitudinal vibration is a partial differential equation of the mechanical motion from which the higher harmonics of rod vibration are generated. The formulations for vibration in magnetostrictive actuators found in the literature only provide for a magnetic field which is generated by a single uniform coil along the length. A coil wound uniformly along the length of the actuator rod has a nearly uniform, axial magnetic field internal to the coil. Since the rod is long and thin, the magnitude of the field is very close to the value for an infinite coil, $H_{\infty} = T\,I$. In this formula, $T$ is the number of turns per unit length of the coil, and $I$ is the current per turn. The gradient in the field of the single uniform coil is steep at the end of the rod, approaching a step function. Approximating the distribution function of magnetic field as a step can be achieved in Eq. (3.10) by replacing the magnetic gradient term on the right hand with zero to represent the uniform field and retaining just the non-homogeneous boundary condition at the free end to represent the step there. This yields the following boundary condition:

$$\frac{\partial \zeta\left(z_L,t\right)}{\partial z} = \frac{\kappa_{eff} H\left(z_L,t\right)}{Y_{eff}^{H}} = \frac{\kappa_{eff} T}{Y_{eff}^{H}} I\left(t\right), \tag{3.28}$$

and following homogeneous differential equation:

$$Y_{eff}^{H}\frac{\partial^2\zeta}{\partial z^2}-\rho\frac{\partial^2\zeta}{\partial t^2}-f\frac{\partial\zeta}{\partial t}=0\,. \tag{3.29}$$

Equation (3.28) approximates the magnetostrictive effect of a uniform coil as a force applied at the end of the rod. While the equation accounts for all the modes, it is driven by only one force acting on the free end. A distributed input with multiple coils provides a way to introduce a driving force at different points in space and time which have different coupling coefficients with the modes of the rod. The distributed force sources can be timed so that their effect on the output is a maximum. This is the basis for the control strategy that underlies the multi-segmented actuator. The actuator control can be designed so that the inputs applied along the length by the multi-coil actuator are all in phase with the desired output resulting in no cancellation by the rod's acoustic response. This effect can be seen more easily in the calculated frequency response given later in this chapter. The optimum input strategy is found in Chapter 6. This section provides the mathematical model that computes the motion of the actuator with the coil current and eddy current as inputs.

**Modal solution to longitudinal vibration equation**

The solution of the damped wave equation is obtained by the integral transform method. The solution to Eq. (3.25) and associated boundary conditions is given in APPENDIX B. The integral transform method converts the partial differential equation into a series of ordinary differential equation. The solution is a series solution using an orthogonal series of trigonometric functions. The solution of the vibration subsystem from the appendix is repeated here. The displacement function is given by.

$$x^N(\xi,t)=\sum_{n=1}^{nmax}\frac{\sin(\beta_n\xi)}{N(\beta_n)}\chi_n^N(t). \tag{3.30}$$

where $N(\beta_n)$ is the normalization parameter for the sine function and $\chi_n^N(t)$ is the amplitude function that solves the following differential equation.

$$\begin{aligned}&\ddot{\chi}_n^N(t)+2\lambda\omega_1\dot{\chi}_n^N(t)+\left(\frac{2\omega_1\beta_n}{\pi}\right)^2\chi_n^N(t)\\&=\left(\frac{2\omega_1}{\pi}\right)^2\sum_{p=1}^{pmax}\sum_{m=1}^{mmax}\sum_{k=1}^{kmax}\frac{\beta_n\eta_pP_{k,m}}{\left(\eta_p^2-\beta_n^2\right)}\chi_{k,m,p}^M(t)+\left(\frac{2\omega_1}{\pi}\right)^2\sum_{j=1}^{jmax}Q_{n,j}x_j^K(t).\end{aligned} \tag{3.31}$$

The variables, $\chi_{k,m,p}^M(t)$ and $x_j^K(t)$, are the state variables from the magnetic subsystem model and coil subsystem model, respectively. The coefficients and parameters are defined in APPENDIX B.

## State Space Modeling

A more compact notation can be developed using matrix arithmetic to replace the indicial equations. First, the state variables are written as vectors. The magnetics states, which are derived in Chapter 4, can be arranged as the following one-dimensional vector

$$\mathbf{x^M}=\begin{bmatrix}X_1^M\\X_2^M\\\vdots\\X_l^M\\\vdots\\X_{lmax}^M\end{bmatrix}, \tag{3.32}$$

where

$$X_l^M=\chi_{k,m,p}^M : l=k+kmax\left[m-1+mmax(p-1)\right]. \tag{3.33}$$

The amplitude variables for the vibration and the coil currents are given in vector form as follows:

$$\mathbf{x^N} = \begin{bmatrix} \mathcal{X}_1^N \\ \mathcal{X}_2^N \\ \vdots \\ \mathcal{X}_n^N \\ \vdots \\ \mathcal{X}_{nmax}^N \end{bmatrix}; \; \mathbf{x^K} = \begin{bmatrix} x_1^K \\ x_2^K \\ \vdots \\ x_j^K \\ \vdots \\ x_{jmax}^K \end{bmatrix}. \tag{3.34}$$

The descriptor form for the vibration equation that combines the vibration subsystem with the other models is given in Eq. (1.10) of Chapter 1. The organization of the matrix equation places the terms involving the highest order state derivatives of each subsystem on the left hand side and the state variable terms and lower order derivatives on the right hand side. Each vector is multiplied by a constant coefficient matrix obtained from the process model. This yields the following equation:

$$\begin{aligned} \mathbf{E}^{11}\ddot{\mathbf{x}}^{\mathbf{N}} + \mathbf{E}^{13}\dot{\mathbf{x}}^{\mathbf{K}} + \mathbf{E}^{14}\dot{\mathbf{x}}^{\mathbf{M}} &= \mathbf{F}^{11}\dot{\mathbf{x}}^{\mathbf{N}} + \mathbf{F}^{12}\mathbf{x}^{\mathbf{N}} \\ &\quad + \mathbf{F}^{13}\mathbf{x}^{\mathbf{K}} + \mathbf{F}^{14}\mathbf{x}^{\mathbf{M}} + \mathbf{G}^{1}\mathbf{u}. \end{aligned} \tag{3.35}$$

where the coefficient matrices can be defined from the coefficients in Eq. (3.31); i.e.,

$$\mathbf{E}^{11} = \mathbf{I}_{nmax \times nmax}. \tag{3.36}$$

$$\mathbf{E}^{13} = \mathbf{0}_{nmax \times jmax}. \tag{3.37}$$

$$\mathbf{E}^{14} = \mathbf{0}_{nmax \times mmax}. \tag{3.38}$$

$$\mathbf{F}^{11} = -2\lambda\omega_1\mathbf{I}_{nmax \times nmax}. \tag{3.39}$$

$$\mathbf{F}^{12} = -\left(\frac{2\omega_1}{\pi}\right)^2 \operatorname{diag}\left(\beta_n^2\right). \tag{3.40}$$

$$\mathbf{F}^{13} = \left[ F_{n,j}^{13} \right] = \left( \frac{2\omega_1}{\pi} \right)^2 Q_{n,j} . \tag{3.41}$$

$$\mathbf{F}^{14} = \left[ F_{n,l}^{14} \right] = \left( \frac{2\omega_1}{\pi} \right)^2 \left[ \frac{\beta_n \eta_p P_{k,m}}{\left( \eta_p^2 - \beta_n^2 \right)} \right]. \tag{3.42}$$

The elements of the $\mathbf{F}^{14}$ array are arranged in a row in the same order as the $\mathbf{X}_M$ vector. The row index is $l = k + kmax\left[ m - 1 + mmax\left( p - 1 \right) \right]$.

The system input (to the amplifiers) does not affect the vibration directly. The effect is felt only through the currents that are generated in the coil. The coil currents are state variables in the coil model derived in Chapter 5. Hence, the input coupling matrix is zero.

$$\mathbf{G}^1 = \mathbf{0} . \tag{3.43}$$

Rewriting the matrix form of the equation, incorporating the zero matrices and the identity matrices yields

$$\ddot{\mathbf{x}}^{\mathbf{N}} = \mathbf{F}^{11}\dot{\mathbf{x}}^{\mathbf{N}} + \mathbf{F}^{12}\mathbf{x}^{\mathbf{N}} + \mathbf{F}^{13}\mathbf{x}^{\mathbf{K}} + \mathbf{F}^{14}\mathbf{x}^{\mathbf{M}} . \tag{3.44}$$

The displacement of the free end is an output that is needed by the control system. It is not given, however, by a single state. It can be expressed in the following form, obtained from Eq.(3.30) by setting $\xi = 1$;

$$\begin{aligned} y(t) = x^N(1,t) &= 2\sum_{n=1}^{nmax} \sin(\beta_n)\, \mathcal{X}_n^N(t), \\ &= 2\sum_{n=1}^{nmax} (-1)^{n-1}\, \mathcal{X}_n^N(t). \end{aligned} \tag{3.45}$$

In general, an output can be written in the following matrix format:

$$y(t) = \mathbf{C}^{11}\dot{\mathbf{x}}^{\mathbf{N}} + \mathbf{C}^{12}\mathbf{x}^{\mathbf{N}} + \mathbf{C}^{13}\mathbf{x}^{\mathbf{K}} + \mathbf{C}^{14}\mathbf{x}^{\mathbf{M}} + \mathbf{D}^{1}\mathbf{u} . \tag{3.46}$$

A comparison of Eqs. (3.45) and (3.46) indicates that the **C** and **D** matrices which compute the displacement at the free end can be expressed as follows:

$$\mathbf{C}^{11} = \mathbf{0}_{1\times nmax}, \tag{3.47}$$

$$\mathbf{C}^{12} = \left[ 2\left(-1\right)^{n-1} \right], \tag{3.48}$$

$$\mathbf{C}^{13} = \mathbf{0}_{1\times jmax}, \tag{3.49}$$

$$\mathbf{C}^{14} = \mathbf{0}_{1\times jmax}, \tag{3.50}$$

$$\mathbf{D}^{1} = \mathbf{0}_{1\times jmax}. \tag{3.51}$$

Eliminating the zero elements from Eq. (3.46) leaves the following equation for the displacement variable.

$$y^{N}\left(t\right) = \mathbf{C}^{12}\mathbf{x}^{N}. \tag{3.52}$$

where $y^{N}$ is the displacement of the actuator tip.

### Time and Frequency Response of the Vibration Model

A simulation of the vibration subsystem as a stand alone model tests the derivation and programming of this part of the model before assembling the full system. The stand alone model captures the dynamics associated with longitudinal vibration and shows that the model reproduces the dynamics expected for a damped wave equation. Additional tests cases are presented in APPENDIX B. The stand alone vibration model evaluates the displacement of the free end of the actuator as a function of the coil current. Both state space and transfer function versions of the model can be obtained. To eliminate the magnetic field due to eddy currents, the eddy current states, $\mathbf{x}^{M}$, may be set

to zero. With this simplification, the displacement is only a function of the coil current, which may be treated as the input for this problem.

$$\ddot{\mathbf{x}}^{\mathbf{N}} = \mathbf{F}^{11}\dot{\mathbf{x}}^{\mathbf{N}} + \mathbf{F}^{12}\mathbf{x}^{\mathbf{N}} + \mathbf{F}^{13}\mathbf{x}^{\mathbf{K}} . \tag{3.53}$$

If a second equation is added to integrate the velocity, $\dot{\mathbf{x}}^{\mathbf{N}}$, then the problem is completely determined.

$$\begin{bmatrix} \ddot{\mathbf{x}}^{N} \\ \dot{\mathbf{x}}^{N} \end{bmatrix} = \begin{bmatrix} \mathbf{F}^{11} & \mathbf{F}^{12} \\ \mathbf{I} & \mathbf{0} \end{bmatrix} \begin{bmatrix} \dot{\mathbf{x}}^{N} \\ \mathbf{x}^{N} \end{bmatrix} + \mathbf{F}^{14}\mathbf{x}^{K} . \tag{3.54}$$

The displacement of the free end is determined by the following equation:

$$y^{N} = \begin{bmatrix} \mathbf{0}_{1\times nmax} & \mathbf{C}^{2} \end{bmatrix} \begin{bmatrix} \dot{\mathbf{x}}^{N} \\ \mathbf{x}^{N} \end{bmatrix}. \tag{3.55}$$

The stand alone system can be put into standard state space form by defining the system matrices as the following.

$$\mathbf{A}^{N} = \begin{bmatrix} \mathbf{F}^{11} & \mathbf{F}^{12} \\ \mathbf{I} & \mathbf{0} \end{bmatrix}. \tag{3.56}$$

$$\mathbf{B}^{N} = \mathbf{F}^{13} . \tag{3.57}$$

$$\mathbf{C}^{N} = \begin{bmatrix} \mathbf{0}_{1\times nmax} & \mathbf{C}^{2} \end{bmatrix}. \tag{3.58}$$

$$\mathbf{D}^{N} = \mathbf{0}_{1\times jmax} \tag{3.59}$$

This vibration model can be simulated using MATLAB[34] to show both time domain and frequency domain response of the actuator. Figure 3.3 shows the time domain response for a set of ten cases in which each coil is individually energized in a step change in the current variable. The model used for the simulation is low order; i.e. *nmax*=10. The step in the input is initiated at $t=5\times10^{-5}$ s. Each trace represents a separate

transient. The plot shows the time delay between the step in coil current and the response of the tip displacement. The pulse originating from the first coil (nearest the free end) arrives at the free end first. The pulses from the coils are separated by a time delay corresponding to the time for an acoustic wave to travel the length of a single coil. The theoretical time delay based on the model parameters is given by:

$$\tau_{\Delta z_c} = \frac{\Delta z_c}{c} = \frac{\pi}{2 j_{max} \omega_1} = 9.1 \times 10^{-6} \text{ s}. \tag{3.60}$$

The delay between the pulses during the initial rise, evaluated numerically from the data in Figure 3.3, is an average of $8.9 \times 10^{-6}$ s.

The truncation error in the modal model is evident in the simulated results. The high frequency ripple in the response is due to the truncation of the Fourier series at ten terms. In addition to the ripple, the plot shows that the response of coil 1, which is nearest the free end, is significantly below the rest. This anomaly is also due to truncation error. The end coil is somewhat less effective than the rest because it extends beyond the active length of the actuator rod, but the effectiveness of the coil only accounts for a small part of the problem. The truncation error is greatest at the free end because the boundary condition used for the series of mode function is a homogeneous derivative condition (Neumann), whereas the boundary condition for the problem is nonhomogeneous derivative. Consequently, the modal solution does not converge on the boundary, only on the interior of the rod. The resulting error is most apparent with the coil input at the free end which has a substantial field diffusing out of the rod. All other coils have nearly zero field at the free end resulting in much smaller error. If a higher order solution is used, for example *nmax*=40, the response of coil 1 becomes consistent with the rest of the coils. The dependence of steady state accuracy and transient response

on the number of modes is shown in APPENDIX B. The effect of the truncation error is not serious. From the plot, the full amplitude current in the first coil causes an error of 0.02 in the displacement. On this basis, the low order model results are considered acceptable.

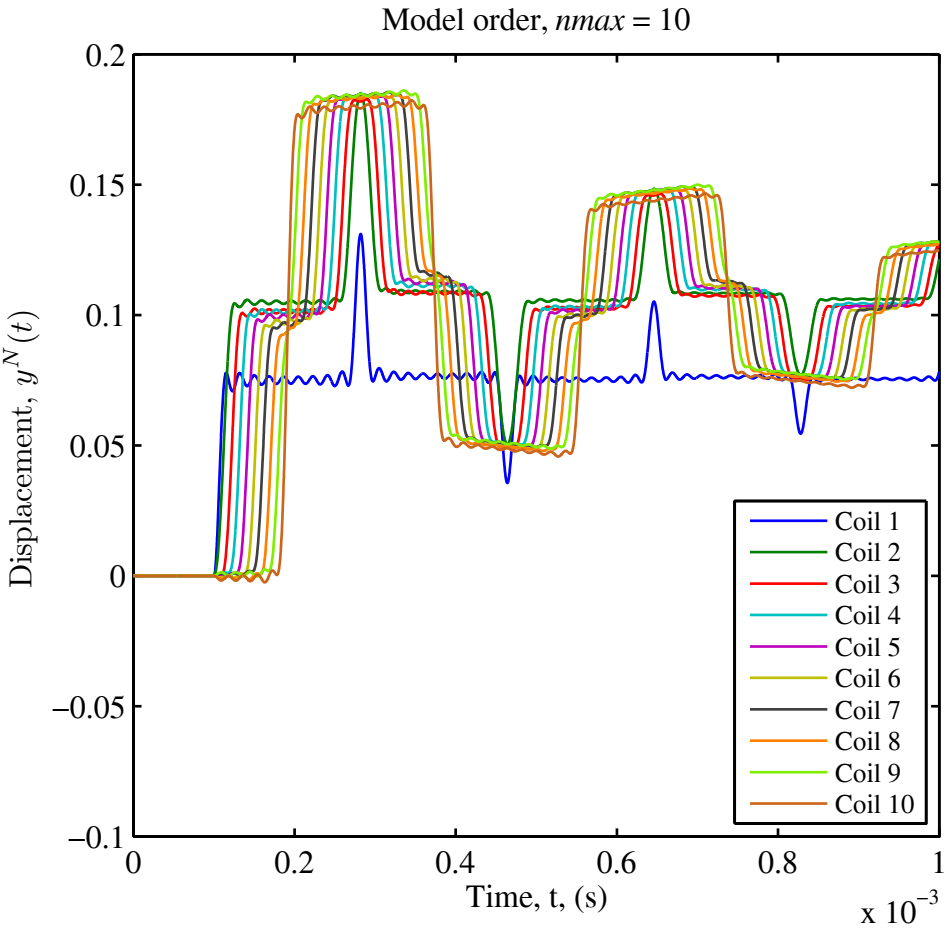


Figure 3.3: Actuator displacement due to step change in coil current

The advantage of the multi-coil actuator can be anticipated from this plot. To get the benefit from the multi-coil design, the inputs to the individual coils need to be separated by a certain time delay to arrive at the actuator tip when needed. To follow a reference trajectory, the input should lead the reference by the acoustic delay between the

coil input and the displacement. The plots also show the ringing as the traveling waves generated by the step inputs travel back and forth along the rod. Following the step, the control system must attenuate the kinetic energy in the acoustic waves so that the rod comes to rest rapidly.

Another type of type response is shown in the three-dimensional surface plot in Figure 3.4. This figure shows the response of spatial distribution of strain, $x^N(\xi,t)$ from Eq. (3.30) to an impulse function given by the following:

$$x_j^K(t) = \delta(t). \tag{3.61}$$

In the case shown, a coil in the middle of the actuator, *j*=6, is energized by the impulse function. The figure shows that the magnetostrictive force pushes outward in both directions, compressing the rod below the energized coil and expanding the rod above. Two pulses are generated that move in opposite directions. The progress of the pulses is shown in the time dimension of the plot. The figure shows the two wave forms crisscrossing and diminishing in amplitude over a few periods of oscillation. The pulses reflect at each end with inversion on the fixed wall where $\xi = 0$ and without inversion at the free end where $\xi = 1$. The plot demonstrates that the model is behaving as expected.

The frequency response model of the vibration model is obtained by applying the Fourier transform to the system in Eq. (3.54). For a linear time-invariant system, this is accomplished by replacing derivatives with ($\frac{d}{dt} \Rightarrow i\omega$). The transformed variable is indicated by the underscore.

$$\frac{\underline{y}(i\omega)}{\underline{\mathbf{x}}^K(i\omega)} = \mathbf{C}^N\left(i\omega\mathbf{I} - \mathbf{A}^N\right)^{-1}\mathbf{B}^N. \tag{3.62}$$

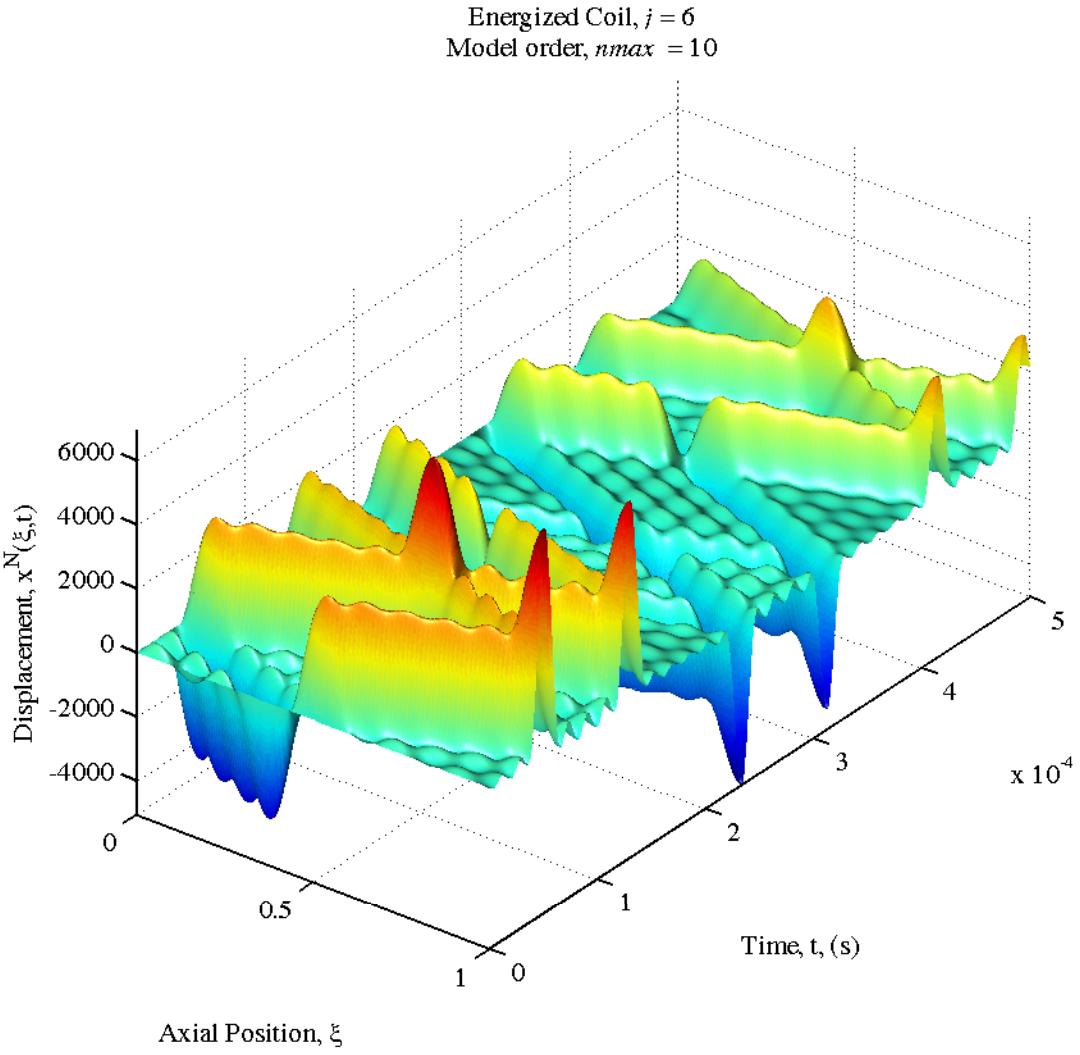


Figure 3.4: Impulse response showing traveling pulse

In this form, the matrix transfer function, $\underline{y}^N(\omega)/\underline{\mathbf{x}}^K(\omega)$, is a row vector ($1\times jmax$) of scalar transfer functions. Each trace represents the response of the displacement of the free end to a unit harmonic signal applied to a particular coil. The input signal is given by:

$$\left|\underline{x}_j^K(\omega)\right| = 1. \tag{3.63}$$

Figure 3.5 is the frequency response of the vibration model which has been computed and plotted using MATLAB. The plot shows the amplitude and phase of the transfer functions in Eq. (3.62) versus frequency. The frequency is normalized using the fundamental frequency of the actuator, $\omega/\omega_1$, so that the resonant frequencies at odd multiples of the base frequency are evident. The amplitude plot shows the resonant peaks and shows that each coil affects the resonance by a different amount. The phase plot shows that the timing relationships for the coils are also different. The phase of each coil changes by 0 or $\pm\pi$ radians as the frequency passes through a resonance. The phase for each coil changes differently. The direction of change is determined by the position of the coil with respect to the nodes and antinodes of the standing waves associated with the resonance.

The frequency response gives the clearest picture for understanding the operation of the multi-coil actuator and its enhanced frequency response. Consider the amplitude and phase at three frequencies $\omega/\omega_1$ =1, 2, and 3. The phases at $\omega/\omega_1$ =1 are all approximately equal to zero so the responses from all coils are nearly in phase. However, the amplitudes are significantly different. To get the greatest response from the actuator for fixed total power delivered to the coils, more current should be sent to coils with high gain and less current to the coils with low gain.

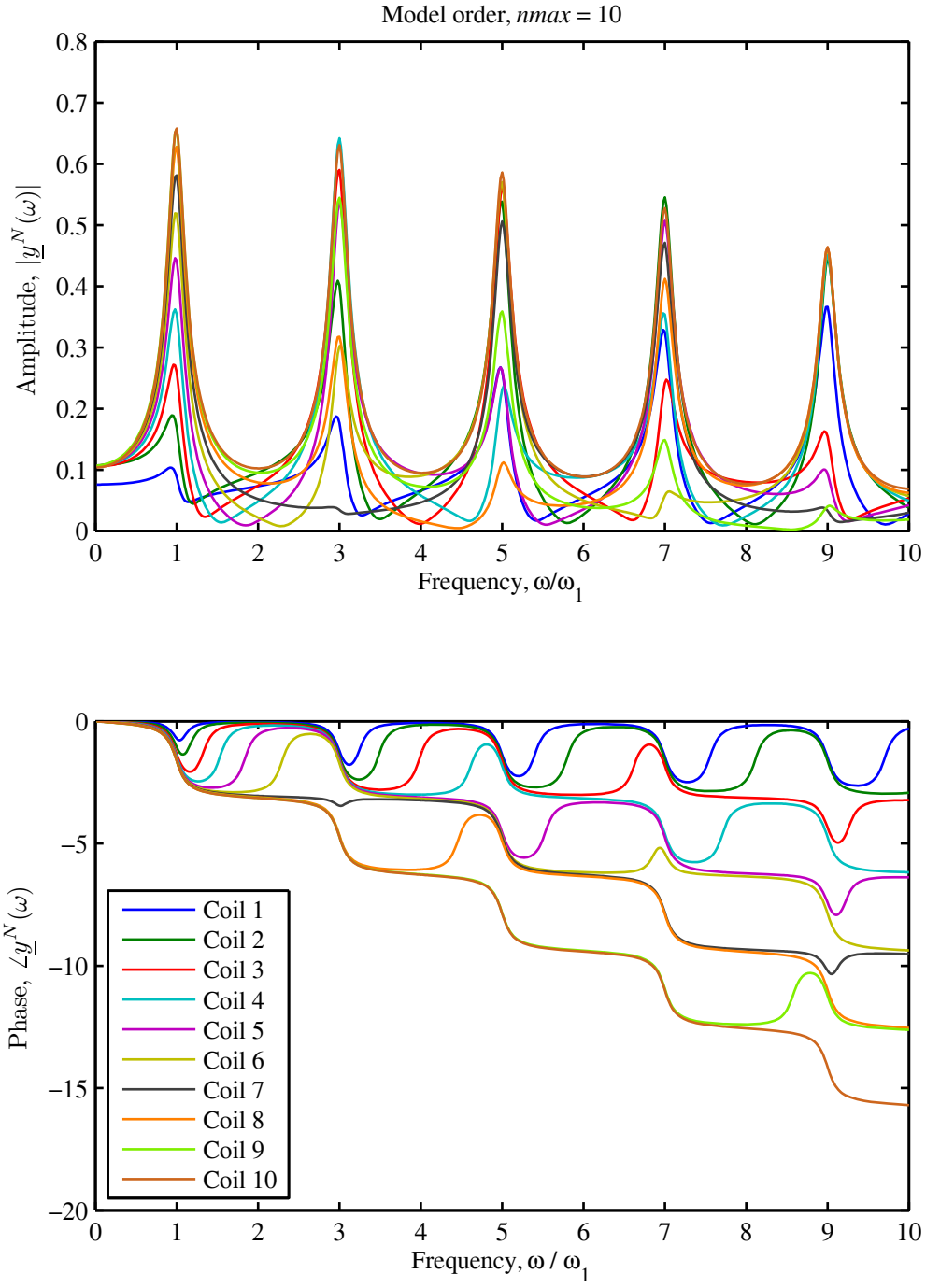


Figure 3.5: Frequency response of actuator to individual coil inputs

Now, consider the amplitude and phase values at $\omega/\omega_1$ =2. At this point, the phase values for coils 1-4 are all close to 0 while the phase for coils 7-10 are all -π. The amplitudes cover a range of values with coils 5 and 6 having the lowest gain. The phase difference means that, if the coils are energized in unison, coils 1-4 would work against coils 7-10 canceling their effect. The overall actuator gain for fixed power would be enhanced if the signals in 7-10 are reversed in sign and the signals sent to 5-6 are zero. Now examine the values at $\omega/\omega_1$ =3. The phases for coils 8-10 are clustered at -3π/2 while coils 1-6 are close to –π/2. Again, the coils are working against each other. Coil 7, which has very low amplitude, is in between. The amplitudes and phases for the input signals can be chosen that give much higher output than operating the coils in unison with the same current. The exact optimum distribution for maximum displacement for fixed total power in coils as a function of frequency is derived in Chapter 6 as the introduction to the optimum control problem. The frequency response plot gives a physical understanding of how the multi-coil actuator can achieve a significant improvement in the bandwidth of the actuator in comparison to a single coil.

**Experimental Determination of Fundamental Frequency and Damping Ratio**

The dimensionless equation for vibration model contains only two parameters: the fundamental frequency, $\omega_1$, and the damping ratio, $\gamma$. The fundamental frequency can be estimated from the Young's modulus, density, and length of the actuator using Eq. (3.23). The material properties of Terfenol have been studied extensively. Engdahl [9, p. 108] gives a range of values for Terfenol-D, 25-35 GPa, that are appropriate for zero dimension models. In Table 2.7, an effective Young's modulus that is calculated from three-dimensional stress and strain relationships. The effective value

$Y_{eff}^{H} = 24.41$ GPa falls near Engdahl's published range. The range of resonant frequencies based on Engdah's data for Young's modulus is useful for comparison. Table 3.1 gives the material data from Engdahl for density and Young's modulus. The length of the actuator rod is from design data. The speed of sound and the fundamental frequency for the actuator are calculated from Engdahl's typical data.

Table 3.1: Fundamental frequency estimate from engineering data

| *Parameter* | *Value* | *Units* |
|---|---|---|
| Density | 9250 | (kg/m$^{3)}$ |
| Young's modulus | 25-35 | (GPa) |
| Length of actuator | 0.1524 [5.875 in] | (m) |
| Speed of sound | 1650-1950 | (m/s) |
| Frequency | 2697- 3190 | (Hz) |
| Frequency | 16,945- 20,049 | (rad/sec) |

The damping ratio is not given in the engineering specifications for the actuator; therefore a simple frequency response experiment using a conventional Etrema actuator (not the ten coil actuator) was performed to estimate a typical value. The procedure used in this research was to fit the model predictions to the experimental data using the damping ratio and fundamental frequency as free parameters.

The experiment to measure damping and fundamental frequency uses a standard Etrema AA-140J025 actuator. The actuator's nominal fundamental frequency is 2400 Hz. A sine wave generated by Wavetek signal generator is applied to the actuator coil through a Crown LVC 608 amplifier. A feedback circuit using the measured current is used for automatic control of the amplitude of current to the actuator. The position is measured using a Philtec Model D63 Fiber Optic Displacement Probe which produces a

voltage linearly related to displacement. The current in the coil is obtained by measuring the voltage across a load resistor in series with the actuator coil. The voltage signals for current and position are monitored by National Instruments digital input and output board on a Dell Precision computer which converted the data to 12 bit digital values. A Labview program operating on the Dell computer captured the time series data and performed a fast Fourier transform (FFT). The amplitude and phase of the current and position at the peak response from the FFT are located in the spectrum and are recorded manually. This procedure is repeated at a series of discrete frequencies, mapping the frequency response one frequency value at a time. The ratio of the magnitude of position to current plotted versus the frequency forms an experimental amplitude plot of the frequency response. The difference of the angles gives the phase plot. The amplitude and phase thus measured are manually transferred into a MATLAB program which plots the data. The modeling equation for a single node model is fitted to the experimental curve using a least sum of the squared differences in the real and imaginary parts. The experimental data can be written as a complex number.

$$\underline{x}_{\exp,j} = \left|\underline{x}\right|_j \left[\cos\left(\alpha_j\right) + i\sin\left(\alpha_j\right)\right], \tag{3.64}$$

where $\left|x\right|_j$ and $\alpha_j$ are the amplitude and phase at the frequency, $\omega_j$.

The model response at $\omega_j$ can be written as complex number as the following. The gain parameter, $g_1$, is needed because the experimental current and displacement are not normalized as in the model.

$$\underline{x}_{\text{model}}\left(\omega\right) = \frac{g_1\omega_1^2}{-\omega^2 - 2\gamma\omega_1\omega^2 i + \omega_1^2}. \tag{3.65}$$

A complex difference can be taken between the experimental and model results.

$$\Delta x_j = \underline{x}_{\text{exp},j} - \underline{x}_{\text{model}}\left(\omega_j\right). \tag{3.66}$$

The sum of the squared differences, *J*, is the quantity which can be minimized to fit $\omega_1$, $\gamma$, and $g_1$. Using the rules for complex arithmetic, sums of the squared differences can be computed by the following:

$$J = \sum_{j=1}^{j_M} \left(\Delta x_j\right)^{\dagger} \left(\Delta x_j\right). \tag{3.67}$$

where $\left(\Delta x_j\right)^{\dagger}$ is the complex conjugate of $\left(\Delta x_j\right)$ and $j_M$ is the number of frequency points in the experimental data.

The results of the parameter fitting experiments are shown in a series of figures. Figure 3.6 shows the amplitude and phase of the displacement in a test that ranged in frequency from 28 Hz to 5000 Hz. Figure 3.7 shows the amplitude of the current for the same experiment. Data for the current are not recorded at every frequency. Interpolated values are generated to fill in the missing data. Both measured and interpolated data are shown in Figure 3.7. The nearly flat response of the current is an indication that the improvised control circuit for current is successful. The phase for the current is nearly zero for all measurements so it is not recorded.

The fit is performed by minimizing the error in the imaginary and real parts individually. Figure 3.8 shows the real and imaginary parts of the measured data and the fitted model. The same data are plotted in Figure 3.6 as magnitude and phase.

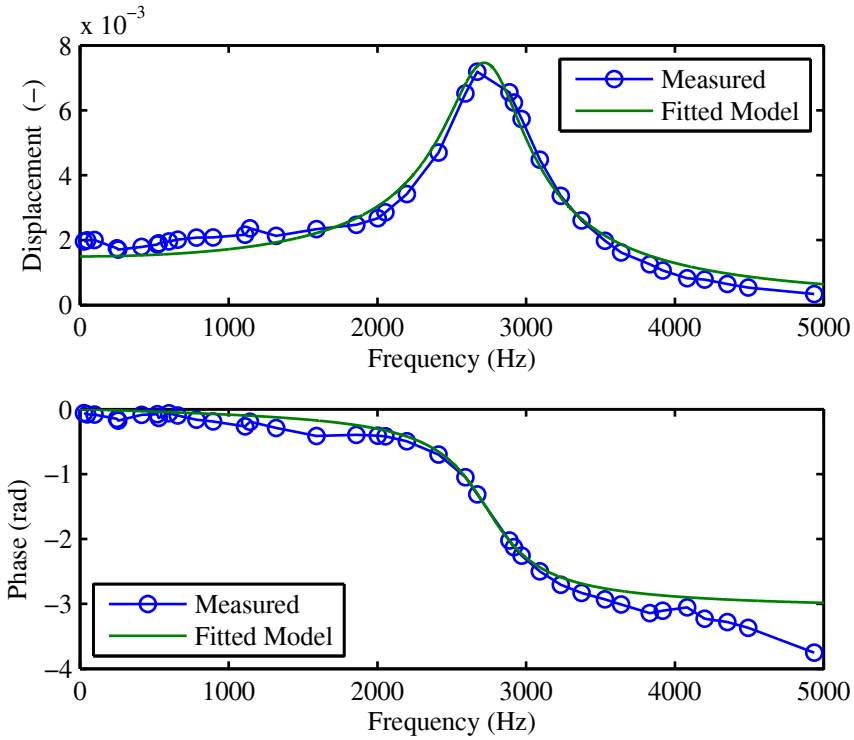


Figure 3.6: Magnitude and phase data for displacement for 28-5000 Hz test

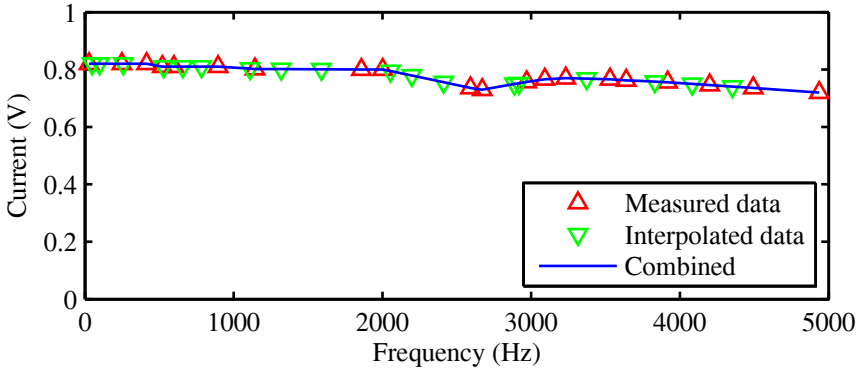


Figure 3.7: Measured and interpolated current data for 28-5000 Hz test

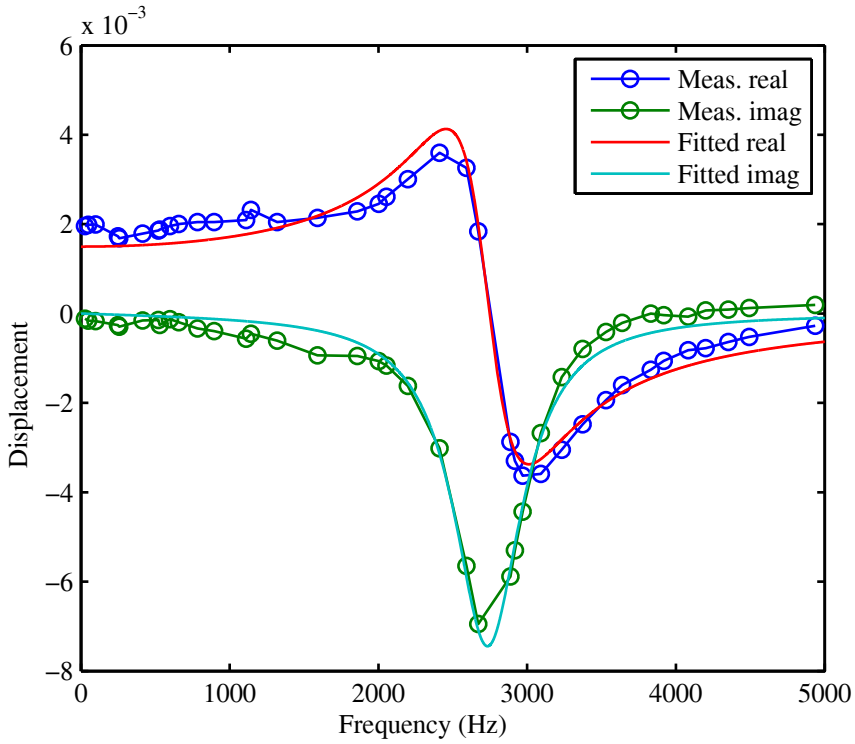


Figure 3.8: Measured and fitted actuator response as real and imaginary components for 28-5000 Hz Test

A second test was performed over a higher frequency range. These data cover the frequency range from 1000 Hz to 10,000 Hz to show the fundamental and first harmonic in the actuator response. The measurements of the current are not recorded in this instance because the current transfer function is nearly a constant in the previous experiment. To fit these data, a second order modal model is needed. The formula for the second order model is computed using a single coil and two vibration modes. The resulting second order model written in terms of frequency response is the following.

$$\underline{x}_{\text{model}}(i\omega) = 16 g_1 \left(\frac{\omega_1}{\pi}\right)^2 \frac{\left(-\omega^2 - 2\gamma\omega_1\omega i + 5\omega_1^2\right)}{\left(-\omega^2 - 2\gamma\omega_1\omega i + 9\omega_1^2\right)\left(-\omega^2 - 2\gamma\omega_1\omega i + \omega_1^2\right)}. \qquad (3.68)$$

The same fitting procedure, except using the second order model, is applied to the second set of data. The magnitude and phase plot of experimental data and the fitted data are shown in Figure 3.9.

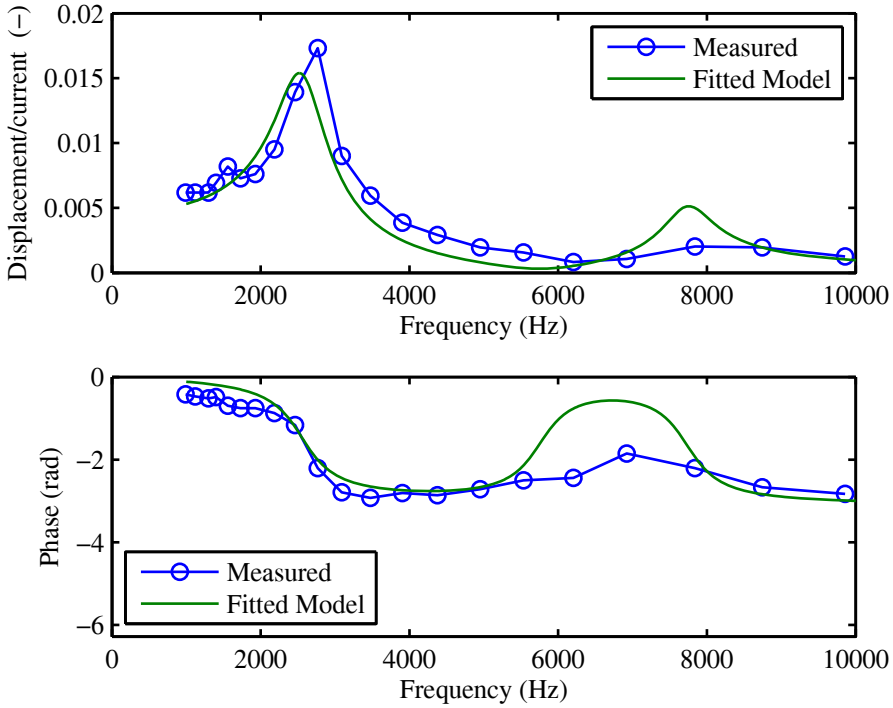


Figure 3.9: Frequency response of displacement for 1000-10,000 Hz

The fitted parameters from the two experiments are summarized in Table 3.2. The gain parameters are not comparable because the calibration of the experiments is different and because the high frequency test did not employ the current transfer function in a ratio. The resonant frequency is close to the value predicted from engineering data. The parameters in Table 3.2 from the 28-5000 Hz test are used in all calculations wherever typical values are needed.

Table 3.2: Actuator modeling data from least squares fit

| Parameter | 28-5000 Hz Test (Figure 3.6) | 1000-10000 Hz Test (Figure 3.9) |
|---|---|---|
| $\omega_1$ | 2747.6 | 2580.2 |
| $\lambda$ | 0.1008 | 0.1369 |
| $g_1$ | 0.0015 | 0.0051 |

**Summary of the Vibration Model**

The vibration model has been developed from the general equations of motion. The effect of magnetostrictive coupling is introduced through a constitutive relation involving the stress and strain and magnetic field. The continuous differential equation is reduced to an infinite series of ordinary differential equations by the integral transform method. The truncated series is used as a state space model of vibration. An integral formulation for coupling coefficients between the eddy current and coil currents in the model is a product of the integral transform method. Methods are presented for evaluating the coefficients either analytically or numerically.

Stand alone calculations of the model are presented to illustrate the time and frequency response of the model. The results illustrate the wave propagation of stress generated by magnetic field from a coil. The simulations illustrate how the time and frequency response of the actuator displacement are affected by the spatial position of the coil. Three-dimensional visualizations illustrate how a pulse of energy from a coil travels acoustically in the rod.

Mathematical tests are constructed in APPENDIX B tests that use the properties of the solution to verify the derivation and programming. The normalization of variables

is used to test the steady state of produced by the model. The eigenvalues computed from the state space model of vibration are compared to an analytical formula. Fourier series solutions that represent the coupling of vibration modes to coil current and to eddy current are evaluated at various numbers of term to assess the truncation error. Time simulations of the model are generated with 20, 40 and 80 vibrational modes to assess the truncation error of the series solution.

# CHAPTER 4

# MAGNETIC MODEL

Magnetic field is the physical phenomenon that couples the longitudinal vibration, the eddy current, and the electronic circuit models together. Each model produces a current density distribution (in the case of vibration, the strain produces magnetization which can be treated as an equivalent current) which in turn produces a magnetic field. The magnetic field acts on the magnetostrictive rod to generate stress which produces the linear motion of the actuator. A time-varying field from any of the current sources also generates an electric field along every current density path by Faraday's law of induction. The induction couples the current of one current distribution to itself by self-induction and to the other current distributions in the actuator through mutual induction. The inductance is the coupling parameter that relates voltage in a circuit or path to the derivative of current in the source distribution.

This chapter on the magnetic model is primarily concerned with deriving spatial distribution functions for the magnetic field and eddy current density. The magnetic field distributions are used in Chapter 3 in the vibration modeling to calculate the coupling coefficients between the vibration modes and the coil and eddy current. The eddy current density distributions are used in Chapter 5 to compute the inductance coefficient between coil and eddy current.

The derivation of the magnetic modeling equations begins with three of the four Maxwell's equations for electromagnetic fields. After applying the quasi-static magnetic field approximation and the linearized constitutive equations, Maxwell's equations are

reduced to a single, three-dimensional, diffusion problem in **H**. All three components of vector field are non-zero; however, only the axial component is needed for the coupling with the vibration model. For the purposes of the actuator model, the magnetic field can be solved for the axial component alone. The fields due to coils and eddy current can be separated in the general equation and solved individually. The coil field is calculated by a detailed representation of the actuator geometry and materials using a finite element magnetics code called FEMM [35]. The eddy current field is obtained by solving the magnetic diffusion equation on the pie-shaped cylinder geometry using a summation of orthogonal modes. Conventional boundary and interface conditions are used by the finite element code to solve the static magnetic diffusion problem. An approximation to the boundary condition is needed for the modal solution to the eddy current's field.

To model the eddy current field, a three-dimensional geometry is needed to represent the pie-shaped cylinder configuration of the laminated rod and the axial dependence of coil current from the multi-coil design. The modal solution to the eddy current field uses a three-dimensional integral transform method to reduce the time dependence to a set of first-order, ordinary differential equations. The solution to the set of differential equations is the amplitude of each of the orthogonal modes of the eddy current's magnetic field. The eigenvalues of the differential equations are the poles of the eddy current model and characterize the frequencies at which each mode's contribution becomes significant. The amplitude variables are the state variables for the state space system. The modal approach results in an efficient, low-order model for the eddy current's three-dimensional effects. For the ten-coil prototype actuator, the full

three-dimensional eddy current effect is captured sufficiently for the frequency range of interest in only ten state variables.

The eddy current density distribution is derived from the eddy current's field distribution. The eddy current density is a function of the same amplitudes and eigenvalues as the magnetic field solution. The spatial modal functions for the density distribution, however, are different.

## Literature Survey on Magnetic Modeling

The difficulty in modeling the magnetics of the actuator rod is that it involves coupled solutions of spatial distributions of magnetostrictive stress, eddy current, and magnetic field in multidimensional, vector relationships. Spatial effects that are frequently neglected in general magnetostrictive actuator models are the primary concern in the multi-coil actuator problem. In particular, the axial dependence of magnetic field, which can be ignored with conventional, single-coil magnetostrictive actuator designs, must be represented accurately in the multi-coil actuator. The gradient in the magnetic field along the length of the actuator rod is the source of the strain distribution along the rod and is the physical process underlying the high frequency response of the multi-coil design. Also, because the goal is to achieve higher frequency response, eddy current, which can frequently be neglected for low frequency applications, becomes a significant issue. Compounding the difficulty of multiple, coupled, differential equations is the need for a low-order model so that real-time control can be based on the model. It is not surprising that it is necessary to start with fundamental equations and to derive an entirely new approach to model the actuator. Despite the lack of a perfectly suited solution in prior work, related work does exist in modeling magnetostrictive actuators and modeling

of magnetics that bears on the formulation and serves as a starting point for this work. This background section on magnetic modeling cites prior modeling work of magnetostrictive devices as well as citing the basic textbook references on magnetics and eddy current modeling that form the starting point for the model that follows. In particular, the features that need to be added to existing models in creating the new model are indicated.

The prior work specifically in modeling of magnetostrictive materials and devices began with the introduction of the "giant" magnetostrictive materials, like Terfenol-D in the 1980's. The works cited in the vibration chapter regarding zero, one-dimensional and two-dimensional mechanical modeling of magnetostrictive transducers are equally applicable to the magnetic modeling. Engdahl's monograph, *Handbook of Giant Magnetostrictive Materials* [9], which is cited many times in this dissertation, is the main compilation of research on the magnetostrictive materials and contains several ways of modeling of the magnetics of Terfenol-D actuators and transducers.

In most applications of magnetostrictive actuators, the actuator rod is fully surrounded by a single uniform coil and is contained within a closed magnetic circuit with low reluctance. At low frequency, eddy current can be neglected. Thus, the magnetic field can be approximated as a uniform field both axially and radially with its value computed from the formula for field inside an infinite solenoid. Under these circumstances, the magnetic "model" reduces to a simple proportionality with current with no spatial or temporal dynamics. This approach is the basis for device models that are focused on investigating the nonlinear and hysteretic effects of magnetostriction. The model is a point or lumped model rather than a spatially distributed model of the actuator.

The assumption in a point model is that all points in the actuator can be represented by average values for the magnetic field, magnetic flux density, stress and strain. The basic point model can be found in Pratt [36]. Other examples include Smith's work on modeling hysteresis as a motion of a magnetic domain wall [37] and Dapino's work characterizing the nonlinear material properties of Terfenol-D using a Tonpilz sonar transducer [38, 39].

Models that account for eddy current effects generally add a radial diffusion equation to the point model representing a solid cylinder. The first publication of eddy current modeling applied to magnetostrictive actuators appears to be Kvarnsjö and Engdahl [40]. Other authors have reported similar models including Evans [41] and Huang [42]. Hall and Flatau present a model of the radial dependence of magnetic field accounting for eddy current using an analytical solution to the radial dependence in the frequency domain [43]. The solution does not represent the azimuthal or axial dependence of magnetic field which are needed for the pie-shaped lamination and the multi-coil effects, but the radial model does have the mathematical advantage (because the axial dimension is neglected) that the interface condition between coil and actuator rod is not approximated as it is in this dissertation.

The formulation for finite element with joint solution of the magnetics and vibration are given by Lhermet for the ATILA code [17] and by Benatar for a finite element solution constructed using general purpose finite element code called FEMLAB (now called COMSOL Multiphysics) [44]. Benatar comments that he encountered problems with memory storage which prevented solving some of the relatively simple geometries with his program. A generalized finite element formulation is presented by

Besbes [45]. The formulation includes linear, nonlinear magnetics with linear elastic properties, and fully nonlinear versions of the constitutive properties. The Besbes' programming is not described, but apparently a solution is obtained for a thin film of material in *x-y* geometry.

The magnetic model development starts with the fundamental laws of classical electrodynamics known as Maxwell's equations. The equations can be found in any standard electrodynamics text [46-48]. Jackson [47] describe a simplification of Maxwell's equations called the quasi-static magnetic approximation that is appropriate for the regime of the problems in which the finite speed of light can be neglected and electromagnetic fields can be treated as if they propagate instantly. This approximation is valid when the product of characteristic length times frequency of interest is small compared to the speed of light in the material as it is in the actuator. The quasi-static magnetic approximation reduces the electromagnetic modeling equation from the usual wave equation to a diffusion equation. Stoll [49] develops the magnetic field diffusion equation from Maxwell's equations. His formulation applies the quasi-static magnetic approximation and is geared specifically to eddy current problems. The derivation in this dissertation follows Stoll's method except that the terms for magnetostriction are added and the anisotropic permeability is retained in the modeling data.

A number of general purpose magnetics codes exist which solve the magnetic diffusion problem numerically. Most magnetics codes are expensive, commercial products that are not available to this research. However, the Finite Element Magnetic Modeling (FEMM) [35] code originally written by David Meeker as a part of his doctoral dissertation at the University of Virginia is a powerful, general purpose, two-dimensional

magnetics code that is made available free of charge by its author. The code is actively maintained by Meeker in his professional work and has a large number of academic users. The FEMM code allows detailed representation of the geometry of the actuator for steady state and harmonic current distributions. The code has proven to be very useful for the magnetic modeling in this paper. However, the finite element solution does not produce results that can be used directly in the control analysis problem. First of all, the code does not include the magnetostriction effect which means that the fields generated by strain magnetization must calculated by some other technique. Second, the code produces spatial distributions of magnetic variables, but these do not translate directly into the matrices needed for a state-space model. A matrix formulation for the magnetics problem is created internally by the code as a part of the finite element solution technique, but, just as in the finite difference approach, it is a very high order matrix and not suitable for control. Thirdly, the finite element code only solves the steady state case and harmonic cases, not the general, time-dependent problem needed for the control design. Fourth, the two-dimensional code in cylindrical coordinates does not have the capability to solve the three-dimensional actuator rod with pie-shaped laminations. The eddy current in the pie-shaped lamination is a concern for the high frequency control that is the objective of the actuator development. The lack of an adequate representation of the pie-shaped cylinder geometry limits the usefulness of FEMM's harmonic solution for the actuator.

Despite the shortcomings of the FEMM code for the actuator control problem, the detailed representation of the actuator geometry and materials makes a much more complete solution of the actuator possible. Detailed maps of the distribution of magnetic

field and magnetic vector potential generated by the steady state coil current can be calculated by the FEMM code. The steady state problem does not produce eddy currents and is not affected by the pie-shaped lamination. The steady state distributions are used to calculate the coupling coefficients between the coil current and the vibration model and to calculate the inductance coefficients for the coil model. Additionally, the maps of magnetic field and eddy current calculated by FEMM have provided considerable insight into the equations which model electromagnetics. Parametric studies varying the geometry and material properties aid the understanding of the dependencies of the problem on physical properties of the materials and the geometry. The FEMM numerical results also provide a point of comparison for the analytical solutions which are also derived and experimental results that are observed. The consistency of results from these three approaches builds confidence that the mathematical problem is correctly understood. A brief description of the problem solved by the FEMM code and the models of the actuator that are used in this analysis are given in APPENDIX C.

Once the magnetics problem is reduced to a diffusion equation, a large body of work on the mathematical methods for solving diffusion problems can be brought to bear to solve the problem. Problems in heat transfer, nuclear reaction dynamics, and chemical processes in addition to the magnetics problems involve the classical diffusion equation. The approach in this paper uses the integral transform method to separate the spatial and temporal parts of the solution. The temporal solution becomes the state space model of the magnetics. Heat transfer texts [27, 50, p. 218-219] are the primary resources used by this author for the integral transform solution technique.

## Geometry of the Actuator Rod

Figure 1.2 shows the general configuration of the actuator. The actuator contains a number of concentric regions for the case, magnetic return path, coil, and actuator rod. The full details of the actuator geometry are solved for the coil current distribution using a steady state FEMM calculation (see APPENDIX C). However, for the purpose of discussing the spatial effects of coil and eddy current fields and the requirements of the magnetic solution, the geometry of the actuator is simplified to just three regions as shown in Figure 4.1: rod, coil, and region outside the coil. The coil is divided into individually controlled coils axially. Each coil produces a magnetic field that is centered within the coil while also diffusing axially and radially. Because the coils are axisymmetric, the fields due to coils are axisymmetric.

Eddy current turns out to be a significant problem for the actuator in the frequency range of interest. At sufficiently high frequency, the eddy current field cancels any field generated by the external circuit inside the conducting material. As discussed in the introduction, the eddy current problem was anticipated before constructing the prototype actuator and the rod was laminated to reduce the eddy current. The insulated boundaries of the pie-shaped segments interrupt the circular eddy current paths and generate electric fields on the surfaces of the radial faces that cause the eddy current to flow around the perimeter of the pie-shaped segment. While the component of current density that is perpendicular to the insulated surface is zero, the current density parallel to the surface is non-zero. The eddy current and the electrical potential gradient that drives the eddy current around the segment's path must have both radial and azimuthal components. Figure 4.2 illustrates the path that the eddy current must take.

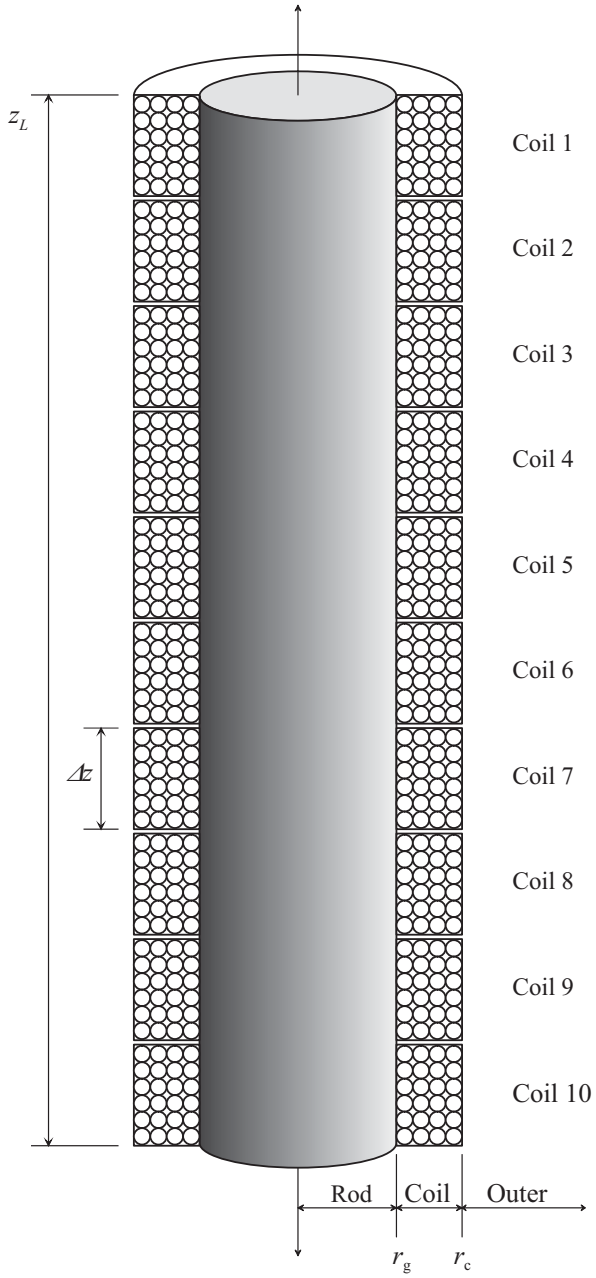


Figure 4.1: Simplified rod and coil geometry for analytical solution of magnetics problem

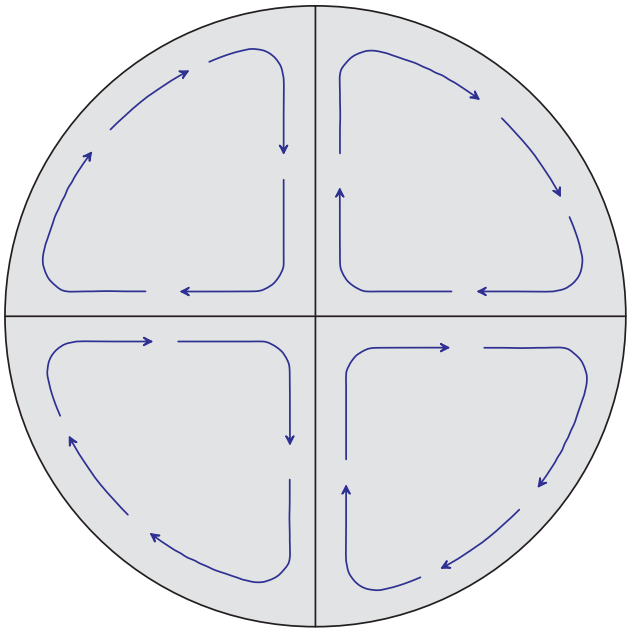

Figure 4.2: Eddy current paths in a pie-shaped cylinder

The length of the path for the electron current (summing all four quadrants together) is greater than a circumferential path around the solid cylinder. The resistivity of a material is the resistance per unit path length (ohms/meter). Thus, the resistance that the electrons see in one transverse of their path is higher for the pie-shaped lamination than for a solid circular cylinder. A longer path has higher resistance and thus lower eddy current. A less obvious result is that the time constant for the magnetic field to diffuse into the center of the pie-shaped segment is reduced as well. The magnetic field diffuses inward from the insulated edges of a conducting region. The coil field travels instantaneously (due to the quasi-steady magnetics approximation) without attenuation from the edge of the cylinder along the radial cuts so that $H_z$ on the radial boundary is unaffected by the eddy current field. The coil magnetic field diffuses into the conducting region from all surfaces of the pie-shaped cylinder. Diffusion into the pie-shaped segment is faster than into the solid circular rod because the average thickness of the pie-

shaped cylinder is less than the solid cylinder. Consequently, the time constants for the magnetic dynamics of the pie-shaped lamination are less than those of the solid cylinder.

The magnetic modeling section derives a dynamic model for eddy current and the field that it produces. The main chapter derives the governing equation from Maxwell's equations and gives sample calculations to illustrate the solution. The details of the integral transform solution of the governing equation and various numerical tests to verify the solution are given in APPENDIX D.

The distribution of field for the eddy current involves all three dimensions because of the radial and azimuthal components of current. The field has non-zero components in all three directions and the field varies in all three dimensions. The axial component eddy current density is zero throughout the actuator. Accounting for the multi- dimensional effects with a low order model is the main challenge of the magnetic model.

### The Governing Equation for Magnetics

The first step in the magnetic model development is to derive the magnetic diffusion equation from Maxwell's equations following the same general steps as given in Stoll while adding the terms for magnetostriction in the constitutive equations and accounting fo anisotropic permeability. Three major approximations are used in solving the magnetics problem:

- The constitutive equations for Terfenol-D are treated as linear thereby neglecting hysteresis, saturation, and other nonlinear effects.
- A quasi-static magnetic field is assumed approximating the speed of electromagnetic waves as infinite.

- The boundary condition for eddy current's magnetic field on the surface of the pie-shaped segment is approximated as being homogeneous (Dirichlet condition).

The section in Chapter 2 discussing the Terfenol-D constitutive equations includes a justification of the linearization approximation and the limitations that the approximation places on the range of solution. The quasi-static magnetics approximation is commonly applied in eddy current problems. It is described and justified for eddy current problems in Jackson [47]. The third is the subject of a detailed discussion the section on boundary and interface conditions in this chapter. The first two approximations are introduced immediately. The third is introduced after separating the problem into the components of the field due to eddy current and due to coil current.

The conventional derivation of the governing equation for magnetic field in eddy current problems starts with Maxwell's equations in which the quasi-static magnetic field has already been applied.

$$\nabla \times \mathbf{H} = \mathbf{J} \tag{4.1}$$

$$\nabla \times \mathbf{E} = -\frac{\partial \mathbf{B}}{\partial t} \tag{4.2}$$

$$\nabla \cdot \mathbf{B} = 0 \tag{4.3}$$

The linearized magnetostriction matrix equations derived in Chapter 2 provide one constitutive equation for this system. Ohm's law provides a second constitutive equation relating electric field to current density.

$$\mathbf{J} = \sigma \mathbf{E} \tag{4.4}$$

$$\mathbf{B} = \boldsymbol{\mu}^{S} \mathbf{H} + \boldsymbol{\kappa} \mathbf{S} \tag{4.5}$$

The next step is to manipulate these five equations algebraically into the form of the diffusion equation. The objective is to eliminate **B**, **E**, and **J** in favor of **H**. First, take curl of Eq. (4.1) and substitute for **J** using Eq. (4.4) to get

$$\begin{aligned} \nabla\times\nabla\times\mathbf{H} &= \nabla\times\mathbf{J} \\ &= \sigma\nabla\times\mathbf{E}. \end{aligned} \tag{4.6}$$

Next, substitute Eq. (4.2) into the right hand side of Eq. (4.6). to get

$$\nabla\times\nabla\times\mathbf{H} = \sigma\nabla\times\mathbf{E} = -\sigma\frac{\partial\mathbf{B}}{\partial t}. \tag{4.7}$$

Using the vector identity $\nabla\times\nabla\times\mathbf{X} = \nabla(\nabla\cdot\mathbf{X}) - \nabla^2\mathbf{X}$, Eq. (4.7) becomes

$$\nabla(\nabla\cdot\mathbf{H}) - \nabla^2\mathbf{H} = -\sigma\frac{\partial\mathbf{B}}{\partial t}. \tag{4.8}$$

The first term can be simplified and the effect of anisotropic diffusion can be brought out by using Maxwell's equation from Eq. (4.3).

$$\nabla\cdot\mathbf{B} = 0 = \nabla\cdot\left[\boldsymbol{\mu}^S\mathbf{H} + \boldsymbol{\kappa}\mathbf{S}\right] = \nabla\cdot\boldsymbol{\mu}^S\mathbf{H} + \nabla\cdot\boldsymbol{\kappa}\mathbf{S}. \tag{4.9}$$

The first term on the right hand side is the conventional linear permeability of magnetic materials. The second term describes the magnetostrictive effect due to strain. The first term on the right hand side of Eq. (4.9) can be expanded into its vector components using the orthotropic permeability of Terfenol from Eq. (2.56).

$$\begin{aligned} \nabla\cdot\boldsymbol{\mu}^S\mathbf{H} &= \left(\frac{\mu_{11}^S}{r}\frac{\partial rH_r}{\partial r} + \frac{\mu_{11}^S}{r}\frac{\partial H_\phi}{\partial\phi} + \frac{\mu_{33}^S\partial H_z}{\partial z}\right) \\ &= \mu_{11}^S\left[\nabla\cdot\mathbf{H} + \left(\frac{\mu_{33}^S}{\mu_{11}^S} - 1\right)\frac{\partial H_z}{\partial z}\right]. \end{aligned} \tag{4.10}$$

The divergence in cylindrical coordinates is defined as

$$\nabla \cdot \mathbf{X} = \left( \frac{1}{r} \frac{\partial r X_r}{\partial r} + \frac{1}{r} \frac{\partial X_\phi}{\partial \phi} + \frac{1 \partial X_z}{\partial z} \right). \tag{4.11}$$

Thus, Eq. (4.10) can be rearranged as follows:

$$\nabla \cdot \boldsymbol{\mu}^S \mathbf{H} = \mu_{11}^S \left[ \nabla \cdot \mathbf{H} + \left( \frac{\mu_{33}^S}{\mu_{11}^S} - 1 \right) \frac{\partial H_z}{\partial z} \right]. \tag{4.12}$$

The magnetostrictive term in Eq. (4.9) can be evaluated using the constant volume approximation from Chapter 2 to give the following.

$$\begin{aligned} \nabla \cdot \boldsymbol{\kappa} \mathbf{S} &= \nabla \cdot \begin{bmatrix} -\frac{\kappa_{51} r}{4} \frac{\partial}{\partial z} \\ 0 \\ \kappa_{33} - \kappa_{13} \end{bmatrix} \frac{\partial \zeta_z}{\partial z} \\ &= \left( \frac{2\kappa_{eff,z} - \kappa_{51}}{2} \right) \frac{\partial^2 \zeta_z}{\partial z^2}. \end{aligned} \tag{4.13}$$

Inserting the result from Eq. (4.10) and Eq. (4.13) into Eq. (4.9) gives the following.

$$\nabla \cdot \mathbf{H} = -\left( \frac{\mu_{33}^S}{\mu_{11}^S} - 1 \right) \frac{\partial H_z}{\partial z} - \frac{1}{\mu_{11}^S} \left( \kappa_{33} - \kappa_{13} - \frac{\kappa_{51}}{2} \right) \frac{\partial^2 \zeta_z}{\partial z^2}. \tag{4.14}$$

Substituting Eq. (4.14) into Eq. (4.8) yields.

$$\nabla \left[ \left( \frac{\mu_{33}^S}{\mu_{11}^S} - 1 \right) \frac{\partial H_z}{\partial z} + \left( \frac{2\kappa_{eff,z} - \kappa_{51}}{2\mu_{11}^S} \right) \frac{\partial^2 \zeta_z}{\partial z^2} \right] + \nabla^2 \mathbf{H} = \sigma \frac{\partial \mathbf{B}}{\partial t}. \tag{4.15}$$

While the above equation has three components, we only need its axial component for the vibration model because the constant volume approach has been applied to reduce the wave equation to one-dimensional axial vibration. The axial component of Eq. (4.15) is given by the following.

$$\left(\frac{\mu_{33}^S}{\mu_{11}^S}-1\right)\frac{\partial^2 H_z}{\partial z^2}+\left(\frac{2\kappa_{eff,z}-\kappa_{51}}{2\mu_{11}^S}\right)\frac{\partial^3 \zeta_z}{\partial z^3}+\nabla^2 \mathrm{H}_z=\sigma\frac{\partial B_z}{\partial t}. \tag{4.16}$$

The scalar Laplacian can be expanded into individual terms. After simplifying and rearranging, the result is the following equation.

$$\frac{1}{r}\frac{\partial H_z}{\partial r}+\frac{\partial^2 H_z}{\partial r^2}+\frac{\partial^2 H_z}{r^2\partial\phi^2}+\frac{\mu_{33}^S}{\mu_{11}^S}\frac{\partial^2 H_z}{\partial z^2}=\sigma\frac{\partial B_z}{\partial t}-\left(\frac{2\kappa_{eff,z}-\kappa_{51}}{2\mu_{11}^S}\right)\frac{\partial^3 \zeta_z}{\partial z^3}. \tag{4.17}$$

The axial component of Eq. (4.5) gives the relationship between the magnetic inductance and the magnetic field and strain. This relationship can be differentiated with time to yield the following.

$$\frac{\partial B_z}{\partial t}=\mu_{33}^S\frac{\partial H_z}{\partial t}+\kappa_{eff,z}\frac{\partial S_z}{\partial t}. \tag{4.18}$$

The strain can be written in terms of displacement as

$$S_z=\frac{\partial \zeta_z}{\partial z}. \tag{4.19}$$

Inserting these results into Eq. (4.17) eliminates $B_z$ from the equation and gives an equation in which the dependent variables are $H_z$ and $S_z$. The left-hand-side of this equation can be recognized as a three-dimensional diffusion equation with anisotropic diffusion coefficients.

$$\begin{aligned}\frac{1}{r}\frac{\partial H_z}{\partial r}+\frac{\partial^2 H_z}{\partial r^2}+\frac{\partial^2 H_z}{r^2\partial\phi^2}+\frac{\mu_{33}^S}{\mu_{11}^S}\frac{\partial^2 H_z}{\partial z^2}-\sigma\mu_{33}^S\frac{\partial H_z}{\partial t}&\\ =\frac{\kappa_{eff,z}}{\mu_{33}^S}\left[\sigma\mu_{33}^S\frac{\partial S_z}{\partial t}-\frac{\mu_{33}^S}{\mu_{11}^S}\left(1-\frac{\kappa_{51}}{2\kappa_{eff,z}}\right)\frac{\partial^2 S_z}{\partial z^2}\right]&.\end{aligned} \tag{4.20}$$

The right hand side can be written in terms of either displacement or strain. The displacement version is given by the following.

$$\frac{1}{r}\frac{\partial H_z}{\partial r}+\frac{\partial^2 H_z}{\partial r^2}+\frac{\partial^2 H_z}{r^2\partial\phi^2}+\frac{\mu_{33}^S}{\mu_{11}^S}\frac{\partial^2 H_z}{\partial z^2}-\sigma\mu_{33}^S\frac{\partial H_z}{\partial t}$$
$$=\frac{\kappa_{eff,z}}{\mu_{33}^S}\frac{\partial}{\partial z}\left[\sigma\mu_{33}^S\frac{\partial\zeta_z}{\partial t}-\frac{\mu_{33}^S}{\mu_{11}^S}\left(1-\frac{\kappa_{51}}{2\kappa_{eff,z}}\right)\frac{\partial^2\zeta_z}{\partial z^2}\right]. \tag{4.21}$$

Equation (4.21) is a general form for magnetic diffusion for both magnetostrictive and conventional magnetic materials. By choosing the material properties appropriately, Eq. (4.21) reduces to a conventional magnetic diffusion problem. For example, by selecting a zero value for the magnetostriction constant ( $\kappa_{eff,z}=0$ ), the terms on the right hand side drop out and the equation represents a non-magnetostrictive material. The effect of anisotropic permeability is captured by the ratio of permeabilities, $\frac{\mu_{33}^S}{\mu_{11}^S}$, in the axial component of the divergence. For an isotropic material, the radial and axial components of permeability are equal, $\mu_{33}^S=\mu_{11}^S$. With this choice of parameters, Eq. (4.21) becomes a conventional isotropic diffusion equation.

The more general form of the material properties permitted by Eq. (4.21) means that the equation can be applied to any region but with the special form it can apply specifically to the rod region. A subscript, *R*, is added to the magnetic field in Eq. (4.21) to indicate the rod region.

$$H_{R,z}=H_z. \tag{4.22}$$

Similarly, the subscript, *C*, is used to indicate the coil region when needed.

To identify the rod region material properties, the following material parameters for the rod are also defined.

$$\begin{aligned}\chi_R &= \frac{\mu_{33}^S}{\mu_{11}^S}.\\ \mu_R &= \mu_{33}^S.\\ \sigma_R &= \sigma.\end{aligned} \tag{4.23}$$

The magnetostrictive term on the right hand side represents the contribution to the magnetic field due to the strain in the rod. Mathematically, this term couples the magnetic field to the vibration model. This term can be replaced by more compact notation to represent the entire group of parameters and variables. The original variables are restored when these expressions are used to compute coupling coefficients between the vibration and mechanical models.

$$\dot{K}^N(z,t) = \frac{\kappa_{eff,z}}{\mu_{33}^S}\frac{\partial}{\partial z}\left[\sigma\mu_{33}^S\frac{\partial\zeta_z(z,t)}{\partial t} - \frac{\mu_{33}^S}{\mu_{11}^S}\left(1-\frac{\kappa_{51}}{2\kappa_{eff,z}}\right)\frac{\partial^2\zeta_z(z,t)}{\partial z^2}\right]. \tag{4.24}$$

The variable $\dot{K}^N(z,t)$ is a function of the axial position and time and has the units of current per unit length. The variable can be interpreted as an equivalent surface current density for the magnetostrictive effect. The superscript, *N*, is chosen as a reminder that the magnetization comes from the strain calculated in the vibration model which is based on Newton's equations of motion. In the formula for $\dot{K}^N$, the second term in the brackets related to curvature of the strain is retained for the moment. It is eventually dropped after the dimensionless variables are introduced and its magnitude can be show to be small relative to the time derivative term.

Inserting the new nomenclature from Eq. (4.23), Eq. (4.22) and (4.24) into Eq. (4.21) gives the form used for deriving the solution of the governing equation for the magnetic field in the actuator rod. In this form, the axial component has been separated from the other two components of the magnetic field.

$$\frac{1}{r}\frac{\partial H_{R,z}}{\partial r}+\frac{\partial^2 H_{R,z}}{\partial r^2}+\frac{\partial^2 H_{R,z}}{r^2\partial\phi^2}+\chi_R\frac{\partial^2 H_{R,z}}{\partial z^2}-\sigma_R\mu_R\frac{\partial H_{R,z}}{\partial t}=\dot{K}^N. \tag{4.25}$$

Inserting the same parameter replacements into $\dot{K}^N$ in Eq. (4.24) gives the result for the forcing term from the vibration equation using the nomenclature for the rod parameters given in Eq. (4.23).

$$\dot{K}^N(z,t)=\frac{\kappa_{eff,z}}{\mu_R}\frac{\partial}{\partial z}\left[\sigma_R\mu_R\frac{\partial\zeta_z(z,t)}{\partial t}-\chi_R\left(1-\frac{\kappa_{51}}{2\kappa_{eff,z}}\right)\frac{\partial^2\zeta_z(z,t)}{\partial z^2}\right]. \tag{4.26}$$

**Boundary, interface, and initial conditions**

Boundary conditions, interface conditions, and initial conditions are needed to close the system of equations. Since the magnetic field is defined over an infinite domain, the boundary condition is that the magnetic field must go to zero at infinity in any direction: i.e.,

$$\lim_{\vec{\mathbf{r}}\to\infty}\mathbf{H}=0. \tag{4.27}$$

A second condition equivalent to a boundary condition is that the magnetic field is finite everywhere. In particular, the magnetic field is finite on the axis of symmetry of the actuator rod.

$$\mathbf{H}<\infty\ \forall\ \vec{\mathbf{r}}. \tag{4.28}$$

Additionally, conditions at the interfaces between dissimilar materials are required. The interface conditions are actually special forms of Maxwell's equations that apply at surfaces of discontinuity in the material properties [48]. The interface equations at the interface between any two dissimilar magnetic materials are given by the following equations:

$$\mathbf{H}_1 \times \hat{e}_n = \mathbf{H}_2 \times \hat{e}_n , \tag{4.29}$$

$$\mathbf{B}_1 \cdot \hat{e}_n = \mathbf{B}_2 \cdot \hat{e}_n , \tag{4.30}$$

where the subscripts 1 and 2 indicate any two materials.

In addition, an insulated boundary, such as the surface of the actuator rod, must have zero current density normal to the surface; i.e.,

$$\mathbf{J}_1 \cdot \hat{e}_n = \mathbf{J}_2 \cdot \hat{e}_n = 0 . \tag{4.31}$$

For a complete solution, the magnetic field problem requires an initial condition specified over the solution domain. This turns out to be an arbitrary condition. The initial condition can be anything if the starting time is set sufficiently before the time frame of interest so that the transient associated with the initial condition has time to die out. The remaining solution is entirely dependent on the forcing function applied over time. Hence, a homogeneous initial condition can be chosen without any loss of generality for this problem.

$$H_R \left( r, \phi, z, 0 \right) = 0 . \tag{4.32}$$

**Separation of diffusion problem into quasi-steady and dynamic solutions**

The complete solution of the time dependent diffusion problem for the complex actuator geometry is a difficult mathematical problem and would be impractical for real-time control. The approach that takes best advantage of the tools that are available combines two solutions: a quasi-steady solution and a transient solution. The quasi-steady solution can be calculated using the finite element code FEMM which is described in APPENDIX C. The dynamic solution is obtained by the method of integral transforms in three dimensions. In obtaining the solutions, it is useful to understand that the quasi-

steady solution gives the field produced by the coils and the dynamic field represents the effect of the eddy current field. The quasi-steady and the dynamic problems can be separated by writing the magnetic field in Eq. (4.25) as the sum of two solutions; i.e.,

$$H_{R,z}\left(r,\phi,z,t\right)=H_R^H\left(r,\phi,z,t\right)+H_R^{FEMM}\left(r,z,t\right), \tag{4.33}$$

where $H_R^{FEMM}\left(r,z,t\right)$ is the quasi-steady solution calculated by FEMM and $H_R^H\left(r,\phi,z,t\right)$ is the dynamic solution. The superscript *H* is used to indicate that the dynamic solution involves an approximation of the boundary condition as a homogeneous field on the surface of the pie-shaped cylinder. This approximation and the justification for it are given later. Substituting Eq. (4.33)into Eq. (4.25) yields:

$$\begin{aligned}\frac{1}{r}\frac{\partial\left(H_R^H+H_R^{FEMM}\right)}{\partial r}+\frac{\partial^2\left(H_R^H+H_R^{FEMM}\right)}{\partial r^2}+\frac{\partial^2\left(H_R^H+H_R^{FEMM}\right)}{r^2\partial\phi^2}\\ +\chi_R\frac{\partial^2\left(H_R^H+H_R^{FEMM}\right)}{\partial z^2}-\sigma_R\mu_R\frac{\partial\left(H_R^H+H_R^{FEMM}\right)}{\partial t}=\dot{K}^N.\end{aligned} \tag{4.34}$$

The quasi-steady problem in the rod region is controlled by an equation similar to Eq. (4.25) with its time derivative terms set to zero. The differential equation for the quasi-steady problem is the same as the steady state FEMM problem. FEMM indirectly solves the following differential equation[§].

$$\frac{1}{r}\frac{\partial H_R^{FEMM}}{\partial r}+\frac{\partial^2 H_R^{FEMM}}{\partial r^2}+\chi_R\frac{\partial^2 H_R^{FEMM}}{\partial z^2}=0. \tag{4.35}$$

The azimuthal contribution to the diffusion is zero, $\frac{\partial^2 H_R^{FEMM}}{r^2\partial\phi^2}=0$, since the laminations of the rod have no effect on the steady state problem. The azimuthal dependence of the

[§] The magnetic potential, **A**, is actually the variable that is solved by FEMM's finite element calculation. The magnetic field is derived from the potential by spatial differentiation. Nevertheless, the derived magnetic field satisfies the equation indicated.

magnetic field comes from the eddy current circulating around the pie-shaped cylinder. The FEMM code solves the steady state magnetic diffusion problem with a detailed representation of the actuator geometry using the exact boundary conditions and interface conditions given by Eqs. (4.27) through (4.30). The source terms in the model are the coil currents. The material properties with anisotropic permeability are modeled by the FEMM code. These features mean that very few approximations are needed to solve the steady state problem and that the FEMM code gives a very accurate simulation of the field due to coil current in the actuator.

The quasi-steady solution gives the field that would be present if the conductivities of all materials were zero (and, consequently, the eddy currents were also zero) and the only current driving the field were imposed by the current in the coils. To emphasize the point, we change the notation.

$$H_R^{FEMM}(r,z,t) = H_R^{FEMM}\left(r,z,\mathbf{I}_C(t)\right). \tag{4.36}$$

In this notation, $\mathbf{I}_C(t)$ indicates a vector of currents in the individual coils.

$$\mathbf{I}_C(t) = \left\{I_{C,1}(t), I_{C,2}(t), \ldots I_{C,jmax}(t)\right\}, \tag{4.37}$$

where $I_{C,j}(t)$ is the current in the *j*-th coil. The quasi-steady solution, $H_R^{FEMM}\left(r,z,\mathbf{I}_C(t)\right)$, depends on the coil currents which in turn may depend on time. However, the relationship between current and field contributes no time dynamics itself. The contribution due to each coil is proportional to the coil current. Since the magnetic field is a linear property, the principle of superposition holds. We can compute $H_R^{FEMM}\left(r,z,\mathbf{I}_C(t)\right)$ as the summation of normalized FEMM cases. The field for an arbitrary combination of coil current is then

$$H_R^{FEMM}\left(r,z,\mathbf{I}_C\left(t\right)\right)=\sum_{j=1}^{jmax}H_{R,j}^{FEMM}\left(r,z\right)I_{C,j}\left(t\right), \tag{4.38}$$

where $H_{R,j}^{FEMM}\left(r,z\right)$ is a steady state FEMM case in which $I_{C,j}\left(t\right)=1$ and the current to all other coils is zero. The parameter, *jmax*, is the number of coils.

The derivative of the quasi-steady solution is obtained by differentiating Eq. (4.38). Hence, derivative can be written as

$$\dot{H}_R^{FEMM}=\frac{dH_R^{FEMM}\left(r,\phi,z,\mathbf{I}_C\left(t\right)\right)}{dt}=\sum_{j=1}^{jmax}H_{R,j}^{FEMM}\left(r,\phi,z\right)\dot{I}_{C,j}\left(t\right). \tag{4.39}$$

Using Eq. (4.35) to eliminate the spatial derivative terms of $H_R^{FEMM}$ in Eq. (4.34) gives the following.

$$\frac{1}{r}\frac{\partial}{\partial r}\left(r\frac{\partial H_R^H}{\partial r}\right)+\frac{1}{r^2}\frac{\partial^2 H_R^H}{\partial\phi^2}+\chi_R\frac{\partial^2\left(H_R^H\right)}{\partial z^2}-\sigma_R\mu_R\frac{\partial\left(H_R^H+H_R^{FEMM}\right)}{\partial t}=\dot{K}^N. \tag{4.40}$$

From the standpoint of the $H_R^H$ problem, the FEMM component is a source term that can be moved to the right hand side of the equation. Placing the $\dot{H}_R^{FEMM}$ on the right hand side as part of the non-homogeneous forcing function yields the form for the equation in dimensioned variables in which the coupling of the eddy current field to the coil and vibration models is explicitly shown; i.e.,

$$\frac{1}{r}\frac{\partial}{\partial r}\left(r\frac{\partial H_R^H}{\partial r}\right)+\frac{1}{r^2}\frac{\partial^2 H_R^H}{\partial\phi^2}+\chi_R\frac{\partial^2 H_R^H}{\partial z^2}-\sigma_R\mu_R\frac{\partial H_R^H}{\partial t}=\sigma_R\mu_R\dot{H}_R^{FEMM}+\dot{K}^N. \tag{4.41}$$

Equivalently, the forcing function can be written in terms of the magnetic induction by recognizing that the time derivative terms can be combined using the constitutive relation. The time derivative of magnetic induction in the of the constitutive

relation, Eq. (4.18), can be written as the following by incorporating the eddy current and coil current components for the magnetic field from Eq. (4.33) and the definition of the strain terms as a surface current as in Eq. (4.74).

$$\sigma_R \frac{\partial B_z}{\partial t} = \sigma_R \mu_R \frac{\partial \left( H_R^H + H_R^{FEMM} \right)}{\partial t} + \dot{K}^N . \tag{4.42}$$

This equation leads to a form that is needed in solving for the eddy current problem.

$$\frac{1}{r}\frac{\partial}{\partial r}\left( r \frac{\partial H_R^H}{\partial r} \right) + \frac{1}{r^2}\frac{\partial^2 H_R^H}{\partial \phi^2} + \chi_R \frac{\partial^2 H_R^H}{\partial z^2} = \sigma_R \frac{\partial B_z}{\partial t} . \tag{4.43}$$

The field that remains to be solved, $H_R^H$, is the field due to eddy current. The desired approach at this point would be to apply the boundary and interface conditions from Eqs. (4.27) through (4.30) and solve the magnetic diffusion equation over all space using the simplified geometry given by Figure 4.1 and Figure 4.2. There are two problems. The first problem is that we want to solve just the axial field problem in Eq. (4.43) but the interface conditions for axial field are not separable from the azimuthal and radial components of magnetic field in the rod. The second problem is that, even if a satisfactorily separated interface condition were available, the problem of a two region scalar diffusion problem in which one region is finite and the other infinite cannot be solved using conventional transcendental functions such as sine, cosines, and Bessel functions. However, both problems can be addressed with a single approximation that requires the eddy current field on the boundary to be zero.

To illustrate the problem of separating the boundary conditions, consider the requirement for interface conditions between the rod and coil region. The goal would be to solve only the axial component of field. The differential equation for the axial

component is given in Eq. (4.41). To complete the problem, two interface equations are needed over the surface of the pie-shaped cylinder. For example, on the interface between the rod and the coil, two linearly independent equations involving the axial field and the first derivative on either side, $H_{R,z}$, $H_{C,z}$, $\frac{\partial H_{R,z}}{\partial r}$, and $\frac{\partial H_{C,z}}{\partial r}$, are needed to close the system. At first this seems plausible since Eq. (4.25) is a scalar equation involving only the axial component of magnetic field. Equations (4.29), (4.30), and (4.31), Maxwell's equations, and the constitutive relations are available to find the desired interface relationships. One equation involving the axial field on each surface is easy to obtain. For example, on the cylindrical surface of the between rod and coil, $r = r_g$, and $0 \le z \le z_L$, $0 \le \phi \le \phi_0$ the axial component of Eq. (4.29) can be written as a scalar equation.

$$H_{R,z}\left(r_g, \phi, z, t\right) = H_{C,z}\left(r_g, \phi, z, t\right). \tag{4.44}$$

Equation (4.44) can be separated into quasi-steady and dynamic components.

$$H_R^H\left(r_g, \phi, z, t\right) + H_R^{FEMM}\left(r_g, z, t\right) = H_C^H\left(r_g, \phi, z, t\right) + H_C^{FEMM}\left(r_g, z, t\right). \tag{4.45}$$

Since the FEMM solution satisfies the interface condition, the dynamic term must satisfy the equation also.

$$H_R^H\left(r_g, \phi, z, t\right) = H_C^H\left(r_g, \phi, z, t\right). \tag{4.46}$$

A second linearly independent relationship is needed to close the system. It is impossible to find a second equation on the cylindrical surface or any other surface of the rod that is not a function of other components of the magnetic field.

Instead of solving the exact eddy current problem, a simplifying approximation is proposed. The homogeneous boundary condition on the surface of the pie-shaped cylinder is a reasonable approximation and makes the field problem solvable.

$$H_R^H\left(r,\phi,z,t\right)=0\,. \tag{4.47}$$

Since the coil region's field is not involved in this equation, only a single condition is needed at the surface. In effect, the second equation to close the system is, $H_{C,z}^{Eddy}\left(r,\phi,z,t\right)=0$, but the field outside the rod region is not needed in the model and no solution is attempted in the coil region.

To illustrate the effect of the homogeneous boundary condition approximation, an example case for a solid (unlaminated) rod can be computed using FEMM to solve a harmonic problem for the actuator geometry. The harmonic problem for the solid rod produces circular current distributions that are larger than the currents in the corresponding laminated rod. Figure 4.3 shows the axial field along the cylindrical surface $\left(r=r_g\right)$ from the bottom to the top of the rod for a case in which two coils near the axial midpoint are energized. The three traces for magnetic field are shown: a FEMM harmonic case, $\omega=10{,}000$ Hz, which represents the total field, $H_R\left(r,\phi,z,t\right)$, a FEMM steady state case $\left(\omega=0\right)$ which represents the field due to just the coil current alone, $H_R^{FEMM}\left(r,z,\mathbf{I}_C\left(t\right)\right)$, and the difference between those two which represents the field due to eddy current, $H_R^H\left(r_g,\phi,z,t\right)=H_R\left(r_g,\phi,z,t\right)-H_R^{FEMM}\left(r_g,z,t\right)$.

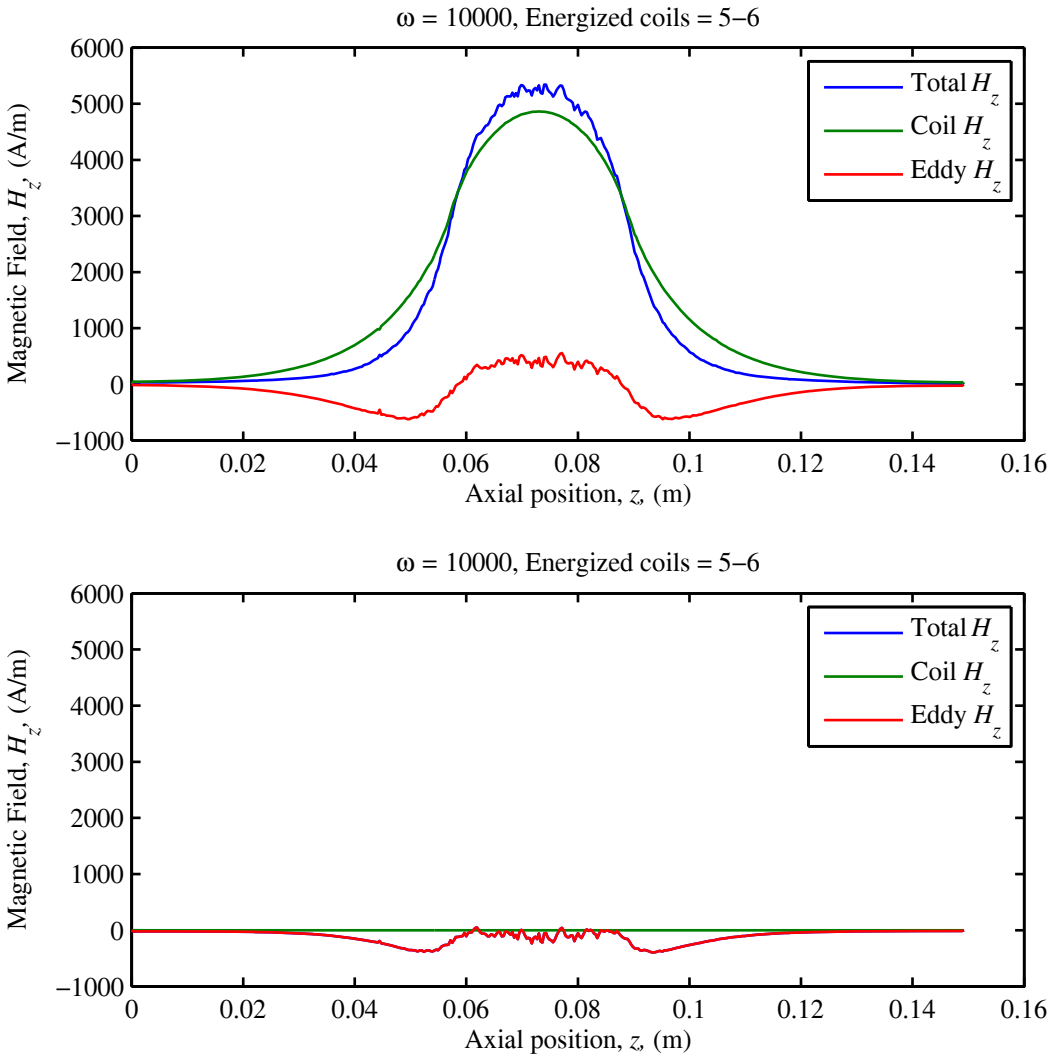


Figure 4.3: Comparison of total, coil current, and eddy current magnetic field along rod surface. Top, $\mathrm{Re}(H_z)$; bottom, $\mathrm{Im}(H_z)$

Figure 4.3 shows that the field due to eddy current is small compared to the field due to coil current which suggests that the homogeneous boundary condition in Eq. (4.47) is a reasonable approximation. The top figure shows the real component of axial field, and the bottom shows the imaginary component. In the lower figure, the total and eddy field are of identical because the coil's field is all real.

The FEMM calculation for an unlaminated, solid cylinder gives a conservatively large estimate of the eddy current field in comparison to the pie-shaped cylinder. The pie-shaped cylinder reduces eddy current and magnetic field resulting in a smaller error in the field calculation due to the boundary condition approximation.

The error due to the homogeneneous boundary approximation can be estimated by considering a third contributor to the magnetic field. The true total field be given by

$$H_{R,z}\left(r,\phi,z,t\right)=H_R^H\left(r,\phi,z,t\right)+H_R^{FEMM}\left(r,z,t\right)+H_R^{BC}\left(r,\phi,z,t\right), \tag{4.48}$$

where $H_R^{BC}\left(r,\phi,z,t\right)$ is the solution to a diffusion problem with the true nonhomegenous boundary condition,

$$\frac{1}{r}\frac{\partial H_R^{BC}}{\partial r}+\frac{\partial^2 H_R^{BC}}{\partial r^2}+\chi_R\frac{\partial^2 H_R^{BC}}{\partial z^2}=0, \tag{4.49}$$

and the boundary condition is given by

$$H_R^{BC}\left(r_g,\phi,z,t\right)=H_C^{Eddy}\left(r_g,\phi,z,t\right). \tag{4.50}$$

Summing the equations shows that the proposed additional term corrects the error due to the homogeneous boundary condition approximation. By applying the maximum principle [51] to Laplace's equation to the case represented by Eqs. (4.49) and (4.50), we can establish maximum error in the interior of the rod due to neglected boundary condition. The maximum principle for a diffusion equation with no sources states that

the solution in the interior must be less than or equal to the maximum value on the boundary. The interion solution must also be greater than the minimum on the boundary. Hence, the limits of the solution can be written as

$$\text{Min}\left[H_C^{Eddy}\left(r_g,\phi,z,t\right)\right] \le H_R^{BC}\left(r,\phi,z,t\right) \le \text{Max}\left[H_C^{Eddy}\left(r_g,\phi,z,t\right)\right] \tag{4.51}$$

We also know that the eddy current field on the surface of the laminated rod must be less than the solution for the unlaminated rod. Hence, the maximum eddy current field on the surface of the rod in Figure 4.1 bounds the error at all interior points. The maximum on the perimeter in Figure 4.1 is approximately 10% of the field at the interior.

The boundary condition approximation of the eddy current problem is not insignificant. However, the eddy current's magnetic field is a secondary effect compared to the coil's field for the frequency range that is needed. The FEMM model is not approximated as homogeneous on the surface and retains the full rigor of the interface conditions defined by Eq. (4.29) and Eq. (4.30).

Another possible boundary condition that could be used for the eddy current problem is a mixed boundary condition of the form

$$\frac{\partial H_R^H\left(r_g,\phi,z,t\right)}{\partial r} + aH_R^H\left(r_g,\phi,z,t\right) = b\,, \tag{4.52}$$

where *a* and *b* are constant or possibly known functions of $\mathbf{I}_C\left(t\right)$. To evaluate the mixed boundary condition as a candidate for the eddy current model, the field, $H_R^H\left(r_g,\phi,z,t\right)$ is plotted versus its partial derivative, $\frac{\partial H_R^H\left(r_g,\phi,z,t\right)}{\partial r}$, for all points along the rod surface to see if a linear relationship emerges. This calculation is performed using the same FEMM model of a solid cylinder that was used for the calculations shown in Figure 4.3.

The partial derivative is evaluated numerically by finite difference. Figure 4.4 gives this plot for the same current distribution case as in Figure 4.3 with coils 5 and 6 energized and frequency $\omega = 10,000$ Hz.

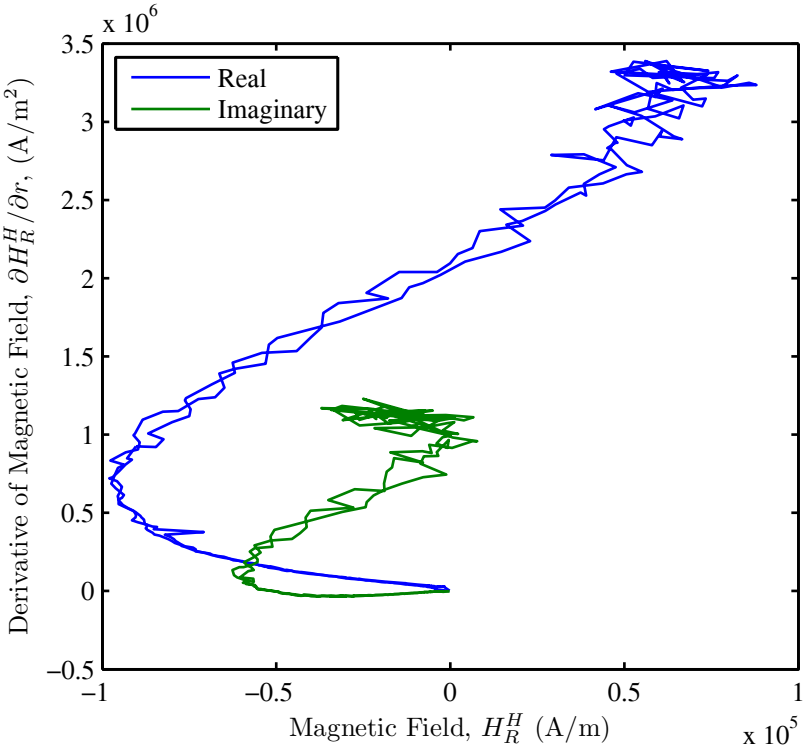


Figure 4.4: Evaluation of linearity of mixed boundary condition

The conclusion that can be reached from Figure 4.4 is that the relationship does not match a mixed boundary condition with constant coefficients. No simple functions for *a* and *b* give a straight line. Figure 4.3 and Figure 4.4 make the case that $H_R^H\left(r_g, \phi, z, t\right) = 0$ is a reasonable approximation and the best available choice for the boundary condition. The diffusion problem with homogeneous (Dirichlet) boundary condition on a pie-shaped cylinder is a problem that can be solved by conventional integral transform methods.

Another alternative is to solve the eddy current field over a three region domain including the rod, coil, and return path. Most of the magnetic flux is channeled from the positive pole of the actuator to the negative pole within the high permeability material in the return path. Consequently the field due to eddy current at the outer surface of the return path is much smaller than on the surface of the rod. The error due to neglecting it is correspondingly smaller in the rod region by the maximum principle. The difficulty is that the solution requires modal functions that span the three regions. The solutions are possible but much more complicated algebraically than the functions over a single region. The ease of solution is viewed to outweigh the error in the eddy current model.

**Dimensionless variables for magnetic modeling**

As in the vibration submodel, dimensionless variables can be defined for the magnetic problem that reduce all parametrically similar problems to a single case. The dimensionless variables for the dependent variables are based on the linearized range for magnetostriction effect found in Chapter 2.

The governing equation and the solutions can be converted to dimensionless units by a set of linear transformations that are defined in Chapter 2. The transformations consist of a scaling factor and an offset. The coil current transformation is given by the following equation. The superscript *K* is used to acknowledge Kirchhoff's laws which are the basis of the circuit equations that are used to compute the coil current.

$$x_j^K = \frac{I_{C,j} - I_{min}}{I_{max} - I_{min}} = \frac{I_{C,j} - I_{min}}{\Delta I}. \tag{4.53}$$

The scaling for the displacement variable is given by the elongation for the maximum and minimum current at steady state and no applied load. The superscript, *N*,

is used to indicate Newton's equations of motion as the source of the displacement model.

$$x^N = \frac{Y_{eff}^H}{\kappa_{eff} z_L T \Delta I}\left(\zeta_z - \zeta_{min}\right). \tag{4.54}$$

The scaling for the magnetic field is defined for the maximum and minimum current and an infinite coil as the following.

$$x^M = \frac{H_R - H_{min}}{H_{max} - H_{min}} = \frac{H_R - H_{min}}{\Delta H} = \frac{H_R - H_{min}}{T \Delta I}. \tag{4.55}$$

In this case, the superscript, *M*, is used to indicate Maxwell's equations which are the basis for the magnetic modeling. The magnetic field is divided into a homogeneous part and quasi-steady part in Eq. (4.33)

$$\begin{aligned} x^M &= \frac{H_R^H + H_R^{FEMM} - H_{min}}{H_{max} - H_{min}} \\ &= \frac{H_R^H}{\Delta H} + \frac{H_R^{FEMM} - H_{min}}{\Delta H}. \end{aligned} \tag{4.56}$$

The two parts can each be defined as a dimensionless variable.

$$\begin{aligned} x_H^M &= \frac{H_R^H}{\Delta H} = \frac{H_R^H}{T \Delta I}. \\ x^{FEMM} &= \frac{H_R^{FEMM} - H_{min}}{\Delta H} = \frac{H_R^{FEMM} - H_{min}}{T \Delta I}. \end{aligned} \tag{4.57}$$

Since the two terms are added together in the total solution, the offset term is necessary for only one of the parts. The offset is chosen to be associated with the quasi-steady term because that leads to a convenient simplification in obtaining the dimensionless current variable. This simplification is given by the following derivation of the FEMM field in terms of the dimensionless coil current variables.

$$
\begin{aligned}
x^{FEMM} &= \frac{\sum_{j=1}^{jmax} H_{R,j}^{FEMM}(r,z) I_{C,j}(t) - H_{min}}{\Delta H} \\
&= \frac{\sum_{j=1}^{jmax} H_{R,j}^{FEMM}(r,z) I_{C,j}(t) - \sum_{j=1}^{jmax} H_{R,j}^{FEMM}(r,z) I_{min}}{T\Delta I} \\
&= \frac{1}{T}\sum_{j=1}^{jmax} H_{R,j}^{FEMM}(r,z)\left(\frac{I_{C,j}(t) - I_{min}}{\Delta I}\right) \\
&= \frac{1}{T}\sum_{j=1}^{jmax} H_{R,j}^{FEMM}(r,z)\, x_j^K .
\end{aligned}
\tag{4.58}
$$

The derivative of $x^{FEMM}$ does not depend on the offset term because the offset is a constant.

$$
\dot{x}^{FEMM} = \frac{d}{dt}\left(\frac{H_R^{FEMM} - H_{min}}{T}\right) = \frac{\dot{H}_R^{FEMM}}{T} = \frac{1}{T}\sum_{j=1}^{jmax} H_{R,j}^{FEMM}(r,z)\dot{x}_j^K . \tag{4.59}
$$

The differential equation in Eq. (4.41) can be converted to dimensionless form by making the following substitutions.

$$
H_R^H(r,\phi,z,t) = T\Delta I x_M^H(r,\phi,z,t). \tag{4.60}
$$

$$
\dot{H}_R^{FEMM}(r,z,t) = T\Delta I \dot{x}^{FEMM}(r,z,t). \tag{4.61}
$$

The dimensionless spatial variables are given by the following replacements.

$$
r = r_g \cdot \rho . \tag{4.62}
$$

$$
z = z_L \cdot \xi . \tag{4.63}
$$

After making the above substitutions and rearranging, the governing equation for the eddy current part of the magnetic model is then given in dimensionless variables by the following.

$$\frac{1}{\rho}\frac{\partial}{\partial\rho}\left(\rho\frac{\partial x_H^M}{\partial\rho}\right)+\frac{\partial^2 x_H^M}{\rho^2\partial\phi^2}+\frac{\chi_R r_g^2}{z_L^2}\frac{\partial^2 x_H^M}{\partial\xi^2}-\sigma_R\mu_R r_g^2\frac{\partial x_H^M}{\partial t}$$
$$=\sigma_R\mu_R r_g^2\dot{x}^{FEMM}+\frac{r_g^2}{T\Delta I}\dot{K}^N. \tag{4.64}$$

The $\dot{K}^N$ term can also be put into dimensionless units to reveal its parameter groups. The entire last term in Eq. (4.64) is converted to dimensionless variables by making the same substitutions as above into the defining equation for $K^N$ from Eq. (4.24). The dimensionless surface current is designated with a lower case, $k^N$, to indicate the transformation.

$$\dot{k}^N=\frac{r_g^2}{T\Delta I}\dot{K}^N=\frac{\kappa_{eff,z}\kappa_{eff}}{Y_{eff}^H\mu_R}\frac{\partial}{\partial\xi}\left[\sigma_R\mu_R r_g^2\frac{\partial x^N}{\partial t}-\frac{\chi_R r_g^2}{z_L^2}\left(1-\frac{\kappa_{51}}{2\kappa_{eff,z}}\right)\frac{\partial^2 x^N}{\partial\xi^2}\right]. \tag{4.65}$$

The homogeneous boundary conditions in dimensionless variables is

$$x_H^M\left(\rho,\phi,\xi,t\right)=0. \tag{4.66}$$

for all points on the surface of the pie-shaped cylinder. The initial condition is homogeneous at all points in the pie-shaped cylinder at $t=0$.

**Estimating Parameter Groups for the Magnetic Model**

Since the dependent variables and position variables in the dimensionless equation are scaled to order unity, the groups of constants in Eq. (4.64) and Eq. (4.65) give some insight into the magnitudes of the terms of the governing equation. The parameters that are needed for the evaluations are given in Table 2.8.

The time variable has not been scaled to be dimensionless; hence the term, $\sigma_T\mu_T r_g^2$, has units of time and represents the magnetic diffusivity. The magnitude

of the diffusivity can be evaluated from the properties of Terfenol-D and the radial dimension of the actuator rod.

$$\sigma_R \mu_R r_g^2 = \left(1.7241\times10^{6}\right)\left(0.8644\times10^{-5}\right)\left(0.0063\right)^2 = 1.5766\times10^{-4}\ s\,. \qquad (4.67)$$

This quantity appears in the denominator of each of the frequency constants for the magnetic solution spatial modes. It can be viewed as an overall time scale factor for magnetics. It is mentioned in Chapter 1 in the argument for addressing the frequency response limitations for the magnetostrictive actuator.

The term, $\frac{\chi_R r_g^2}{z_L^2}$, combines factors representing the anisotropy in magnetic permeability, $\chi_R$, and the length to radius ratio and gives an effective aspect ratio of the cylinder. Since the anisotropy factor is a number less than one, the cylinder is effectively longer and thinner from the standpoint of magnetic diffusion than the actual dimensions. The actual length to radius ratio is approximately 24. The dimensionless parameter gives an effective length to radius ratio for the actuator rod.

$$\left(\frac{1}{\chi_R}\right)^{\frac{1}{2}} \frac{z_L}{r_g} = \left(\frac{8.6444\times10^{-6}}{2.2678\times10^{-6}}\right)^{\frac{1}{2}} \left(\frac{5.875}{0.25}\right) = 45.9\,. \qquad (4.68)$$

The ratio is also an indication of the order of the modes in radial and axial direction that give comparable diffusion. Since there are ten coils in the prototype actuator, the model needs ten or more axial modes to model the coupling of the coils to the rod. The 45-th axial mode has about the same axial diffusion as the radial diffusion of the first radial mode. The minimum number of axial modes needed to represent the multi-coil actuator is roughly equal to the number of coils. With ten coils in the actuator, this means that only a one or two radial modes need to be retained in the model to

represent the radial diffusion to the same degree of approximation as the ten axial modes represent the axial diffusion.

The factor $\frac{\kappa_{eff,z} d_{33}}{\mu_R}$ gives a relative weighting of the vibration modes to the axial eddy current modes. The value of the factor is given by

$$\frac{\kappa_{eff,z}\kappa_{eff}}{Y_{eff}^{H}\mu_R} = \frac{(192.34)\left(1.1\times10^{-8}\right)}{0.2268\times10^{-5}} = 0.9329 . \tag{4.69}$$

Since the factor is close to unity, the time derivative terms for the coil $\dot{x}^{FEMM}$ and for the vibration $\dot{x}^{N}$ contribute approximately equally to the eddy current model dynamics.

The $\dot{K}^{N}$ term defined in dimensionless variables in Eq. (4.65) is the coupling term between the vibration model and the magnetic model. The term contains a time derivative, $\sigma_R \mu_R r_g^2 \frac{\partial x^N}{\partial t}$, and a curvature term, $\frac{\chi_R r_g^2}{z_L^2}\left(1-\frac{\kappa_{51}}{2\kappa_{eff,z}}\right)\frac{\partial^2 x^N}{\partial \xi^2}$. With the variables in dimensionless units, an estimate the relative magnitude of the time derivative and curvature terms can be calculated to see if it is reasonable to neglect the curvature term. In dimensionless units, the time derivative term is on the order of the frequency in radian/second.

$$\frac{\partial x^N}{\partial t} \approx \omega . \tag{4.70}$$

The curvature term can be estimated from the highest spatial mode that contributes to the solution. The curvature is the square of the axial mode's highest spatial eigenvalue. For a ten coil actuator, the maximum value is reasonably estimated as the

tenth mode (based on ten coils). The solution derived in the section that follows shows that for the unloaded rod the curvature of the tenth mode is given by

$$\frac{\partial^2 x^N}{\partial \xi^2} \approx \left[ \left( \frac{2 \cdot n - 1}{2} \right) \pi \right]^2 . \tag{4.71}$$

If we choose the maximum frequency of interest as 10,000 Hz and the tenth vibration mode, $n$=10, as the highest mode to be considered contributing to the response, then the relative magnitudes of the dimensionless time derivative term and the curvature term can be estimated as follows.

Time derivative term

$$\sigma_R \mu_R r_g^2 \frac{\partial x^N}{\partial t} \approx \sigma_R \mu_R r_g^2 \omega = 1.5766 \times 10^{-4} \cdot 10^4 \cdot 2\pi = 9.9 . \tag{4.72}$$

Curvature term

$$\begin{aligned} \frac{\chi_R r_g^2}{z_L^2} \left( 1 - \frac{\kappa_{51}}{2\kappa_{eff,z}} \right) \frac{\partial^2 x^N}{\partial \xi^2} &\approx \frac{\chi_R r_g^2}{z_L^2} \left( 1 - \frac{\kappa_{51}}{2\kappa_{eff,z}} \right) \beta_{10}^2 \\ &= \left( \frac{1}{45.9} \right)^2 \cdot \left( 1 - \frac{155.56}{2 \cdot 275.86} \right) \cdot 29.8^2 \\ &= 0.3038 \\ &\approx 0. \end{aligned} \tag{4.73}$$

By this estimation, the curvature term is a factor of 30 smaller than the time derivative term and can be dropped. This approximation simplifies the vibration term to the following.

$$\dot{K}^N = \sigma_R \kappa_{eff,z} \frac{\partial}{\partial z} \left[ \frac{\partial \zeta_z}{\partial t} \right]. \tag{4.74}$$

**Solution of the Magnetic Diffusion Problem**

The derivation of the solution of Eq. (4.64) by the integral transform method is given in APPENDIX D. The resulting modal equations for the solution are repeated here. The total magnetic field combines the fields of the coils and the eddy currents.

$$x^M\left(\rho,\phi,\xi,t\right)=x^{FEMM}\left(\rho,\phi,\xi,\mathbf{x}^{\mathbf{K}}\left(t\right)\right)+x_H^M\left(\rho,\phi,\xi,t\right). \tag{4.75}$$

where $x^M\left(\rho,\phi,\xi,t\right)$ is the dimensionless magnetic field in the axial direction, $x^{FEMM}\left(\rho,\phi,\xi,\mathbf{x}^{\mathbf{K}}\left(t\right)\right)$ is the FEMM solution the field due to the current in the coils without eddy current effects given by Eq. (4.58), and $\mathbf{x}^{\mathbf{K}}\left(t\right)$ is a vector of the dimensionless coil currents. The solution for the eddy current field, $x_H^M\left(\rho,\phi,\xi,t\right)$, which is derived in APPENDIX D, is given as the following summation of azimuthal, radial, and axial modes.

$$x_H^M\left(\rho,\phi,\xi,t\right)=\sum_{k=1}^{kmax}\sum_{m=1}^{mmax}\sum_{p=1}^{pmax}\mathcal{X}_{k,m,p}^M\left(t\right)\frac{\sin\left(\gamma_m\phi\right)\mathrm{J}_{\gamma_m}\left(\varepsilon_{k,m}\rho\right)\sin\left(\eta_p\xi\right)}{N\left(\varepsilon_{k,m},\gamma_m\right)N\left(\gamma_m\right)N\left(\eta_p\right)}. \tag{4.76}$$

The set of three constants, *N*, in the denominator are the normalization coefficients for the orthogonal modal functions and are given in the appendix.

The amplitude functions are given by the solution to a system of ordinary differential equations.

$$\dot{\mathcal{X}}_{k,m,p}^M+\sum_{n=1}^{nmax}\Upsilon_{k,m,p,n}\dot{\mathcal{X}}_n^N\left(t\right)+\sum_{j=1}^{jmax}\Theta_{k,m,p,j}\dot{x}_j^K\left(t\right)=-\alpha_{k,m,p}\mathcal{X}_{k,m,p}^M. \tag{4.77}$$

The coefficient terms, $\Upsilon_{k,m,p,n}$, $\Theta_{k,m,p,j}$, and $\alpha_{k,m,p}$ are defined in APPENDIX D. The terms, $\dot{\mathcal{X}}_n^N\left(t\right)$ and $\dot{x}_j^K\left(t\right)$, couple the eddy current field to the fields generated by the

magnetostrictive strain and coil current, respectively. The variables are the state variables from the vibration and coil circuit subsystem models.

### Time and Frequency Response Using the Magnetic Model

This section presents sample results using the magnetics submodel as a stand alone calculation. The purpose of the stand alone model calculations is to show that the results are plausible and to show graphically the magnitude and delay of the eddy current effect. One of the approximations of the magnetic model is the truncation of the series. The effect of truncation is shown by comparing a high-order and a low-order model. Additional results and numerical tests of the solution are given in APPENDIX D.

Results are shown in two types of plots, spatial plots and frequency response plots. The spatial plot shows magnetic field versus position while holding frequency constant. The second type of calculation gives the frequency response plot in which the frequency is varied. The variable that is plotted versus frequency is the average field in a transverse section. The transverse sections are located at the midpoint of each coil. The forcing function for both types of cases is a harmonic current in a single coil. The vibration inputs are specified as zero, $\dot{\boldsymbol{\chi}}_n^N(t) = 0$ in all the sample cases. A schematic illustrating the arrangement of the actuator showing energized coil and elevations for midplane of coils is shown in Figure 4.5

In both spatial and frequency response calculations, the amplitude functions, $\boldsymbol{\chi}_{k,m,p}^M$, are calculated as functions of frequency. The Fourier transform is applied to Eq. (4.77) to compute the amplitudes as functions of frequency. In this equation, the vibration inputs are set to zero. The underscore indicates the frequency transformation.

$$i\omega \underline{\chi}^{M}_{k,m,p}\left(i\omega\right)+\sum_{j'=1}^{jmax}\Theta_{k,m,p,j'}i\omega \underline{x}^{K}_{j'}\left(i\omega\right)=-\alpha_{k,m,p}\underline{\chi}^{M}_{k,m,p}\left(i\omega\right). \tag{4.78}$$

A case in which the coils are individually energized can be specified as $\left|\underline{x}^{K}_{j'}\left(\omega\right)\right|=1$ for $j'=j$, and $\underline{x}^{K}_{j'}\left(\omega\right)=0$ for $j'\neq j$. With this restriction, the amplitude function can be written as a transfer function.

$$\frac{\underline{\chi}^{M}_{k,m,p}\left(i\omega\right)}{\underline{x}^{K}_{j}\left(i\omega\right)}=-\frac{i\omega\Theta_{k,m,p,j}}{\left(i\omega+\alpha_{k,m,p}\right)}. \tag{4.79}$$

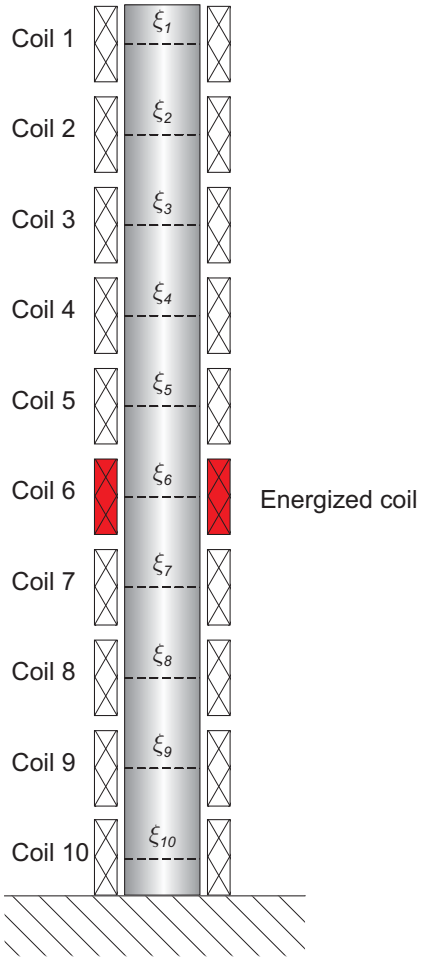


Figure 4.5: Arrangement of the magnetic model for sample calculation

The transfer function of the dimensionless field due to eddy current can be obtained by performing the Fourier transform on Eq. (4.76) and substituting in the results from Eq. (4.79).

$$\begin{aligned}\frac{\underline{x}_H^M(\rho,\phi,\xi,i\omega)}{\underline{x}_j^K(i\omega)} &= \sum_{k=1}^{kmax}\sum_{m=1}^{mmax}\sum_{p=1}^{pmax}\frac{\underline{\chi}_{k,m,p}^M(i\omega)}{\underline{x}_j^K(i\omega)}\frac{\sin(\gamma_m\phi)\mathrm{J}_{\gamma_m}(\varepsilon_{k,m}\rho)\sin(\eta_p\xi)}{N(\varepsilon_{k,m},\gamma_m)N(\gamma_m)N(\eta_p)} \\ &= -\sum_{k=1}^{kmax}\sum_{m=1}^{mmax}\sum_{p=1}^{pmax}\frac{i\omega\Theta_{k,m,p,j}}{(i\omega+\alpha_{k,m,p})}\frac{\sin(\gamma_m\phi)\mathrm{J}_{\gamma_m}(\varepsilon_{k,m}\rho)\sin(\eta_p\xi)}{N(\varepsilon_{k,m},\gamma_m)N(\gamma_m)N(\eta_p)}.\end{aligned} \tag{4.80}$$

The transfer function form of the coil field due to single energized coil is given by transforming Eq. (4.75) and applying the condition that only the *j*-th coil is energized

$$\frac{\underline{x}^{FEMM}(\rho,\phi,\xi,\omega)}{\underline{x}_j^K(\omega)} = \frac{1}{T}H_{R,j}^{FEMM}(r_g\rho,z_L\xi). \tag{4.81}$$

The coil current transfer function is independent of frequency. For a unit amplitude input ($\left|\underline{x}_j^K(\omega)\right|=1$), Eqs. (4.80) and (4.81) for the total field give the following.

$$\begin{aligned}\underline{x}^M(\rho,\phi,\xi,i\omega) &= \frac{1}{T}H_{R,j}^{FEMM}(r_g\rho,z_L\xi) \\ &\quad -\sum_{k=1}^{kmax}\sum_{m=1}^{mmax}\sum_{p=1}^{pmax}\frac{i\omega\Theta_{k,m,p,j}}{(i\omega+\alpha_{k,m,p})}\frac{\sin(\gamma_m\phi)\mathrm{J}_{\gamma_m}(\varepsilon_{k,m}\rho)\sin(\eta_p\xi)}{N(\varepsilon_{k,m},\gamma_m)N(\gamma_m)N(\eta_p)}.\end{aligned} \tag{4.82}$$

This function is evaluated and plotted using MATLAB. The sample case for the spatial plot has frequency of $\omega = 2\pi\cdot 10,000$ radians/second. The effect of truncation error on the calculation can be assessed by comparing two cases. The first case is calculated with a relatively high-order solution. The maximum orders of the three components are: radial, *kmax*=10; azimuthal, *mmax*=10; and axial, *pmax*=20. This is a much higher order solution than can be used in the control algorithm. The high-order case is intended to show that the solution is smooth and convergent. The high order

solution should be close to the true solution. The low-order solution gives the minimum number of terms and represents the preferred number of states for real-time control.

Two cross-sectional views of the results are shown. The first view, in Figure 4.6, is a plot of amplitude and phase in a transverse ( $\rho - \phi$ ) section of the rod at the midplane of the energized coil.

The magnetic field for the harmonic case is a complex number so it is converted into absolute magnitude and phase for the plots. The absolute magnitude plot shows the dip in the field in the middle of each quadrant due to eddy current. The field is depressed about ten per cent at the center of the pie-shaped section. The phase shows that the field is delayed with respect to the input. A phase of 0.5 radians at 10,000 Hz corresponds to a time delay of

$$\tau_M = \frac{\angle \underline{x}^M}{2\pi\Omega} = \frac{0.5}{2\pi \cdot 10,000} = 8\times10^{-6} \text{ s}. \tag{4.83}$$

The magnetic field delay is comparable to the delay from acoustic effects. For example, the time delay for an acoustic wave to pass through a single coil is

$$\tau_{\Delta z_c} = \frac{\Delta z_c}{c} = \frac{\pi}{20\omega_1} = 9.1\times10^{-6} \text{ s}. \tag{4.84}$$

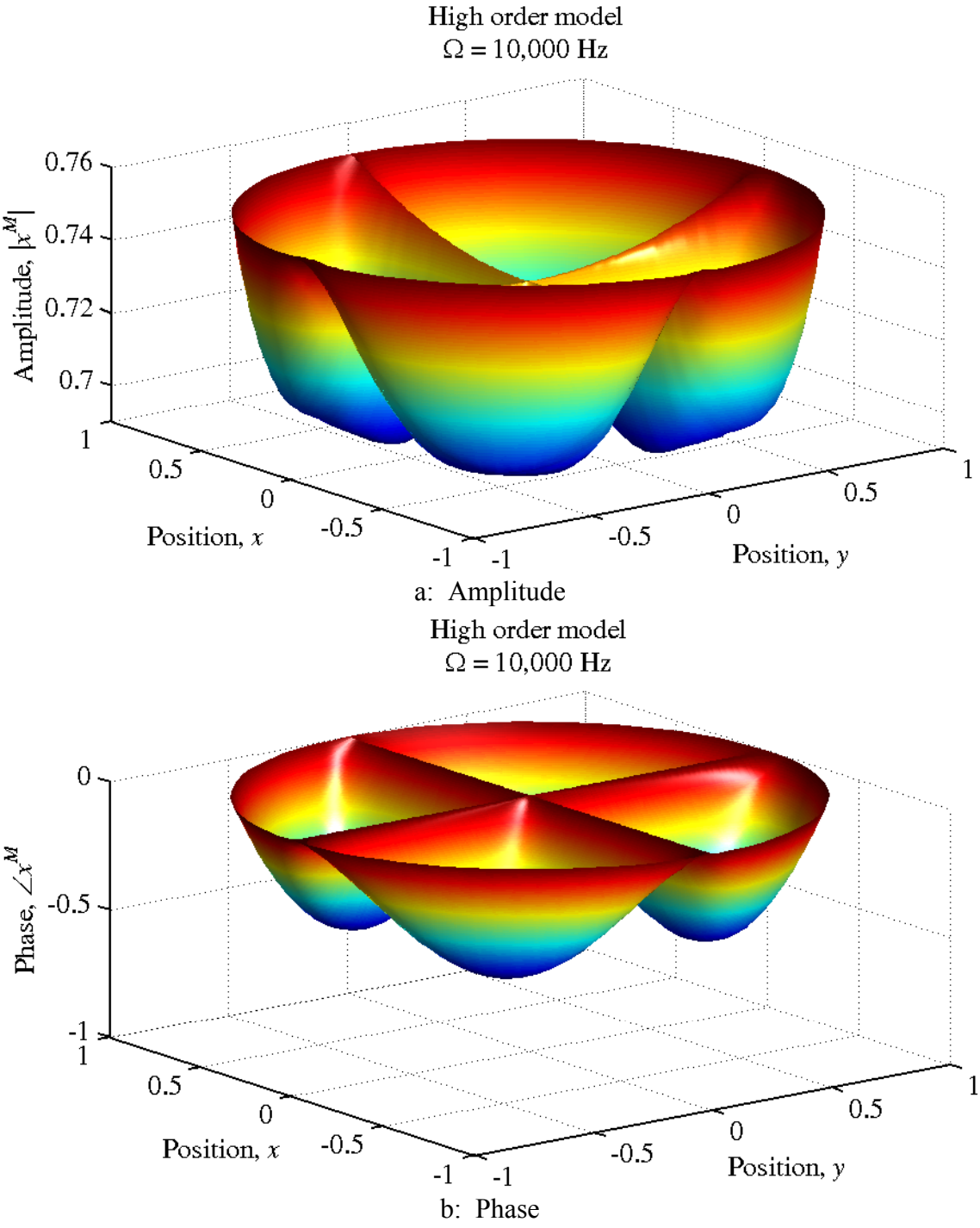


Figure 4.6: High-order model of magnetic field through a transverse section view of the actuator rod.

Another spatial plot, in Figure 4.7, shows an axial section view ( $\rho - \xi$ ) through the diameter of the rod. The section passes through the center of the pie-shaped quadrant ( $\phi = \frac{\pi}{4}$ ).

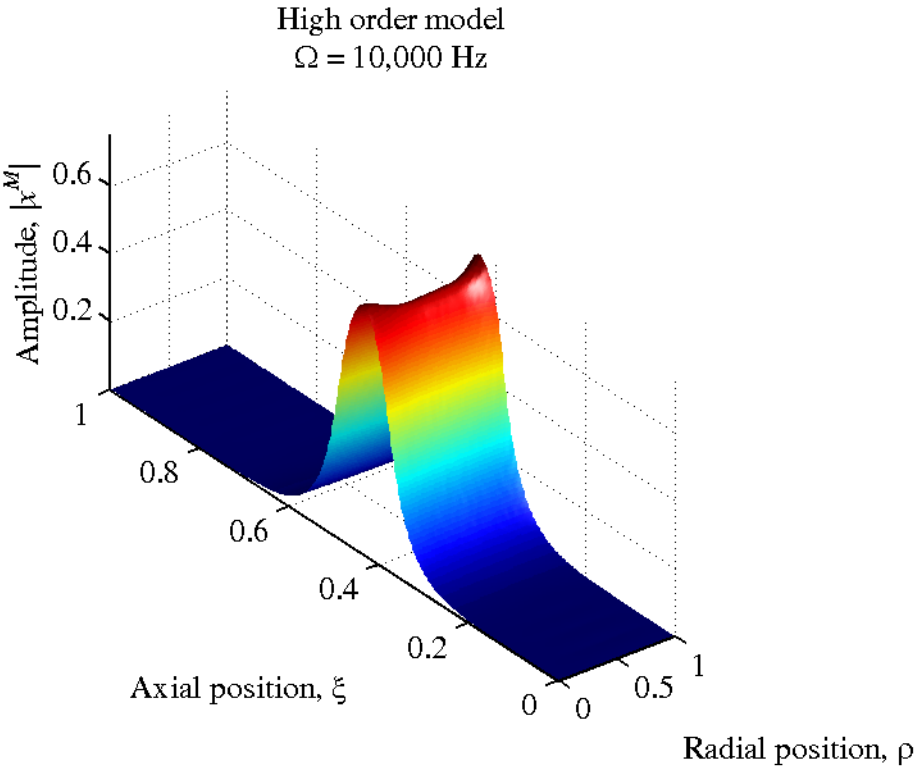


Figure 4.7: High-order model of magnetic field through an axial section view of the actuator rod.

For comparison, Figure 4.8 and Figure 4.9 show the FEMM results for the same radial and axial section views at steady state. The coil field is independent of frequency. The difference between the full magnetic model and FEMM results is the result of the eddy current field. The FEMM field in the transverse plane is an azimuthally symmetric shallow bowl. The ridges in the amplitude plot of Figure 4.6a are the same depth as the bowl in Figure 4.8. The axial section view is similar to Figure 4.7 but shows no saddle-like dip in the middle of the coil, corresponding to the eddy current effect.

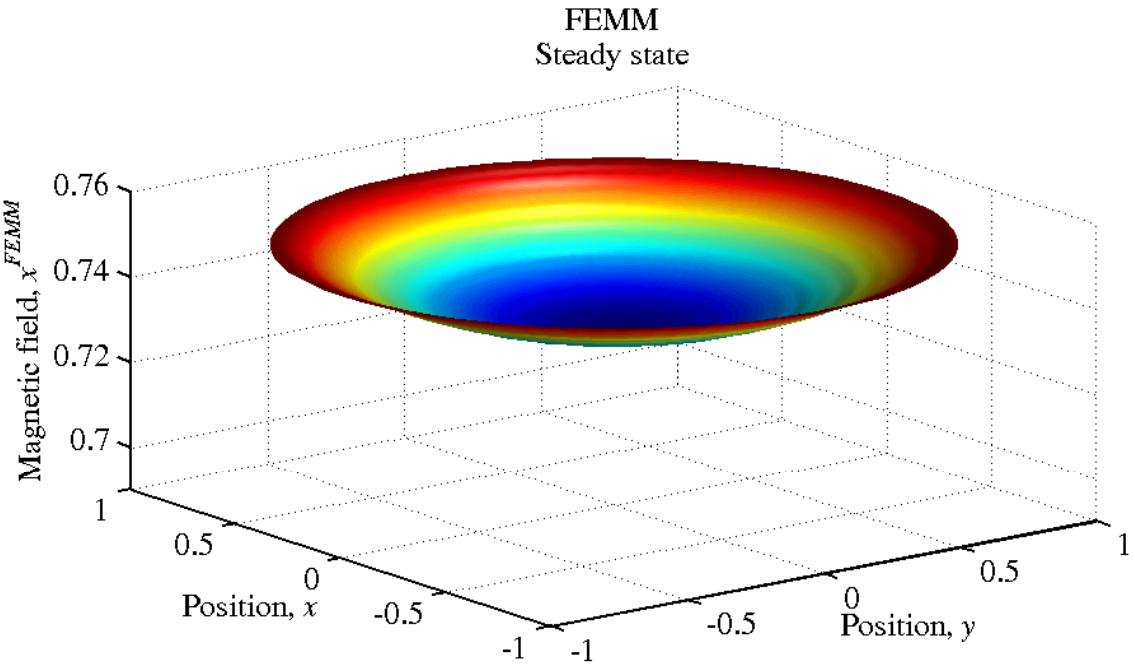


Figure 4.8: Steady state magnetic field through a radial section view due to coil current calculated by FEMM

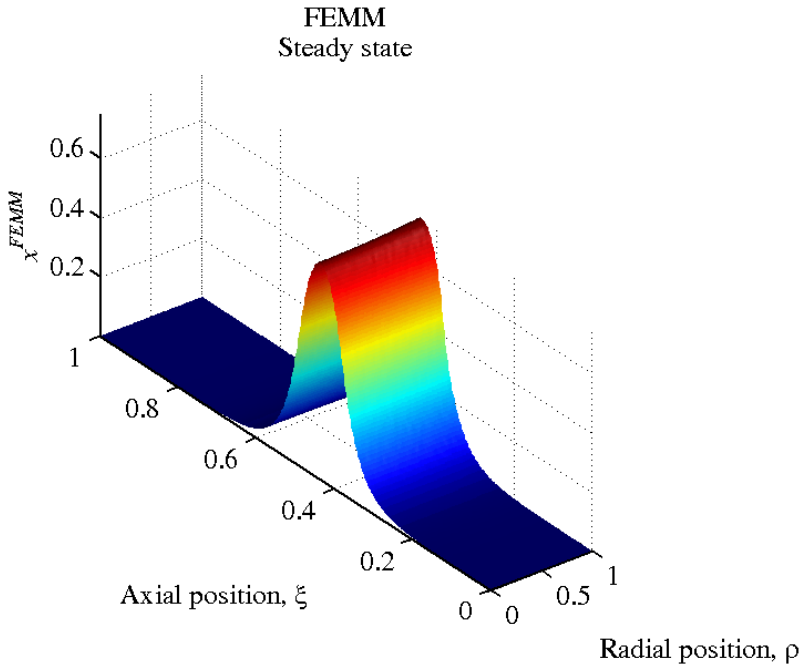


Figure 4.9: Steady state magnetic field through an axial section view due to coil current calculated by FEMM

A second case in which the number of modes is reduced to a minimum is shown in Figure 4.10 and Figure 4.11. The number of terms it each series for the magnetic modes in the low-order solution are: radial - *kmax*=1, azimuthal - *mmax*=1, and axial - *pmax*=10. The same types of transverse and axial section view plots are shown for the low-order case. The case shows that the distribution functions using just one radial and one azimuthal mode are not greatly different than the high order case. These plots suggest that the low order solution is reasonable for frequencies up to 10,000 Hz.

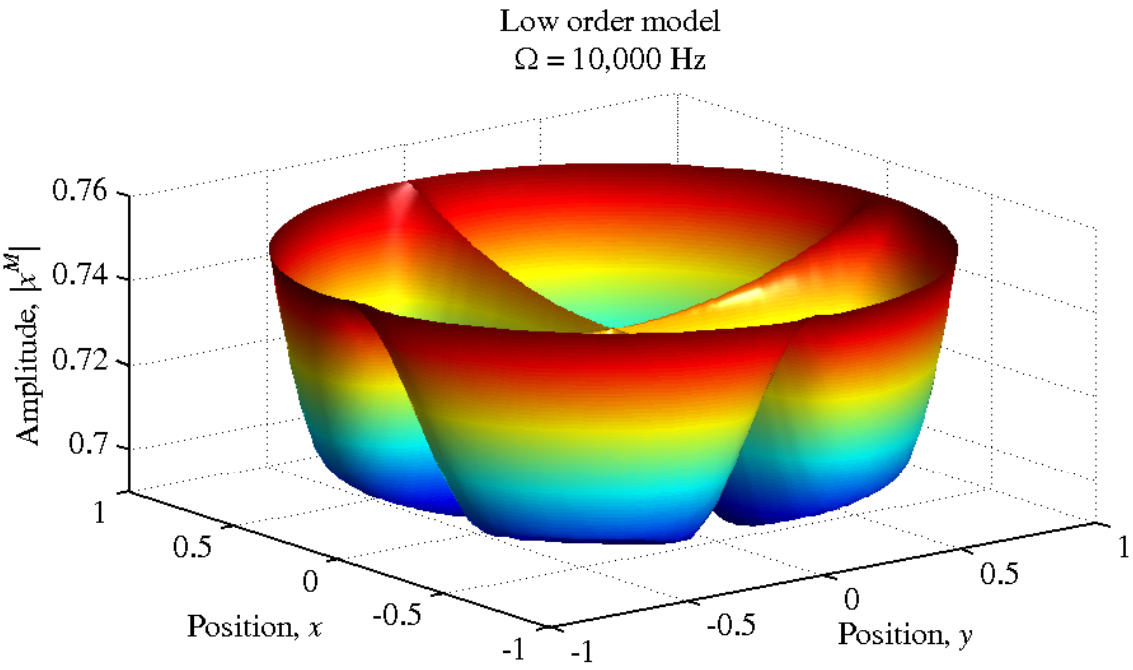


Figure 4.10: Low order model of magnetic field through a transverse section view of actuator rod

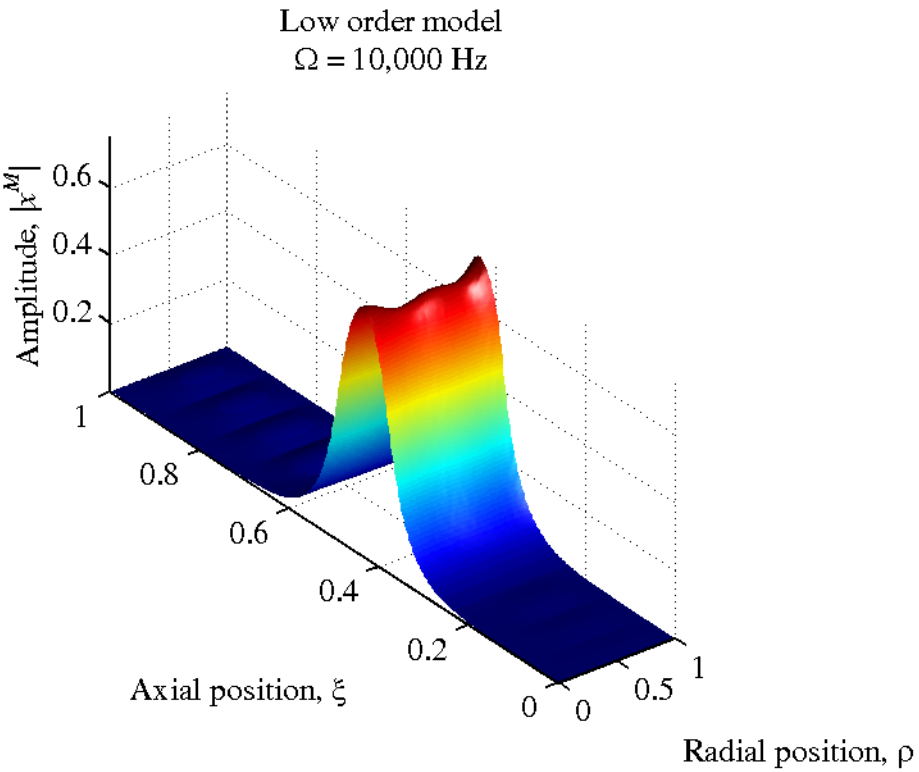


Figure 4.11: Low order model of magnetic field through an axial section view

Another type of example problem can be constructed to evaluate the frequency dependence of the magnetic field. In this case, we define a set of output variables in which the magnetic field is averaged across a transverse section of the rod. The transverse average field is the variable used by the vibration model to compute the distribution of magnetostrictive stress in the rod. The frequency response shows how the average field at an axial position changes with frequency.

The transverse average of dimensionless field for the coils from FEMM at the midplanes of the coils can be obtained by averaging the result in Eq. (4.82) across the pie segment.

$$\frac{\breve{\underline{x}}^M\left(\xi_{j'},\omega\right)}{\underline{x}_j^K\left(\omega\right)}=\frac{2}{\phi_0}\int_{\phi=0}^{\phi_0}\int_{\rho=0}^{1}\frac{\underline{x}^M\left(\rho,\phi,\xi_{j'},\omega\right)}{\underline{x}_j^K\left(\omega\right)}\rho d\rho d\phi$$
$$=\frac{2}{\phi_0 T}\int_{\phi=0}^{\phi_0}\int_{\rho=0}^{1}H_{R,j}^{FEMM}\left(r_g\rho,z_L\xi_{j'}\right)\rho d\rho d\phi \tag{4.85}$$
$$-\frac{2}{\phi_0}\sum_{k=1}^{kmax}\sum_{m=1}^{mmax}\sum_{p=1}^{pmax}\frac{i\omega\Theta_{k,m,p,j}}{\left(i\omega+\alpha_{k,m,p}\right)}\int_{\phi=0}^{\phi_0}\int_{\rho=0}^{1}\frac{\sin\left(\gamma_m\phi\right)\mathrm{J}_{\gamma_m}\left(\varepsilon_{k,m}\rho\right)\sin\left(\eta_p\xi_{j'}\right)}{N\left(\varepsilon_{k,m},\gamma_m\right)N\left(\gamma_m\right)N\left(\eta_p\right)}\rho d\rho d\phi$$

where

$$\xi_{j'}=\text{Axial midpoint of the } j' \text{ coil} \tag{4.86}$$

The formula is given for an arbitrary angular dimension, $\phi_0$, of the laminated segment. For the case computed, the angle is a quadrant of a circle, $\phi_0=\frac{\pi}{2}$.

Equation (4.85) can be simplified with the following definitions,

$$\breve{x}_{R,j}^{FEMM}\left(\xi_{j'}\right)=\frac{2}{T}\int_{\rho=0}^{1}H_{R,j}^{FEMM}\left(r_g\rho,z_L\xi_{j'}\right)\rho d\rho \tag{4.87}$$

$$P_{k,m}=\frac{2}{\phi_0}\frac{\int_{\phi=0}^{\phi_0}\sin\left(\gamma_m\phi\right)d\phi\int_{\rho=0}^{1}\mathrm{J}_{\gamma_m}\left(\varepsilon_{k,m}\rho\right)\rho d\rho}{N\left(\varepsilon_{k,m},\gamma_m\right)N\left(\gamma_m\right)N\left(\eta_p\right)}. \tag{4.88}$$

Inserting the definitions into Eq. (4.85)

$$\frac{\breve{\underline{x}}^M\left(\xi_{j'},\omega\right)}{\underline{x}_j^K\left(\omega\right)}=\breve{x}_{R,j}^{FEMM}\left(\xi_{j'}\right)-\sum_{p=1}^{pmax}\sum_{m=1}^{mmax}\sum_{k=1}^{kmax}\frac{i\omega\Theta_{k,m,p,j}}{\left(i\omega+\alpha_{k,m,p}\right)}P_{k,m}\sin\left(\eta_p\xi_{j'}\right) \tag{4.89}$$

This calculation can be computed for any energized coil and axial position for *jmax*×*jmax* array of results. Figure 4.12 shows a calculation in which the sixth coil, *j*=6, is energized and all ten axial positions are evaluated, $j'=1-10$. The calculation in Figure 4.12 is the high order case. The top line in the figure is the field at the midplane

of the energized coil at $\xi_6$. The two lines for the field on either side of coil 6 for the levels at $\xi_5$ and $\xi_7$ lie almost on top of one another and are about a factor of ten lower in amplitude. These lines represent the field in the rod which has diffused axially along the rod on either side of the energized coil. The magnetic field at positions which are farther from the energized coil are quite weak, a factor of 100 smaller than the field inside the energized coil shown by the top line.

The line for $\xi_6$ shows the effect of eddy current on the driving force for the actuator. The effect of the eddy current shows up as a first order attenuation beginning at a frequency of about 10,000 Hz. The average field at the midplane of the coil diminishes as a first order system above this point.

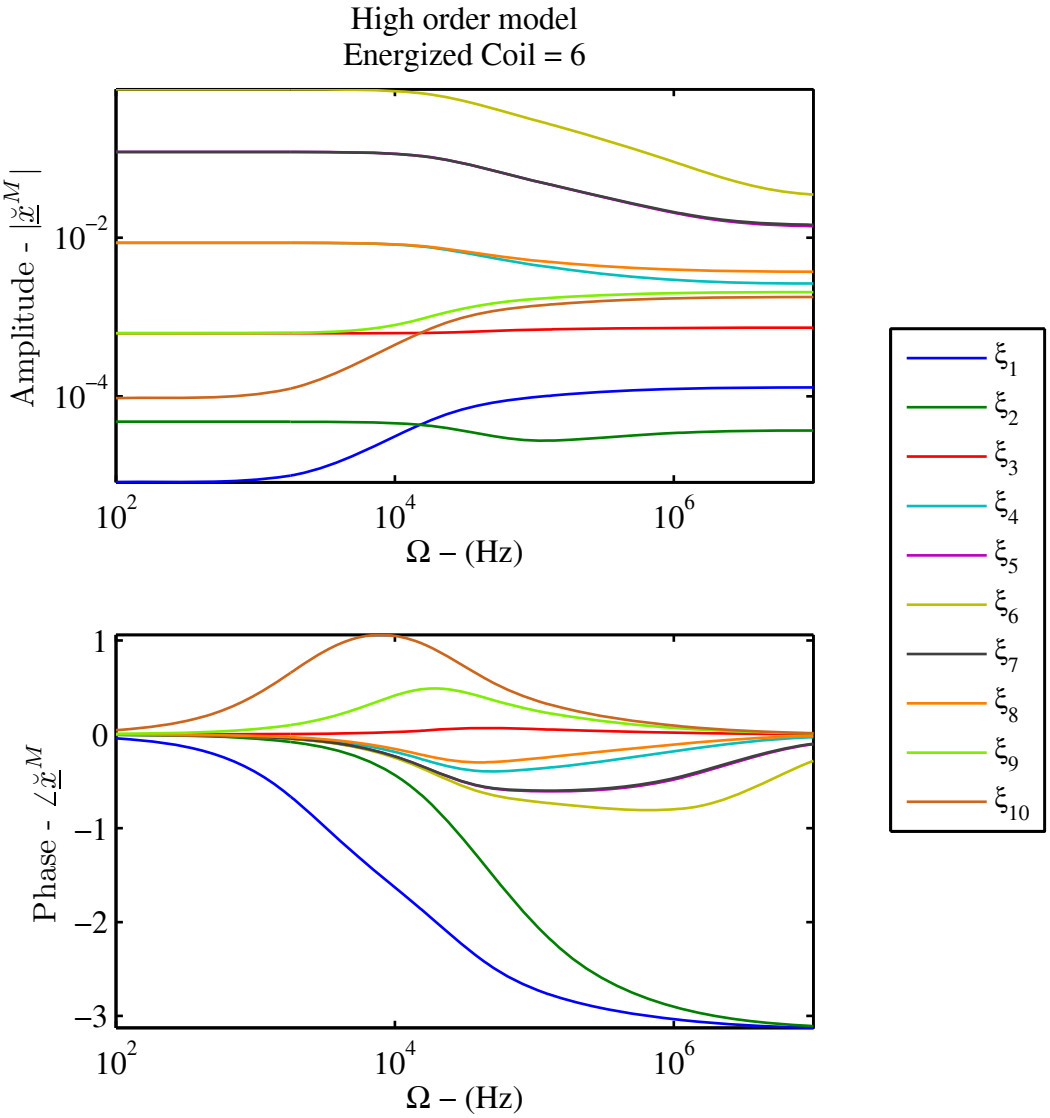


Figure 4.12: Frequency response of the average field at various axial positions for the high order magnetic model for a single energized coil

Figure 4.13 shows the same calculation except that the model is the low order case. The amplitude at low frequency is the same and response begins to roll off at the same frequency. The difference between the high order and low order cases can be seen in the attenuation the top line at $\xi_6$ at high frequency. The attenuation of the low order case flattens out at about 200,000 Hz rather than continuing toward zero field. The figure illustrates the expected result that the high order terms in the series are necessary for matching the field distribution at high frequency. The upper limit on frequency for which the low order model can be satisfactorily used is the frequency at which the response begins to flatten out. The low order response begins to deviate above $\Omega = 100,000$ Hz. Higher frequency calculations would require a higher order spatial model.

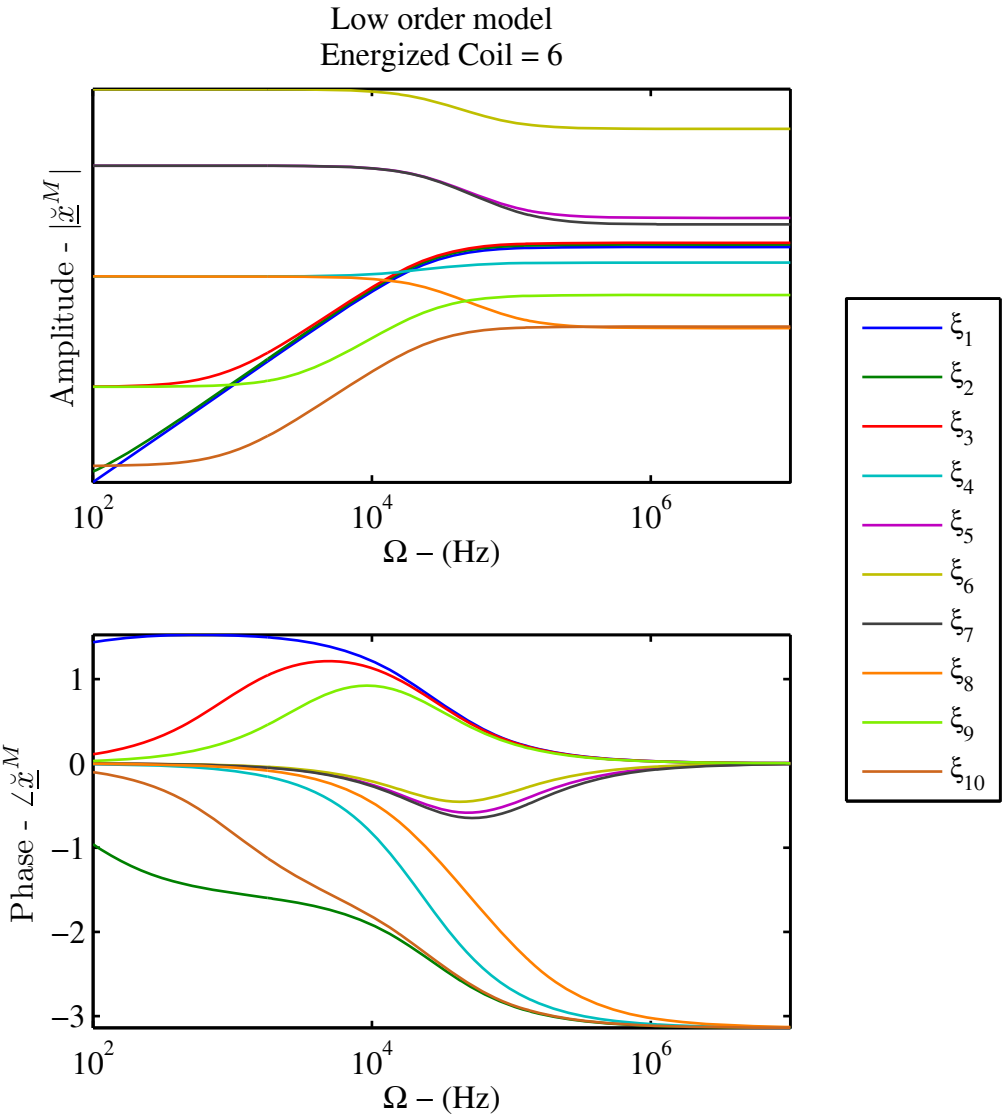


Figure 4.13: Frequency response of the average magnetic field at various axial positions for the low order system in response to a single energized coil

## State Space Magnetics Model

The derivation of the magnetic field has been working toward the state space form. The next step is to write Eq. (4.77) in the form of a descriptor state space system that can be combined with the vibration and circuit models of the actuator as indicated in Chapter 2. The technique is to write each subsystem in the following matrix form.

$$\mathbf{E}\dot{\mathbf{x}} = \mathbf{F}\mathbf{x} + \mathbf{G}\mathbf{u}\,. \tag{4.90}$$

In this form, all the terms that are coupled through their highest order derivatives are on the left hand side and multiplied by the **E** matrix. All the terms that are coupled through their states or lower orders of derivatives are multiplied by the **F** matrix. The matrices are subdivided into a four-by-four array according to the subdivision of the state vector. The magnetics model supplies the fourth row of the four-by-four system. Hence, we write out each submatrix individually as the following equation.

$$\begin{aligned}\mathbf{E}^{41}\ddot{\mathbf{x}}^{N} + \mathbf{E}^{43}\dot{\mathbf{x}}^{K} + \mathbf{E}^{44}\dot{\mathbf{x}}^{M} \\ = \mathbf{F}^{41}\dot{\mathbf{x}}^{N} + \mathbf{F}^{42}\mathbf{x}^{N} + \mathbf{F}^{43}\mathbf{x}^{K} + \mathbf{F}^{44}\mathbf{x}^{M} + \mathbf{G}^{4}\mathbf{u}.\end{aligned} \tag{4.91}$$

By comparison to Eq. (4.77), it is evident that a number of the matrices are zero matrices.

$$\begin{aligned}\mathbf{E}^{41} &= \mathbf{0}. \\ \mathbf{F}^{42} &= \mathbf{0}. \\ \mathbf{F}^{43} &= \mathbf{0}. \\ \mathbf{G}^{4} &= \mathbf{0}.\end{aligned} \tag{4.92}$$

Equation (4.77) also shows that $\mathbf{E}^{44} = \mathbf{I}$. Incorporating these simplifications into Eq. (4.92) leaves the version of the state space equation which can be combined with the other subsystems as the following.

$$\mathbf{E}^{43}\dot{\mathbf{x}}^{\mathbf{K}} + \dot{\mathbf{x}}^{\mathbf{M}} = \mathbf{F}^{41}\dot{\mathbf{x}}^{\mathbf{N}} + \mathbf{F}^{44}\mathbf{x}^{\mathbf{M}}\,. \tag{4.93}$$

The elements of the non-zero coefficient matrices can be written as

$$\begin{aligned} E_{l,j}^{43} &= \Theta_{k,m,p,j}. \\ F_{l,n}^{41} &= -\Upsilon_{k,m,p,n}. \\ F_{l,l'}^{44} &= -\delta_{ll'}\alpha_{k,m,p}. \end{aligned} \tag{4.94}$$

where the index, $l = k + kmax\left[m - 1 + mmax\left(p - 1\right)\right]$, is the index computation that stacks the three-dimensional *k*, *m*, and *p* elements into a vector. The index *n* corresponds to the elements of the vibration states. The index, *j*, corresponds to the elements of the coil current states. The $F_{l,l'}^{44}$ term gives a matrix with the elements of $\alpha_{k,m,p}$ on the diagonal.

## Combined Magnetics and Vibration State Space Model

The magnetics and vibration models can be combined in a state space model for sample calculations. In this model the derivative of coil current is the input to the magnetics model whereas the coil current itself is the input to the vibration model. First, we write the vibration and magnetics equations in descriptor form with the coil current in the input position of the equation.

$$\ddot{\mathbf{x}}^{\mathbf{N}} = \mathbf{F}^{11}\dot{\mathbf{x}}^{\mathbf{N}} + \mathbf{F}^{12}\mathbf{x}^{\mathbf{N}} + \mathbf{F}^{14}\mathbf{x}^{\mathbf{M}} + \mathbf{F}^{13}\mathbf{x}^{\mathbf{K}}. \tag{4.95}$$

$$\dot{\mathbf{x}}^{\mathbf{M}} = \mathbf{F}^{41}\dot{\mathbf{x}}^{\mathbf{N}} + \mathbf{F}^{44}\mathbf{x}^{\mathbf{M}} - \mathbf{E}^{43}\dot{\mathbf{x}}^{\mathbf{K}}. \tag{4.96}$$

Equations (4.95) and (4.96) can be written as a matrix equation. Notice that the coil current derivative input. $\dot{\mathbf{x}}^{\mathbf{K}}$, is integrated to get the current in the third row.

$$\begin{bmatrix} \ddot{\mathbf{x}}^{\mathbf{N}} \\ \dot{\mathbf{x}}^{\mathbf{N}} \\ \dot{\mathbf{x}}^{\mathbf{K}} \\ \dot{\mathbf{x}}^{\mathbf{M}} \end{bmatrix} = \begin{bmatrix} \mathbf{F}^{11} & \mathbf{F}^{12} & \mathbf{F}^{13} & \mathbf{F}^{14} \\ \mathbf{I} & \mathbf{0} & \mathbf{0} & \mathbf{0} \\ \mathbf{0} & \mathbf{0} & \mathbf{0} & \mathbf{0} \\ \mathbf{F}^{41} & \mathbf{0} & \mathbf{0} & \mathbf{F}^{44} \end{bmatrix} \begin{bmatrix} \dot{\mathbf{x}}^{\mathbf{N}} \\ \mathbf{x}^{\mathbf{N}} \\ \mathbf{x}^{\mathbf{K}} \\ \mathbf{x}^{\mathbf{M}} \end{bmatrix} + \begin{bmatrix} \mathbf{0} \\ \mathbf{0} \\ \mathbf{I} \\ -\mathbf{E}^{43} \end{bmatrix} \dot{\mathbf{x}}^{\mathbf{K}}. \tag{4.97}$$

To clarify the input derivative for current from the state derivative for current, the equation can be rewritten as the following.

$$\begin{bmatrix} \ddot{\mathbf{x}}^{\mathbf{N}} \\ \dot{\mathbf{x}}^{\mathbf{N}} \\ \dot{\mathbf{x}}^{\mathbf{K}} \\ \dot{\mathbf{x}}^{\mathbf{M}} \end{bmatrix} = \begin{bmatrix} \mathbf{F}^{11} & \mathbf{F}^{12} & \mathbf{F}^{13} & \mathbf{F}^{14} \\ \mathbf{I} & \mathbf{0} & \mathbf{0} & \mathbf{0} \\ \mathbf{0} & \mathbf{0} & \mathbf{0} & \mathbf{0} \\ \mathbf{F}^{41} & \mathbf{0} & \mathbf{0} & \mathbf{F}^{44} \end{bmatrix} \begin{bmatrix} \dot{\mathbf{x}}^{\mathbf{N}} \\ \mathbf{x}^{\mathbf{N}} \\ \mathbf{x}^{\mathbf{K}} \\ \mathbf{x}^{\mathbf{M}} \end{bmatrix} + \begin{bmatrix} \mathbf{0} \\ \mathbf{0} \\ \mathbf{I} \\ -\mathbf{E}^{43} \end{bmatrix} \dot{\mathbf{u}}^{\mathbf{K}} . \tag{4.98}$$

This system can be written as a state space system

$$\begin{bmatrix} \ddot{\mathbf{x}}^{\mathbf{N}} \\ \dot{\mathbf{x}}^{\mathbf{N}} \\ \dot{\mathbf{x}}^{\mathbf{K}} \\ \dot{\mathbf{x}}^{\mathbf{M}} \end{bmatrix} = \mathbf{A}^{\mathbf{NM}} \begin{bmatrix} \dot{\mathbf{x}}^{\mathbf{N}} \\ \mathbf{x}^{\mathbf{N}} \\ \mathbf{x}^{\mathbf{K}} \\ \mathbf{x}^{\mathbf{M}} \end{bmatrix} + \mathbf{B}^{\mathbf{NM}} \dot{\mathbf{u}}^{\mathbf{K}} . \tag{4.99}$$

where

$$\mathbf{A}^{\mathbf{NM}} = \begin{bmatrix} \mathbf{F}^{11} & \mathbf{F}^{12} & \mathbf{F}^{13} & \mathbf{F}^{14} \\ \mathbf{I} & \mathbf{0} & \mathbf{0} & \mathbf{0} \\ \mathbf{0} & \mathbf{0} & \mathbf{0} & \mathbf{0} \\ \mathbf{F}^{41} & \mathbf{0} & \mathbf{0} & \mathbf{F}^{44} \end{bmatrix} . \tag{4.100}$$

$$\mathbf{B}^{\mathbf{NM}} = \begin{bmatrix} \mathbf{0} \\ \mathbf{0} \\ \mathbf{I} \\ -\mathbf{E}^{43} \end{bmatrix} . \tag{4.101}$$

The displacement can be computed from this model using the $\mathbf{C}^2$ from Eq. 3.55.

$$y^{\mathbf{NM}} = \begin{bmatrix} \mathbf{0}_{1\times nmax} & \mathbf{C}^2 & \mathbf{0}_{1\times jmax} & \mathbf{0}_{1\times lmax} \end{bmatrix} \begin{bmatrix} \dot{\mathbf{x}}^{\mathbf{N}} \\ \mathbf{x}^{\mathbf{N}} \\ \mathbf{x}^{\mathbf{K}} \\ \mathbf{x}^{\mathbf{M}} \end{bmatrix} = \mathbf{C}^{\mathbf{NM}} \begin{bmatrix} \dot{\mathbf{x}}^{\mathbf{N}} \\ \mathbf{x}^{\mathbf{N}} \\ \mathbf{x}^{\mathbf{K}} \\ \mathbf{x}^{\mathbf{M}} \end{bmatrix}. \tag{4.102}$$

The time response for a step change transient analogous to the vibration model in Figure 3.3 is shown in Figure 4.14. To get a step change in current when the input is the derivative of current, we must apply an impulse to the derivative input.

$$\dot{u}_j^K = \delta(t). \tag{4.103}$$

The impulse input is equivalent to setting the initial condition to the following.

$$\mathbf{x}_0 = \mathbf{B}^{\mathbf{MV}}\mathbf{u}^{\mathbf{K}}, \tag{4.104}$$

where $u_j^K = 1$ and $u_{j'}^K = 0$ for all $j' \neq j$.

The response of the combined model shows ringing that is similar to the vibration model's step response, but the attenuation of the displacement response is clearly evident. Instead of a sharp step-like response in the vibration model, the displacement has the exponential rise of a first-order response to a step. This is the expected effect of a diffusion equation opposing the step response.

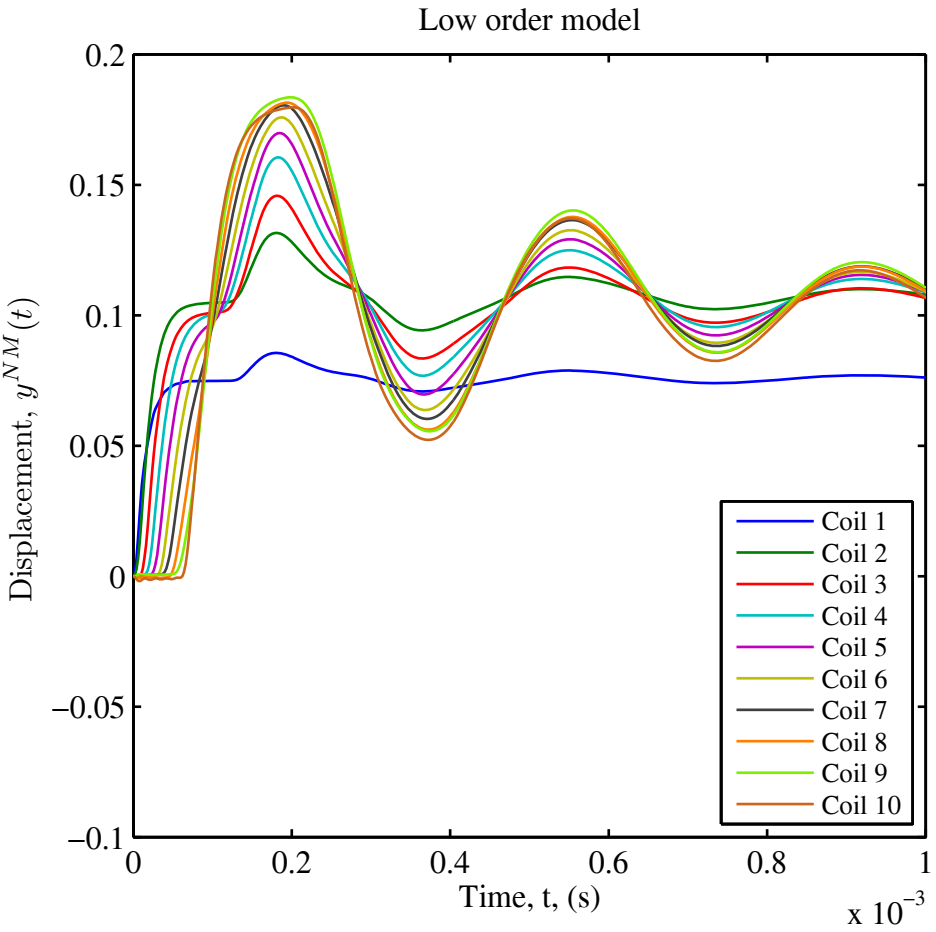


Figure 4.14: Actuator displacement for the combined magnetic and vibration model due to a step change in coil current

The frequency response form of the combined vibration and magnetic model can be obtained by transforming the state space system in Eqs. (4.99) and (4.102) and solving algebraically for $\frac{\underline{\underline{y}}^{\mathbf{NM}}}{\underline{\mathbf{u}}^{\mathbf{K}}}$.

$$\frac{\underline{\underline{y}}^{\mathbf{NM}}}{\underline{\mathbf{u}}^{\mathbf{K}}} = \mathbf{C}^{\mathbf{NM}} \left( i\omega \mathbf{I} - \mathbf{A}^{\mathbf{NM}} \right)^{-1} \mathbf{B}^{\mathbf{NM}} \left( i\omega \right). \tag{4.105}$$

The input derivative is transformed in the above expression, $\dot{\mathbf{u}}^{\mathbf{K}} \Rightarrow i\omega \underline{\mathbf{u}}^{\mathbf{K}}$, which gives the extra $i\omega$ factor on the right. The frequency response plot for a series of cases in which the inputs are individually energized is given in Figure 4.15. This figure is analogous to frequency response for the vibration model in Figure 3.5.

The frequency response shows the strong attenuation in the displacement due to the eddy current as frequency increases, whereas the vibration alone had much higher high frequency response. The eddy current attenuation has an even more significant effect for the combined vibration and magnetic models than the magnetic model alone because the vibration also generates a changing magnetic induction which adds to the coil current generating the eddy current. The eddy current effect acts as a magnetic drag on the vibration of the rod. The magnetic drag effect increases dramatically with frequency above the first radial mode's frequency constant.

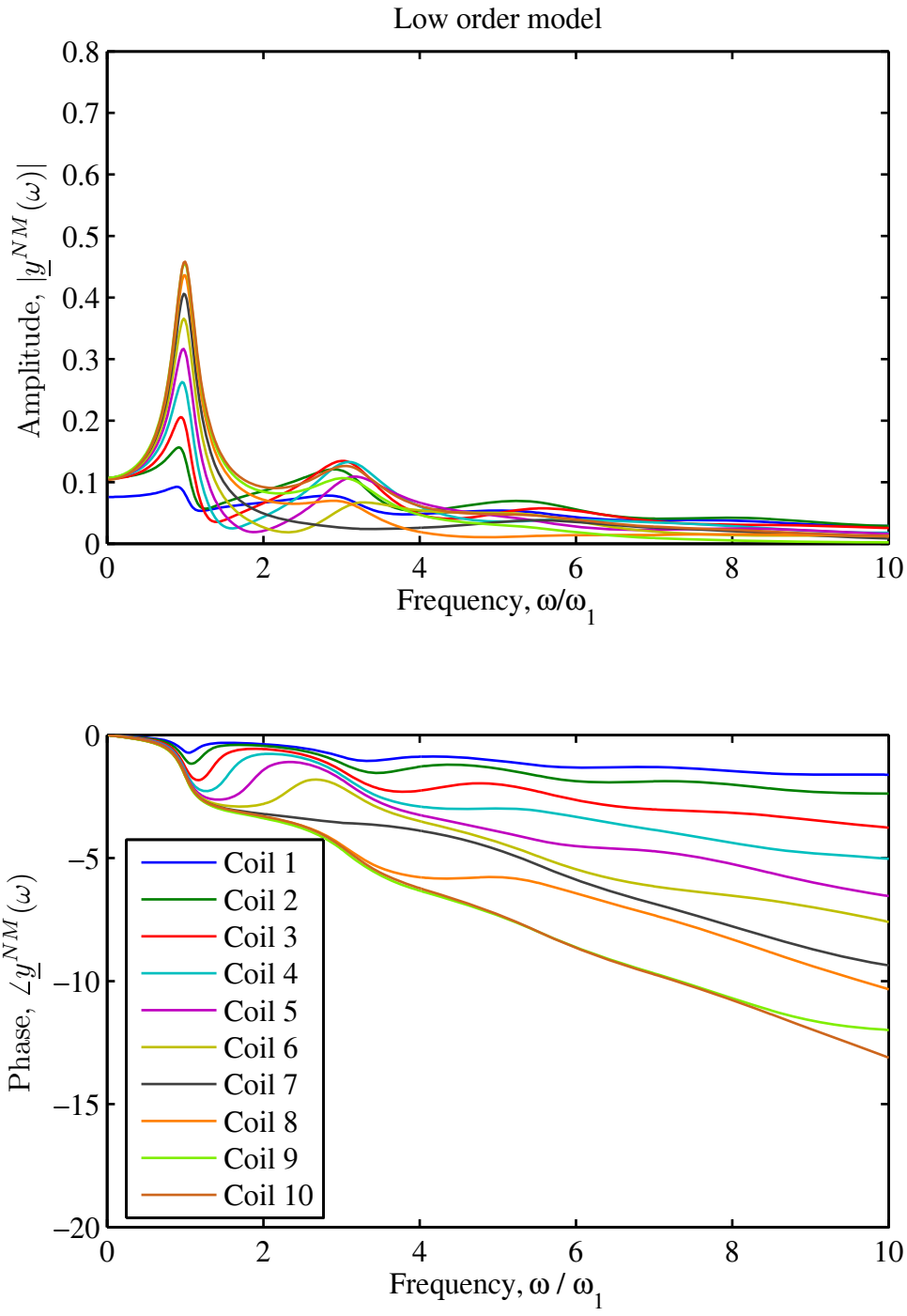


Figure 4.15: Frequency response of actuator displacement for the combined vibration and magnetics model

The eddy current attenuation of the vibration response makes a significant impact on the actuator design for high speed actuator response. The main frequency range of interest is the range up to $\omega/\omega_1 = 4$, ($\Omega = 4 \cdot 2747$ Hz $\approx 10,000$ Hz). In this range the attenuation is significant, but the actuator still responds. At frequency greater than 10,000 Hz, the loss in response means that the eddy current effect would prevent significant actuation. For that range of frequency, the actuator design must be modified to reduce the eddy current by including more laminations. The magnetic model includes a design parameter, $\phi_0$, representing the angular dimension of the pie-shaped segment of the actuator rod. The prototype is divided into quadrants so $\phi_0 = \frac{\pi}{2}$. The eddy current can be reduced by decreasing $\phi_0$. Another frequency response is shown in Figure 4.16 in which the angle is set to $\phi_0 = \frac{\pi}{16}$ or 32 pie segments. The finely laminated rod significantly reduces the eddy current effect and restores the frequency response out to very high frequency. The magnetic model development including eddy current effects is a key tool to designing actuators with high frequency response.

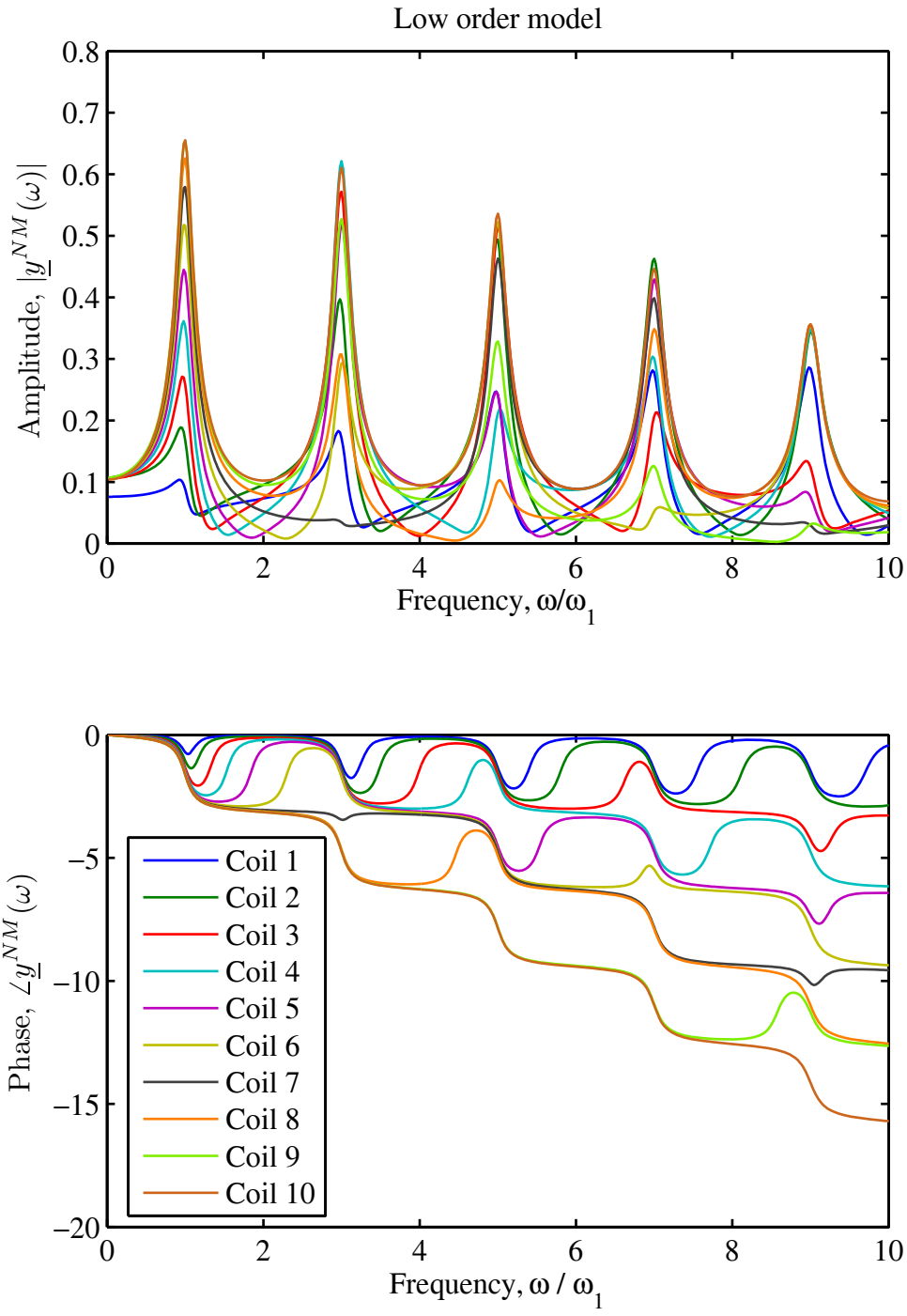


Figure 4.16: Frequency response of the finely laminated actuator rod, $\phi_0 = \frac{\pi}{16}$

## Current Density Solution

Any time-varying magnetic field in the actuator rod induces a voltage in the coils through Faraday's law. A component of that voltage depends on the induction due to the eddy current density distribution. To model this effect, one of the inductance coefficients that is derived in Chapter 5 depends on the azimuthal component of eddy current density distribution. In this section, formulae for the radial and azimuthal components of current density are derived in terms of the magnetic field solution. The current density distribution of the actuator rod is not linearly independent of the magnetic field. In this section, the relationship between the magnetic field and the current density is derived. The operation is not as simple as evaluating $\nabla \times \mathbf{H} = \mathbf{J}$ because only the axial component of the field has been derived thus far. The solution for current density must account for the radial, azimuthal, and axial dependence of the field. To get the full, three-dimensional dependence, we have to return to Maxwell's equations. First, a governing equation for the current density is derived starting with one of Maxwell's equations from Eq. (4.2)

$$\nabla \times \mathbf{E} = -\frac{\partial \mathbf{B}}{\partial t}, \tag{4.106}$$

and Ohm's law,

$$\mathbf{E} = \frac{\mathbf{J}}{\sigma}. \tag{4.107}$$

Substitute Eq. (4.107) into Eq. (4.106) to obtain

$$\nabla \times \mathbf{J} = -\sigma \frac{\partial \mathbf{B}}{\partial t}. \tag{4.108}$$

The axial component of the Eq. (4.108) can be obtained by performing the curl operation on the vector. The axial component of current density is zero by the orientation of the coil current.

$$\nabla \times \mathbf{J} = \nabla \times \begin{bmatrix} J_r \\ J_\phi \\ 0 \end{bmatrix} = \frac{1}{r} \begin{vmatrix} \hat{e}_r & r\hat{e}_\phi & \hat{e}_z \\ \frac{\partial}{\partial r} & \frac{\partial}{\partial \phi} & \frac{\partial}{\partial z} \\ J_r & rJ_\phi & 0 \end{vmatrix} = \begin{bmatrix} -\frac{\partial J_\phi}{\partial z} \\ \frac{\partial J_r}{\partial z} \\ \frac{1}{r}\left( \frac{\partial r J_\phi}{\partial r} - \frac{\partial J_r}{\partial \phi} \right) \end{bmatrix}. \tag{4.109}$$

The axial component of Eq. (4.108) can be written as a scalar equation involving the radial and azimuthal current densities.

$$\frac{1}{r}\left( \frac{\partial r J_\phi}{\partial r} - \frac{\partial J_r}{\partial \phi} \right) = -\sigma \frac{\partial B_z}{\partial t}. \tag{4.110}$$

A second equation involving the components of current density can be obtained from the conservation of charge equation.

$$\nabla \cdot \mathbf{J} = \frac{1}{r}\left[ \frac{\partial r J_r}{\partial r} + \frac{\partial J_\phi}{\partial \phi} \right] = 0. \tag{4.111}$$

These equations can be put in to dimensionless form with the variable substitutions from Chapter 2.

$$b = \frac{B - B_{min}}{\Delta B} = \frac{B - B_{min}}{\mu^T T \Delta I}. \tag{4.112}$$

$$\xi = \frac{z}{z_L}. \tag{4.113}$$

$$\rho = \frac{r}{r_g}. \tag{4.114}$$

Note that the permeability, $\mu^T$, is not the same parameter as $\mu_R$.

We can derive a scaling factor for $J_r(r,\phi,z,t)$ and $J_\phi(r,\phi,z,t)$ to create a dimensionless current density.

$$j_r = \frac{r_g J_r}{T\Delta I},\ j_\phi = \frac{r_g J_\phi}{T\Delta I}. \tag{4.115}$$

Inserting these definitions into Eq. (4.110) and Eq. (4.111) gives the dimensionless form of the current density equations.

$$\frac{1}{\rho}\left(\frac{\partial \rho j_\phi}{\partial \rho} - \frac{\partial j_r}{\partial \phi}\right) = -\sigma\mu^T r_g^2 \frac{\partial b_z}{\partial t}. \tag{4.116}$$

$$\frac{1}{\rho}\left(\frac{\partial \rho j_r}{\partial \rho} + \frac{\partial j_\phi}{\partial \phi}\right) = 0. \tag{4.117}$$

The goal of the derivation is to use Eq. (4.116) and Eq. (4.117) to find series solutions that are similar in form to the magnetic field solution. The general form of the solution that is sought is given by the following two equations.

$$j_\phi(\rho,\gamma,\xi,t) = \sum_{k=1}^{kmax}\sum_{m=1}^{mmax}\sum_{p=1}^{pmax} \frac{\mathcal{J}_{\phi,k,m,p}(t) R_\phi(\varepsilon_{k,m}\rho)\Phi_\phi(\gamma_m\phi) Z_\phi(\eta_p\xi)}{N_\phi(\gamma_m) N_\phi(\varepsilon_{k,m},\gamma_m) N_\phi(\eta_p)}, \tag{4.118}$$

$$j_r(\rho,\gamma,\xi,t) = \sum_{k=1}^{kmax}\sum_{m=1}^{mmax}\sum_{p=1}^{pmax} \frac{\mathcal{J}_{r,k,m,p}(t) R_r(\varepsilon_{k,m}\rho)\Phi_r(\gamma_m\phi) Z_r(\eta_p\xi)}{N_r(\gamma_m) N_r(\varepsilon_{k,m},\gamma_m) N_r(\eta_p)}, \tag{4.119}$$

where $j_r(\rho,\gamma,\xi,t)$ and $j_\phi(\rho,\gamma,\xi,t)$ are dimensionless current density functions, $R_r(\varepsilon_{k,m}\rho)$, $\Phi_r(\gamma_m\phi)$, and $Z_r(\eta_p\xi)$ are modal functions for the radial component of current density, and $R_\phi(\varepsilon_{k,m}\rho)$, $\Phi_\phi(\gamma_m\phi)$, and $Z_\phi(\eta_p\xi)$ are modal functions for the azimuthal component of current density. The solution of current density is not

independent of the magnetics solution so it is to be expected that the amplitude functions, $\mathcal{I}_{r,k,m,p}(t)$ and $\mathcal{I}_{\phi,k,m,p}(t)$ are related to the amplitude functions for the magnetic modes, $\chi^{M}_{k,m,p}(t)$. The details of the derivation of the functions are given in APPENDIX D. The results are repeated here for completeness.

$$\mathcal{I}_{r,k,m,p} = \left(1+\frac{\chi_R r_g^2 \eta_p^2}{z_L^2 \varepsilon_{k,m}^2}\right)\chi^{M}_{k,m,p}(t). \tag{4.120}$$

$$\mathcal{I}_{\phi,k,m,p}(t) = \left(1+\frac{\chi_R r_g^2 \eta_p^2}{z_L^2 \varepsilon_{k,m}^2}\right)\chi^{M}_{k,m,p}(t). \tag{4.121}$$

$$R_r\left(\varepsilon_{k,m} r\right) = \frac{\gamma_m \mathrm{J}_{\gamma_m}\left(\varepsilon_{k,m}\rho\right)}{\rho}. \tag{4.122}$$

$$R_\phi\left(\varepsilon_{k,m}\rho\right) = \left[\varepsilon_{k,m}\mathrm{J}_{\gamma_m+1}\left(\varepsilon_{k,m}\rho\right) - \frac{\gamma_m \mathrm{J}_{\gamma_m}\left(\varepsilon_{k,m}\rho\right)}{\rho}\right]. \tag{4.123}$$

$$\Phi_r\left(\gamma_m\phi\right) = \cos\left(\gamma_m\phi\right). \tag{4.124}$$

$$\Phi_\phi\left(\gamma_m\phi\right) = \sin\left(\gamma_m\phi\right). \tag{4.125}$$

$$Z_\phi\left(\eta_p\xi\right) = \sin\left(\eta_p\xi\right). \tag{4.126}$$

$$Z_r\left(\eta_p\xi\right) = \sin\left(\eta_p\xi\right). \tag{4.127}$$

The eigenvalues for the modes are the same as for the magnetic field problem and are defined in APPENDIX D.

The vector current density in dimensioned units is needed for the coil circuit coupling to eddy current because the calculation involves dimensioned parameters from FEMM. The vector current density in dimensioned units is given by

$$\mathbf{J}^M\left(r,\phi,z,t\right)=\frac{T\Delta I}{r_g}\begin{bmatrix} j_r\left(\dfrac{r}{r_g},\phi,\dfrac{z}{z_L},t\right) \\ j_\phi\left(\dfrac{r}{r_g},\phi,\dfrac{z}{z_L},t\right) \\ 0 \end{bmatrix}. \tag{4.128}$$

The radial and azimuthal components of the current density distribution functions can be grouped into a single vector function for use in the induction calculation. Let

$$\mathbf{f}^M_{k,m,p}\left(r,\phi,z\right)=\frac{T\Delta I}{r_g}\begin{bmatrix} \gamma_m\left(1+\dfrac{\chi_R r_g^2\eta_p^2}{z_L^2\varepsilon_{k,m}^2}\right)\dfrac{\mathrm{J}_{\gamma_m}\left(\dfrac{\varepsilon_{k,m}r}{r_g}\right)\cos\left(\gamma_m\phi\right)\sin\left(\dfrac{\eta_p z}{z_L}\right)}{\rho N_r\left(\gamma_m\right)N_r\left(\varepsilon_{k,m},\gamma_m\right)N_r\left(\eta_p\right)} \\ \left(1+\dfrac{\chi_R r_g^2\eta_p^2}{z_L^2\varepsilon_{k,m}^2}\right)\dfrac{\begin{bmatrix}\varepsilon_{k,m}\mathrm{J}_{\gamma_m+1}\left(\dfrac{\varepsilon_{k,m}r}{r_g}\right) \\ -\dfrac{r_g}{r}\gamma_m\mathrm{J}_{\gamma_m}\left(\dfrac{\varepsilon_{k,m}r}{r_g}\right)\end{bmatrix}\sin\left(\gamma_m\phi\right)\sin\left(\dfrac{\eta_p z}{z_L}\right)}{N\left(\gamma_m\right)N\left(\varepsilon_{k,m},\gamma_m\right)N\left(\eta_p\right)} \\ 0 \end{bmatrix}. \tag{4.129}$$

With this definition of the spatial distribution function, the dimensioned current density can be written in terms of the dimensionless eddy current states as

$$\mathbf{J}^M\left(r,\phi,z,t\right)=\sum_{k=1}^{kmax}\sum_{m=1}^{mmax}\sum_{p=1}^{pmax}\mathbf{f}^M_{k,m,p}\left(r,\phi,z\right)\mathcal{X}^M_{k,m,p}\left(t\right). \tag{4.130}$$

This is the form for current density that is most convenient for computing the inductance coefficients in Chapter 5.

**Frequency Response of the Eddy Current Density Model**

The eddy current model can be evaluated using MATLAB to illustrate the properties of the current distribution under an oscillatory input current to the coil. The frequency dependent amplitude functions are given in Eq. (4.79). The current density can be evaluated using these amplitudes and the distribution function in Eq. (4.118) along with the associated spatial functions for the coil field and eddy current field. The vibration component of magnetization is set to zero in these calculations. Figure 4.17 shows the real component of current density, $\mathrm{Re}(j_\phi(\rho,\gamma,\xi,t))$ through an axial, $\rho-\xi$ plane. Only the azimuthal current density is plotted. The inductance coefficients which are computed in the following chapter ultimately depend only on the azimuthal component. The radial component current density is an intermediate step in the derivation of the azimuthal component.

The response of the eddy current is to cancel the field from the coil current. The coil current is positive so the eddy current reaches a peak in the negative direction on the outer surface of the rod just inside the energized coil. The positive peak near the centerline is due to conservation of charge. No charge can build up at any point in the interior of the rod; therefore, the net current through the axial section must be zero, and the area under the curve in Figure 4.17 must integrate to zero. The positive and negative components represent the circulation of the eddy current around the pie-shaped cylinder as illustrated in Figure 4.2

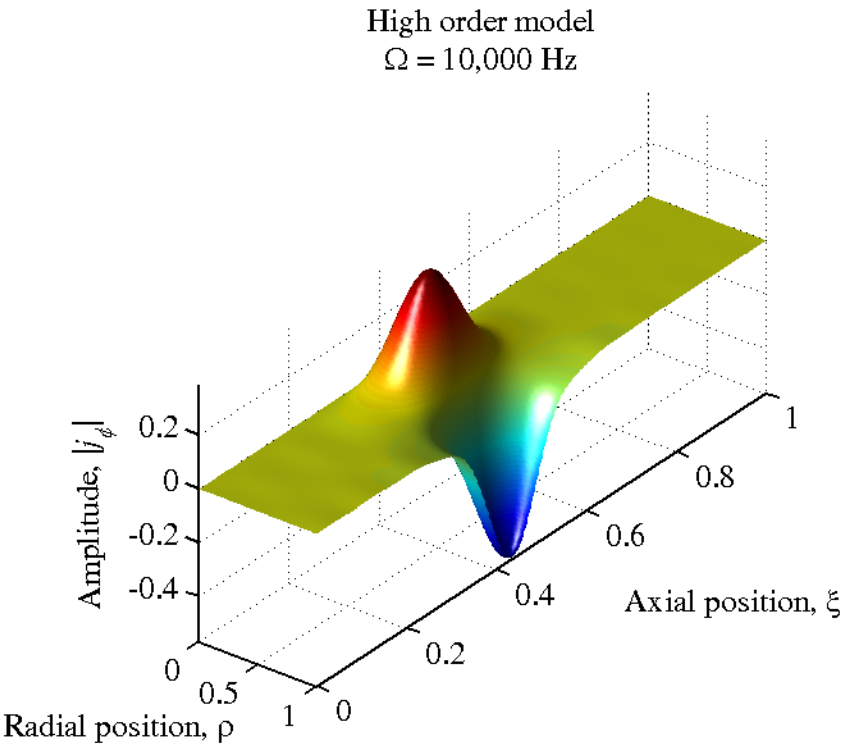


Figure 4.17: Real component of eddy current density distribution in an axial section view

The real and imaginary components of azimuthal current distribution in a transverse section view are shown in Figure 4.18 and Figure 4.19. Both current distributions in the transverse section view show the negative peak at the outer radius of the cylinder and the corresponding positive peak near the centerline. The current density must be zero normal to any insulated surface. So, the azimuthal current density goes to zero on the insulated boundaries between the pie segments.

The general features of the current density solution conform to expectations. The modal model of eddy current distribution in a transverse section view is also compared the current density computed by the FEMM infinite cylinder problem in APPENDIX D.

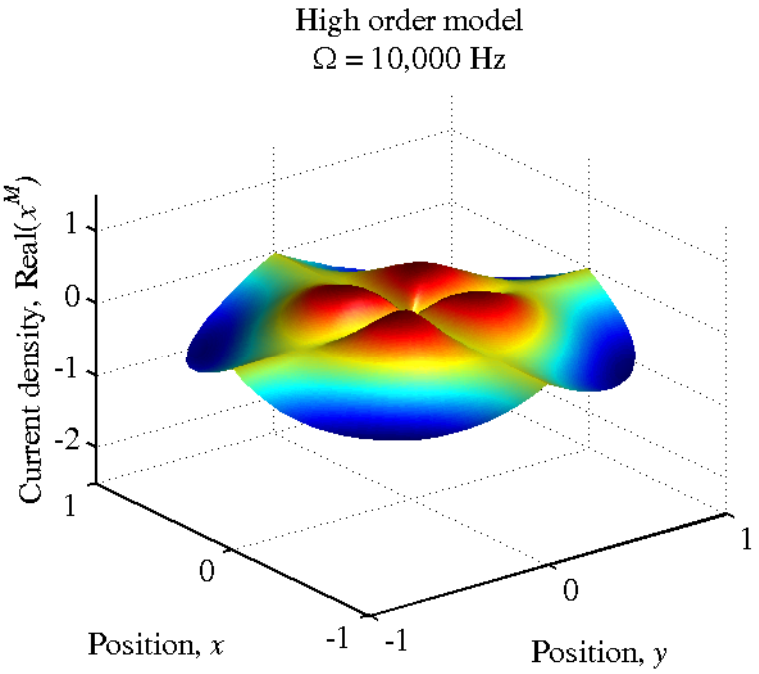


Figure 4.18: Real component of current density distribution in a transverse section view

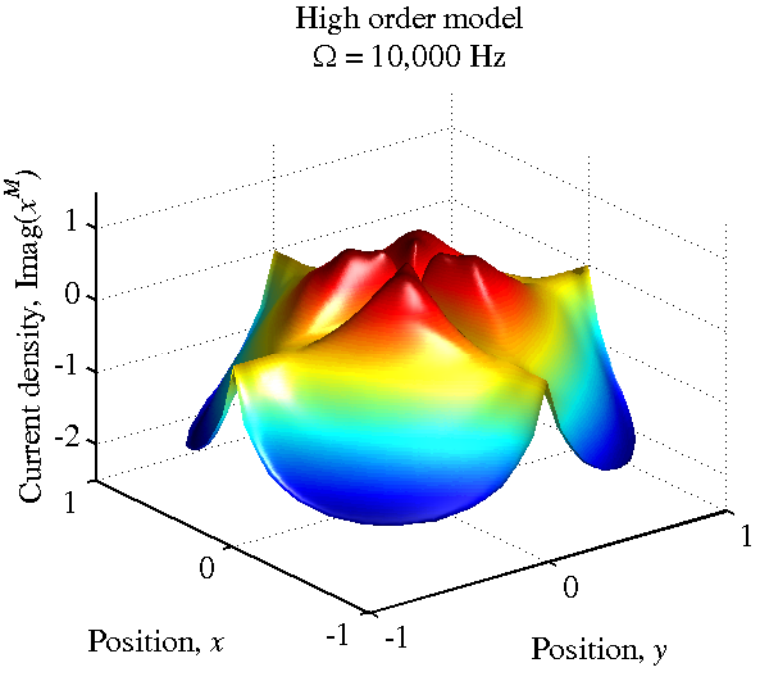


Figure 4.19: Imaginary component of current density distribution in a transverse section view

## Summary of the Magnetic Model

The governing equation for magnetics is derived from Maxwell's equations. The equation is simplified using the quasi-steady magnetics approximation of the electromagnetic wave equation to obtain a diffusion equation representing the magnetic field. The magnetostrictive effect is added through a constitutive relation relating magnetic induction to magnetic field and strain. The magnetic field problem is separated into two terms, one representing the field of the coil and the other representing the field due to eddy current. This separation allows the field from the coil to be simulated by the finite element code, FEMM. The eddy current's magnetic field is obtained from a modal solution of a three-dimensional diffusion problem. The homogeneous boundary condition approximation is introduced to make the equation for the eddy current's magnetic field solvable. The solution is obtained by the method of integral transform which reduces the partial differential equation in time and three spatial variables to a set of ordinary differential equations in the time variable. Each differential equation represents the amplitude of a spatial mode of the eddy current's magnetic field. A related problem to obtain the eddy current density distribution from the magnetic field solution is also solved. The eddy current density distribution is needed to compute the inductance between the eddy current and the coil. The total number of state variables for the magnetic model is only ten states to represent a three-dimensional distribution of magnetic field and eddy current in the ten coil actuator. This is a significantly more compact model than might have been anticipated and is one of the results of the project that may be useful in other magnetostrictive actuator research.

Spatial distributions of magnetic field are evaluated and plotted to visualize the solution of the magnetic field problem. These calculations illustrate the axial distribution of magnetic field that is the source of the localized stress used in the multi-coil design to distribute the energy input in space and time for more efficient operation. The visualization of the magnetic field in the transverse plane illustrates that the additional lamination of the actuator rod in the prototype design did not eliminate eddy current. The eddy current effect produces a significant loss in actuator response at the upper end of the frequency range of interest.

The magnetic model is combined with the vibration model to show the coupled system involving the damped wave equation for the vibration model with the diffusion equation for the magnetic field. The stand alone simulations show that the magnetic drag term is greater than the frictional drag at high frequency and is responsible for a significant attenuation of the response. A calculation using a modified, high speed actuator design is shown which increases the number of laminations to recover the very high frequency response.

Test calculations are provided in APPENDIX D based on limiting cases in which the magnetic model solution must approach a known distribution. One limiting case can be constructed by allowing the driving frequency to approach infinity. The magnetic induction in the interior of the rod must approach zero. The eddy current induction must build sufficiently to cancel the source distribution exactly. Since the series solution for the eddy current induction distribution is truncated, the cancelation is approximate. The test cases verify the derivation and programming of the coupling coefficients between eddy current model and the vibration and coil current models.

An innovative test case is also constructed in which the two-dimensional FEMM code is used to simulate the transverse plane of the actuator rod. The calculation approximates the rod as a uniform infinite cylinder. With some special interpretation, the results from FEMM can be compared to the eddy current density and magnetic field distributions from the modal series solution developed for the research. The modal model is executed with all coils operating in unison to approximate the infinite rod and the distributions functions are evaluated at the axial midplane of the actuator. This simulation is used to evaluate the number of terms in the eddy current modal solution that are needed for accurate simulation of the field. At 10,000 Hz, the calculations show that one radial mode, one azimuthal mode and ten axial mode functions are sufficient for the problem.

A test is devised using the symbolic mathematical manipulation program in MATLAB to differentiate the modal solution of current density to test that the solution solves the original differential equation. A series of differential and algebraic operations using Maxwell's equations generates the analytical solutions for the modes of magnetic potential, magnetic induction, magnetic field, and back again to current density. Reproducing the original modal current density function by way of a computer program to perform the algebraic steps provides an independent test of modal functions used for the magnetic field and current density solution.

# A MULTI-COIL MAGNETOSTRICTIVE ACTUATOR: DESIGN, ANALYSIS, AND EXPERIMENT

## VOLUME II

by

Thomas L. Wilson, Jr.

# CHAPTER 5

# COIL CIRCUIT MODEL

Each of the drive coils in the multi-coil actuator is contained in a separate, individually controlled circuit consisting of a coil, load resistor, and amplifier. The control input is computed by the digital control system and is applied to the amplifier's input. The control input must then go through the amplifier circuitry and the coil circuit to reach the magnetostrictive rod. The dynamics of the amplifier and coil circuit affect the model-based control strategy. The magnetic model section discusses the inductive coupling between the coils, eddy current, and vibration. The inductive coupling of a coil with other current sources is important because the coils, eddy current, and vibration are physically close to one another in the actuator device. The induced currents work against the input current that the control algorithm would ideally need for optimal actuator response. The amplifier in the circuit is configured as a current-controlled device whose internal feedback is designed to compensate for the induced voltages, but the compensation is not perfect and the dynamics of the circuit need to be considered in conjunction with the dynamics of eddy current and vibration for an accurate representation of the process in the control algorithm.

The only significant, new approximation added to the actuator model in this section is the approximation that the amplifier is a proportional gain device. This approximation neglects the higher frequency dynamics of the amplifier's internal feedback network. The coil model is also affected by approximations from the vibration

and eddy current models because it uses their current density distributions in the inductance calculation.

The voltages around the coil circuit loop are given by Kirchhoff's law for closed loop. The main objective of the development of the circuit model is to account for the self inductances of the coil and the mutual inductance between the coil and all other current sources in the model. The inductances are determined by an application of Faraday's law. Each mode of eddy current or vibration can be thought of as a coil with a density of turns at every point in space equal to the modal current density distribution function. The inductance calculation integrates that current density distribution weighted with the coil's magnetic potential at that point in space. Since each mode shape is fixed, the calculation yields an array of constants which represent the inductances between the current density distributions of the eddy current and vibration modes and the coil.

The differential form of Faraday's law is one of Maxwell's equations and is the starting point for the derivation. The inductances are solved using the current density distributions for vibration and eddy current that have been derived in Chapter 3 and Chapter 4. The calculation depends on the magnetic potential that is calculated by the FEMM model of the actuator that is described in Appendix C. The coil circuit model derivation results in a state space equation in descriptor form for the coil circuit. The state variables in the coil circuit model are the normalized coil currents. In addition, the outputs for coil voltage and power are computed from the state space system. APPENDIX F derives the general coupling of a coil with the magnetic potential which is used in the formulation of the inductances. APPENDIX G gives the details of the solution for each coefficient.

## Literature Survey on the Coil Circuit Modeling

Mathematical models of a complete coil circuit of a magnetostrictive device are rarely reported in the literature. Modeling for the two main components, the amplifiers and magnetostrictive devices, are typically found in separate references. The literature survey covers the references to coil and amplifier topics separately with the coil model discussed first.

The magnetostrictive device has a dual nature as both actuator and sensor. Just as an externally supplied current in the coil produces a strain in the rod, a strain in the actuator produces a current in the coil. Models dealing with the voltage or current induced in a coil from magnetostriction are mainly concerned with using the magnetostrictive device as a sensor. In many instances, separate coils for sensing and driving the device are provided in the design [52, 53]. The sensing coils are modeled using the Faraday law applied to a coil. The early articles by Pratt [36] and Calkins [54] are relevant because they recognize that sensing and driving could be accomplished in a single coil. The models of inductive coupling are mainly lumped models with a single average magnetization in the device and a single average current. A typical case is Dapino's lumped parameter model which is used to fit of several magnetostrictive parameters simultaneously. To model the pickup coil, Dapino applies the Faraday-Lenz law of magnetic induction to calculate the field in a coil as the integral of voltage across a pickup coil. Dapino also uses a direct measurement of the magnetic field at the surface of the coil to show that the magnetic end effects of the coil are actually not negligible [38]. Hall devises a feedback control circuit to compensate for nonlinearity of a magnetostrictive transducer [43]. The design of the feedback circuit requires a simple

model of the drive circuit. In two versions of the circuit, the feedback control was tried with both current-controlled and voltage-controlled configurations of the drive amplifiers. Both types of amplifiers are modeled as proportional amplifiers in which the output is proportional to the error (either current or voltage error). Hall's paper is the only reference obtained in which the amplifier is explicitly part of the model.

The coil modeling requirements of the multi-coil magnetostrictive actuator are different than other magnetostrictive actuator models because of the spatially distributed nature of the coils, vibration, and eddy current density distributions. To develop the multiple interactions between the current sources in the model, the research returns to basic textbook references in electricity and magnetism. Modeling of inductive coupling between coils is commonly found in elementary physics and electromagnetic texts [46-48]. The approach in this model is the same as conventional coil-to-coil inductance but is adapted so that the inductive coupling between each coil and modal function for the eddy current and vibration can also be computed. The equation for inductive coupling is derived from Maxwell's equations and the constitutive relations for the materials.

The amplifier is the other dynamic component of the coil circuit. The current controlled amplifier produces an output current proportional to the input voltage. In the actuator experiment, the current feedback (as opposed to the more conventional voltage feedback) works to counteract any current induced in the coil by inductive coupling to other coils, vibration, and eddy currents and causes the coil current to track control demand more closely.

Mathematical models of amplifiers are commonly found in textbooks. The references [55] and [56] give examples of simple dynamic models of an amplifier in a

circuit. The typical textbook models of amplifiers are constant gain devices producing an output voltage proportional to the input voltage. Operational amplifiers, for example, are idealized as constant, very high gain devices with infinite input impedance and zero output impedance. The main point in modeling the operational amplifier is to compute the steady state gain when various forms of compensation and feedback are applied. The calculation of gain of the circuit only requires the resistances in the circuit and does not depend on the dynamic components such as the inductance or capacitance. The output of the calculation is simply the linear, steady state gain. In models that are one step up from the steady-state gain calculation, the operational amplifier or transistor is modeled as a perfect gain device plus a capacitor in parallel. This model is converted to frequency domain and algebraic computations in the complex plane are used to evaluate gain and phase as a function of frequency. This type of model is used to design feedback compensation of amplifiers. Since audio amplifiers, like the ones used in this research, are multi-stage devices with complex feedback schemes, the frequency response models become high-order transfer functions. Modeling of a detailed circuit is a usually handled by computer simulation. One of the early circuit modeling codes is SPICE (Simulation Program with Integrated Circuit Emphasis) which was developed at University of California at Berkeley in the 1970's by Nagel and others [57, 58]. The modeling approach of SPICE has been widely adopted and many commercial electronic analysis codes trace their modeling origins to the SPICE code. SPICE was originally intended for integrated circuit design but has become a general-purpose tool for all types of electronic circuits. SPICE represents each discrete transistor, resistor, inductor, and capacitor in the circuit individually. The power of the code comes from the library of models of

nonlinear devices such as MOSFET's and bipolar transistors which can be incorporated into a circuit as building blocks. Steady state, dynamic and frequency domain results can be calculated from the same SPICE model. For an electronic circuit simulation representing all the discrete components in an audio amplifier, the model might be small compared to an integrated circuit but still results in a high order model for the purposes of control. Moreover, the input data for the discrete components in the amplifier used in the research are not available. Since the amplifier used in this research is rated for less than ±3 dB variation in gain from DC to 20 kHz, the amplifier frequency dynamics only begin to come into play at the upper end of the range of the actuator problem. Based on this understanding of the dynamics, a simple, proportional gain approximation of the amplifier, like the models in Ogata[55], should suffice.

**Governing Equation for the Coil Circuit**

The coil circuit consists of three components: a coil, an amplifier and a resistor connected in series. The starting point for the model of the circuit is Kirchhoff's loop equation around the coil circuit. In the loop equation, the sum of the voltages around any closed loop must be zero.

$$\mathscr{V}_{Amp,j} - \mathscr{V}_j^K - I_j^K \mathscr{R}_L = 0\,, \tag{5.1}$$

where $\mathscr{V}_{Amp,j}$ is the voltage supplied by the amplifier, $\mathscr{V}_j^K$ is the voltage drop across the coil, $I_j^K$ is the current in the circuit, and $R_L$ is the resistance of the load resistor in the circuit.

A load resistor is included in the circuit to match the impedance of the circuit to the output impedance of the amplifier. The audio amplifier is designed for a load

impedance of 4 ohms. Audio amplifiers, like the ones used for the experiment, when used to power loudspeakers are high pass filters with cut-off frequency of about 20-50 Hz. The circuit can rely mainly on the inductive component from coil of the loudspeaker to provide load impedance. The magnetostrictive actuator, however, includes a DC bias. The inductive load becomes zero at DC so a resistive element is needed in the circuit to stabilize the amplifier feedback under DC conditions. The resistance of the load resistor is selected to be 4 ohms to match the impedance of the output stage of the amplifier.

The voltage across the coil consists of a purely resistive loss in the coil wire and an inductive component. The dimensionless variables are more conveniently defined when these inductive and resistive components are separated. Let

$$\mathscr{V}_j^K = \mathscr{V}_{Inductive,j} + I_j^K \mathscr{R}_C . \tag{5.2}$$

With this definition, the loop equation becomes the following:

$$\mathscr{V}_{Amp,j} - \mathscr{V}_{Inductive,j} - I_j^K \left( \mathscr{R}_L + \mathscr{R}_C \right) = 0 . \tag{5.3}$$

While amplifier dynamic modeling could be elaborate, the choice in this model is to take the simplest possible approach. The amplifier in the prototype actuator's drive circuit is configured as a current-controlled or transconductance amplifier. This configuration typically is high gain and is fast responding. Based on this characteristic, the approach in this dissertation is to approximate the amplifier voltage as a proportional gain device.

$$\mathscr{V}_{Amp,j}(t) = \mathscr{G}\left( U_j(t) - I_j^K(t) \right). \tag{5.4}$$

The proportional nature of the feedback results in a steady state error between $U_j(t)$ and $I_j^K(t)$. The steady state error is made small by designing the amplifier so that

the gain $\mathscr{G}$ is large. The name "transconductance" amplifier recognizes that the gain of the device in units of resistance. The gain multiplies the amplifier input by a negative resistance to provide a source term for the differential equation. Including the proportional gain model of the actuator in Eq. (5.3) yields the following.

$$\mathscr{V}_{Inductive,j} + \left(\mathscr{G} + \mathscr{R}_L + \mathscr{R}_C\right) I_j^K = \mathscr{G} U_j(t). \tag{5.5}$$

A simplified inductive voltage that includes just the self-inductance of the coil reveals the basic character of the coil dynamics.

$$\mathscr{L} \dot{I}_j^K(t) + \left(\mathscr{G} + \mathscr{R}_L + \mathscr{R}_C\right) I_j^K = \mathscr{G} U_j(t). \tag{5.6}$$

where $\mathscr{L}$ is the self inductance of the *j*-th coil. This equation is a first order, inductive-resistive system. A frequency constant of the circuit, $\omega_{inductive,j}$, can be defined which characterizes the dominant pole of the inductive-resistive circuit. The numerator in Eq. (5.7) sums of all the resistance elements including the transconductance gain of the amplifier, load resistor, and the resistance of the coil. It can be seen from this frequency constant that a gain which makes the steady state error small has the additional effect of making the pole occur at high frequency.

$$\omega_{inductive,j} = \frac{\left(\mathscr{G} + \mathscr{R}_L + \mathscr{R}_C\right)}{\mathscr{L}^K}. \tag{5.7}$$

The gain in this expression represents a dynamic feedback rather than a steady state relation between the input demand and output current. The gain for this type of application is not given in amplifier design data because the gain actually depends on the load. An approximate value must be inferred from the frequency range of the amplifier.

The gain is estimated by using the nominal amplifier cut-off frequency in radians per second for $\omega_{inductive}$ and then solving for the corresponding gain, $\mathscr{G}$.

The main work of this chapter is to define the self and mutual inductance coefficients for the coil and other current density distributions. The general equation for induced voltage can be written out from elementary physics without yet knowing the formulations of the coefficients. The voltage induced in a coil due to time-varying currents can be expressed as a set of inductance coefficients times the current derivatives for all the sources of induction.

$$\mathscr{V}_{Inductive,j} = \sum_{j'=1}^{jmax} \mathscr{L}^{K}_{j',j} \dot{I}^{K}_{j'}(t) + \sum_{k=1}^{kmax} \sum_{m=1}^{mmax} \sum_{p=1}^{pmax} \mathscr{L}^{M}_{k,m,p,j} \dot{I}^{M}_{k,m,p}(t) + \sum_{n=1}^{nmax} \mathscr{L}^{N}_{n,j} \dot{I}^{N}_{n}(t). \qquad (5.8)$$

The constants, $\mathscr{L}^{K}_{j',j}$, $\mathscr{L}^{M}_{k,m,p,j}$, and $\mathscr{L}^{N}_{n,j}$, represent inductances between the $j$-coil to the other coils, eddy current modes, and vibration modes respectively. The variable, $\dot{I}^{K}_{j'}$, represents the derivative of current in the $j'$-th coil. The variables, $\dot{I}^{M}_{k,m,p}$ and $\dot{I}^{N}_{n}$, represent the derivatives of the amplitude functions for the eddy current and vibration modes scaled to units of equivalent current. These quantities are proportional to the dimensionless amplitude functions, $\dot{I}^{M}_{k,m,p}(t) = \Delta I \, \dot{\chi}^{H}_{M,k,m,p}$ and $\dot{I}^{N}_{n}(t) = \Delta I \, \dot{\chi}^{N}_{n}(t)$, and are ultimately replaced by the dimensionless quantities in the derivation. The inductances are fixed coefficients that depend only on the geometry and material properties of the actuator.

**Dimensionless variables for the coil circuit model**

The coil circuit equation is transformted into dimensionless units using the approach that has been applied to the vibration and magnetic field problems. As in the

vibration model and the magnetics field model, the range and offset of the dependent variables are set by the linear range of the coil current at steady state. The transformations of the variables defined in the Chapter 2 are applied to the coil equation variables. The current is defined as the following.

$$x_j^K = \frac{I_j^K - I_{min}}{\Delta I}. \tag{5.9}$$

The amplifier input is scaled in units of current also.

$$u_j^K = \frac{U_j - I_{min}}{\Delta I}. \tag{5.10}$$

An additional parameter, the dimensionless voltage, is needed for the circuit equation. The inductive voltage of the coil is zero at steady state so the scaling and offset for the amplifier voltage are given by the voltage drop across the loop resistance.

$$\Delta\mathscr{V} = \Delta I\left(\mathscr{R}_L + \mathscr{R}_C\right). \tag{5.11}$$

The dimensionless voltages are given by:

$$v_{Amp,j} = \frac{\mathscr{V}_{Amp,j}}{\Delta\mathscr{V}} = \frac{\mathscr{V}_{Amp,j}}{\Delta I\left(\mathscr{R}_L + \mathscr{R}_C\right)}. \tag{5.12}$$

In dimensionless units, the proportional model of the amplifier can be written as

$$v_{Amp,j}(t) = \frac{\mathscr{G}}{\left(\mathscr{R}_L + \mathscr{R}_C\right)}\left[u_j(t) - x_j^K(t)\right]. \tag{5.13}$$

The inductive voltage, in dimensionless units is given by:

$$v_{Inductive,j} = \frac{\mathscr{V}_{Inductive,j}}{\Delta\mathscr{V}} = \frac{\mathscr{V}_{Inductive,j}}{\Delta I\left(\mathscr{R}_L + \mathscr{R}_C\right)}. \tag{5.14}$$

The dimensionless version of the loop equation is found by substituting the dimensionless variables into Eq. (5.3) and simplifying the result.

$$\mathscr{v}_{Inductive,j}(t)+\left[\frac{\mathscr{G}}{\mathscr{R}_L+\mathscr{R}_C}+1\right]x_j^K(t)=\frac{\mathscr{G}}{\left(\mathscr{R}_L+\mathscr{R}_C\right)}u_j(t). \tag{5.15}$$

To make the notation more compact, let the following dimensionless gain for the amplifier be defined.

$$\mathscr{G}_{amp}=\frac{\mathscr{G}}{\mathscr{R}_L+\mathscr{R}_C}. \tag{5.16}$$

$$\mathscr{v}_{Inductive,j}(t)+\left(\mathscr{G}_{amp}+1\right)x_j^K(t)=\mathscr{G}_{amp}u_j(t). \tag{5.17}$$

The transformation in Eq. (5.14) can also be applied to Eq. (5.8).

$$\begin{aligned}\mathscr{v}_{Inductive,j}=\Bigg[&\sum_{j'=1}^{jmax}L_{j,j'}^K\dot{x}_{j'}^K(t)+\sum_{k=1}^{kmax}\sum_{m=1}^{mmax}\sum_{p=1}^{pmax}L_{j,k,m,p}^M\dot{\boldsymbol{\pi}}_{k,m,p}^M(t)\\&+\sum_{n=1}^{nmax}L_{j,n}^N\dot{\boldsymbol{\pi}}_n^N(t)\Bigg].\end{aligned} \tag{5.18}$$

where the dimensionless inductance coefficients are defined as:

$$L_{j,j'}^K=\frac{\mathscr{L}_{j,j'}^K}{\left(\mathscr{R}_L+\mathscr{R}_C\right)}. \tag{5.19}$$

$$L_{j,k,m,p}^M=\frac{\mathscr{L}_{j,k,m,p}^M}{\left(\mathscr{R}_L+\mathscr{R}_C\right)}. \tag{5.20}$$

$$L_{j,n}^N=\frac{\mathscr{L}_{j,n}^N}{\left(\mathscr{R}_L+\mathscr{R}_C\right)}. \tag{5.21}$$

**Solving for the inductance coefficients**

The inductance coefficients can be derived from the Faraday's law of induction. Faraday's law in differential form is one of Maxwell's equations.

$$\nabla \times \mathbf{E} = -\frac{\partial \mathbf{B}}{\partial t}. \tag{5.22}$$

In APPENDIX F, this equation is integrated twice to get the following form for the coil voltage.

$$\mathscr{V}_j^K = \frac{T}{\left(r_c - r_g\right)} \int_{V_{C,j}} \hat{e}_\phi \bullet \dot{\mathbf{A}} dV + I_j^K \mathscr{R}_C . \tag{5.23}$$

where $\mathbf{A}$ is the magnetic potential, $T$ is the number of turns per unit length, $V_{C,j}$ is the volume of the coil, $r_c$ and $r_g$ are the inner and outer radii of the coil. The outer radius of the rod and the inner radius of the coil are assumed to be equal. By comparison to Eq. (5.2), the inductive component of the coil voltage can be identified as

$$\mathscr{V}_{Inductive,j} = \frac{T}{\left(r_c - r_g\right)} \int_{V_{C,j}} \hat{e}_\phi \bullet \dot{\mathbf{A}} dV . \tag{5.24}$$

The differential equation for magnetic potential is derived in Appendix C in the section that describes the FEMM model. Equation C.5 gives a form for the potential that shows it is a linear function of the current density. We repeat the equation for the discussion.

$$\nabla \times \left[ \upsilon(\mathbf{r}) \nabla \times \mathbf{A}(\mathbf{r}) \right] = \mathbf{J}(\mathbf{r}) . \tag{5.25}$$

The linear properties of Eq. (5.25) mean that the potential can be expressed as an algebraic function of the current density distribution functions. Let the solution to Eq. (5.25) be written in the following way to show the linear dependence of the function

**A** on **J**. The square brackets are used to indicate that **A** depends on **J** over all space not just the value of **J** at **r**.

$$\mathbf{A}(\mathbf{r},t)=\mathbf{A}\left[\mathbf{r}\,|\,\mathbf{J}(\mathbf{r}',t)\right]\forall\mathbf{r}'. \tag{5.26}$$

where the notation suggests the linear dependence of **A** on **J**

The current density can be written as the sum of all the current density modal functions and their associated amplitude functions.

$$\begin{aligned}\mathbf{J}(\mathbf{r}',t)=&\sum_{j=1}^{jmax}\mathbf{f}_j^K(\mathbf{r}')x_j^K(t)+\sum_{k=1}^{kmax}\sum_{m=1}^{mmax}\sum_{p=1}^{pmax}\mathbf{f}_{k,m,p}^M(\mathbf{r}')\mathcal{X}_{k,m,p}^M(t)\\&+\sum_{n=1}^{nmax}\mathbf{f}_n^N(\mathbf{r}')\mathcal{X}_n^N(t).\end{aligned} \tag{5.27}$$

where the functions, $\mathbf{f}_j^K(r,\phi,z)$, $\mathbf{f}_{k,m,p}^M(r,\phi,z)$, and $\mathbf{f}_n^N(r,\phi,z)$ are the spatial current density distribution functions for coil current, eddy current, and vibration in dimensioned units. The corresponding amplitudes functions are $x_j^K(t)$, $\mathcal{X}_{k,m,p}^M(t)$, and $\mathcal{X}_n^N(t)$.

The principle of superposition applies to linear equations so this expression can be written as the following where **A**[-] implies the same mathematical operation in each instance.

$$\begin{aligned}\mathbf{A}(\mathbf{r},t)=&\sum_{j=1}^{jmax}\mathbf{A}\left[\mathbf{r}\,|\,\mathbf{f}_j^K(\mathbf{r}')\right]x_j^K(t)\\&+\sum_{k=1}^{kmax}\sum_{m=1}^{mmax}\sum_{p=1}^{pmax}\mathbf{A}\left[\mathbf{r}\,|\,\mathbf{f}_{k,m,p}^M(\mathbf{r}')\right]\mathcal{X}_{k,m,p}^M(t)\\&+\sum_{n=1}^{nmax}\mathbf{A}\left[\mathbf{r}\,|\,\mathbf{f}_n^N(\mathbf{r}')\right]\mathcal{X}_n^N(t).\end{aligned} \tag{5.28}$$

Differentiating Eq. (5.28) and substituting the result into the integral in Eq. (5.24) yields the following.

$$\mathscr{V}_{Inductive,j} = \frac{T}{\left(r_c - r_g\right)}\Bigg[\sum_{j'=1}^{jmax}\int_{V_{C,j}} \hat{\mathbf{e}}_\phi \cdot \mathbf{A}\left[\mathbf{r}\,|\,\mathbf{f}_j^K\left(\mathbf{r}'\right)\right]dV\dot{x}_{j'}^K\left(t\right) + \sum_{k=1}^{kmax}\sum_{m=1}^{mmax}\sum_{p=1}^{pmax}\int_{V_{C,j}} \hat{\mathbf{e}}_\phi \cdot \mathbf{A}\left[\mathbf{r}\,|\,\mathbf{f}_{k,m,p}^M\left(\mathbf{r}'\right)\right]dV\dot{\chi}_{k,m,p}^M\left(t\right) + \sum_{n=1}^{nmax}\int_{V_{C,j}} \hat{\mathbf{e}}_\phi \cdot \mathbf{A}\left[\mathbf{r}\,|\,\mathbf{f}_n^N\left(\mathbf{r}'\right)\right]dV\dot{\chi}_n^N\left(t\right)\Bigg]. \tag{5.29}$$

Converting the voltage to dimensionless form yields the following.

$$v_{Inductive,j} = \frac{T}{\left(r_c - r_g\right)\left(\mathscr{R}_L + \mathscr{R}_C\right)\Delta I}\Bigg[\sum_{j'=1}^{jmax}\int_{V_{C,j}} \hat{\mathbf{e}}_\phi \cdot \mathbf{A}\left[\mathbf{r}\,|\,\mathbf{f}_j^K\left(\mathbf{r}'\right)\right]dV\dot{x}_{j'}^K\left(t\right) + \sum_{k=1}^{kmax}\sum_{m=1}^{mmax}\sum_{p=1}^{pmax}\int_{V_{C,j}} \hat{\mathbf{e}}_\phi \cdot \mathbf{A}\left[\mathbf{r}\,|\,\mathbf{f}_{k,m,p}^M\left(\mathbf{r}'\right)\right]dV\dot{\chi}_{k,m,p}^M\left(t\right) + \sum_{n=1}^{nmax}\int_{V_{C,j}} \hat{\mathbf{e}}_\phi \cdot \mathbf{A}\left[\mathbf{r}\,|\,\mathbf{f}_n^N\left(\mathbf{r}'\right)\right]dV\dot{\chi}_n^N\left(t\right)\Bigg]. \tag{5.30}$$

The **A** and **f** terms are kept in dimensioned form so that the input and output from FEMM can be used in their native units. The integral terms are constants that are functions of the geometry and material properties of the actuator. Equation (5.30) now resembles the desired inductance formula in Eq. (5.18). The formulae for the inductances in dimensionless units are given by the following:

$$L_{j,j'}^K = \frac{T}{\left(r_c - r_g\right)\left(\mathscr{R}_L + \mathscr{R}_C\right)\Delta I}\int_{V_{C,j}} \hat{\mathbf{e}}_\phi \cdot \mathbf{A}\left[\mathbf{r}\,|\,\mathbf{f}_j^K\left(\mathbf{r}'\right)\right]dV\,. \tag{5.31}$$

$$L_{j,k,m,p}^M = \frac{T}{\left(r_c - r_g\right)\left(\mathscr{R}_L + \mathscr{R}_C\right)\Delta I}\int_{V_{C,j}} \hat{\mathbf{e}}_\phi \cdot \mathbf{A}\left[\mathbf{r}\,|\,\mathbf{f}_{k,m,p}^M\left(\mathbf{r}'\right)\right]dV\,. \tag{5.32}$$

$$L_{j,n}^N = \frac{T}{\left(r_c - r_g\right)\left(\mathscr{R}_L + \mathscr{R}_C\right)\Delta I}\int_{V_{C,j}} \hat{\mathbf{e}}_\phi \cdot \mathbf{A}\left[\mathbf{r}\,|\,\mathbf{f}_n^N\left(\mathbf{r}'\right)\right]dV\,. \tag{5.33}$$

**Evaluation of the inductance using reciprocity**

While the coupling coefficient problem is solved by Eqs. (5.31) through (5.33), the calculation of magnetic potential using Eq. (5.25) over the coil volume due to each of the current density distributions is a particularly arduous analytical task. A FEMM calculation of the potential is advantageous because it accounts for all the geometric details of the actuator design rather than the simplified geometry used to represent the magnetic field for eddy current or vibration. The difficulty is that the FEMM code only provides two types of current sources: uniform sources which can be used to model the coil and point sources which represent an infinitesimal wire loop in the axisymmetric geometry. Unfortunately, the current density distributions for the modal functions of vibration and eddy current cannot be easily or accurately defined in terms of point and uniform current sources. One of the useful mathematical properties of Eq. (5.25) is the principle of reciprocity which allows the target and source in the inductance calculation to be interchanged. Consequently, the coil's potential is integrated over the volumes of the various current density distributions rather than integrating the current density distribution's potential over the coil volume. The coil's potential function can be calculated by FEMM using the same cases used to evaluate the coupling coefficients in the vibration and eddy current modeling chapters so the coil potential distribution is a mathematical result that is already in hand.

The principle of reciprocity of inductances means that the inductance between any two current loops or current density distributions is the same if the role of source and target are reversed. The following description illustrates the principle. Consider two volumes, $V_1$ and $V_2$, and two prescribed current density distribution in those volumes, $\mathbf{J}_1$

and $\mathbf{J}_2$. In this scenario, $\mathbf{J}_1$ is zero outside of $V_1$ and $\mathbf{J}_2$ is zero outside of $V_2$. The vector potential, $\mathbf{A}\left[\mathbf{r} \mid \mathbf{J}_1\left(\mathbf{r}', t\right)\right]$, is the potential function over all space corresponding to $\mathbf{J}_1$ alone with $\mathbf{J}_2 = 0$. The vector potential, $\mathbf{A}\left[\mathbf{r} \mid \mathbf{J}_2\left(\mathbf{r}', t\right)\right]$, is the reverse case in which $\mathbf{J}_2$ is energized and $\mathbf{J}_1$=0. The reciprocity relation can then be stated as:

$$\int_{V_1} \mathbf{J}_1\left(\mathbf{r}\right) \bullet \mathbf{A}\left[\mathbf{r} \mid \mathbf{J}_2\left(\mathbf{r}', t\right)\right] dV = \int_{V_2} \mathbf{J}_2\left(\mathbf{r}\right) \bullet \mathbf{A}\left[\mathbf{r} \mid \mathbf{J}_1\left(\mathbf{r}', t\right)\right] dV \,. \tag{5.34}$$

The reciprocity relationship is a consequence of Green's first identity for vector fields applied to the magnetic potential differential equation, Eq. (5.25). The reciprocity relation can be used to manipulate the expressions for the induction coefficient in Eqs. (5.31) through (5.33) into a form that can be computed using FEMM cases in which the coil current is the current source.

The reciprocity equation can be applied to the evaluation of the inductance calculation in Eq. (5.34). Let $V_1$ and its associated current density distribution, $\mathbf{J}_1$, be the coil volume and current density in the inductance calculation.

$$V_1 = V_{C,j} \,. \tag{5.35}$$

$$\mathbf{J}_1\left(\mathbf{r}\right) = \mathbf{f}_j^K\left(r, \phi, z\right) = \frac{T\Delta I}{\left(r_c - r_g\right)} \hat{\mathbf{e}}_\phi \,. \tag{5.36}$$

The second current density distribution and volume can be any current mode in the actuator model and its associated volume.

$$V_2 = V_x \,. \tag{5.37}$$

$$\mathbf{J}_2\left(\mathbf{r}\right) = \mathbf{f}^x\left(\mathbf{r}\right), \tag{5.38}$$

where $x$ may be $K$, $M$, or $N$ representing any coil current, eddy current mode, or vibration mode.

The FEMM cases used to calculate the potential due to coil current are designed with a current density distribution equal to one amp in each turn of the coil. This current density gives a uniform current density over the coil area that differs from the $\mathbf{f}_j^K(\mathbf{r})$ by the factor $\Delta I$.

$$\mathbf{J}_j^{FEMM}(r,\phi,z) = \frac{T}{(r_c - r_g)}\hat{\mathbf{e}}_\phi . \tag{5.39}$$

The corresponding magnetic potential is then:

$$\mathbf{A}\left[\mathbf{r} \mid \mathbf{J}_1(\mathbf{r}',t)\right] = \mathbf{A}\left[\mathbf{r} \mid \mathbf{f}_j^K(\mathbf{r}')\right] = \Delta I\, A_j^{FEMM}(\mathbf{r}) . \tag{5.40}$$

The equivalences defined in Eqs. (5.35) through (5.40) can be substituted into the reciprocity equation.

$$\int_{V_{C,j}} \frac{T\Delta I}{(r_c - r_g)}\hat{\mathbf{e}}_\phi \bullet \mathbf{A}\left[\mathbf{r} \mid \mathbf{f}^x(\mathbf{r}')\right] dV = \int_{V_x} \mathbf{f}^x(\mathbf{r}) \bullet \Delta I\, A_j^{FEMM}(r,\phi,z)\hat{\mathbf{e}}_\phi dV . \tag{5.41}$$

Divide both sides by $\left(\mathscr{R}_L + \mathscr{R}_C\right)\Delta I$

$$\begin{aligned} &\frac{T}{(r_c - r_g)\left(\mathscr{R}_L + \mathscr{R}_C\right)\Delta I}\int_{V_{C,j}} \hat{\mathbf{e}}_\phi \bullet \mathbf{A}\left[\mathbf{r} \mid \mathbf{f}^x(\mathbf{r}')\right] dV \\ &\qquad = \frac{1}{\left(\mathscr{R}_L + \mathscr{R}_C\right)\Delta I}\int_{V_x} \mathbf{f}^x(\mathbf{r}) \bullet A_j^{FEMM}(\mathbf{r})\hat{\mathbf{e}}_\phi dV . \end{aligned} \tag{5.42}$$

The left hand side has been manipulated to be in the same form as the inductance coefficients in Eqs. (5.31) through (5.33). Thus, the reciprocal form of the inductance coefficient is the right hand side of Eq. (5.42).

$$L^x = \frac{1}{\left(\mathscr{R}_L + \mathscr{R}_C\right)\Delta I}\int_{V_x} \mathbf{f}^x\left(\mathbf{r}\right)\bullet A_j^{FEMM}\left(\mathbf{r}\right)\hat{\mathbf{e}}_\phi dV\,. \tag{5.43}$$

The inductance formulation in Eq. (5.43) can be calculated with existing information from current density distributions derived in the vibration and magnetic models and the potential calculated by FEMM. APPENDIX G gives the evaluation of the coefficients using the previously derived current density formulae. APPENDIX G also gives a test of the inductance coefficients that uses Green's first identity for vector functions to develop a proportionality relationship between the coupling coefficients developed in the vibration, magnetic, and coil circuit models.

**State Space Equation**

The plan for combining the coil circuit model with the full system that is given in Chapter 1 requires that the coil current model be defined in the descriptor state space form. The terms in the descriptor form for the coil circuit which are potentially non-zero are the following:

$$\begin{aligned}&\mathbf{E}^{31}\ddot{\mathbf{x}}^{\mathbf{N}} + \mathbf{E}^{33}\dot{\mathbf{x}}^{\mathbf{K}} + \mathbf{E}^{34}\dot{\mathbf{x}}^{\mathbf{M}}\\ &\qquad = \mathbf{F}^{31}\dot{\mathbf{x}}^{\mathbf{N}} + \mathbf{F}^{32}\mathbf{x}^{\mathbf{N}} + \mathbf{F}^{33}\mathbf{x}^{\mathbf{K}} + \mathbf{F}^{34}\mathbf{x}^{\mathbf{M}} + \mathbf{G}^{3}\mathbf{u}.\end{aligned} \tag{5.44}$$

The coil current differential equation can be assembled using the loop equation from Eq. (5.17) and the inductive voltage in Eq. (5.18). The terms are arranged to correspond to the order of the terms in Eq. (5.44)

$$\begin{aligned}&\sum_{j'=1}^{jmax} L_{j,j'}^K \dot{x}_{j'}^K\left(t\right) + \sum_{k=1}^{kmax}\sum_{m=1}^{mmax}\sum_{p=1}^{pmax} L_{j,k,m,p}^M \dot{\mathscr{X}}_{k,m,p}^M\left(t\right)\\ &\qquad = -\sum_{n=1}^{nmax} L_{j,n}^N \dot{\mathscr{X}}_n^N\left(t\right) - \left(\mathscr{G}_{amp}+1\right)x_j^K\left(t\right) + \mathscr{G}_{amp}u_j\left(t\right).\end{aligned} \tag{5.45}$$

The rearrangement of the three dimensional array of states for the magnetics as a linear vector has been given in Chapter 3 and 4. The definitions of the state vectors are repeated here for reference. The magnetics vector is defined as

$$\mathbf{x^M} = \begin{bmatrix} X_1^M \\ X_2^M \\ \vdots \\ X_l^M \\ \vdots \\ X_{lmax}^M \end{bmatrix}, \tag{5.46}$$

where the index, $l = k + kmax\left[ m - 1 + mmax\left( p - 1 \right) \right]$, is computed to stack the three dimensional *k*, *m*, and *p* elements into a one-dimensional vector.

$$X_l^M = \mathcal{X}_{k,m,p}^M . \tag{5.47}$$

The amplitude variables for the vibration and the coil currents are already in vector form.

$$\mathbf{x^N} = \begin{bmatrix} \mathcal{X}_1^N \\ \mathcal{X}_2^N \\ \vdots \\ \mathcal{X}_n^N \\ \vdots \\ \mathcal{X}_{nmax}^N \end{bmatrix}; \; \mathbf{x}^K = \begin{bmatrix} x_1^K \\ x_2^K \\ \vdots \\ x_j^K \\ \vdots \\ x_{jmax}^K \end{bmatrix}. \tag{5.48}$$

The index *n* corresponds to the elements of the vibration states. The index, *j*, corresponds to the elements of the coil current states.

The required matrices for the state system form are given by

$$\mathbf{E}^{31} = \mathbf{0}_{jmax \times nmzx} . \tag{5.49}$$

$$\mathbf{E}^{33} = \left[ L_{j,j'}^K \right]. \tag{5.50}$$

$$\mathbf{E}^{34} = \left[ L^{M}_{j,l} \right] = \left[ L^{M}_{j,k,m,p} \right]. \tag{5.51}$$

$$\mathbf{F}^{31} = -\left[ L^{N}_{j,n} \right]. \tag{5.52}$$

$$\mathbf{F}^{32} = \mathbf{0}_{jmax \times nmax}. \tag{5.53}$$

$$\mathbf{F}^{33} = -\left( \mathscr{G}_{amp} + 1 \right) \mathbf{I}_{jmax \times jmax}. \tag{5.54}$$

$$\mathbf{F}^{34} = \mathbf{0}_{jmax \times lmax}. \tag{5.55}$$

$$\mathbf{G}^{3} = \mathscr{G}_{amp} \mathbf{I}_{jmax \times jmax}. \tag{5.56}$$

Equation (5.44) can be rewritten omitting the zero elements.

$$\begin{aligned} &\mathbf{E}^{33} \dot{\mathbf{x}}^{\mathbf{K}} + \mathbf{E}^{34} \dot{\mathbf{x}}^{\mathbf{M}} \\ &\qquad = \mathbf{F}^{31} \dot{\mathbf{x}}^{\mathbf{N}} + \mathbf{F}^{33} \mathbf{x}^{\mathbf{K}} + \mathbf{G}^{3} \mathbf{u}. \end{aligned} \tag{5.57}$$

**Output variables for the coil model**

Coil current

The coil currents are measured variables. The output matrix to select these states is used in the design of the state estimation algorithm.

$$\mathbf{y}^{I} = \mathbf{I} \mathbf{x}^{\mathbf{K}}. \tag{5.58}$$

Amplifier voltage

The dimensionless amplifier voltage is given by:

$$\mathbf{y}^{V} = \mathbf{C}^{33} \mathbf{x}^{\mathbf{K}} + \mathbf{D}^{3} \mathbf{u}, \tag{5.59}$$

where

$$\mathbf{C}^{33} = -\left(\mathscr{G}_{amp} + 1\right)\mathbf{I}_{jmax \times jmax},$$
$$\mathbf{D}^{3} = \mathscr{G}_{amp}\mathbf{I}_{jmax \times jmax}. \tag{5.60}$$

Power calculation.

The power consumed at each time step is $\sum I^2 R$ where the terms are summed over the number of coils. A dimensionless quantity proportional to power can be computed as the following.

$$\mathscr{E} = \left(\mathbf{x}^{\mathbf{K}}\right)^{T} \mathbf{x}^{\mathbf{K}}. \tag{5.61}$$

**Time and Frequency Response of the Coil Circuit Model**

The coil model can be analyzed as a stand alone model for both time and frequency response. The following equations reduce the state space descriptor model in Eq. (5.57) to a stand alone case. The only change required from the fully coupled model is to set the terms for eddy current and vibration effects to zero. The state space equations for the stand alone coil circuit model are given by.

$$\mathbf{E}^{33}\dot{\mathbf{x}}^{\mathbf{K}} = \mathbf{F}^{33}\mathbf{x}^{\mathbf{K}} + \mathbf{G}^{3}\mathbf{u}. \tag{5.62}$$

Converting from descriptor to standard state space form gives

$$\dot{\mathbf{x}}^{\mathbf{K}} = \mathbf{A}^{K}\mathbf{x}^{\mathbf{K}} + \mathbf{B}^{K}\mathbf{u}. \tag{5.63}$$

where $\mathbf{A}^{K} = \left(\mathbf{E}^{33}\right)^{-1}\mathbf{F}^{33}$ and $\mathbf{B}^{K} = \left(\mathbf{E}^{33}\right)^{-1}\mathbf{G}^{3}$. The output variables for the coil model are coil current and amplifier voltage which are computed from the state by the output matrices given in Eqs. (5.58) and (5.60).

In addition to the inductances formulated in this chapter, the coil circuit model depends on the data for the resistor and amplifier parameters. When the equations are

converted to dimensionless variables, these amplifier gain and resistance parameters combine into a ratio, $\mathscr{G}_{amp}$, which is the only new parameter needed to model the coil circuit. The feedback gain, in this sense, is not the steady state relationship between the input to the amplifier and output current. The feedback gain determines the frequency constant of the coil circuit. Also, since the amplifier is modeled with only proportional feedback, the gain parameter also determines the steady state offset of the circuit. Based on the amplifier's specifications for ±3 dB for 0 Hz to 20,000 Hz, the gain is chosen to give a frequency constant for the basic inductive resistive circuit of 20,000 Hz. The gain which gives this frequency constant can be solved from the Eqs. (5.7) and (5.16).

$$\omega_{inductive,j} = \frac{\left(\mathscr{G} + \mathscr{R}_L + \mathscr{R}_C\right)}{\mathscr{L}^K_{j,j}} = \frac{\left(\mathscr{G}_{amp} + 1\right)}{L^K_{j,j}}. \tag{5.64}$$

Solving this equation for the gain and using the value of self-inductance of a coil calculated by FEMM, $L^K_{j,j}$ for $j$=6 gives the following estimation of the gain parameter.

$$\mathscr{G}_{amp} = L^K_{j,j}\omega_{inductive,j} - 1 = 0.4312\times10^{-4}\cdot 2\pi\cdot 20,000 - 1 = 4.4192. \tag{5.65}$$

The steady state error for the proportional control can be solved by substituting this gain into the differential equation and solving for steady state. Setting the derivative to zero in Eq. (5.62) and using the definition of $\mathbf{F}^{33}$ and $\mathbf{G}^3$ from Eqs. (5.54) and (5.56) gives the following value for the steady state error.

$$\left(\frac{\mathbf{x^K}}{\mathbf{u}}\right)_{SS} = \frac{\mathscr{G}_{amp}}{\mathscr{G}_{amp}+1} = 0.8155. \tag{5.66}$$

A simulation generated by MATLAB for coil current in response to a step change in the demand is shown in Figure 5.1. In this transient, the current demand for $j$=6 is

energized while the other demands are held steady at zero. The amplifiers in the other circuits remain on in an effort to maintain the current at the demand of zero. The dynamics of the active coil circuit are basically the same as an isolated coil, resistor and amplifier. The current follows an exponential rise to the demand current. The multiple coils add a coupled behavior which can be seen in the response. The magnetic field generated by the active coil generates an electric field in the opposite direction in the other coils. The mutual inductance between a coil and its adjacent neighbors is about 25% of its self-inductance. This coupling is diminished by the feedback control of the circuit which works to cancel any induced current. With a high feedback gain, the induced current can be nearly canceled. The current in coils $j$=5 and 7 lie on top of one another. The current drops to about -0.075 following the step and then returns to zero. The amplitude of the induced current in coils farther from the energized coil is smaller. The current in coils 4 and 8 responds more strongly to the induced current in coils 5 and 7 than to the current in the energized coil. The current in those coil increases by a very small amount. Coils farther away have no perceptible current at the scale shown. The results when other coils are energized with a step demand are essentially the same, so only one coil is shown.

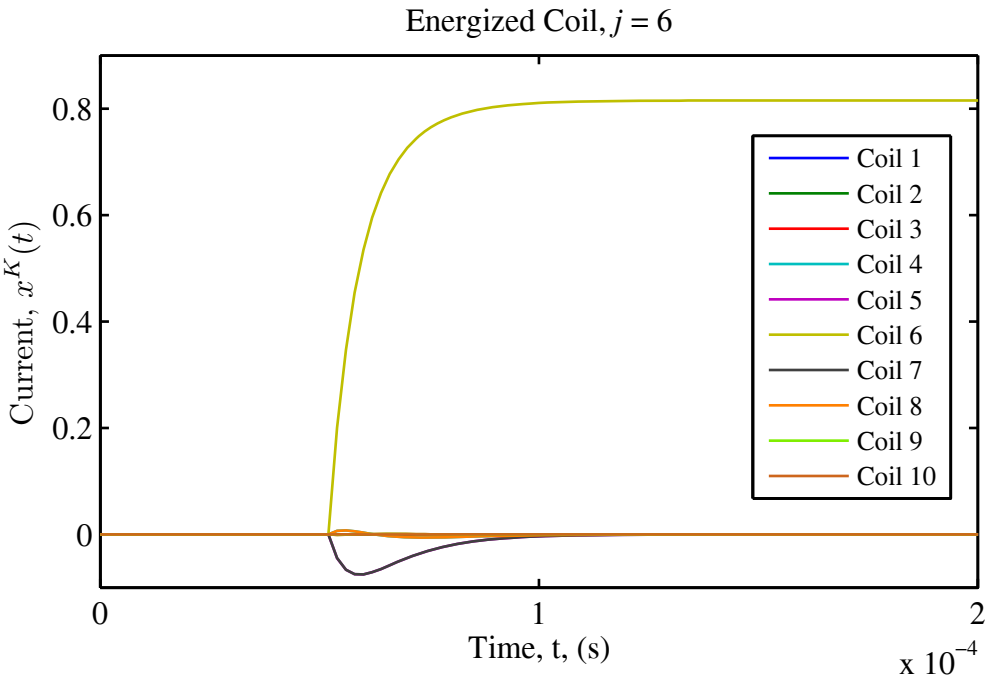


Figure 5.1: Step response of coil current from stand alone coil circuit model

Figure 5.2 shows the amplifier voltages for the same step transient. For the energized coil, the voltage response to a step in current demand is a spike in amplifier voltage which then decays down to the steady state value. The peak voltage that can be generated by the amplifier is the most limiting quantity for high speed performance of the actuator. The maximum voltage that an amplifier can generate is limited by the "rail" voltages of the amplifier power supply applied at the power terminals of the output transistors. The output of the amplifier saturates at the voltage of its power supply. Typically, a transistor is limited to about 40 volts across a single stage. The peak voltage of $\mathscr{v}_{Amp,6} = 4.5$ in dimensionless units from the figure can be converted into the dimensioned quantity.

$$\mathscr{V}_{Amp,6=}\Delta I\left(\mathscr{R}_L+\mathscr{R}_C\right)\mathscr{v}_{Amp,6} = 1.5\cdot 4\cdot 4.5 = 27 \text{ volts} \tag{5.67}$$

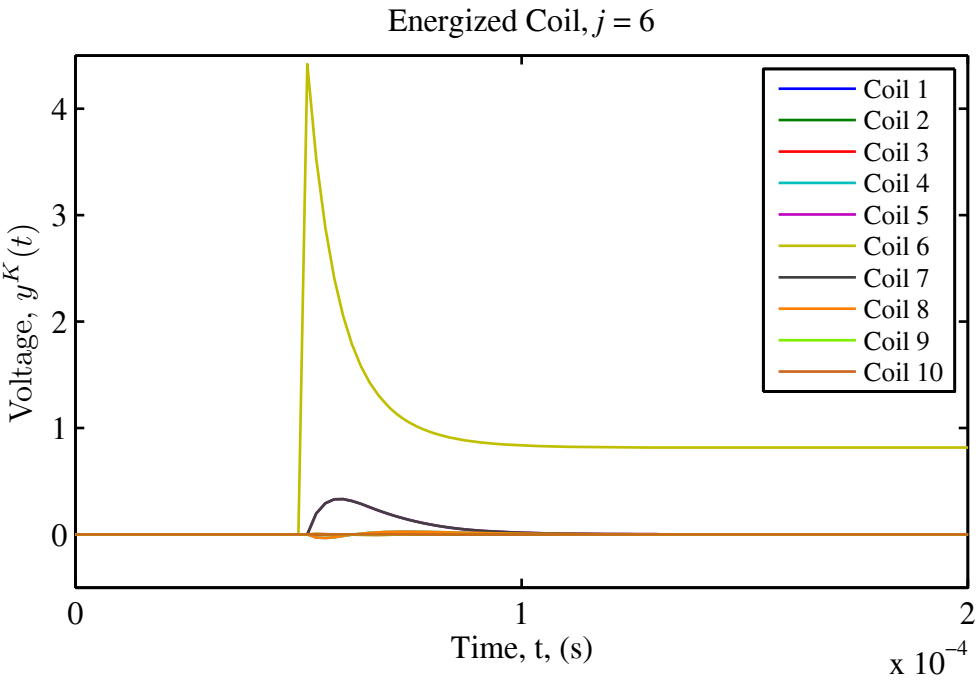


Figure 5.2: Step response of amplifier voltage from stand alone coil circuit model

Even though the feedback gain parameter is roughly estimated, the simulated voltage is within a reasonable range, and the transient behavior is consistent with the expected behavior of an audio amplifier.

The frequency response of the coil circuit can also be simulated using the stand alone model. Figure 5.3 shows the current in each loop for a single energized coil versus frequency. The top line is the response of current in the active coil. The other coils show the effect of the induced current from the active coil. The shape of the energized coil is approximately that of a first order lag response representing an isolated inductive resistive circuit. However, the shape is not precisely first order due to the presence of other coils. The gain parameter in Eq. (5.65) is determined using just the coil's self inductance. The mutual inductance also acts on the coil current retarding the current response. The mutual inductance between coils spreads the energy to the other coil

circuits and creating a response over range of frequencies about the corner frequency defined by the self-inductance. This effect is evident in the coil current frequency response as the amplitude plot begins to drop below the 20,000 Hz point but drops more gradually than a first order system. The energy transferred to the neighboring coil circuits is evident in the induced currents that rise from zero at DC to peak at the break frequency and then drop as the drive current drops.

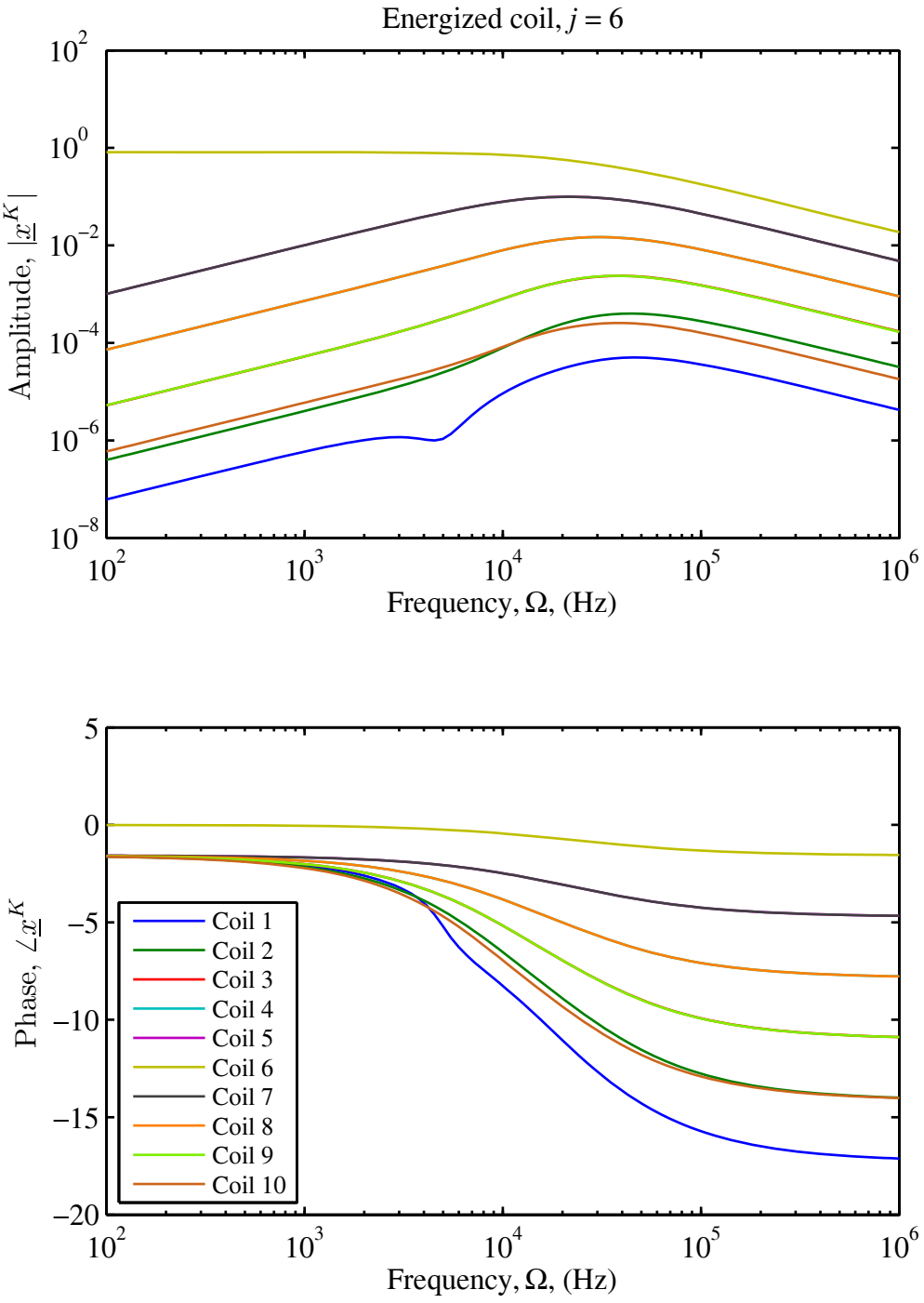


Figure 5.3: Frequency response of coil current for stand alone coil circuit model

The frequency response of voltage over current is shown in Figure 5.4. The voltage response of an isolated inductive resistive circuit has a behavior of a lead-lag component. The derivative action comes from the coil inductance and the proportional action from the voltage drop across the load resistor. The effect of the mutual inductance on the voltage is to smear out the lead effect slightly. On the scale shown, the phase angle of the active coil shows very little positive shift at the break frequency. On a finer scale plot, the peak of the phase can be observed to be 0.7 radians.

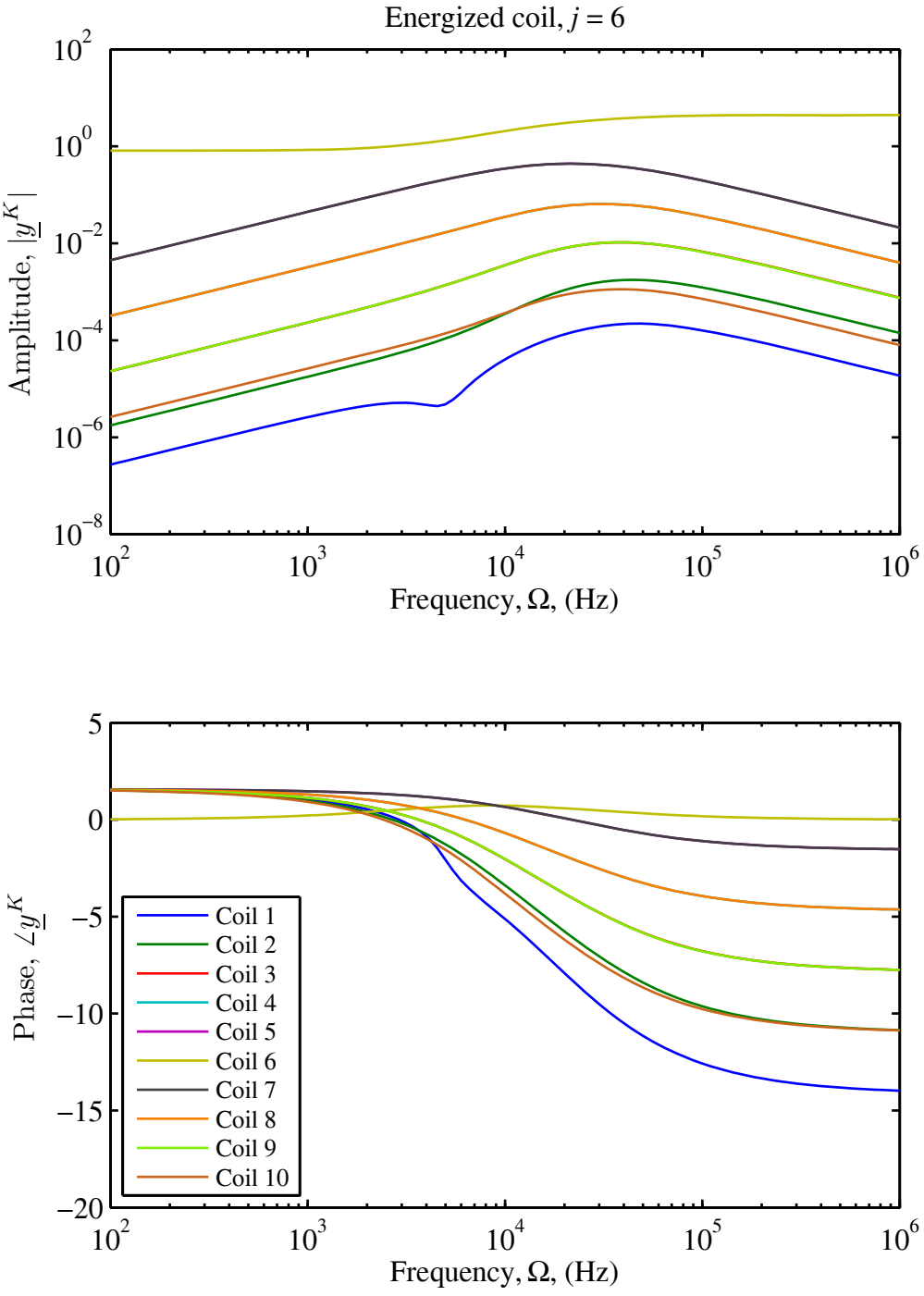


Figure 5.4: Frequency response of amplifier voltage for coil current model

**Combined Vibration, Magnetic and Coil State Space Model**

The individual subsystem models have been prepared for a very straightforward assembly by defining each subsystem in the descriptor form using a predefined format for the state vector and coefficient matrices specified in Eq. (1.10). The combined system is assembled by inserting the matrices in Eqs. (3.44), (4.87) and (5.57) into a single system matrix. The descriptor form of the state space system is rewritten here. Matrices that have been determined to be zero matrices or the identity matrices in the modeling are indicated as such in the completed system model.

$$\begin{bmatrix} \mathbf{I} & \mathbf{0} & \mathbf{0} & \mathbf{0} \\ \mathbf{0} & \mathbf{I} & \mathbf{0} & \mathbf{0} \\ \mathbf{0} & \mathbf{0} & \mathbf{E}^{33} & \mathbf{E}^{34} \\ \mathbf{0} & \mathbf{0} & \mathbf{E}^{43} & \mathbf{I} \end{bmatrix} \begin{bmatrix} \dot{\mathbf{x}}^{\mathbf{N}} \\ \dot{\mathbf{x}}^{\mathbf{N}} \\ \dot{\mathbf{x}}^{\mathbf{K}} \\ \dot{\mathbf{x}}^{\mathbf{M}} \end{bmatrix} = \begin{bmatrix} \mathbf{F}^{11} & \mathbf{F}^{12} & \mathbf{F}^{13} & \mathbf{F}^{14} \\ \mathbf{I} & \mathbf{0} & \mathbf{0} & \mathbf{0} \\ \mathbf{F}^{31} & \mathbf{0} & \mathbf{F}^{33} & \mathbf{0} \\ \mathbf{F}^{41} & \mathbf{0} & \mathbf{0} & \mathbf{F}^{44} \end{bmatrix} \begin{bmatrix} \dot{\mathbf{x}}^{\mathbf{N}} \\ \mathbf{x}^{\mathbf{N}} \\ \mathbf{x}^{\mathbf{K}} \\ \mathbf{x}^{\mathbf{M}} \end{bmatrix} + \begin{bmatrix} \mathbf{0} \\ \mathbf{0} \\ \mathbf{G}^{3} \\ \mathbf{0} \end{bmatrix} \mathbf{u} \tag{5.68}$$

The main outputs needed for the control system modeling are coil current and displacement of the free end. The voltage of the amplifier is also determined to ensure that the control system does not to give an unrealistic voltage demand. The formulae to compute the measured values from the state variables and inputs are written here for completeness of the full system model. A cross reference to the equation number of the defining equation is given to tie the outputs of the full model to their derivation.

Displacement, Eq. (3.52)

$$y^{N}(t) = \begin{bmatrix} \mathbf{0} & \mathbf{C}^{12} & \mathbf{0} & \mathbf{0} \end{bmatrix} \begin{bmatrix} \dot{\mathbf{x}}^{\mathbf{N}} \\ \mathbf{x}^{\mathbf{N}} \\ \mathbf{x}^{\mathbf{K}} \\ \mathbf{x}^{\mathbf{M}} \end{bmatrix} \tag{5.69}$$

Amplifier voltage, Eq. (5.58)

$$\mathbf{y}^{\mathbf{V}} = \begin{bmatrix} \mathbf{0} & \mathbf{0} & \mathbf{C}^{33} & \mathbf{0} \end{bmatrix} \begin{bmatrix} \dot{\mathbf{x}}^{\mathbf{N}} \\ \mathbf{x}^{\mathbf{N}} \\ \mathbf{x}^{\mathbf{K}} \\ \mathbf{x}^{\mathbf{M}} \end{bmatrix} + \mathbf{D}^{3}\mathbf{u} \tag{5.70}$$

Coil current, Eq. (5.60)

$$\mathbf{y}^{\mathbf{I}} = \begin{bmatrix} \mathbf{0} & \mathbf{0} & \mathbf{I} & \mathbf{0} \end{bmatrix} \mathbf{x}^{\mathbf{K}} \tag{5.71}$$

The descriptor form is converted to standard state space form by the algebraic solution of the system. The MATLAB program solves the state matrices using the "\" operator rather than matrix inversion to compute the conventional state space coefficient matrices. The low order models of vibration and magnetics are used in the simulation. The maximum orders of the low order case for magnetics are: radial, *kmax*=1; azimuthal, *mmax*=1; and axial, *pmax*=10. The maximum order for the vibration model is *nmax*=10.

A time simulation shown in Figure 5.5 is a step change transient analogous to the step changes in Figure 3.3 and Figure 4.14. The effect of adding the coil circuit to the model is subtle but significant. The effect of the proportional gain in the amplifer model is to decrease the amplitude by the steady state error. The mutual inductance with neighboring coils adds to the magnetic drag from the eddy current model. As a result of the increased drag, the displacement shows more rapid decay of the ringing following the step than in Figure 4.14. The first order rise in current leads to a slower response to the input step with the slope of the initial rise being slightly lower. The lines for the first and last coils are delayed somewhat more than the rest. The inductances of the end coils are greater than the coils in the middle of the rod because of the flux peak at either end. The magnetic flux peaks at the ends of the actuator rod because of the high permeability

material used in the return path. The net effect that is evident from the figure is that the coil circuit dynamics increase the magnetic drag and filter the current demand through a low pass filter. Both effects work against the improvements in actuator speed that can be achieved with the multi-coil actuator.

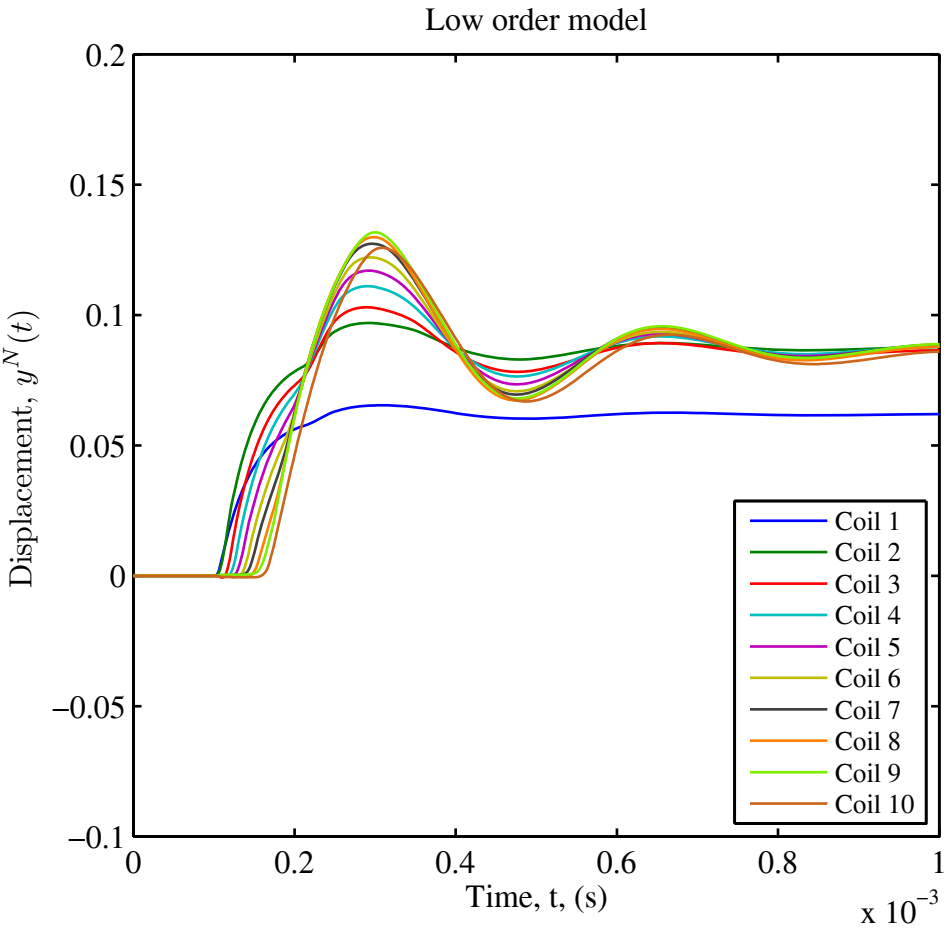


Figure 5.5: Step change for combined vibration, magnetic and coil circuit model.

Figure 5.6 shows the coil current response to a step in a single coil. In this transient, the coil closest to the wall, $j$=10, is energized. The coil on the end is chosen to show the acoustic pulse passing through each coil as it travels the length of the rod. The wave passing effect is not as easy to follow when other coils are energized because a coil

in the middle of the rod generates two pulses traveling in opposite directions. The coil current in the coil adjacent to the energized coil, $j$=9, is mainly affected by the induction from its neighbor. The induction from the energized coil drives a negative current in $j$=9. The effect of the magnetostrictive strain pulse travels through the ninth coil and appears as a small positive peak on the overall negative trace. The traveling pulse appears on the current traces for the other coils also as it travels down the actuator rod.

The figure for coil current is an indication of the behavior of the multi-coil actuator as a sensor. The peak current from the magnetostrictive pulse is about 10% of the step current. This result, as shown, gives a very measurable effect. An even higher response can be obtained by lowering the amplifier gain. The potential for applications of the multi-coil device as a high speed, high amplitude acoustic sensor is evident from this plot.

The induced response of coil current due to the coupling of the acoustic pulse to coil current is detrimental to the high speed performance of the device as an actuator. The induced current represents energy which is lost from the acoustic wave and is dissipated by the coil circuit's resistance. The high speed response of the actuator is improved by increasing the amplifier gain so that the amplifier works against the induced current keeping the coil current closer to zero. Increasing the amplifier gain also increases the frequency constant of the circuit model, which improves high speed performance.

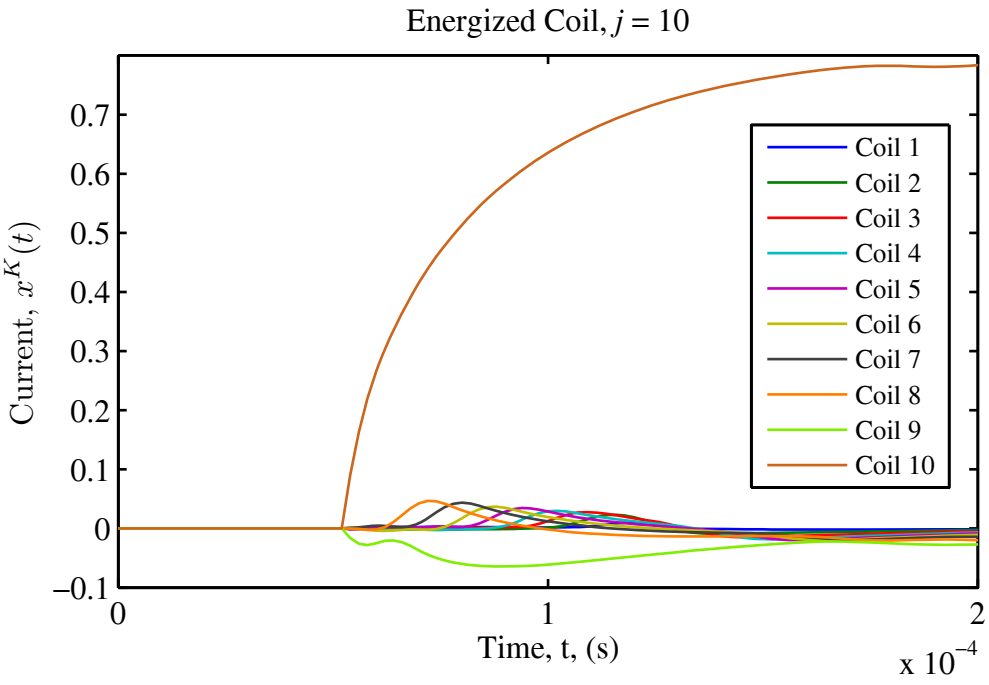


Figure 5.6: Step response of coil current from combined vibration, magnetics, and coil circuit model

Figure 5.7 shows the frequency response for displacement for a unit current demand applied to each coil. This plot is comparable to the frequency response plots shown in Figure 3.5 and Figure 4.15.

The attenuation of the response by the coil circuit is even more apparent in the frequency response than in the step change transient. The amplitude of the first peak is approximately 0.2 which is down from 0.45 in the model of magnetics and vibration in Figure 4.15 down from 0.65 in the plot of vibration alone in Figure 3.5. The reduced response is due to the filtering effect of the resistive inductive circuit and the steady state error from the proportional gain modeling of the amplifier.

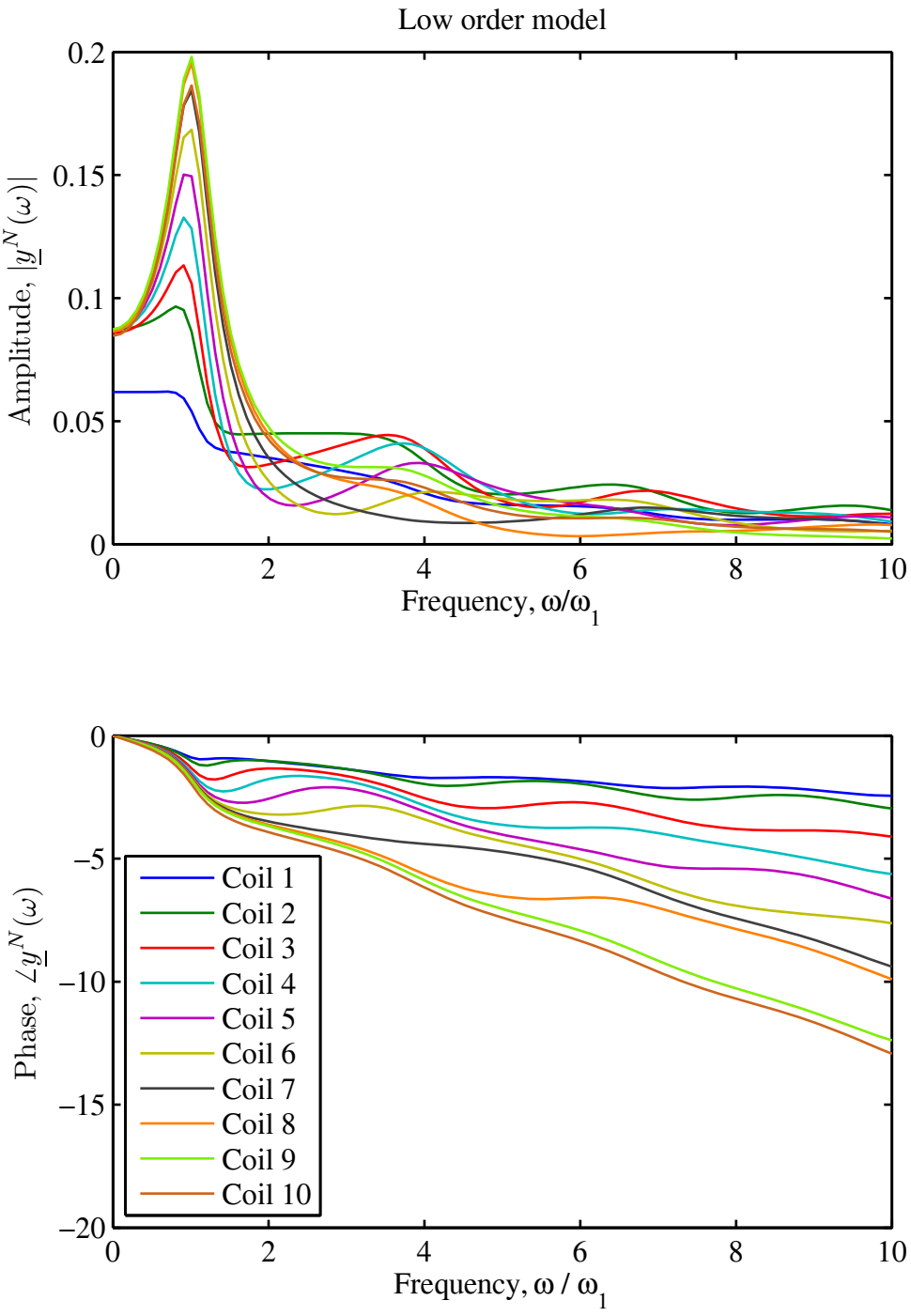


Figure 5.7: Frequency response of displacement to current demand for combined vibration, magnetics, and coil circuit model

The frequency response of coil current to a demand applied to a single coil circuit is shown in Figure 5.8. This trace is similar to Figure 5.3 but with the additions of the effects of vibration and eddy current models.

The frequency response of coil current can be divided into three frequency sections. The frequency response below 1000 Hz is the steady state response. The dynamics of the actuator do not come into play. The middle range between 1000 and 20,000 is characterized by interactions among the vibration and eddy current subsystem models giving complex character to the response. The high range response is dominated by the filtering of the coil circuit model. The energized coil's amplitude response in the top line of the figure is characterized by the gradual drop in amplitude starting around 1000 Hz. The mutual inductance effects start at about this value. The high frequency response is not accurate because of the limited number of terms in the vibration and eddy current models. The lack of high frequency terms is unimportant in light of the attenuation from the coil circuit model.

Despite the heavy attenuation that has been discovered through modeling of the eddy current and coil circuit, the multi-coil actuator still has dynamics that can be exploited for high speed response. The range of frequency response that is targeted for enhancement in this research is from the first resonance at about 2500 Hz up to about 10,000 Hz. In this range, the frequency response of coil current and displacement show some differences in amplitude and phase that come into play as the control algorithm optimizes the distribution of current to different coils to increase speed although not so much as the vibration model alone would have indicated.

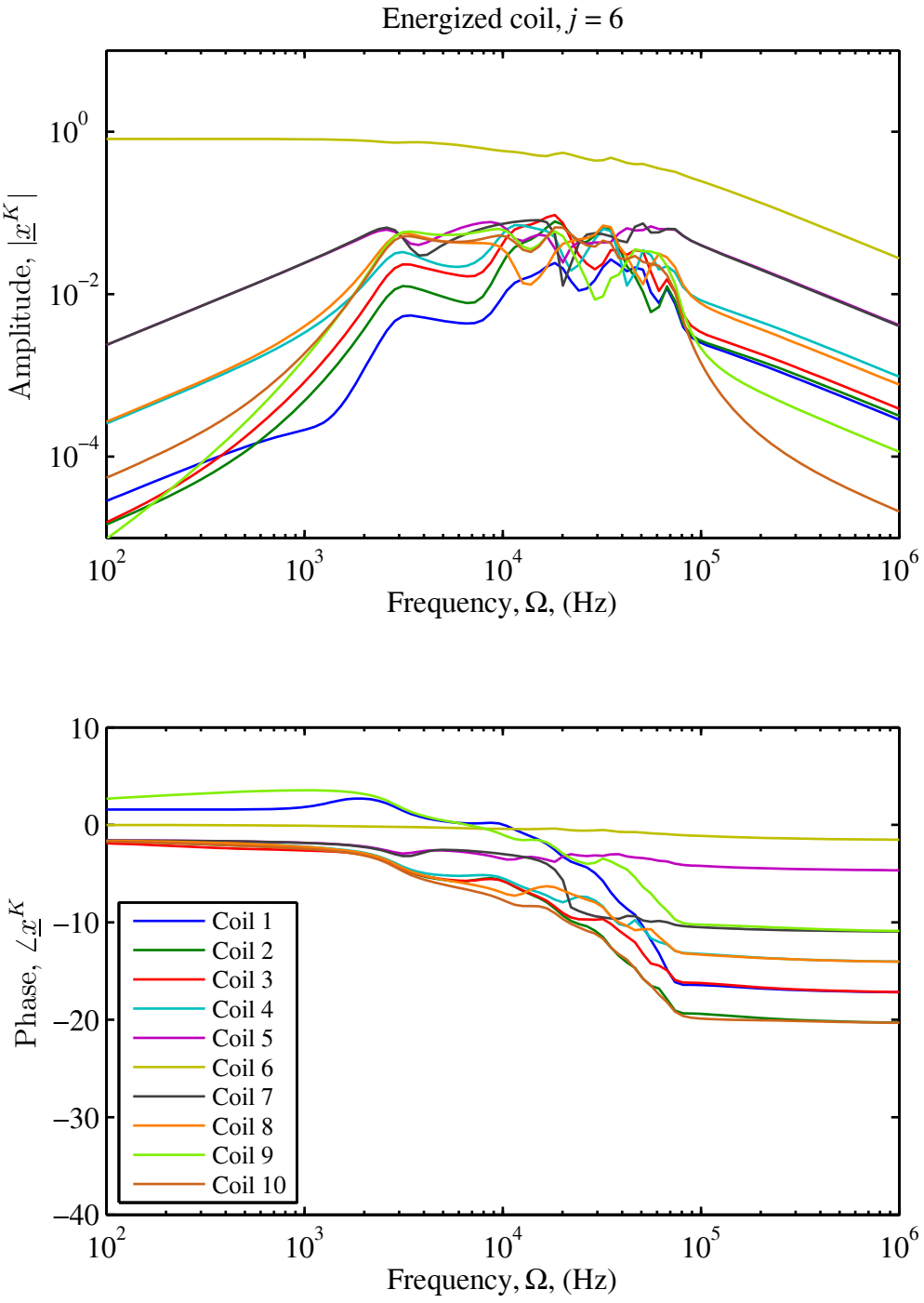


Figure 5.8: Frequency response of coil current to a current demand in $j$=6

The conclusion that can be reached from the results of full system model is that the entire actuator system needs to support the frequency response objective. A very high frequency response from 25,000 to 100,000 Hz is possible using the ten coil actuator with the vibration model but not when the limitations of eddy current and amplifier dynamics are considered. To gain very high frequency response, the actuator must be subdivided into more pie segments as indicated in Figure 4.16 to reduce eddy current and a faster amplifier must be used. As an indication of the response that could be achieved with these modifications to the design, the frequency response plot for 32 pie segments rather than four and amplifier gain set a factor of twenty higher is shown in Figure 5.9:

Frequency response of displacement for high speed actuator model, $\phi_0 = \frac{\pi}{16}$ and . This figure shows that high frequency response is obtainable with the proper choice of design parameters.

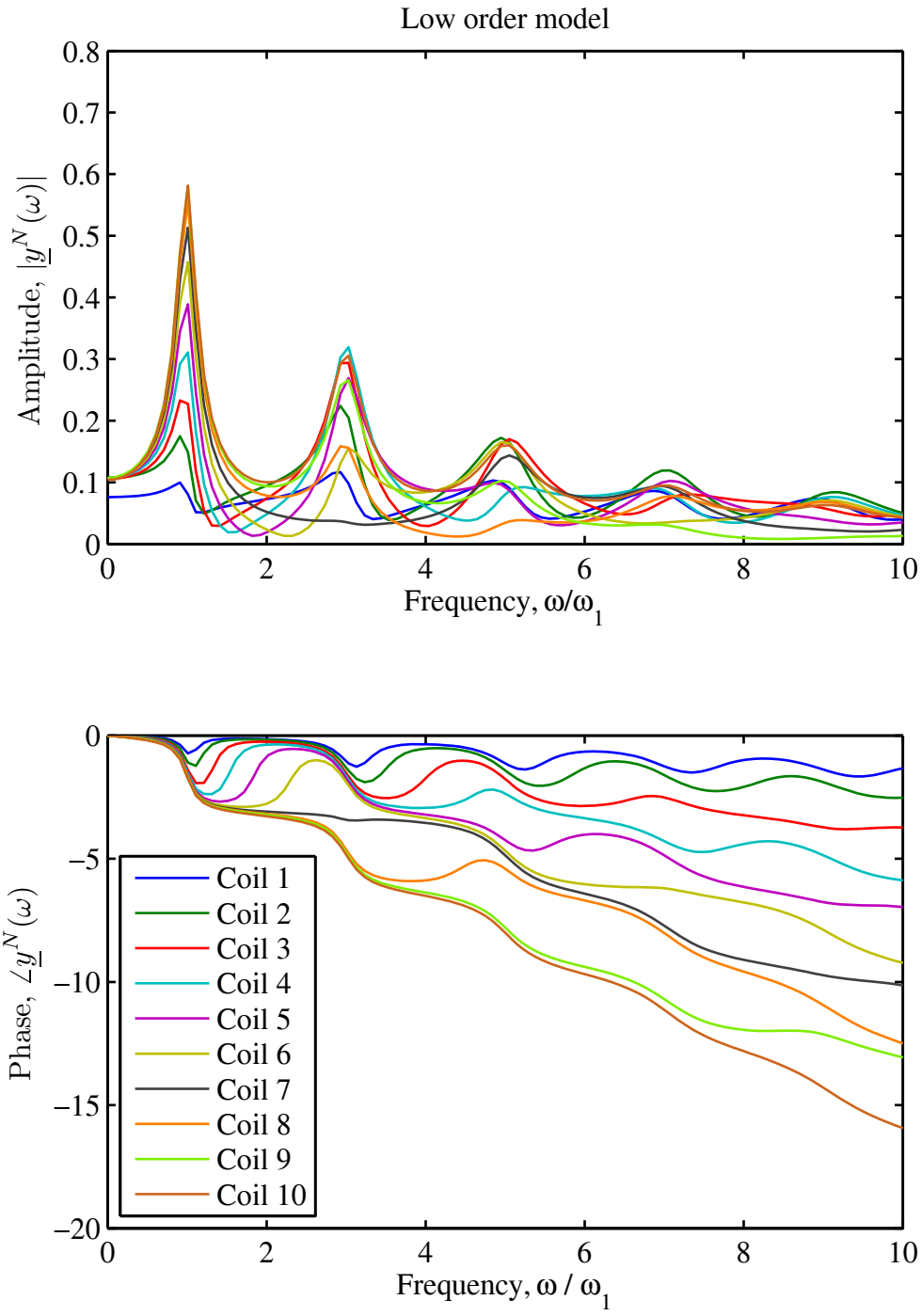


Figure 5.9: Frequency response of displacement for high speed actuator model, $\phi_0 = \frac{\pi}{16}$ and $\mathscr{G}_{amp,highspeed} = 20 \cdot \mathscr{G}_{amp}$

## Summary of Coil Circuit Model

A coil circuit model is derived in this chapter which describes the dynamics of the coil, amplifier, and load resistor. The current controlled amplifier in the model is approximated as a proportional device that has gain in units of resistance so that the resulting circuit is an inductive-resistive circuit. The inductive-resistive formulation generates a single state variable representing the current for each circuit. The model of the coil includes voltages induced by all current density distributions in the model including the effects on the coil from other coils and from the modal distributions of eddy current and magnestostrictive strain. An innovative method of calculation of the inductance coefficients for the modal current density distributions using the reciprocity principle is developed. The reciprocity method of calculation requires only the modal current density distribution and a steady-state FEMM calculation of the magnetic potential distribution in the rod resulting from each coil current to calculate the inductance coefficients.

Stand alone calculations in the time and frequency domain illustrate the inductive resistive behavior of the coil circuit and the inductive coupling of coils to each other. Simulations combining the vibration, magnetics and coil circuit models illustrate the full open loop system response. The simulations of current in coils that are not energized show the current generated as an acoustic pulse passes through the coil. This behavior gives the effectiveness of the actuator as a sensor. The induction effect from magnetostrictive strain also contributes to the magnetic drag. The increased attenuation of the displacement due to the circuit's contribution to drag is shown by the frequency

response of displacement to current in comparison to the response of vibration and magnetic simulations without the coil circuit.

An innovative test of the coil circuit model is devised using Green's first identity for vector fields. The test gives an equality between coupling coefficients from the vibration, magnetic, and coil models that can be checked. A constant proportionality between pairs of state space coefficient matrices is derived. Since the coefficients in each part of model are derived independently, the test uses each model to check the other two.

# CHAPTER 6

# MODEL PREDICTIVE CONTROL FOR THE MAGNETOSTRICTIVE ACTUATOR

The purpose of a control system is to alter the natural dynamics of a device for a specific desired effect. In the case of the magnetostrictive actuator, the goal is to take advantage of the spatially distributed inputs of the multi-coil device to overcome the limitation of the actuator's vibration resonance and extend the frequency range over which the actuator can respond effectively and accurately to demands. The spatially distributed inputs provide different amplitude and phase responses at the tip of the actuator as a function of frequency as shown in Figure 5.5 and Figure 5.7. The demands to the individual coils can be timed so that their collective effects arrive simultaneously to move the end of the actuator along a desired trajectory. The individual coils are also timed to cancel undesirable effects of reflected wave motion. The coils can each act individually to cancel the reflected wave that results from actuation as the wave front passes through each coil.

The research in this dissertation investigates whether multiple coils are more effective than a single coil for fast actuation. Before embarking on the time domain control algorithm problem to investigate the improvement, a simpler problem in the frequency domain can be formulated to show the theoretical advantage of multiple coils over a single coil. The actuator problem can be optimized in the frequency domain to show that a multiple coil actuator can track a sinusoidal reference signal of given amplitude and frequency using less power than a single coil actuator. This calculation

describes the advantage of the multi-coil actuator in terms of an improvement in the efficiency of converting electrical energy into linear motion. The frequency domain optimization is an algebraic problem equivalent to finding the minimum of a parabolic surface in a *jmax* dimensional space where *jmax* is the number of coils. This is a relatively easy problem to understand and to solve. The single coil problem can be made to track the reference sinusoidal signal but does not have any additional degrees of freedom for optimization or minimization of power. The comparison of the power consumed for the single and multiple coil cases makes a quantitative argument for the effectiveness of the multi-coil design.

The main objective of this chapter is the derivation of a control algorithm that uses the multiple coils effectively in a practical, real-time control system. Following a reference trajectory is a control problem that falls under the general heading of tracking or servo problems. The optimal frequency response shows a positive phase angle between the optimal current demand and the tip displacement. Positive phase suggests that the control algorithm should look ahead to the future reference trajectory specified for the actuator response and should provide a feedforward signal that anticipates the required future response. The need for tracking and feedforward action points toward model predictive control (MPC) as a candidate strategy for the control design. MPC falls into the same general category of optimal control as linear quadratic control (LQC) because the optimization is also based on a quadratic performance index. The model predictive control strategy is a mathematical technique which uses a model of the plant to predict the behavior of the plant from the current time to a future time horizon. The

strategy adjusts the inputs from the current time to the prediction horizon to minimize the quadratic performance index.

The multi-coil actuator control design can be based on the basic model predictive control strategy; however, some difficulties are encountered. The main mathematical difficulty is that the actuator has more inputs available than variables controlled to setpoints. The excess means that the steady state for the problem is underdetermined. The underdetermined situation can also be described as a system that has spare degrees of freedom. Most control processes are designed to have the same number of inputs (or manipulated variable) as variables controlled to setpoints. Such systems are called "square" systems. The spare degrees of freedom problem is unusual in model predictive control literature. The main new contribution to control theory in this dissertation comes from working out the resolution to the problems of steady state offset and non-equilibrium distribution of current that can occur because of the spare degrees of freedom. The problem is resolved by incorporating approaches analogous to conventional proportional and integral error feedback into the model predictive method.

In addition to the calculation of demands for the control law, the control system must provide estimation of full state from the available measurements and must deal with the problem of time delay. The combined model of vibration, magnetics, and coil circuits developed in Chapters 3, 4, and 5, when reduced to the low order case, has forty state variables. The prototype actuator system only measures eleven variables. Since the control algorithm requires the full state vector of forty state variables, it must be estimated from the available measurements. A standard Kalman estimator based on the

linear model of the actuator is developed for the real time control program. Conventional estimation techniques are used for designing the estimator feedback gain.

The speed of response of the actuator depends, in part, on the size of the time step of the real time system. The calculations in the control and estimation algorithm can consume a substantial amount of the computational time. With the hardware used for the experimental system, a number of compromises in the estimation and control algorithm have to be made in the interest of reducing the computation time. The approximations include reducing the order of the state space system (by a quasi-steady approximation) and using a single step calculation of the estimation algorithm rather than a prediction and correction step. The model reduction is a compromise between the time step needed for high speed control and the fidelity of the estimation and control computations.

The time delay of the digital system must also be addressed. The digital control system consists of a computational loop of operations in which the data are sampled and converted from analog values to digital, the state estimation and next set of values of the coil current demands are computed, and then the demands are converted back into analog form and sent to the amplifiers. The total time delay for the loop is significant compared to the time scale of interest. The current value of control demand is consequently based on a sample of data that may be several time steps old. The control algorithm must account for the time delay by predicting the behavior of the actuator over the computational delay. This prediction task is grouped with the estimation calculations and is based on the linear prediction model of the actuator.

The results for the control design developed in this chapter are presented for a set of simulated transients. The simulated results provide a clearer evaluation of the multi-

coil design than the experimental results in Chapter 7. The benefit of the multi-coil design only becomes fully realized when the time step is on the order of the time for an acoustic wave to pass through a single coil. The fastest time step that can be achieved with the prototype hardware is a factor of ten slower than this desired time step. The simulations using a smaller time step show the capability of the actuator without the limitation of the particular hardware available for the experiment. Simulations of the actuator with model reduction and the hardware time step are also shown for comparison to the examples using the full model with faster sampling to validate the model simplified model.

## Literature Survey on Control of Magnetostrictive Actuators and Model Predictive Control

The survey of research related to control of magnetostrictive actuators covers two separate subject areas. First, topics related to control using magnetostrictive actuators are covered. The history of magnetostrictive actuators is briefly traced leading up to current research which shapes the response of the actuator using models based on the physics of the process. This survey establishes the state of the art of control theory using magnetostrictive actuators and places the current work in context of the broader field. The second area is the discussion of model predictive control (MPC). Although a relatively recent development, model predictive control has enjoyed broad application in industry. The advantage of the method for the application of fast actuation is that model predictive control includes both feedforward and feedback elements in a unified but relatively simple mathematical structure. The main goal of the literature survey is to establish links to the basic references on model predictive control that provide the

underlying theory. The application literature is also reviewed for a few examples of applications that are mathematically similar to the multi-coil actuator, such as systems with vibrational modes, and for instances in which the spare degrees of freedom problem is addressed.

**Magnetostrictive actuator control**

Following the first reports of Terfenol in the literature, a number of publications in the 1980's investigated potential applications for the new giant magnetostrictive material. Most of the publications involved using the material in applications such as valve actuation, micro positioning, or vibration dampening which would require a feedback circuit. The early articles focused on the feasibility of the application based on the Terfenol's material properties without actually placing the device in a feedback loop [6, 59]. The earliest research that placed a prototype actuator in a feedback application seems to be Hiller who gave a description of using a simple proportional feedback of position error to cancel a vibration disturbance applied to the base of the actuator while at the same time tracking a reference position signal [60]. An article by Greenough [5] describes efforts to compensate for nonlinearities and load dependent gain in the Terfenol response. The article describes shaping the response with two feedback controllers and indicates a digital implementation using a "transputer". Mathematical details of the control algorithm are not given. Hall reported a compensation algorithm for a prototype device in which a measured acceleration signal was fed back through a proportional-differential control to compensate for the nonlinearity of the magnetostrictive material through classical feedback [43]. Hall's control scheme is a model-based control system that incorporates a theoretical transfer function of the actuator's open loop response to set

the system gain. The idea of Hall's design was to overcome Terfenol's nonlinearities and gain shifts due to load and temperature by incorporating linear feedback so that the actuator's compensated response matched the ideal linear device more closely.

In an early application of Terfenol to vibration control, Bryant reported a design for vibration control of a table supported by three Terfenol actuators[7]. This is perhaps the first example in which the control scheme involved a multi-input and multi-output arrangement. In the experiment, the three-legged platform was mounted on a shaker table which acted as a disturbance. The feedback control was designed to maintain a steady table top surface while vibration was applied by the shaker table. The physics of the problem involves complex coupled vibration dynamics in three dimensions. The control design, however, was not based on a physical model of either the actuators or table dynamics. Instead, a proportional-integral-differential feedback was applied and then tuned manually by trial and error techniques to obtain an approximate classical control algorithm. The feedback was then refined by an artificial neural network control that adaptively adjusted the response for greatest attenuation.

Moon developed a structural vibration control method using magnetostrictive actuators [61]. An experimental system consisting of a simple aluminum beam supported on each end by a magnetostrictive actuator was used for experimental verification of the concept. The vibration model of the beam has similar mathematical properties to the vibration component of the multi-coil actuator but in a much lower frequency range. The first resonance of the beam occurs at 50 Hz. In Moon's mathematical model of the system, the magnetostrictive actuators are proportional devices.

A number of characteristics set the proposed multi-coil actuator apart from the early controls. The common characteristic of the early Terfenol actuator applications is that the frequency range is well below the first resonance of the actuator. At low frequency, the actuator can be satisfactorily modeled as a linear, instantaneous component. The advantages that are brought out by multiple coils are only evident when the bandwidth extends above the first longitudinal resonance. Also, the magnetostrictive device given in the literature is a single-input, single-output system. The only multivariate problems occur when multiple actuators are employed. Separate actuators do not involve magnetic coupling among the inputs and lack the coupled sensing and actuation dynamics of the multi-coil device.

**Compensation for hysteresis and saturation nonlinearities**

Recent efforts in control of magnetostrictive actuators have centered on handling the saturation and hysteresis of the magnetostrictive material. Hughes and Wen recognized the applicability of Preisach operators (on-off operator with dead band like a thermostat) to represent the hysteresis of piezoceramics and shape memory alloys [20]. Their paper went on to suggest an open loop, inverse operator to compensate for the nonlinearities. Smith proposed a similar model of the hysteresis and a feedback control of a cantilevered beam using optimum control theory to compensate for the nonlinear response of a magnetostrictive actuator [33]. The vibration of the cantilever beam is a process model in the same mathematical family as longitudinal vibration of the multi-coil actuator. Smith applied this control scheme in a practical application to control chatter and vibration in the cutting tool of a milling operation. He presented a control algorithm with two types of compensation, an inverse operator for the saturation nonlinearity and

feedback control to compensate for hysteresis in the magnetostrictive positioner [62]. Nealis applied robust control techniques to Smith's nonlinear model to improve the noise rejection characteristics of the feedback portion of the design [63]. Tan and Baras combined an inverse of the Preisach operator with the inverse of the saturation nonlinearity in the forward loop of a controller in a static compensation algorithm. This differs from the previous controls in that the feedback portion of the control is nonlinear. Ventakaraman with Tan and Krishnaprasad extended Tan's earlier work by developing an approximate inverse operator that includes a rate-dependent dynamic model of hysteresis as part of the inverse compensator [64].

The inverse control schemes can be thought of as compensating for the nonlinear material properties in much the same way that a pair of eyeglasses compensates for poor focus of the eye. The inverse of the mathematical shape of the response is applied to the demand as a pre-filter resulting in an overall linear response. The experimental and simulated results give good evidence of the success of the algorithms in representing the nonlinear processes and the ability of inverse operators to compensate for them. The nonlinear control research is complementary to the present research in the multi-coil actuator. The nonlinear control applies a very successful approach to the material model but then treats the actuator without spatial distribution effects. The multi-coil actuator handles the spatial distribution of properties with detailed spatially distributed models of the magnetic field and vibrational stress and strain but then approximates the magnetostrictive material properties as linear. A combined model representing both nonlinearity and spatial distributions seems mathematically feasible. The difficulty of the

combined model is the number of calculations that the hysteresis modeling adds to the control algorithm. A combined model is recommended for future work.

**Background on model predictive control**

The model predictive control (MPC) method is a recent development in control theory but has become widely applied in control of chemical plants and oil refineries. The basic formulation that is used as the starting point for the control algorithm in this research can be found in standard texts on the subject[12, 13]. Either of these two references provides sufficient background on the basic MPC method. The approach used in the multi-coil actuator is the simplest case given in the early chapters of these texts, an unconstrained problem with no random disturbances. The history of development and references to the current trends are given in a survey of the field [65]. This article, originally written in 1998, has been updated and republished several times as new research has been added to the field.

The multi-coil actuator is a special case of predictive control because the number of inputs is greater than the number of variables controlled to a setpoints. The situation is generally described as non-square and possessing spare degrees of freedom. The basic textbook references do not provide much information on this class of problems. Maciejowski [12] mentions the topic briefly in a section listing problems "which are potentially very important, but which are mostly still at the research stage." For spare degrees of freedom, he suggests solving a steady-state problem to compute an optimum steady state distribution of inputs based on a steady state cost function. The control problem is then modified to use the steady state optimum values as the setpoints for any spare inputs. The control problem with augmented setpoints is square. In their survey

paper, Qin and Badgwell discuss non-square systems and mention the technique of squaring the system by using a steady state optimization to calculate auxiliary setpoints. Rossiter [13] specifically does not address non-square problems in his monograph. He states, "When MPC is applied to a nonsquare system the precise objectives and associated tuning are process dependent and nongeneric; hence, we omit this topic."

Published applications of non-square systems are fairly rare and are lacking in any mathematical generality. Two examples mentioning non-square problems in recent work are Magni [66] and Shead [67]. The example problem in the Magni paper involves a fermentation process with two inputs and a single output. The control scheme involves appending integrators to the system model to guarantee no steady state error. The same mathematical idea, but with a different method of introducing the integrators, is used in this dissertation's design of the actuator control. Shead's paper is primarily about a technique for handling fewer actuators than setpoints. The particular non-square problem that Shead addresses is a heavy oil fractionator in which the system changes from square to insufficient in degrees of freedom because one or more actuators fails or reaches a limit. Shead's scheme, which he calls the operability method, involves steady state optimization of a variable to an interval rather than a setpoint. Shead points out that the operability method can be applied to the spare degrees of freedom problem also.

**Similar control problems**

The actuator control problem presents a unique combination of features and requirements because of the novelty of the design itself. One would not expect to find control research that is closely related. However, problems from other fields have similar mathematical properties. The survey sought related problems both to gain the benefit of

their research in solving the difficulties of the actuator control and to determine whether the present control research would have wider applicability. The main characteristic of the actuator to achieve the higher speed actuation is to exploit the higher vibrational modes. To devise a control system, the vibration is expressed in a modal model and modern optimal control techniques are applied. The search found two research areas that share the same modeling and control approach: active structure control and thermoacoustic combustion control.

The most closely related field is the active control of structures which is described in detail in Gawronski's monograph, *Advanced Structural Dynamics and Active Control of Structures*[22]. One of the practical applications for active structural control is in positioning large satellite tracking antennae and radio telescopes that must be aimed toward a target. Vibration in such systems can be best expressed as a modal plant model, similar mathematically to the vibration model of the actuator, and the control can be derived from the state space form of the equations. The radio telescope structure is very lightly damped and the vibration interferes with receiving a precise signal. The similarity of the structural dynamics problem is the representation of the dynamics of the antenna as a modal model with multiple inputs and outputs for sensing and controlling both the positioning and the vibration. The structural dynamics problems are different from the multi-coil actuator in several significant ways. The number of sensors and actuators in the structural system is usually designed to be equal so the control system does not encounter the problem of spare degrees of freedom. The frequency range of the structural vibration problem is much lower. The dominant frequencies occur below 300 Hz. This means that the dynamics of the actuators tend to be much faster than the

structural dynamics, and the actuators can be modeled as proportional devices with no dynamics of their own that are important to the control problem. The actuators are point sources of force and do not have a mathematical analogy to the coupling of inputs through a diffusion process like the magnetic field. However, the main difference is the objective of control. In the actuator, the goal is to move the tip rapidly, usually from closed to open and then back. The technique is to use the distributed controls to put energy into the high frequency modes and then to draw the kinetic energy rapidly back out again. Damping the high frequency modes works against the desired speed of response. For the antenna aiming problem, the natural damping is very light and vibration is unwanted. The control objective is to take energy out of the vibration modes. The control approach is to design an algorithm that damps each mode specifically. The control algorithm drives the amplitude of the targeted mode to zero, in effect, applying a setpoint of zero to the state variable for the mode's amplitude. Nevertheless, the design process and computations follow along similar lines and use similar mathematical tools. The active structural control work was found to have a number of useful parallels to the actuator problem. In particular, the techniques used in this research for balanced realization and model reduction are based in part on the methods given by Gawronski.

The cantilevered beam problem has been investigated by a number of researchers in the field of active structure control as a simple academic problem leading to more complex vibration control applications. The transverse vibration in the cantilevered beam and longitudinal vibration in the actuator rod are mathematically the same problem. Hanagud applied the piezoceramic devices to a cantilevered beam to investigate sensing and controlling vibration [68]. His aim was to develop an active control method for

vibration in the vertical stabilizer of high performance aircraft. Multiple piezoelectric devices are used so the vibration case is a multivariate problem like the actuator, and the modal vibrational model and optimal performance index in his example are similar to the actuator problem. Again, the differences are in the objective of control, damping versus speed, and the frequency range of interest. The control method that Hanagud chose for the design the structural feedback in the cantilevered beam is the linear quadratic control (LQC) method.

A comparison between LQC and MPC methods for vibration control of a cantilevered beam using piezoelectric sensors and transducers is given by Nelson [69]. His study found that the MPC method gave superior results. Another comparable aspect of his study to the present work is that he also encountered problems with DC offset using the MPC and reformulated the cost of control effort in terms of the control demand rather than the change in demand as is usually done in MPC.

Another problem that bears a mathematical similarity to the actuator problem is thermoacoustic combustion. Schuermans combined a modal model of the combustion chamber acoustics with an impulse model of the flame front. The dynamics of the combustion are represented by a distribution of straight delays in which the delay is a Gaussian distributed variable. Schuermans' acoustic model combines a series of one-dimensional flow elements to represent moderately complex geometries of combustion chambers in the state space format. The control method designs an algorithm that damps each acoustic mode individually. The Schuermans' example problem contains 24 burners and, at most, two controlled modes so the problem has the property of spare degrees of freedom. He uses the Moore-Penrose pseudo-inverse in calculating the optimum control

gains. The pseudo-inverse is a method of solving a least squares optimization problem. Schuermans comments that the number of sensors and actuators need not be the same. The terminology of the combustion control problem is very different than the actuator problem but the underlying mathematics is actually very similar. The main differences between the combustion and the actuator problems are that the frequency range of interest is lower and the objective of the thermoacoustic problem is to draw energy out of the high frequency modes rather than put energy into those modes.

## Optimization in the Frequency Domain

The actuator problem is a case of "spare degrees of freedom" in which the number of inputs exceeds the number of controlled variables. This situation occurs less frequently than square systems in which the inputs and outputs are equal in number or the situation in which the number of controlled variables exceeds the number of inputs. It seems plausible that spare degrees of freedom should offer some advantage in control, but the literature on control offers very little in the way of general guidance on the devising such a control system. This section provides a simple algebraic optimization of the spare degrees of freedom problem in the frequency domain that is based on minimizing the energy consumed by the actuator while following a sinusoidal reference signal exactly. The derivation serves as a mathematical illustration of the advantage that the spare degrees of freedom situation presents. The optimization in the frequency domain finds the optimum input distribution for the multi-coil actuator in amplitude and phase as a function of frequency. The response of the single coil actuator following the same signal is also determined to show the conditions under which the multiple coils give an advantage and to calculate the magnitude of the improvement as function of

frequency. The frequency domain solution for the single coil is an algebraic equation that does not involve optimization. The frequency domain solution provides insight into the control advantages that can be gained by applications with spare degrees of freedom and how multiple inputs work.

A general frequency response function with spare degrees of freedom can be represented as the following equation. The output, in this case, is a scalar while the input is a vector. This is the version of the equation that is needed for the actuator problem, but a more general case could be devised in which the output is also vector, but lower dimension than the input. The optimization solution presented here does not depend in any unique way on the actuator transfer function other than the characteristic that it is a multi-input, single-output transfer function. The frequency response function can be thought of as an arbitrary vector function. The multi-input, single-output problem can be written as simply;

$$\underline{y}^{N}(i\omega) = \mathbf{T}(i\omega) \cdot \underline{\mathbf{u}}(i\omega). \tag{6.1}$$

In this notation, the underscore is used to indicate a frequency response transform of the time domain function. The frequency response function for the actuator is obtained from the state space model as the following.

$$\frac{\underline{y}^{\mathbf{N}}(i\omega)}{\underline{\mathbf{u}}(i\omega)} = \mathbf{C}^{\mathbf{P}}\left(i\omega\mathbf{I} - \mathbf{A}^{\mathbf{P}}\right)^{-1}\mathbf{B}^{\mathbf{P}} + \mathbf{D}^{\mathbf{P}} = \mathbf{T}(i\omega). \tag{6.2}$$

In the actuator problem, the controlled variable is $\underline{y}^{\mathbf{N}}(i\omega)$ which is a scalar variable representing the displacement of the free end of the actuator at a given driving frequency, $\omega$. The control input, $\underline{\mathbf{u}}(i\omega)$, is a vector of current demands which are applied at the amplifier inputs. The model of the actuator is given by the linear state

space coefficient matrices, $\mathbf{A}^{\mathbf{P}}$, $\mathbf{B}^{\mathbf{P}}$, $\mathbf{C}^{\mathbf{P}}$, and $\mathbf{D}^{\mathbf{P}}$, which represent the coupled dynamics of the vibration, eddy current, and coil circuit models. The frequency response, $\mathbf{T}(i\omega)$, is a row vector of scalar transfer functions representing the dynamics of the displacement in response to each of the individual current inputs. At any given frequency, the transfer function, $\mathbf{T}(i\omega)$, can be evaluated to yield a set of complex constants. The basic frequency domain control problem is to find a set of inputs that give the desired reference value of the controlled variable.

$$\underline{r}(i\omega) = \underline{y}^{\mathbf{N}}(i\omega) = \mathbf{T}(i\omega) \cdot \underline{\mathbf{u}}(i\omega). \tag{6.3}$$

In the frequency domain, the reference signal, $\underline{r}(i\omega)$, is a sinusoidal signal of amplitude, $|\underline{r}|$ and frequency, $\omega$, in radians per second. The unknowns are the control inputs in the equation, $\underline{\mathbf{u}}(i\omega)$. For a square system, the reference value problem in Eq. (6.3) has a single unique solution. For example, if the input is a scalar like the output, then the solution is given by

$$\underline{u}(i\omega) = T(i\omega)^{-1} \underline{r}(i\omega). \tag{6.4}$$

In control literature, this is called the inverse dynamics solution. The difficulty of the control problem with spare degrees of freedom is that the number of unknowns in Eq. (6.3) is greater than the number of equations and the problem has no unique solution. In the general case for the spare degrees of freedom, some of the solutions would be truly undesirable. The problem can be made unique, and the spare degrees of freedom can be put to good use by adding a requirement for the solution of Eq. (6.3) to also minimize some useful performance index. The typical (and mathematically easiest) condition to minimize is a quadratic function.

$$\mathcal{F} = \frac{1}{2}\underline{\mathbf{u}}^{\dagger}\underline{\mathbf{u}}. \tag{6.5}$$

The frequency input is a complex number so the quantity, $\underline{\mathbf{u}}^{\dagger}$, represents the complex conjugate and transpose of $\underline{\mathbf{u}}$. In the actuator problem, the quadratic term is the sum of the squares of the current demands. Power applied to the actuator is proportional to the sum of squared currents so minimizing $\mathcal{F}$ represents the minimum power demand to the actuator. In a more general derivation, the performance index could include a weight matrix, $\mathcal{F} = \frac{1}{2}\underline{\mathbf{u}}^{\dagger}\mathbf{R}\underline{\mathbf{u}}$. Since the inputs in the actuator problem all represent equal power sources, it makes sense for the weight matrix to be the identity matrix for this problem. The problem now is to minimize $\mathcal{F}$ subject to the reference condition in Eq. (6.3). Optimization with a constraint can be solved using Lagrange multipliers [70]. The method of Lagrange multipliers solves an auxiliary function, $\tilde{\mathcal{F}}$, that contains the original performance index plus the constraint times the Lagrange multiplier. Minimizing this auxiliary function and satisfying the constraint equation gives the solution to the constrained optimization problem. The auxiliary optimization problem with the Lagrange multiplier term is the following.

$$\begin{aligned}\tilde{\mathcal{F}} &= \frac{1}{2}\underline{\mathbf{u}}^{\dagger}\underline{\mathbf{u}} + \lambda\left(\underline{r} - \underline{y}\right) \\ &= \frac{1}{2}\underline{\mathbf{u}}^{\dagger}\underline{\mathbf{u}} + \lambda\left(\underline{r} - \mathbf{T}\cdot\underline{\mathbf{u}}\right).\end{aligned} \tag{6.6}$$

The optimum is found by taking the partial derivative with respect to the input and setting it equal to zero.

$$\begin{aligned}\frac{\partial \tilde{\mathscr{F}}}{\partial \underline{\mathbf{u}}} &= \mathbf{0}, \\ &= \frac{\partial}{\partial \underline{\mathbf{u}}}\left[\frac{1}{2}\underline{\mathbf{u}}^{\dagger}\underline{\mathbf{u}} + \lambda\left(\underline{r} - \mathbf{T}\cdot\underline{\mathbf{u}}\right)\right], \\ &= \underline{\mathbf{u}}^{\dagger} - \lambda\mathbf{T}.\end{aligned} \tag{6.7}$$

Taking the complex conjugate of both sides gives the solution for the optimum input.

$$\underline{\mathbf{u}} = \lambda\mathbf{T}^{\dagger}. \tag{6.8}$$

The Lagrange multiplier can be obtained by substituting the solution for $\underline{\mathbf{u}}$ into Eq. (6.3).

$$\begin{aligned}\underline{r} &= \mathbf{T}\cdot\underline{\mathbf{u}}(i\omega) \\ &= \mathbf{T}\cdot\lambda\mathbf{T}^{\dagger}.\end{aligned} \tag{6.9}$$

Solving for $\lambda$ and inserting the result into Eq. (6.8) gives the final result.

$$\underline{\mathbf{u}} = \frac{\mathbf{T}^{\dagger}}{\mathbf{T}\cdot\mathbf{T}^{\dagger}}\underline{r}. \tag{6.10}$$

This remarkably simple solution gives a clear insight into the advantage of multi-coil actuator. The complex conjugate has the opposite phase angle to the original variable.

$$\angle\mathbf{T} = -\angle\mathbf{T}^{\dagger}. \tag{6.11}$$

This result gives the mathematical basis for the intuitive notion that the demand should lead the demand function by the same phase angle that the response of $\underline{y}^{N}$ lags that demand. The input function's angle cancels the output lag giving a response with zero phase error.

The amplitude of the input also has the expected response. The denominator of Eq. (6.10) of can be written as the absolute magnitude of the vector squared

$$\underline{\mathbf{u}} = \frac{\mathbf{T}^{\dagger}}{|\mathbf{T}|^2}\underline{r}\,. \tag{6.12}$$

Taking the magnitude of both sides gives.

$$|\underline{\mathbf{u}}| = \frac{1}{|\mathbf{T}|}\underline{r}\,. \tag{6.13}$$

This equation shows that the magnitude of the input must follow the reciprocal of the magnitude of the frequency response function. If the frequency response diminishes with frequency, which is the case for most physical systems, then the input must become proportionately larger to maintain the same amplitude.

For the multi-coil actuator to be more efficient at high frequency than the single coil, the power consumed by the multi-coil actuator must be less than the power consumed by the single coil actuator while tracking the same reference input. The power consumed by the actuator can be obtained by substituting the optimum back into the equation for $\mathscr{F}$ .

$$\mathscr{F} = \frac{1}{2}\underline{\mathbf{u}}^{\dagger}\underline{\mathbf{u}} = \frac{1}{2}\left(\frac{\mathbf{T}\underline{r}}{\mathbf{T}\cdot\mathbf{T}^{\dagger}}\right)\left(\frac{\mathbf{T}^{\dagger}\underline{r}}{\mathbf{T}\cdot\mathbf{T}^{\dagger}}\right) = \frac{\underline{r}^2}{2\mathbf{T}\cdot\mathbf{T}^{\dagger}}\,. \tag{6.14}$$

For comparison, the power consumed by a single coil actuator can also be obtained. This solution can be derived from the original transfer function by setting all the inputs equal to the same value.

$$\underline{y}^N(i\omega) = \mathbf{T}(i\omega) \cdot \begin{bmatrix} 1 \\ 1 \\ \vdots \\ 1 \end{bmatrix} \underline{u}_{single}(i\omega). \tag{6.15}$$

This equation can be simplified by writing the summation in terms of an average value of the transfer function vector.

$$\overline{T}(i\omega) = \frac{1}{n_u} \mathbf{T}(i\omega) \cdot \begin{bmatrix} 1 \\ 1 \\ \vdots \\ 1 \end{bmatrix}. \tag{6.16}$$

where $n_u$ is the number of inputs. Note that the average is not in bold font, indicating that it is a scalar.

With only a single degree of freedom, the reference condition can be solved for the single coil problem, but no additional optimization is possible.

$$\underline{r} = \underline{y}^N_{single}(i\omega) = n_u \overline{T}(i\omega) \underline{u}_{single}. \tag{6.17}$$

Since the average is a simple complex number the equation can be solved for $\underline{u}_{single}$.

$$\underline{u}_{single} = \frac{\underline{r}}{n_u \overline{T}(i\omega)}. \tag{6.18}$$

The power consumed by the single coil actuator is given by

$$\begin{aligned} \mathscr{T}_{single} &= \frac{1}{2} \underline{\mathbf{u}}^{\dagger} \underline{\mathbf{u}} = \frac{1}{2} \underline{u}^{\dagger}_{single} \begin{bmatrix} 1 & 1 & \dots & 1 \end{bmatrix} \begin{bmatrix} 1 \\ 1 \\ \vdots \\ 1 \end{bmatrix} \underline{\mathbf{u}}_{single} \\ &= \frac{n_u}{2} \left| \underline{u} \right|^2_{single}. \end{aligned} \tag{6.19}$$

Substituting the reference solution gives

$$\mathscr{F}_{single} = \frac{n_u}{2}\left|\frac{\underline{r}}{n_u \overline{T}\left(i\omega\right)}\right|^2 = \frac{1}{2n_u}\left|\frac{\underline{r}}{\overline{T}\left(i\omega\right)}\right|^2 . \tag{6.20}$$

The fundamental question of the research project is whether the power consumed by the multi-coil actuator with optimal input is less than the power for the single coil actuator for the same response. In the simplest possible terms, the dissertation reduces to evaluating whether the following inequality is true.

$$\mathscr{F} \overset{?}{\leq} \mathscr{F}_{single} . \tag{6.21}$$

Substituting Eqs. (6.14) and (6.20) into Eq. (6.21) provides the answer to the question and shows by how much the power is reduced.

$$\frac{\left|\underline{r}\right|^2}{2\mathbf{T}\cdot\mathbf{T}^{\dagger}} \overset{?}{\leq} \frac{1}{2n_u}\left|\frac{\underline{r}}{\overline{T}\left(i\omega\right)}\right|^2 . \tag{6.22}$$

The next few steps solve for an equivalent expression that can be more readily interpreted. First, the reciprocal of both sides is taken. This operation requires that the inequality be reversed. Common factors are all positive so they may be canceled without changing the direction of the inequality. After making these changes, Eq. (6.22) becomes the following.

$$\mathbf{T}\cdot\mathbf{T}^{\dagger} \overset{?}{\geq} n_u \left|\overline{T}\left(i\omega\right)\right|^2 . \tag{6.23}$$

The equation is equal to the following.

$$\begin{bmatrix} T_1 & T_2 & \dots & T_{n_u} \end{bmatrix} \cdot \begin{bmatrix} T_1^\dagger \\ T_2^\dagger \\ \vdots \\ T_{n_u}^\dagger \end{bmatrix} \overset{?}{\geq} n_u \overline{T} \cdot \overline{T}^\dagger . \tag{6.24}$$

The following identity can be defined by multiplying both sides of Eq. (6.16) by $\overline{T}^\dagger$.

$$\begin{aligned} \begin{bmatrix} T_1 & T_2 & \dots & T_{n_u} \end{bmatrix} \cdot \begin{bmatrix} 1 \\ 1 \\ \vdots \\ 1 \end{bmatrix} \overline{T}^\dagger &= n_u \overline{T} \cdot \overline{T}^\dagger . \\ \begin{bmatrix} T_1 & T_2 & \dots & T_{n_u} \end{bmatrix} \cdot \begin{bmatrix} \overline{T}^\dagger \\ \overline{T}^\dagger \\ \vdots \\ \overline{T}^\dagger \end{bmatrix} &= n_u \overline{T} \cdot \overline{T}^\dagger . \end{aligned} \tag{6.25}$$

The following identity can be defined by taking the complex conjugate of both sides of Eq. (6.25). Since the right hand side is the product of two complex numbers, and not a vector, the operation is commutative.

$$\begin{bmatrix} \overline{T} & \overline{T} & \dots & \overline{T} \end{bmatrix} \cdot \begin{bmatrix} T_1^\dagger \\ T_2^\dagger \\ \vdots \\ T_{n_u}^\dagger \end{bmatrix} = n_u \overline{T}^\dagger \cdot \overline{T} = n_u \overline{T} \cdot \overline{T}^\dagger . \tag{6.26}$$

Now, subtract Eqs. (6.25) and (6.26) from the inequality in Eq. (6.24)

$$\begin{bmatrix} T_1 & T_2 & \dots & T_{n_u} \end{bmatrix} \cdot \begin{bmatrix} T_1^\dagger \\ T_2^\dagger \\ \vdots \\ T_{n_u}^\dagger \end{bmatrix} - \begin{bmatrix} T_1 & T_2 & \dots & T_{n_u} \end{bmatrix} \cdot \begin{bmatrix} \overline{T}^\dagger \\ \overline{T}^\dagger \\ \vdots \\ \overline{T}^\dagger \end{bmatrix} - \begin{bmatrix} \overline{T} & \overline{T} & \dots & \overline{T} \end{bmatrix} \cdot \begin{bmatrix} T_1^\dagger \\ T_2^\dagger \\ \vdots \\ T_{n_u}^\dagger \end{bmatrix} \overset{?}{>} -n_u \overline{T} \cdot \overline{T}^\dagger. \tag{6.27}$$

The right hand side of Eq. (6.24) can be written as

$$n_u \overline{T} \cdot \overline{T}^\dagger = \begin{bmatrix} \overline{T} & \overline{T} & \dots & \overline{T} \end{bmatrix} \cdot \begin{bmatrix} \overline{T}^\dagger \\ \overline{T}^\dagger \\ \vdots \\ \overline{T}^\dagger \end{bmatrix}. \tag{6.28}$$

After inserting this equation into Eq. (6.27) and bringing all terms to the left hand side, it becomes evident that the equation can be factored.

$$\begin{bmatrix} T_1 & T_2 & \dots & T_{n_u} \end{bmatrix} \cdot \begin{bmatrix} T_1^\dagger \\ T_2^\dagger \\ \vdots \\ T_{n_u}^\dagger \end{bmatrix} - \begin{bmatrix} T_1 & T_2 & \dots & T_{n_u} \end{bmatrix} \cdot \begin{bmatrix} \overline{T}^\dagger \\ \overline{T}^\dagger \\ \vdots \\ \overline{T}^\dagger \end{bmatrix} - \begin{bmatrix} \overline{T} & \overline{T} & \dots & \overline{T} \end{bmatrix} \cdot \begin{bmatrix} T_1^\dagger \\ T_2^\dagger \\ \vdots \\ T_{n_u}^\dagger \end{bmatrix} + \begin{bmatrix} \overline{T} & \overline{T} & \dots & \overline{T} \end{bmatrix} \cdot \begin{bmatrix} \overline{T}^\dagger \\ \overline{T}^\dagger \\ \vdots \\ \overline{T}^\dagger \end{bmatrix} \overset{?}{\geq} 0. \tag{6.29}$$

The top line can be factored for **T** and the second line can be factored for $\overline{T}$

$$\begin{bmatrix} T_1 & T_2 & \dots & T_{n_u} \end{bmatrix} \cdot \begin{bmatrix} T_1^\dagger - \overline{T}^\dagger \\ T_2^\dagger - \overline{T}^\dagger \\ \vdots \\ T_{n_u}^\dagger - \overline{T}^\dagger \end{bmatrix} - \begin{bmatrix} \overline{T} & \overline{T} & \dots & \overline{T} \end{bmatrix} \cdot \begin{bmatrix} T_1^\dagger - \overline{T}^\dagger \\ T_2^\dagger - \overline{T}^\dagger \\ \vdots \\ T_{n_u}^\dagger - \overline{T}^\dagger \end{bmatrix} \stackrel{?}{\geq} 0. \tag{6.30}$$

Factoring again yields an expression that is clearly positive or zero.

$$\begin{bmatrix} T_1 - \overline{T} & T_2 - \overline{T} & \dots & T_{n_u} - \overline{T} \end{bmatrix} \cdot \begin{bmatrix} T_1^\dagger - \overline{T}^\dagger \\ T_2^\dagger - \overline{T}^\dagger \\ \vdots \\ T_{n_u}^\dagger - \overline{T}^\dagger \end{bmatrix} \stackrel{?}{\geq} 0. \tag{6.31}$$

In this form, the inequality is clearly true. In addition, the only way that equality can hold is if

$$\begin{bmatrix} T_1^\dagger \\ T_2^\dagger \\ \vdots \\ T_{n_u}^\dagger \end{bmatrix} = \begin{bmatrix} \overline{T}^\dagger \\ \overline{T}^\dagger \\ \vdots \\ \overline{T}^\dagger \end{bmatrix}. \tag{6.32}$$

This condition for equality says that the only way that a multi input device operating with optimum inputs can consume the same power as the single actuator device (all inputs operating in unison) is when all the elements in the vector $\mathbf{T}(i\omega)$ are equal for all frequencies. For the multi-coil actuator, any difference in phase or amplitude among the transfer functions from the average can be used to make the multi-coil actuator work more efficiently than the single coil actuator. As the difference of each input from the average increases, the gain in efficiency also increases. A corrolary can show that the

multi-coil actuator can move faster than a single coil if both are constrained with same power.

To illustrate the magnitude of the efficiency improvement, the power parameters, $\mathscr{F}$ and $\mathscr{F}_{single}$ are plotted versus frequency in Figure 6.1. The transfer function model is the full system model (vibration, magnetics, and coil current using the low-order number of terms) shown graphically in Figure 5.7. Figure 6.2 shows the ratio $\mathscr{F}_{single} / \mathscr{F}$. This figure shows that the maximum improvement occurs in the resonance region of the vibration model and that ratio ranges between 10 and 100 in this frequency range.

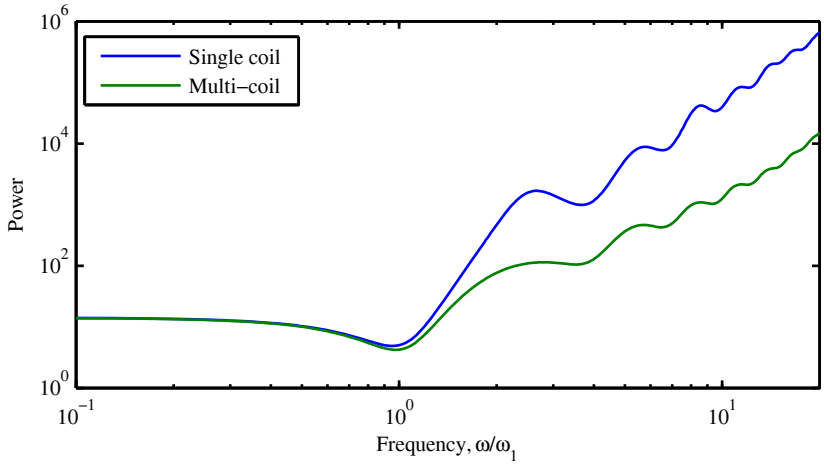


Figure 6.1: Power required for multi-coil and single coil actuators, nominal design

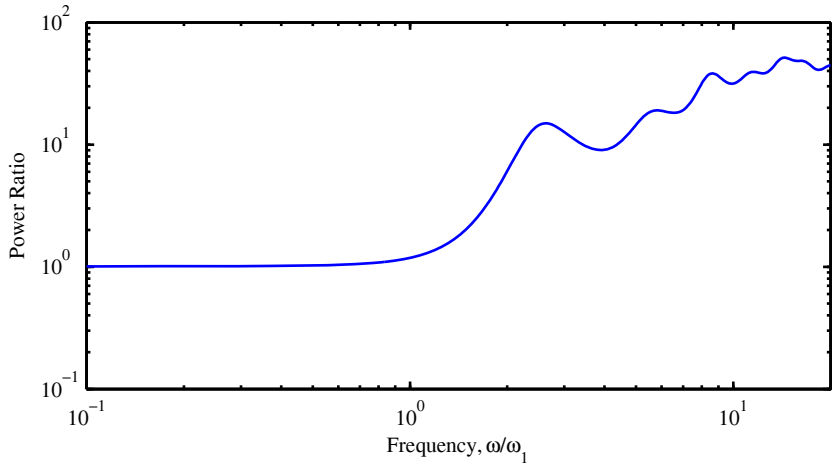


Figure 6.2: Ratio of single coil to multi-coil power, $\mathcal{F}_{single} / \mathcal{F}$ .

The multi-coil actuator shows significant reduction in power in the range from $\omega = \omega_1$ to $10\omega_1$ with the ratio shown in Figure 6.2 of a factor of 20 to 50 less power required by the multi-coil actuator. The enthusiasm for this success should be moderated by the observation that at 10,000 Hz even the multi-coil actuator requires nearly 100 times the power at 0 Hz to maintain the full amplitude response. This level of power is not feasible. The increase in power is primarily a consequence of the magnetic drag due to eddy current. The improvement is more feasible if the actuator is modified as shown in Figure 5.9 for high speed design with more pie segments and faster amplifiers. Figure 6.3 shows the optimum power for the high speed design

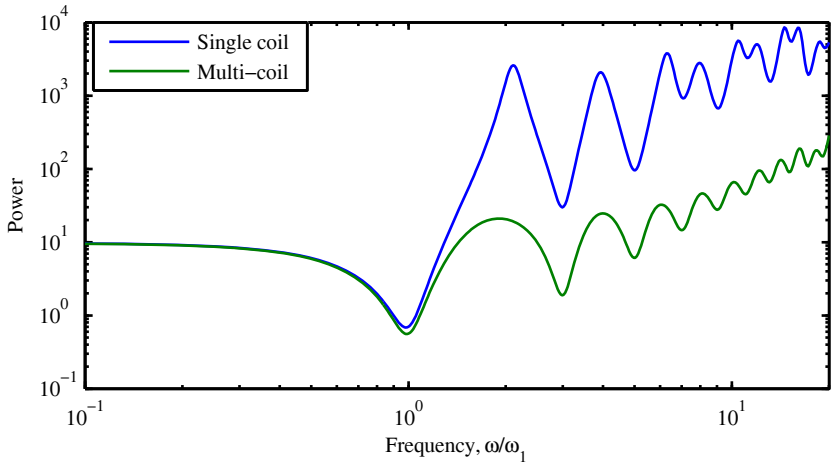


Figure 6.3: Power required for multi-coil and single coil actuators, high speed design

The power in the high speed design at the upper frequency range of the multi-coil actuator remains in a feasible range, within a factor of ten of the DC power.

The derivation of the optimum input for the frequency response problem in this section is one of the main conclusions of the dissertation. The derivation and numerical results show very clearly that the multi-coil actuator meets the expected potential for a faster device than the single coil. However, some shortcomings of the frequency analysis should be pointed out. The main point is that matching the displacement and the reference trajectory exactly using the Lagrange multiplier method does not lead to a robust control algorithm. In practice, a small amount of difference between the reference and the displacement must be tolerated to reduce the power requirement and make the control less sensitive to noise and modeling errors. The control strategies that are considered in the following section use a cost function including both control error (difference between reference and measure) and control effort (power demand) to balance out the desirable features of robustness, tracking, and minimizing the power. The degree

of improvement shown by this optimization in the frequency domain may be considered the maximum achievable improvement in power without consideration of robustness.

## Model Predictive Control Strategy

The frequency domain analysis in the previous section provides a simple, analytical result that shows that the multi-coil actuator can produce a given amplitude response while consuming less power than a single coil actuator, or alternatively, a multi-coil actuator can give higher amplitude response for a fixed input power. The frequency response results prove the multi-coil concept can always provide an improvement in the actuator response if there are differences in the phase and gain response to the different inputs; however, it is difficult to judge how well that advantage translates into improvement in the time response. The operation of the multi-coil actuator as a practical device requires a real-time control design that takes advantage of the timing of the inputs.

This section derives a servo control design for the actuator and provides example transients to illustrate the benefit of multiple input coils in following typical wave forms that might be needed for applications such as a operating a valve or canceling vibration. The same strategy is used to provide the control algorithm for both simulated and experimental results. This chapter gives the simulated results of the closed loop system. Experimental results are given in Chapter 7. The simulated results show the advantage of multiple coils more clearly than the experimental because the time step of the simulated transient is not restricted by the hardware limits of the experimental system.

Just as in the frequency domain analysis, the control objective for the actuator is to find the input demand versus time for the ensemble of coil inputs so that the actuator tip follows a specified trajectory while consuming the minimum electrical power. To

demonstrate improvement, the multi-coil control concept has to be compared against a well-tuned, conventional single coil actuator. The goal of the comparison is to show that the minimum power for the multi-coil actuator is significantly less than the single coil and that high frequency response can be achieved with realistic current and voltage from the driving amplifiers.

The model predictive control algorithms for single coil and multi-coil actuator are designed using the same approach. The simulation models for both cases are also the same. The single coil model is implemented using the same modification to the multi-coil mode that was used in the frequency domain section. The same current demand is applied to each amplifier of the multi-coil model thus causing all circuits to operate in unison as if the actuator were a single coil. The voltage of the single coil is computed as the sum of the voltages across the individual coils as if the coils are wired in series. It should be noted that other approaches to convert the multi-coil model to an equivalent single coil model are possible. The dynamics of ten individual coil circuits each with an amplifier operating on the same input signal is not precisely the same as a single coil circuit with one uniform coil along the full length, one load resistor, and one amplifier. The advantages of the approach taken are that it is simple to implement, involving multiplication by a column of ones, and gives little chance for an error to affect the comparison. The control designs are equivalent in the sense that the performance index that is optimized involves the power applied to the coil and the same weighting of the control error.

The following sections start with a brief review of the conventional derivation of the prediction equations and model predictive control. These equations follow the usual

practice of formulating the prediction model in terms of the change in input at each time step. Simulated results are generated to show how the predictive control is able to use the anticipated trajectory to project the optimum current demands and improve on the response of the single coil actuator. Then, the undesirable attributes of the conventional MPC for a control problem with spare degrees of freedom are demonstrated. A series of modifications to conventional predictive control are then presented that lead to a resolution of the problems and a suitable control algorithm for the system with spare degrees of freedom. Each variation of the control algorithm is simulated in closed loop form for both the multi-coil and single coil actuator to compare their responses.

## General Equations for Model Predictive Control

The MPC method starts with the state space form of the plant model but then algebraically manipulates that form to eliminate the state variable, **x**. The predictive form of the equations depends on the current state of the system (an initial condition) and all future inputs, **u**, but not explicitly on the predicted states. The MPC prediction model is only different from the standard state space system in the form of the equations. The underlying plant model is the same as the state space model. The prediction equations are particularly useful for solving the minimization problem because the only unknown variables appearing in the performance index are the control demands, thus avoiding the algebraic difficulty of additional dependent variables in the performance index.

The predictive control problem is almost always solved for the discrete time case which can be written for a general state space system as the following,

$$\begin{aligned} \mathbf{x}_{i+1} &= \mathbf{A}\mathbf{x}_i + \mathbf{B}\mathbf{u}_{i+1}. \\ \mathbf{y}_{i+1} &= \mathbf{C}\mathbf{x}_{i+1} + \mathbf{D}\mathbf{u}_{i+1}. \end{aligned} \tag{6.33}$$

where $i$ is the index for the advancement of time, $t_i = i\Delta t$. The overlap of nomenclature with the usage of $i$ as the imaginary constant and as the time index in this section is unfortunate but is tolerated since subscript in the discrete time problem is not likely to be confused with the imaginary constant.

The predictive control formulation follows the notation and derivation given by Rossiter [13] for model predictive control. The output at each step can be obtained by substituting the state from the preceding step. The following equations illustrate a series of substitutions relating $\mathbf{x}_{i_0+i}$ to $\mathbf{x}_{i_0}$ and $\left[\mathbf{u}_{i_0+1}, \mathbf{u}_{i_0+2}, \cdots \mathbf{u}_{i_0+i_H}\right]$ and eliminating the intervening state variables on the right hand side. The $i_0$ index refers to the current time. The solution represents the response over the prediction interval from $i_0$ to the time horizon at $i_0 + i_H$.

$$\mathbf{x}_{i_0+1} = \mathbf{A}\mathbf{x}_{i_0} + \mathbf{B}\mathbf{u}_{i_0+1}. \tag{6.34}$$

$$\begin{aligned} \mathbf{x}_{i_0+2} &= \mathbf{A}\mathbf{x}_{i_0+1} + \mathbf{B}\mathbf{u}_{i_0+2} \\ &= \mathbf{A}\left(\mathbf{A}\mathbf{x}_{i_0} + \mathbf{B}\mathbf{u}_{i_0+1}\right) + \mathbf{B}\mathbf{u}_{i_0+2} \\ &= \mathbf{A}^2\mathbf{x}_{i_0} + \mathbf{A}\mathbf{B}\mathbf{u}_{i_0+1} + \mathbf{B}\mathbf{u}_{i_0+2}. \end{aligned} \tag{6.35}$$

$$\begin{aligned} \mathbf{x}_{i_0+3} &= \mathbf{A}\mathbf{x}_{i_0+2} + \mathbf{B}\mathbf{u}_{i_0+3} \\ &= \mathbf{A}\left(\mathbf{A}^2\mathbf{x}_{i_0} + \mathbf{A}\mathbf{B}\mathbf{u}_{i_0+1} + \mathbf{B}\mathbf{u}_{i_0+2}\right) + \mathbf{B}\mathbf{u}_{i_0+3} \\ &= \mathbf{A}^3\mathbf{x}_{i_0} + \mathbf{A}^2\mathbf{B}\mathbf{u}_{i_0+1} + \mathbf{A}\mathbf{B}\mathbf{u}_{i_0+2} + \mathbf{B}\mathbf{u}_{i_0+3}. \end{aligned} \tag{6.36}$$

$$\vdots$$

$$\mathbf{x}_{i_0+i_H} = \mathbf{A}^{i_H}\mathbf{x}_{i_0} + \mathbf{A}^{i_H-1}\mathbf{B}\mathbf{u}_{i_0+1} + \mathbf{A}^{i_H-2}\mathbf{B}\mathbf{u}_{i_0+2} + \cdots + \mathbf{A}\mathbf{B}\mathbf{u}_{i_0+i_H-1} + \mathbf{B}\mathbf{u}_{i_0+i_H}. \tag{6.37}$$

These equations can be written more compactly if the inputs at each time point are stacked in a single vector. The notation draws on the MATLAB ":" notation in the

subscript to indicate that the vector includes a range of values over time. The length of the vector is $i_H \cdot n_u$ by 1.

$$\mathbf{u}_{i_0+1:i_0+i_H} = \begin{bmatrix} \mathbf{u}_{i_0+1} \\ \mathbf{u}_{i_0+2} \\ \vdots \\ \mathbf{u}_{i_0+i_H} \end{bmatrix}. \tag{6.38}$$

The output vector, state vector, and reference trajectory can be similarly stacked in single-column vectors.

$$\mathbf{x}_{i_0+1:i_0+i_H} = \begin{bmatrix} \mathbf{x}_{i_0+1} \\ \mathbf{x}_{i_0+2} \\ \vdots \\ \mathbf{x}_{i_0+i_H} \end{bmatrix}; \mathbf{y}_{i_0+1:i_0+i_H} = \begin{bmatrix} \mathbf{y}_{i_0+1} \\ \mathbf{y}_{i_0+2} \\ \vdots \\ \mathbf{y}_{i_0+i_H} \end{bmatrix}; \mathbf{r}_{i_0+1:i_0+i_H} = \begin{bmatrix} \mathbf{r}_{i_0+1} \\ \mathbf{r}_{i_0+2} \\ \vdots \\ \mathbf{r}_{i_0+i_H} \end{bmatrix}. \tag{6.39}$$

The group of equations from Eq. (6.34) through (6.37) can be written as a single matrix equation.

$$\mathbf{x}_{i_0+1:i_0+i_H} = \begin{bmatrix} \mathbf{A} \\ \mathbf{A}^2 \\ \vdots \\ \mathbf{A}^{i_H} \end{bmatrix} \mathbf{x}_{i_0} + \begin{bmatrix} \mathbf{B} & \mathbf{0} & \cdots & \mathbf{0} \\ \mathbf{AB} & \mathbf{B} & \mathbf{0} & \vdots \\ \vdots & & \ddots & \mathbf{0} \\ \mathbf{A}^{i_H-1}\mathbf{B} & \cdots & \mathbf{AB} & \mathbf{B} \end{bmatrix} \mathbf{u}_{i_0+1:i_0+i_H}. \tag{6.40}$$

The output vector can be written by multiplying each term by the **C** matrix and adding the pass-through **D** term.

$$\mathbf{y}_{i_0+1:i_0+i_H} = \begin{bmatrix} \mathbf{CA} \\ \mathbf{CA}^2 \\ \vdots \\ \mathbf{CA}^{i_H} \end{bmatrix} \mathbf{x}_{i_0} + \begin{bmatrix} \mathbf{CB} & \mathbf{0} & \cdots & \mathbf{0} \\ \mathbf{CAB} & \mathbf{CB} & \mathbf{0} & \vdots \\ \vdots & & \ddots & \mathbf{0} \\ \mathbf{CA}^{i_H-1}\mathbf{B} & \cdots & \mathbf{CAB} & \mathbf{CB} \end{bmatrix} \mathbf{u}_{i_0+1:i_0+i_H}$$
$$+ \begin{bmatrix} \mathbf{D} & \mathbf{0} & \cdots & \mathbf{0} \\ \mathbf{0} & \mathbf{D} & \mathbf{0} & \vdots \\ \vdots & & \ddots & \mathbf{0} \\ \mathbf{0} & \cdots & \mathbf{0} & \mathbf{D} \end{bmatrix} \mathbf{u}_{i_0+1:i_0+i_H}; \tag{6.41}$$
$$= \begin{bmatrix} \mathbf{CA} \\ \mathbf{CA}^2 \\ \vdots \\ \mathbf{CA}^{i_H} \end{bmatrix} \mathbf{x}_{i_0} + \begin{bmatrix} \mathbf{CB}+\mathbf{D} & \mathbf{0} & \cdots & \mathbf{0} \\ \mathbf{CAB} & \mathbf{CB}+\mathbf{D} & \mathbf{0} & \vdots \\ \vdots & & \ddots & \mathbf{0} \\ \mathbf{CA}^{i_H-1}\mathbf{B} & \cdots & \mathbf{CAB} & \mathbf{CB}+\mathbf{D} \end{bmatrix} \mathbf{u}_{i_0+1:i_0+i_H}.$$

The first term on the right is the "free" output and represents the trajectory of $\mathbf{y}_{i_0:i_0+i_H}$ if all the future inputs were zero. It is multiplied by the current state of the plant which serves as an initial condition to the prediction. The second term represents the effect of the future inputs on the output. The output at the first time step, $\mathbf{y}_{i_0+1}$, depends only on the input at the first time step, $\mathbf{u}_{i_0+1}$. The second output depends on the inputs at the first and second time steps. The last step depends on all the time steps in the time horizon preceding it. The transformation matrices are constants. Conventional nomenclature in predictive control names these arrays **P** and **H**.

$$\mathbf{P} = \begin{bmatrix} \mathbf{CA} \\ \mathbf{CA}^2 \\ \vdots \\ \mathbf{CA}^{i_H} \end{bmatrix}; \ \mathbf{H} = \begin{bmatrix} \mathbf{CB}+\mathbf{D} & \mathbf{0} & \cdots & \mathbf{0} \\ \mathbf{CAB} & \mathbf{CB}+\mathbf{D} & \mathbf{0} & \vdots \\ \vdots & & \ddots & \mathbf{0} \\ \mathbf{CA}^{i_H-1}\mathbf{B} & \cdots & \mathbf{CAB} & \mathbf{CB}+\mathbf{D} \end{bmatrix}. \tag{6.42}$$

Equation (6.41) can be rewritten in terms of the matrices of Eq. (6.42).

$$\mathbf{y}_{i_0+1:i_0+i_H} = \mathbf{P}\mathbf{x}_{i_0} + \mathbf{H}\mathbf{u}_{i_0+1:i_0+i_H}. \tag{6.43}$$

The form given in Eq. (6.43) is the most useful for the multi-coil actuator problem; however, conventional model predictive control is formulated in terms of the change in input per time step rather than the input itself. The change in input is given by

$$\Delta \mathbf{u}_{i_0+i} = \mathbf{u}_{i_0+i} - \mathbf{u}_{i_0+i-1}. \tag{6.44}$$

The $\Delta \mathbf{u}$ formulation is advantageous for square systems or in cases in which the number of inputs is less than the number of outputs. The resulting MPC law for the $\Delta \mathbf{u}$ formulation does not have any offset for square systems or it has the least squares offset for system in which the number of outputs that are being controlled exceeds the inputs. Unfortunately, the $\Delta \mathbf{u}$ formulation is a source of difficulty in solving the actuator problem with spare degrees of freedom. For the spare degrees of freedom problem, the $\Delta \mathbf{u}$ formula does not minimize power which can result in an undesirable, unequal distribution of power among the control inputs. The problem is that no cost term in the $\Delta \mathbf{u}$ cost index drives the system toward the minimum power distribution.

The presentation of predictive control theory starts with the conventional $\Delta \mathbf{u}$ formulation and shows that the multi-coil actuator can achieve a faster response than a single coil actuator. Then, the undesirable properties of the $\Delta \mathbf{u}$ formulation are illustrated. The derivation then reverts back to the formulation in $\mathbf{u}$ to introduce a series of modifications to the basic MPC approach that satisfactorily resolves the problem with multiple inputs and a single output.

A minor revision to the matrices converts Eq. (6.43) from the $\mathbf{u}$ formulation to the equivalent $\Delta \mathbf{u}$ formulation. First, we define the integrator and differentiator matrices. The integrator matrix in discrete time is given by

$$\begin{bmatrix} F_{i_0+1} \\ F_{i_0+2} \\ F_{i_0+3} \\ F_{i_0+4} \\ F_{i_0+5} \end{bmatrix} = \begin{bmatrix} 1 & 0 & 0 & 0 & 0 \\ 1 & 1 & 0 & 0 & 0 \\ 1 & 1 & 1 & 0 & 0 \\ 1 & 1 & 1 & 1 & 0 \\ 1 & 1 & 1 & 1 & 1 \end{bmatrix} \begin{bmatrix} f_{i_0+1} \\ f_{i_0+2} \\ f_{i_0+3} \\ f_{i_0+4} \\ f_{i_0+5} \end{bmatrix} + \begin{bmatrix} F_{i_0} \\ F_{i_0} \\ F_{i_0} \\ F_{i_0} \\ F_{i_0} \end{bmatrix}. \tag{6.45}$$

The integrator matrix gives rectangular integration of the input vector over time. The second term is the initial condition for the integral. Each integral requires one past value from the point prior to the horizon interval.

The corresponding differentiation matrix is given by

$$\begin{bmatrix} f_{i_0+1} \\ f_{i_0+2} \\ f_{i_0+3} \\ f_{i_0+4} \\ f_{i_0+5} \end{bmatrix} = \begin{bmatrix} 1 & 0 & 0 & 0 & 0 \\ -1 & 1 & 0 & 0 & 0 \\ 0 & -1 & 1 & 0 & 0 \\ 0 & 0 & -1 & 1 & 0 \\ 0 & 0 & 0 & -1 & 1 \end{bmatrix} \begin{bmatrix} F_{i_0+1} \\ F_{i_0+2} \\ F_{i_0+3} \\ F_{i_0+4} \\ F_{i_0+5} \end{bmatrix} - \begin{bmatrix} F_{i_0} \\ 0 \\ 0 \\ 0 \\ 0 \end{bmatrix}. \tag{6.46}$$

Conveniently, the integrator and differentiator matrices are inverses of one another. For the multi-input case, each "1" and "0" in the integration and differentiator matrices becomes an identity matrix of square dimension $n_u$. The integrator and differentiator matrices are given the following names in the formulation.

$$\mathbf{S} = \underbrace{\begin{bmatrix} \mathbf{I} & \mathbf{0} & \mathbf{0} & \mathbf{0} & \mathbf{0} \\ \mathbf{I} & \mathbf{I} & \mathbf{0} & \mathbf{0} & \mathbf{0} \\ \mathbf{I} & \mathbf{I} & \mathbf{I} & \mathbf{0} & \mathbf{0} \\ \mathbf{I} & \mathbf{I} & \mathbf{I} & \mathbf{I} & \mathbf{0} \\ \mathbf{I} & \mathbf{I} & \mathbf{I} & \mathbf{I} & \mathbf{I} \end{bmatrix}}_{n_u \cdot i_H} \Bigg\} n_u \cdot i_H \,. \tag{6.47}$$

$$\mathbf{D} = \begin{bmatrix} \mathbf{I} & \mathbf{0} & \mathbf{0} & \mathbf{0} & \mathbf{0} \\ -\mathbf{I} & \mathbf{I} & \mathbf{0} & \mathbf{0} & \mathbf{0} \\ \mathbf{0} & -\mathbf{I} & \mathbf{I} & \mathbf{0} & \mathbf{0} \\ \mathbf{0} & \mathbf{0} & -\mathbf{I} & \mathbf{I} & \mathbf{0} \\ \mathbf{0} & \mathbf{0} & \mathbf{0} & -\mathbf{I} & \mathbf{I} \end{bmatrix}, \tag{6.48}$$

where each $\mathbf{I}$ in the matrices is an $n_u \times n_u$ identity matrix.

A special identity matrix is needed to represent the initial conditions as a matrix multiplication.

$$\underline{\mathbf{I}} = \begin{bmatrix} \mathbf{I} \\ \mathbf{I} \\ \\ \vdots \\ \mathbf{I} \end{bmatrix} \Bigg\} n_u \cdot i_H . \tag{6.49}$$

Thus, the forward and inverse relationships between $\mathbf{u}_{i_0:i_0+i_H}$ and $\mathbf{\Delta u}_{i_0:i_0+i_H}$ are given by

$$\begin{aligned} \mathbf{u}_{i_0+1:i_0+i_H} &= \mathbf{S}\mathbf{\Delta u}_{i_0+1:i_0+i_H} + \underline{\mathbf{I}}\mathbf{u}_{i_0}, \\ \mathbf{\Delta u}_{i_0+1:i_0+i_H} &= \mathbf{D}\mathbf{u}_{i_0+1:i_0+i_H}. \end{aligned} \tag{6.50}$$

Inserting the definitions of the integrator and special identity matrices into Eq. (6.43) gives the prediction equation in terms of $\mathbf{\Delta u}$.

$$\mathbf{y}_{i_0+1:i_0+i_H} = \mathbf{P}\mathbf{x}_{i_0} + \mathbf{H}\left(\mathbf{S}\mathbf{\Delta u}_{i_0+1:i_0+i_H} + \underline{\mathbf{I}}\mathbf{u}_{i_0}\right). \tag{6.51}$$

In the nomenclature of Maciejowski, this system is written as

$$\mathbf{y}_{i_0+1:i_0+i_H} = \mathbf{P}\mathbf{x}_{i_0} + \mathbf{\Theta}\mathbf{\Delta u}_{i_0+1:i_0+i_H} + \mathbf{T}\mathbf{u}_{i_0}, \tag{6.52}$$

where $\mathbf{\Theta} = \mathbf{H}\mathbf{S}$ and $\mathbf{T} = \mathbf{H}\underline{\mathbf{I}}$.

Equations (6.43) and (6.52) are the basis for the optimization calculations in conventional MPC. The equations depend on an initial state vector, $\mathbf{x}_{i_0}$, and an initial position for the control input, $\mathbf{u}_{i_0}$, which are known at the start of the prediction interval. The predictive control scheme finds the inputs $\Delta\mathbf{u}_{i_0+1:i_0+i_H}$ (or $\mathbf{u}_{i_0+1:i_0+i_H}$) that minimize a quadratic performance index. The solution of the minimization problem is the subject of the next section. When the full state is not directly measureable, as in the actuator problem, an estimator of the state is needed. A Kalman estimator is designed in APPENDIX J for the actuator to complete a control design that can be realized on the prototype actuator.

**Quadratic Performance Index for Model Predictive Control**

The minimization of a quadratic performance index is the fundamental mathematical technique in optimal control theory to design both linear quadratic regulators and estimators. The minimization of a quadratic performance index is at the heart of model predictive control as well. The quadratic performance index is convenient for optimization because, after taking the partial derivatives, the problem which remains to be solved to find the optimum is the solution of a linear system of equations. The derivation of the basic MPC algorithm presented here owes mainly to Maciejowski, but innumerable similar versions of the basic derivation are available in the literature. The version presented here is the simplest case with no random disturbances and no constraints on the control inputs or outputs. The main deviation from the standard MPC problem which is developed for the multi-coil actuator is the special case with spare degrees of freedom. This special case is not affected by the omission of the constraints

and random disturbances. These terms can be included in a more general formulation of the problem without changing the results developed here regarding spare degrees of freedom.

As presented by both Rossiter and Maciejowski, the customary optimization problem in predictive control is based on minimizing the change in the input, $\mathbf{\Delta u}$, and the control error, $\mathbf{r}-\mathbf{y}$ [12, 13].

$$\mathscr{J} = \mathbf{\Delta u}^T_{i_0+1:i_0+i_H}\mathbf{R}\mathbf{\Delta u}_{i_0:i_0+i_H} + \left(\mathbf{r}_{i_0+1:i_0+i_H} - \mathbf{y}_{i_0:i_0+i_H}\right)^T \mathbf{Q}\left(\mathbf{r}_{i_0+1:i_0+i_H} - \mathbf{y}_{i_0+1:i_0+i_H}\right). \qquad (6.53)$$

The specification of the performance index in terms of $\mathbf{r}-\mathbf{y}$ allows the trajectory of the reference input **r** to enter the equation. The reference trajectory may be time-varying. By including the control error in the cost function, a difference in the tracking accuracy is tolerated if there is a corresponding reduction in the control effort term. A strategy in which the output is constrained to follow the reference exactly is considered in a later section.

The performance index is written using square weight matrices, **R** and **Q**. The weight matrices may be chosen on a number of different mathematical bases. In predictive control, it is sometimes advantageous to vary the weight with time so that near term estimates are more lightly weighted than far term. However, the decision to introduce time-based weighting is usually the result of simulations in which it becomes apparent that a time-varying weight addresses some problem. In most cases, the weights are set initially to be equal over time and that choice is never changed. When the output and input are not scaled to have the same range, the weight matrices are also used to correct the scaling, in effect using the weight matrices to normalize the variables. In the actuator development problem, the state space model has been formulated in

dimensionless variables so that the input, **u**, and output, **y** nominally range from 0 to 1. The inputs are all equal in their contribution to the power consumed so it makes some sense for the weights of the all inputs (i.e. coil currents) over all time to be the same. Hence the weight matrix for the inputs is chosen as, $\mathbf{R} = \mathbf{I}$. The control output in the actuator problem is the scalar displacement. Each output in the prediction interval is weighted. The relative weight between the inputs and outputs is still undetermined. The relative weight between control error and control effort is commonly used as a tuning parameter to determine the trade-off between the closeness of the tracking and the sensitivity to noise. In this respect, the weighting in MPC is used in much the same way as in conventional feedback control design. These design decisions for the performance index mean that we can set $\mathbf{Q} = q^2\mathbf{I}$ where the relative weight between inputs and outputs, $q^2$, is a constant to be determined by experimentation. The basic MPC method does not provide a guarantee of stability. Most systems, including the multi-coil actuator, become unstable if $q^2$ is chosen too large.

The simplified weighting scheme gives the following cost function.

$$\mathscr{F} = \Delta\mathbf{u}_{i_0+1:i_0+i_H}^T \Delta\mathbf{u}_{i_0+1:i_0+i_H} + q^2 \left(\mathbf{r}_{i_0+1:i_0+i_H} - \mathbf{y}_{i_0:i_0+i_H}\right)^T \left(\mathbf{r}_{i_0+1:i_0+i_H} - \mathbf{y}_{i_0+1:i_0+i_H}\right). \tag{6.54}$$

The performance index is converted into a quadratic function of the input by substituting in the predictive model as defined in Eq. (6.52).

$$\begin{aligned}\mathscr{F} = \Delta\mathbf{u}_{i_0+1:i_0+i_H}^T \Delta\mathbf{u}_{i_0+1:i_0+i_H} + q^2 \left(\mathbf{r}_{i_0+1:i_0+i_H} - \mathbf{P}\mathbf{x}_{i_0} - \boldsymbol{\Theta}\Delta\mathbf{u}_{i_0+1:i_0+i_H} - \mathbf{T}\mathbf{u}_{i_0}\right)^T \cdot \\ \left(\mathbf{r}_{i_0+1:i_0+i_H} - \mathbf{P}\mathbf{x}_{i_0} - \boldsymbol{\Theta}\Delta\mathbf{u}_{i_0+1:i_0+i_H} - \mathbf{T}\mathbf{u}_{i_0}\right).\end{aligned} \tag{6.55}$$

The quadratic form emerges after expanding the output term and rearranging the equation. The equation is written as the following

$$\begin{aligned}\mathscr{F} = {} & q^2\left(\mathbf{r}_{i_0+1:i_0+i_H}-\mathbf{P}\mathbf{x}_{i_0}-\mathbf{T}\mathbf{u}_{i_0}\right)^T\left(\mathbf{r}_{i_0+1:i_0+i_H}-\mathbf{P}\mathbf{x}_{i_0}-\mathbf{T}\mathbf{u}_{i_0}\right)\\ & -2q\Delta\mathbf{u}^T_{i_0+1:i_0+i_H}\boldsymbol{\Theta}^T\left(\mathbf{r}_{i_0+1:i_0+i_H}-\mathbf{P}\mathbf{x}_{i_0}-\mathbf{T}\mathbf{u}_{i_0}\right)\\ & +\Delta\mathbf{u}^T_{i_0+1:i_0+i_H}\left(\mathbf{I}+q^2\boldsymbol{\Theta}^T\boldsymbol{\Theta}\right)\Delta\mathbf{u}_{i_0+1:i_0+i_H}.\end{aligned} \tag{6.56}$$

In this equation, $\mathbf{r}_{i_0+1:i_0+i_H}$, $\mathbf{x}_{i_0}$, and $\mathbf{u}_{i_0}$ are known constants. The changes in input, $\Delta\mathbf{u}_{i_0+1:i_0+i_H}$, are the quantities that are to be adjusted to minimize the performance index. The quadratic form is clearly evident in the equation. The first term on the right hand side is a constant vector, the second term is linear in $\Delta\mathbf{u}_{i_0+1:i_0+i_H}$, and the third term is second order in $\Delta\mathbf{u}_{i_0+1:i_0+i_H}$. Taking the partial derivative of the performance index with respect to the input vector and setting each partial to zero provides the necessary condition for an extremum. The extremum condition yields a system of $i_H \cdot n_u$ equations with the same number of unknowns.

$$\frac{\partial\mathscr{F}}{\partial\Delta\mathbf{u}_{i_0+1:i_0+i_H}} = \mathbf{0}. \tag{6.57}$$

$$-2q^2\boldsymbol{\Theta}^T\left(\mathbf{r}_{i_0+1:i_0+i_H}-\mathbf{P}\mathbf{x}_{i_0}-\mathbf{T}\mathbf{u}_{i_0}\right)+2\Delta\mathbf{u}^T_{i_0+1:i_0+i_H}\left(\mathbf{I}+q^2\boldsymbol{\Theta}^T\boldsymbol{\Theta}\right)=\mathbf{0}. \tag{6.58}$$

At least formally, the solution for $\Delta\mathbf{u}_{i_0:i_0+i_H}$ that minimizes the performance index is the following.

$$\Delta\mathbf{u}^T_{i_0+1:i_0+i_H} = q\boldsymbol{\Theta}\left(\mathbf{r}_{i_0+1:i_0+i_H}-\mathbf{P}\mathbf{x}_{i_0}-\mathbf{T}\mathbf{u}_{i_0}\right)^T\left(\mathbf{I}+q^2\boldsymbol{\Theta}^T\boldsymbol{\Theta}\right)^{-1}. \tag{6.59}$$

The optimal solution using the matrix inverse is theoretically valid, but the calculation using the matrix inverse is a poor choice numerically. The matrix, $\boldsymbol{\Theta}^T\boldsymbol{\Theta}$, is inherently poorly conditioned. For values of $q^2$ that are high enough to give good tracking, the inverse operation is nearly singular and Eq. (6.59) gives inaccurate results.

The difficulty with the near singularity of the prediction matrix can be mitigated by reformulating the optimization problem as a least squares problem. The least squares form of the quadratic minimization avoids taking any inverses or forming the product $\boldsymbol{\Theta}^T\boldsymbol{\Theta}$. The least squares solution is stable and numerically accurate to the convergence criteria of the solution algorithm even if $\boldsymbol{\Theta}^T\boldsymbol{\Theta}$ is singular. To put the predictive control optimization problem in the form of a least squares problem, the first step is to formulate the quadratic cost minimization as an over-determined system of linear equations. An abbreviated version of the derivation found in Maciejowski [12, p. 77] is presented here. The least squares computation method is used to solve this and all subsequent variations of the MPC optimization problem.

A vector is formed in which the elements of the performance index are stacked one on top of the other.

$$\begin{bmatrix} q\left(\mathbf{r}_{i_0+1:i_0+i_H} - \mathbf{P}\mathbf{x}_{i_0} - \mathbf{T}\mathbf{u}_{i_0} - \boldsymbol{\Theta}\Delta\mathbf{u}_{i_0+1:i_0+i_H}\right) \\ \Delta\mathbf{u}_{i_0+1:i_0+i_H} \end{bmatrix} \tag{6.60}$$

The performance index is given by the square length of the vector. The minimum performance index corresponds to the minimum length of this vector. In other words, the cost function is given by the following square length of the vector.

$$\begin{aligned} \mathscr{F} &= \left\| \begin{bmatrix} q\left(\boldsymbol{\Theta}\Delta\mathbf{u}_{i_0+1:i_0+i_H} - \left(\mathbf{r}_{i_0+1:i_0+i_H} - \mathbf{P}\mathbf{x}_{i_0} - \mathbf{T}\mathbf{u}_{i_0}\right)\right) \\ \Delta\mathbf{u}_{i_0+1:i_0+i_H} \end{bmatrix} \right\|^2 \\ &= \begin{bmatrix} q\left(\boldsymbol{\Theta}\Delta\mathbf{u}_{i_0+1:i_0+i_H} - \left(\mathbf{r}_{i_0+1:i_0+i_H} - \mathbf{P}\mathbf{x}_{i_0} - \mathbf{T}\mathbf{u}_{i_0}\right)\right)^T & \Delta\mathbf{u}_{i_0+1:i_0+i_H}^T \end{bmatrix} \\ &\quad \bullet \begin{bmatrix} q\left(\boldsymbol{\Theta}\Delta\mathbf{u}_{i_0+1:i_0+i_H} - \left(\mathbf{r}_{i_0+1:i_0+i_H} - \mathbf{P}\mathbf{x}_{i_0} - \mathbf{T}\mathbf{u}_{i_0}\right)\right) \\ \Delta\mathbf{u}_{i_0+1:i_0+i_H} \end{bmatrix}. \end{aligned} \tag{6.61}$$

The $\mathbf{\Delta u}_{i_0+1:i_0+i_H}$ that gives the minimum length of the vector is given by least squares solution of the following system of equations.

$$\begin{bmatrix} q\left(\mathbf{\Theta\Delta u}_{i_0+1:i_0+i_H} - \left(\mathbf{r}_{i_0+1:i_0+i_H} - \mathbf{Px}_{i_0} - \mathbf{Tu}_{i_0}\right)\right) \\ \mathbf{\Delta u}_{i_0+1:i_0+i_H} \end{bmatrix} = \mathbf{\delta}, \tag{6.62}$$

where $\mathbf{\delta}$ is the residuals vector. The vector can be separated into a sum of two parts.

$$\begin{bmatrix} q\mathbf{\Theta} \\ \mathbf{I} \end{bmatrix} \mathbf{\Delta u}_{i_0+1:i_0+i_H} - \begin{bmatrix} q\left(\mathbf{r}_{i_0+1:i_0+i_H} - \mathbf{Px}_{i_0} - \mathbf{Tu}_{i_0}\right) \\ \mathbf{0} \end{bmatrix} = \mathbf{\delta} \tag{6.63}$$

In this form, the number of unknowns is $n_u \cdot i_h$. The number of equations is $2 \cdot n_u \cdot i_h$. The least squares solution of Eq. (6.63) minimizes the length of the residuals vector. The least squares solution to a system of linear equations is such an important mathematical problem in matrix algebra that MATLAB includes a special arithmetic operator, "\" in addition to the normal four arithmetic operators; "+", "-","×", "/", to indicate a least squares problem. In MATLAB notation, the least squares solution to Eq. (6.63) is written as

$$\mathbf{\Delta u}_{i_0+1:i_0+i_H} = \begin{bmatrix} q\mathbf{\Theta} \\ \mathbf{I} \end{bmatrix} \setminus \begin{bmatrix} q\left(\mathbf{r}_{i_0+1:i_0+i_H} - \mathbf{Px}_{i_0} - \mathbf{Tu}_{i_0}\right) \\ \mathbf{0} \end{bmatrix}. \tag{6.64}$$

Using this form of the solution to the quadratic cost minimization tells MATLAB to bring to bear the numerical techniques of the least squares solution rather than matrix inversion on equation to be solved

A control law in terms of a fixed gain matrix can be obtained by separating the least squares calculation into two parts. The first part contains the solution of the least squares problem of involving constant matrices. This part of the solution can be pre-

computed and stored. The second part is a multiplication by a vector containing the time-varying components in the equation. The bulk of the optimal control computation is expended in solving the least squares problem. The reformulated version of the control law represents a substantial computational savings over Eq. (6.64).

$$\begin{aligned}\mathbf{K}_{Full} &= \begin{bmatrix} q\boldsymbol{\Theta} \\ \mathbf{I} \end{bmatrix} \quad \backslash \quad \begin{bmatrix} q\mathbf{I} \\ \mathbf{0} \end{bmatrix}. \\ \boldsymbol{\Delta}\mathbf{u}_{i_0+1:i_0+i_H} &= \mathbf{K}_{Full}\left(\mathbf{r}_{i_0+1:i_0+i_H} - \mathbf{P}\mathbf{x}_{i_0} - \mathbf{T}\mathbf{u}_{i_0}\right).\end{aligned} \tag{6.65}$$

A simple multiplication shows that Eq. (6.65) is equivalent to Eq. (6.64).

The concept of the receding horizon means that the control is optimized over the time interval from $i_0+1$ to $i_0+i_H$ but only the values of $\boldsymbol{\Delta}\mathbf{u}_{i_0+1}$ are actually used. The optimization starts over at $\boldsymbol{\Delta}\mathbf{u}_{i_0+2}$ and recomputes over the interval from $i_0+2$ to $i_0+i_H+1$. The receding horizon only requires the first set of control inputs, $\boldsymbol{\Delta}\mathbf{u}_{i_0+1}$, from Eq. (6.65). The number of online calculations can be reduced by selecting just the part of the $\mathbf{K}_{Full}$ that is needed to compute $\boldsymbol{\Delta}\mathbf{u}_{i_0+1}$, and discarding the rest of the matrix. Mathematically, this operation can be performed by multiplying both sides of Eq. (6.65) by a matrix $\begin{bmatrix}\mathbf{I} & \mathbf{0} & \cdots & \mathbf{0}\end{bmatrix}$.

$$\begin{aligned}\boldsymbol{\Delta}\mathbf{u}_{i_0+1} &= \begin{bmatrix}\mathbf{I} & \mathbf{0} & \cdots & \mathbf{0}\end{bmatrix}\boldsymbol{\Delta}\mathbf{u}_{i_0+1:i_0+i_H} \\ &= \begin{bmatrix}\mathbf{I} & \mathbf{0} & \cdots & \mathbf{0}\end{bmatrix}\mathbf{K}_{Full}\left(\mathbf{r}_{i_0+1:i_0+i} - \mathbf{P}\mathbf{x}_{i_0} - \mathbf{T}\mathbf{u}_{i_0}\right) \\ &= \mathbf{K}_{\Delta u}\left(\mathbf{r}_{i_0+1:i_0+i_H} - \mathbf{P}\mathbf{x}_{i_0} - \mathbf{T}\mathbf{u}_{i_0}\right),\end{aligned} \tag{6.66}$$

where $\mathbf{K}_{\Delta u} = \begin{bmatrix}\mathbf{I} & \mathbf{0} & \cdots & \mathbf{0}\end{bmatrix}\mathbf{K}_{Full}$. $\mathbf{I}$ and $\mathbf{0}$ are the identity and zero matrices with dimensions, $n_u \times n_u$. The number of $\mathbf{0}$ matrices is $i_H - 1$. Of course, the matrix $\mathbf{K}_{\Delta u}$ can also be obtained by using the MATLAB ":" operator to select the first $n_u$ rows of $\mathbf{K}_{Full}$.

The final form of the MPC law is a proportional gain matrix multiplying a time-varying vector. The proportional gain matrix form of the control law for MPC is analogous to classical proportional control or conventional LQC control.

The control law required requires three inputs: $\mathbf{r}_{i_0+1:i_0+i_H}$ which is the reference trajectory from the current time to the prediction horizon, $\mathbf{x}_{i_0}$ which is the current value of the state, and $\mathbf{u}_{i_0}$ which is the current value of the control input. In the experimental system, the current value of the state comes from a Kalman estimator with a predictor to advance from the delayed measurement point to the current time. The equations for the estimated state are given in APPENDIX J. However, the estimation can be avoided in the preliminary simulations to simplify the test case and focus just on the control problem. The separation principle applies to MPC so the Kalman estimator can be designed later without affecting the design of the MPC.

The following equations summarize the calculation of the simulated model. The calculation consists of three parts, 1) the calculation of the new control increment, 2) integration of the control increment, and 3) the calculation of the new state.

$$\begin{aligned}\Delta\mathbf{u}_{i+1} &= \mathbf{K}_{\Delta u}\left(\mathbf{r}_{i+1:i+i_H} - \mathbf{P}\mathbf{x}_i - \mathbf{T}\mathbf{u}_i\right).\\ \mathbf{u}_{i+1} &= \mathbf{u}_i + \Delta\mathbf{u}_{i+1}.\\ \mathbf{x}_{i+1} &= \mathbf{A}\mathbf{x}_i + \mathbf{B}\mathbf{u}_{i+1}.\end{aligned} \tag{6.67}$$

The observed variables for displacement, $y^N$; voltage, $\mathbf{y}^V$; and coil current, $\mathbf{y}^I$ are computed from the formulae given for the open loop models in Chapter 5 in Equations (5.69), (5.70), and (5.71).

**Simulated Results Using Conventional MPC Design**

In the following test calculations, the combined actuator model including the dynamics of vibration, eddy current, and coil current is used as the plant model. The particular version is the low order model with the best estimate parameters for the prototype actuator. In the design of the MPC given by Eq. (6.66), the simulations are calculated without an observer as if the state, $\mathbf{x}_{i_0}$, were measured.

The calculations are shown for a discrete time solution in which the time step is substantially faster than can be achieved with the experimental setup for the actuator. The higher speed sampling is chosen to show the performance achievable with predictive control without the artificial limitation of the sampling time of the experimental system.

The physical parameters for the state space actuator model are given in Table 2.8. In addition, the tuning parameters for the MPC system design are given in Table 6.1. A derivation of the time step and the prediction horizon are given in APPENDIX H.

Table 6.1: Actuator modeling and control design parameters for predictive control

| Parameter | Value | Description |
|---|---|---|
| $n_s$ | 40 | Number of states. (The low order model is used: 10 coil currents, 10 eddy current modes, 10 second order vibration modes). |
| $n_u$ | 10 | Number of control inputs (i.e. amplifier demand signals). |
| $n_y$ | 11 | Number of observations (10 coil currents and 1 displacement). |
| $i_H$ | 120 | Prediction horizon |
| $T_S$ | $2\times10^{-6}$ s | Time step** |
| $q^2$ | 1000 | Relative weight for control error to control input |

** Time step for simulated transients

The test transients consist of a suite of three reference trajectories: the step change transient, the square pulse transient, and the swept frequency sine wave.

**Step change transient**

The step change transient is perhaps the most widely used test case in time domain control analysis. The 100 % step change is, in effect, the fundamental transient. All other transients can be constructed by summing a series of smaller, individual steps. The main features of MPC that are evident in the step change results also apply to the more complex wave forms that are presented next. The step change test case is programmed with a quiescent interval slightly longer than the prediction horizon preceding the step change. This quiescent interval shows that the predictive aspect of the MPC algorithm begins to affect the control inputs well before the actual step occurs. The anticipatory behavior is the main advantage that MPC possesses over conventional feedback control.

Figure 6.4 shows the reference trajectory and the calculated responses for the ten coil and single coil simulations. Both models follow the reference closely. The multi-coil actuator rises faster than the single coil. The peak velocity at the time of the step is a factor of 1.89 faster for the multi-coil. Overshoot and settling time are also less for the multi-coil actuator. Figure 6.5 shows the current demand computed by the MPC algorithm for both multi-coil and single coil. The single coil current is similar in magnitude but follows along a line on the outer edge of the envelope of traces for the multi-coil current. Each coil current for the multi-coil actuator is approximately the same magnitude or slightly smaller than the single coil current. The plots of tracking and

current show that the multi-coil actuator provides a modest improvement in both current and tracking results.

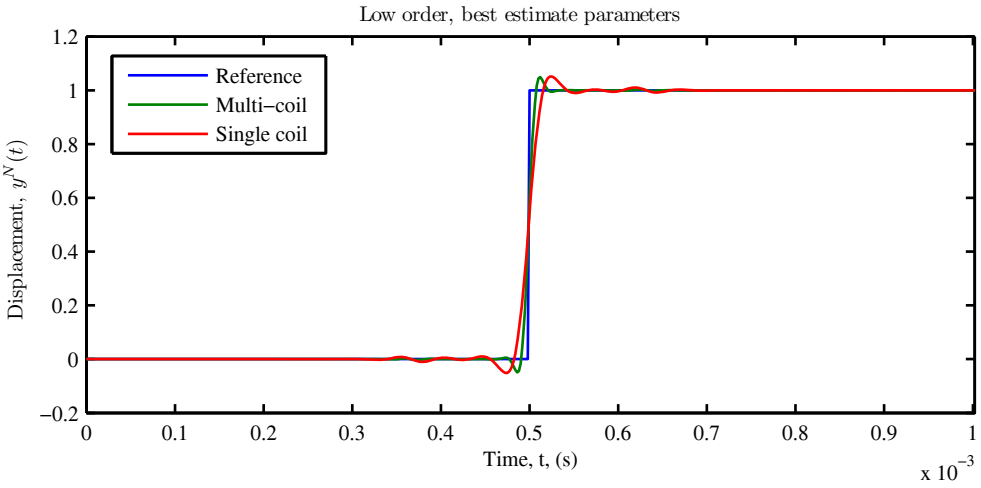


Figure 6.4: Multi-coil and single coil actuators tracking a step change reference trajectory

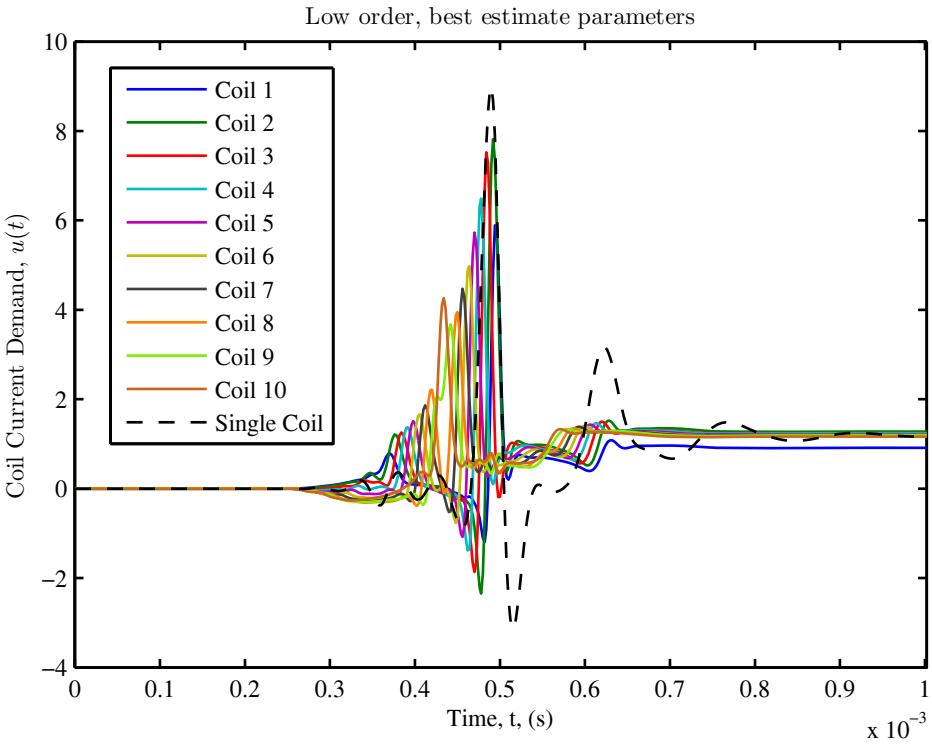


Figure 6.5: Current demand for step change for multi-coil and single coil actuators

The difference between the multi-coil and single coil performance is more evident in the plots of voltage and power. Figure 6.6 shows the power in the coil. Maximum power for the transient, which occurs at the time of the step, is a factor of 8.60 higher for the single coil than the multi-coil. This is a significant difference but is a smaller improvement than the factor of 10 to 50 predicted by the frequency optimization in Figure 6.2. The difference is a consequence of choosing a different performance index for the MPC optimization than for the frequency domain optimization. The frequency domain optimization constrains the response to follow the reference exactly, whereas the MPC balances control error against control effort allowing the displacement to vary from the reference to reduce the change in the demand. The output represents a compromise between control effort and control accuracy. The weighting factor, $q$, which is the relative cost of the control effort to control error, has been selected for these transients to give close tracking between the measured response and the reference but not to give indistinguishable lines. The compromise yields a low gain on high frequency errors and relatively smooth control inputs. In the time domain results, the difference between the multi-coil and single coil is a combination of speed of response and power consumption. The speed of the multi-coil actuator is a factor of 1.88 faster, and the peak power is a factor of 8.60 less. In contrast, the frequency optimization, the entire difference is contained in the power ratio.

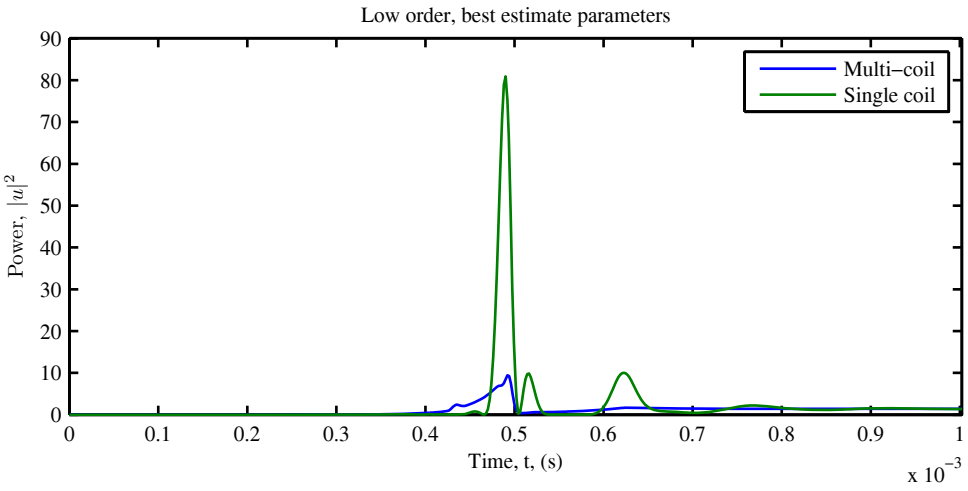


Figure 6.6: Power for step change for multi-coil and single coil

The voltage plot in Figure 6.7 shows an even larger improvement for the multi-coil. In this figure, the peak dimensionless voltage of the single coil is 400 which corresponds to an actual voltage of $y^V_{single} \cdot \Delta I \cdot R = 400 \cdot 1.5 \cdot 4 = 2400\,V$. The single coil voltage is a factor of 11.5 higher than the highest multi-coil voltage. The peak voltage necessary for the single coil is considerably greater than the voltage that an audio amplifier can produce. In contrast, the peak voltage of the multi-coil in dimensioned variables is on the order of 200 V which is also high but close to feasible for an amplifier. The peak voltage can be changed by adjusting the weight factor, $q$, in the cost function. Lowering $q$ reduces the peak voltage but also reduces the maximum speed. The relative benefit in voltage between the single and multi-coil remains roughly the same as $q$ is tuned.

The multi-coil improvement in voltage comes largely from subdividing the coil not from the optimal control of the spatial distribution of coils. Each of the individual coils in the multi-coil actuator has one tenth the inductance of the single coil. Since the

inductive voltage is proportional to the inductance, the voltage is reduced by a factor of ten by subdividing alone without considering the effect from the optimal control of the individual coils. The point of this plot is that a faster response cannot be achieved with a single coil actuator by increasing the gain alone. The voltage becomes too high. The subdivision of the coils is necessary to reduce coil voltage even if the multi-input multi-output control algorithm is not used.

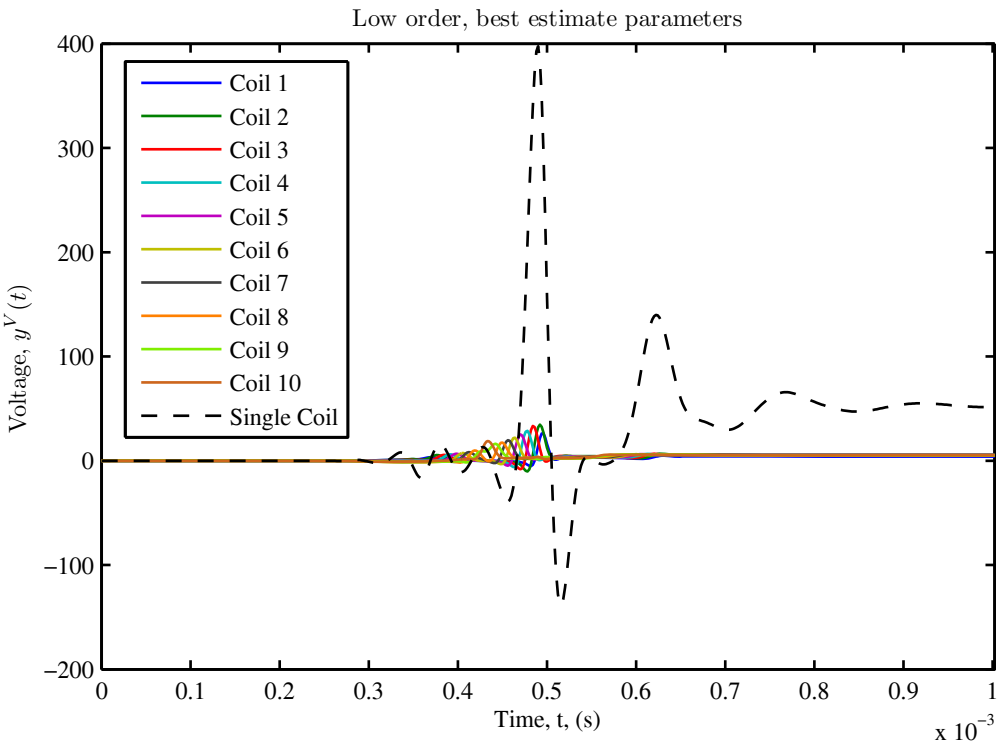


Figure 6.7: Voltage across amplifier for multi-coil and single coil

In Figure 6.2, the group of coil currents from the MPC controller track closely together but do not follow identical paths. The currents follow roughly parallel tracks that are shifted in time with respect to one another, but the pattern is not easy to see. The trend of the group of currents is more evident in a three dimensional plot in which coil current is plotted versus the time and the coil index. The surface plotting routine

interpolates and smoothes the coil current as if the index were a continuous variable; nevertheless, the three-dimensional plot shows the trends of the current distribution in the coils more clearly than the two-dimensional plot. Figure 6.8 shows the same data for coil demand given in Figure 6.5 but plotted this time in a three-dimensional plot. The plot is turned so that time increases from right to left to give a better viewing angle of the current distribution. Lighting and shading effects are used to bring out the details of the surface. The transient can be divided into four phases: the pre-step preparation phase, the step, the wave cancellation phase, and the final plateau. The step occurs at $t=5\times10^{-4}$ seconds. The current begins to respond at $t=2.6\times10^{-4}$ when the step demand enters the far end of the prediction horizon. The pre-step phase appears as a zig-zag pattern of ridges as energy is added to the wave front being created in the rod. The magnitude of the current demand rises as the step approaches, reaching a peak at the time of the step. Following the step, the control system draws the kinetic energy from the rod to stop the resonance. A zig-zag pattern plateau steps in the current demand following the step cancels the kinetic energy in the wave as it reflected back and forth along the actuator. In the final phase a quiescent plateau is formed starting from a diagonal ridge beginning about $t=6\times10^{-4}$

Figure 6.8 shows how the multi-coil actuator achieves the large improvement in power compared to the single coil. The angle of the diagonal ridges in the *j*-*t* plane corresponds to the acoustic wave speed. The anticipatory action of the MPC begins to add energy to a wave front when the step enters the prediction horizon. The wave front is timed so that it reaches the tip at the time of the step. Energy is added to the wave front exactly in phase with the energy already stored in the wave. No energy is added that

cancels the high frequency components. Following the step, the feedback effects are designed to damp out acoustic oscillations with the same use of spatial distribution of current in the coil to draw kinetic energy out of the rod. This period of stopping the motion appears first as a bumpy, quilted surface just after the impulse wave passes through just before the step. This period extracts high frequency kinetic energy from the rod. Following the step in the reference trajectory, the control algorithm produces a zig-zag pattern of steps in demand that bring the rod to rest.

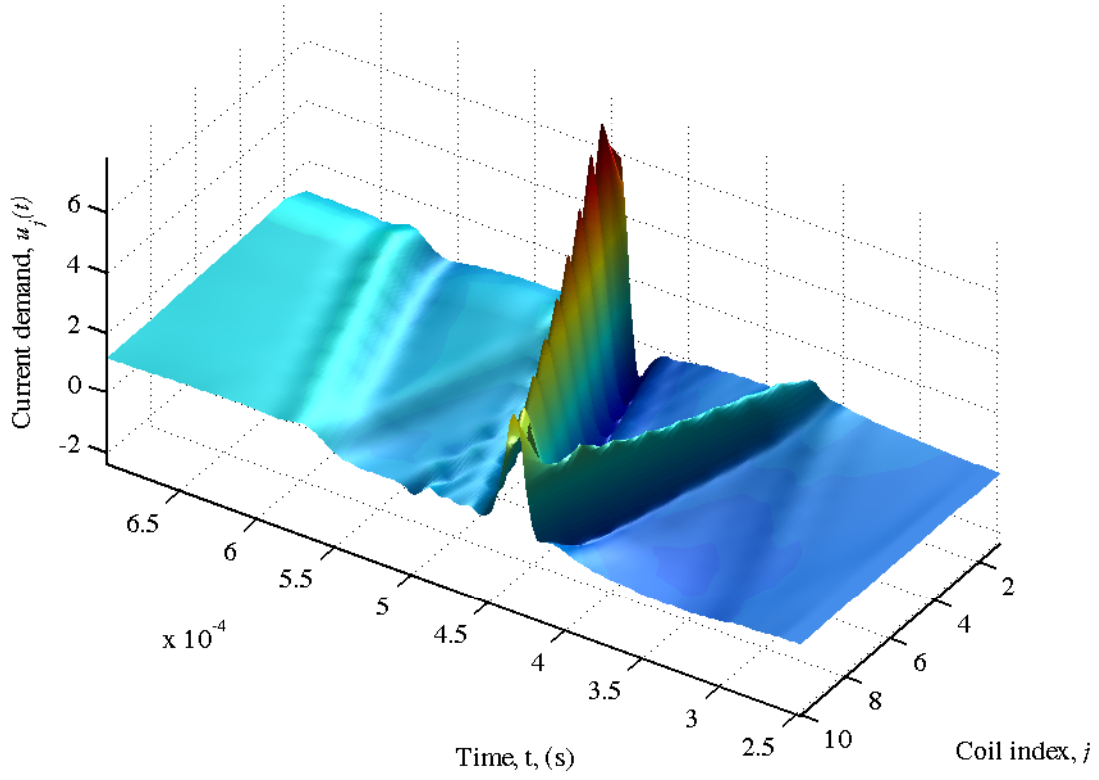


Figure 6.8: Current demand versus coil index and time

The model used to calculate the results in Figure 6.8 uses the best estimate design parameters for the prototype. This model has fairly high magnetic damping which has to be overcome by the input current. Even more advantage for the multi-coil actuator can

be gained if the actuator design is modified to reduce the magnetic drag due to eddy currents by subdividing into more laminations or if faster amplifiers (or smaller load resistors) are used to make the electronic circuit faster.

**Square pulses**

The square pulse transient is a sequence of three, nearly square pulses. The pulses are, by design, not quite square. The step is actually a steep ramp. The duration of the ramp is the chosen to be the time step of the experiment setup, 70 μs. The use of a fixed ramp rate makes comparisons of results using different time steps more meaningful. In particular, the peak voltages and currents are more nearly comparable to simulations in which the time step is set equal to the experimental time step.

The ramp is a milder transient than the step change. Figure 6.9 shows even closer tracking for both single and multi-coil for the transient than the step change. The reference and multi-coil displacements are covered by the single coil in the figure.

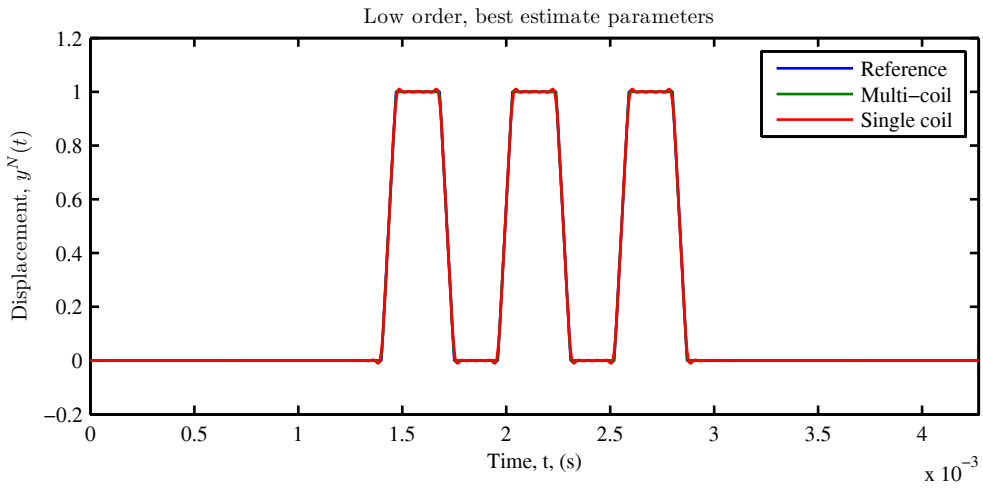


Figure 6.9: Multi-coil and single coil actuators tracking three square pulses

The power and voltage in the square pulse case shown in Figure 6.10 and Figure 6.11 follow similar trends as the step change transient. Since the ramp rate is slower in this case, the difference between multi-coil and single coil is less pronounced. Nevertheless, the maximum power and voltage of the ten coil controller are lower than the single coil case and are feasible levels for real amplifiers.

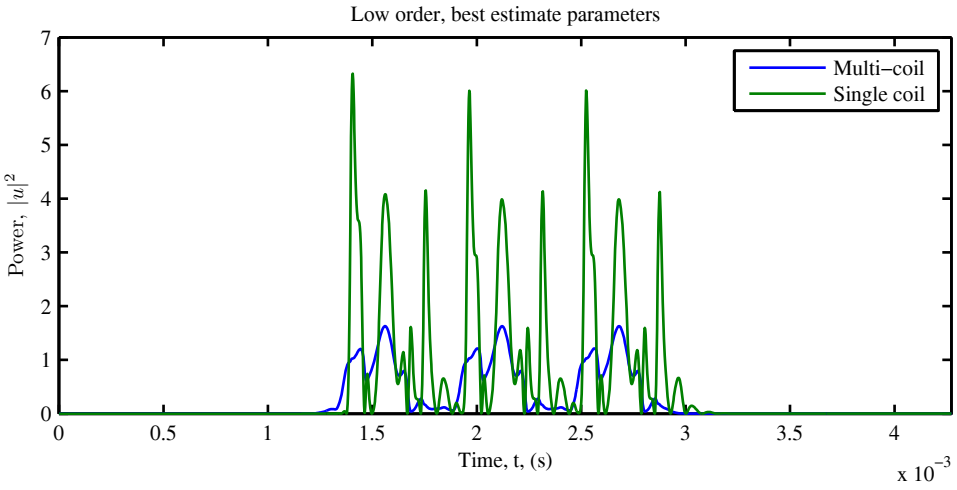


Figure 6.10: Power for square pulses for multi-coil and single coil

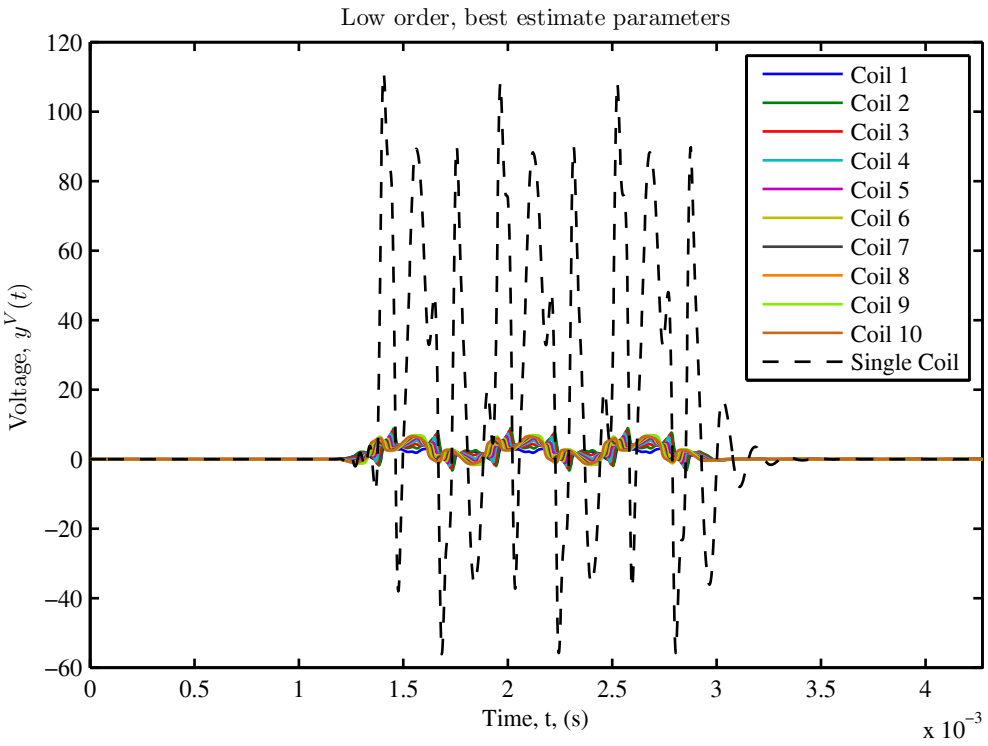


Figure 6.11: Voltage across amplifier for square pulses for multi-coil and single coil

Figure 6.12 gives the three dimensional view of the coil current demand for the transient. The features of the transient due to each step in the three pulses overlap with one another thus giving more complex patterns but the understanding of the features is basically the same as in the single step change. The four phases of the MPC's control response that were introduced to explain the features of the step change transient show up in the three pulse transient as well. A ridge of current precedes each edge of a pulse that anticipates the step. A spike is generated in the coil at the free end at the time of the step. The cancellation phase to draw energy out of reflected waves follows the step. The pulses are close enough together that the effects of each step have not decayed away completely before the next pulse begins. The results of the three pulse transient address the question of whether the actuator can handle an arbitrary wave form as well as it

performs on a single isolated step change transient. The results show that the complexity of the three pulse transient does not introduce any new types of features or lead to undesirable transient performance by the control algorithm. The anticipatory ridges leading up to the steps are evident at the edge of each pulse. The ridges are less sharp than for the step change because the pulse edge is actually a steep ramp.

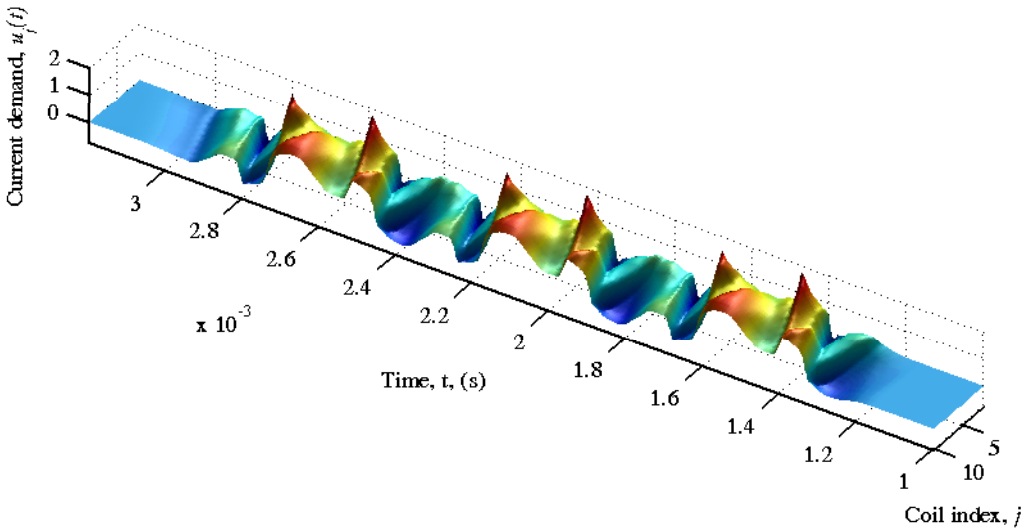


Figure 6.12: Current demand versus coil index and time for square pulse transient

**Swept Frequency Sine Wave**

In this transient, the reference trajectory is a sine wave in which the frequency gradually shifts. The purpose of the transient is to show the amplitude of the actuator response over a range of frequencies in the time domain. The transient gives similar information about the discrete time control algorithm performance that a Bode plot gives. The time domain is used rather than discrete frequency response because the predictive aspect of the control algorithm cannot be represented in a traditional frequency response.

The transient demonstrates the ability of the actuator to respond to an oscillatory demand with shifting frequency or phase in applications such as vibration cancelation or combustion instability. The duration of the transient is $2.2\times10^{-3}$ seconds. The frequency increases linearly from 0 to 10,000 Hz over the transient. The target for the research project for the multi-coil actuator is to increase the frequency response to 10,000 Hz. This transient shows that goal is met by this design. The Nyquist frequency for the time step ( $T_s = 2\times10^{-6} s$ ) used in the simulations is 250,000 Hz. This is sufficiently small that time step effects are not evident in the results. The time step is sufficiently small that decreasing it does not change the results.

Figure 6.13 shows the reference signal, and the response for the ten coil and single coil actuator. The axis is labeled with frequency rather than time to relate the results to the frequency response. The frequency, $\Omega = 0\ Hz$ , corresponds to $t = 0\ s$. The frequency $\Omega = 10,000\ Hz$ corresponds to $t = 2.2\times10^{-3}\ s$ . The single and multi-coil actuators match the reference so closely that only the topmost line is visible up to approximately 7000 Hz where the single coil actuator begins to fall off. The multi-coil actuator lies on top of the reference except for just the tips of the wave above 9000 Hz.

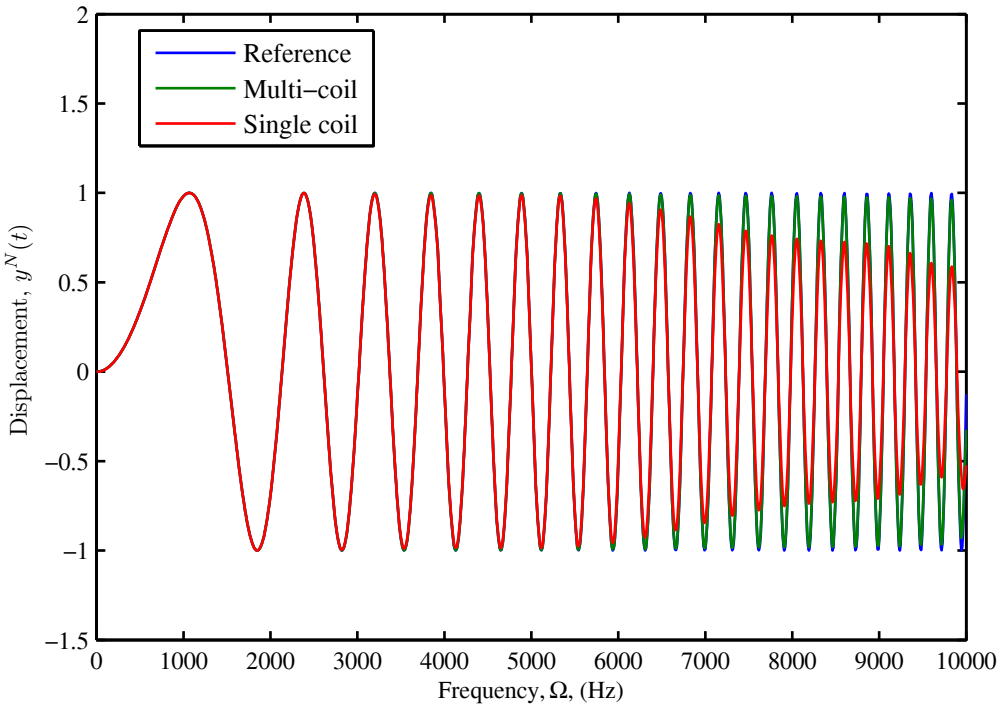


Figure 6.13: Tracking for swept frequency transient

The power for the transient is shown in Figure 6.14. As in the previous transients, the power of the single coil is significantly higher than physically realizable. The power for the multi-coil is also somewhat higher than what may be achievable with audio amplifiers. This is an indication that the weighting of the control error, $q$, may be too high for the actual prototype.

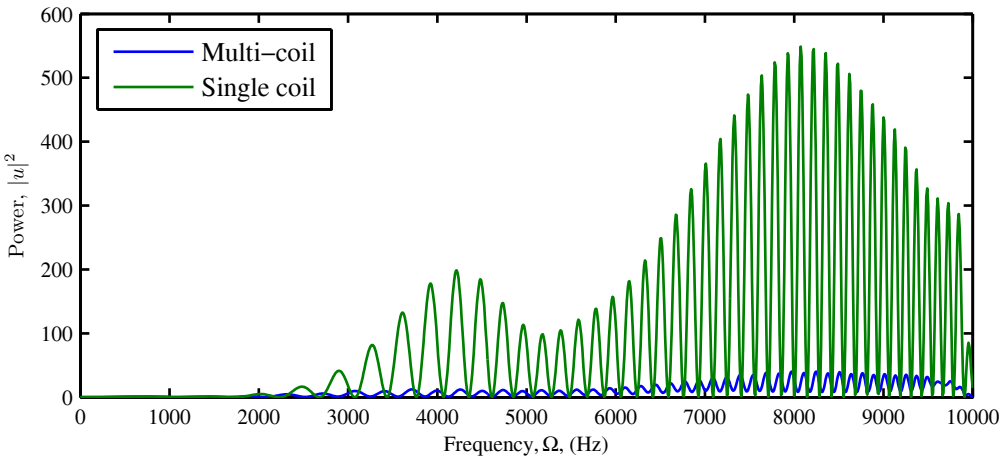


Figure 6.14: Power for swept frequency transient

The three-dimensional plot of current demand versus index and frequency (time) is shown in Figure 6.15. The frequency starts on the right side at a frequency of 0 Hz. The distribution of current is uniform in the *j* dimension, indicating that each coil receives the same demand. The shape in the coil direction changes as the frequency increases. At the high frequency end of the plot, the shape is approaching the ridge-like shape seen for the step change. This shape means that the distribution of current demands is approaching equal magnitude sine waves with a constant phase shift between each coil demand. The amount of phase shift corresponds to the acoustic propagation delay. The high frequency result confirms the "phasing" that Neumeier anticipated when this project was conceived [71]. The intermediate results are different than simple phase shift. The profile in the coil index direction gradually shifts from a flat profile through range of changing harmonic profiles until the ridge-like phased response is reached at high frequency. At frequencies near the first resonance, the profile is the quarter sine wave profile. As frequency increases, higher spatial harmonics are energized giving other wave-like profiles. This aspect of the plot gives a visual illustration of the physics

of the optimum current distribution and the coupling between specific spatial modes and the frequency of the stimulus. From the point of view of the control design, the transient shows a smooth, equal amplitude tracking throughout the frequency range and success in meeting the goal of increasing the frequency response of the actuator in the targeted frequency range.

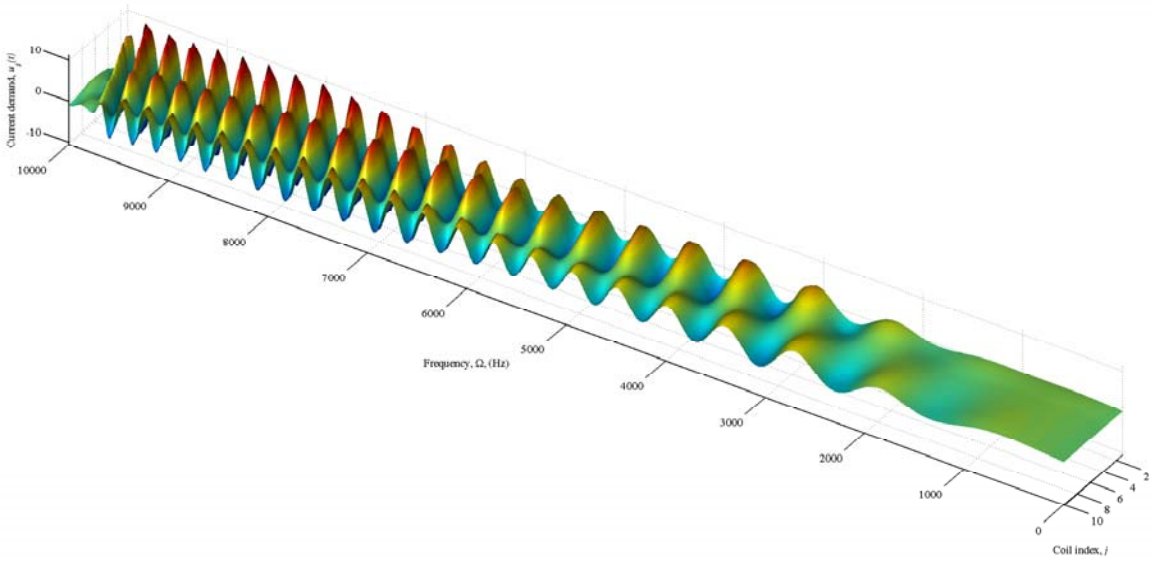


Figure 6.15: Current demand for swept frequency transient

**The non-uniform power distribution problem**

The results for conventional MPC presented thus far are completely satisfactory and are successful in showing that the multi-coil actuator is capable of achieving a faster response at practical levels of power and voltage than a single coil actuator. The previous transients do not demonstrate the shortcomings of the conventional change-driven MPC scheme to handle the spare degrees of freedom situation. The spare degrees of freedom mean that there is not a unique equilibrium state for the actuator. One of the consequences of the change driven cost function of the conventional MPC is that the system can come to rest at any combination of control inputs for which the control error

is zero. This is an undesirable situation because many combinations of current distribution that give zero control error could damage the actuator or amplifiers. This problem is discussed more fully later in this section. It is important to devise a control algorithm that handles all conceivable dynamic conditions successfully and drives the current demand toward the uniform distribution of current demand at steady state. The non-uniform power distribution problem is first demonstrated with a transient simulation and illustrative calculations and then modifications are introduced to the MPC algorithm to resolve the problem.

The step change transient can be used to demonstrate that the actuator can come to rest satisfying the control error requirement perfectly while the current demands are not uniform. The step change reference trajectory from Figure 6.4 can be simulated again except that the initial condition for the current demands are as follows, $\mathbf{u}_0^T = [1, -1, 1, -1, \ldots -1]$. The displacement for the modified case is identical to the response shown in Figure 6.4 so the plot is not repeated. The current demands are the same shape as in Figure 6.5 except that they are offset up and down by the initial conditions. The initial, non-uniform distribution of current persists for the duration of the transient and would continue on indefinitely. The conventional change-driven MPC scheme does not drive a non-uniform distribution of current in the coils toward a uniform distribution (equal current in each coil) at steady state.

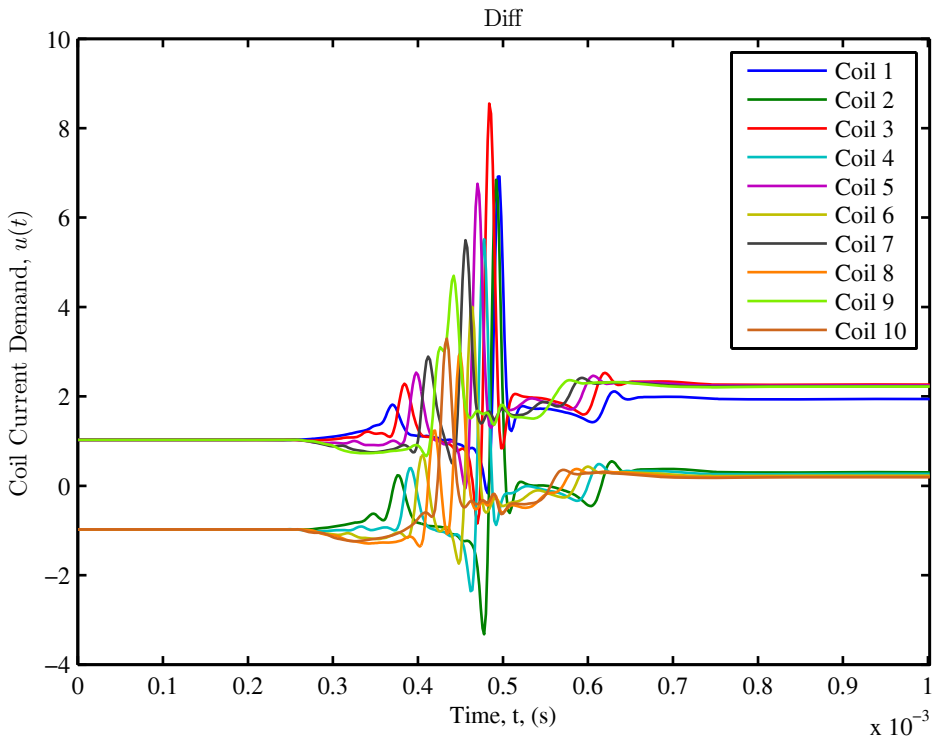


Figure 6.16: Current demand for step change transient starting from $\mathbf{u}_0^T = [1, -1, 1, -1, \ldots -1]$

The problem with the change-driven optimization can be traced to the performance index. The problem can be illustrated by evaluating the equilibrium condition using Eq. (6.33) and Eq. (6.66). At equilibrium, the control error, $\mathbf{r}_{i_0+1:i_0+i_H} - \mathbf{y}_{i_0+1:i_0+i_H} = 0$, in Eq. (6.33) is satisfied exactly at the current time and all future points by the current value of the control, $\mathbf{u}_{i_0}$. Also, actuator current calculated by Eq. (6.66) at equilibrium does not change so $\Delta\mathbf{u}_{i_0:i_0+i_H} = 0$. The actuator can come to rest with a non-uniform power distribution. The equilibrium condition for the system can be solved to show that anhe multi-coil actuator does not have a unique equilibrium.. At equilibrium, the state system is steady at an equilibrium value as given by the following equation.

$$\begin{aligned}\mathbf{x}_{eq} &= \mathbf{A}\mathbf{x}_{eq} + \mathbf{B}\mathbf{u}_{eq}.\\ \mathbf{r} &= \mathbf{C}\mathbf{x}_{eq} + \mathbf{D}\mathbf{u}_{eq}.\end{aligned} \tag{6.68}$$

Eliminating the state vector gives the following equation.

$$\mathbf{r} = \left[\mathbf{C}\left(\mathbf{I}-\mathbf{A}\right)^{-1}\mathbf{B} + \mathbf{D}\right]\mathbf{u}_{eq}. \tag{6.69}$$

For the actuator with spare degrees of freedom, Eq. (6.69) constitutes one equation with $n_u$ control inputs as unknowns. Any combination of inputs satisfying Eq. (6.69) also satisfies Eq. (6.63) exactly. All the residuals of the least squares problem in Eq. (6.63) are exactly zero. This is clearly a minimum for the performance index, but it is not a unique minimum. The problem of equalizing the distribution of current is not addressed by the performance index for the change driven MPC. The lack of a unique minimum power solution at steady state is a significant problem for safe control of the actuator because some solutions that satisfy Eq. (6.69) yield a power distribution that would destroy either the amplifiers or the actuator. Consider the following numerical example of the non-equilibrium problem. The system responds approximately equally to each coil. Hence, the matrix in Eq. (6.69) is given by

$$\left[\mathbf{C}\left(\mathbf{I}-\mathbf{A}\right)^{-1}\mathbf{B} + \mathbf{D}\right] = \frac{1}{10}\begin{bmatrix}1 & 1 & 1 & 1 & 1 & 1 & 1 & 1 & 1 & 1\end{bmatrix}. \tag{6.70}$$

At full stroke, output is given by $\mathbf{r} = \mathbf{y} = 1$. The steady state, the equilibrium condition for full stroke can be satisfied by any combination of positive or negative currents adding to ten. For example, a distribution of coil current in which $u_1 = 10$ and all other control inputs are zero satisfies Eq. (6.69). Equation (6.63) is also satisfied by the asymmetric current distribution at steady state and yields zero residuals. The power consumed by that distribution is given by $\mathbf{u}^T\mathbf{u} = 100$ and all of the power is deposited in

the first coil. This current distribution exceeds both the coil's and amplifier's rated current. The magnetic field in the energized segment of the rod exceeds the saturation limit for the magnetostrictive material. An even higher power would be generated in the actuator if a combination of negative and positive numbers was chosen. In practice, the actuator would drift along the surface defined by Eq. (6.69) until a damaging combination of inputs was encountered.

The optimum distribution from the standpoint of power consumption is to distribute that current nearly[††] evenly among the individual coils. For full stroke output, $y$=1, the current distribution that produces full stroke and consumes the minimum power is approximately

$$\mathbf{u}_{\infty} = \begin{bmatrix} 1 \\ 1 \\ \vdots \\ 1 \end{bmatrix}. \tag{6.71}$$

The power consumed by this current distribution is $\mathbf{u}^T\mathbf{u} = 10$. Power is a factor of 10 less than the previous non-uniform example and is distributed uniformly along the rod. The goal of the control algorithm should be to force a non-uniform distributions toward the uniform, minimum power condition at steady state. Optimizing power (rather than increment in power) solves the problem of spare degrees of freedom and gives a unique and desirable steady state condition.

The problem with the conventional MPC algorithm lies in the performance index based on $\Delta\mathbf{u}^T\Delta\mathbf{u}$. This performance index minimizes the incremental change in power at

[††] The actual optimum distribution is not quite a uniform distribution due to end effects and the location of the coils with respect to the rod in the actuator design. The coils are not equally effective at moving the actuator tip. The precise distribution is close to uniform and the distinction is unimportant for analyzing the spare degrees of freedom problem.

each step. There is no penalty in the cost for an unequal distribution for the absolute magnitude of the current. The solution to the problem is to base the cost of control in the performance index on $\mathbf{u}^T\mathbf{u}$ rather than $\Delta\mathbf{u}^T\Delta\mathbf{u}$. The following section starts by introducing the $\mathbf{u}^T\mathbf{u}$ formulation in the cost index and then, in a series of further modifications, deals with other problems that arise due to the modification.

**Alternatives to Standard MPC to Address the Spare Degrees of Freedom Problem**

Only minor modifications to the conventional MPC are needed to generate an acceptable control performance for the actuator with spare degrees of freedom. Three alternatives are presented in this section. All three involve using $\mathbf{u}^T\mathbf{u}$ rather than $\Delta\mathbf{u}^T\Delta\mathbf{u}$ in the performance index. When $\mathbf{u}^T\mathbf{u}$ is the input cost in the performance index, then the optimization drives the distribution of current to the uniform distribution as required for minimizing power thus rectifying the problem with the $\Delta\mathbf{u}^T\Delta\mathbf{u}$ optimization.

The three approaches are 1) the least squares power with an exact trajectory tracking, 2) least squares power and proportional control error, and 3) least squares power and proportional and integral control errors. The least squares power refers to the $\mathbf{u}^T\mathbf{u}$ in the cost function rather than $\Delta\mathbf{u}^T\Delta\mathbf{u}$. The square proportional and square integral control errors are the form of the reference tracking error in the cost function. We will abbreviate the names of the schemes sometimes as: 1) exact, 2) proportional error, and 3) proportional-integral error. These approaches can be viewed as an evolution of the problem resolution over time. The first two alternative control schemes correct the equilibrium problem but create different problems of their own. The last variation which

includes the control error and the integral of the control error in the cost function so that it is analogous to classical proportional-integral control.

**Least squares power with exact trajectory.**

The exact trajectory method is a time domain version of the frequency domain optimization presented at the beginning of this chapter. The performance index for the exact trajectory control algorithm minimizes $\mathbf{u}^T\mathbf{u}$ subject to the constraint $\mathbf{r} = \mathbf{y}$ at every point in the prediction horizon. Interestingly, this case represents an extension of the type of solution presented by Book [72] and Kwon and Book [73] called inverse dynamic tracking control. The proposed exact trajectory case combines inverse dynamics with model predictive control. The non-uniform current distribution problem is handled by this formulation.

The optimization with the control error constraint is solved using the method of Lagrange multipliers [70] just as in the frequency domain optimization. The exact trajectory requires that each output in the prediction horizon conform exactly to the reference. The number of constraints is equal to the number of points in the prediction horizon. The set of constraint equations is solved exactly at each point from the current time to the prediction horizon. The optimization then minimizes the sum of squares of current at each predicted point. The performance index for the exact trajectory with the auxiliary constraint for the exact trajectory is given by the following:

$$\tilde{\mathscr{F}} = \frac{1}{2}\mathbf{u}_{i_0+1:i_0+i_H}^T\mathbf{u}_{i_0+1:i_0+i_H} + \boldsymbol{\lambda}\left(\mathbf{r}_{i_0+1:i_0+i_H} - \mathbf{y}_{i_0+1:i_0+i_H}\right), \tag{6.72}$$

where $\boldsymbol{\lambda}$ is a vector of Lagrange mulitipliers that appends the constraint equation at each point in the prediction horizon to the performance index. Substituting the prediction equation from Eq. (6.43) into Eq. (6.72) give the following:

$$\tilde{\mathscr{F}} = \frac{1}{2}\mathbf{u}_{i_0+1:i_0+i_H}^T \mathbf{u}_{i_0+1:i_0+i_H} + \boldsymbol{\lambda}\left(\mathbf{r}_{i_0+1:i_0+i_H} - \mathbf{P}\mathbf{x}_{i_0} + \mathbf{H}\mathbf{u}_{i_0+1:i_0+i_H}\right) \tag{6.73}$$

Taking the partial yields

$$\frac{\partial \mathscr{F}}{\partial \mathbf{u}_{i_0+1:i_0+i_H}} = \mathbf{u}_{i_0+1:i_0+i_H}^T - \boldsymbol{\lambda}\mathbf{H} = 0\,. \tag{6.74}$$

Solving for the control input gives

$$\mathbf{u}_{i_0+1:i_0+i_H} = \mathbf{H}^T\boldsymbol{\lambda}^T\,. \tag{6.75}$$

The Lagrange multipliers can be evaluated by substituting into the constraint equations. The constraint equation can be written as

$$\mathbf{r}_{i_0+1:i_0+i_H} - \mathbf{y}_{i_0+1:i_0+i_H} = \mathbf{0}\,. \tag{6.76}$$

Equation (6.43) can be used to write Eq. (6.76) in terms of known inputs and the unknown control input.

$$\mathbf{r}_{i_0+1:i_0+i_H} = \mathbf{y}_{i_0+1:i_0+i_H} = \mathbf{P}\mathbf{x}_{i_0} + \mathbf{H}\mathbf{u}_{i_0+1:i_0+i_H}\,. \tag{6.77}$$

This problem can be formulated as least squares problem analogous to Eq. (6.62). First, we write the problem as two vector equations in vector unknowns.

$$\begin{aligned} \mathbf{u}_{i_0+1:i_0+i_H} \quad & -\mathbf{H}^T\boldsymbol{\lambda}^T = \mathbf{0}. \\ \mathbf{H}\mathbf{u}_{i_0+1:i_0+i_H} \quad & = \mathbf{r}_{i_0+1:i_0+i_H} - \mathbf{P}\mathbf{x}_{i_0}. \end{aligned} \tag{6.78}$$

This system can be written as a matrix equation.

$$\begin{bmatrix} \mathbf{I} & -\mathbf{H}^T \\ \mathbf{H} & \mathbf{0} \end{bmatrix} \begin{bmatrix} \mathbf{u}_{i_0+1:i_0+i_H} \\ \boldsymbol{\lambda}^T \end{bmatrix} = \begin{bmatrix} \mathbf{0} \\ \mathbf{r}_{i_0+1:i_0+i_H} - \mathbf{P}\mathbf{x}_{i_0} \end{bmatrix}. \tag{6.79}$$

This system of equations is square and consists of an equal number, $(n_u+1)\cdot i_h$, of equations and unknowns. Despite the problem being square, the solution can be solved using the least squares operator, "\", to take advantage of the numerical robustness of the MATLAB's least squares method.

$$\begin{bmatrix} \mathbf{u}_{i_0+1:i_0+i_H} \\ \boldsymbol{\lambda}^T \end{bmatrix} = \begin{bmatrix} \mathbf{I} & -\mathbf{H}^T \\ \mathbf{H} & \mathbf{0} \end{bmatrix} \backslash \begin{bmatrix} \mathbf{0} \\ \mathbf{r}_{i_0+1:i_0+i_H} - \mathbf{P}\mathbf{x}_{i_0} \end{bmatrix}. \tag{6.80}$$

The exact trajectory method can be converted to a gain matrix applied at each step using the same procedure as in Eq. (6.65) and Eq. (6.66).

$$\begin{aligned} \mathbf{K}_{Full} &= \begin{bmatrix} \mathbf{I} & -\mathbf{H}^T \\ \mathbf{H} & \mathbf{0} \end{bmatrix} \backslash \begin{bmatrix} \mathbf{0} \\ \mathbf{I} \end{bmatrix}. \\ \mathbf{u}_{i_0+1:i_0+i_H} &= \mathbf{K}_{Full}\left(\mathbf{r}_{i_0+1:i_0+i_H} - \mathbf{P}\mathbf{x}_{i_0}\right). \end{aligned} \tag{6.81}$$

Reducing the full matrix to just the first time step is given by the same types of matrix multiplication as in Eq. (6.66) give the following:

$$\mathbf{u}_{i_0:i_0+i_H} = \begin{bmatrix} \mathbf{I} & \mathbf{0} & \cdots & \mathbf{0} \end{bmatrix} \mathbf{K}_{Full}\left(\mathbf{r}_{i_0+1:i_0+i_H} - \mathbf{P}\mathbf{x}_{i_0}\right), \tag{6.82}$$

$$\mathbf{u}_{i_0+1} = \mathbf{K}_{Exact}\left(\mathbf{r}_{i_0:i_0+i} - \mathbf{P}\mathbf{x}_{i_0}\right), \tag{6.83}$$

where $\mathbf{K}_{Exact} = \begin{bmatrix} \mathbf{I} & \mathbf{0} & \cdots & \mathbf{0} \end{bmatrix} \mathbf{K}_{Full}$. $\mathbf{I}$ and $\mathbf{0}$ are the identity and zero matrices with dimensions $n_u \times n_u$. It is an interesting result that the exact scheme gives the same form of control law as the conventional MPC and is derived by very analogous mathematical steps.

**Test calculations using the exact scheme**

The exact scheme is suggested as a starting point for the evolution of the control algorithm, but the strategy is not expected to yield good control. Confining the trajectory exactly to the reference trajectory is an unnecessarily difficult constraint. The scheme is particularly sensitive to small perturbations. Noise is amplified with a very high gain. Very small perturbations due to numerical modeling error and finite precision arithmetic can be expected to yield extraordinarily noisy results. Even though a noisy response may be expected, it is somewhat surprising that the exact trajectory scheme is not even stable for the single coil actuator. However, this turns out to be the case. Since the single coil actuator is unstable, only the results of the multi-coil actuator are shown.

To illustrate the performance, the three square pulse transient is simulated. Figure 6.17 and Figure 6.18 show the response of the ten coil actuator model for the exact trajectory control law in Eq. (6.83). The actuator model, data, and reference transient are the same as used for the conventional MPC problem. The initial conditions for the current inputs are the problematic case, $\mathbf{u}_{i_0}^T = [1, -1, 1, -1, \ldots -1]$. The noise of the system response is decreased by using a larger time step so the simulations are run using $T_s = 7\times10^{-6}$ seconds. Using the same time step as the conventional MPC, $T_s = 2\times10^{-6}$, gives extraordinarily high spikes in current at the corners of the pulses.

Figure 6.17 plots the reference trajectory and simulated displacement. As required by the exact trajectory control law, the two lines are exactly equal so that only the simulated displacement is visible. Figure 6.18 shows the current demand; however, the individual traces are not discernible in the noise of the coil currents. The case is really two transients. The first part is the response to the initial condition in which the

proportional error drives the uneven distribution of current in the initial condition toward zero. The second part shows the response to the three square pulse reference trajectory. The non-uniform current distribution problem is clearly solved as the initial unequal distribution in current demand is driven to zero by the time, $t = 0.1\times10^{-3}$ seconds. The current demands however display wide swings that are clearly undesirable and do not match the smooth ridges predicted by the conventional MPC. The perturbations stimulating the noise in the current in this simulation are due to the inaccuracy inherent in finite precision arithmetic. Actual control applications in which instrumentation noise is also present would be even noisier.

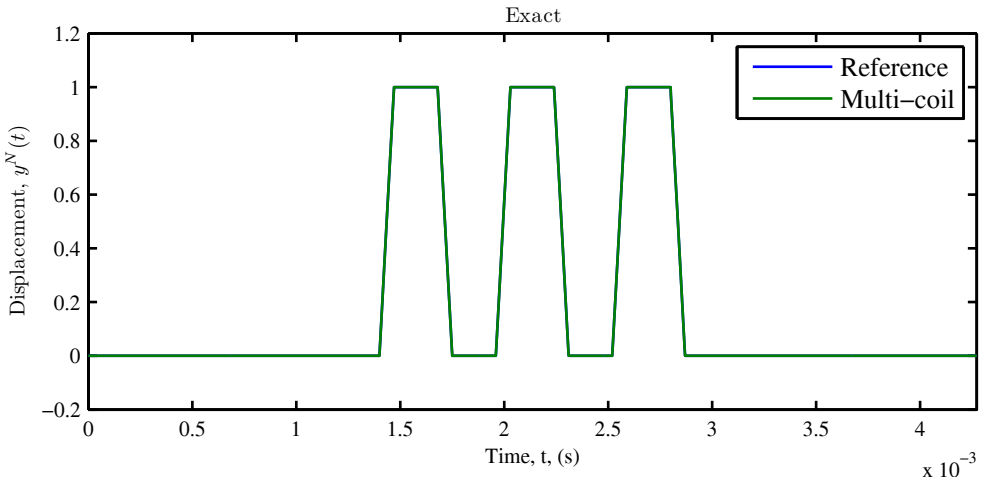


Figure 6.17: Exact trajectory reference tracking

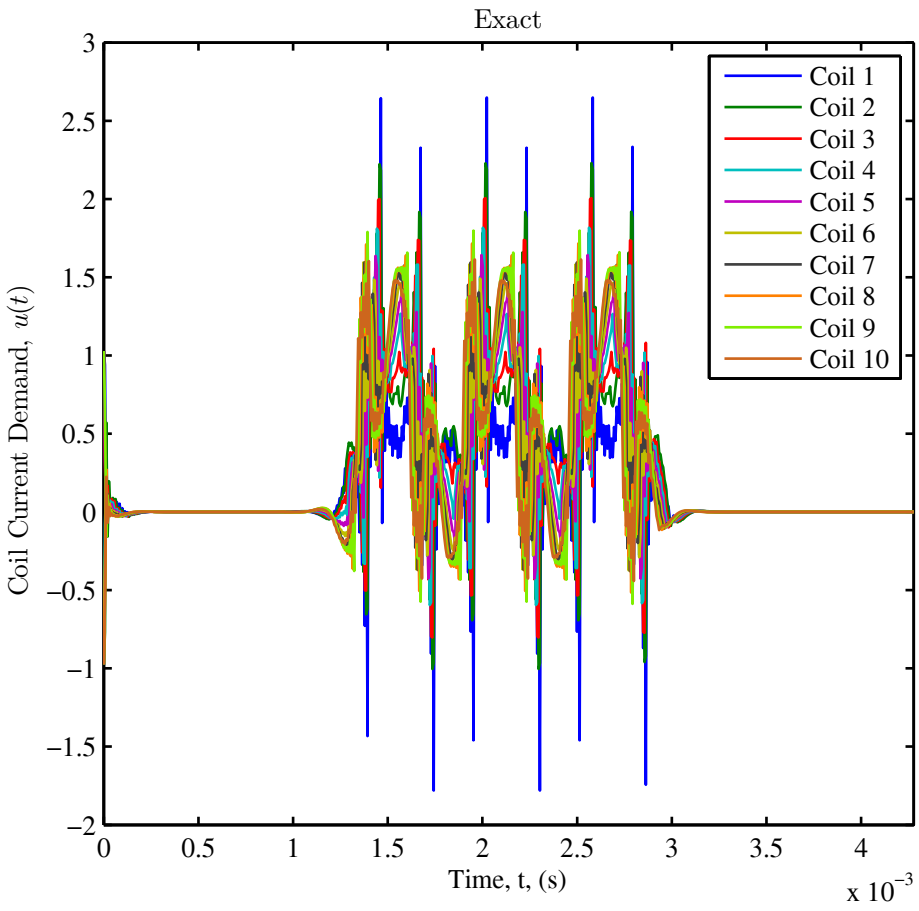


Figure 6.18: Current demand for exact trajectory control

Despite solving the non-uniform current distribution problem, the exact trajectory formulation turns out not to yield satisfactory control because of sensitivity to noise. To address the noise problem, the algorithm should have very low gain at high frequency while maintaining the equilibrium power distribution that the exact solution has at low frequency. To achieve this objective, an alternative cost function is introduced using the weighted square of the control error in the cost function instead of the exact tracking constraint.

**Least squares power and proportional control error.**

Another control algorithm can be devised by replacing $\Delta\mathbf{u}$ in the conventional MPC cost function of Eq. (6.53) with $\mathbf{u}$.

$$\mathscr{J} = \mathbf{u}^T_{i_0+1:i_0+i_H}\mathbf{u}_{i_0+1:i_0+i_H} + q^2\left(\mathbf{r}_{i_0+1:i_0+i_H} - \mathbf{y}_{i_0+1:i_0+i_H}\right)^T\left(\mathbf{r}_{i_0+1:i_0+i_H} - \mathbf{y}_{i_0+1:i_0+i_H}\right). \tag{6.84}$$

The cost function is essentially a version of the linear quadratic cost function of conventional optimal control. If the reference is set to zero $\mathbf{r}_{i_0+1:i_0+i_H} = \mathbf{0}$ and the $\mathbf{y}_{i_0+1:i_0+i_H} = \mathbf{C}\mathbf{x}_{i_0+1:i_0+i_H}$, then the performance index can be written as

$$\mathscr{J} = \mathbf{u}^T_{i_0+1:i_0+i_H}\mathbf{u}_{i_0+1:i_0+i_H} + \mathbf{x}^T_{i_0+1:i_0+i_H}q^2\mathbf{C}^T\mathbf{C}\mathbf{x}_{i_0+1:i_0+i_H}. \tag{6.85}$$

The cost function in Eq. (6.84), which we refer to as the proportional error cost function, allows the optimization scheme to balance the control error with control effort over the prediction horizon. With this formulation, a control error is tolerated if the power consumption is reduced. This optimization scheme is much less noisy than the exact trajectory when the proportional weight factor, $q^2$, is properly chosen. In the limit as $q^2$ increases to infinity, the proportional control scheme approaches the same result (including noise sensitivity) as the exact trajectory scheme. Because the cost depends on $\mathbf{u}^T_{i_0+1:i_0+i_H}\mathbf{u}_{i_0+1:i_0+i_H}$, it can be expected that this cost function also solves the equilibrium current distribution problem. However, the proportional error approach causes a different problem. The proportional error scheme leads, just as it does in LQC, to a steady state offset between the reference and controlled variable.

The minimization solution of the input power and square control error problem follows the same steps as Eq. (6.54) through (6.63) except that $\mathbf{\Delta u}$, $\mathbf{\Theta}$, and $\mathbf{T}$ are

replaced by $\mathbf{u}$, $\mathbf{H}$, and $\mathbf{0}$. The first step in the solution is to substitute the predictive model defined in Eq. (6.43) into Eq. (6.84).

$$\mathscr{F} = \mathbf{u}_{i_0+1:i_0+i_H}^T \mathbf{u}_{i_0+1:i_0+i_H} + q^2 \left(\mathbf{r}_{i_0+1:i_0+i_H} - \mathbf{P}\mathbf{x}_{i_0} - \mathbf{H}\mathbf{u}_{i_0+1:i_0+i_H}\right)^T \left(\mathbf{r}_{i_0+1:i_0+i_H} - \mathbf{P}\mathbf{x}_{i_0} - \mathbf{H}\mathbf{u}_{i_0+1:i_0+i_H}\right). \tag{6.86}$$

The optimum solution is given by $\dfrac{\partial \mathscr{F}}{\partial \mathbf{u}_{i_0+1:i_0+i_H}} = 0$ and can be solved by matrix inversion, but, as in the change driven derivation, the least squares formulation is preferred for numerical calculation. The least squares formulation of Eq. (6.86) is found by minimizing the length of the following vector.

$$\begin{bmatrix} q\left(\mathbf{r}_{i_0+1:i_0+i_H} - \mathbf{P}\mathbf{x}_{i_0} - \mathbf{H}\mathbf{u}_{i_0+1:i_0+i_H}\right) \\ \mathbf{u}_{i_0+1:i_0+i_H} \end{bmatrix} \tag{6.87}$$

The minimum length vector s given by the least squares solution of the following over-determined system of equations.

$$\begin{bmatrix} q\mathbf{H}\mathbf{u}_{i_0+1:i_0+i_H} - q\left(\mathbf{P}\mathbf{x}_{i_0} - \mathbf{r}_{i_0+1:i_0+i_H}\right) \\ \mathbf{u}_{i_0+1:i_0+i_H} \end{bmatrix} = \boldsymbol{\delta}. \tag{6.88}$$

Equation (6.88) can be factored to separate the unknown vector $\mathbf{u}_{i_0:i_0+i_H}$

$$\begin{bmatrix} q\mathbf{H} \\ \mathbf{I} \end{bmatrix} \mathbf{u}_{i_0+1:i_0+i_H} - \begin{bmatrix} q\left(\mathbf{P}\mathbf{x}_{i_0} - \mathbf{r}_{i_0+1:i_0+i_H}\right) \\ \mathbf{0} \end{bmatrix} = \boldsymbol{\delta}. \tag{6.89}$$

Equation (6.89) can be minimized by MATLAB's least squares operator.

$$\mathbf{u}_{i_0+1:i_0+i_H} = \begin{bmatrix} q\mathbf{H} \\ \mathbf{I} \end{bmatrix} \backslash \begin{bmatrix} q\left(\mathbf{r}_{i_0+1:i_0+i_H} - \mathbf{P}\mathbf{x}_{i_0}\right) \\ \mathbf{0} \end{bmatrix}. \tag{6.90}$$

The remaining steps obtain the constant gain matrix for a proportional control law following the same procedure as Eq. (6.65). First, the constant matrices involved in the least squares operation are separated from the time-varying portion.

$$\begin{aligned}\mathbf{K}_{Full} &= \begin{bmatrix} q\mathbf{H} \\ \mathbf{I} \end{bmatrix} \quad \backslash \quad \begin{bmatrix} q\mathbf{I} \\ \mathbf{0} \end{bmatrix}. \\ \mathbf{u}_{i_0+1:i_0+i_H} &= \mathbf{K}_{Full}\left(\mathbf{r}_{i_0+1:i_0+i_H} - \mathbf{P}\mathbf{x}_{i_0}\right).\end{aligned} \tag{6.91}$$

As in Eq. (6.66), the control vector for the next time step is obtained by selecting the first $n_u$ columns of $\mathbf{K}_{Full}$.

$$\begin{aligned}\mathbf{u}_{i_0+1} &= \begin{bmatrix}\mathbf{I} & \underline{\mathbf{0}} & \cdots & \underline{\mathbf{0}}\end{bmatrix}\mathbf{u}_{i_0+1:i_0+i_H} \\ &= \begin{bmatrix}\mathbf{I} & \underline{\mathbf{0}} & \cdots & \underline{\mathbf{0}}\end{bmatrix}\mathbf{K}_{Full}\left(\mathbf{r}_{i_0+1:i_0+i_H} - \mathbf{P}\mathbf{x}_{i_0}\right) \\ &= \mathbf{K}_P\left(\mathbf{r}_{i_0+1:i_0+i_H} - \mathbf{P}\mathbf{x}_{i_0}\right),\end{aligned} \tag{6.92}$$

where $\mathbf{K}_P = \begin{bmatrix}\mathbf{I} & \underline{\mathbf{0}} & \cdots & \underline{\mathbf{0}}\end{bmatrix}\mathbf{K}_{Full}$ is the gain matrix for the proportional error scheme. The gain matrix for the least squares with proportional error is exactly the same form as the conventional change driven MPC algorithm and the exact algorithm. Only the values of the matrix are different.

**Test Calculations Using MPC with Proportional Error**

The step change transient is used to illustrate the performance of the MPC scheme based on the proportional error cost function. The weighting factor has the same value used in the conventional, change-driven MPC. The value is chosen to be $q^2 = 1000$.

The initial condition for the current is chosen to be $\mathbf{u}_0^T = [1, -1, 1, -1, \ldots -1]$ to assess how well the proportional error cost function is able to drive the non-uniform

currents toward a uniform distribution. The rest of the parameters are the same as given in Table 6.1.

Figure 6.19 and Figure 6.20 give the simulated results for the tracking and current demand. The current demand results show that proportional error control scheme addresses the two problems that have been identified so far. In Figure 6.20, the initial non-uniform distribution of current quickly approaches the uniform current distribution which demonstrates that the problem of non-uniform current distribution is solved by the proportional controller. In Figure 6.20, the noise seen in the exact scheme has been significantly reduced. The time step used for the conventional MPC, $T_s = 2\times10^{-6}$, is used for these calculations.

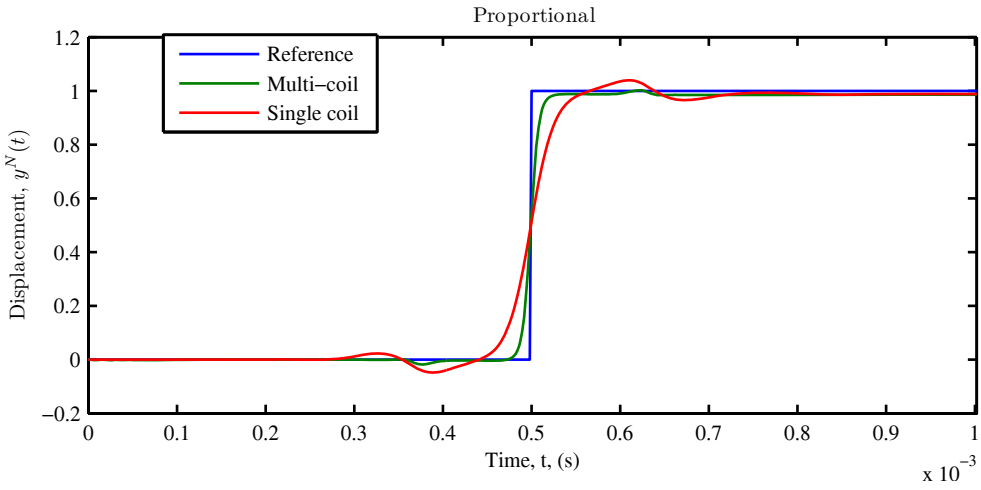


Figure 6.19: Tracking for proportional error control algorithm on step transient

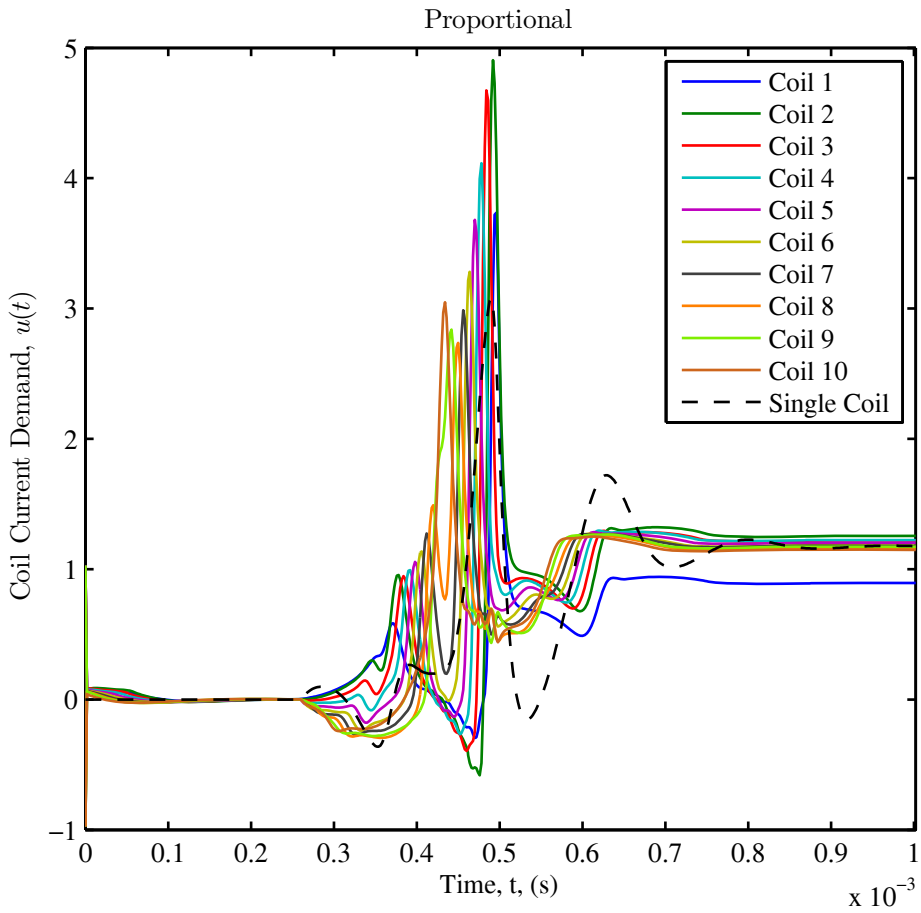


Figure 6.20: Current demand for the proportional error on the step change transient

The proportional error strategy introduces a new problem which is evident in the tracking results. The control error does not approach zero asymptotically at steady state. Figure 6.19 shows that the final steady state value for $y$ deviates slightly from the reference. The source of the offset is the cost function. The least squares optimization is a compromise between the norm of control effort, $\mathbf{u}^T\mathbf{u}$, and the norm of the control error $(\mathbf{r}-\mathbf{y})^T(\mathbf{r}-\mathbf{y})$ so that the sum is minimized. At any non-zero reference condition, the $\mathbf{u}^T\mathbf{u}$ value is non-zero. The minimization algorithm balances the control error against the

power term so that neither is exactly zero at the minimum. Hence, the control error does not approach zero asymptotically.

The steady state offset can be calculated analytically. The steady state condition is given by the condition at which $\mathbf{u}_\infty$, $y_\infty$, and $r_\infty$ are all steady at their equilibrium conditions. Since the outputs are all steady, $\mathbf{x}_\infty = \mathbf{x}_{i+1} = \mathbf{x}_i$, Eq. (6.33) can be solved for relationships between the equilibrium variables.

$$\begin{aligned} \mathbf{x}_\infty &= \left[ \left( \mathbf{I} - \mathbf{A} \right)^{-1} \mathbf{B} + \mathbf{D} \right] \mathbf{u}_\infty, \\ y_\infty &= \mathbf{C} \left( \mathbf{I} - \mathbf{A} \right)^{-1} \mathbf{B} \mathbf{u}_\infty. \end{aligned} \tag{6.93}$$

Let $\mathbf{M} = \mathbf{C} \left( \mathbf{I} - \mathbf{A} \right)^{-1} \mathbf{B} + \mathbf{D}$ and then write the equation for equilibrium as

$$y_\infty = \mathbf{M} \mathbf{u}_\infty . \tag{6.94}$$

The $\mathbf{u}_\infty$ that minimizes the performance index equation can be obtained by the following steps.

$$\mathscr{J}_\infty = \mathbf{u}_\infty^T \mathbf{u}_\infty + q^2 \left( \mathbf{r}_\infty - \mathbf{y}_\infty \right)^T \left( \mathbf{r}_\infty - \mathbf{y}_\infty \right). \tag{6.95}$$

Substitute in Eq. (6.94) to eliminate $\mathbf{y}_\infty$.

$$\mathscr{J}_\infty = \mathbf{u}_\infty^T \mathbf{u}_\infty + q^2 \left( \mathbf{r}_\infty - \mathbf{M} \mathbf{u}_\infty \right)^T \left( \mathbf{r}_\infty - \mathbf{M} \mathbf{u}_\infty \right). \tag{6.96}$$

Take the partial derivative with respect to the vector $\mathbf{u}_\infty$.

$$\frac{\partial \mathscr{J}_\infty}{\partial \mathbf{u}_\infty} = 2 \mathbf{u}_\infty^T + 2 q^2 \left( \mathbf{r}_\infty - \mathbf{M} \mathbf{u}_\infty \right)^T \left( -\mathbf{M} \right) = \mathbf{0}. \tag{6.97}$$

Solve for $\mathbf{u}_\infty$.

$$\mathbf{u}_\infty^T\left(\mathbf{I}+q^2\mathbf{M}^T\mathbf{M}\right)=q^2\mathbf{r}_\infty^T\mathbf{M}.$$
$$\mathbf{u}_\infty=q^2\left(\mathbf{I}+q^2\mathbf{M}^T\mathbf{M}\right)^{-1}\mathbf{M}^T\mathbf{r}_\infty. \tag{6.98}$$

Insert the result back into the equilibrium model. In our problem, the output and reference are scalars so the equation can be written as a ratio.

$$\frac{y_\infty}{r_\infty}=q^2\mathbf{M}\left(\mathbf{I}+q^2\mathbf{M}^T\mathbf{M}\right)^{-1}\mathbf{M}^T. \tag{6.99}$$

Equation (6.99) can be evaluated numerically using the actuator model to show the offset for the step change. The offset calculated from Eq. (6.99) is the value as in the simulated results shown in Figure 6.19.

$$\frac{y_\infty}{r_\infty}=0.9862. \tag{6.100}$$

The steady state offset can be made arbitrarily small by increasing the weight on the control error, $q^2$ ,but this re-introduces the noise problem which was seen in the exact trajectory control. In general, a steady state offset cannot be tolerated in servo control so another modification must be introduced to address the steady state offset problem. The last variation in model predictive control introduces integral error to the performance index. Stabilizing the integral term guarantees that the control error approaches zero asymptotically. This approach is developed in the next section.

Other differences in the performance can also be noted. The tracking of the reference in Figure 6.19 is slightly slower than the conventional MPC algorithm in Figure 6.4: Multi-coil and single coil actuators tracking a step change reference trajectory. The difference in speed is due to the change in cost function. Since the average magnitude of $\Delta\mathbf{u}^T\Delta\mathbf{u}$ is smaller than the magnitude of $\mathbf{u}^T\mathbf{u}$, the effective weight of control effort

versus control error in the cost function is shifted toward control effort by the revised cost function. The increase in the control effort term means that cost optimum occurs for a higher value of control error resulting in less control action. The weight factor on the control error, $q^2$, is tuned in the research by trial and error to give best results for the proportional control scheme and held constant in all other control schemes.

The swept frequency transient in Figure 6.21 shows the attenuation of the response as frequency increases.

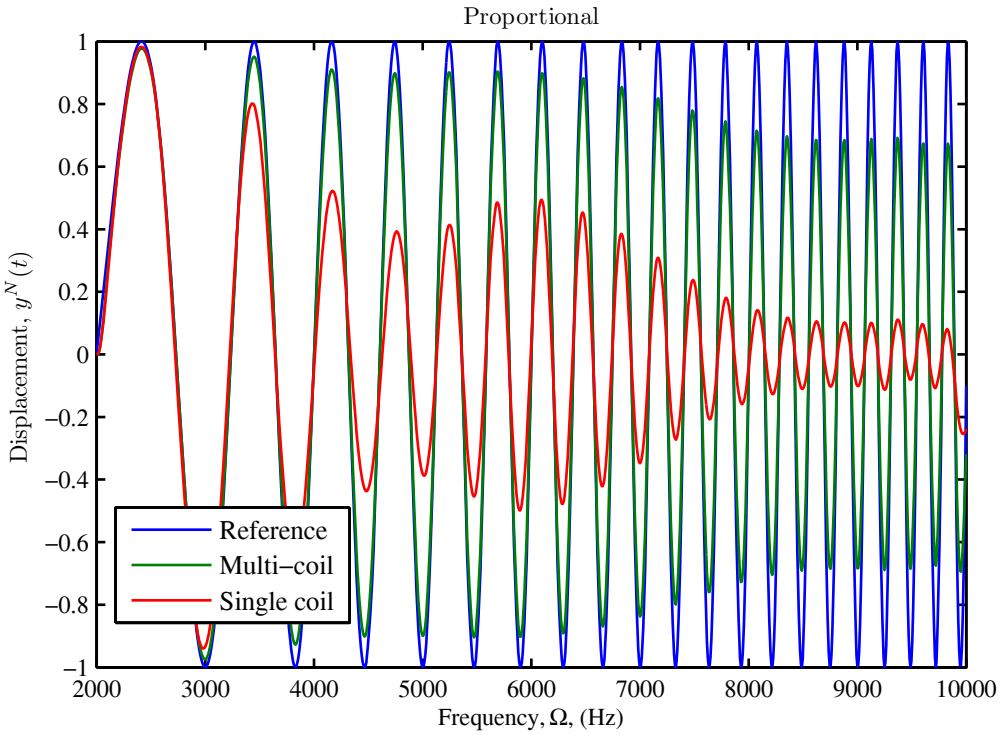


Figure 6.21: Swept frequency response for the proportional error MPC.

The response of the multi-coil actuator begins to fall off at 3000 Hz and then levels off again at about the 8000 Hz. The frequency response of the proportional error control scheme is lower than the conventional MPC in Figure 6.13 at all frequencies. The multi-coil begins to drop at 3500 Hz and continues downward until flattening out at

0.7 amplitude at 8000 Hz. The response indicates the weight on the control error is effectively less relative to the control effort (now in terms of input power) in the proportional scheme than the conventional MPC. This is a difference in tuning. The response could be made the more nearly the same by increasing $q^2$ for the proportional scheme. The tuning for the proportional scheme using the same value $q^2 = 1000$ effectively lowers the feedback gain relative to the gain of conventional MPC control using the same numerical value of the weight factor. The lower gain is a better choice for a real system because the maximum current demand is lower and remains within a feasible range for real amplfiers and because the algorithm has lower sensitivity to noise.

**Least squares power and proportional and integral control error**

Applying integral action to the control error is the classical method to eliminate steady state offset. In predictive control, an approach that is analogous to classical integral action can be implemented to achieve the same effect by adding the square of the integral control error to the cost function.

The purpose of including integral action in the controller is to counteract any steady state offset that may occur in the control. The offset calculated in Eq. (6.100) is simply due to the proportional error control scheme. The offset can also be caused by modeling error. The magnetostrictive actuator is particularly subject to modeling error because of the unmodeled temperature dependence of the magnetostriction constant. The temperature of the material changes due to heating from ohmic and hysteretic losses in the magnetostrictive material, causing the $d_{33}$ coefficient to change. In the experimental results, changes as large as 40% in the magnetostriction constant have been observed in

calibration tests. The integral control action described in this section corrects for offset due to both calibration and the proportional error formulation.

In the predictive control method, integral action is added by including the square of the integral of the control error in the performance index. A similar approach is used with LQC controller by D'Azzo to solve the LQC problem with steady state offset in tracking control applications [74, p. 630-631]. Magni included an auxiliary integrator of the control error in his MPC scheme [66]. Integrating the control error gives a term in the performance index which increases over time when any offset is present. Stabilizing the integral error drives the error itself to zero asymptotically.

In the following performance index, the integral action is added to performance index from Eq.(6.84).

$$\begin{aligned}\mathscr{J} = {} & \mathbf{u}_{i_0+1:i_0+i_H}^T \mathbf{u}_{i_0+1:i_0+i_H} + q_P^2 \left(\mathbf{r}_{i_0+1:i_0+i_H} - \mathbf{y}_{i_0+1:i_0+i_H}\right)^T \left(\mathbf{r}_{i_0+1:i_0+i_H} - \mathbf{y}_{i_0+1:i_0+i_H}\right) \\ & + q_I^2 \left( \int_{t=0}^{t_{i_0+1:i_0+i_H}} \mathbf{r}(t) - \mathbf{y}(t)\, dt \right)^T \left( \int_{t=0}^{t_{i_0+1:i_0+i_H}} \mathbf{r}(t) - \mathbf{y}(t)\, dt \right).\end{aligned} \tag{6.101}$$

where $q_P$ and $q_I$ are the weights for proportional and integral action. The notation for the upper limit of the integral term means a vector of integrals in which the upper limit ranges over the prediction horizon. The vector can be written explicitly as the following.

$$\int_{t=0}^{t_{i_0+1:i_0+i_H}} \left[\mathbf{r}(t) - \mathbf{y}(t)\right] dt = \begin{bmatrix} \int_{t=0}^{t_{i_0+1}} \left[\mathbf{r}(t) - \mathbf{y}(t)\right] dt \\ \int_{t=0}^{t_{i_0+2}} \left[\mathbf{r}(t) - \mathbf{y}(t)\right] dt \\ \vdots \\ \int_{t=0}^{t_{i_0+i_H}} \left[\mathbf{r}(t) - \mathbf{y}(t)\right] dt \end{bmatrix}. \tag{6.102}$$

Each integral term can be converted into a summation over the discrete time steps.

$$\int_{t=0}^{t_{i_0+i}} \left[\mathbf{r}(t)-\mathbf{y}(t)\right] dt = \sum_{i'=0}^{i} \left[\mathbf{r}(t_{i'})-\mathbf{y}(t_{i'})\right] T_s$$
$$= \sum_{i'=0}^{i} (\mathbf{r}_{i'}-\mathbf{y}_{i'}) T_s. \tag{6.103}$$

The summation representing the integral term can be divided into two time intervals: the interval up to the current time and interval from the current time to the endpoint of the prediction horizon.

$$\int_{t=0}^{t_{i0+i}} \left[\mathbf{r}(t)-\mathbf{y}(t)\right] dt = T_s \left[ \sum_{i'=0}^{i_0} (\mathbf{r}_{i'}-\mathbf{y}_{i'}) + \sum_{i'=i_0+1}^{i} (\mathbf{r}_{i'}-\mathbf{y}_{i'}) \right]. \tag{6.104}$$

The evaluation of the first term is a straightforward summation of past control errors.

$$E_{i_0} = T_s \sum_{i'=0}^{i_0} (\mathbf{r}_{i'}-\mathbf{y}_{i'}). \tag{6.105}$$

This term is calculated as a running total in the control program as if it were an additional state variable in the discrete model.

$$E_{i_0} = E_{i_0-1} + T_s \left(r_{i_0} - y_{i_0}\right). \tag{6.106}$$

The second integration segment involves the control inputs in the prediction horizon and is part of the solution that can be varied to reach an optimum control.

$$T_s \sum_{i'=i_0+1}^{i_0:i_0+i_H} (\mathbf{r}_{i'}-\mathbf{y}_{i'}) = \mathbf{S}_e \left(\mathbf{r}_{i_0+1:i_0+i_H} - \mathbf{y}_{i_0+1:i_0+i_H}\right)$$
$$= \mathbf{S}_e \left(\mathbf{r}_{i_0+1:i_0+i_H} - \mathbf{P}\mathbf{x}_{i_0} - \mathbf{H}\mathbf{u}_{i_0+1:i_0+i_H}\right), \tag{6.107}$$

where $\mathbf{S}_e$ is the integration matrix that sums the control error from $i_0+1$ to $i_0+i'$. Each row of $\mathbf{S}_e$ contains a group of 1's over the elements that are summed to perform the integration at that time step.

$$\mathbf{S}_e = T_s \begin{bmatrix} 1 & 0 & \cdots & 0 \\ 1 & 1 & 0 & \vdots \\ \vdots & & \ddots & 0 \\ 1 & \cdots & 1 & 1 \end{bmatrix}. \tag{6.108}$$

The objective now is to rearrange terms in Eq. (6.107) so that the solution to the cost minimization can be posed as a least squares problem. In the following equation, the time-varying terms $\mathbf{r}_{i_0+1:i_0+i_H}$, $\mathbf{x}_{i_0}$, and $E_{i_0}$ are grouped as a vector. The terms involving the unknown control input, $\mathbf{u}_{i_0+1:i_0+i_H}$ are also factored. The vector form of the integral can be written as

$$\begin{aligned} \int_{t=0}^{t_{i_0+1:i_0+i_H}} \left[\mathbf{r}(t) - \mathbf{y}(t)\right] dt &= \left\{ \mathbf{S}_e \left( \mathbf{r}_{i_0+1:i_0+i_H} - \mathbf{P}\mathbf{x}_{i_0} - \mathbf{H}\mathbf{u}_{i_0+1:i_0+i_H} \right) + \begin{bmatrix} 1 \\ 1 \\ \vdots \\ 1 \end{bmatrix} E_{i_0} \right\}, \\ &= \begin{bmatrix} \mathbf{S}_e & -\mathbf{S}_e\mathbf{P} & \begin{bmatrix} 1 \\ 1 \\ \vdots \\ 1 \end{bmatrix} \end{bmatrix} \begin{bmatrix} \mathbf{r}_{i_0+1:i_0+i_H} \\ \mathbf{x}_{i_0} \\ E_{i_0} \end{bmatrix} - \mathbf{S}_e\mathbf{H}\mathbf{u}_{i_0+1:i_0+i_H}, \\ &= \tilde{\mathbf{P}}_I \begin{bmatrix} \mathbf{r}_{i_0+1:i_0+i_H} \\ \mathbf{x}_{i_0} \\ E_{i_0} \end{bmatrix} - \mathbf{S}_e\mathbf{H}\mathbf{u}_{i_0+1:i_0+i_H}, \end{aligned} \tag{6.109}$$

where

$$\tilde{\mathbf{P}}_I = \begin{bmatrix} \mathbf{S}_e & -\mathbf{S}_e\mathbf{P} & \begin{bmatrix} 1 \\ 1 \\ \vdots \\ 1 \end{bmatrix} \end{bmatrix}. \tag{6.110}$$

The integral term, $E_{i_0}$, term is multiplied by a column vector of ones to add the past integral to each term.

To make the proportional and integral terms in the performance index parallel in form to the integral term, the proportional error term can be written as a function of the same stacked vector of $\mathbf{r}_{i_0+1:i_0+i_H}$, $\mathbf{x}_{i_0}$, and $E_{i_0}$. The proportional error is given by the equation

$$\begin{aligned}\mathbf{r}_{i_0+1:i_0+i_H} - \mathbf{y}_{i_0+1:i_0+i_H} &= \mathbf{r}_{i_0+1:i_0+i_H} - \mathbf{P}\mathbf{x}_{i_0} - \mathbf{H}\mathbf{u}_{i_0:i_0+i_H} \\ &= \tilde{\mathbf{P}}_P \begin{bmatrix} \mathbf{r}_{i_0+1:i_0+i_H} \\ \mathbf{x}_{i_0} \\ E_{i_0} \end{bmatrix} - \mathbf{H}\mathbf{u}_{i_0:i_0+i_H},\end{aligned} \tag{6.111}$$

where

$$\tilde{\mathbf{P}}_P = \begin{bmatrix} \mathbf{I} & -\mathbf{P} & \begin{bmatrix} 0 \\ 0 \\ \vdots \\ 0 \end{bmatrix} \end{bmatrix}. \tag{6.112}$$

The integral term, $E_{i_0}$, term is multiplied by a column vector of zeros in this case to fill out the $\tilde{\mathbf{P}}_P$ matrix to the same width as the $\tilde{\mathbf{P}}_I$. The control optimization can now be defined as a least squares problem. The vector whose length is minimized for the proportional-integral control is the following.

$$\begin{bmatrix} q_I \left( \tilde{\mathbf{P}}_I \begin{bmatrix} \mathbf{r}_{i_0+1:i_0+i_H} \\ \mathbf{x}_{i_0} \\ E_{i_0} \end{bmatrix} - \mathbf{S}_e \mathbf{H}\mathbf{u}_{i_0+1:i_0+i_H} \right) \\ q_p \left( \tilde{\mathbf{P}}_P \begin{bmatrix} \mathbf{r}_{i_0+1:i_0+i_H} \\ \mathbf{x}_{i_0} \\ E_{i_0} \end{bmatrix} - \mathbf{H}\mathbf{u}_{i_0+1:i_0+i_H} \right) \\ \mathbf{u}_{i_0+1:i_0+i_H} \end{bmatrix} \tag{6.113}$$

The remaining steps solve for the gain matrix by the same steps as the previous derivations. The control gain is determined by the least squares solution to the following over-determined system of equations.

$$\begin{bmatrix} q_I\left(\tilde{\mathbf{P}}_I\begin{bmatrix}\mathbf{r}_{i_0+1:i_0+i_H}\\ \mathbf{x}_{i_0}\\ E_{i_0}\end{bmatrix}-\mathbf{S}_e\mathbf{H}\mathbf{u}_{i_0:i_0+i_H}\right)\\ q_p\left(\tilde{\mathbf{P}}_P\begin{bmatrix}\mathbf{r}_{i_0+1:i_0+i_H}\\ \mathbf{x}_{i_0}\\ E_{i_0}\end{bmatrix}-\mathbf{H}\mathbf{u}_{i_0+1:i_0+i_H}\right)\\ \mathbf{u}_{i_0+1:i_0+i_H}\end{bmatrix}=\boldsymbol{\delta}. \tag{6.114}$$

The motivation for the grouping of terms is now apparent because the least squares problem can be written as a vector problem analogous to Eq. (6.89)

$$\begin{bmatrix} q_I\mathbf{S}_e\mathbf{H}\\ q_p\mathbf{H}\\ \mathbf{I}\end{bmatrix}\mathbf{u}_{i_0+1:i_0+i_H}=\begin{bmatrix} q_I\tilde{\mathbf{P}}_I\\ q_p\tilde{\mathbf{P}}_P\\ \mathbf{0}\end{bmatrix}\begin{bmatrix}\mathbf{r}_{i_0+1:i_0+i_H}\\ \mathbf{x}_{i_0}\\ E_{i_0}\end{bmatrix}. \tag{6.115}$$

Solving by least squares gives a constant matrix multiplied by a time varying vector.

$$\mathbf{u}_{i_0+1:i_0+i_H}=\begin{bmatrix} q_I\mathbf{S}_e\mathbf{H}\\ q_p\mathbf{H}\\ \mathbf{I}\end{bmatrix}\backslash\begin{bmatrix} q_I\tilde{\mathbf{P}}_I\\ q_p\tilde{\mathbf{P}}_P\\ \mathbf{0}\end{bmatrix}\begin{bmatrix}\mathbf{r}_{i_0+1:i_0+i_H}\\ \mathbf{x}_{i_0}\\ E_{i_0}\end{bmatrix}. \tag{6.116}$$

The constant part of the control law can be separated from the time-varying components.

$$\mathbf{K}_{Full} = \begin{bmatrix} q_I \mathbf{S}_e \mathbf{H} \\ q_p \mathbf{H} \\ \mathbf{I} \end{bmatrix} \backslash \begin{bmatrix} q_I \tilde{\mathbf{P}}_I \\ q_p \tilde{\mathbf{P}}_P \\ \mathbf{0} \end{bmatrix},$$
$$\mathbf{u}_{i_0+1:i_0+i_H} = \mathbf{K}_{Full} \begin{bmatrix} \mathbf{r}_{i_0+1:i_0+i_H} \\ \mathbf{x}_{i_0} \\ E_{i_0} \end{bmatrix}. \tag{6.117}$$

The remaining step is to extract the rows of the gain matrix for the next time step in the same way as in Eq.(6.92).

$$\begin{aligned} \mathbf{u}_{i_0+1} &= \begin{bmatrix} \underline{\mathbf{1}} & \underline{\mathbf{0}} & \cdots & \underline{\mathbf{0}} \end{bmatrix} \mathbf{u}_{i_0+1:i_0+i_H}, \\ &= \begin{bmatrix} \underline{\mathbf{1}} & \underline{\mathbf{0}} & \cdots & \underline{\mathbf{0}} \end{bmatrix} \mathbf{K}_{Full} \begin{bmatrix} \mathbf{r}_{i_0+1:i_0+i_H} \\ \mathbf{x}_{i_0} \\ E_{i_0} \end{bmatrix}, . \\ &= \mathbf{K}_{P+I} \begin{bmatrix} \mathbf{r}_{i_0+1:i_0+i_H} \\ \mathbf{x}_{i_0} \\ E_{i_0} \end{bmatrix}. \end{aligned} \tag{6.118}$$

This control law can be evaluated using the same equations in Eq. (6.67) plus the equation for the integral error, $E_{i_0}$, from Eq. (6.106). The control is calculated from the control law in Eq. (6.118).

**Test calculations using MPC with proportional and integral error**

The suite of three transients for step, pulse and swept frequency with plots showing the reference tracking, power, and three-dimensional current demand for the proportional and integral MPC algorithm are collected in Figure 6.22 through Figure 6.30. The same three transients have been presented for the conventional MPC earlier in this chapter. The transients show that the performance of the conventional MPC has been maintained in the final algorithm while solving the problems of non-uniform current

distribution, noise, and steady state offset. The features of the control response are largely the same as the conventional MPC. The discussion of the control features for the conventional system also applies to these transients so limited discussion of the results is needed. Certain differences do occur as a result of the integral error term.

In general, the tracking of the proportional-integral MPC is slower than the conventional MPC. The single coil is a great deal slower and has lower cutoff frequency response than the multi-coil. The performance index causes the controller to balance the optimization between tracking and power consumption. Because of the effective difference in weight in the performance index, the improvement of multi-coil over single coil in this set of transients is shifted more toward better tracking rather than reduced power. The power consumption of the single coil is a factor of two higher than the multi-coil whereas it is a factor of eight in the conventional MPC results. On the other hand, the speed of the multi-coil actuator on the step response in Figure 6.22 is three times faster than the single coil where it is less than twice as fast for the conventional MPC. The attenuation in frequency response in the swept frequency transient in Figure 6.28 shows the single coil actuator dropping down to a negligible response above 7000 Hz while the multi-coil actuator continues to respond with 70% of full amplitude up to the 10,000 Hz. It is important to realize that the differences between the conventional MPC and the proportional-integral are primarily tuning differences. The same level of tracking is achievable with either design with the proper choice of weight factors. The weight factors have been held constant despite the change in the formulation of the cost function because there is no formula for equivalent tuning. The tuning is a trial and error process. The tuning parameters are held constant to eliminate any bias in the selection.

The multi-coil actuator shows very precise tracking of the reference in the step change and pulse transients. The overshoot is negligible and the settling time is on the order of $5\times10^{-5}$ seconds. The single coil actuator has noticeably poorer control performance. The performance of the multi-coil design represents results that could be achieved in practice. The parameters of the amplifiers and magnetostrictive actuator are realistic estimates. The time step is quite fast, $2\times10^{-6}$ seconds, but is achievable, not with the prototype control hardware, but with digital signal processing computer hardware. On the whole, this is an extraordinarily fast, accurate actuator that is feasible to build.

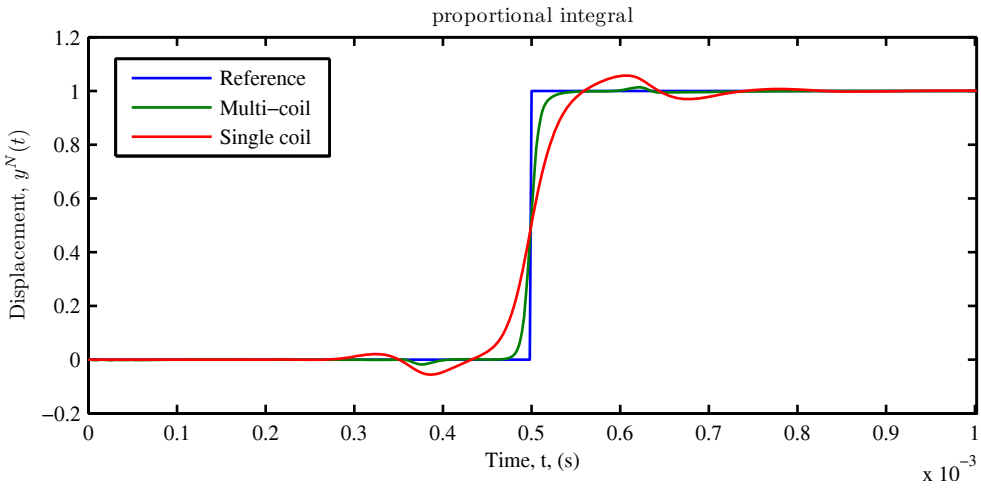


Figure 6.22: Tracking the reference for proportional-integral MPC on a step change

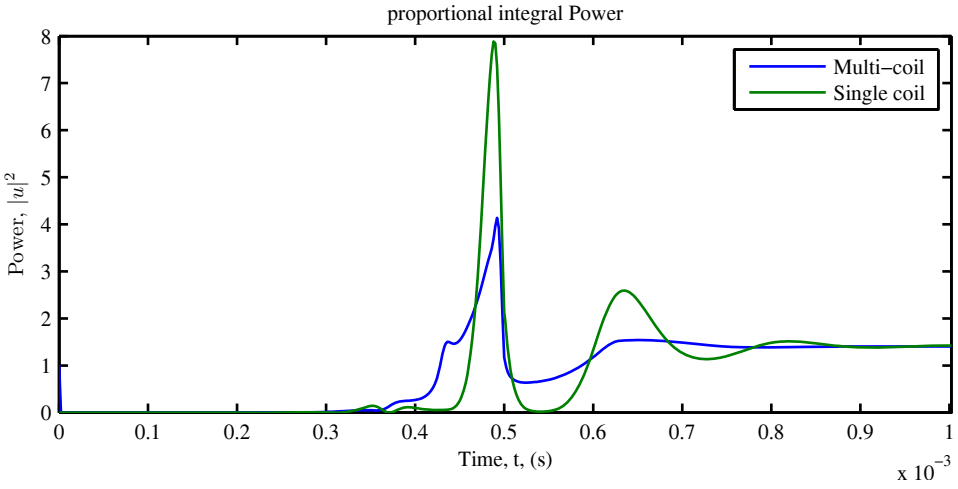


Figure 6.23: Power for proportional-integral MPC on a step change

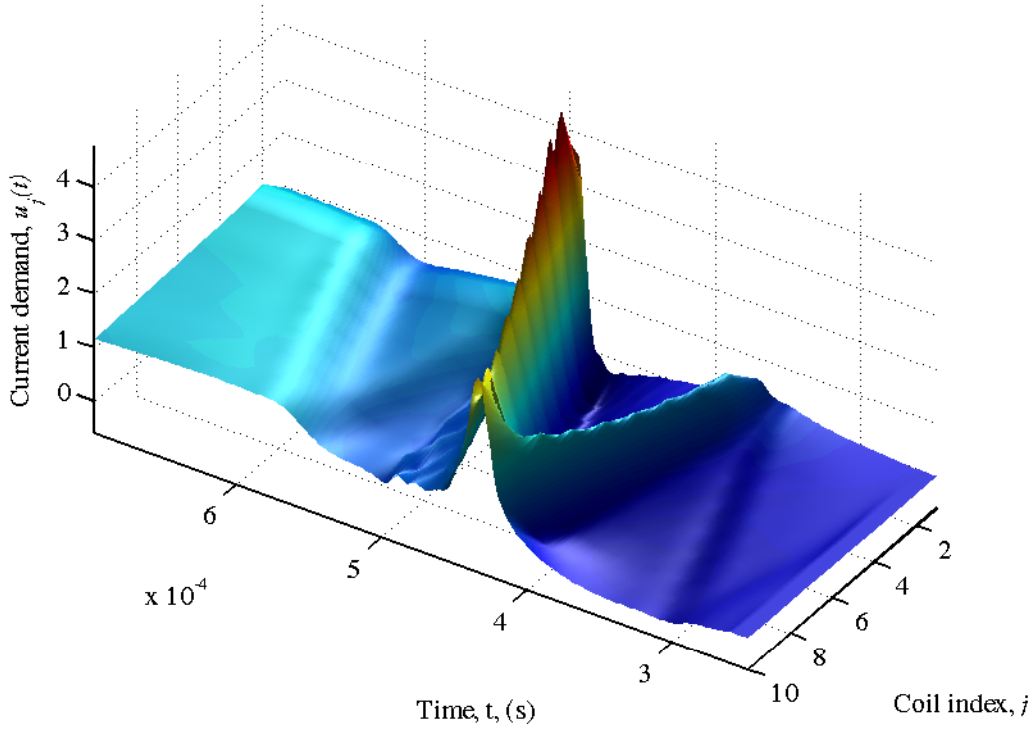


Figure 6.24: Current demand for proportional-integral MPC on a step change transient

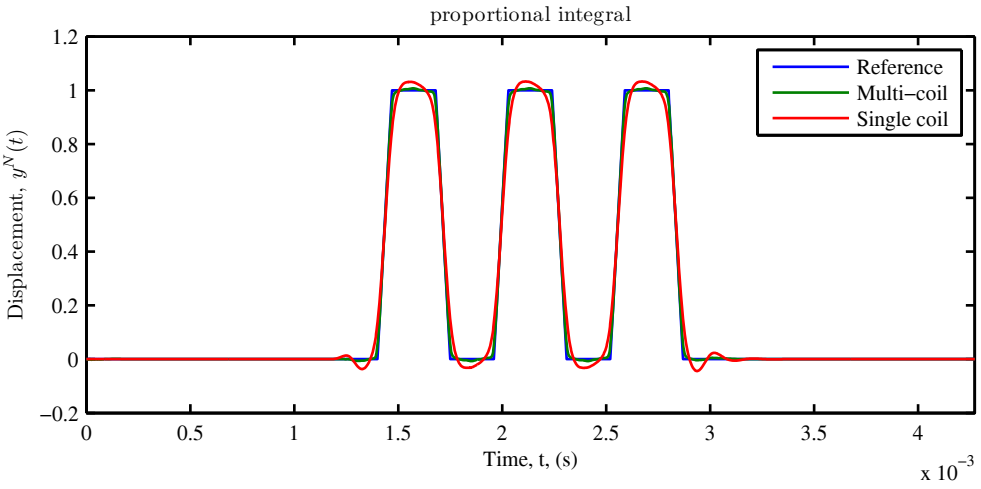


Figure 6.25: Tracking the reference for proportional-integral MPC on a three pulse transient

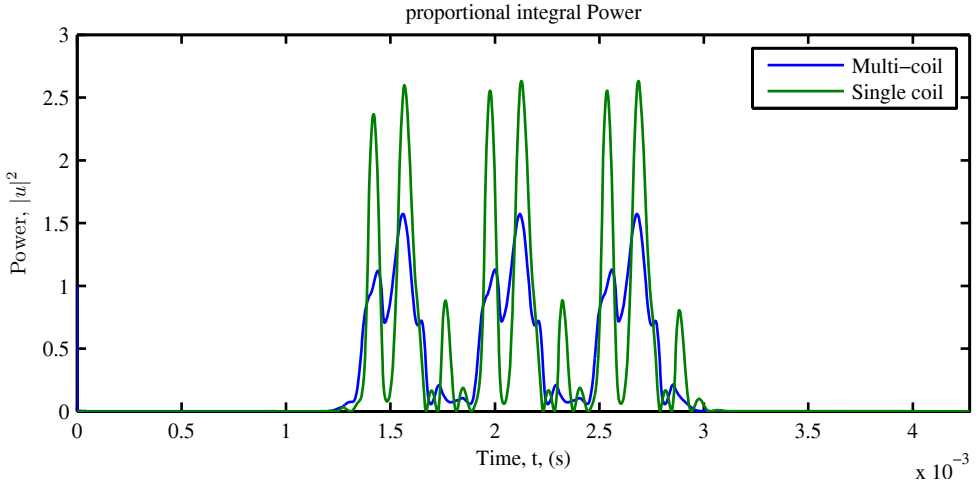


Figure 6.26: Power for proportional-integral MPC on a three pulse transient

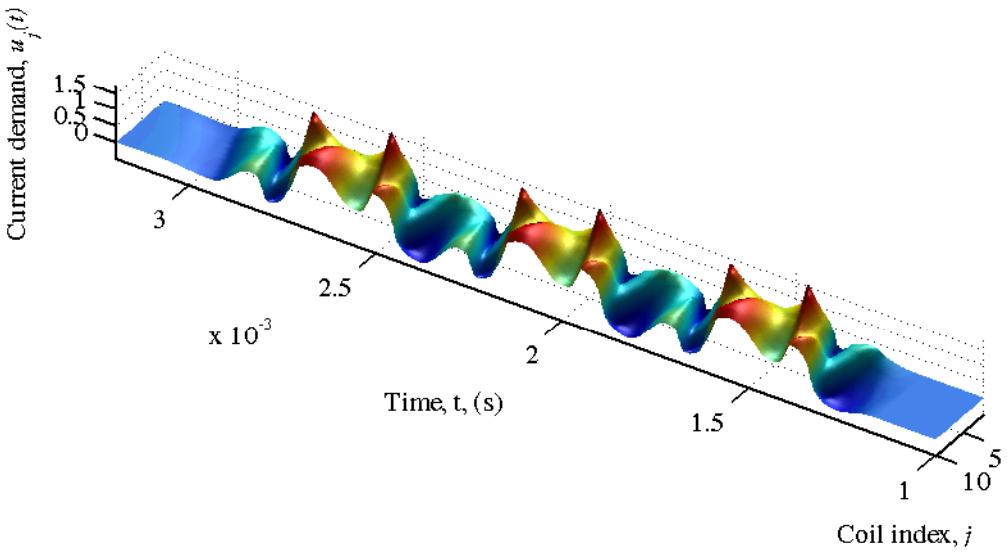


Figure 6.27: Current demand for proportional-integral MPC on a three pulse transient

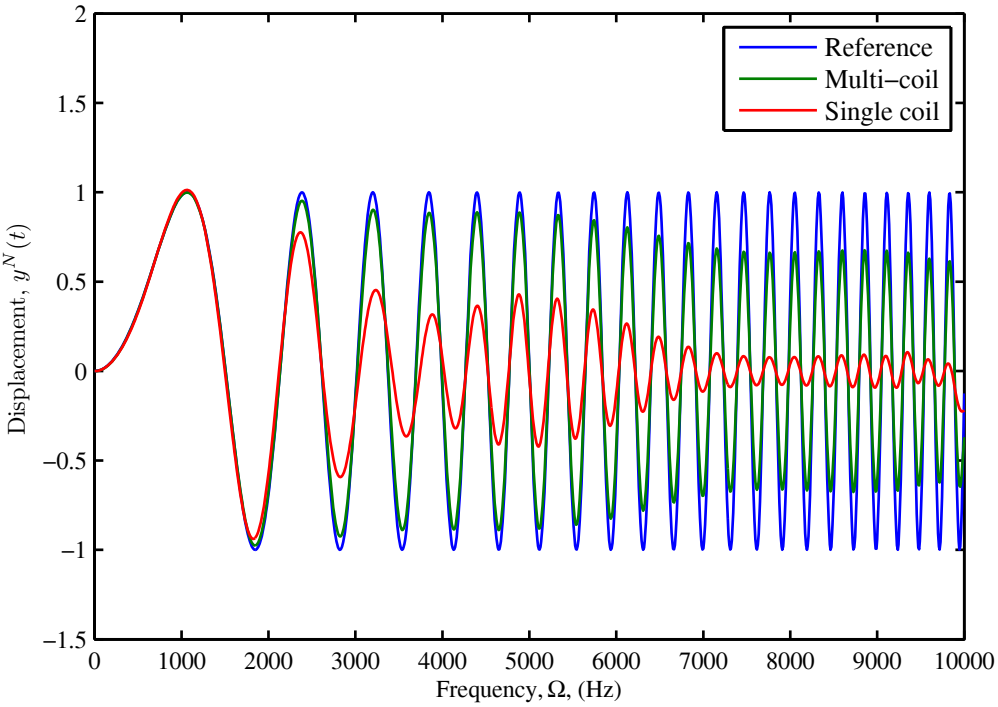


Figure 6.28: Tracking the reference for proportional-integral MPC on a swept frequency transient

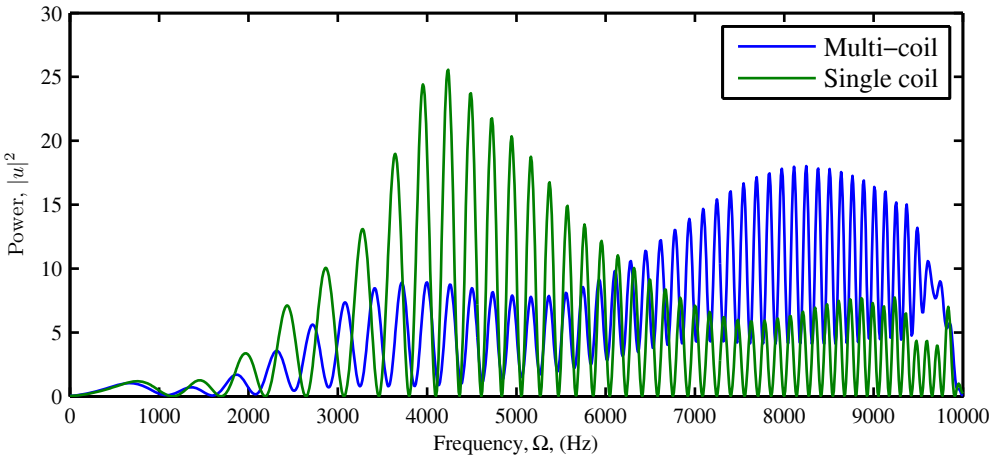


Figure 6.29: Power for proportional-integral MPC on a swept frequency transient

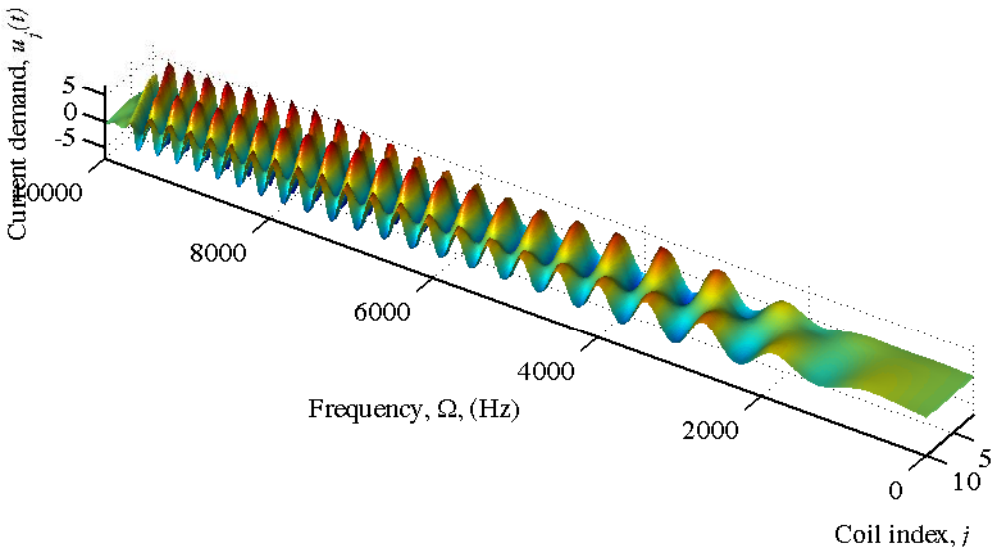


Figure 6.30: Current demand for proportional-integral MPC on a swept frequency transient

## Summary of the MPC Development

The MPC algorithm with proportional and integral error terms is the final form of the control algorithm. The control algorithm and model demonstrate the capability of the multi-coil concept to operate with much less power and voltage than a single coil actuator with a comparably tuned controller. Depending on tuning the control design, the multi-coil actuator can operate faster than a single coil while using the same power or can operate with less power for following the same transient. The MPC algorithm produces a simple proportional control law that can be readily implemented in real time. Work remains on the control algorithm to deal with the practical limitations of incomplete measurements of the state of the system and time delay. APPENDIX I, APPENDIX J, and APPENDIX K deal with model reduction, the Kalman state estimator and the Smith predictor, and the combined control system for implementation on the prototype. However, the development of a proportional-integral control algorithm marks the conclusion of the theoretical development of an improved actuator. The results show that the idea is feasible and demonstrate how it works. The fundamental problems of modeling the device and designing a control system which optimizes the response have been completed successfully. The control results show how a control design can take advantage of the dynamic characteristics of the multi-coil actuator to achieve improved speed of response and reduced power. The essential step of the research is to show that multi-coil actuator provides significant improvement over the single coil actuator, improvement that cannot be achieved with a single coil actuator. The plots of power and voltage of the single and multi-coil actuator show that the multi-coil actuator is an order

of magnitude less for both parameters. The levels of power and voltage for the single coil are not physically achievable.

The model predictive control using various combinations of proportional error, integral error, control input and the change in control input suggest that a more general form of the MPC cost function can be defined that may have broader application than the actuator problem. Various orders of integration and differentiation of the control error or control input can be included in the cost function by raising the integration and differentiation matrices to a corresponding power in the cost function over the prediction horizon. The linear combination of the integral and differential terms is, in effect, a digital filter. The MPC can be tuned for robustness to error as a function of frequency by tuning the filtering parameters. Development of robustness in the MPC using filter design techniques is suggested as future work.

# CHAPTER 7

# THE MULTI-COIL ACTUATOR EXPERIMENTS

The experimental results from the multi-coil actuator prototype system provide the final test for the dissertation problem. The experimental system is limited by the minimum sampling time that can be achieved with the input and output boards for the control computer. Despite the time step limitations of the hardware, the experimental results provide a valid, if limited, demonstration of the effect of multiple coils. The main goal is to provide experimental verification of the simulation results of the actuator and controls that are presented in Chapter 6. The experimental confirmation of the modeling and controls provides some assurance that the simulated results using a faster time step are an accurate prediction of the performance that can be achieved with a faster control system.

Two groups of transients are presented: open loop and closed loop. The open loop transients are generated by providing a pseudo-random binary sequence (PRBS) as the current demand to each coil. The PRBS transients are performed without any control feedback from the MPC algorithm. These results are used for confirming the modeling of the actuator. The closed loop transients present the same suite of three reference trajectories that are used in the MPC development in Chapter 6 to illustrate the performance of the control algorithm on the prototype actuator. Predicted transients using the simulation model operating at the experimental system's time step are given in APPENDIX K. The closed loop transients are the step change, three square pulse, and

swept frequency. These transients provide the evidence that the benefits of increased speed and reduced power of the multi-coil actuator can be observed experimentally.

This chapter also describes the hardware and software for the prototype system. The actuator is a modified version of a commercially available magnetostrictive actuator. The prototype control system is a general-purpose, laboratory computer system equipped with input and output boards which convert data from analog measurements to digital data for processing and the convert the control system demand back into analog to control the prototype actuator. The software for the digital control system retrieves the measured data from the data acquisition system, performs the computations for estimation and model predictive control, issues the control commands, regulates the timing of the main control loop, and logs data for post-processing.

## Experimental System

The experimental system consists of the prototype actuator, the power electronics for driving the coils, the control computer with input and output devices, and the sensing devices for measuring the displacement and coil current. The circuit for each coil consists of the coil in the actuator, a 4 ohm load resistor, and one channel of a power amplifier. Figure 7.1 is a schematic of the system. To simplify the representation of the wiring for ten coils, the schematic borrows Simulink's *mux* and *demux* symbols for multiplexing, and de-multiplexing composite signals. The heavy lines represent a composite signal containing ten cables. In the actual experiment, the signals are not multiplexed. Each of the ten cables is routed point to point.

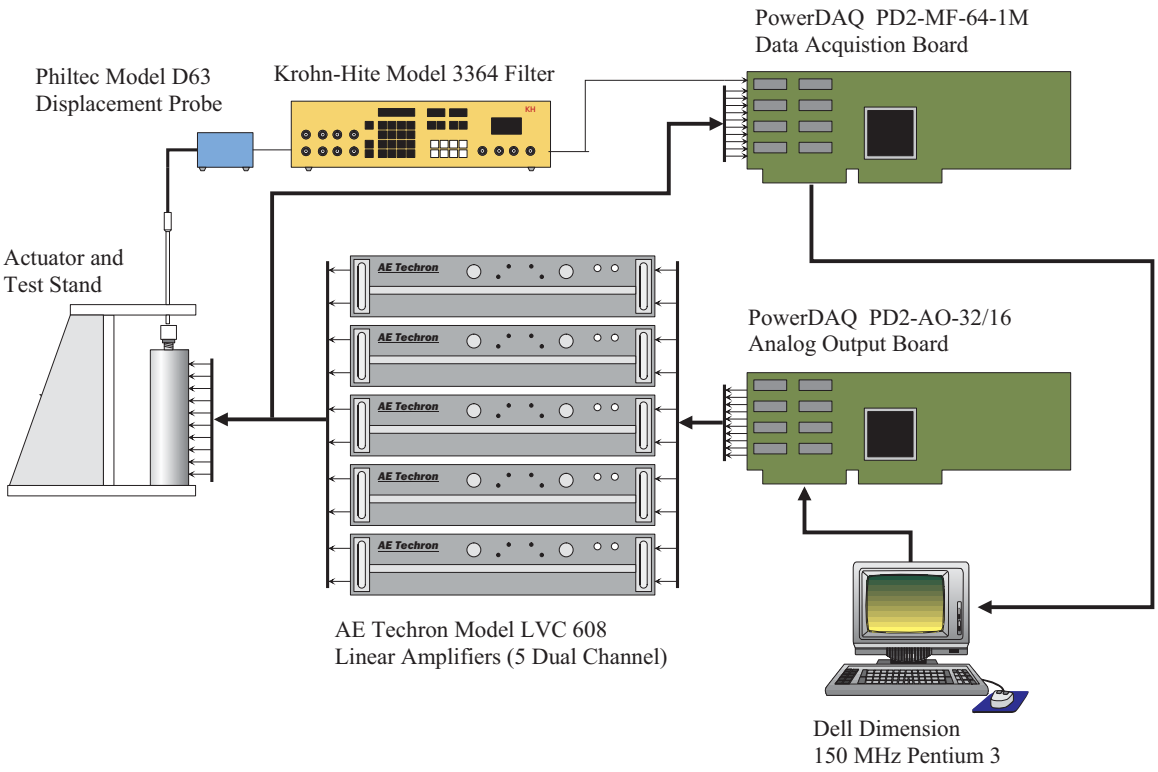


Figure 7.1: Schematic of experimental system

Figure 7.2 shows the prototype actuator built by Etrema to Georgia Tech's specification. The features of the prototype are described in Chapter 1.

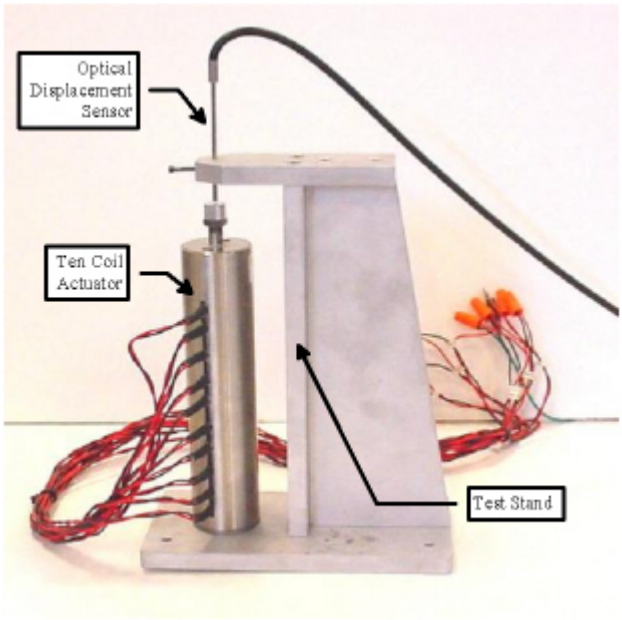


Figure 7.2: Prototype actuator mounted in test stand

The amplifiers for the experimental setup consist of five, dual-channel, AE Techron Model LV608 modules. The LV608 is a modified version of the Crown Macro-Tech 602. The Crown amplifier is usually found in high-power audio applications. The Crown amplifier offers excellent dynamic range and overload protection. The amplifiers can supply 290 watts rms into 4 ohms with less than 0.1% total harmonic distortion at rated power at 20,000 Hz. These amplifiers are rack mounted and are wired to a patch panel built for the experiment to facilitate interfacing the amplifiers to the actuator and the control computer. The load resistors in the coil circuit are each 4 ohm wire-wound, power resistors rated for 4 amperes.

The LV608 amplifiers provide several configuration choices. The LV608 is a dual-channel device but may be operated with the two channels bridged to double the

voltage or in parallel to double the current of a single channel. In the actuator experiment, the LV608's are operated as two independent channels with each channel configured as a DC-coupled, voltage-to-current converter. The input for an audio amplifier is normally configured as AC coupled. Any DC level in the input signal is blocked by a small capacitor and large shunt resistor in the input stage. Only the time-varying component of the input signal passes through to the output stage. In the actuator experiment, a DC offset is required to bias the magnetic field of the actuator so that the actuator operates in its linear region for magnetostriction. The DC coupling of the LV608 bypasses the capacitor in the input stage and permits the DC component of the input signal to pass through to the output.

Another modification to the usual audio amplifier configuration is to select current-controlled feedback. A typical audio amplifier produces an output voltage proportional to its input voltage. The current controlled amplifier or transconductance amplifier produces an output current proportional to the input voltage. In the actuator experiment, the current feedback works to counteract any current induced in the coil by inductive coupling to other coils and eddy currents and causes the coil current to track control demand more closely. Without the current controlled compensation, the induced current would otherwise work against the desired axial variation of magnetic field that is set at the amplifier input and increase the magnetic drag.

The control computer for the performing the control algorithm computations and logging data is an Intel Pentium 3 operating at 150 MHz. The input board is a PowerDAQ PD2-MF-64-1M/12L and the output board is a PowerDAQ PD2-AO-32/16. The input and output boards are installed in the control computer. The computer system

operates under a proprietary, real-time operating system called QNX. QNX is a derivative of Unix with extensions for real time data acquisition and control. The control program to implement data logging and the linear state space controls is written in C specifically for the experiment. The PowerDaq data acquisition system comes with a library of C routines for controlling the data acquisition process. These routines are accessed as needed in the prototype control program. Data from the tests are recorded into a file that can be transferred by Ethernet data link using FTP (file transfer protocol) to a Windows-based PC for data analysis and plotting using MATLAB. To minimize the computational load, no screen display output capabilities are used on the control computer. The same program can run either the closed loop or open loop experiments by selection of a switch setting at the start of a run.

Both the control computer and the I/O boards are slower than ideal for the actuator application. Either one alone would limit the time step of the experimental system to larger values than the simulations of Chapter 6 indicate are needed for taking advantage of the multi-coil actuator. The limiting time step of the current experimental hardware is fixed by the settling time of the analog to digital conversion on the PowerDAQ data acquisition boards. If faster time steps are attempted with the current system, the sampled data do not have time to settle to a steady value giving erratic data. The speed of the computer for performing the control algorithm on the control computer is also a potential limitation on the current system. The control computations take place in parallel with the data sampling. The computation loop with the reduced-order, (20-state) system consumes nearly the full time step of 70 microseconds on the control

computer. The computation would become the critical path if the I/O speed were increased.

The time step limitation of the experimental system is not a major technical obstacle for future research. The computer and data acquisition boards are approximately ten years old. Commercial digital control hardware is available today that can achieve the sampling rates needed to gain the full benefit of the multi-coil actuator. Consumer grade microprocessors available today are factors of 20 to 30 or even 50 times faster than the computer used for this experiment. The PowerDaq line of data acquisition boards made by United Electronics now has individual digital to analog converters that can sample 12 bit results at 2 megahertz. The boards are available with as many as eight A/D converters on a single board to process multiple channels in parallel rather than multiplexing all channels through a single A/D converter as on the experimental setup. Hence, the sampling time could be reduced as low as 0.5 microseconds with newer hardware.

Sensor dynamics have not been considered in the theoretical actuator model. The measured variables consist of the ten current signals and the displacement. A voltage signal proportional to current is an output of the amplifier. The current signal is patched directly to the input of the PowerDaq board. No sensor dynamics or signal processing are needed for the current measurement. The sensor dynamics for the displacement measurement however need to be considered in the experimental results. The displacement measurement system shown in Figure 7.1 consists of two components, the optical probe and the signal processing filter. The actuator displacement is measured by a Philtec Fiber Optic displacement probe (Philtec Model D63). The displacement probe

measures the gap between the tip of the probe and a mirrored surface using the method of reflectance. A polished aluminum reflective surface attached to the actuator's lead screw provides a high reflectivity surface to produce a good signal to the detector. The output of the displacement probe produces a decreasing voltage versus gap. The actuator's displacement measurement is set so that the operating point is at the steepest part of the downward curve at approximately 4 volts.

The full-scale voltage signal for the measured displacement when all the coils are changed in unison from the minimum to maximum current (0.75 A to 2.25 see Table 2.9) yields a maximum change in the probe's signal from 4 to 3.75 volts. The difficulty that the displacement probe's sensing response presents for displacement measurement is that the resolution of the analog to digital conversion is reduced to a 0.25 volt interval out of a 10 volt range (-5 to +5 volts). A signal conditioning filter (Krohn-Hite Model 3364 Filter) is used to remove the DC offset and apply a constant gain to expand the sensor voltage range to full scale of the analog to digital converter's range. The front panel settings of the filter are set for a fourth order Butterworth filter with gain of 20 to 40 dB and cutoff frequency of between 10 and 50 Hz. The gain of 40 dB corresponds to an algebraic multiplier of 100 which increases the displacement signal from a single coil to full scale of the analog to digital converter for the PRBS tests. A smaller gain is used for the reference suite of transients in which the displacement involves multiple energized coils yielding larger displacements. The experimental system uses a filter inversion algorithm to recover an estimate of the actual displacement from the filtered displacement signal. APPENDIX L discusses the modeling of the Krohn-Hite filter and the Philtec displacement probe

The real-time software for the control experiment is limited to the essential operations because of the need to run the program as fast as possible. The control calculations are contained in an iterative loop that reads data from the experiment, computes the control, and outputs the control demands to the experiment. The control computation consists of a loop calculation to implement the matrix multiplications for the estimator and controls. The control program runs with all processes and interrupts on the control computer disabled except the control program. The timing of the control loop uses the processor's clock as the timing device. Two sources of error in the timing of the loop can potentially affect the control loop. First, while the CPU clock speed is a repeatable measurement of time, the time per cycle is only approximately known. The rated CPU speed is used in the program for the clock time. The clock rate may vary from the rated by a few percent. This clock rate error is not a significant source of error for the control program because repeatability is the main issue. Another source of potentially larger timing inaccuracy is the loop count per time step. At the end of each control loop's computations, the clock cycles are read iteratively until the number of cycles for the time step is exceeded. The timing of the control loop is approximate because the number of cycles for each loop can vary (for unknown reason) from the desired number for the control loop. Because of this variability in machine cycles, the control program simply restarts the control test if the number of cycles in a time step exceeds a maximum limit specified in the control program. Hence, the time per step varies between the minimum and maximum number of clock cycles per time step specified in the program.

The process for verifying the programming of the control program is a comparison of the matrix calculations in the C program to the same MATLAB

calculation in the simulated transients in Chapter 6. For the control program test, the data acquisition portion of the C program is replaced by a simulation program of the actuator so that the C program and MATLAB program perform exactly the same computation by different coding. The verification is not quite exact because the matrices are transferred from MATLAB to the C program as text files with decimal values of the coefficients which can differ in the least significant bits from the binary versions of the coefficients. The comparison of the C and MATLAB simulations shows that the simulated results are the same to 4 or 5 decimal digits.

## Experimental Results

The experiment results for both open and closed loop modes of operation are presented in this section. The control demands for the open loop cases are given by predefined series of values. The closed loop demands are computed in real-time by the MPC algorithm using the measured data from the actuator system. Results from two types of transients are shown. In the first group of results, a pseudo-random binary sequence (PRBS) is used to stimulate the actuator in open loop fashion. The displacement and current from the PRSB transient for the experimental and simulated actuator are compared to show how well the model reproduces the actual device. The second group of transients is the same suite of three reference transients used in Chapter 6 to illustrate the performance of the MPC algorithm. These results are used to show that the benefit from optimum control of the multiple coils is evident in the experimental results. For a comparison, the reference transients are run in open and closed loop. In the open loop reference transients, all amplifiers are driven with the reference trajectory signal in unison so that the multi-coil actuator acts like a single coil device. The benefit

of the optimization of the multi-coil device, although weaker than the results at high frequency sampling rates in the simulated results of CHAPTER 6, is evident in a slight reduction in power in the multi-coil devices in comparison to the single coil. The magnitude of the effect is consistent with predicted results using the $T_s = 70\times10^{-6}$ s time step shown in APPENDIX K.

**Pseudo-random binary sequence**

The pseudo-random binary sequence (PRBS) is a series of demand values that are randomly chosen as either 0 or 1 using a numerical random number generator. The random sequence gives a wide, flat spectral density for a given time step and sample size. Comparing a model and experiment using the PRBS transient is generally considered the most rigorous test of a model's fidelity. The PRBS test is frequently used to stimulate a process to develop a system model by the method of system identification. The original plan for the PRBS experiment was to analyze the actuator modeling data using 'grey box' system identification from MATLAB's System Identification Toolboox to refine the parameter estimates for the coefficients in the constitutive relationships of the magnetostrictive material. The modeling results turned out to be satisfactory with the original engineering data so the system identification calculations were not completed. The transient results are presented for the PRBS for the experiment and simulated actuator. The only parameter change introduced by the PRBS transient is a minor tuning of the amplifier gain. The cut-off frequency for the amplifier, which is used in setting the amplifier feedback gain, is reduced from 20,000 Hz to 10,000 Hz to improve the match of the rise time of the measured current. As discussed in Chapter 5, tuning the cut-off frequency is expected because the amplifier parameter depends on the load and needs to

be determined experimentally. Reducing the amplifier cut-off frequency makes the amplifiers slower and has a significant effect on the actuator performance. Slowing the amplifier response has the effect of reducing the benefit that can be gained by the multi-coil actuator because the current signals cannot rise as sharply to create precisely defined wave fronts. The amplifier dynamics are a design parameter of the system that must be considered in future work to achieve the desired frequency response of the overall system. The results in Chapter 6 are computed using the 20,000 Hz parameter for the amplifiers. The predictions for the experimental system in reflect the lowered cut-off frequency parameter.

The PRBS is generated by the MATLAB function, *idinput*, and downloaded to the control computer. The sequence of 0's and 1's generates a current demand of either 0.75 or 2.25 ampères in dimensioned units. For the test case, the sequence is applied to a single coil demand at a time while all other coil demands are held constant at the minimum value for the current range (0.75 amps). The minimum current provides the magnetic bias needed for the magnetostrictive material to be in its linear range. The same pseudo-random sequence is applied to each coil in a separate transient. The multi-coil actuator gives a nonlinear response if the unenergized coils are not biased.

For comparison, the PRBS transient is also applied to the simulation model of the actuator from Chapter 5. The time step for the simulated transient is $T_s = 1.4 \times 10^{-6} s$ to eliminate any potential accuracy problems due to undersampling. The intermediate values of the simulated results also provide information about the high frequency components of the response that are not evident in the slower experimental results. The comparisons of the simulated and experimental results are given in Figure 7.3, Figure 7.4,

and Figure 7.5. The total number of data samples in each transient needs to be an even power of two for signal processing. The length of the PRBS transient consists of a sample of $2^{13} = 8192$ time steps of the experimental system at $T_s = 70 \times 10^{-6} s$ for a total duration of 0.5734 seconds. Only a short segment of that data can be shown in the figures. The chosen segment has a long step and then a series of fast on-off steps that give the model a rigorous test. This fidelity of the sample shown is representative of the entire test.

The model of displacement in Figure 7.3 gives a very good comparison of the major peaks of the transient. The fit is best for coil 10 and becomes progressively poorer for coils 8 down to 2. The increase in error versus position is believed to be the result of an approximation of the boundary condition used for the vibration model. The model assumes no load on the actuator even though the mass of the actuator push rod, friction, and preload spring contribute a dynamic load on the magnetostrictive rod.

The important property of the multi-coil actuator that is exploited by the MPC to make it faster than the single coil is the difference in amplitude and phase response of the individual coils. To illustrate the difference in time response among the coils, we combine the PRBS transients for coils 2, 4, 6, 8, and 10 on the same plot. The displacement data from Figure 7.3 are plotted again on Figure 7.6 and Figure 7.7. The simulated results in Figure 7.6 show the expected time delay and variation in amplitude among the individual coils that result from the spatial distribution of the inputs. The experimental results in Figure 7.7 show the same overall shape for the peaks as the calculated response but lack the time resolution to see the time delay for each coil individually. The difference in resolution of the time response illustrates the handicap

that the sampling time presents to the MPC for achieving significant performance improvement. The modeling, on the other hand, is successful. The overall character of the response is clearly the same. The two figures demonstrate that the prototype multi-coil device possesses a degree of differentiation in the timing of response that is accurately represented by the actuator model.

The current in each energized coil is also compared in Figure 7.4. The only parameter that is adjusted in the model is the amplifier cut-off frequency. That change was made on the basis of the comparison in Figure 7.4. Before tuning the cut-off frequency parameter, the rise time for model's current was substantially faster than the experiment. The time constant of the inductive resistive circuit response is increased by decreasing the cut-off frequency, yielding the comparison that is shown. The plot for the current in the coil adjacent to the energized coil is shown in the Figure 7.5. This plot shows the effect of induced voltage on the coil.

The fidelity between the model and the experimental results is quite good considering that the speed of the transient is at the limits of monitoring capability for the data acquisition system. The results shown here are the "raw" comparison. The engineering estimates for the parameters which were made initially (except for the amplifier parameter) are not changed to improve the fit. No evidence of major unmodeled dynamics appears in the results. The main features of the transient are evident in both the model and experimental results but perhaps have different magnitude. This result suggests that a task to refine parameter estimates in the model using system identification could significantly improve the comparison.

The modeling approximations that are introduced in the development are confirmed. The approximation to linearize the magnetostrictive properties in Chapter 2 and the homogeneous approximation of the eddy current's boundary condition in Chapter 3 appear to be satisfactory. The circuit model approximating the feedback gain of the amplifier as a linear device appears to be a valid approach as indicated by the comparison of predicted and measured current for the energized coil. The peaks of induced current in the coil adjacent to the energized in Figure 7.5 are overpredicted by the model by about a factor of two. The reason for this is not known. The modeling error is not significant to the test. The induced current is quite small relative to the current in the energized coil. The deviation in current in the unenergized coils appears more significant because it is not shown in comparison to a full scale current. The comparison could mean that a higher value for the permeability parameter of the magnetostrictive rod is needed or that unmodeled dynamics in the current sensing circuit or current feedback circuit of the amplifier should be identified.

In the presentation of results, the measured data are time-shifted two steps to correct for measurement delay as closely as possible and line up the input with the response in time. The experimental data indicate that perhaps a fractional time step would yield a better comparison. The time shift in the Smith predictor in the control algorithm is restricted to integer steps of the experimental time step which explains the choice of an integer value, but the Smith predictor could be changed to use a fractioinal time step with some more complicated prediction mathematics. The time shift appears greater in the displacement results than in the current results. Hysteresis in magnetization also manifests as an apparent time delay in transients involving step changes and would

affect displacement more than current. Including a model of hysteresis could also improve the time comparison.

The conclusion to be drawn from the PRBS test is that the model of the actuator system is largely successful and could easily be improved by tuning for a better fit. Since the control results hinge on the underlying model, it could be argued that the PRBS results are more significant indication of the success of the mulit-coil actuator than the closed loop results in the following section.

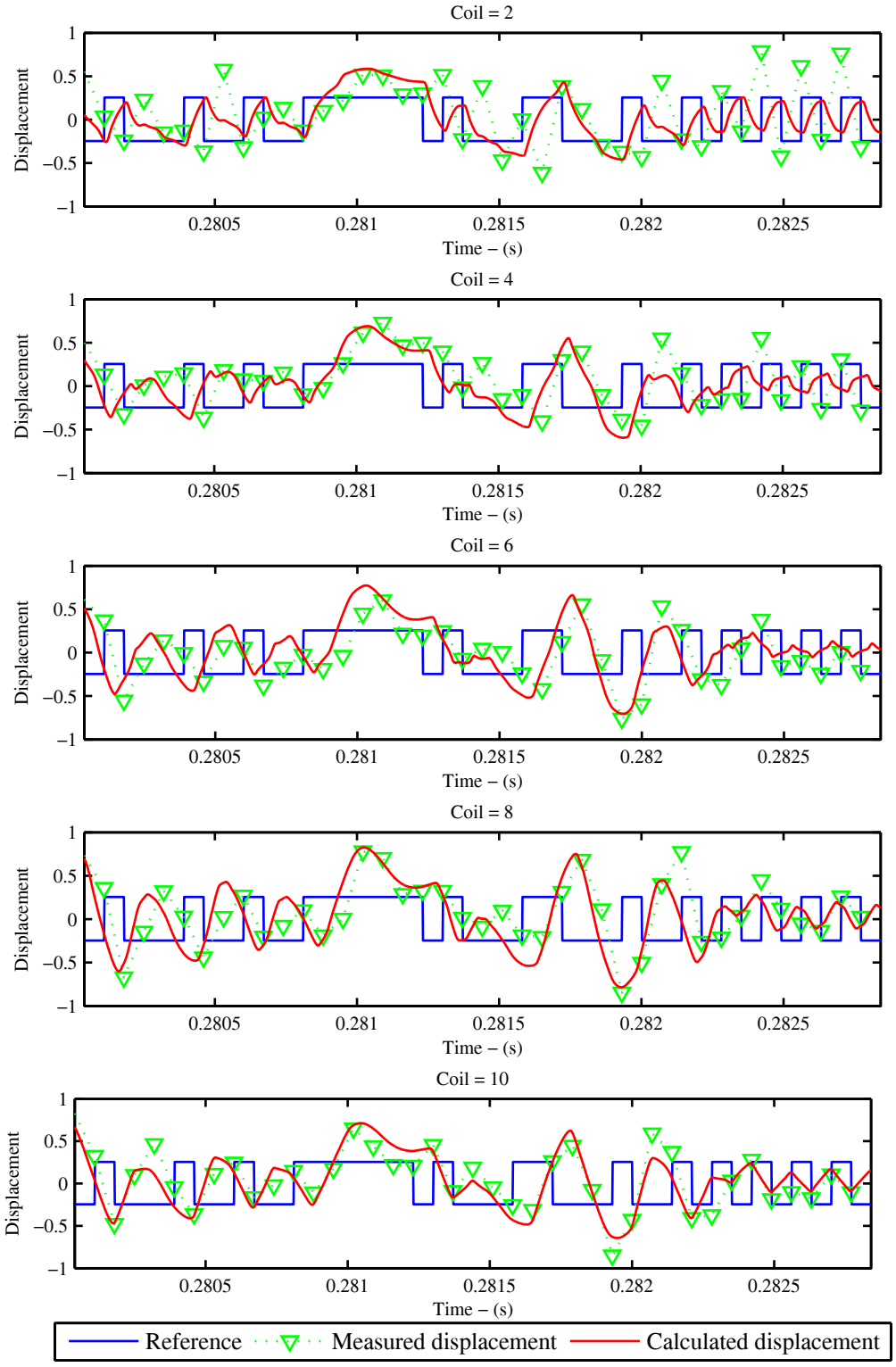


Figure 7.3: Displacement for simulated and experimental models on PRBS transient

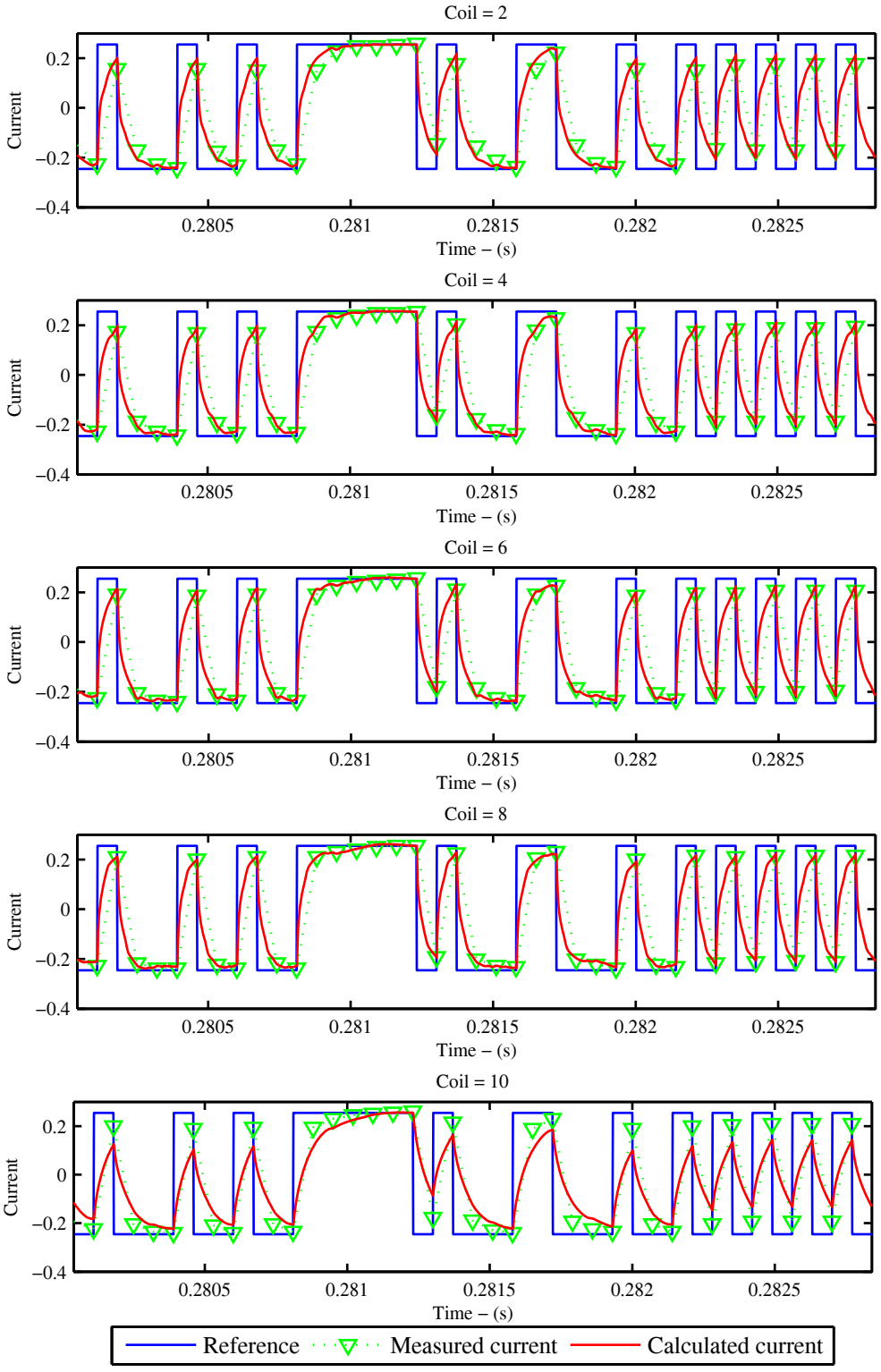


Figure 7.4: Current in energized coil for PRBS transient

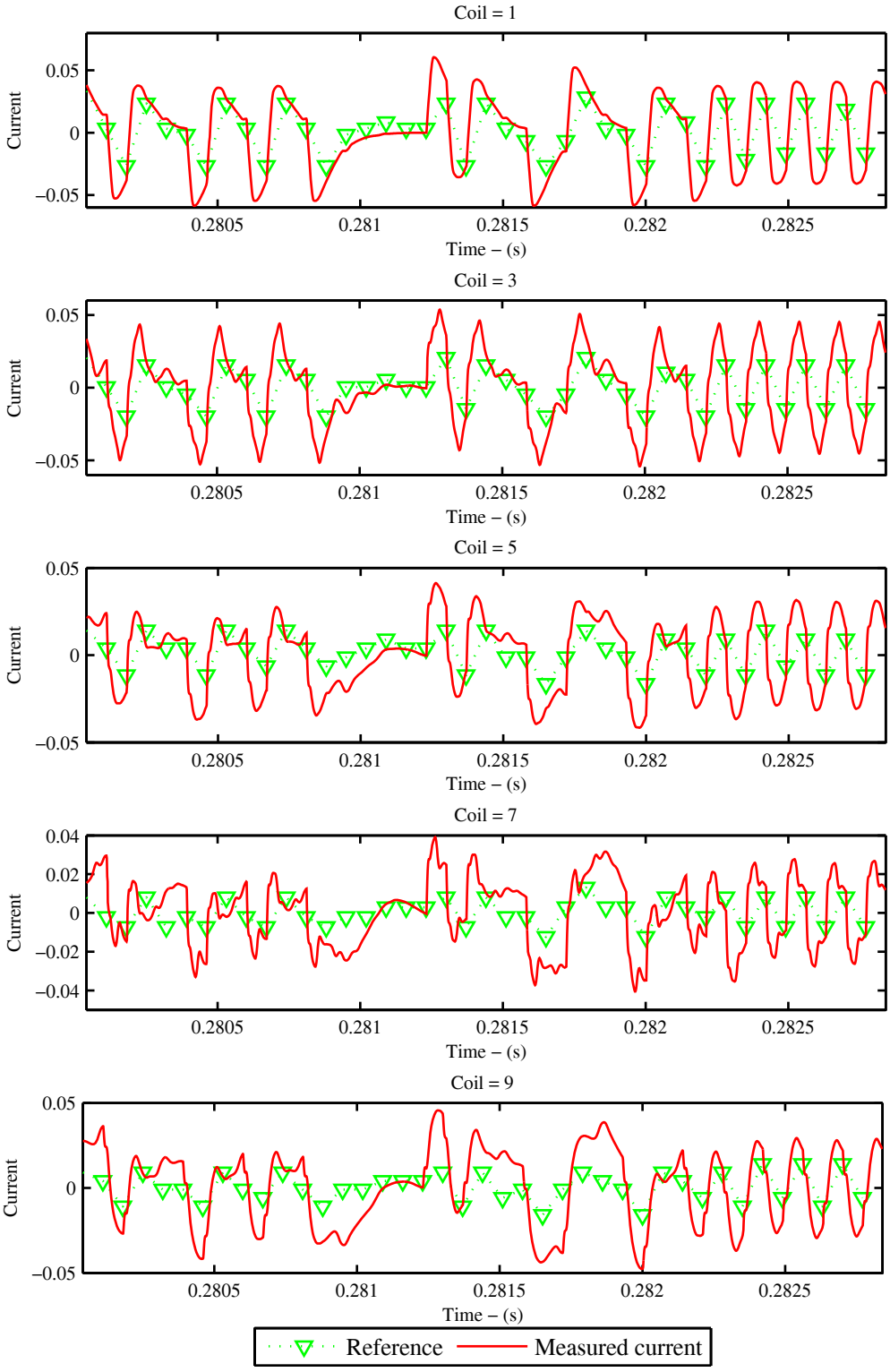


Figure 7.5: Current in coil adjacent to energized coil for PRBS

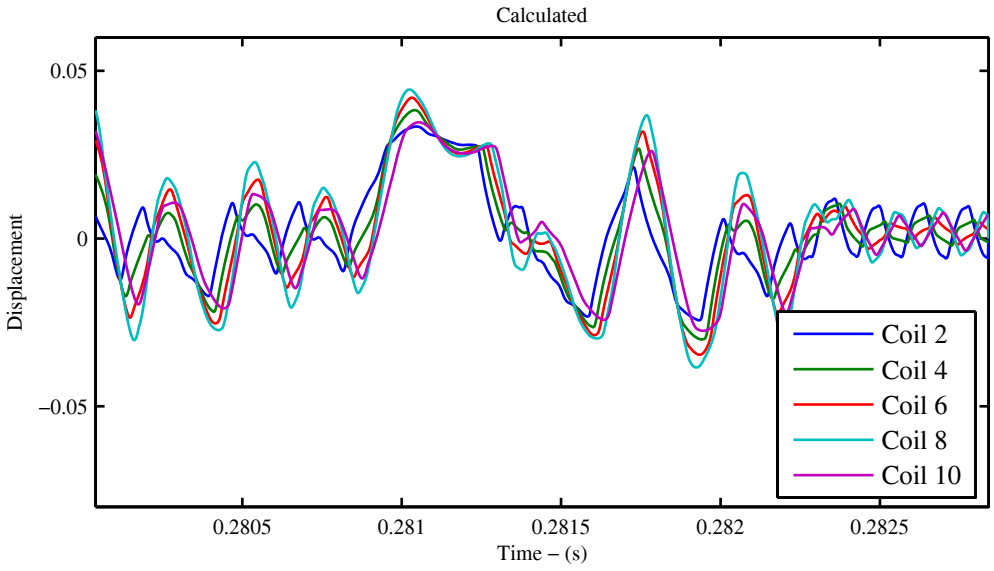


Figure 7.6: Calculated displacement for coils 2, 4, 6, 8 and 10 on PRBS transient

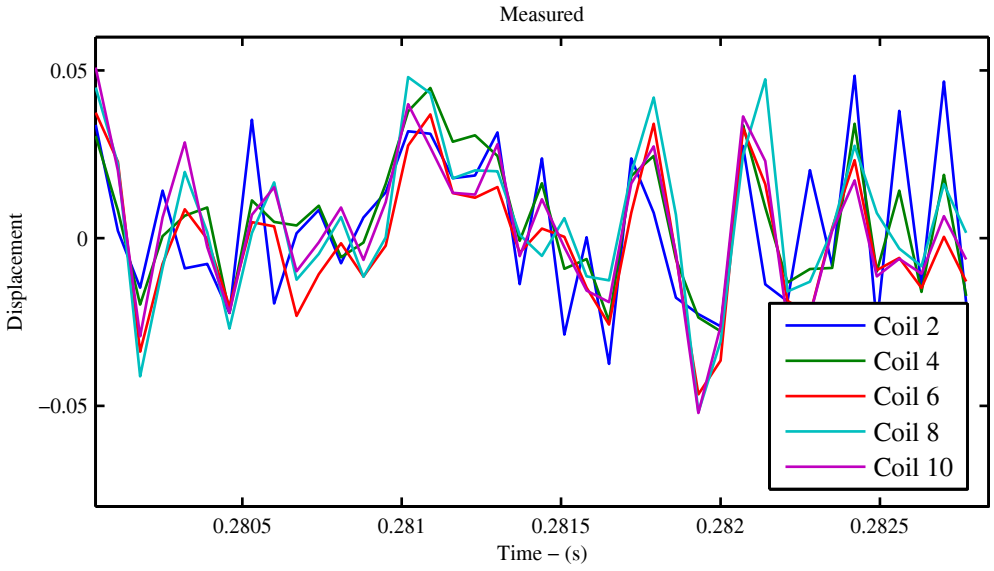


Figure 7.7: Measured displacement for coils 2, 4, 6, 8 and 10 on PRBS transient

**Closed loop reference tracking transients**

The same three transients that are used in Chapter 6 to illustrate the performance of the MPC algorithm in simulated cases are repeated in this chapter using the prototype actuator. The transients include the step change, three square pulses, and swept frequency transients. The actuator model used to design the proportional-integral MPC for the experimental system is the reduced order controller with 20 states. The control algorithm in the experimental system includes the Kalman state estimator and Smith predictor described in APPENDIX J. The combined controller is described in APPENDIX K

The data and parameters for the control algorithm are as close as practical to the parameters for the cases in Chapter 6 at the faster time step but cannot be the same. The prediction horizon is the same duration rounded to the nearest integer number of time steps as in Chapter 6. The time delay is the value observed in the PRBS transients. The weights on the proportional and integral error in the MPC optimization are reduced based on the predicted effect of time step on tuning that is described in APPENDIX K. The control algorithm for the experiment is tuned for stability and low sensitivity to noise. The tuning is adjusted by setting the weight on the control error in the MPC optimization algorithm. The weight for the proportional error in the experimental system control is $q_P^2 = 100$, whereas the weight for the simulations in Chapter 6 with a faster time step is $q_P^2 = 1000$. The reduction in the control error term of the cost function improves the damping of the control response but it also results in slower response and greater steady state offset from the proportional error. The tuning choice for slower, more stable response is evident in all the experimental runs. The steady state offset from proportional

control also increases. A corresponding effect from reducing the weight is that the power term is more significant in the cost function than the control error. The optimization emphasizes a reduction in power rather than reduction in control error in the results presented. Numerical values for the key parameters in the MPC design calculation are given in Table 7.1.

Table 7.1: MPC algorithm parameters

| Variable | Value | Units | Description |
|---|---|---|---|
| $q_P^2$ | 100 | (-) | Proportional error weight factor |
| $q_I^2$ | $2000 / T_s$ | $s^{-2}$ | Integral error weight factor[7] |
| $q_E^2$ | 0.001 | (-) | Estimator weight factor |
| $f_D$ | 0.1 | (-) | Displacement weight factor in estimator |
| $i_H$ | 3 | (-) | Prediction horizon, (number of time steps) |
| $n_K$ | 2 | (-) | Time delay (number of time steps) |
| $T_s$ | $70\times10^{-6}$ | | Time step |
| $ns$ | 20 | (-) | Number of states in reduced order model |

Another tuning difference between the simulated results and the experiment is that the integral error of the measured displacement has to be disabled. The measured signal for displacement goes through the Krohn-Hite filter and then is processed by the digital inverse filter. The resulting estimate of displacement drifts with respect to the actual displacement due to small differences between Krohn-Hite filter and the inversion of that filter in the control system. The build-up of the integral error is a false error signal that drives the current demand off center and potentially could damage the amplifiers. Removing integral action over past measured variables eliminates the problem with the false drift in the displacement sensor but also removes the correction of the signal for any

[7] The integral weight is only used on the portion of control error integrated over the prediction horizon. See discussion of the heading for

true offset between the reference signal and the actual displacement. Eliminating the integration of measured displacement error means that steady state errors are not compensated in the experimental results. In the MPC, the integral error actually consists of two terms, the integral over past values that depends on measured data and the integral over the prediction horizon that does not depend on the measurements. The integration of the error over the predicted time horizon is retained in the control algorithm because it is not affected by the signal processing error. However, it has a small effect on the steady state offset because the prediction time interval is short and the integral action does not have time to accumulate error. Moreover, the integral error calculated over the prediction horizon has no effect on the offset due to measurement error because predictions are not dependent on the measurement error. The predicted interval only works to counteract the offset to proportional control. The drift in calibration of the actuator due to temperature variation accounts for most of the steady state offset observed between the measured trajectory and the reference. The displacement measurement is calibrated periodically in the experiments, but the effect of miscalibration is still evident in the closed loop results.

The model used in computing the MPC matrices for the closed loop control cases in this section is not exactly the same as the model shown in the PRBS or the simulated results in Chapter 6. After the closed loop data were taken, additional tests of the model equations were constructed to verify the modeling and programming. In particular, the Green's identity tests in Appendix G were developed. In the course of evaluating the test results, several minor programming errors and poor approximations were identified in the model. These errors were corrected in the simulation cases in Chapter 3 through 6 and the PRBS cases in this chapter; however, the closed loop experimental results presented

in this chapter dissertation are not repeated with the corrected model owing to the difficulty of re-assembling the experimental system.

The effect of the modeling errors on control is assessed in the APPENDIX N. The assessment is a test in which the measured data from the closed loop transient are processed by the final corrected MPC algorithm to compute the output that the corrected outputs. The demands which are computed from the corrected MPC design model are compared to the demands from control algorithm actually used in the experiment. The computation shows that the differences between the experimental and corrected MPC demands, while significant, are not so severe as to bring the fairly modest conclusions about the experimental results into doubt. The control performance is certainly improved by greater fidelity, but at the available speed of the experimental system, no strong conclusions from the experimental results about the invention are possible. The goal of the experimental testing is to verify that the actuator behaves as expected in this experimental system. The conclusion can be drawn based on the group of results despite the modeling errors. The model and controls behave as expected and the results and programming developed here can be used as the basis for future research using faster hardware to provide a more conclusive statement about the actuator performance. The open loop experiments, in which modeling errors have been corrected, show that the corrected model is sufficiently accurate that simulated results of the multi-coil using a faster time step are reasonable predictions of future experiments with a faster computer system. The modeling errors actually give an inadvertent benefit. The results with a known error in the model show that the control algorithm is robust to a certain class of

modeling errors. The optimization is affected by the modeling error, but the solution remains stable and continues to provide effective, if suboptimal, control.

The model data are plotted in a group of three figures for each transient. The first and second are line plots that show the terms in the cost function for the control error and the control effort. The performance index in the MPC optimization combines the square of the difference between the reference trajectory and the measured displacement, $(r-y)^2$ which represents the control error and the power demand, $|\mathbf{u}|^2 / n_u$ which represents the control effort.

The first plot in each set is the reference trajectory plot that shows the input reference signal, *r*, and the actuator's displacement response, *y*. The time delay in the measured displacement is removed by shifting the measured data by the computational delay so that the outputs to line up with actual time at which they were recorded. For comparison, the corresponding experimental results from the open loop case are also shown on the reference trajectory. The open loop case for the experiment uses the reference trajectory as the input to each coil,

$$u_{open,j}(t_i) = r(t_i), \tag{7.1}$$

causing all coils to operate in unison. The open loop case simulates a single coil actuator without any compensation. This is slightly different than the single coil with compensation presented in Chapter 6 for comparison.

The second plot compares the power from closed and open loop cases. The power term is actually the demand for power computed from the current demand as $|\mathbf{u}|^2 / n_u$ where $\mathbf{u}$ is the dimensionless demand and $n_u$ is the number of coils. The demand

for power differs from the actual power delivered by the amplifier output to the actuator by the delay contributed by the amplifier.

The open loop power in the same figure is numerically equal to $r^2$. By Eq. (7.1), the power for the open loop can be calculated as the following.

$$\left|\mathbf{u}_{open}\right|^2 / n_u = r^2 . \tag{7.2}$$

This value is plotted on the power plot for comparison.

The third plot in the set of experimental results for each transient is the three dimensional current demand plots for the closed loop cases. The plot shows current demand versus coil index and time for the transient. The current demand plot for the MPC algorithm illustrates how the optimization distributes the current in space to minimize the power and reference tracking error. The three dimensional plot gives a visualization of the spatial distribution effects resulting from the multi-coil actuator.

**Discussion of the step change transient**

The experimental step change event provides the same type of information about multi-coil actuator performance as the transient with faster time step, $T_s = 2\times10^{-6}$, in Figure 6.4 through Figure 6.15. Predicted results for the slower time step are given in Figure K.7 through Figure K.15.

The actuator's reference tracking is shown in Figure 7.8. The magnitude of the displacement is slightly different between the open loop and closed loop response. The difference is a consequence of the calibration of the experiment and the steady state offset that occurs with proportional control. Because of the filtered displacement measurement, the integral error cannot be used to correct for the offset. The shape of the response other

than amplitude is almost the same for open and closed loop in both speed and settling time.

The power consumed is shown in Figure 7.9. The power of the closed loop settles out at a lower value because of the steady state offset inherent in proportional control. The power to hold the displacement at the lower value is correspondingly less. The power plot indicates one slight advantage for the multi-coil design. The rate of change of power is less. The current demand for the multi-coil actuator changes more gradually which is less demanding on the amplifiers.

The three dimensional plot of the current demand is shown in Figure 7.10. The MPC algorithm using a time step of $T_s = 70\times10^{-6}$ does not produce the zig-zag pattern of current demand leading up to the step change that characterizes the simulated cases at faster time step, $T_s = 2\times10^{-6}$, in Figure 6.24. This distinctive zig-zag feature of the control algorithm is the clearest evidence of how the multi-coil actuator achieves its enhanced performance. The behavior is not possible in the slower case because the time step for the experiment is almost as long as the time for a pulse to travel from one end of the actuator to the other. However, the distribution of input energy shifts subtly from one end of actuator to the other to optimize total power for the transient in a profile that is shaped like the second spatial mode for vibration. This behavior is evidence that the algorithm continue to seek an optimum current distribution despite the increase in time step.

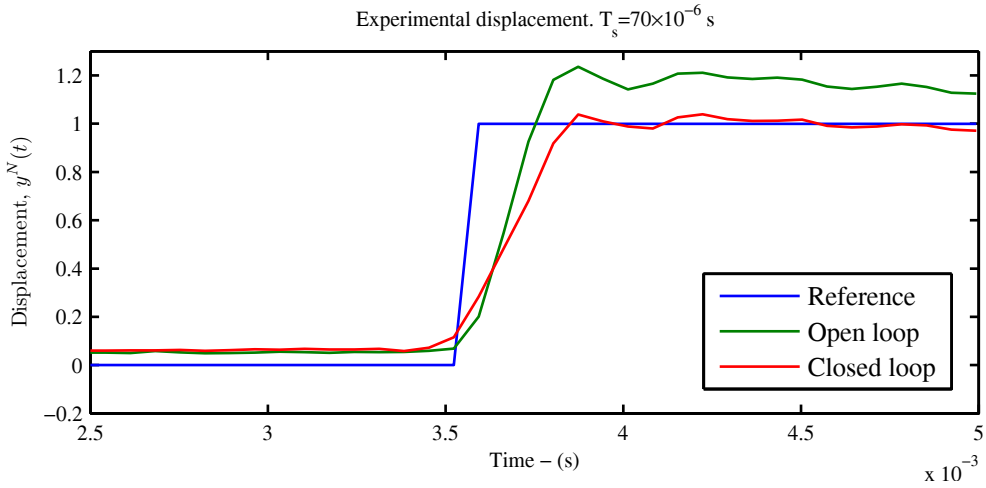


Figure 7.8: Open and closed loop response of displacement on step change transient for prototype actuator

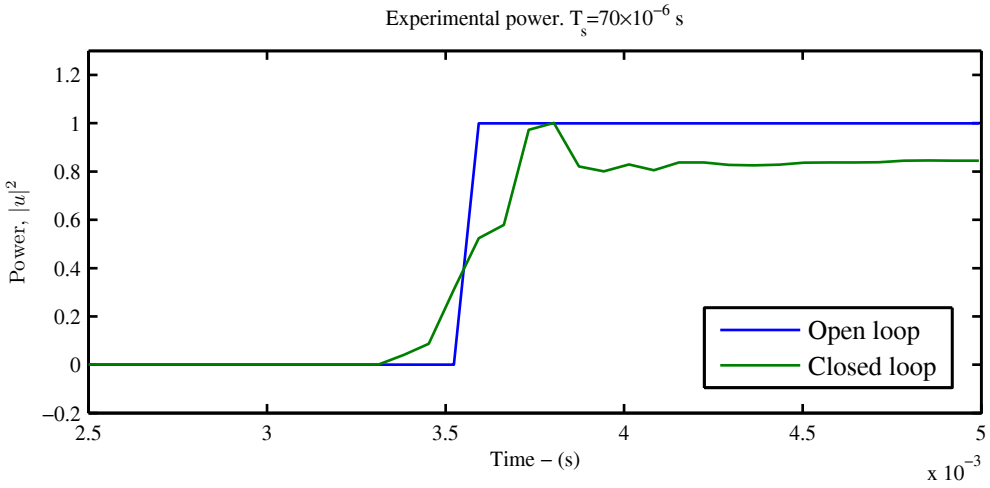


Figure 7.9: Open and closed loop response of power on step change transient for prototype actuator

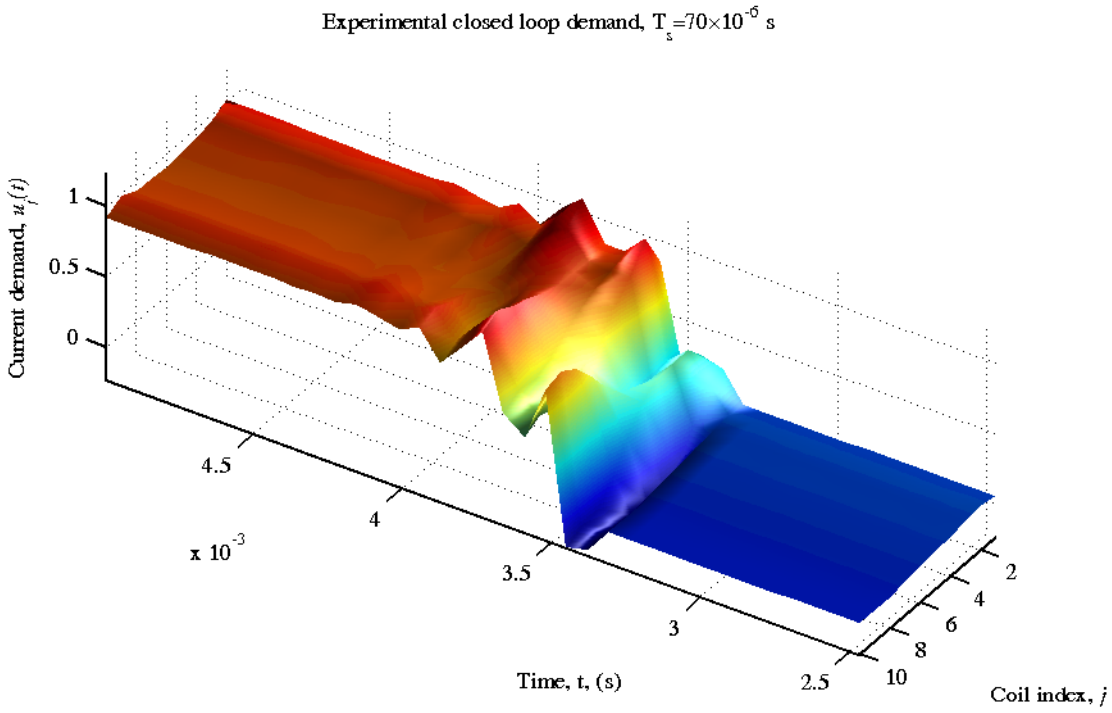


Figure 7.10: Closed loop current demand versus coil index and time on step change transient

**Discussion of the three square pulse transient**

The three square pulse transient is presented in Figure 7.11, Figure 7.12, and Figure 7.13. The simulated results for the same transient executed with faster time step are given in Figure 6.9 through Figure 6.12. The predicted results for the actuator response at the same slower time step are given in Figure K.10 through Figure K.12.

The open loop displacement in Figure 7.11 is significantly larger than the closed loop. At the same time, the power in Figure 7.12 shows that the power consumed by the open loop is correspondingly higher. The MPC finds an optimum that uses less power but accepts a larger control error. This effect is a consequence of the weight factors that sacrifice tracking accuracy for stability. The error in the model used for the MPC design discussed in APPENDIX N may also contribute to the diminished experimental response. The predicted response for the same transient in APPENDIX K shows considerably larger amplitude response for the closed loop control. The control algorithm in the experimental system is designed with a modeling error that underpredicts magnetic drag. The current demand produced by the experimental system is therefore smaller than needed to overcome the actual drag. The result is the lower amplitude displacement shown in the figure.

The open loop experimental results for displacement in Figure 7.11 and corresponding predicted open loop using the corrected model in Figure K.10 provide a useful validation of the model. The experimental and predicted displacements are remarkably close. The predicted response for displacement in the closed loop in Figure K.10 is considerably higher in amplitude than the closed loop displacement in the experimental results in Figure 7.11. It is believed that repeating the control experiment

with the corrected the control model would yield higher amplitude displacement response like the predictions.

The three dimensional current demand in Figure 7.13 shows the same shifting of current from one end of the actuator to the other that is seen in the step change transient. The results are very similar in overall shape to the predicted current demand as well. The general agreement in the current demand suggests that the programming of the algorithm is correct and only a correction of the actuator modeling matrices is needed for closer comparison.

**Three square pulses**

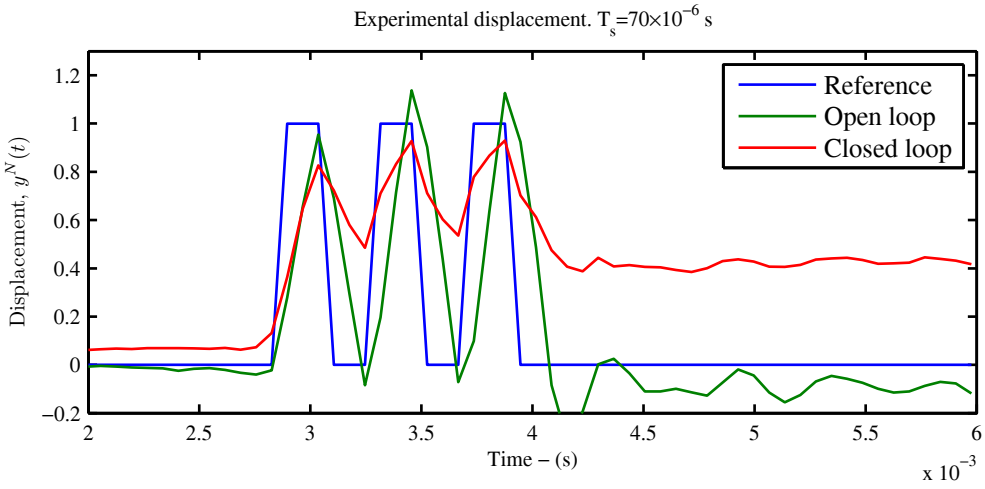


Figure 7.11: Open and closed loop response of displacement on three square pulses for prototype actuator

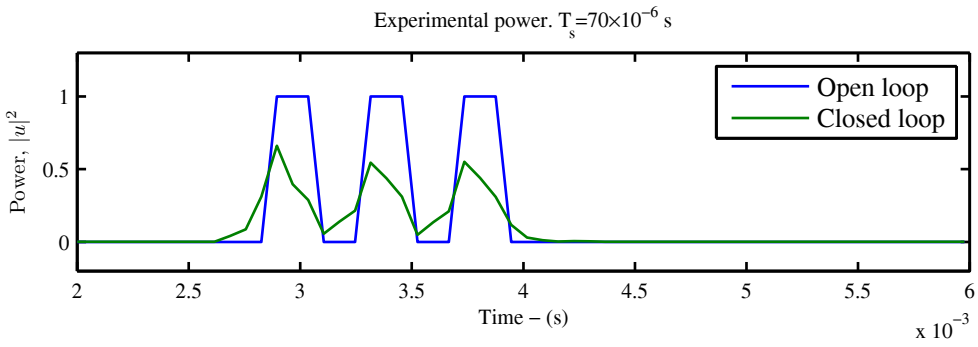


Figure 7.12: Open and closed loop response of power on three square pulses for prototype actuator

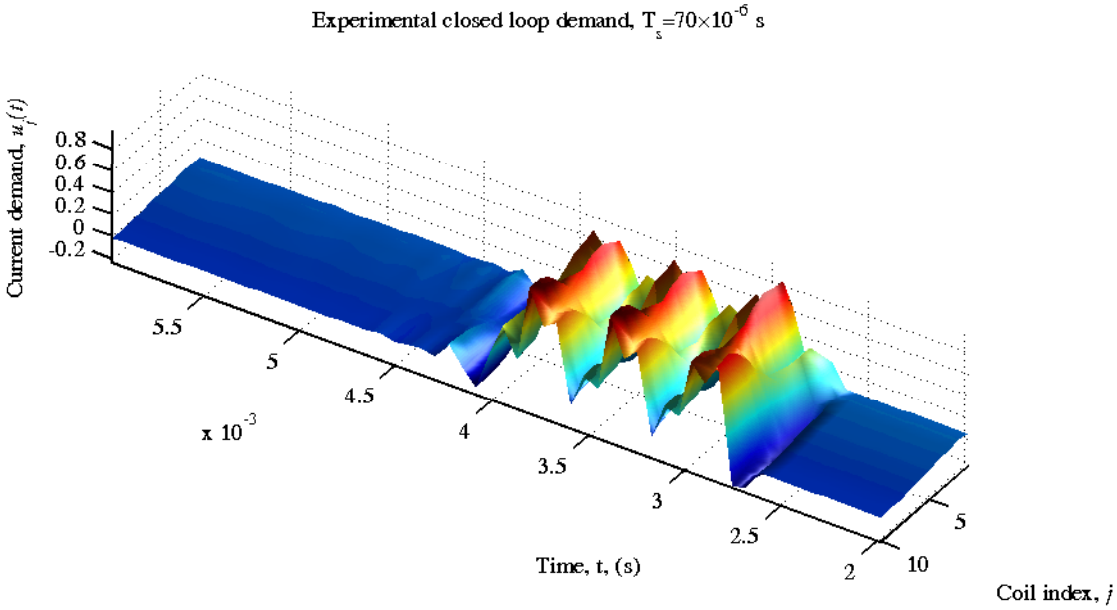


Figure 7.13: Closed loop current demand versus coil index and time on three square pulse

**Discussion of the experimental swept frequency transient**

The range of frequencies in the swept frequency transient in Figure 7.14, Figure 7.15, and Figure 7.16 is less than range in the corresponding transient for the fast time stsep transient in Figure 6.28, Figure 6.29, and Figure 6.30 because of the slower time step. The swept frequency reference trajectory is constructed so that the frequency goes from $\Omega = 200$ Hz to $\Omega = \frac{1}{4T_s} = 3571$ Hz over a time span of 0.012 seconds. The swept frequency transient for the fast time step simulation ranges from 0 to 10,000 Hz in a transient lasting 0.0022 seconds. The upper end of the frequency range in the experimental transient is half the Nyquist frequency which is the maximum frequency that can be reached. The data in the reference signal exhibit a deterioration of the representation of the sinusoidal shape at the upper limit of the discrete sampling frequency range. The purpose of the transient is to provide a strenuous test for the actuator that simulates a wide frequency range. No particular attention is given to the lack of a sinusoidal shape at the upper frequency end. Both the prediction with slow time step in Figure K.13, Figure K.14, and Figure K.15 and the experiment in Figure 7.14, Figure 7.15, and Figure 7.16 are given the same stimulus so the experimental and predicted results are comparable.

The swept frequency transient offers evidence that a faster experimental system would be able to take full advantage of the benefit of the multi-coil actuator shown in Chapter 6 with the faster time step. The amplitude of the closed loop displacement, although less than the reference, is nearly constant from the beginning of the transient to the end. The upper end of frequency at 3571 Hz is well beyond the first resonance at 2747 Hz. The amplitude of the open loop response goes nearly to zero at the upper end

of frequency. The distribution of current to the coils successfully overcomes the high frequency attenuation that reduces the amplitude of the open loop response.

The three dimensional plot of current demand in Figure 7.16 shows that the spatial distribution of demand approaches the shape of the second mode of vibration at the upper end of the frequency range. This spatial distribution is the same shape seen in the fast time step results at comparable frequency.

The results of the swept frequency transient are very encouraging that the performance of the actuator could achieve the high frequency goals of the design if the sampling time were sufficiently fast.

**Swept Frequency**

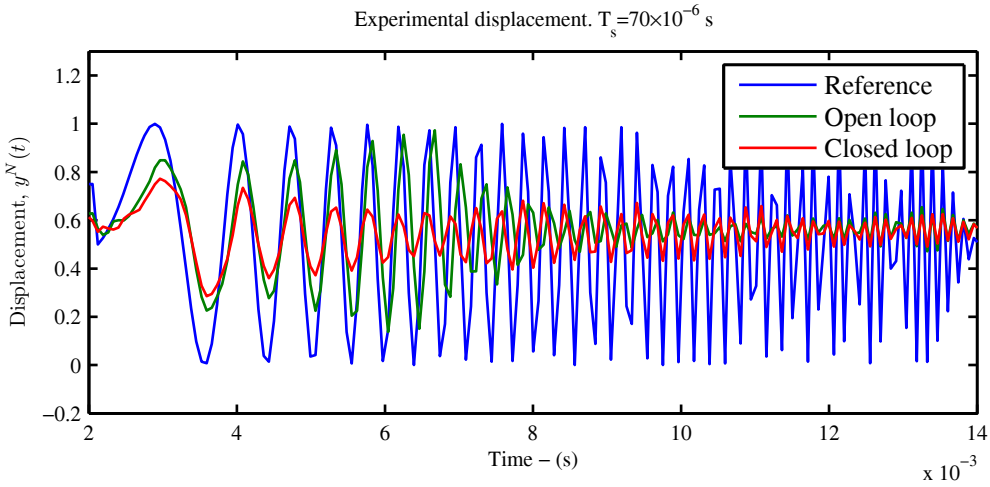


Figure 7.14: Open and closed loop response of displacement on swept frequency transient for prototype actuator

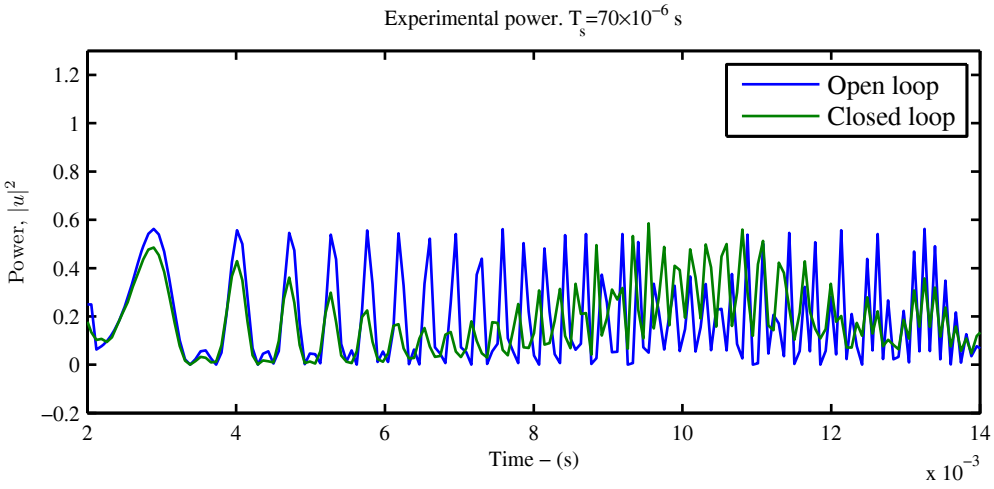


Figure 7.15: Open and closed loop response of power on swept frequency transient for prototype actuator

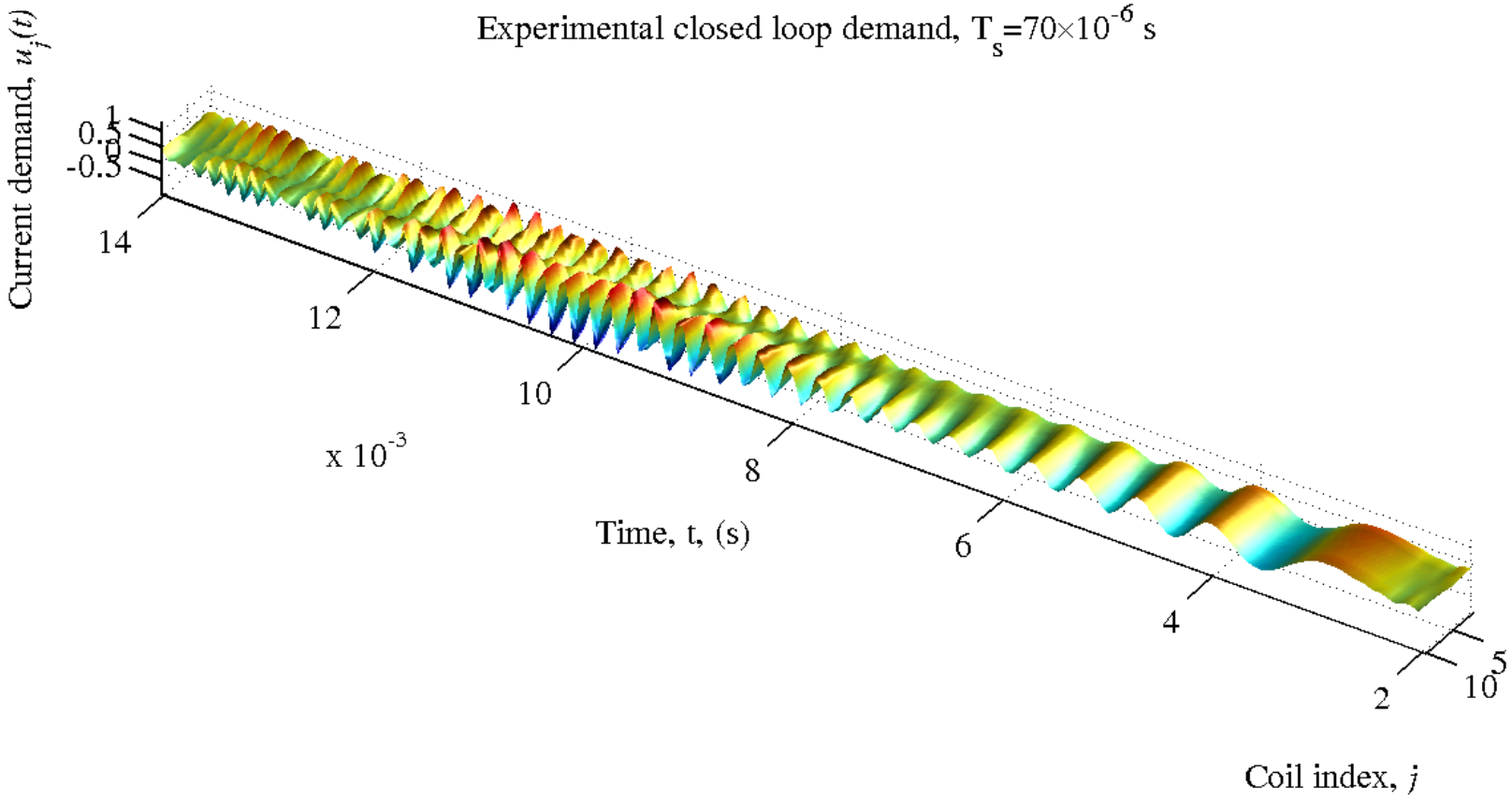


Figure 7.16: Current demand versus coil index and time for closed loop system on swept frequency transient

## Summary of the Experimental Results

The experimental results produce three main findings. First, the modeling is validated. The developed model of the actuator and controls reproduces the dynamic performance in the prototype actuator system. The agreement between experiments in this chapter and predictions in both open loop and closed loop operation gives considerable confidence that the greater performance improvements predicted with a faster time step can be realized with faster computer hardware. The approximations in the model, such as linearizing the magnetostriction process, approximating the eddy current field as homogeneous on the rod boundary, and modeling the amplifier as a linear feedback device, are also validated. No significant unmodeled dynamics are encountered.

Second, the experimental multi-coil prototype reduces power and/or improves tracking as specified in the performance index. The magnitude of the improvement in the multi-coil actuator at the experimental time step is predictably modest, but the optimum sought by the MPC algorithm does not vanish. The benefits of the MPC optimization gradually degenerate as the time step increases. The control then approaches the same control that one would get with a single coil. No numerical problems are encountered in the calculating the control matrices for the algorithm or in calculating the stable closed loop demands in the real-time experiment on the control computer.

Third, the control algorithm can be implemented successfully in a digital computer and executed in real time. The experiment quantifies the maximum performance for sampling data and computing the algorithm on the prototype system's hardware. The performance of the control hardware shows what components need to be

upgraded for a more complete test of the actuator. Based on the timing of the control program calculation and the sampling rate of the data acquisition system in the experiment, a revised experiment can be designed with very precise specification of the performance of the amplifiers, computer, and data acquisition hardware. As an added benefit, the experiment also forces the research to address the problems of model reduction, measurement delay, and state estimation to produce a workable control algorithm. The experiment shows that these features can be added to the MPC algorithm without affecting the performance of the multi-coil actuator.

# CHAPTER 8

# CONCLUSIONS

This research investigates whether a multi-coil magnetostrictive actuator offers a significant advantage in speed over a conventional single coil actuator. The result of the study shows that an optimally controlled multi-coil actuator is a more efficient linear motor and is capable of tracking a rapidly changing reference signal more closely while using less power than a single coil actuator. For example, in a numerical simulation of a step change transient, the multi-coil actuator responds three times faster than a comparably tuned single coil while using less than half the peak power. Similar results are obtained for a three pulse transient simulating a multi-pulse fuel injection. A swept frequency transient shows that the multi-coil actuator responds with more than 60% of full amplitude from 0 to 10,000 Hz. The amplitude of the single coil actuator is the same as the multi-coil at 0 Hz but progressively less as frequency increases. Above 7000 Hz, the amplitude of the single coil response is less than 10%. Visualizations of the control input on the example transients using three dimensional plots present the results in a form that leads to an understanding of how the distributions of input over space and time along the rod can lead to a more efficient actuator design. The plots show that the inputs to individual coils can be timed to account for the acoustic propagation delay between input and output and thus give an optimum response.

The contributions of the thesis are the prototype of the multi-coil actuator with design features to minimize eddy current, a mathematical model that couples the effects of vibration, eddy current, and coil current, an optimal control algorithm based on model

predictive control strategy, and experimental system to verify the modeling and control. The modeling results presented as time and frequency domain simulations provide an understandings the physics of the process and give confidence that the model produces reasonable results. The modeling and controls are presented with the details of the derivations so that the future research can build upon this work. The model derivations are also verified extensively using mathematical tests of the solutions that have been developed as part of the research.

Investigating the multi-coil actuator has led to advances in modeling techniques for magnetostrictive actuators. As in many engineering problems, the important dynamics cannot be isolated in a single equation or physical phenomenon. The overall process of the magnetostrictive actuator involves coupled systems for the vibration, eddy current and coil currents. All of these processes have significant effects on the actuator dynamics within the time scale for high speed actuation. The model development shows how the coupling coefficients between the processes can be developed from a first principles derivation starting from the fundamental laws of physics and using the constitutive equations of magnetostriction. The solutions to the vibration and magnetics equations give formulae for the coupling coefficients that are integrals of products of mode functions. The integrals can be evaluated numerically or analytically for the state space model. The coil current model makes an innovative use of a two-dimensional finite element magnetic modeling code (FEMM) of the multi-coil actuator to obtain the steady state magnetic field distribution of the coils. FEMM's detailed representation of the actuator geometry and materials gives the coil field a much greater fidelity than would be available if the coil field were solved with the simplified geometry that can be

handled analytically. The magnetic field distributions, represented as tabular functions of coil index and position, are used in calculating the coupling coefficients between the three models. The analytical formulation using one-dimensional modal functions to represent the vibration and three dimensional modal functions for the magnetic field of the eddy current leads to a compact solution of the modeling problem which in turn is essential to solve the optimal control problem numerically. The state space model having a total of forty state variables is shown to provide adequate accuracy for the control study. The forty state model contains twenty states associated with vibration modes, ten states for eddy current modes, and ten states representing coil current. The order of the model is sufficiently low and the mathematical properties of the resulting state space matrices are sufficiently well-conditioned that the control calculations present no numerical problems.

The model development and open loop transients using the model are the basis for understanding the efficiency advantage of the multi-coil actuator. Simulations in the time and frequency domain using the vibration model, both as stand alone simulation and combined with the eddy current and coil current models, lead to an understanding of the acoustic propagation effect that underlies the advantage of the multi-coil actuator. Energy added to the vibration process by coil current must propagate from the coil to the tip at the sound of speed in the actuator. The time delay between energy input and its effect on displacement must be accounted for in the control system algorithm. Similarly, the frequency response results illustrate that the actuator's response to different coils can be out of phase with one another because of the propagation delay effect. The input energy is lost if the wave generated by one coil cancels the wave by another coil. The

cancellation mechanism for energy loss is the property of the actuator that can be overcome by multiple coils. Energy from each coil can be timed so that its effect is a maximum to achieve the desire response and does not cancel the energy from other coils.

The full system model combining vibration, eddy current, and coil current models shows the significance of the eddy current and coil current as loss mechanisms. The eddy current draws energy from the vibration model and coil model through induction and dissipates that energy rapidly in ohmic losses. The simulations that combine the eddy current with vibration show that high frequency response is greatly attenuated by the magnetic drag of eddy currents. The coil currents have a similar magnetic drag effect. The current induced by other coils and by vibration in the rod is lost in that circuit's resistance. The simulations of the step change and frequency response show that magnitude of the loss mechanism at high frequency for the coil circuit's drag effect is on the same order of magnitude as the eddy current loss. For example, the amplitude (normalized to unit gain) at the first resonant peak drops from 0.65 for the vibration alone case to 0.45 for the vibration plus eddy current to 0.22 for vibration, eddy current, and coil current models. The combined system simulations demonstrate that the eddy current and coil current dynamics cannot be neglected in designing a control algorithm. The combined process simulation also suggests that very high frequency response (e.g., above 10,000 Hz) is not possible with the prototype actuator, but an actuator that is designed with more segments of lamination or perhaps as a wound tape of magnetostrictive material could achieve even faster response than the prototype results presented in this study.

The major approximations in the model are the linearization of constitutive equations of magnetostriction and approximation the boundary condition of eddy current field on the surface of the rod as homogeneous. Both of these approximations greatly simplify the model and are shown to be valid for this initial study. Further refinement of the model with more exact approximations is possible. For example, the Preisach operator method of modeling hysteresis can be added to the simulation. This type of nonlinear model has been successfully applied to lumped models of magnetics and control. By adding spatial dependence to the operator, the technique could be applied to the multi-coil actuator model. The difficulty of the Preisach model of hysteresis is the problem of nonlinear control of the resulting actuator model. The second major approximation in the model is the homogeneous boundary condition for the eddy current model which accounts for perhaps 10% error in the magnetic field under worst conditions. The error can be made much smaller by applying the homogeneous boundary condition approximation at the outer surface of the flux return path rather than on the surface of the actuator rod. The magnetic field is much lower at this boundary because most of the magnetic flux is contained with the return path. By neglecting a boundary term that is much smaller, the magnetic field in the interior of the rod is subject to smaller error giving a much more accurate approximation to the overall magnetic field. The difficulty in extending the region of solution to include the coil and return path is that the modal functions are multi-region functions and thus are much more complicated algebraically.

The main objective of the research is to show that a multi-coil actuator, if optimally controlled, can achieve a significant improvement over a single coil actuator.

The second half of the research problem is to use the mathematical model of the actuator in a model-based control strategy to determine whether additional coils provide any significant advantage. The control problem is a tracking problem in which the objective is to find the coil current demand that causes the displacement to follow a reference trajectory. The multi-coil actuator control problem is somewhat unusual since it involves multiple inputs controlling a single variable to a reference condition. This underdetermined situation, called spare degrees of freedom, gains its advantage over a system with equal number of inputs and outputs by distributing the spare inputs so that some additional parameter of the system is optimized. To show how the spare degrees of freedom works to make a multi-coil actuator track more closely or use less power than a single coil, a derivation is offered in this dissertation for an optimization of the actuator response in the frequency domain. The problem is to find the current distribution among the coils that causes the displacement to track a sinusoidal reference signal exactly while the sum of squares of current demand is a minimum. The solution of the optimization problem illustrates the advantage of the multi-coil actuator. The phase of the optimum current for each coil with respect to the reference turns out to be the negative of the phase between the displacement and the coil current demand. In other words, the optimal coil current demand must lead the reference by the same amount of time that the displacement lags the coil current demand. The net phase from reference demand to displacement is then zero. The amplitude of the optimum demand is the reciprocal of the amplitude of the transfer function between displacement and current. In other words, if the output response to a particular coil is less than the average of all coils (at a given frequency), the optimum current demand to that coil is proportionately less. For comparison, the ratio of

power consumed by an optimally controlled multi-coil actuator and the power of a single coil actuator tracking the same sinusoidal reference signal is calculated. The results show that ten to 100 times more power is consumed by the single coil actuator than the multi-coil in the frequency range from the resonance to 10,000 Hz. This calculation shows the theoretical maximum efficiency of the multi-coil design relative to the single coil. The actual improvement that can be realized in the time domain control is less because of finite sample time and because the exact tracking assumed in the frequency domain optimization turns out to be very sensitive to noise. The actual optimal control problem in the time domain is solved by the model predictive control for a discrete time model of the actuator in the research also.

A model predictive control algorithm is developed to realize a practical control system that takes advantage of the multi-coil actuator. The predictive aspect of the model predictive control allows the algorithm to look ahead to the future reference trajectory and anticipate the current control demand that optimizes the future response. The predictive aspect of the control compensates for the acoustic wave transport delay between the coil inputs and the displacement. The optimized control design puts energy into the rod's vibrational model in advance of a change in the reference position so that the resulting displacement arrives at the time required by the reference trajectory. Simulated transients using a computation time step that is small compared to the acoustic propagation time show the advantage of the multi-coil actuator on a range of transients including step change, three square pulses, and swept frequency. The simulated transients show an order of magnitude better power, voltage, and reference tracking with the multi-coil actuator than a single coil actuator with similarly tuned predictive control.

The current and voltage for the multi-coil device are feasible for conventional amplifiers, whereas the current and voltage for the single coil case are not.

One of the incidental contributions of this research is a modification of conventional model predictive control to accommodate the spare degrees of freedom situation. The modification is to use actuator input demand, proportional control error and integral control in the quadratic performance index that is optimized over the prediction horizon. (In contrast, the conventional model predictive control uses the change in input demand and proportional error.) The resulting control law for the modified performance index is a proportional gain matrix that is no more difficult than the conventional control law for implementation in the real time control algorithm. The model predictive control algorithm for the multi-coil actuator is a matrix multiplication that can computed at the high speed needed to demonstrate the actuator performance. The modified model predictive control algorithm is a general result that is applicable to any control application with spare degrees of freedom.

A prototype actuator was designed and built for this research and an experimental system assembled to test the concept. The experimental system for the actuator research consists of a prototype multi-coil actuator, the electronics to power the multiple, and a digital control system for computing the real-time control program and logging the experimental data. The design of the prototype multi-coil actuator is presented as part of this research. The prototype includes ten coils arranged axially in a modified version of a commercial magnetostrictive actuator. The prototype actuator differs from commercial actuators because of design features to reduce eddy currents that would otherwise prevent the actuator from achieving the desired frequency response. The innovative features

include laminating the actuator rod in four, quadrant-shaped cylinders and the use of low conductivity materials. The other major components in the experimental system are commercial items that were either available in laboratory resources or purchased for this project.

The experimental system is limited by its sampling speed in demonstrating the high speed actuator performance. The control system is limited to a time step greater than 70 μs by the settling time of the analog to digital conversion of the digital input board. This time step is approximately ten times greater than the time for a pulse to travel through a single coil. Consequently, the experimental system cannot input current demands to individual controls with the time differences that provide the improvement. Despite the time step limitation of the hardware, the experimental results provide a valid, if limited, verification of the simulation results. The experimental results confirm the modeling and controls and provide assurance that the simulated results using a faster time step are an accurate prediction of the performance that can be achieved with a faster control system.

The experimental system is used to confirm the modeling in both open loop and closed loop experiments. The stimulus for the open loop is a pseudo-random binary sequence as the current demand at the amplifier. This pseudorandom input is a stringent test that exercises the full frequency response of the actuator model within the limitations of the sampling time. The comparison, presented without tuning the input data to improve the match, confirms that the model is satisfactory. The comparison between model and data can be improved in future work by applying techniques of system

identification to fit the parameters of the model such as the constants of the magnetostrictive constitutive equations and amplifier gains to the experimental data.

Some additional features of control need to be developed for the closed-loop, real-time experiment. The control algorithm for the real-time experiment includes model reduction to reduce computation time, adds a Kalman state estimator to predict the full state of the actuator from the measured variables, and develops a new type of Smith predictor to correct for digital time delay. The Smith predictor formulation in conjunction with model predictive control is an original contribution that has not been reported previously. The real-time control algorithm with the added features is simulated numerically at the fast time step needed to show that the advantage of the control algorithm is not compromised by the additional features of the real-time control program. The control program and simulated plant are also executed at the time step of the experimental system to predict results for the experiment.

The experimental tests of the multi-coil actuator confirm the modeling, show that the model predictive control with proportional and integral error and other features developed in this research can be implemented in a real-time control system, and demonstrate the advantage, insofar, as possible with the available sampling time, that a multi-coil actuator reduces power and/or improves the reference tracking capability of the actuator. The agreement between experiments and predictions in both open loop and closed loop operation gives confidence that the greater performance improvements predicted with a faster time step can be realized with faster experimental hardware. The magnitude of the improvement in the multi-coil actuator at the experimental time step is predictably modest, but the optimum sought by the model predictive control algorithm

does not vanish. The benefits of the model predictive control optimization degenerate gracefully as time step increases. The multi-coil control response approaches the same control that one would get with a single coil. The experiment quantifies the performance of a real-time system for sampling data and computing the algorithm. The performance of the control hardware shows what components need to be upgraded for a more complete test of the multi-coil actuator performance. The timing on this experimental system can be extrapolated to the sampling rates and processor speed needed in future tests to demonstrate the predicted performance enhancement that the multi-coil actuator offers.

# A MULTI-COIL MAGNETOSTRICTIVE ACTUATOR: DESIGN, ANALYSIS, AND EXPERIMENT

## VOLUME III

by

Thomas L. Wilson, Jr.

# APPENDIX A

# MAGNETOSTRICTIVE CONSTITUTIVE EQUATIONS TESTING

One of the convenient mathematical properties of the matrix form of the magnetostrictive constitutive relationships is that many identities can be found that allow the original nine element linear constitutive relations and the various manipulated versions to be compared with each other to check the algebra.

### Matrix transformation test

A simple test for the derived magnetostrictive matrices, $\mathbf{Y}^{\mathbf{H}}$, $\boldsymbol{\kappa}$, and $\boldsymbol{\mu}^{\mathbf{S}}$, in comparison to the original nine component matrices, $\mathbf{s}^{\mathbf{H}}$, $\mathbf{d}$, and $\boldsymbol{\mu}^{\mathbf{T}}$ can be constructed by closing the algebraic loop back to the starting point.

$$\begin{aligned} \mathbf{B} &= \boldsymbol{\kappa}'\mathbf{S} + \boldsymbol{\mu}^{\mathbf{S}}\mathbf{H}, \\ \mathbf{T} &= \mathbf{Y}^{\mathbf{H}}\mathbf{S} - \boldsymbol{\kappa}\mathbf{H}. \end{aligned} \tag{A.1}$$

Consider a case with no external load, steady state, and a specified magnetic field. Since the problem is steady state, no unbalanced forces may act on the rod. The magnetostrictive forces balance the elastic forces at every point; hence, the stress everywhere must be zero, $\mathbf{T} = [0]$. From this condition, the equilibrium condition for the strain and magnetic field from Eq. (2.13) is obtained by inserting $\mathbf{T} = \mathbf{0}$ into the second relation in Eq. (A.1).

$$\begin{aligned} \mathbf{0} &= \mathbf{Y}^{\mathbf{H}}\mathbf{S} - \boldsymbol{\kappa}\mathbf{H}, \\ \mathbf{S} &= \left(\mathbf{Y}^{\mathbf{H}}\right)^{-1}\boldsymbol{\kappa}\mathbf{H}. \end{aligned} \tag{A.2}$$

Insert Eq. (A.2) into the top equation of the magnetostrictive relations in Eq. (A.1).

$$\begin{aligned}\mathbf{B} &= \boldsymbol{\kappa}'\left(\mathbf{Y}^{\mathbf{H}}\right)^{-1}\boldsymbol{\kappa}\mathbf{H} + \boldsymbol{\mu}^{\mathbf{S}}\mathbf{H} \\ &= \left[\boldsymbol{\kappa}'\left(\mathbf{Y}^{\mathbf{H}}\right)^{-1}\boldsymbol{\kappa} + \boldsymbol{\mu}^{\mathbf{S}}\right]\mathbf{H}.\end{aligned} \tag{A.3}$$

From the definition of $\boldsymbol{\kappa}$ in Eq. (2.18),

$$\mathbf{S} = \mathbf{d}\cdot\mathbf{H}. \tag{A.4}$$

Insert $\mathbf{T} = [0]$ into Eq. (2.13),

$$\begin{aligned}\mathbf{B} &= \mathbf{d}'[\mathbf{0}] + \boldsymbol{\mu}^{\mathbf{T}}\mathbf{H} \\ &= \boldsymbol{\mu}^{\mathbf{T}}\mathbf{H}.\end{aligned} \tag{A.5}$$

Equate Eq. (A.3) and Eq. (A.5),

$$\left[\boldsymbol{\kappa}'\left(\mathbf{Y}^{\mathbf{H}}\right)^{-1}\boldsymbol{\kappa} + \boldsymbol{\mu}^{\mathbf{S}}\right]\mathbf{H} = \boldsymbol{\mu}^{\mathbf{T}}\mathbf{H}. \tag{A.6}$$

Equation (A.6) gives the identity,

$$\left(\boldsymbol{\mu}^{\mathbf{T}}\right)^{-1}\left[\boldsymbol{\kappa}'\left(\mathbf{Y}^{\mathbf{H}}\right)^{-1}\boldsymbol{\kappa} + \boldsymbol{\mu}^{\mathbf{S}}\right]\mathbf{H} = \mathbf{I}. \tag{A.7}$$

This result brings the equation back to the starting point and provides a quick numerical check of the programming of the formulae in the MATLAB program for transforming the magnetostrictive relationships. The test can be applied to both the three-dimensional and the two dimensional constitutive equations. Data from Table 2.2 and Table 2.3 are evaluated using the identity matrix test. The MATLAB calculation gives the identity matrix to machine precision for both Table 2.2 and Table 2.3.

By analogous steps, the following identity should also hold.

$$\mathbf{I} = \left(\boldsymbol{\mu}^{\mathbf{S}}\right)^{-1}\left[\mathbf{-d}'\left(\mathbf{s}^{\mathbf{H}}\right)^{-1}\mathbf{d} + \boldsymbol{\mu}^{\mathbf{T}}\right]. \tag{A.8}$$

This test gives the identity matrix to machine accuracy for both three-dimensional and two dimensional cases.

**Constant volume test**

The validity of the approximation of constant volume used in reducing the constitutive relation for the vibration can be tested by applying an axial magnetic induction and evaluating the volume change. In this test, no external stress is applied. The approximation is valid if the volume is constant or nearly so. The first step is to define the volume change in terms of the components of strain.

The volume of an unperturbed volume element in Cartesian coordinates is

$$V = \Delta x \, \Delta y \, \Delta z \, . \tag{A.9}$$

The volume change under the six element stress and strain formulation in Cartesian coordinates can be computed as

$$\begin{aligned} V_p &= \left( \Delta x + \frac{\partial \zeta_x}{\partial x} \Delta x \right) \left( \Delta y + \frac{\partial \zeta_y}{\partial y} \Delta y \right) \left( \Delta z + \frac{\partial \zeta_z}{\partial z} \Delta z \right) \\ &= \left( 1 + \frac{\partial \zeta_x}{\partial x} \right) \left( 1 + \frac{\partial \zeta_y}{\partial y} \right) \left( 1 + \frac{\partial \zeta_z}{\partial z} \right) \Delta x \, \Delta y \, \Delta z \\ &= \left( 1 + S_1 \right) \left( 1 + S_2 \right) \left( 1 + S_3 \right) \Delta x \, \Delta y \, \Delta z. \end{aligned} \tag{A.10}$$

Taking the ratio of the volumes in Eq. (A.10) and (A.9) to eliminate $\Delta x \, \Delta y \, \Delta z$ makes the equation dimensionless.

$$\frac{V_p}{V} = \left( 1 + S_1 \right) \left( 1 + S_2 \right) \left( 1 + S_3 \right) . \tag{A.11}$$

The strains under the application of magnetic field can be evaluated numerically by Eq. (A.2) for any vector, **H**. A maximum magnetic field can be evaluated using the maximum current, $I_{max} = 2.25 \, \text{A}$, and number of turns in the coil, $T = 6614 \, \text{turns/m}$, which gives $H_z = T \cdot I_{max} = 14882 \, \text{A/m}$. Equations (A.2) and (A.11) can be evaluated using this maximum value of $H_z$ along with the data in Table 2.3 and Table 2.4. The

result for the strains and the volume ration are given in Table A.1 This test confirms that a maximum axial field results in negligible volume change, thus justifying the constant volume approximation.

Table A.1: Volume change for six element matrices for an applied magnetic field

| **H** [Amp/m] | $S_1$ | $S_2$ | $S_3$ | $V_p / V$ |
|---|---|---|---|---|
| $\begin{bmatrix} 0 \\ 0 \\ 14882 \end{bmatrix}$. | $-0.789\times10^{-4}$ | $-0.789\times10^{-4}$ | $0.1637\times10^{-3}$ | 1.000005933 |

The constant volume test can be applied in cylindrical coordinates also. The volume of a thin ring is given by

$$\begin{aligned} V &= \pi\left[\left(r+\Delta r\right)^2 - r^2\right]\Delta z \\ &= \pi\left[2r\Delta r + \Delta r^2\right]\Delta z \\ &= \pi\Delta r\left[2r+\Delta r\right]\Delta z. \end{aligned} \tag{A.12}$$

The perturbed volume is given by

$$\begin{aligned} V_p &= \pi\left[2\left(r+\zeta_r\right)\left(1+\frac{\partial\zeta_r}{\partial r}\right)\Delta r + \left(1+\frac{\partial\zeta_r}{\partial r}\right)^2\Delta r^2\right]\left(1+\frac{\partial\zeta_z}{\partial z}\right)\Delta z \\ &= \pi\left(1+\frac{\partial\zeta_r}{\partial r}\right)\Delta r\left[2\left(r+\zeta_r\right)+\left(1+\frac{\partial\zeta_r}{\partial r}\right)\Delta r\right]\left(1+\frac{\partial\zeta_z}{\partial z}\right)\Delta z. \end{aligned} \tag{A.13}$$

The uniform density approximation gives the following relationship.

$$\frac{\zeta_r}{r} = \frac{\partial\zeta_r}{\partial r}. \tag{A.14}$$

Thus, the term in square brackets in Eq. (A.13) can be written as

$$\left[2\left(r+\zeta_r\right)+\left(1+\frac{\partial\zeta_r}{\partial r}\right)\Delta r\right]=2\left(1+\frac{\partial\zeta_r}{\partial r}\right)r+\left(1+\frac{\partial\zeta_r}{\partial r}\right)\Delta r$$
$$=\left(1+\frac{\partial\zeta_r}{\partial r}\right)\left(2r+\Delta r\right). \tag{A.15}$$

Making this substitution into (A.13) gives

$$V_p=\pi\left(1+\frac{\partial\zeta_r}{\partial r}\right)^2\Delta r\left(2r+\Delta r\right)\left(1+\frac{\partial\zeta_z}{\partial z}\right)\Delta z$$
$$=\pi\Delta r\left(2r+\Delta r\right)\Delta z\left(1+\frac{\partial\zeta_r}{\partial r}\right)^2\left(1+\frac{\partial\zeta_z}{\partial z}\right) \tag{A.16}$$

Taking the ratio of $V_p/V$ gives

$$\frac{V_p}{V}=\frac{\pi\Delta r\left(2r+\Delta r\right)\Delta z\left(1+\frac{\partial\zeta_r}{\partial r}\right)^2\left(1+\frac{\partial\zeta_z}{\partial z}\right)}{\pi\Delta r\left(2r+\Delta r\right)\Delta z}$$
$$=\left(1+\frac{\partial\zeta_r}{\partial r}\right)^2\left(1+\frac{\partial\zeta_z}{\partial z}\right) \tag{A.17}$$

In terms of the strain elements, this ratio can be written as the following.

$$\frac{V_p}{V}=\left(1+S_{rr}\right)^2\left(1+S_{zz}\right) \tag{A.18}$$

From the orthotropic symmetry, the strains in all directions in the *x*-*y* plane are equal.

$$S_{rr}=S_1=S_2 \tag{A.19}$$

Hence, the constant volume test applied to the cylindrical version of the constitutive relations gives the same result as given in Table A.1.

The constant volume approximation in Chapter 2 gives a relationship between radial and axial strain in which the volume is constrained to be constant. The constraint is approximate because second order terms are neglected in Eq. (2.48). The validity of

this approximation can be assessed by inserting the strain relationships from Eq. (2.51) into Eq. (A.18).

$$\begin{aligned}\frac{V_p}{V} &= \left(1+S_{rr}\right)^2\left(1+S_{zz}\right) \\ &= \left(1-\frac{1}{2}S_{zz}\right)^2\left(1+S_{zz}\right) \\ &= 1-\frac{3}{4}S_{zz}{}^2+\frac{1}{4}S_{zz}{}^3\end{aligned} \tag{A.20}$$

The expression is accurate to first order as expected based on the approximation in Eq. (2.48). Inserting the numerical value, $S_{zz} = S_3 = 0.1637\times10^{-3}$, from Table A.1 gives the following estimate assessment of the accuracy of the constant volume expression with second order effects.

$$\frac{V_p}{V} == 1-\frac{3}{4}\left(0.1637\times10^{-3}\right)^2+\frac{1}{4}\left(0.1637\times10^{-3}\right)^3 = 0.9999999953 \tag{A.21}$$

# APPENDIX B

# SOLUTION OF THE VIBRATION PROBLEM BY INTEGRAL TRANSFORM

This appendix gives the solution to the damped wave equation by the integral transform method. The coefficients that couple the vibration model to the magnetics model and the coil circuit model are computed. Test calculations are also shown to verify the derivations and coding.

The derivation finds a solution for the displacement of the rod from a neutral position using the product of orthogonal spatial functions and time dependent amplitude functions. The amplitude functions become the state space variables of the state space model.

The governing equation and boundary conditions are derived in the main text as a damped wave equation with a distributed source.

Governing equation

$$\frac{\partial^2 x^N}{\partial \xi^2} - \left(\frac{\pi}{2\omega_1}\right)^2 \left(\frac{\partial^2 x^N}{\partial t^2} + 2\lambda\omega_1 \frac{\partial x^N}{\partial t}\right) = \frac{\partial h}{\partial \xi}. \tag{B.1}$$

Boundary conditions

$$\begin{aligned} x^N(0,t) &= 0, \\ \frac{\partial x^N(1,t)}{\partial \xi} &= h(1,t). \end{aligned} \tag{B.2}$$

Initial conditions

$$x^N(\xi,0)=0,$$
$$\frac{\partial x^N(\xi,0)}{\partial t}=0. \tag{B.3}$$

The integral transform method described by Özişik [27] can be applied to Eq. (3.25)to reduce the equation to an ordinary differential equation in time. The integral transform for $\xi$ is defined as the following.

$$\bar{x}_n^N(t)=\int_0^1 x^N(\xi,t)\,Z(\beta_n,\xi)\,d\xi. \tag{B.4}$$

The inverse transform is given by

$$x^N(\xi,t)=\sum_{n=1}^{\infty}\frac{Z(\beta_n,\xi)}{N(\beta_n)}\bar{x}_n^N(t). \tag{B.5}$$

The transform function, $Z(\beta_n,\xi)$, is the solution to the associated homogeneous ordinary differential equation and boundary conditions in which $\beta_n$ is a parameter.

$$\frac{d^2Z(\beta_n,\xi)}{d\xi^2}+\beta_n^2Z(\beta_n,\xi)=0\,. \tag{B.6}$$

$$Z(\beta_n)=0.$$
$$\frac{\partial Z(\beta_n,1)}{\partial\xi}=0. \tag{B.7}$$

The eigenfunctions and eigenvalues satisfy the differential equation and the boundary conditions

$$Z(\beta_n,\xi)=\sin(\beta_n\xi);\ \beta_n=\frac{(2n-1)\pi}{2};\ n=1,\ 2,\ 3,\ \ldots. \tag{B.8}$$

The normalization constant for $Z(\beta_n,\xi)$ is

$$N(\beta_n) = \int_0^1 \sin^2(\beta_n \xi) d\xi, \\ = \frac{1}{2}. \tag{B.9}$$

Applying the integral transform solution to each term reduces the problem to an ordinary, second-order differential equation in the transformed variable. The last term on the second and third lines arises as a consequence of the nonhomogeneous boundary condition term.

$$-\beta_n^2 \chi_n^N(t) - \left(\frac{\pi}{2\omega_1}\right)^2 \left(\ddot{\chi}_n^N(\beta_n, t) + 2\lambda\omega_1 \dot{\chi}_n^N(t)\right) \\ = \int_{\xi=0}^1 \left[\frac{\partial h(\xi,t)}{\partial \xi}\right] \sin(\beta_n \xi) d\xi + \sin(\beta_n \xi)\Big|_{\xi=1} h(1,t) \\ = \int_{\xi=0}^1 \left[\frac{\partial h(\xi,t)}{\partial \xi}\right] \sin(\beta_n \xi) d\xi + (-1)^{n-1} h(1,t). \tag{B.10}$$

Rearrange and simplify

$$\ddot{\chi}_n^N(t) + 2\lambda\omega_1 \dot{\chi}_n^N(t) + \left(\frac{2\omega_1 \beta_n}{\pi}\right)^2 \chi_n^N(t) \\ = \left(\frac{2\omega_1}{\pi}\right)^2 \left[-\int_{\xi=0}^1 \frac{\partial h(\xi,t)}{\partial \xi} \sin(\beta_n \xi) d\xi + (-1)^{n-1} h(1,t)\right]. \tag{B.11}$$

The integral on the right hand side involves results for $h(\xi.t)$ which are calculated using the FEMM code. For numerical accuracy of the integration, it is preferable not to differentiate the FEMM data before integrating. The integrand, $\frac{\partial h}{\partial \xi}\sin(\beta_n \xi)$, can be integrated by parts to recast the integral in terms of $h$.

$$\int_{\xi=0}^{1} \frac{\partial h(\xi,t)}{\partial \xi} \sin(\beta_n \xi)\, d\xi = h(\xi,t)\sin(\beta_n \xi)\Big|_{\xi=0}^{1} - \beta_n \int_{\xi=0}^{1} h(\xi,t)\cos(\beta_n \xi)\, d\xi$$
$$= (-1)^{n-1} h(1,t) - \beta_n \int_{\xi=0}^{1} h(\xi,t)\cos(\beta_n \xi)\, d\xi. \tag{B.12}$$

Substituting Eq. (B.12) into Eq. (B.11) gives the basic form of the transformed system. Conveniently, the boundary condition terms cancel.

$$\ddot{\chi}_n^N(t) + 2\lambda\omega_1 \dot{\chi}_n^N(t) + \left(\frac{2\omega_1 \beta_n}{\pi}\right)^2 \chi_n^N(t)$$
$$= \left(\frac{2\omega_1}{\pi}\right)^2 \beta_n \int_{\xi=0}^{1} h(\xi,t)\cos(\beta_n \xi)\, d\xi. \tag{B.13}$$

The modeling equation is neatly divided into the vibration model on the left and the coupling term on the right. The remaining work is to transform the right hand side into a summation consisting of fixed coefficients that depend only on the spatial distribution functions and the time-varying state variables from the magnetic and coil circuit models. The magnetic field distribution functions are obtained from the solution to the magnetic problem Appendix D. The axial component of field in the magnetic model is a function of all three spatial variables whereas the $h(\xi,t)$ function is just a function of the axial variable. The magnetic field is averaged over the rod cross section to reduce the dimensions. The magnetic field consists of the parts of field from true currents. It may be surprising that the strain does not appear on the right hand side. The field due to strain is incorporated into the equation by the definition of the magnetostrictive coefficients. If the constitutive relation had been formulated with magnetic induction as the input rather than field, the strain term would have appeared explicitly on the right hand side.

$$h(\xi,t) = h^H(\xi,t) + h^{FEMM}(\xi,t)$$
$$= \frac{2}{\phi_0}\int_{\rho=0}^{1}\int_{\phi=0}^{\phi_0}\left(x_H^M(\rho,\phi,\xi,t) + x^{FEMM}(\rho,\xi,t)\right)\rho d\phi d\rho \tag{B.14}$$

The integration for the radial average can be shown more clearly by performing the operations separately.

$$h^H(\xi,t) = \frac{2}{\phi_0}\int_{\rho=0}^{1}\int_{\phi=0}^{\phi_0} x_H^M(\rho,\phi,\xi,t)\,\rho d\phi d\rho$$
$$= \frac{2}{\phi_0}\int_{\rho=0}^{1}\int_{\phi=0}^{\phi_0}\left[\sum_{k=1}^{kmax}\sum_{m=1}^{mmax}\sum_{p=1}^{pmax}\chi_{k,m,p}^M(t)\frac{\sin(\gamma_m\phi)\mathrm{J}_{\gamma_m}(\varepsilon_{k,m}\rho)\sin(\eta_p\xi)}{N(\varepsilon_{k,m},\gamma_m)N(\gamma_m)N(\eta_p)}\right]\rho d\phi d\rho \tag{B.15}$$
$$= \sum_{p=1}^{pmax}\sin(\eta_p\xi)\left[\sum_{m=1}^{mmax}\sum_{k=1}^{kmax}\chi_{k,m,p}^M(t)\frac{2\int_{\phi=0}^{\phi_0}\sin(\gamma_m\phi)d\phi\int_{\rho=0}^{1}\mathrm{J}_{\gamma_m}(\varepsilon_{k,m}\rho)\rho d\rho}{\phi_0 N(\varepsilon_{k,m},\gamma_m)N(\gamma_m)N(\eta_p)}\right].$$

The integration of the radial and azimuthal terms and associated normalization factors yields a matrix of constants. A grouped constant, $P_{k,m}$, can be defined to hold the result. The radial and axial integrations can performed analytically, but the resulting formula includes a Bessel function that is not provided in the MATLAB library. The radial integration is performed by numerical quadrature rather than by the evaluation of the analytical solution.

$$P_{k,m} = \frac{4}{\phi_0\gamma_m}\frac{\int_{\rho=0}^{1}\mathrm{J}_{\gamma_m}(\varepsilon_{k,m}\rho)\rho d\rho}{N(\varepsilon_{k,m},\gamma_m)N(\gamma_m)N(\eta_p)}. \tag{B.16}$$

The simplified form of $h^H(\xi,t)$ can be written in terms of the array of constants

$$h^H(\xi,t) = \sum_{p=1}^{pmax}\left\{\left[\sum_{m=1}^{mmax}\sum_{k=1}^{kmax}\chi_{k,m,p}^M(t)P_{k,m}\right]\sin(\eta_p\xi)\right\}. \tag{B.17}$$

The transverse average of the FEMM term is also computed numerically from a table of magnetic field values computed by FEMM and stored.

$$
\begin{aligned}
h^{FEMM}(\xi,t) &= \frac{2}{\phi_0}\int_{\rho=0}^{1}\int_{\phi=0}^{\phi_0} x^{FEMM}(\rho,\xi,t)\rho d\phi d\rho \\
&= \frac{2}{\phi_0}\int_{\rho=0}^{1}\int_{\phi=0}^{\phi_0} \frac{1}{T}\sum_{j=1}^{jmax} H_{R,j}^{FEMM}\left(r_g\rho, z_L\xi\right) x_{K,j}\rho d\phi d\rho \\
&= \frac{2}{\phi_0}\sum_{j=1}^{jmax} x_j^K\left[\frac{1}{T}\int_{\rho=0}^{1}\int_{\phi=0}^{\phi_0} H_{R,j}^{FEMM}\left(r_g\rho,\, z_L\xi\right)\rho d\phi d\rho\right] \\
&= \frac{2}{\phi_0}\sum_{j=1}^{jmax} x_j^K\left[\frac{\phi_0}{T}\int_{\rho=0}^{1} H_{R,j}^{FEMM}\left(r_g\rho,\, z_L\xi\right)\rho d\rho\right] \\
&= \sum_{j=1}^{jmax} x_j^K\left[\frac{2}{T}\int_{\rho=0}^{1} H_{R,j}^{FEMM}\left(r_g\rho,\, z_L\xi\right)\rho d\rho\right].
\end{aligned}
\tag{B.18}
$$

The radial average of the flux due to the *j*-th coil is given by the following.

$$
\breve{x}_{R,j}^{FEMM}(\xi) = \frac{2}{T}\int_{\rho=0}^{1} H_{R,j}^{FEMM}\left(r_g\rho, z_L\xi\right)\rho d\rho. \tag{B.19}
$$

The notation for radial averaging is indicated by a *breve*, diacritical mark, "˘", superimposed on the variable. The average is computed numerically using Simpson's rule integration.

The coil component of the field can be written as a linear combination of the normalized coil currents and the $\breve{x}_{R,j}^{FEMM}(\xi)$ functions.

$$
h^{FEMM}(\xi,t) = \sum_{j=1}^{jmax} x_j^K(t)\,\breve{x}_{R,j}^{FEMM}(\xi). \tag{B.20}
$$

The results of the averaging operations can be inserted into the transformed differential equation Eq. (B.13).

$$\beta_n \int_{\xi=0}^{1} h(\xi,t)\cos(\beta_n\xi)\,d\xi = \beta_n \int_{\xi=0}^{1} \left[h^H(\xi,t)+h^{FEMM}(\xi,t)\right]\cos(\beta_n\xi)\,d\xi. \quad \text{(B.21)}$$

The terms on the right hand side are evaluated individually. The first term accounts for the eddy current's field, the second the coil's field. The first term is evaluated by integrating the series solution analytically term by term.

$$\begin{aligned}&\beta_n \int_{\xi=0}^{1} h^H(\xi,t)\cos(\beta_n\xi)\,d\xi \\ &\qquad = \beta_n \sum_{p=1}^{pmax}\left\{\left[\sum_{m=1}^{mmax}\sum_{k=1}^{kmax} \mathcal{X}^M_{k,m,p}(t)\,P_{k,m}\right]\int_{\xi=0}^{1}\sin(\eta_p\xi)\cos(\beta_n\xi)\,d\xi\right\}.\end{aligned} \quad \text{(B.22)}$$

The eigenfunctions are not orthogonal so each product is non-zero.

$$\int_{\xi=0}^{1}\cos(\beta_n\xi)\sin(\eta_p\xi)\,d\xi = \frac{\cos\left[(\beta_n-\eta_p)\xi\right]}{2(\beta_n-\eta_p)} - \frac{\cos\left[(\beta_n+\eta_p)\xi\right]}{2(\beta_n+\eta_p)}\Bigg|_{\xi=0}^{1}. \quad \text{(B.23)}$$

The formulae for the eigenvalues are the following.

$$\begin{aligned}\beta_n &= \left(\frac{2n-1}{2}\right)\pi, \\ \eta_p &= p\pi.\end{aligned} \quad \text{(B.24)}$$

These formulae may be inserted into Eq. (B.23) to evaluate the limits of the integral.

$$\int_{\xi=0}^{1}\cos(\beta_n\xi)\sin(\eta_p\xi)\,d\xi = \frac{2\left[\begin{array}{r}-2p\cos(p\pi)\sin(n\pi)+2n\sin(p\pi)\cos(n\pi)\\ -\sin(p\pi)\cos(n\pi)+2p\end{array}\right]}{\pi\left(-4p^2+4n^2-4n+1\right)}. \quad \text{(B.25)}$$

Noting that $\sin(n\pi)=0$ and $\sin(p\pi)=0$ simplifies the numerator considerably. In the following equation, the first step inserts the zero terms in the numerator and the second step recovers the formula for the eigenvalues.

$$\int_{\xi=0}^{1} \cos\left(\beta_n \xi\right) \sin\left(\eta_p \xi\right) d\xi = \frac{p}{\pi\left(p^2 - \left(\frac{2n-1}{2}\right)^2\right)} = \frac{\eta_p}{\left(\eta_p^2 - \beta_n^2\right)}. \tag{B.26}$$

This result may be inserted into Eq. (B.22).

$$\beta_n \int_{\xi=0}^{1} h^H\left(\xi,t\right) \cos\left(\beta_n \xi\right) d\xi = \sum_{p=1}^{pmax} \sum_{m=1}^{mmax} \sum_{k=1}^{kmax} \mathcal{X}_{k,m,p}^{M}\left(t\right) \frac{\beta_n \eta_p P_{k,m}}{\left(\eta_p^2 - \beta_n^2\right)}. \tag{B.27}$$

Equation (B.27) expresses the coupling from the *n*-th vibration mode to the (*k,m,p*)-th eddy current modes. The result is a linear combination the eddy current mode's amplitude functions. The multiplying factors in the linear combination are constants that are properties of the modal solution of the cylindrical geometry. No material properties are involved in the coefficients nor are any dimensions of the rod.

The term from Eq. (B.21) involving the coil currents is the following. This term is integrated numerically using the FEMM results.

$$\begin{aligned} \beta_n \int_{\xi=0}^{1} h^{FEMM}\left(\xi,t\right) \cos\left(\beta_n \xi\right) d\xi &= \beta_n \int_{\xi=0}^{1} \sum_{j=1}^{jmax} x_j^K\left(t\right) \breve{x}_{R,j}^{FEMM}\left(\xi\right) \cos\left(\beta_n \xi\right) d\xi \\ &= \sum_{j=1}^{jmax} \left[ x_j^K\left(t\right) \beta_n \int_{\xi=0}^{1} \breve{x}_{R,j}^{FEMM}\left(\xi\right) \cos\left(\beta_n \xi\right) d\xi \right]. \end{aligned} \tag{B.28}$$

Another coefficient matrix can be defined using the result of the integral.

$$Q_{n,j} = \beta_n \int_{\xi=0}^{1} \breve{x}_{R,j}^{FEMM}\left(\xi\right) \cos\left(\beta_n \xi\right) d\xi. \tag{B.29}$$

Inserting $Q_{n,j}$ into Eq. (B.28) gives the more compact form of the equation.

$$\beta_n \int_{\xi=0}^{1} h^{FEMM}\left(\xi,t\right) \cos\left(\beta_n \xi\right) d\xi = \sum_{j=1}^{jmax} \left[ x_j^K\left(t\right) Q_{n,j} \right]. \tag{B.30}$$

At this point, all the necessary equations to solve the vibration model are specified in indicial form. The results of Eq. (B.27) and Eq. (B.30) can be inserted into Eq. (B.13) to form a complete, albeit unwieldy equation for the time dynamics of a vibration mode.

$$\begin{aligned}\ddot{\mathcal{X}}_n^N(t)+2\lambda\omega_1\dot{\mathcal{X}}_n^N(t)+\left(\frac{2\omega_1\beta_n}{\pi}\right)^2\mathcal{X}_n^N(t)\\ =\left(\frac{2\omega_1}{\pi}\right)^2\sum_{p=1}^{pmax}\sum_{m=1}^{mmax}\sum_{k=1}^{kmax}\frac{\beta_n\eta_p P_{k,m}}{\left(\eta_p^2-\beta_n^2\right)}\mathcal{X}_{k,m,p}^M(t)+\left(\frac{2\omega_1}{\pi}\right)^2\sum_{j=1}^{jmax}Q_{n,j}x_j^K(t).\end{aligned} \tag{B.31}$$

The solution for the displacement is obtained by the summation of the products of the amplitude and the modal functions.

$$\begin{aligned}x^N(\xi,t)&=\sum_{n=1}^{nmax}\frac{Z(\beta_n,\xi)}{N(\beta_n)}\mathcal{X}_n^N(t)\\&=2\sum_{n=1}^{nmax}\sin(\beta_n\xi)\mathcal{X}_n^N(t),\end{aligned} \tag{B.32}$$

where $\beta_n=\frac{(2n-1)\pi}{2}$; $n=1,\ 2,\ 3,\ \ldots$ and $N(\beta_n)=\frac{1}{2}$. The state variables in this solution are the amplitude functions, $\mathcal{X}_n^N(t)$. Equation (B.31) is a linear equation for the state derivatives of the vibration model. The magnetics model supplies the states for the eddy current states, $\mathcal{X}_{k,m,p}^M(t)$, and the coil model supplies the coil current state variables, $x_j^K$.

The dimensioned form of the displacement can be obtained by inverting the linear transformation in Eqs. **(2.75)** through **(2.77)**.

$$\begin{aligned}\zeta_z(z,t)&=\frac{\kappa_{eff}Tz_L}{Y_{eff}^H}\left[\Delta I\,x^N\left(\frac{z}{z_L},t\right)+I_{min}\right]\\&=\frac{\kappa_{eff}Tz_L\Delta I}{Y_{eff}^H}\left[2\sum_{n=1}^{nmax}\sin\left(\beta_n\frac{z}{z_L}\right)\mathcal{X}_n^N(t)+\frac{I_{min}}{\Delta I}\right].\end{aligned} \tag{B.33}$$

The dimensioned strain can also be written in terms of the dimensionless amplitude functions.

$$\begin{aligned} S_z(z,t) &= \frac{\partial \zeta_z(z,t)}{\partial z} \\ &= \frac{\kappa_{eff} T z_L \Delta I}{Y_{eff}^H}\left[2\sum_{n=1}^{nmax}\frac{\beta_n}{z_L}\cos\left(\beta_n\frac{z}{z_L}\right)\varkappa_n^N(t)\right] \\ &= \frac{\kappa_{eff} T \Delta I}{Y_{eff}^H}\left[2\sum_{n=1}^{nmax}\beta_n\cos\left(\beta_n\frac{z}{z_L}\right)\varkappa_n^N(t)\right]. \end{aligned} \tag{B.34}$$

## Test Calculations of the Vibration Model

The test calculations evaluate the vibration model against several theoretical results.

### Steady state calculations

The state space model can be solved at steady conditions as a test of the derivation. The steady state case provides a test of both the normalization approach and the coding of the model.

The model's steady state is obtained by setting all the time derivatives in Eq. (3.44) to zero.

$$0 = \mathbf{F}^{12}\mathbf{x}_{SS}^N + \mathbf{F}^{13}\mathbf{x}_{SS}^K. \tag{B.35}$$

Solving for $\mathbf{x}^N$, we have

$$\mathbf{x}_{SS}^N = -\left(\mathbf{F}^{12}\right)^{-1}\mathbf{F}^{13}\mathbf{x}_{SS}^K. \tag{B.36}$$

Inserting this solution into the output formula for tip displacement yields

$$y_{SS} = -\mathbf{C}^2\left(\mathbf{F}^{12}\right)^{-1}\mathbf{F}^{13}\mathbf{x}_{SS}^K. \tag{B.37}$$

Any array of currents may be inserted into Eq. (B.37) to evaluate the displacement of the actuator. A problem with all coils energized at their maximum normalized current, $\mathbf{x}_{SS}^{K} = \mathbf{1}_{jmax\times 1}$, gives a condition approximating the infinite solenoid and should give approximately unity. Applying the test vector to the system matrices of the vibration problem with modal order $nmax = 10$ yields a numerical value of

$$y_{SS} = 1.0421 \tag{B.38}$$

The steady state elongation can also be solved using the original wave equation setting all time derivatives to zero. This steady solution is the solution to the following system of equations.

Steady state governing equation

$$\frac{d^2 x_A^N(\xi)}{d\xi^2} = \frac{dh_{SS}(\xi)}{d\xi}. \tag{B.39}$$

Boundary conditions

$$\begin{aligned} x_A^N(0) &= 0, \\ \frac{dx_A^N(1)}{d\xi} &= h_{SS}(1). \end{aligned} \tag{B.40}$$

The solution is obtained by integrating twice.

$$x_A^N(\xi) = C_1\xi + C_2 + \int_{\xi'=0}^{\xi} h_{SS}(\xi')d\xi'. \tag{B.41}$$

The undetermined coefficients are found by evaluating the boundary conditions,

$$\begin{aligned} C_1 &= 0, \\ C_2 &= 0. \end{aligned} \tag{B.42}$$

The solution for the steady problem is thus

$$x_A^N(\xi) = \int_{\xi'=0}^{\xi} h_{SS}(\xi')d\xi'. \tag{B.43}$$

The steady state magnetic field is given by the FEMM solution. Any field distribution can be evaluated using Eq. (B.20).

$$h_{SS}(\xi) = h^{FEMM}(\xi) = \sum_{j=1}^{jmax} x_{SS,j}^K \breve{x}_{R,j}^{FEMM}(\xi). \tag{B.44}$$

The steady state displacement as a function of the normalized coil currents is given by the following.

$$x_A^N(\xi) = \int_{\xi'=0}^{\xi} \sum_{j=1}^{jmax} x_{SS,j}^K \breve{x}_{R,j}^{FEMM}(\xi')d\xi'. \tag{B.45}$$

Evaluating this condition at the free end yields a second calculation of the position at the free end that just involves integrating the FEMM cases. The result is evaluated numerically by applying Simpson's rule to the FEMM cases for each energized coil.

$$x_A^N(1) = \sum_{j=1}^{jmax} x_{SS,j}^K \int_{\xi'=0}^{1} \breve{x}_{R,j}^{FEMM}(\xi')d\xi'. \tag{B.46}$$

The result for a case with all coils energized, $x_{SS,j}^K = 1$ for all $j$, is the following numerical value.

$$x_A^N(1) = 1.0419. \tag{B.47}$$

Equation (B.47) gives an excellent comparison with Eq. (B.38). The fact that the steady state elongation for both solutions is somewhat more than unity is a result of the normalization. The normalization is set by the field for an infinite solenoid, $H = T \cdot I$. Since the actuator is finite and has a flux return path, the actual field in the actuator

differs from the infinite solenoid. This difference is calculated by the FEMM model. A portion of the field follows the closed loop around the rod and return path forming a magnetic circuit. Since the permeability of the materials in the return path is somewhat higher than Terfenol-D, magnetic field is somewhat peaked at each end of the actuator rod.

The displacement for any set of values for the coil currents can be calculated by Eq. (B.37) and Eq. (B.46). Table B.1 lists a number of cases and the displacement calculated by the two methods. The cases are all constructed to give $\sum_{j=1}^{jmax} x_{SS,j}^{K} = 10$. All of the cases should give approximately one unit steady state displacement. The displacement is not exactly one unit because the coils are not equally effective because of end effects in the actuator geometry; however, the two solutions should be the same. The deviations between the solutions in the two rightmost columns are an indication of the steady state accuracy of the modal solution. The worst deviation occurs for case 4. In this case, all the current is in the first coil which is the coil at the free end. The Fourier fit is particularly poor when the function fitted does not satisfy the same boundary condition as the modal function. The modal function $\cos(\beta_n \xi)$ is zero at the free end. Hence, all cases with a significant current in the first coil can be expected to have poor steady state accuracy. This is the only major drawback to the modal approach. Of course, accuracy is improved by increasing the number of axial modes.

Table B.1: Steady state accuracy of the modal vibration model

| | *Coil index* | | | | | | | | | | *Steady state displacement* | |
|---|---|---|---|---|---|---|---|---|---|---|---|---|
| *Case* | *1* | *2* | *3* | *4* | *5* | *6* | *7* | *8* | *9* | *10* | $y_{SS}$ | $x_A^N$ |
| *1* | 1 | 1 | 1 | 1 | 1 | 1 | 1 | 1 | 1 | 1 | 1.0316 | 1.0618 |
| *2* | 2 | 2 | 2 | 2 | 2 | 0 | 0 | 0 | 0 | 0 | 1.0034 | 1.0624 |
| *3* | 0 | 0 | 0 | 0 | 0 | 2 | 2 | 2 | 2 | 2 | 1.0598 | 1.0611 |
| *4* | 10 | 0 | 0 | 0 | 0 | 0 | 0 | 0 | 0 | 0 | 0.7588 | 1.0530 |
| *5* | 0 | 10 | 0 | 0 | 0 | 0 | 0 | 0 | 0 | 0 | 1.0712 | 1.0640 |
| *6* | 0 | 0 | 10 | 0 | 0 | 0 | 0 | 0 | 0 | 0 | 1.0532 | 1.0650 |
| *7* | 0 | 0 | 0 | 10 | 0 | 0 | 0 | 0 | 0 | 0 | 1.0684 | 1.0652 |
| *8* | 0 | 0 | 0 | 0 | 10 | 0 | 0 | 0 | 0 | 0 | 1.0655 | 1.0650 |
| *9* | 0 | 0 | 0 | 0 | 0 | 10 | 0 | 0 | 0 | 0 | 1.0619 | 1.0649 |
| *10* | 0 | 0 | 0 | 0 | 0 | 0 | 10 | 0 | 0 | 0 | 1.0697 | 1.0650 |
| *11* | 0 | 0 | 0 | 0 | 0 | 0 | 0 | 10 | 0 | 0 | 1.0591 | 1.0650 |
| *12* | 0 | 0 | 0 | 0 | 0 | 0 | 0 | 0 | 10 | 0 | 1.0704 | 1.0636 |
| *13* | 0 | 0 | 0 | 0 | 0 | 0 | 0 | 0 | 0 | 10 | 1.0381 | 1.0471 |
| *14* | 2 | 0 | 2 | 0 | 2 | 0 | 2 | 0 | 2 | 0 | 1.0035 | 1.0623 |
| *15* | 0 | 2 | 0 | 2 | 0 | 2 | 0 | 2 | 0 | 2 | 1.0597 | 1.0612 |

The steady state test is only influenced by some of the matrices in the model. Only the matrices multiplying the current or displacement states, $\mathbf{F}^{12}$, $\mathbf{F}^{13}$, and $\mathbf{C}^{2}$, are involved in the calculation. The matrix, $\mathbf{F}^{13}$, which couples coil current with vibration is the main item that is checked is by the steady state calculation.

**Eigenvalue test**

The eigenvalues of the state space problem can be calculated directly from the indicial differential equation Eq. (B.31) as the roots of the following.

$$\omega_n^2 + 2\lambda\omega_1 s_n + \left(\frac{2\omega_1\beta_n}{\pi}\right)^2 = 0. \tag{B.48}$$

The analytical eigenvalues are given by

$$\omega_n = \omega_1 \left( -\lambda \pm i \sqrt{\left( \frac{2\beta_n}{\pi} \right)^2 - \lambda^2} \right). \tag{B.49}$$

where $i = \sqrt{-1}$. These eigenvalues can be compared to the eigenvalues calculated numerically by MATLAB for the $\mathbf{A}^N$ matrix for the vibration model.

$$\det\left( s\mathbf{I} - \mathbf{A}^N \right) = \det \begin{bmatrix} s\mathbf{I} - \mathbf{F}^{11} & -\mathbf{F}^{12} \\ -\mathbf{I} & s\mathbf{I} \end{bmatrix} = 0. \tag{B.50}$$

Table B.2 gives the first ten complex eigenvalues from Eq. (B.49) and Eq.(B.50). For the test calculation, $\lambda = 0.1$ and the number of axial modes in the MATLAB model is $nmax = 10$. The values as shown are divided by the first resonance, $\omega_1$, so that the imaginary part is more recognizable as an odd multiple of the fundamental frequency as *n* increases. The MATLAB calculation uses a value of $\omega_1 = 2\pi \times 2747.1$ in calculating the actual matrices. To give a sense of the frequency range, the eigenvalue for $n = 5$ corresponds to a frequency of 13,750 Hz, which is just a little above the target of a cut-off frequency of 10,000 Hz. The eigenvalues of the modal model agree exactly with the analytical formula. The calculation provides a convincing test of the programming of the matrices, $\mathbf{F}^{11}$ and $\mathbf{F}^{12}$.

Table B.2: Comparison of eigenvalues, $\omega_n$, of wave equation from the analytical formula and system matrix

| *Index* | *Eigenvalues* $\omega_n / \omega_1$ | |
|---|---|---|
| *n* | *Analytical* | *Matrix* |
| *1* | 0.1 ± 0. 9950i | 0.1 ± 0.9950i |
| *2* | 0.1 ± 2.9983i | 0.1 ± 2.9983i |
| *3* | 0.1 ± 4.9990i | 0.1 ± 4.9990i |
| *4* | 0.1 ± 6.9993i | 0.1 ± 6.9993i |
| *5* | 0.1 ± 8.9994i | 0.1 ± 8.9994i |
| *6* | 0.1 ±10.9995i | 0.1 ±10.9995i |
| *7* | 0.1 ±12.9996i | 0.1 ±12.9996i |
| *8* | 0.1 ±14.9997i | 0.1 ±14.9997i |
| *9* | 0.1 ±16.9997i | 0.1 ±16.9997i |
| *10* | 0.1 ±18.9997i | 0.1 ±18.9997i |

**Fourier series approximation tests**

The coupling coefficients between the vibration model and the magnetic and coil models represent force applied to the rod by an external forcing function on the displacement modes of the vibration model. If a steady state problem is constructed for the rod displacement, it is clear that the coupling coefficients are the coefficients of a Fourier series that approximate the external function. Equation (B.26) gives a series of coefficients that fit the sine function using a cosine series. For a finite number of terms, the following is approximately true.

$$\sin\left(\eta_p \xi\right) \approx \sum_{n=1}^{nmax} A_{pn} \cos\left(\beta_n \xi\right), \tag{B.51}$$

where

$$A_{pn} = \frac{2\eta_p}{\left(\eta_p^2 - \beta_n^2\right)}. \tag{B.52}$$

Comparing the original sine function to the Fourier series checks the programming of the matrix coefficients and tests the sufficiency of the number of terms to reproduce the input curve. The comparison is shown in Figure B.1 for three cosine series approximations to the sine function with three values of the wave number, $p = 1$, 3, and 10. The comparisons on each plot are the original sine function and the cosine series in Eq. (B.51). The cosine series is shown for $nmax = 10$ and 20.

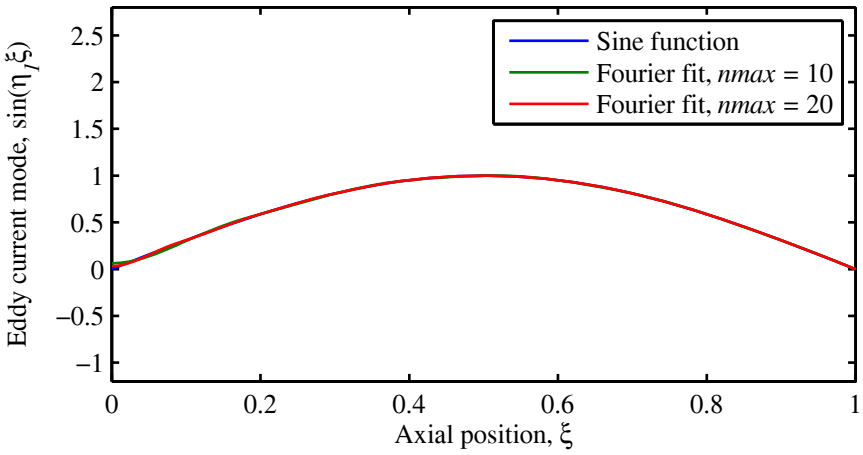


Case 1: $\sin(\beta_1 \xi)$

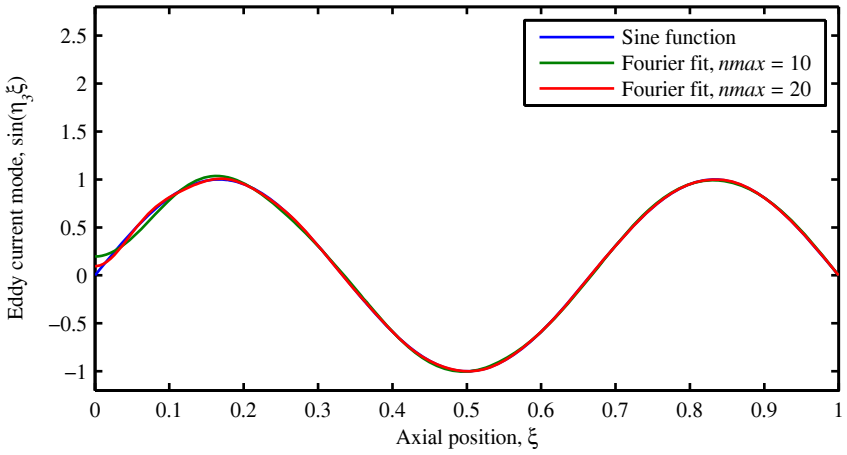


Case 2: $\sin(\beta_3 \xi)$

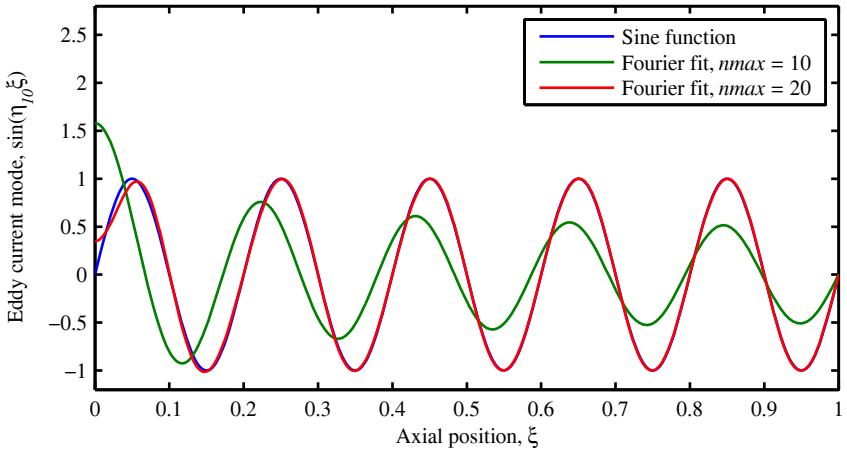


Case 3: $\sin(\beta_{10} \xi)$

Figure B.1: Comparison of Fourier fit of the cosine series to sine function

Equation (B.29) leads to a Fourier series representation of the average axial field due the energized coils from the FEMM distribution which can be compared with the original FEMM distribution from Eq. (B.20).

$$h^{FEMM}(\xi) = \sum_{j=1}^{jmax} \breve{x}_{R,j}^{FEMM}(\xi) x_j^K . \tag{B.53}$$

$$h_{inv}^{FEMM}(\xi) = \sum_{j=1}^{jmax} \sum_{n=1}^{nmax} \frac{2Q_{n,j}}{\beta_n} \cos(\beta_n \xi) x_j^K . \tag{B.54}$$

Figure B.2 shows the comparison of the Fourier fit and the original FEMM function for Eqs. (B.53) and (B.54). The Fourier series is shown for *nmax*=10 and 20. The case number refers to the distribution of input currents, $x_j^K$, as given in Table B.2. The first case with all coils energized illustrates the problem of fitting a nonhomogeneous source function with a homogeneous modal function. The fit at the homogenous right boundary is not accurate. The average behavior is correct.

The second plot shows the peak for a single energized coil at level 2. This plot shows the local distribution of magnetic field and some effect from the boundary condition approximation.

The third plot shows the field for coil current pattern of alternating on-off coils. The case shows the effect of magnetic diffusion to spread out and attenuate the flux localization that is being used to cause an axial distribution of magnetic field. The peaks and valleys of the field profile are the effect that distributes energy along the rod.

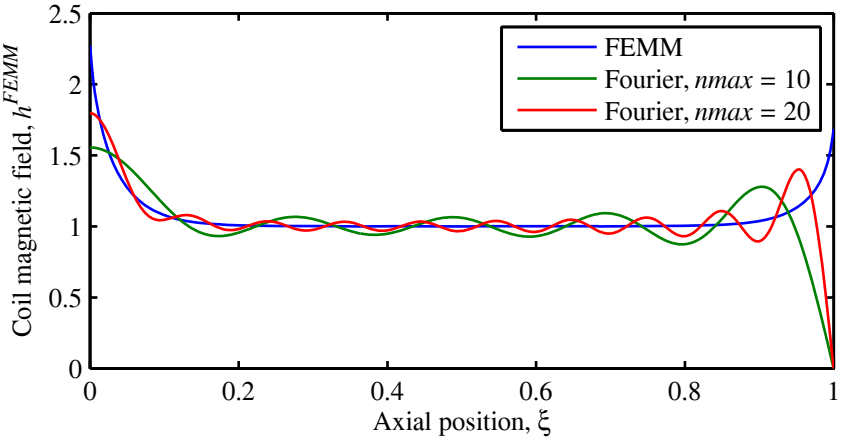


Case 1. All coils energized

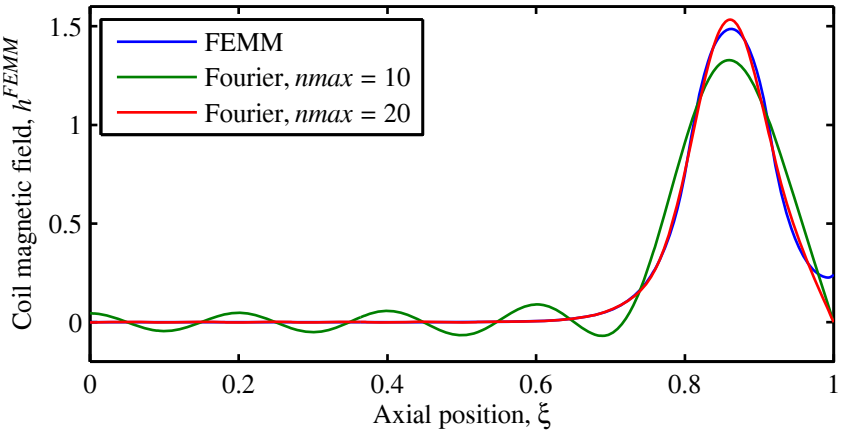


Case 5: Coil 2 energized

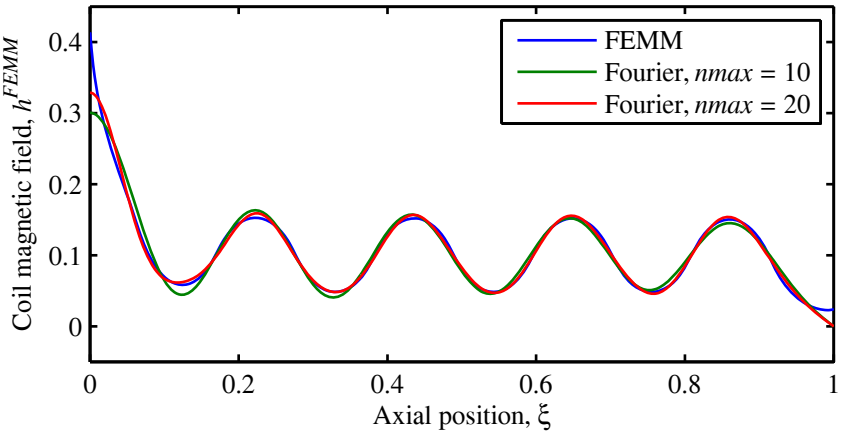


Case 15: Alternating coils energized. 2, 4, 6, 8, 10.

Figure B.2: Comparison of Fourier fit of magnetic field to FEMM distribution

**Vibration model order comparison**

The truncation error in the modal solution can be assessed by a group of cases in which the order is varied. The step change transient shown in Figure 3.3 can be repeated varying the number of vibration modes in the solution. The transients are calculated using the stand alone vibration model given by Eqs. (3.54) through (3.59). Results for *nmax*=10, 20, 40, and 80 are shown in Figure B.3 through Figure B.6.

The traces become progressively smoother and the trace of coil 1 moves closer to the rest of the coil responses as *nmax* increases. Both effects are indications of the expected reduction of truncation error as order increases. The lowest order system, *nmax*=10, is used in the control simulations to keep the model as small as possible but with an understanding of the magnitude of the truncation error.

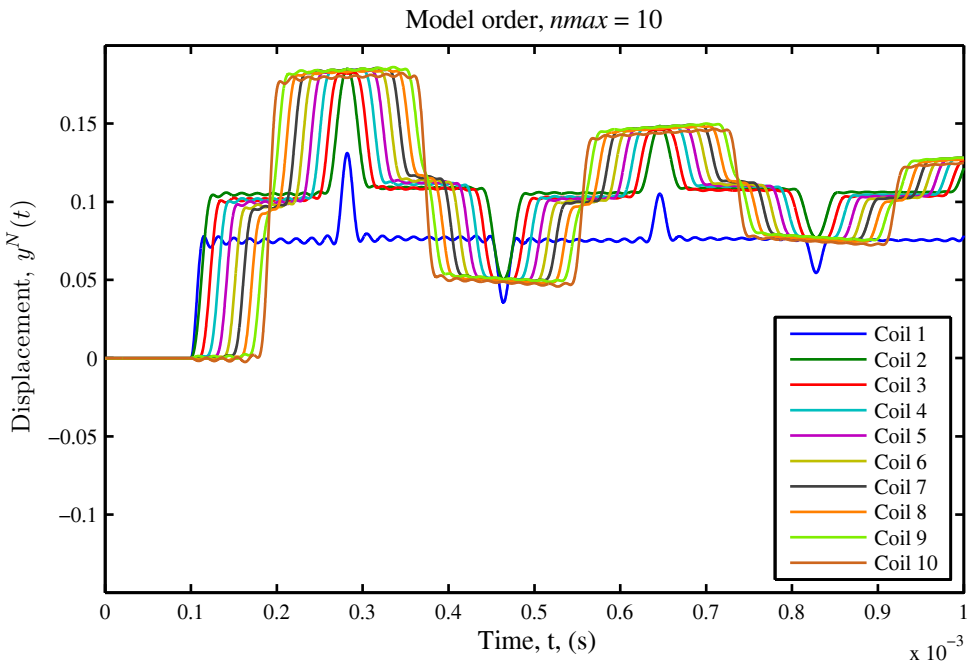


Figure B.3: Step change transient for vibration model, *nmax*=10

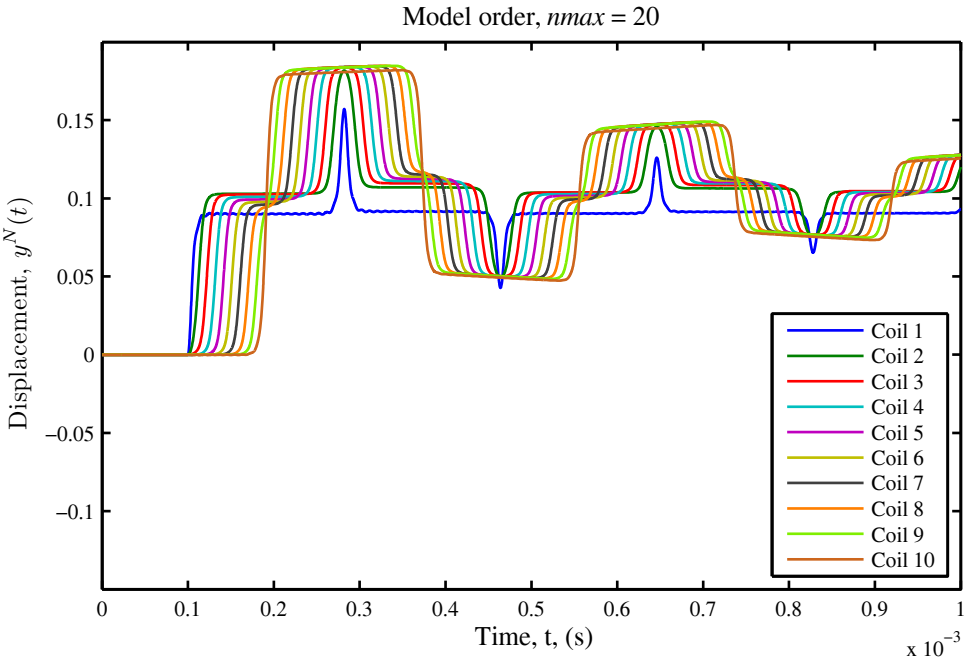


Figure B.4: Step change transient for vibration model, *nmax*=20

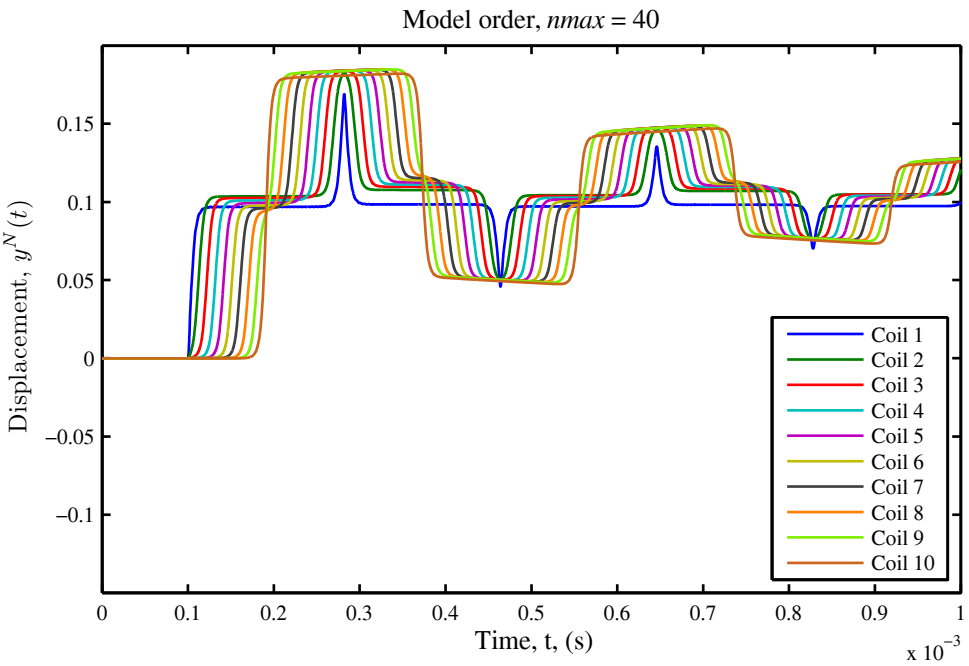


Figure B.5: Step change transient for vibration model, *nmax*=40

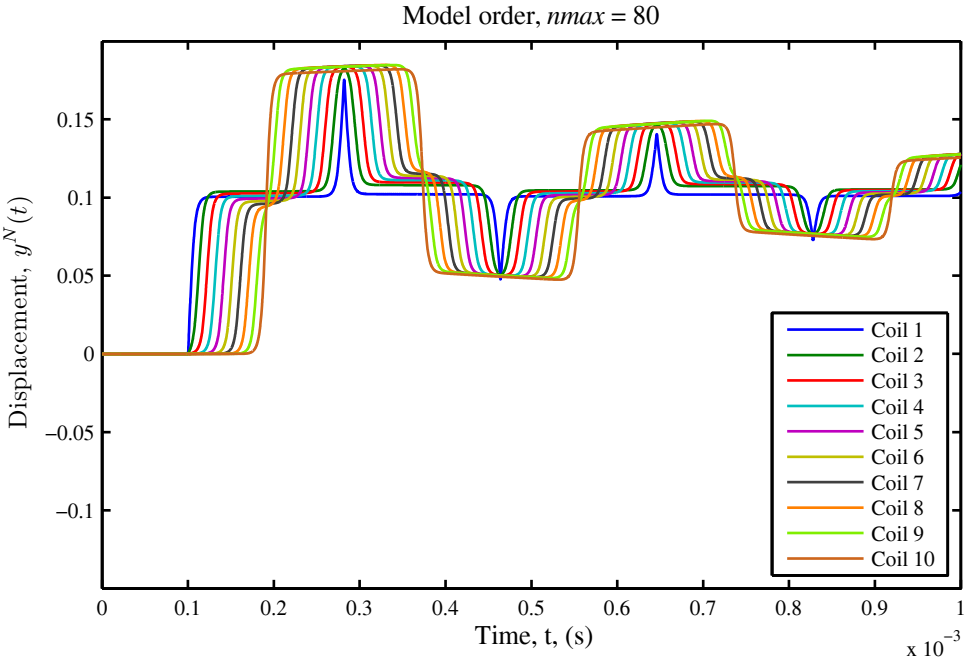


Figure B.6: Step change transient for vibration model, *nmax*=80

# APPENDIX C

# FEMM MODELING

The Finite Element Magnetic Modeling (FEMM) code, written by David Meeker [35], solves static and low frequency problems in magnetics. The following description of the code is an abbreviated version of the description given in the FEMM user manual. The nomenclature in this derivation is slightly modified from Meeker's to coincide with the nomenclature used in this dissertation.

The equations solved by FEMM are based on Maxwell's equation. The equations are formulated in terms of the vector potential. Other magnetic variables, such as magnetic field, magnetic induction, and eddy current density are obtained by differentiating the potential numerically. The magnetostatic problem can be derived in terms of magnetic potential from Maxwell's equations, the constitutive relations, and the definition of magnetic potential. The needed equations are Maxwell's equations,

$$\nabla \times \mathbf{H} = \mathbf{J}\,, \tag{C.1}$$

$$\nabla \cdot \mathbf{B} = 0\,, \tag{C.2}$$

subject to the linear constitutive relation,

$$\boldsymbol{\mu}^{-1}\mathbf{B} = \mathbf{H}\,. \tag{C.3}$$

The vector potential is defined as

$$\mathbf{B} = \nabla \times \mathbf{A}\,. \tag{C.4}$$

Substituting Eq. (C.3) and Eq. (C.4) into Eq. (C.1) gives

$$\nabla \times \boldsymbol{\mu}^{-1}\left(\nabla \times \mathbf{A}\right) = \mathbf{J}\,. \tag{C.5}$$

blem solves for **A** that satisfies Eq. (C.5) and the boundary conditions in the presence of the source current.

FEMM also solves the harmonic case, in which the source currents are sinusoidally varying functions of time. The harmonic problem can be reduced to an equation that is algebraic in frequency by the Fourier transformation in time.

In addition to Eqs. (C.1) through (C.3), the harmonic problem requires another one of Maxwell's equation,

$$\nabla \times \mathbf{E} = -\frac{\partial \mathbf{B}}{\partial t}, \tag{C.6}$$

and Ohm's law in differential form,

$$\mathbf{J} = \sigma \mathbf{E}. \tag{C.7}$$

Substituting Eq. (C.4) into Eq. (C.6) and rearranging gives an equation that can be integrated.

$$\nabla \times \left( \mathbf{E} + \frac{\partial \mathbf{A}}{\partial t} \right) = 0. \tag{C.8}$$

The integral is given by

$$\mathbf{E} + \frac{\partial \mathbf{A}}{\partial t} = \mathbf{C}, \tag{C.9}$$

where **C** represents an undetermined constant function of integration. The electric field can be eliminated in favor of current density using Eq. (C.7).

$$\mathbf{J} = -\sigma \frac{\partial \mathbf{A}}{\partial t} + \sigma \nabla \mathscr{V} + \mathbf{J}_{src}. \tag{C.10}$$

Meeker defines the constant function as the sum of two terms.

$$\sigma \mathbf{C} = \sigma \nabla \mathscr{V} + \mathbf{J}_{src} . \tag{C.11}$$

where $\nabla \mathscr{V}$ is an externally applied voltage gradient and $\mathbf{J}_{src}$ is an externally applied current source.

Combining Eqs. (C.5), (C.10), and (C.11) gives the time dependent potential problem.

$$\nabla \times \boldsymbol{\mu}^{-1} \left( \nabla \times \mathbf{A} \right) = -\sigma \frac{\partial \mathbf{A}}{\partial t} + \sigma \nabla \mathscr{V} + \mathbf{J}_{src} . \tag{C.12}$$

The harmonic problem converts the differential time dependence into an algebraic function by the Fourier or phasor transform. The forcing functions are assumed to be sinusoidal functions of a single frequency, $\omega$. The time derivative becomes an algebraic multiplication, $\frac{\partial}{\partial t} \Rightarrow i\omega$. The transformed variable is a function of frequency rather than time. The transformed variables are indicated by an underscore applied to the transformed variable.

$$\nabla \times \boldsymbol{\mu}^{-1} \left( \nabla \times \underline{\mathbf{A}} \right) = -i\omega\sigma \underline{\mathbf{A}} + \sigma \nabla \underline{\mathscr{V}} + \underline{\mathbf{J}}_{src} . \tag{C.13}$$

This differential equation is only slightly different than the static problem in Eq. (C.5) and can be solved by comparable, finite-element methods.

The FEMM problem is further simplified by considering only two-dimensional problems, either axisymmetric or planar. In either of the geometries which are solved by FEMM, two of the three components of $\underline{\mathbf{A}}$ are exactly zero, so the problem reduces to a scalar equation. The non-zero component of $\underline{\mathbf{A}}$ is the axial direction for the planar case or the azimuthal direction for the axisymmetric case.

## FEMM Model of the Multi-coil Actuator

The input to the FEMM code includes the dimensions and material types for different regions of the device being simulated, the source current distribution, and the boundary conditions. The dimensions for the FEMM model of the actuator are obtained from drawings of the prototype actuator supplied by Etrema. The mechanical design drawing, shown in Figure C.1: Mechanical design drawing of prototype actuator, was supplied without internal dimensions by Etrema to protect their proprietary actuator designs. The geometrical data were estimated by measuring the drawing and scaling the results by the external dimensions of the actual device. The method assumes that the only change made by Etrema to the drawing was erasing the dimensions. The external dimensions of the device are known to be to scale with the drawing. Some error is inevitably introduced into the FEMM calculations by the inaccuracies of measuring the drawing, but this is the best information available.

The material properties needed for the simulation are the permeabilities and conductivities of each material. Most materials are available from the library of materials in the FEMM code. A magnetic stainless steel (416 stainless) is used for the return path in the actuator design. A nonmagnetic stainless steel (304 stainless) is used for the case and other parts. A high permeability, low conductivity material called T4 is used to turn the flux at the end of the rod. The T4 is a proprietary material whose properties were provided by Etrema. The properties of Terfenol-D are derived in Chapter 2 from published data.

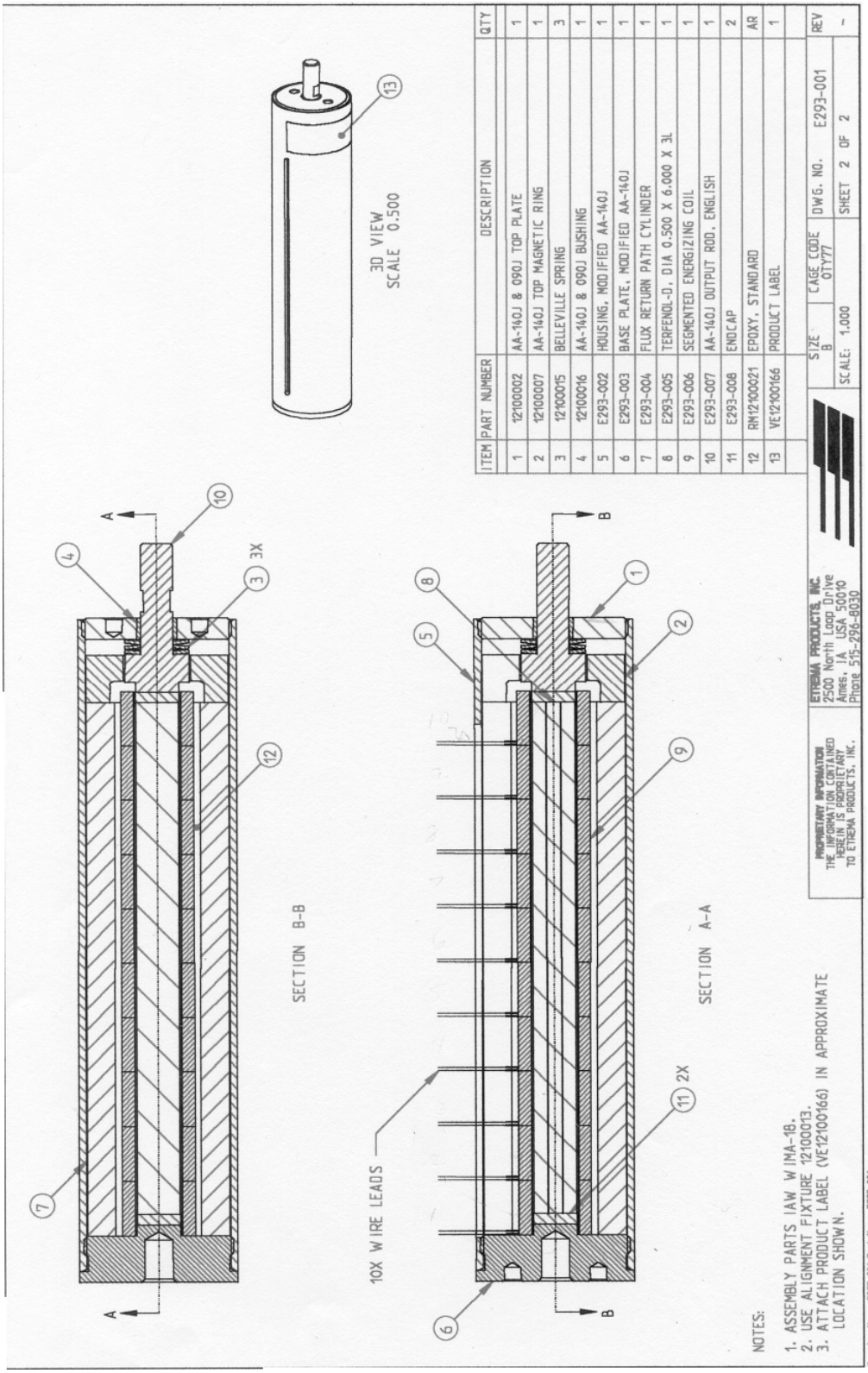


Figure C.1: Mechanical design drawing of prototype actuator

The actuator problem requires an infinite boundary condition. FEMM provides a special technique to approximate the infinite or open boundary on a finite domain. At large distances, a magnetic device's field approaches asymptotically the field of a simple device such as a dipole, quadrupole, or higher order device depending on the symmetry of the current distribution. The long axial rod dimension with coils all arranged axially means that, from a great distance, the field of the actuator is closely approximated by a dipole. To represent this field on a fixed boundary, a large volume about the device is defined. The boundary condition is then specified as a mixed boundary chosen to represent the asymptotic limit of the dipole field on the surface. The boundary on the central axis is specified as $\mathbf{A}=0$ which completes the boundary conditions needed for the FEMM problem.

The FEMM actuator model consisting of the geometrical and material data is retained in a read-only file to protect against unintentional saving of changes. The cases are run by loading the standard model and then changing any problem-dependent parameters. The code can be executed interactively or in a batch mode using a scripting language called LUA. The FEMM cases for this research usually involved a large number of related runs so all the production calculations were conducted using LUA scripts. The LUA scripts and the model file provide a convenient way to recreate previous runs if parameters need to be changed. The LUA language provides output utilities to write results to an external file. This feature is used to generate results that can be imported into MATLAB for plotting or calculation of the state space model.

FEMM also provides a graphical interface to display results interactively. The FEMM interface is used to generate the plots for this section. In all other sections of this

report, graphics for computed results are generated with MATLAB which are vector format. The FEMM plots are in the form of bit mapped images which have limited resolution.

The geometry of the actuator model drawn using FEMM's input processor is shown in Figure C.2. The left axis of the image is the centerline of the actuator. The semi-circular region around the actuator approximates the infinite boundary.

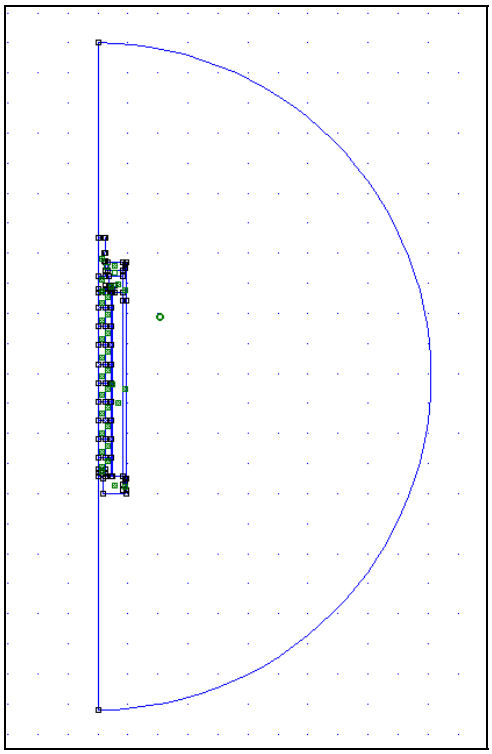

Figure C.2: FEMM model of the actuator geometry

A close up of the top part of the actuator showing material names and the finite element mesh is shown in Figure C.3. The material "copper" is an unenergized coil. The material "copper with current" is energized. The mesh is specified to be finer in the rod region to give smooth results for the magnetic field used in the actuator model.

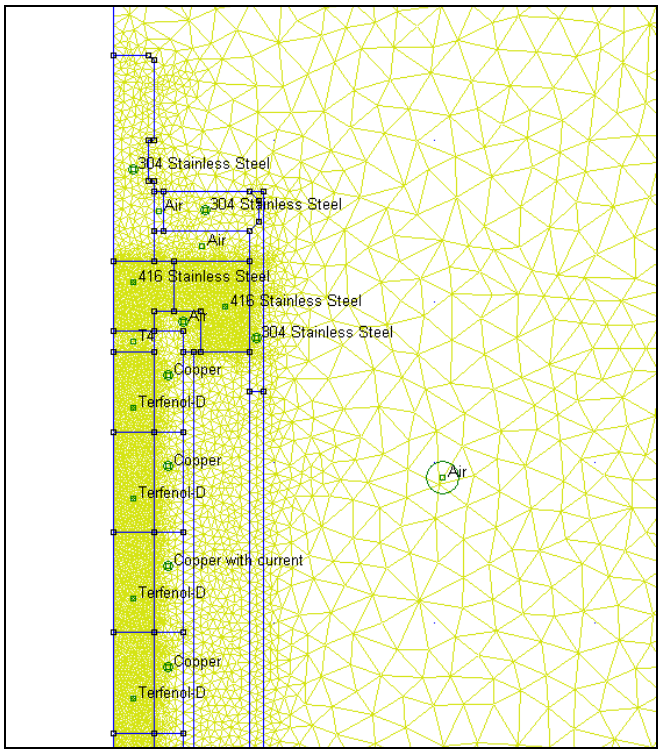


Figure C.3: Detail of the upper part of the FEMM model to illustrate the mesh and block names

Figure C.4 shows the distribution of flux for the same model. A single coil, third from the top, is energized. The plot shows the magnitude of induction, $|\mathbf{B}|$, as a colored density plot. The lines of induction (direction of the flux) are shown as a contour map. A close-up is shown to give a better view of the energized region.

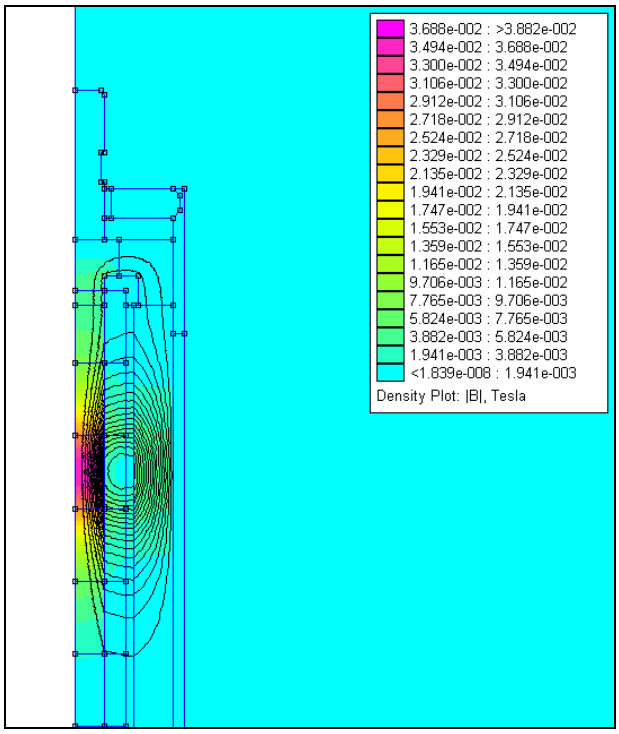


Figure C.4: Map of density and flux contour lines of magnetic flux for a static current case

## A FEMM Model of an Infinite Pie-shaped Cylinder

A general, three-dimensional model of the pie-shaped cylinder cannot be simulated using FEMM because FEMM is limited to two-dimensional problems either, *r*-*z* or *x*-*y*; however, the *x*-*y* problem can be used to simulate the transverse area of an infinite, pie-shaped cylinder. The special case requires a trick in recognizing the similarity between the equation for magnetic field and the equation for vector potential in FEMM's two-dimensional problem space.

The infinite pie-shaped cylinder problem means that the cylinder and coil are infinite and uniform in the axial direction. Under this geometry, the solution does not vary axially. The solution of the FEMM infinite cylinder problem is approximately the

same as the model of the finite actuator when all coils are energized and the flux is evaluated at the axial midplane. The approximation of the actuator as an infinite cylinder is valid since the actuator is a long, thin rod.

The simplifying characteristic of the infinite cylinder problem is that the field on the surface of the rod is uniform and independent of any currents on the interior of the rod. The field on the surface is equal to the infinite solenoid field, $H_z = TI$, independent of any eddy current on the interior of the rod. For the infinite, uniform coil and cylinder, the homogeneous boundary condition is an exact equation, not an approximation as it is for the finite rod. Because of this simplification, the infinite cylinder problem can be solved as a boundary value problem for magnetic field. Even with this simplification, a trick is needed to use FEMM to solve the infinite cylinder problem. The trick is that the differential equation for magnetic field problem turns out to be mathematically the same equation as the equation for $\underline{\mathbf{A}}$ that FEMM solves in *x*-*y* geometry. To illustrate this useful result, consider the magnetic field equation for the actuator rod from Eq. (4.25).

$$\frac{1}{r}\frac{\partial H_{R,z}}{\partial r}+\frac{\partial^2 H_{R,z}}{\partial r^2}+\frac{\partial^2 H_{R,z}}{r^2\partial\phi^2}+\chi_R\frac{\partial^2 H_{R,z}}{\partial z^2}-\sigma_R\mu_R\frac{\partial H_{R,z}}{\partial t}=\dot{K}^N. \qquad \text{(C.14)}$$

Dropping the effects of magnetostriction, $\dot{K}^N = 0$ and the axial term, $\frac{\partial^2 H_{R,z}}{\partial z^2} = 0$ (because of the infinite cylinder idealization), the equation becomes the following.

$$\frac{1}{r}\frac{\partial H_{R,z}}{\partial r}+\frac{\partial^2 H_{R,z}}{\partial r^2}+\frac{\partial^2 H_{R,z}}{r^2\partial\phi^2}-\sigma_R\mu_R\frac{\partial H_{R,z}}{\partial t}=0. \qquad \text{(C.15)}$$

Transforming the independent variables from $r-\phi$ to $x-y$ gives

$$\frac{\partial^2 H_{R,z}}{\partial x^2}+\frac{\partial^2 H_{R,z}}{\partial y^2}=\sigma_R\mu_R\frac{\partial H_{R,z}}{\partial t}. \qquad \text{(C.16)}$$

The axial component of vector potential can be put into the same form. Starting with Eq. (C.12), we first assume a pie-shaped region of an isotropic material with permeability and conductivity, $\mu_R$ and $\sigma_R$ and set the current source and voltage gradient terms to zero.

$$\nabla\times(\nabla\times\mathbf{A}) = -\sigma_R\mu_R\frac{\partial\mathbf{A}}{\partial t}. \tag{C.17}$$

By a well-known result, we can use the matrix identity

$$\nabla\times(\nabla\times\mathbf{A}) = \nabla(\nabla\cdot\mathbf{A}) - \nabla^2\mathbf{A}, \tag{C.18}$$

and assert a permissible constraint on A,

$$\nabla\cdot\mathbf{A} = 0. \tag{C.19}$$

Equation (C.17) becomes

$$\nabla^2\mathbf{A} = \sigma_R\mu_R\frac{\partial\mathbf{A}}{\partial t}. \tag{C.20}$$

With planar symmetry, the assumption is that the shape in the *x*-*y* plane is infinite in the axial direction (out of the page). Hence, the *x* and *y* components of **A** must be zero, $A_x = A_y = 0$, and $\frac{\partial^2 A_z}{\partial z^2} = 0$. Substituting these terms into Eq. (C.20) gives

$$\frac{\partial^2 A_z}{\partial x^2} + \frac{\partial^2 A_z}{\partial y^2} = \sigma_R\mu_R\frac{\partial A_z}{\partial t}. \tag{C.21}$$

Thus, the differential equation for the magnetic potential, Eq. (C.16) and the equation for magnetic field, Eq. (C.21), are exactly the same. Furthermore, because $\nabla\times\mathbf{A} = \mathbf{B}$ and $\nabla\times\mathbf{H} = \mathbf{J}$, the current density in the rod can be obtained from the **B** field of the FEMM problem. The boundary condition magnetic field at the surface of the pie-shaped region is given by the formula for the infinite solenoid.

$$A_{\text{inf}} = H_z = T \cdot I \,, \tag{C.22}$$

where $T$ is the turns per meter and $I$ is the current per turn. This uniform boundary condition can be specified in FEMM as a harmonically varying boundary, thus producing a time-varying magnetic field that generates eddy currents on the interior of the pie-shaped cylinder.

The difference between the magnetic field problem which we are using and FEMM's intended vector potential problem is the direction that current is flowing in the case being represented. For the potential problem that FEMM was designed to solve, the current sources and voltage gradients and any resulting eddy currents are in the axial or out-of-page direction. The magnetic field problem represents a case in which current is circulating around the pie-shaped segment in paths parallel to the page.

Figure C.5 illustrates the pie-shaped model as it is represented in the FEMM preprocessor program. The interior arcs are defined so that the contours may be used in the postprocessor as lines along which the field and current are plotted.

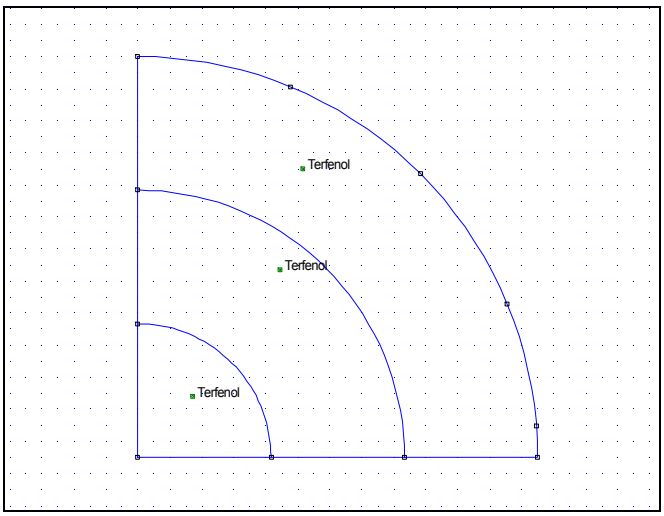


Figure C.5: FEMM layout of pie-shaped cylinder

As an example of the FEMM calculation of the pie-shaped cylinder, a harmonic case is presented in which the amplitude of the boundary conditions is specified as $|H_z| = |T \cdot I| = 1$, and the frequency is set as $\omega = 2\pi \cdot 2500 = 1.57 \times 10^4$ radians per second. The FEMM results for current density are shown in Figure C.6. The color density in this plot represents the magnitude of current density (in the interpretation of this problem). The contours represent the lines of current density. The current flow is a maximum near the center of each boundary segment. The current density is zero in each corner. The FEMM legend labels the results as $|\mathbf{B}|$ in units of Tesla. For our purposes, the results should be interpreted as $|\mathbf{J}|$ in A/m$^2$.

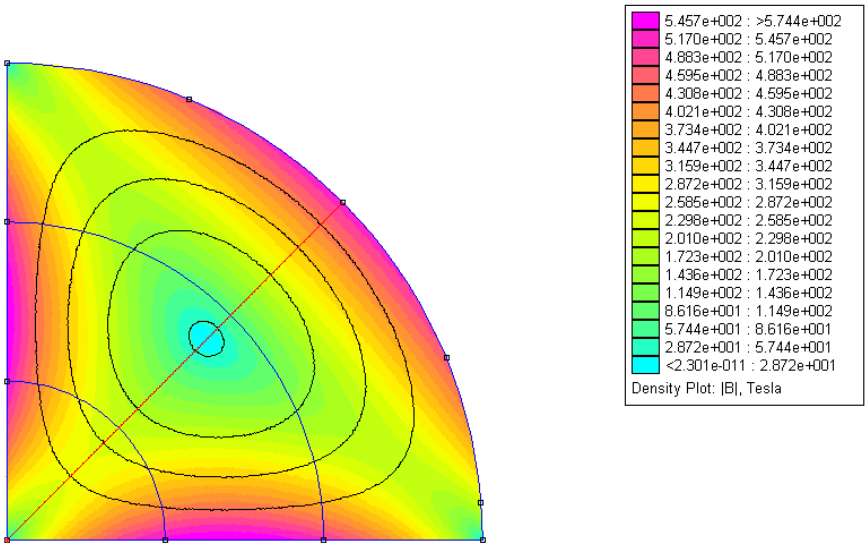


Figure C.6: Current density for a segment calculated by FEMM cwith $\omega = 2\pi \cdot 2500$

A FEMM plot of potential along a contour can also be shown which represents the magnetic field, $H_z$. The contour is along the radial line bisecting the pie-shaped region (shown as a red line in Figure C.6). Figure C.7 shows the real, imaginary, and

absolute magnitude of $A_z$ in units of Webers per meter which should be interpreted as $H_z$ in units of amperes per meter for the special interpretation of the results used here.

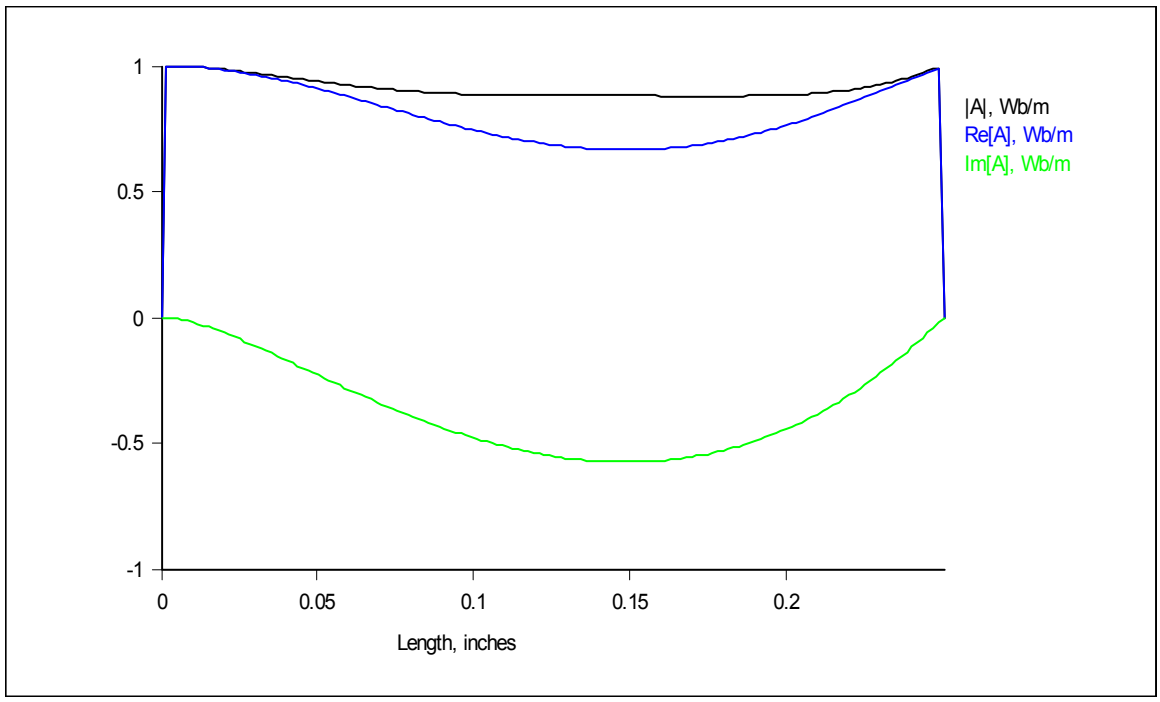


Figure C.7: FEMM plot showing magnetic field along a radial line for case $\omega = 2\pi \cdot 2500$

The FEMM results for the pie-shaped infinite cylinder are used primarily as a benchmark for the modal solution to the pie-shaped cylinder. The FEMM cases are able to verify the derivation and the programming of radial and azimuthal modes of the modal magnetic model. These comparisons are given in APPENDIX D.

# APPENDIX D

# SOLUTION OF THE MAGNETIC DIFFUSION EQUATION

## The Three-Dimensional Integral Transform Method

The magnetic diffusion equation, derived in the main text is repeated here for convenience.

$$\frac{1}{\rho}\frac{\partial}{\partial\rho}\left(\rho\frac{\partial x_H^M}{\partial\rho}\right)+\frac{\partial^2 x_H^M}{\rho^2\partial\phi^2}+\frac{\chi_R r_g^2}{z_L^2}\frac{\partial^2 x_H^M}{\partial\xi^2}-\sigma_R\mu_R r_g^2\frac{\partial x_H^M}{\partial t} = \sigma_R\mu_R r_g^2\dot{x}^{FEMM}+\frac{r_g^2}{T\Delta I}\dot{K}^N. \tag{D.1}$$

The integral transform solution to the magnetic diffusion equation in Eq. (D.1) involves three spatial transformations for the azimuthal, radial, and axial variables. Because of the dependence of the radial modes on the azimuthal modes through the order of the Bessel function, the solution is considerably more convenient if the azimuthal transformation is performed first. The azimuthal transform and its inverse are given by

$$\bar{x}_H^M(\rho,\gamma,\xi,t)=\int_0^{\phi_0} x_H^M(\rho,\gamma,\xi,t)\Phi(\gamma,\phi)\,d\phi, \tag{D.2}$$

$$x_H^M(\rho,\phi,\xi,t)=\sum_{\gamma=1}^{\infty}\frac{\Phi(\gamma,\phi)}{N(\gamma)}\bar{x}_H^M(\rho,\gamma,\xi,t). \tag{D.3}$$

The transform function is the solution to the associated homogeneous ordinary differential equation and boundary conditions in which $\gamma$ is a parameter.

$$\frac{d^2\Phi(\gamma,\phi)}{d\phi^2}+\gamma^2\Phi(\gamma,\phi)=0. \tag{D.4}$$

$$\Phi(\gamma,0)=0.$$
$$\Phi(\gamma,\phi_0)=0. \tag{D.5}$$

The solutions for $\Phi$ and $\gamma$ are the eigenfunctions and eigenvalues respectively of the azimuthal problem. The following solutions satisfy the differential equation and the boundary conditions.

$$\Phi(\gamma_m,\phi)=\sin(\gamma_m\phi);\ \gamma_m=\frac{\pi}{\phi_0}(2m-1);\ m=1,\ 2,\ 3,\ \ \ldots \tag{D.6}$$

For the pie-shaped segment, the angle is given by $\phi_0=\frac{\pi}{2}$ and $\gamma_m=2,\ 6,\ 10,\ ...$ The eigenvalues for $\gamma=\frac{\pi}{\phi_0}(2,\ 4,\ 6,\ \ldots)$ also satisfy the boundary conditions and differential equation but are eliminated by the requirement that the magnetic field must be symmetric about the $\phi_0/2$ radius. The proof of symmetry is not shown but can be obtained by showing that the problem is unchanged by a rotation of $\phi_0$ and by reflection about the $\phi_0/2$ axis.

The normalization constant for $\Phi(\gamma_m,\phi)$ is

$$\begin{aligned} N(\gamma_m)&=\int_0^{\phi_0}\sin^2(\gamma_m\phi)d\phi \\ &=\frac{\phi_0}{2}. \end{aligned} \tag{D.7}$$

A second integral transform for the *r* variable can be applied. The transform and inverse are given by

$$\tilde{\bar{x}}_H^M(\varepsilon_{k,m},\gamma_m,\xi,t)=\int_0^1\rho' R_{\gamma_m}(\varepsilon_{k,m},\rho')\bar{x}_H^M(\rho',\gamma_m,\xi,t)\,d\rho'. \tag{D.8}$$

$$\bar{x}_H^M\left(\rho,\gamma_m,\xi,t\right)=\sum_{k=1}^{\infty}\frac{\tilde{\bar{x}}_H^M\left(\varepsilon_{k,m},\gamma_m,\xi,t\right)}{N\left(\varepsilon_{k,m},\gamma_m\right)}R_{\gamma_m}\left(\varepsilon_{k,m},\rho\right). \tag{D.9}$$

The radial transform in Eq. (D.8) is indicated by stacking the ~ on top of the previous symbol. The eigenvalue of the azimuthal transform, $\gamma_m$, gives the order of the Bessel equation. The associated homogeneous spatial problem for $R_{\gamma_m}\left(\varepsilon_{k,m},\rho\right)$ is Bessel's equation of order $\gamma_m$.

$$\frac{1}{\rho}\frac{d}{dr}\left(\rho\frac{dR_{\gamma_m}\left(\varepsilon_{k,m},\rho\right)}{d\rho}\right)-\frac{\gamma_m^2}{\rho^2}R_{\gamma_m}\left(\varepsilon_{k,m},\rho\right)+\varepsilon_{k,m}^2R_{\gamma_m}\left(\varepsilon_{k,m},\rho\right)=0. \tag{D.10}$$

The boundary conditions for the radial eigenfunctions are the following.

$$\begin{aligned}&R_{\gamma_m}\left(\varepsilon_{k,m},1\right)=0.\\&R_{\gamma_m}\left(\varepsilon_{k,m},\rho\right)<\infty.\end{aligned} \tag{D.11}$$

The solutions are Bessel's functions, $\mathrm{J}_{\gamma_m}\left(\varepsilon_{k,m}\rho\right)$ and $\mathrm{Y}_{\gamma_m}\left(\varepsilon_{k,m}\rho\right)$. The functions of the second kind are eliminated by the requirement that the magnetic field be bounded at $\rho=0$. The radial functions are given by

$$R_{\gamma_m}\left(\varepsilon_{k,m},\rho\right)=\mathrm{J}_{\gamma_m}\left(\varepsilon_{k,m}\rho\right), \tag{D.12}$$

where the eigenvalues, $\varepsilon_{k,m}$, are the roots of the equation

$$\mathrm{J}_{\gamma_m}\left(\varepsilon_{k,m}\right)=0, \tag{D.13}$$

and the order of the Bessel function is given by: $\gamma_m=\frac{\pi}{\phi_0}(1,\,3,\,5,\,\ldots)$. The normalization constant for the *r* transform, $N\left(\varepsilon_{k,m},\gamma_m\right)$ is given by the integral.

$$N\left(\varepsilon_{k,m},\gamma_m\right)=\int_0^1 \rho' \mathrm{J}^2_{\gamma_m}\left(\varepsilon_{k,m}\rho'\right)d\rho' \\ =\frac{\mathrm{J}^2_{\gamma_m+1}\left(\varepsilon_{k,m}\right)}{2}. \tag{D.14}$$

The $\xi$ transform is similar to the $\phi$ transform.

$$\tilde{\tilde{x}}^M_H(\varepsilon_{k,m},\gamma_m,\eta_p,t)=\int_0^1 \tilde{\tilde{x}}^M_H\left(\varepsilon_{k,m},\gamma_m,\xi,t\right)Z\left(\eta_p,\xi\right)d\xi. \tag{D.15}$$

$$\tilde{\tilde{x}}^M_H\left(\varepsilon_{k,m},\gamma_m,\xi,t\right)=\sum_{\gamma=1}^{\infty}\frac{Z\left(\eta_p,\xi\right)}{N\left(\eta_p\right)}\tilde{\tilde{x}}^M_H(\varepsilon_{k,m},\gamma_m,\eta_p,t). \tag{D.16}$$

The transform function is the solution to the associated homogeneous ordinary differential equation and boundary conditions in which $\eta$ is a parameter.

$$\frac{d^2Z\left(\eta_p,\xi\right)}{d\xi^2}+\eta_p^2Z\left(\eta,\xi\right)=0. \tag{D.17}$$

$$Z(\eta_p,0)=0. \\ Z\left(\eta_p,z_L\right)=0. \tag{D.18}$$

The eigenfunctions and eigenvalues are chosen to satisfy the differential equation and the boundary conditions

$$Z\left(\eta_p,\xi\right)=\sin\left(\eta_p\xi\right);\ \eta_p=\pi p;\ p=1,\ 2,\ 3,\ \ldots. \tag{D.19}$$

Unlike the azimuthal transform, the odd functions are retained for the $\xi$ transform.

The normalization constant for $Z\left(\eta_p,\xi\right)$ is

$$N\left(\eta_p\right)=\int_0^1 \sin^2\left(\eta_p\xi\right)dz \\ =\frac{1}{2}. \tag{D.20}$$

The three spatial integral transforms are applied to the differential equation for $x_M^H$ in Eq. (4.41) one at a time. The transforms of the spatial derivative terms are evaluated by using Green's theorem and applying the boundary conditions of the problem. Applying the transformation of the azimuthal variable to the differential term give the following.

$$\int_0^{\phi_0} \frac{1}{\rho^2} \frac{\partial^2 x_H^M(\rho,\phi,\xi,t)}{\partial\phi^2} \sin(\gamma_m\phi)\, d\phi = -\frac{\gamma_m^2}{\rho^2} \bar{x}_H^M(\rho,\gamma_m,\xi,t). \tag{D.21}$$

The remaining terms in Eq. (4.41) are unchanged by the transformation. The governing equation after applying the integral transform in the $\phi$ direction is given by the following.

$$\begin{aligned} \frac{1}{\rho}\frac{\partial}{\partial r}\left(\rho \frac{\partial \bar{x}_H^M(\rho,\gamma_m,\xi,t)}{\partial\rho}\right) - \frac{\gamma_m^2}{\rho^2}\bar{x}_{H,m}^M(\rho,\gamma_m,\xi,t) + \frac{\chi_R r_g^2}{z_L^2}\frac{\partial^2 \bar{x}_H^M(\rho,\gamma_m,\xi,t)}{\partial\xi^2} \\ -\sigma_R\mu_R r_g^2 \frac{\partial \bar{x}_H^M(\rho,\gamma_m,\xi,t)}{\partial t} = \sigma_R\mu_R r_g^2 \dot{\bar{x}}_{M,m}^{FEMM} + \frac{r_g^2}{T\Delta I}\dot{\bar{K}}_m^N. \end{aligned} \tag{D.22}$$

The transformation of the right hand side of the equation is indicated by the overbar. A subscript "m" is added to indicate the index of the transformation.

The next transformation removes the radial dependence. Applying the integral transformation in the radial variable defined in Eq. (D.8) to the first two terms in Eq. (D.22) yields the following expression. The simplified result on the right hand side is obtained using Green's theorem and the boundary conditions.

$$\begin{aligned} \int_{\rho=0}^{1} \left[\frac{1}{\rho}\frac{\partial}{\partial\rho}\left(\rho\frac{\partial \bar{x}_H^M(\rho,\gamma_m,z,t)}{\partial\rho}\right) - \frac{\gamma_m^2}{\rho^2}\bar{x}\bar{x}_H^M(\rho,\gamma_m,\xi,t)\right] \mathrm{J}_{\gamma_m}(\varepsilon_{k,m}\rho)\rho\, d\rho \\ = -\varepsilon_{k,m}^2 \tilde{\bar{x}}_H^M(\varepsilon_{k,m},\gamma_m,\xi,t). \end{aligned} \tag{D.23}$$

The remaining terms in Eq. (D.22) are unchanged by the transformation.

$$-\varepsilon_{k,m}^2 \tilde{\tilde{x}}_H^M\left(\varepsilon_{k,m},\gamma_m,z,t\right)+\frac{\chi_R r_g^2}{z_L^2}\frac{\partial^2 \tilde{\tilde{x}}_H^M\left(\varepsilon_{k,m},\gamma_m,\xi,t\right)}{\partial z^2}$$
$$-\sigma_R\mu_R r_g^2\frac{\partial \tilde{\tilde{x}}_H^M\left(\varepsilon_{k,m},\gamma_m,\xi,t\right)}{\partial t}=\sigma_R\mu_R r_g^2\dot{\tilde{\tilde{x}}}_{k,m}^{FEMM}+\frac{r_g^2}{T\Delta I}\dot{\tilde{\tilde{K}}}_{k,m}^N. \tag{D.24}$$

The final transformation to remove the axial variable follows the same pattern as the other two and leaves an ordinary differential in the thrice transformed magnetic field. The result is an ordinary differential equation in $t$ with parameters $\varepsilon_{k,m}$, $\gamma_m$, and $\eta_p$.

$$-\varepsilon_{k,m}^2 \hat{\tilde{\tilde{x}}}_H^M\left(\varepsilon_{k,m},\gamma_m,\eta_p,t\right)-\frac{\chi_R r_g^2\eta_p^2}{z_L^2}\hat{\tilde{\tilde{x}}}_H^M\left(\varepsilon_{k,m},\gamma_m,\eta_p,t\right)$$
$$-\sigma_R\mu_R r_g^2\dot{\hat{\tilde{\tilde{x}}}}_H^M\left(\varepsilon_{k,m},\gamma_m,\eta_p,t\right)=\sigma_R\mu_R r_g^2\dot{\hat{\tilde{\tilde{x}}}}_{k,m,p}^{FEMM}+\frac{r_g^2}{T\Delta I}\dot{\hat{\tilde{\tilde{K}}}}_{k,m,p}^N. \tag{D.25}$$

The notation using three superimposed diacritical marks to indicate the three successive transformations is clumsy. To simplify the notation, let the triply transformed variables be replaced by variables in script font.

$$\mathcal{x}_{k,m,p}^M=\hat{\tilde{\tilde{x}}}_H^M\left(\varepsilon_{k,m},\gamma_m,\eta_p,t\right). \tag{D.26}$$

$$\mathcal{x}_{M,k,m,p}^{FEMM}=\hat{\tilde{\tilde{x}}}_{M,k,m,p}^{FEMM}. \tag{D.27}$$

$$\dot{\mathcal{K}}_{M,k,m,p}=\dot{\tilde{\tilde{K}}}_{M,k,m,p}. \tag{D.28}$$

The eigenvalue terms for the radial and axial transformations are grouped as a single parameter. The new parameter has units of radians per second.

$$\alpha_{k,m,p}=\frac{\left(\varepsilon_{k,m}^2+\frac{\chi_R r_g^2\eta_p^2}{z_L^2}\right)}{\sigma_R\mu_R r_g^2}. \tag{D.29}$$

Incorporating the new notation into Eq. (D.25) and simplifying gives an ordinary differential equation.

$$\dot{\chi}^{M}_{k,m,p} + \frac{\dot{\kappa}^{N}_{k,m,p}}{\sigma_R \mu_R T \Delta I} + \dot{\chi}^{FEMM}_{k,m,p} = -\alpha_{k,m,p} \chi^{M}_{k,m,p} \,. \tag{D.30}$$

In this equation, $\chi^{M}_{k,m,p}$ is a scalar function of time and represents the amplitude of the ($k$, $m$, $p$) mode of the magnetic field due to eddy current. The $\chi^{M}_{k,m,p}$ term is used as the state variable in the modal magnetic model. The other derivative terms on the left hand side represent the coupling of the ($k$, $m$, $p$) mode to the vibration model and the coil model. These coupling terms can be evaluated as a linear combination of the corresponding state variables and coupling coefficients from the vibration and circuit models. These terms are evaluated in the remainder of this section.

The full solution by the integral transform method consists of a summation of the amplitude functions and the associated modal shapes.

$$x^{M}_{H}(\rho,\phi,\xi,t) = \sum_{k=1}^{kmax} \sum_{m=1}^{mmax} \sum_{p=1}^{pmax} \chi^{M}_{k,m,p}(t) \frac{\sin(\gamma_m \phi) \mathcal{J}_{\gamma_m}(\varepsilon_{k,m}\rho) \sin(\eta_p \xi)}{N(\varepsilon_{k,m},\gamma_m) N(\gamma_m) N(\eta_p)}. \tag{D.31}$$

Now, we turn to the evaluation of the transforms, $\dot{\kappa}^{N}_{k,m,p}$ and $\dot{\chi}^{FEMM}_{k,m,p}$. These terms can be evaluated by integrating the transformation equation. We begin with the $\chi^{FEMM}_{M,k,m,p}$ terms. The integral transform of the FEMM term can be written as follows

$$\dot{\chi}^{FEMM}_{k,m,p}(t) = \int_{\xi=0}^{1} \int_{\rho=0}^{1} \int_{\phi=0}^{\phi_0} \dot{x}^{FEMM}(\rho,z,t) \sin(\gamma_m \phi) \mathcal{J}_{\gamma_m}(\varepsilon_{k,m}\rho) \sin(\eta_p \xi) \rho d\phi d\rho d\xi \tag{D.32}$$

The FEMM results are computed in dimensioned units for field and position so it is necessary to convert the FEMM dimensioned variables to dimensionless before performing the integration.

$$\dot{\mathcal{H}}_{k,m,p}^{FEMM}(t)=\int_{\xi=0}^{1}\int_{\rho=0}^{1}\int_{\phi=0}^{\phi_0}\frac{\dot{H}_R^{FEMM}\left(r_g\rho,z_L\xi,t\right)}{T\Delta I}\sin\left(\gamma_m\phi\right)\mathfrak{J}_{\gamma_m}\left(\varepsilon_{k,m}\rho\right)\cdot\sin\left(\eta_p\xi\right)\rho d\phi d\rho d\xi. \tag{D.33}$$

Substituting the result given in Eq. (4.39) which represents the $\dot{H}_R^{FEMM}$ as the superposition of individual shape functions for the magnetic field due to each coil gives the following.

$$\begin{aligned}\dot{\mathcal{H}}_{k,m,p}^{FEMM}(t)&=\int_{\xi=0}^{1}\int_{\rho=0}^{1}\int_{\phi=0}^{\phi_0}\frac{\dot{H}_R^{FEMM}\left(r_g\rho,z_L\xi,t\right)}{T\Delta I}\sin\left(\gamma_m\phi\right)\mathfrak{J}_{\gamma_m}\left(\varepsilon_{k,m}\rho\right)\cdot\sin\left(\eta_p\xi\right)\rho d\phi d\rho d\xi\\&=\int_{\xi=0}^{1}\int_{\rho=0}^{1}\int_{\phi=0}^{\phi_0}\left[\frac{1}{T\Delta I}\sum_{j=1}^{jmax}H_{R,j}^{FEMM}\left(r_g\rho,z_L\xi,t\right)\dot{I}_{C,j}(t)\right]\sin\left(\gamma_m\phi\right)\mathfrak{J}_{\gamma_m}\left(\varepsilon_{k,m}\rho\right)\cdot\sin\left(\eta_p\xi\right)\rho d\phi d\rho d\xi\\&=\sum_{j=1}^{jmax}\frac{\dot{I}_{C,j}(t)}{\Delta I}\int_{\xi=0}^{1}\int_{\rho=0}^{1}\int_{\phi=0}^{\phi_0}\left[\frac{H_{R,j}^{FEMM}\left(r_g\rho,z_L\xi,t\right)}{T}\right]\sin\left(\gamma_m\phi\right)\mathfrak{J}_{\gamma_m}\left(\varepsilon_{k,m}\rho\right)\cdot\sin\left(\eta_p\xi\right)\rho d\phi d\rho d\xi.\end{aligned} \tag{D.34}$$

The triple integral yields a four-dimensional array of constants that is independent of time. We can define a coefficient matrix $\Theta_{k,l,m,j}$ for convenience. The subscripts *k*, *m*, *p* indicate the magnetic mode for radial, azimuthal, and axial components. The subscript *j* points to the energized coil.

$$\Theta_{k,m,p,j}=\frac{1}{T}\int_{\xi=0}^{1}\int_{r=0}^{1}\int_{\phi=0}^{\phi_0}H_{R,j}^{FEMM}\left(r_g\rho,z_L\xi\right)\sin\left(\gamma_m\phi\right)\mathfrak{J}_{\gamma_m}\left(\varepsilon_{k,m}\rho\right)\cdot\sin\left(\eta_p\xi\right)\rho d\phi d\rho d\xi. \tag{D.35}$$

The azimuthal integration can be performed analytically since the FEMM results do not depend on $\phi$.

$$\int_0^{\phi_0} \sin\left(\gamma_m \phi\right) d\phi = -\frac{\cos\left(\gamma_m \phi\right)}{\gamma_m}\bigg|_0^{\phi_0} = \frac{2}{\gamma_m}. \tag{D.36}$$

Thus, the coefficient can be written as the following.

$$\Theta_{k,m,p,j} = \frac{2}{T\gamma_m} \int_{\xi=0}^{1} \int_{r=0}^{1} H_{R,j}^{FEMM}\left(r_g \rho, z_L \xi\right) \mathfrak{J}_{\gamma_m}\left(\varepsilon_{k,m} \rho\right) \sin\left(\eta_p \xi\right) \rho d\rho d\xi. \tag{D.37}$$

The coil current's contribution to the mode differential equation in Eq. (D.30) can now be written as

$$\dot{\chi}_{k,m,p}^{FEMM}\left(t\right) = \sum_{j=1}^{jmax} \Theta_{k,m,p,j} \dot{x}_j^K\left(t\right). \tag{D.38}$$

The solution for $\Theta_{k,m,p,j}$ requires $H_{R,j}^{FEMM}\left(r,z\right)$ as a function of the currents in the individual coils. To obtain the distributions, a series of FEMM cases are solved in which the coils are energized one at a time. Each coil is energized with a steady current density ($\Omega$=0 Hz) equivalent to a current of one ampere per turn ($I_{C,j}\left(t\right)=1$) while the rest of the coils are specified to have zero current. The FEMM calculations are performed for each case and the values for the magnetic field are recorded in a two-dimensional grid in the *r*-*z* plane from $0 \le r \le r_g$ and $0 \le z \le z_L$. The grid spacing is $3.175\times10^{-4}$ m (0.0125 in) axially and $6.35\times10^{-5}$ m (0.0025 in) radially. This mesh size gives an array of 471 by 101 points over the axial and radial dimensions of the rod. The results are written to a file which is then transferred into MATLAB to perform the integration in Eq. (D.37). The *r*-*z* integration is performed using two-dimensional Simpson's rule for numerical integration [75].

The physical meaning of the $\Theta_{k,m,p,j}$ coefficient is the fraction of the electromotive force from the time-varying current in the *j*-th coil that goes into the (*k, m, p*) mode of the eddy current's magnetic field. The modes themselves represent fixed distributions of field that, when linearly combined with the associated amplitude function, sum to give the field due to eddy current. The $\Theta_{k,m,p,j}$ coefficients diminish as the indices increase which means that higher frequency modes receive a smaller fraction of the energy. The frequency constant, $\alpha_{k,m,p}$, which is given by Eq. (D.29), represents the decay rate of the mode. Energy entering the higher modes decays away exponentially with this rate constant. The decay rate also increases with the indices; therefore, higher frequency modes dissipate their energy more rapidly than the lower modes. Truncating the series is equivalent to causing the energy that would have entered those modes to decay away immediately. In effect, the truncation is the same as approximating the terms with the large decay constants as having infinite decay constants.

The coupling coefficients between the eddy current field and the field generated by strain are derived by a similar triple integral transformation. The vibration model in Chapter 3 is a modal solution for strain versus position. The integration of the product of the two spatial functions can be solved analytically. The axial functions are trigonometric series for both magnetics and vibration, but the boundary conditions for the two problems are different. The vibration modes are not orthogonal to the magnetics modes. Thus, each vibration mode couples with each current mode. The transformation of the vibration submodel solution is given by:

$$\frac{r_g^2 \dot{\kappa}_{k,m,p}^N}{T\Delta I} = \frac{\kappa_{eff,z} d_{33}}{\mu_R} \int_{\xi=0}^{1} \int_{\rho=0}^{1} \int_{\phi=0}^{\phi_0} \frac{\partial}{\partial \xi} \left[ \sigma_R \mu_R r_g^2 \frac{\partial x^N}{\partial t} \right] \cdot \sin(\gamma_m \phi) \mathrm{J}_{\gamma_m}(\varepsilon_{k,m} \rho) \sin(\eta_p \xi) \rho d\phi d\rho d\xi. \tag{D.39}$$

where $x^N$ is the displacement variable in dimensionless form. The modal solution to the vibration problem is given by Eq. (D.40) from Appendix B. The equation is repeated here for reference.

$$x^N(\xi, t) = \sum_{n=1}^{nmax} \chi_n^N(t) \frac{\sin(\beta_n \xi)}{N(\beta_n)}. \tag{D.40}$$

where the eigenvalues are given by $\beta_n = \frac{(2n-1)\pi}{2}$ and the normalization factor for the modal function is given by

$$N(\beta_n) = \int_{\xi=0}^{1} \sin^2(\beta_n \xi) d\xi = \frac{1}{2}. \tag{D.41}$$

Since $x_N(\xi, t)$ does not depend on $\phi$ or $\rho$, the radial and azimuthal integral transformations in Eq. (D.39) can be evaluated independent of the vibration model given in Eq (D.40). The formula for the integral of the Bessel function is too long to reproduce. It can be obtained with MATLAB's Symbolic Toolbox [34]. The integrals can be collected into a coefficient.

$$\begin{aligned} \Gamma_{k,m} &= \int_{\phi=0}^{\phi_0} \sin(\gamma_m \phi) d\phi \int_{\rho=0}^{1} \mathrm{J}_{\gamma_m}(\varepsilon_{k,m} \rho) \rho d\rho \\ &= \frac{2}{\gamma_m} \int_{\rho=0}^{1} \mathrm{J}_{\gamma_m}(\varepsilon_{k,m} \rho) \rho d\rho. \end{aligned} \tag{D.42}$$

The remaining integrations in Eq. (D.39) are evaluated by substituting in the modal form from Eq. (D.40) and integrating analytically.

$$\begin{aligned}\int_{\xi=0}^{1}\frac{\partial}{\partial\xi}\left(\frac{\partial x^N}{\partial t}\right)\sin\left(\eta_p\xi\right)d\xi &= \int_{\xi=0}^{1}\frac{\partial}{\partial t}\left\{\frac{\partial}{\partial\xi}\left[\sum_{n=1}^{nmax}\chi_n^N(t)2\sin\left(\beta_n\xi\right)\right]\right\}\sin\left(\eta_p\xi\right)d\xi \\ &= \int_{\xi=0}^{1}\left[\sum_{n=1}^{nmax}\dot{\chi}_n^N(t)2\beta_n\cos\left(\beta_n\xi\right)\right]\sin\left(\eta_p\xi\right)d\xi \\ &= \sum_{n=1}^{nmax}\left[\dot{\chi}_n^N(t)2\beta_n\int_{\xi=0}^{1}\cos\left(\beta_n\xi\right)\sin\left(\eta_p\xi\right)d\xi\right] \\ &= \sum_{n=1}^{nmax}\left[\dot{\chi}_n^N(t)\frac{2\beta_n\eta_p}{\left(\eta_p^2-\beta_n^2\right)}\right].\end{aligned} \tag{D.43}$$

Reassembling the individual integrations from Eqs. (D.42) and (D.42) and rearranging the result into the form required for Eq. (D.39) gives the following equation.

$$\frac{\dot{\kappa}_{k,m,p}^N}{\sigma_R\mu_R T\Delta I} = \frac{\kappa_{eff,z}d_{33}\Gamma_{k,m}}{\mu_R}\sum_{n=1}^{nmax}\left[\dot{\chi}_n^N(t)\frac{2\beta_n\eta_p}{\left(\eta_p^2-\beta_n^2\right)}\right]. \tag{D.44}$$

Let the following coefficient matrix be defined to group the constants for future use. The coefficient is defined by extracting the constant factors from Eq. (D.44)

$$\Upsilon_{k,m,p,n} = \frac{\kappa_{eff,z}d_{33}}{\mu_R}\frac{2\beta_n\eta_p\Gamma_{k,m}}{\left(\eta_p^2-\beta_n^2\right)}. \tag{D.45}$$

Inserting the coefficient names into Eq. (D.44) gives the following

$$\frac{\dot{\kappa}_{k,m,p}^N}{\sigma_R\mu_R T\Delta I} = \sum_{n=1}^{nmax}\Upsilon_{k,m,p,n}\dot{\chi}_n^N(t). \tag{D.46}$$

Equation (D.30) can be written in terms of the state variables and coefficient matrices from Eq. (D.38) and Eq. (D.46). The terms are re-ordered in anticipation of writing the system in the descriptor form of the state space model defined in Eq. (4.91).

$$\sum_{j=1}^{jmax}\Theta_{k,m,p,j}\dot{x}_j^K(t)+\dot{\chi}_{k,m,p}^M = -\sum_{n=1}^{nmax}\Upsilon_{k,m,p,n}\dot{\chi}_n^N(t)-\alpha_{k,m,p}\chi_{k,m,p}^M. \tag{D.47}$$

### Test Calculations of the Magnetic Field in the Pie-Shaped Cylinder Model

A number of stand alone calculations can be performed with the magnetic model to check the solution and to gain insight into the physical processes being modeled. The test calculations are based on limiting cases in which the magnetic model solution must approach a known distribution. One type of limiting case can be constructed by allowing the driving frequency to approach infinity. Either a vibration mode or a coil current can be driven with infinite frequency. In either case, the magnetic induction in the interior of the rod must approach zero. The eddy current induction must build sufficiently to cancel the source distribution exactly. Since the series solution for the eddy current induction distribution is truncated, the cancelation is approximate. The test cases can be used to confirm the derivation and programming of the vibration and coil current coupling coefficients and to determine number of terms in the series that are needed for a valid approximation of the source distribution.

Another type of limiting case can be constructed by considering the solution when the rod length approaches infinity. The infinite rod case can be modeled using the FEMM code by using the trick described in APPENDIX C. A modal magnetic solution approximating the infinite rod can be evaluated using the modal magnetic model by simply energizing all coils and evaluating the solution at the axial midplane. Since the rod is long and thin, the field at the axial midplane approaches the FEMM infinite rod distribution.

## Spatial Distribution of Magnetic Field at Infinite Frequency for Coil Current and Vibration

### Coil current case

First, consider the case of the magnetic field in which the frequency of the applied coil current approaches infinity. In this test case, the vibration is set to zero. Mathematically, the vibration can be forced to be zero by choosing the magnetostriction coefficient to be zero, $d_{33} = 0$ so that the vibration term in Eq. (D.47) is zero.

$$\sum_{n=1}^{nmax} \Upsilon_{k,m,p,n} \dot{\chi}_n^N(t) = 0. \tag{D.48}$$

When the actuator is stimulated using coil current with infinite frequency, the eddy current builds sufficiently to cause the magnetic field in the interior of the actuator to be zero.

$$\lim_{\omega\to\infty} \frac{\underline{x}^M(\rho,\phi,\xi,\omega)}{\underline{x}_j^K(\omega)} = 0. \tag{D.49}$$

The amplitude function from Eq. (4.79) at infinite frequency is given by

$$\lim_{\omega\to\infty} \frac{i\omega}{i\omega + \alpha_{k,m,p}} = 1. \tag{D.50}$$

Using these two facts, we obtain the following equation from Eq. (4.82) for a case in which the *j*-th coil is energized and all other coils are not energized.

$$\frac{1}{T}\frac{H_{R,j}^{FEMM}(r_g\rho, z_L\xi)}{\hat{x}_j^K} \approx \sum_{k=1}^{kmax}\sum_{m=1}^{mmax}\sum_{p=1}^{pmax} \Theta_{k,m,p,j} \frac{\sin(\gamma_m\phi)\mathrm{J}_{\gamma_m}(\varepsilon_{k,m}\rho)\sin(\eta_p\xi)}{N(\varepsilon_{k,m},\gamma_m)N(\gamma_m)N(\eta_p)}. \tag{D.51}$$

The left hand side is the coil's field calculated by FEMM. The right hand side is the eddy current field calculated from the modal solution. The relationship is only

approximately equal because the eddy current series is truncated to a finite number of terms. The summation on the right hand side is also the inverse of the transform given by Eq. (D.35). To indicate the inverse transform the function, the function on the right hand side can be called, $x_{INV,j}^{FEMM}(r,z)$, and compared that with the original FEMM results. The inverse transform is given by

$$x_{INV,j}^{FEMM}(r,\phi,z)=\sum_{k}\sum_{m}\sum_{p}\frac{\Theta_{k,m,p,j}}{N(\gamma_m)N(\varepsilon_{k,m},\gamma_m)N(\eta_p)}\sin(\gamma_m\phi)\mathfrak{J}_{\gamma_m}\left(\frac{\varepsilon_{k,m}r}{r_g}\right)\sin\left(\frac{\eta_p z}{z_L}\right). \tag{D.52}$$

The test calculation compares the modal solution to the original FEMM distribution to determine how closely the following approximation holds.

$$x_{INV,j}^{FEMM}(r,\phi,z)\approx x_{R,j}^{FEMM}(r,z)=\frac{H_{R,j}^{FEMM}(r,z)}{T}. \tag{D.53}$$

Figure D.1 and Figure D.2 show the coil's magnetic field in a rectangular *r*-*z* plane for cases with energized coils at *j*=1 and 5. The figure in the top pane is coil's magnetic field calculated by FEMM, $x_{R,j}^{FEMM}(r,z)$. The figures below are the inverse transforms of the field, $x_{INV,j}^{FEMM}(r,\phi,z)$, calculated using Eq. (D.52) for the high and low order models. The maximum orders of the dimension of the high order case are: radial, *kmax*=10; azimuthal, *mmax*=10; and axial, *pmax*=20. The maximum orders of the low order case are: radial, *kmax*=1; azimuthal, *mmax*=1; and axial, *pmax*=10. The inverse transform includes $\phi$ dependence because the modal result varies in the azimuthal direction due to truncation error. In the axial section view, the cutting angle is positioned at the azimuthal midplane of the pie-segment, $\phi=\frac{\phi_0}{2}=\frac{\pi}{4}$. The aspect ratio for the plots

is set so that the *r*-*z* region suggests a long thin rod, but the dimensions are not to scale. The scale of the radial direction is expanded slightly to show the radial dependence more clearly.

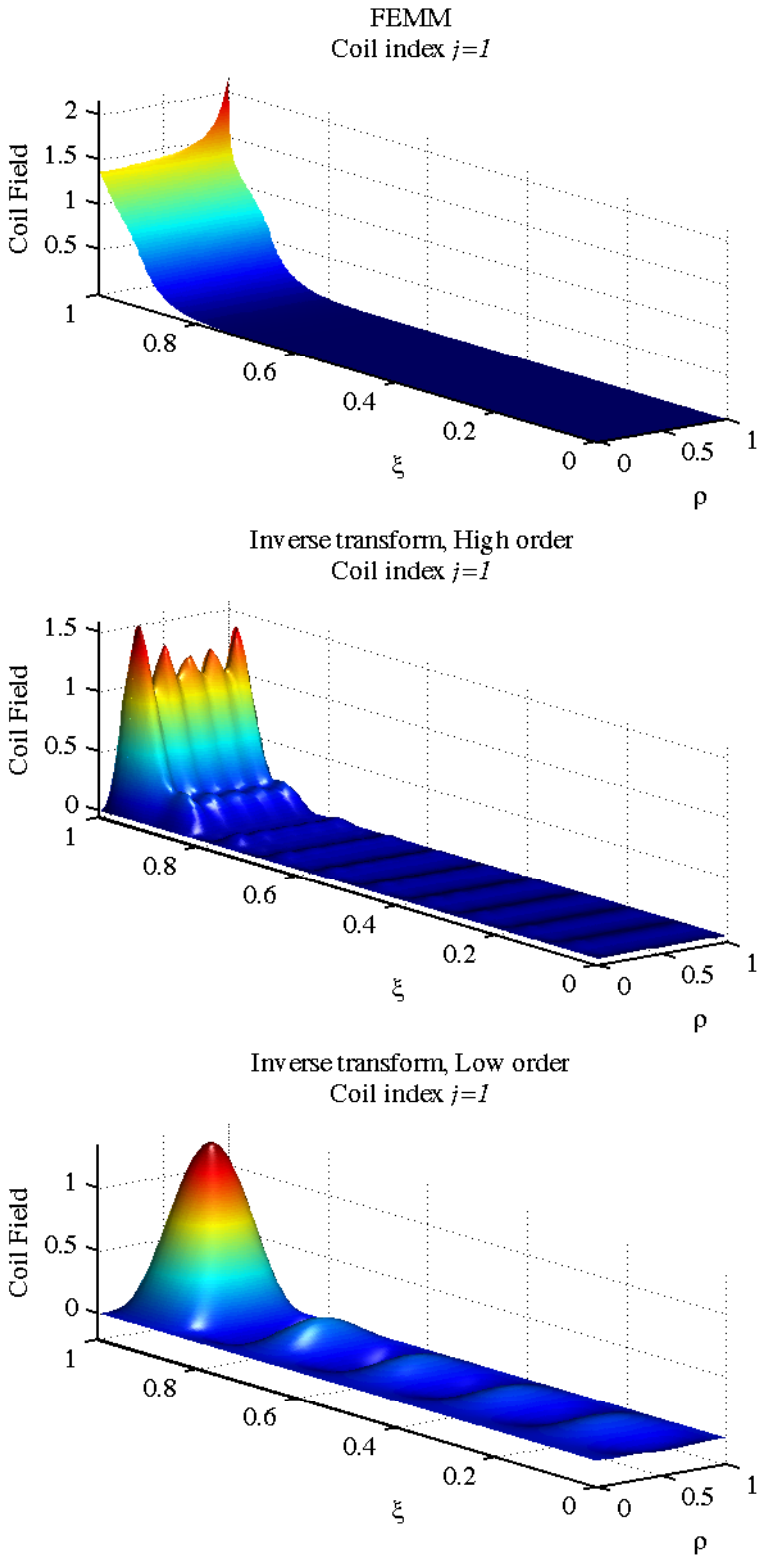


Figure D.1: Comparison of coil's magnetic field from FEMM and inverse transform, coil index, j=1

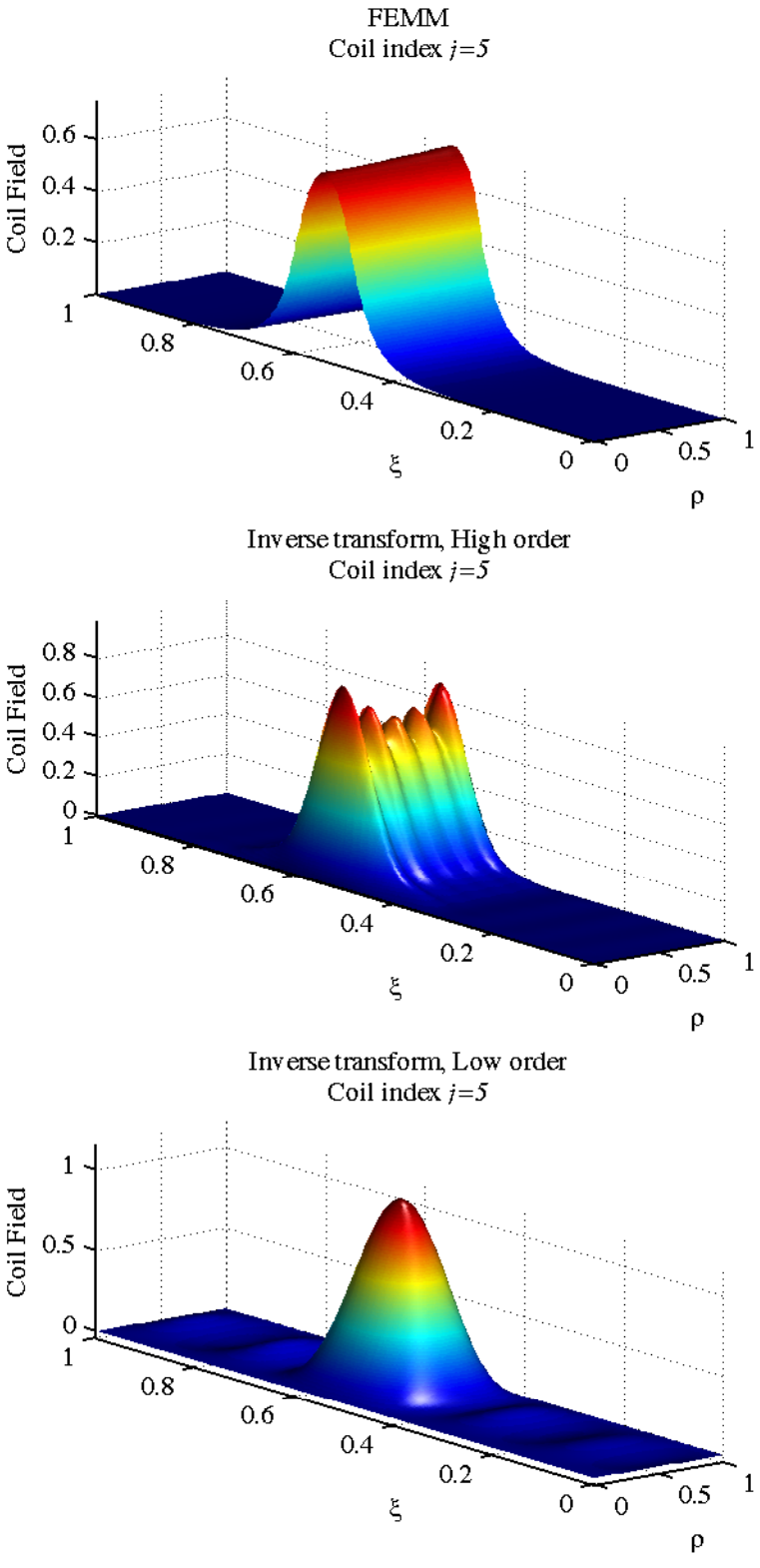


Figure D.2: Comparison of magnetic fields from FEMM and its inverse transform; coil index, j=5

The plots for energized coils at $j$=1 and 5 are representative of the results for all ten coils. The figures for $j$=1 and 10 are close to mirror images. The shapes for $j$=2 through 9 are all approximately the same. The figures show that the field spreads axially above and below the region of the coil that generates it. The FEMM field peaks at either end of the rod because of the high permeability of the return path. The FEMM field also has a slight peak at the outer cylindrical surface of the rod adjacent to the energized coil compared to the centerline. The inverse transform results are noticeably more oscillatory in space that the original FEMM results. The results appear to be correct in an average sense, but the series solution does not converge closely to the original function even for the high order case. The non-homogeneous boundary condition near the edge is the cause of the somewhat bumpy fit. While the fit does not look impressive, the accuracy of the inverse transform fit is not a major concern in the actuator model. The infinite frequency case converges more slowly than any finite frequency. Consider the frequency dependent factor in Eq. (4.82). For finite frequency, the factor is less than one and diminishes with higher order terms because the frequency constant, $\alpha_{k,m,p}$, increases with order.

$$\left| \frac{i\omega}{i\omega + \alpha_{k,m,p}} \right| < 1 . \tag{D.54}$$

The infinite frequency cases in Figure D.1 and Figure D.2 represent the worst case comparison for convergence. The actual frequency range of interest is between 0 and 10,000 Hz. Over this range, the field due to the eddy current is much closer to homogeneous on the rod surface, and the solution converges more rapidly. The main point of the test is to provide evidence that the numerical integration which is used to

obtain $\Theta_{k,m,p,j}$ is programmed correctly. This is indicated by the fact that the average behavior of the fit is correct.

To compare the quantitative results more closely, the values of $x_{R,j}^{FEMM}(r,z)$ and $x_{INV,j}^{FEMM}(r,\phi,z)$ for the low and high order cases can be plotted along a line on the same plot. Figure D.3 and Figure D.4 compare in the axial and radial directions respectively for energized coil, *j*=5. In the radial direction, the angle that is chosen for the plot is the midplane of the pie-segment, $\phi = \frac{\phi_0}{2} = \frac{\pi}{4}$ and the midplane of the energized coil, $\xi = \xi_5$. For the axial plot, the same angular position is shown and the radial position is set at $\rho = 0.6$ near the minimum of the eddy current field in the transverse plane.

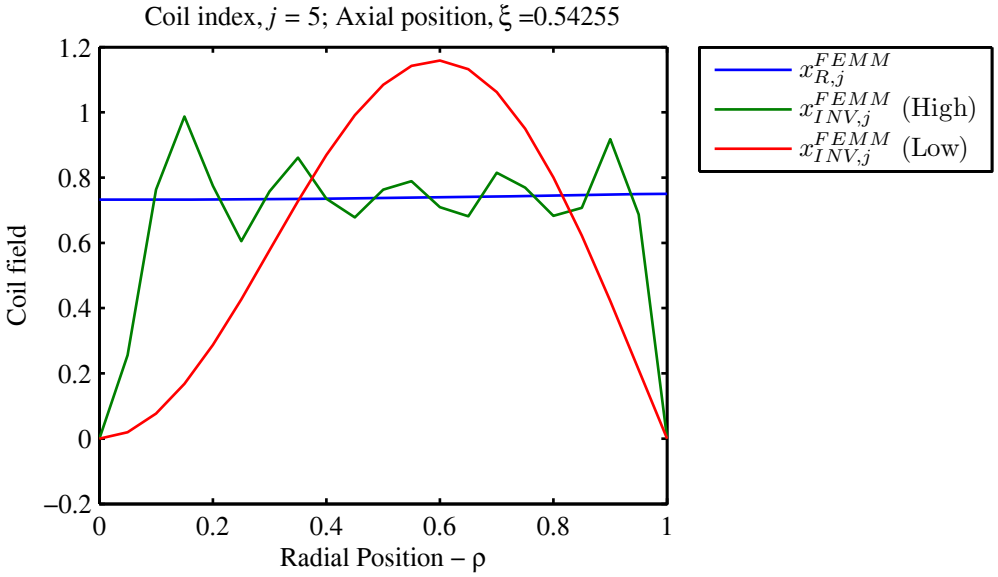


Figure D.3: Comparison of radial fit of FEMM by the inverse transform for high and low order models for energized coil, j=5

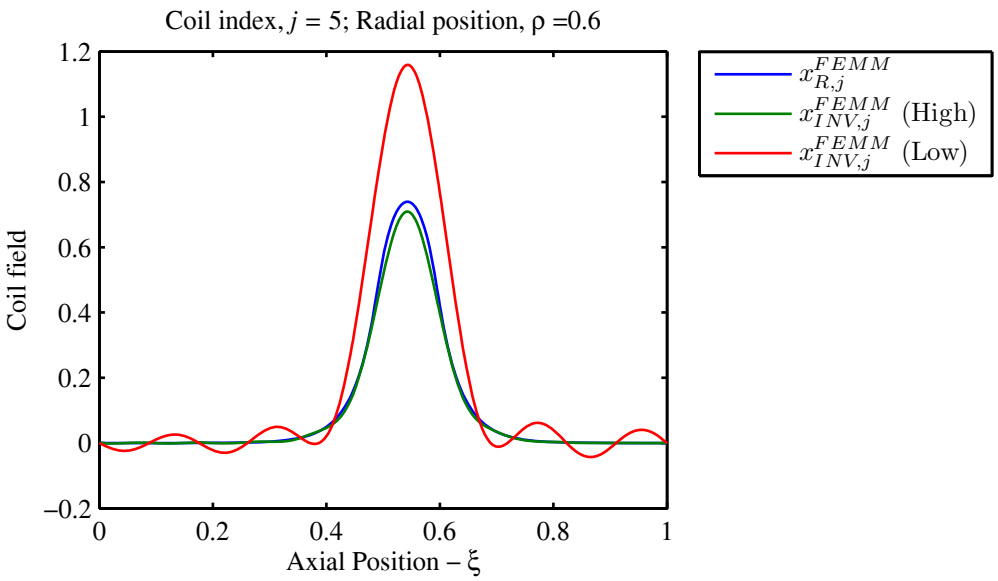


Figure D.4: Comparison of axial fit of FEMM by the inverse transform for high and low order models for energized coil, *j*=5.

**Vibration driven case**

The vibration driven case is constructed in a similar fashion to the coil current case. As the vibration frequency approaches infinity, the eddy current induction must match the induction from vibration. The idea of an infinite frequency of vibration requires some mental ingenuity to conceive. The source term in the diffusion equation is chosen to be a single spatial vibration mode. The limiting case is constructed by increasing the frequency of that mode to infinity. In reality, each spatial mode is associated with a single, particular frequency that is determined by the length the rod, the speed of sound in the material, and the harmonic chosen. The infinite frequency case is a purely mathematical construction. For a physical interpretation, one can imagine it as the effect of a material whose density can be decreased (or its Young's modulus increased) at will. The infinite frequency is the limiting case as the density is decreased to zero while keeping all other properties the same.

The description of the vibration problem is different from the coil problem because it is necessary to be precise about the difference between the magnetic induction and magnetic field. By the conventional definition, a magnetization is not a magnetic field even though it has the same units. Only real currents, such as coil currents and eddy current, produce magnetic field. The magnetization produced by strain does produce magnetic induction (magnetic flux density) and can be thought of as an equivalent current density. In the case of a coil current with infinite frequency, we can speak of the field canceling, but in reality, it is induction that goes to zero. For real currents and linear magnetic materials, the field and induction are simply proportional. In the case of vibration, the strain produces magnetization. The vibration case requires that the magnetic induction, **B**, must be zero rather than the magnetic field, **H**. To make this point with an equation, the induction at the limiting frequency is given by the following

$$\lim_{\omega\to\infty} \mathbf{B} = \lim_{\omega\to\infty} \mu_0 \left(\mathbf{H} + \mathbf{M}\right) = 0 \,. \tag{D.55}$$

where in this case **H** is the field from eddy current and **M** is the total magnetization due to the strain and to the ferromagnetic properties of the material. The magnetic induction from strain is canceled by the eddy current's induction.

$$\begin{aligned} \mu_0 \left(\mathbf{H} + \mathbf{M}\right) &= \mu_0 \left(\mathbf{H} + \mathbf{M}_{Ferro} + \mathbf{M}_{Strain}\right) \\ &= \mu_0 \left(\mathbf{H} + \mathrm{X}_M \mathbf{H} + \mathbf{M}_{Strain}\right) \\ &= \mu_0 \left(1 + \mathrm{X}_M\right) \mathbf{H} + \mu_0 \mathbf{M}_{Strain}, \end{aligned} \tag{D.56}$$

where $\mathrm{X}_M$ is the magnetic susceptibility. The constitutive equation for magnetostrictgive materials gives the following equations for the terms in Eq. (D.56).

$$\mu_R = \mu_0 \left(1 + \mathrm{X}_M\right). \tag{D.57}$$

$$\mu_0 M_z = k_{eff,z} S_z = k_{eff,z} \frac{\partial \zeta_z}{\partial z}. \tag{D.58}$$

Setting the net axial component of induction to zero and setting coil current to zero yields the terms for eddy current and strain.

$$B_z = \mu_R H_R^H + k_{eff,z} \frac{\partial \zeta_z}{\partial z} = 0. \tag{D.59}$$

The transformations for dimensionless units for magnetic induction are given in Chapter 2. The following is the transformation for magnetic induction.

$$b = \frac{B}{\mu_R T \Delta I}. \tag{D.60}$$

Applying the transformation for induction to the first term in Eq. (D.59) gives the same transformation as the magnetic field.

$$x_H^M = \frac{\mu_R H_R^H}{\mu_R T \Delta I} = \frac{H_R^H}{T \Delta I}. \tag{D.61}$$

Applying the same transformation to the magnetization due to strain term gives

$$m_z = \frac{\mu_0 M_z}{\mu_R T \Delta I_z} = \frac{k_{eff,z}}{\mu_R T \Delta I} \frac{\partial \zeta_z}{\partial z}. \tag{D.62}$$

The dimensionless transformations for $z$ and $\zeta_z$ from Eq. (4.54) and Eq. (4.63) can be inserted into Eq. (D.62) to give the dimensionless magnetization as a function of the dimensionless strain.

$$\begin{aligned} m_z &= \frac{k_{eff,z}}{\mu_R T \Delta I} \frac{\partial}{\partial (z_z \xi)} \left[ \frac{\kappa_{eff} z_L T \Delta I}{Y_{eff}^H} x^N \right] \\ &= \frac{k_{eff,z}}{\mu_R} \frac{\kappa_{eff}}{Y_{eff}^H} \frac{\partial x^N}{\partial \xi}. \end{aligned} \tag{D.63}$$

The limiting case for frequency can now be written in terms of the transformed variables.

$$\lim_{\omega\to\infty}\left[\underline{x}_H^M(\rho,\phi,\xi,\omega)+\underline{m}_z(\omega)\right]=0. \tag{D.64}$$

Now we want to evaluate the terms in the equation using the modal solutions for vibration and eddy current.

Using an identity defined in Chapter 2, $\frac{\kappa_{eff}}{Y_{eff}^H}=d_{33}$, and the modal solution of the vibration model from Eq. (D.40), the magnetization can be written as

$$\begin{aligned} m_z(\xi,t) &= \frac{k_{eff,z}d_{33}}{\mu_R}\frac{\partial}{\partial\xi}\left[\sum_{n'=1}^{nmax}\chi_{n'}^N(t)\frac{\sin(\beta_{n'}\xi)}{N(\beta_{n'})}\right] \\ &= \frac{k_{eff,z}d_{33}}{\mu_R}\sum_{n'=1}^{nmax}\chi_{n'}^N(t)2\beta_{n'}\cos(\beta_{n'}\xi). \end{aligned} \tag{D.65}$$

A single vibration mode can be selected for the purposes of the mathematical test. Let the vibration in $n'=n$ be defined as a harmonic driving function with frequency $\omega$ while all other modes are zero.

$$\left|\underline{\chi}_n^N(\omega)\right|=1. \tag{D.66}$$

The phasor transform of $m_z(t)$ for the single vibration mode is then

$$\frac{\underline{m}_z(\omega)}{\underline{\chi}_n^N(\omega)}=\frac{k_{eff,z}d_{33}}{\mu_R}2\beta_n\cos(\beta_n\xi). \tag{D.67}$$

Equation (D.47) can be transformed selecting only the *n*-th vibration mode and setting the coil current term to zero.

$$\begin{aligned} &\underline{\chi}_{k,m,p}^M(\omega)+\Upsilon_{k,m,p,n}\underline{\chi}_n^N(\omega)=-\alpha_{k,m,p}\underline{\chi}_{k,m,p}^M. \\ &\frac{\underline{\chi}_{k,m,p}^M(\omega)}{\underline{\chi}_n^N(\omega)}=\frac{-i\omega\Upsilon_{k,m,p,n}}{(i\omega+\alpha_{k,m,p})}. \end{aligned} \tag{D.68}$$

$$\lim_{\omega\to\infty}\frac{-i\omega\Upsilon_{k,m,p,n}}{\left(i\omega+\alpha_{k,m,p}\right)}=-\Upsilon_{k,m,p,n}. \tag{D.69}$$

As $\omega\to\infty$,

$$\frac{\underline{\chi}^{M}_{k,m,p}}{\underline{\chi}^{N}_{n}}=-\Upsilon_{k,m,p,n}. \tag{D.70}$$

Thus, the magnetic field due to eddy current at infinite frequency of the vibration is given by inserting Eq. (D.70) into Eq. (4.80).

$$\begin{aligned}\underline{x}^{M}_{H}\left(\rho,\phi,\xi,\omega\right)&=\sum_{k=1}^{kmax}\sum_{m=1}^{mmax}\sum_{p=1}^{pmax}\underline{\chi}^{M}_{k,m,p}\left(\omega\right)\frac{\sin\left(\gamma_m\phi\right)\mathrm{J}_{\gamma_m}\left(\varepsilon_{k,m}\rho\right)\sin\left(\eta_p\xi\right)}{N\left(\varepsilon_{k,m},\gamma_m\right)N\left(\gamma_m\right)N\left(\eta_p\right)}\\&=-\sum_{k=1}^{kmax}\sum_{m=1}^{mmax}\sum_{p=1}^{pmax}\Upsilon_{k,m,p,n}\underline{\chi}^{N}_{n}\left(\omega\right)\frac{\sin\left(\gamma_m\phi\right)\mathrm{J}_{\gamma_m}\left(\varepsilon_{k,m}\rho\right)\sin\left(\eta_p\xi\right)}{N\left(\varepsilon_{k,m},\gamma_m\right)N\left(\gamma_m\right)N\left(\eta_p\right)}.\end{aligned} \tag{D.71}$$

$$\frac{\underline{x}^{M}\left(\rho,\phi,\xi,\omega\right)}{\underline{\chi}^{N}_{n}\left(\omega\right)}=-\sum_{k=1}^{kmax}\sum_{m=1}^{mmax}\sum_{p=1}^{pmax}\Upsilon_{k,m,p,n}\frac{\sin\left(\gamma_m\phi\right)\mathrm{J}_{\gamma_m}\left(\varepsilon_{k,m}\rho\right)\sin\left(\eta_p\xi\right)}{N\left(\varepsilon_{k,m},\gamma_m\right)N\left(\gamma_m\right)N\left(\eta_p\right)}. \tag{D.72}$$

Equating eddy current and vibration terms gives the comparison that serves as the test of the vibration model.

$$\cos\left(\beta_n\xi\right)\approx-\frac{\mu_R}{2\beta_n k_{eff,z}d_{33}}\sum_{k=1}^{kmax}\sum_{m=1}^{mmax}\sum_{p=1}^{pmax}\Upsilon_{k,m,p,n}\frac{\sin\left(\gamma_m\phi\right)\mathrm{J}_{\gamma_m}\left(\varepsilon_{k,m}\rho\right)\sin\left(\eta_p\xi\right)}{N\left(\varepsilon_{k,m},\gamma_m\right)N\left(\gamma_m\right)N\left(\eta_p\right)}. \tag{D.73}$$

The function on the right is the three-dimensional, inverse transform of the function on the left. Following the nomenclature of the coil model, this quantity is called the inverse transform of the cosine function.

$$\underline{x}^{\cos}_{INV,n}\left(\rho,\phi,\xi\right)=\frac{\mu_R}{2\beta_n k_{eff,z}d_{33}}\sum_{k=1}^{kmax}\sum_{m=1}^{mmax}\sum_{p=1}^{pmax}\Upsilon_{k,m,p,n}\frac{\sin\left(\gamma_m\phi\right)\mathrm{J}_{\gamma_m}\left(\varepsilon_{k,m}\rho\right)\sin\left(\eta_p\xi\right)}{N\left(\varepsilon_{k,m},\gamma_m\right)N\left(\gamma_m\right)N\left(\eta_p\right)}. \tag{D.74}$$

The vibration case can be compared in a surface plot in the same way as the coil case. The cosine forcing functions $\cos(\beta_3\xi)$ and $\cos(\beta_5\xi)$ are shown in Figure D.5 and Figure D.6. The cosine function is shown in the top panel the lower two panels are the inverse transform for the high and low order solutions.

Figure D.7 compares the high order and low order and the original cosine function on the same figure. The magnetic field is plotted along an axial line. The same three mode cases are shown as in Figure D.5 and Figure D.6.

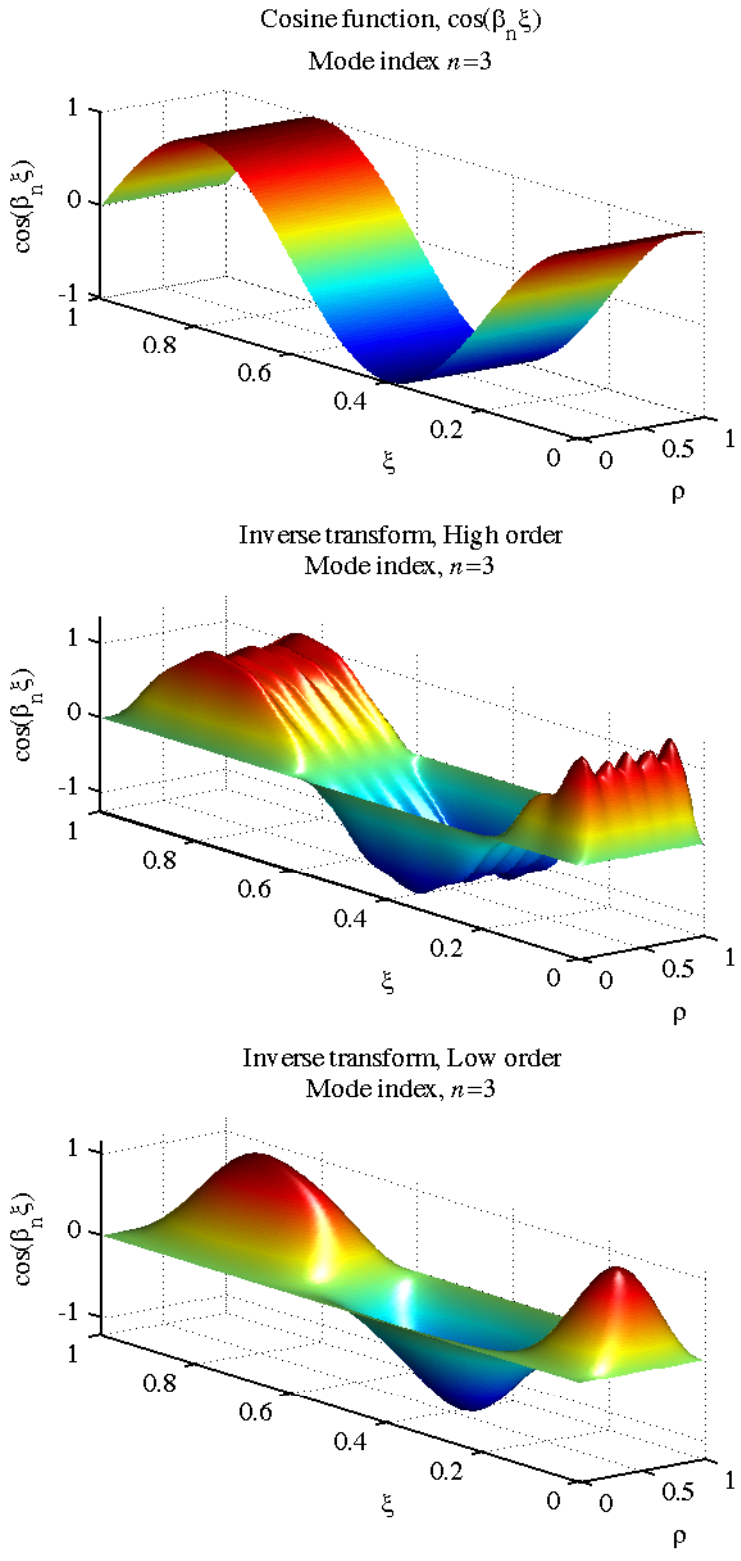


Figure D.5: Comparison of magnetic fields from a vibration mode and its inverse transform; mode index, $n$=3.

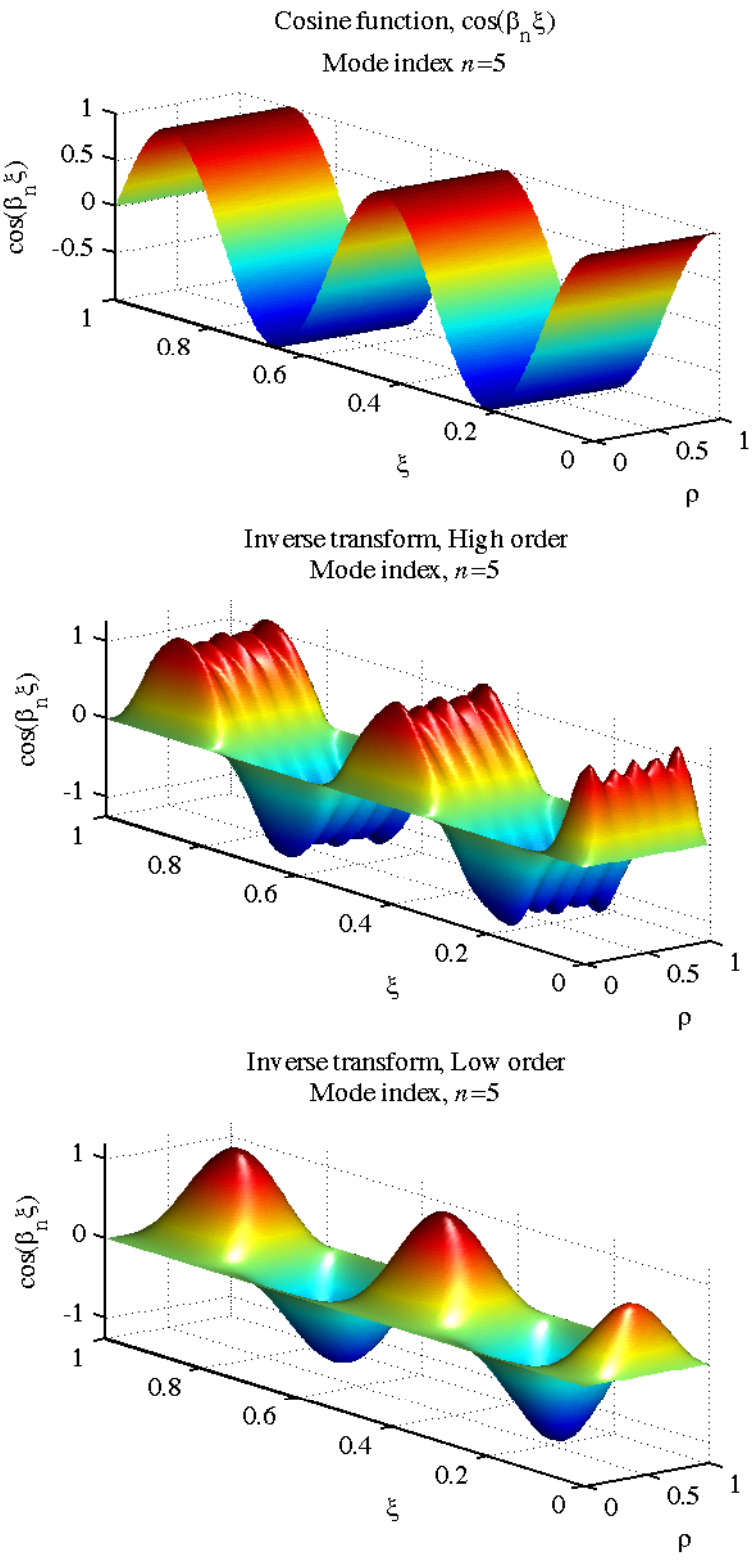


Figure D.6: Comparison of magnetic fields from a vibration mode and its inverse transform; mode index, $n$=5.

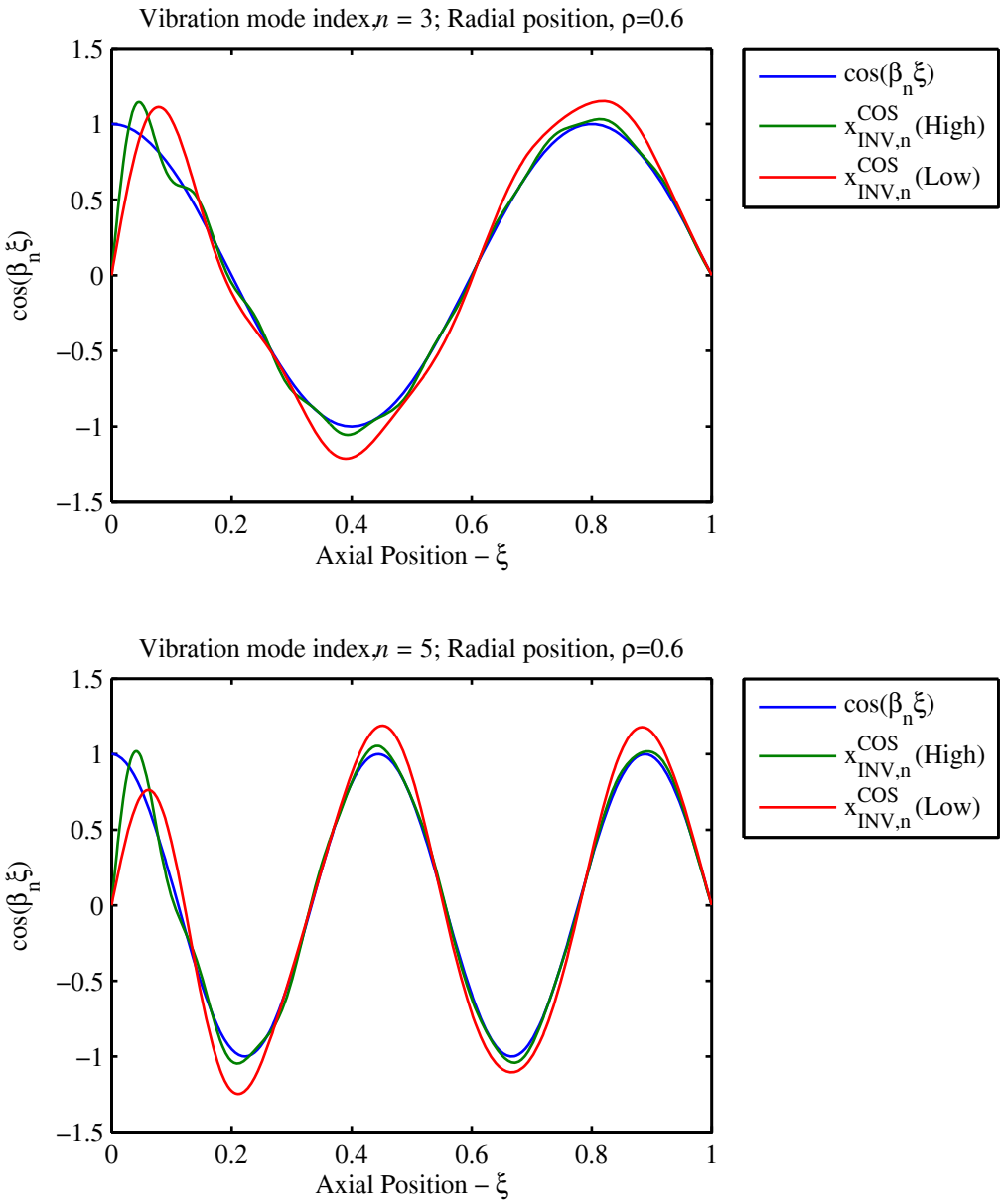


Figure D.7: Comparison of high and low order inverse transforms to vibration forcing function

**Infinite frequency for the state space results**

To check the state space matrices, the limiting case at infinite frequency can be applied again. The descriptor form of the state space model in Eq. (4.93) can be written as

$$\mathbf{E}^{43}\dot{\mathbf{x}}^{\mathbf{K}} + \dot{\mathbf{x}}^{\mathbf{M}} = \mathbf{F}^{41}\dot{\mathbf{x}}^{\mathbf{N}} + \mathbf{F}^{44}\mathbf{x}^{\mathbf{M}}. \tag{D.75}$$

Assuming the vibration term is zero gives an equation that can be solved for the magnetic field vector.

$$\dot{\mathbf{x}}^{\mathbf{M}} = \mathbf{F}^{44}\mathbf{x}^{\mathbf{M}} - \mathbf{E}^{43}\dot{\mathbf{x}}^{\mathbf{K}}. \tag{D.76}$$

Using the formula for field at the midplane from Eq. (4.89) gives the following definition of an output variable representing the average field at each axial elevation, $\xi = \xi_j$.

$$\underline{y}_j = \sum_{p=1}^{pmax}\sum_{m=1}^{mmax}\sum_{k=1}^{kmax} \underline{\mathcal{Z}}^{M}_{k,m,p}(t) P_{k,m} \sin\left(\eta_p \xi_j\right) + \sum_{j'=1}^{jmax} \underline{x}^{K}_{j'}(t) \breve{x}^{FEMM}_{R,j'}\left(\xi_j\right). \tag{D.77}$$

This equation can be written as a state space output equation in a state space by the following variable definitions

$$\underline{\mathbf{y}} = \mathbf{C}\underline{\mathbf{x}}^{\mathbf{M}} + \mathbf{D}\underline{\mathbf{x}}^{\mathbf{K}}. \tag{D.78}$$

The observation matrices are obtained by comparison of Eqs. (D.77) and (D.78).

$$C_{j,l} = P_{k,m} \sin\left(\eta_p \xi_j\right), \tag{D.79}$$

where $l = k + kmax\left[m - 1 + mmax\left(p - 1\right)\right]$, and

$$D_{j,j'} = \breve{x}^{FEMM}_{R,j'}\left(\xi_j\right). \tag{D.80}$$

Equations (D.76) can be transformed by the Fourier transformation and solved for the eddy current amplitude functions. The equation in terms of the state variables is

$$
\begin{aligned}
i\omega \underline{\mathbf{x}}^{\mathbf{M}} &= \mathbf{F}^{44}\underline{\mathbf{x}}^{\mathbf{M}} - i\omega\mathbf{E}^{43}\underline{\mathbf{x}}^{\mathbf{K}}. \\
\underline{\mathbf{x}}^{\mathbf{M}} &= -i\omega\left(i\omega\mathbf{I} - \mathbf{F}^{44}\right)^{-1}\mathbf{E}^{43}\underline{\mathbf{x}}^{\mathbf{K}}.
\end{aligned}
\tag{D.81}
$$

Inserting this result into the transformed version of Eq. (D.78) gives

$$
\underline{\mathbf{y}} = \left[-\mathbf{C}i\omega\left(i\omega\mathbf{I} - \mathbf{F}^{44}\right)^{-1}\mathbf{E}^{43} + \mathbf{D}\right]\underline{\mathbf{x}}^{\mathbf{K}}. \tag{D.82}
$$

The limit as $\omega \to \infty$ simplifies Eq. (D.82) to the following.

$$
\mathbf{0} = \left[\mathbf{C}\mathbf{E}^{43} + \mathbf{D}\right]\underline{\mathbf{x}}^{\mathbf{K}}. \tag{D.83}
$$

This result gives a relationship among the matrices that can be calculated as a test.

$$
\mathbf{I} \approx -\mathbf{D}^{-1}\mathbf{C}\mathbf{E}^{43}. \tag{D.84}
$$

The equation is not exact because of truncation error. Equation (D.84) serves as a test of the programming of the matrices. Figure D.8 and Figure D.9 are surface plots of the elements of Eq. (D.84) to illustrate the approximation to the identity matrix produced by the quantity, $-\mathbf{D}^{-1}\mathbf{C}\mathbf{E}^{43}$, when the matrices are defined for the low order and high order models.

The diagonal in Figure D.8 gives a peak just a little less than one which shows that the matrix for the high order system is reasonably close to the identity matrix. The same plot for the low order case in Figure D.9 gives a lower value on the diagonal and noticeable more bumps on the off-diagonal locations. This plot is an indication of the energy lost through truncation of the high frequency modes.

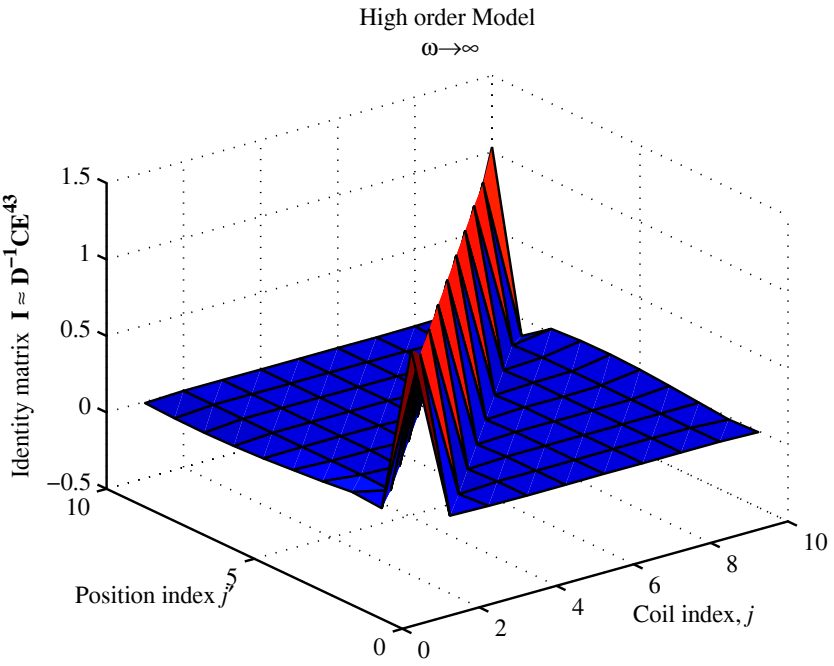


Figure D.8: Approximation to identity matrix for high order model by $-\mathbf{D}^{-1}\mathbf{C}\mathbf{E}^{43}$ matrix

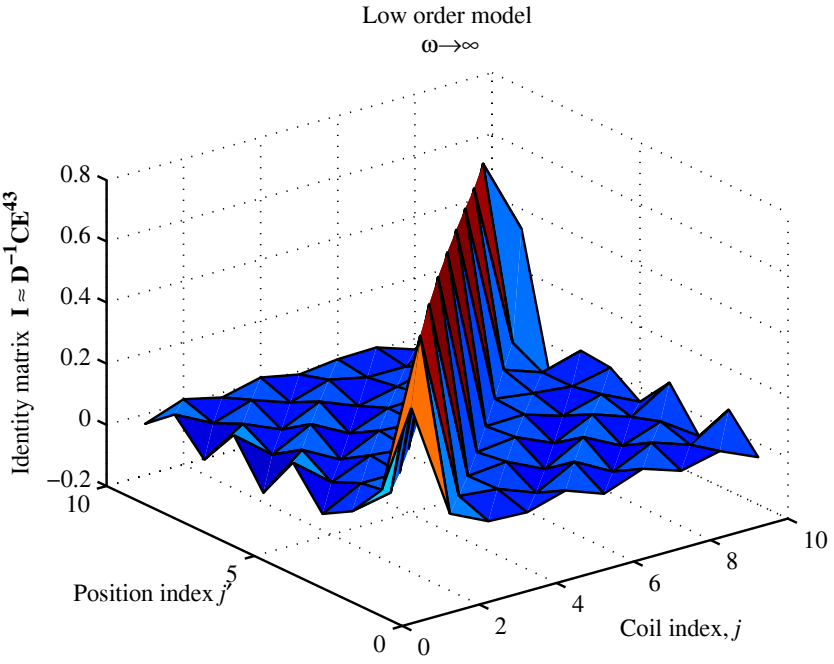


Figure D.9: Approximation to identity matrix for low order model by $-\mathbf{D}^{-1}\mathbf{C}\mathbf{E}^{43}$ matrix

### Infinite cylinder problem

Another limiting case is the case in which length of the actuator rod is infinite. This simplifies the magnetics problem to a planar, *x*-*y* problem. The FEMM calculation of the infinite, pie-shaped cylinder is described in APPENDIX C. The corresponding calculation using the modal magnetic model is a case in which all coils are energized and the field is evaluated at the axial midplane of the rod, $\xi = 0.5$. The frequency dependent amplitude values are given by Eq. (4.79). The series solution is evaluated using Eq. (4.75).

Figure D.10 shows the comparison of the FEMM infinite cylinder case and the modal models with all coils energized. The case is evaluated at a frequency of 10,000 Hz. The plot shows the FEMM result and the high and low order modal magnetic solutions for the real and imaginary components. The high order solution shows excellent agreement and generally confirms the derivation and programming of the modal solution. The modal solution converges quickly and thus the results are substantially better than the infinite frequency results. Another reason the agreement is good is that, for the infinite rod geometry, the homogeneous boundary condition approximation used for the magnetic field is not an approximation at all. The eddy current's magnetic field is exactly zero on the boundary for the infinite cylinder case.

The low order solution proves to be a satisfactory approximation to the shape as well. The imaginary component of the low order solution, shown in the lower panel of Figure D.10, is slightly less accurate than the real component. This is expected since the imaginary part is related to the derivative of the eddy current flux. Truncation error in a series solutions always increases with differentiation in time or spatial variables.

The low order model consists of just a single mode for the radial and azimuthal dependence of the magnetic field (*kmax*=1 and *mmax*=1). The fact that the first mode approximates the spatial distribution flux reasonably well at 10,000 Hz suggests that, for all frequencies up to 10,000 Hz, the shape of the spatial distribution for the eddy current field is approximately fixed and all profiles for the field, for both imaginary and real components, only vary in amplitude. This turns out to be a satisfactory approximation in both time and frequency domain.

Figure D.11 illustrates the shape function for the real component of field in the transverse plane for FEMM, the high order model, and the low order model. The purpose of the plot is to show the similarity in appearance between the three cases. This figure indicates that the fundamental mode for the radial and azimuthal components of the eddy current is sufficient to represent the dynamics for frequencies up to 10,000 Hz. This approximation improves at lower frequency but, of course, breaks down at higher frequency.

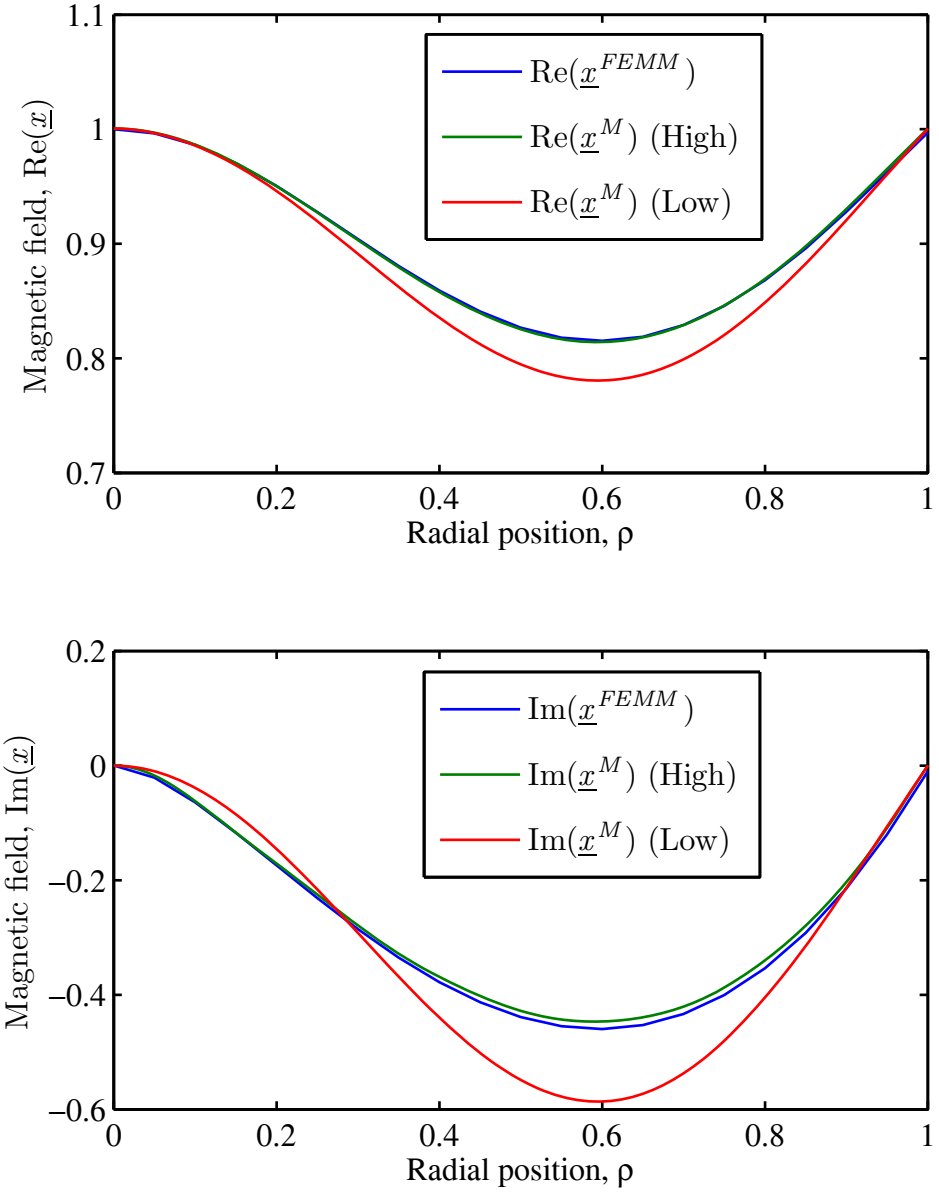


Figure D.10: Comparison of magnetic field calculated by the FEMM infinite cylinder model to the high and low order modal magnetic models on a radial line

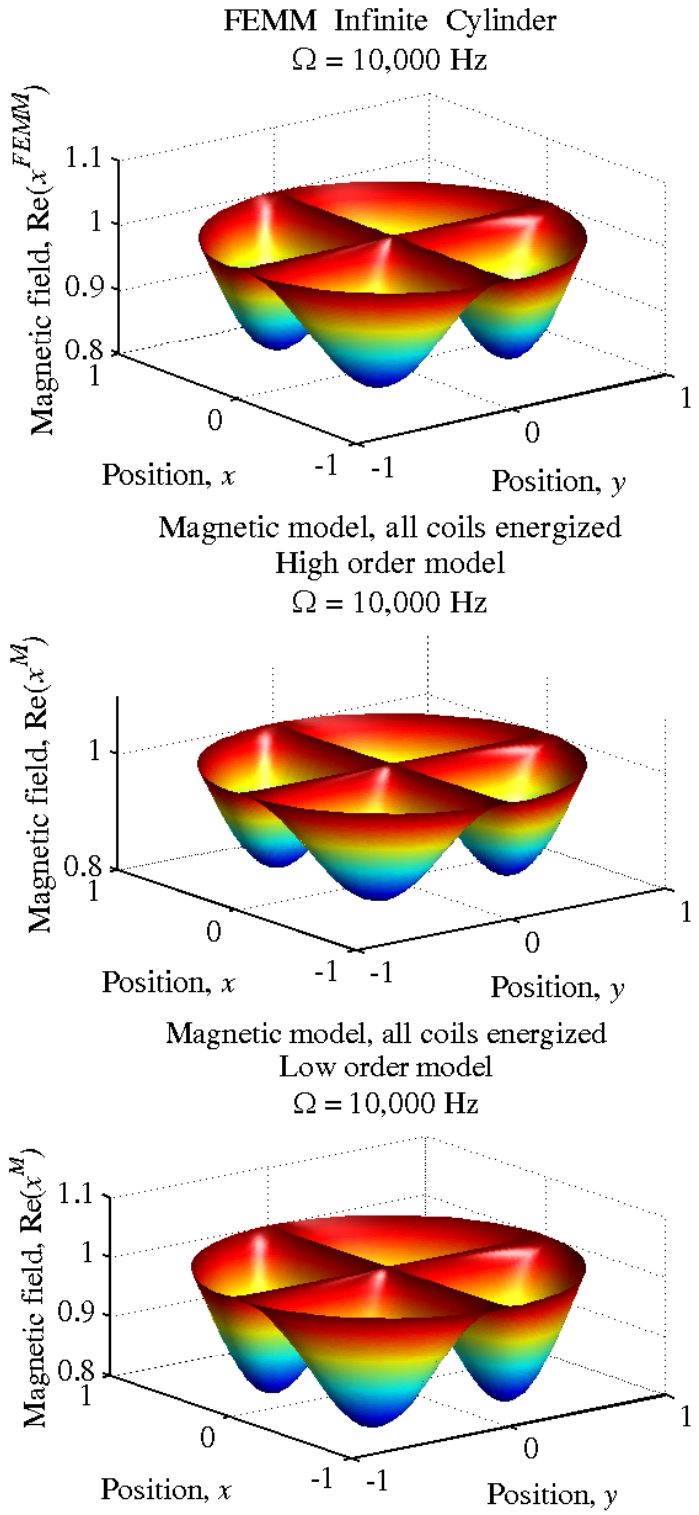


Figure D.11: Comparison of real component of magnetic field spatial distributions from FEMM infinite cylinder, high order model, and low order model.

# APPENDIX E

# EDDY CURRENT DENSITY DISTRIBUTION

## Algebraic Solution for the Eddy Current Density Distribution

The eddy current density distributions are used in the calculation of inductance coefficients between coil and eddy currents. The solution for the eddy current density distribution is similar in form to the magnetic field series and is based on that solution.

The differential equations for the radial and azimuthal components of eddy current are derived in CHAPTER 4.

$$\frac{1}{\rho}\left(\frac{\partial \rho j_\phi}{\partial \rho}-\frac{\partial j_r}{\partial \phi}\right)=-\sigma\mu^T r_g^2\frac{\partial b_z}{\partial t}. \tag{E.1}$$

$$\frac{1}{\rho}\left(\frac{\partial \rho j_r}{\partial \rho}+\frac{\partial j_\phi}{\partial \phi}\right)=0. \tag{E.2}$$

The goal of the derivation is to use Eq. (E.1) and Eq. (E.2) to find series of the following general form.

$$j_\phi(\rho,\gamma,\xi,t)=\sum_{k=1}^{kmax}\sum_{m=1}^{mmax}\sum_{p=1}^{pmax}\frac{\mathcal{J}_{\phi,k,m,p}(t)R_\phi\left(\varepsilon_{k,m}\rho\right)\Phi_\phi\left(\gamma_m\phi\right)Z_\phi\left(\eta_p\xi\right)}{N_\phi\left(\gamma_m\right)N_\phi\left(\varepsilon_{k,m},\gamma_m\right)N_\phi\left(\eta_p\right)}. \tag{E.3}$$

$$j_r(\rho,\gamma,\xi,t)=\sum_{k=1}^{kmax}\sum_{m=1}^{mmax}\sum_{p=1}^{pmax}\frac{\mathcal{J}_{r,k,m,p}(t)R_r\left(\varepsilon_{k,m}\rho\right)\Phi_r\left(\gamma_m\phi\right)Z_r\left(\eta_p\xi\right)}{N_r\left(\gamma_m\right)N_r\left(\varepsilon_{k,m},\gamma_m\right)N_r\left(\eta_p\right)}. \tag{E.4}$$

The eigenvalues of the functions are assumed, for the moment, to be the same as the eigenvalues of the magnetic field solution. This assumption is verified after solutions are obtained.

The problem is to relate the functions and coefficients in $j_\phi(\rho,\gamma,\xi,t)$ and $j_r(\rho,\gamma,\xi,t)$ to the corresponding solutions for the magnetic field. From Eq. (D.31), the solution of the axial magnetic field due to eddy current is the following.

$$x_H^M(\rho,\phi,\xi,t)=\sum_{k=1}^{kmax}\sum_{m=1}^{mmax}\sum_{p=1}^{pmax}\chi_{k,m,p}^M(t)\frac{\sin(\gamma_m\phi)\mathrm{J}_{\gamma_m}(\varepsilon_{k,m}\rho)\sin(\eta_p\xi)}{N(\varepsilon_{k,m},\gamma_m)N(\gamma_m)N(\eta_p)}. \tag{E.5}$$

The next step is to eliminate $b_z$ in Eq. (E.1) in favor of $\chi_{k,m,p}^H(t)$. This can be accomplished by applying the integral transform to the differential equation for $x_H^M$. The differential equation for the eddy current magnetic field from Eq. (4.43) in terms of dimensionless variables can be written as the following.

$$\frac{1}{\rho}\frac{\partial}{\partial\rho}\left(\rho\frac{\partial x_H^M}{\partial\rho}\right)+\frac{\partial^2 x_H^M}{\rho^2\partial\phi^2}+\frac{\chi_R r_g^2}{z_L^2}\frac{\partial^2 x_H^M}{\partial\xi^2}=\sigma_R\mu^T r_g^2\frac{\partial b_z}{\partial t}. \tag{E.6}$$

The three-dimensional integral transform for the magnetic field solution can be applied to the left hand side of Eq. (E.6). The result was previously obtained in APPENDIX D with the result given by Eq. (D.25). The left hand side simplifies to the following.

$$\begin{aligned}-\int_{\xi=0}^{1}\int_{\rho=0}^{1}\int_{\phi=0}^{\phi_0}&\left[\frac{1}{\rho}\frac{\partial}{\partial\rho}\left(\rho\frac{\partial x_H^M}{\partial\rho}\right)+\frac{\partial^2 x_H^M}{\rho^2\partial\phi^2}+\frac{\chi_R r_g^2}{z_L^2}\frac{\partial^2 x_H^M}{\partial\xi^2}\right]\\ &\cdot\sin(\gamma_m\phi)\mathrm{J}_{\gamma_m}(\varepsilon_{k,m}\rho)\sin(\eta_p\xi)\rho d\phi d\rho d\xi=-\left(\varepsilon_{k,m}^2+\frac{\chi_R r_g^2\eta_p^2}{z_L^2}\right)\chi_{k,m,p}^M(t).\end{aligned} \tag{E.7}$$

The right hand side of Eq. (E.6) can be written as a transformed variable, $\dot{\varepsilon}_{k,m,p}(t)$

$$\int_{\xi=0}^{1}\int_{\rho=0}^{1}\int_{\phi=0}^{\phi_0}\frac{\partial b}{\partial t}\sin(\gamma_m\phi)\mathrm{J}_{\gamma_m}(\varepsilon_{k,m}\rho)\sin(\eta_p\xi)rd\phi drd\xi=\dot{\varepsilon}_{k,m,p}(t). \tag{E.8}$$

Substituting Eq. (E.7) and Eq. (E.8) into Eq. (E.6) gives the following formula for the transformed magnetic induction.

$$\sigma_R \mu^T r_g^2 \dot{\mathcal{B}}_{k,m,p}(t) = -\left(\varepsilon_{k,m}^2 + \frac{\chi_R r_g^2 \eta_p^2}{z_L^2}\right) \mathcal{H}_{k,m,p}^M(t). \tag{E.9}$$

Thus, the inverse transform of $b_z$ can be written in terms of the amplitude functions of magnetic field, $\mathcal{H}_{k,m,p}^H(t)$.

$$\begin{aligned} \sigma_R \mu^T r_g^2 \frac{\partial b_z}{\partial t} = -\sum_{k=1}^{kmax} \sum_{m=1}^{mmax} \sum_{p=1}^{pmax} \Bigg[ & \left(\varepsilon_{k,m}^2 + \frac{\chi_R r_g^2 \eta_p^2}{z_L^2}\right) \\ & \cdot \frac{\mathcal{J}_{\gamma_m}(\varepsilon_{k,m}\rho)\sin(\gamma_m\phi)\sin_\phi(\eta_p\xi)\mathcal{H}_{k,m,p}^M(t)}{N(\gamma_m)N(\varepsilon_{k,m},\gamma_m)N(\eta_p)} \Bigg]. \end{aligned} \tag{E.10}$$

Now, the terms in the proposed series solutions for current density can be matched with the elements of the solution in Eq. (E.10) to determine the functions and constants in the solution.

Applying the derivative operations on the left hand side of Eq. (E.1) to the series solutions in Eq. (E.3) and Eq. (E.4) gives the following partial derivatives

$$\begin{aligned} \frac{\partial \rho j_\phi}{\partial \rho} &= \frac{\partial}{\partial \rho}\left[\rho \sum_{k=1}^{kmax} \sum_{m=1}^{mmax} \sum_{p=1}^{pmax} \frac{\mathcal{J}_{\phi,k,m,p}(t) R_\phi(\varepsilon_{k,m}\rho)\Phi_\phi(\gamma_m\phi)Z_\phi(\eta_p\xi)}{N_\phi(\gamma_m)N_\phi(\varepsilon_{k,m},\gamma_m)N_\phi(\eta_p)}\right] \\ &= \sum_{k=1}^{kmax} \sum_{m=1}^{mmax} \sum_{p=1}^{pmax} \frac{\mathcal{J}_{\phi,k,m,p}(t)\Phi_\phi(\gamma_m\phi)Z_\phi(\eta_p\xi)}{N_\phi(\gamma_m)N_\phi(\varepsilon_{k,m},\gamma_m)N_\phi(\eta_p)} \frac{d}{d\rho}\left[\rho R_\phi(\varepsilon_{k,m}\rho)\right]. \end{aligned} \tag{E.11}$$

$$\begin{aligned} \frac{\partial j_r}{\partial \phi} &= \frac{\partial}{\partial \phi} \sum_{k=1}^{kmax} \sum_{m=1}^{mmax} \sum_{p=1}^{pmax} \frac{\mathcal{J}_{r,k,m,p}(t) R_r(\varepsilon_{k,m}\rho)\Phi_r(\gamma_m\phi)Z_r(\eta_p\xi)}{N_r(\gamma_m)N_r(\varepsilon_{k,m},\gamma_m)N_r(\eta_p)} \\ &= \sum_{k=1}^{kmax} \sum_{m=1}^{mmax} \sum_{p=1}^{pmax} \frac{\mathcal{J}_{r,k,m,p}(t) R_r(\varepsilon_{k,m}\rho)Z_r(\eta_p\xi)}{N_r(\gamma_m)N_r(\varepsilon_{k,m},\gamma_m)N_r(\eta_p)} \frac{d\Phi_r(\gamma_m\phi)}{d\phi}. \end{aligned} \tag{E.12}$$

It is desirable for Eq. (E.1) to hold term-by-term. We propose tentatively that the two series are equal term-by-term to see if a solution can be found under this constraint. If the series solutions are equal term-by-term, then the following equalities for the modal

functions must hold so that the azimuthal and axial dependence can be factored out of each term.

$$\Phi_r\left(\gamma_m\phi\right)=\cos\left(\gamma_m\phi\right). \tag{E.13}$$

$$\Phi_\phi\left(\gamma_m\phi\right)=\sin\left(\gamma_m\phi\right). \tag{E.14}$$

$$Z_\phi\left(\eta_p\xi\right)=\sin\left(\eta_p\xi\right). \tag{E.15}$$

$$Z_r\left(\eta_p\xi\right)=\sin\left(\eta_p\xi\right). \tag{E.16}$$

For these functions, the normalization constants for the radial and axial modes of current density and eddy current field are equal.

$$N_r\left(\eta_p\right)=N_\phi\left(\eta_p\right)=N\left(\eta_p\right)=\frac{1}{2}. \tag{E.17}$$

$$N_r\left(\gamma_m\right)=N_\phi\left(\gamma_m\right)=N\left(\gamma_m\right)=\frac{\phi_0}{2}. \tag{E.18}$$

Now we write term-by-term equality for Eq. (E.1) canceling out the common factors from each.

$$\begin{aligned}
&\frac{1}{\rho}\left\{\frac{\mathcal{J}_{\phi,k,m,p}\left(t\right)}{N_\phi\left(\varepsilon_{k,m},\gamma_m\right)}\frac{d}{d\rho}\left[\rho R_\phi\left(\varepsilon_{k,m}\rho\right)\right]-\left[-\frac{\gamma_m\mathcal{J}_{r,k,m,p}\left(t\right)R_r\left(\varepsilon_{k,m}\rho\right)}{N_r\left(\varepsilon_{k,m},\gamma_m\right)}\right]\right\}\\
&\qquad=-\left[-\left(\varepsilon_{k,m}^2+\frac{\chi_R r_g^2\eta_p^2}{z_L^2}\right)\frac{\mathcal{X}_{k,m,p}^M\left(t\right)\mathrm{J}_{\gamma_m}\left(\varepsilon_{k,m}\rho\right)}{N\left(\varepsilon_{k,m},\gamma_m\right)}\right].\\
&\frac{1}{\rho}\left\{\frac{\mathcal{J}_{\phi,k,m,p}\left(t\right)}{N_\phi\left(\varepsilon_{k,m},\gamma_m\right)}\frac{d}{d\rho}\left[\rho R_\phi\left(\varepsilon_{k,m}\rho\right)\right]+\frac{\gamma_m\mathcal{J}_{r,k,m,p}\left(t\right)R_r\left(\varepsilon_{k,m}\rho\right)}{N_r\left(\varepsilon_{k,m},\gamma_m\right)}\right\}\\
&\qquad=\left(\varepsilon_{k,m}^2+\frac{\chi_R r_g^2\eta_p^2}{z_L^2}\right)\frac{\mathrm{J}_{\gamma_m}\left(\varepsilon_{k,m}\rho\right)\mathcal{X}_{k,m,p}^M\left(t\right)}{N\left(\varepsilon_{k,m},\gamma_m\right)}.
\end{aligned} \tag{E.19}$$

From Eq. (E.19) it is evident that if the system is to be solvable then the amplitude functions must be proportional to one another.

$$\mathcal{I}_{\phi,k,m,p}(t) \;\alpha\; \mathcal{I}_{r,k,m,p}(t) \alpha\; \mathcal{X}^{M}_{k,m,p}(t). \tag{E.20}$$

The problem is reduced to finding the constants of proportionality and the form for the radial functions that asatisfy the equation. If the amplitude functions are all proportional, then there is no need to have different normalization factors for each of the radial functions. The constants can be absorbed into the proportionality constant between $\mathcal{I}_{\phi,k,m,p}(t)$, $\mathcal{I}_{r,k,m,p}(t)$, and $\mathcal{H}^{H}_{k,m,p}(t)$. We may set the *N*'s equal with no loss of generality.

$$N_{\phi}\left(\varepsilon_{k,m},\gamma_{m}\right) = N_{r}\left(\varepsilon_{k,m},\gamma_{m}\right) = N\left(\varepsilon_{k,m},\gamma_{m}\right). \tag{E.21}$$

Simplifying Eq. (E.19) using the equality defined for the normalization constants, Eq. (E.21) gives the following:

$$\begin{aligned}\frac{1}{\rho}\left\{\mathcal{I}_{\phi,k,m,p}(t)\frac{d}{d\rho}\left[\rho R_{\phi}\left(\varepsilon_{k,m}\rho\right)\right] + \gamma_{m}\mathcal{I}_{r,k,m,p}(t) R_{r}\left(\varepsilon_{k,m}\rho\right)\right\} \\ = \left(\varepsilon^{2}_{k,m} + \frac{\chi_{R} r_{g}^{2}\eta_{p}^{2}}{z_{L}^{2}}\right)\mathbb{J}_{\gamma_{m}}\left(\varepsilon_{k,m}\rho\right)\mathcal{X}^{M}_{k,m,p}(t).\end{aligned} \tag{E.22}$$

The series solutions for current density from Eqs. (E.3) and (E.4) can be substituted into the conservation of charge condition in Eq. (4.111). Applying term-by-term equality of the series yields the following equation.

$$\begin{aligned}&\mathcal{I}_{r,k,m,p}(t)\frac{d}{d\rho}\left[\rho R_{r}\left(\varepsilon_{k,m}\rho\right)\right] + \gamma_{m}\mathcal{I}_{\phi,k,m,p}(t) R_{\phi}\left(\varepsilon_{k,m}\rho\right) = 0. \\ &\frac{\mathcal{I}_{r,k,m,p}(t)}{\gamma_{m}\mathcal{I}_{\phi,k,m,p}(t)}\frac{d}{d\rho}\left[\rho R_{r}\left(\varepsilon_{k,m}\rho\right)\right] = -R_{\phi}\left(\varepsilon_{k,m}\rho\right).\end{aligned} \tag{E.23}$$

The next step is to use Eq. (E.23) to eliminate the $R_\phi\left(\varepsilon_{k,m}\rho\right)$ term from Eq. (E.22). We differentiate Eq. (E.23).

$$-\frac{\mathcal{J}_{r,k,m,p}(t)}{\gamma_m \mathcal{J}_{\phi,k,m,p}(t)}\frac{d}{d\rho}\left\{\rho\frac{d}{d\rho}\left[\rho R_r\left(\varepsilon_{k,m}\rho\right)\right]\right\}=\frac{d}{d\rho}\left[\rho R_\phi\left(\varepsilon_{k,m}\rho\right)\right]. \tag{E.24}$$

Substitute Eq. (E.24) into Eq. (E.22).

$$\begin{aligned}-\frac{\mathcal{J}_{\phi,k,m,p}(t)}{\gamma_m}\frac{\mathcal{J}_{r,k,m,p}(t)}{\gamma_m \mathcal{J}_{\phi,k,m,p}(t)}\frac{d}{d\rho}\left\{\rho\frac{d}{dr}\left[rR_r\left(\varepsilon_{k,m}\rho\right)\right]\right\}+\mathcal{J}_{r,k,m,p}(t)R_r\left(\varepsilon_{k,m}\rho\right)&\\ =\frac{1}{\gamma_m}\left(\frac{\varepsilon_{k,m}^2}{r_g^2}+\frac{\chi_R\eta_p^2}{z_L^2}\right)\rho\mathrm{J}_{\gamma_m}\left(\varepsilon_{k,m}\rho\right)\mathcal{X}_{k,m,p}^M(t).&\end{aligned} \tag{E.25}$$

Rearranging and canceling factors yields the following equation.

$$\begin{aligned}\frac{1}{\rho^2}\frac{d}{d\rho}\left\{\rho\frac{d}{d\rho}\left[\rho R_r\left(\varepsilon_{k,m}\rho\right)\right]\right\}-\frac{\gamma_m^2}{\rho^2}R_r\left(\varepsilon_{k,m}\rho\right)&\\ +\gamma_m\left(\varepsilon_{k,m}^2+\frac{\chi_R r_g^2\eta_p^2}{z_L^2}\right)\frac{\mathcal{X}_{k,m,p}^H(t)}{\mathcal{J}_{r,k,m,p}(t)}\frac{\mathrm{J}_{\gamma_m}\left(\varepsilon_{k,m}\rho\right)}{\rho}=0.&\end{aligned} \tag{E.26}$$

Equation (E.26) makes it clear that $\mathcal{X}_{k,m,p}^H(t)$ and $\mathcal{J}_{r,k,m,p}(t)$ must be proportional for a solution to exist. One more rearrangement puts the equation in a form that has a recognizable solution. First, the derivative term is expanded.

$$\frac{1}{\rho^2}\frac{d}{dr}\left\{\rho\frac{d}{d\rho}\left[\rho R_r\left(\varepsilon_{k,m}\rho\right)\right]\right\}=\frac{d^2R_r\left(\varepsilon_{k,m}\rho\right)}{d\rho^2}+\frac{3}{\rho}\frac{dR_r\left(\varepsilon_{k,m}\rho\right)}{d\rho}+\frac{R_r\left(\varepsilon_{k,m}\rho\right)}{\rho^2}. \tag{E.27}$$

Inserting that result into Eq. (E.26) gives

$$\begin{aligned}\frac{d^2R_r\left(\varepsilon_{k,m}\rho\right)}{d\rho^2}+\frac{3}{\rho}\frac{dR_r\left(\varepsilon_{k,m}\rho\right)}{d\rho}+\frac{\left(1-\gamma_m^2\right)}{\rho^2}R_r\left(\varepsilon_{k,m}\rho\right)&\\ +\gamma_m\left(\varepsilon_{k,m}^2+\frac{\chi_R r_g^2\eta_p^2}{z_L^2}\right)\frac{\mathcal{X}_{k,m,p}^M(t)}{\mathcal{J}_{r,k,m,p}(t)}\frac{\mathrm{J}_{\gamma_m}\left(\varepsilon_{k,m}\rho\right)}{\rho}=0.&\end{aligned} \tag{E.28}$$

Now, if we set following terms equal, then we have a solution for Eq. (E.28).

$$\mathcal{J}_{r,k,m,p}(t)=\left(1+\frac{\chi_R r_g^2 \eta_p^2}{z_L^2 \varepsilon_{k,m}^2}\right)\mathcal{H}_{k,m,p}^{M}(t). \tag{E.29}$$

$$R_r\left(\varepsilon_{k,m} r\right)=\frac{\gamma_m \mathrm{J}_{\gamma_m}\left(\varepsilon_{k,m}\rho\right)}{\rho}. \tag{E.30}$$

Substituting the solution back into the differential equation gives

$$\begin{aligned}\frac{d^2 R_r\left(\varepsilon_{k,m}\rho\right)}{d\rho^2}+\frac{3}{\rho}\frac{dR_r\left(\varepsilon_{k,m}\rho\right)}{d\rho}\\ +\frac{\left(1-\gamma_m^2\right)}{\rho^2}R_r\left(\varepsilon_{k,m}\rho\right)+\varepsilon_{k,m}^2 R_r\left(\varepsilon_{k,m}\rho\right)=0.\end{aligned} \tag{E.31}$$

This equation can be recognized as one of the forms of the generalized Bessel equation derived by Douglas and reported in [27]. The generalized Bessel equation is defined as an equation of the following form.

$$\begin{aligned}\frac{d^2 R(\rho)}{d\rho^2}+\left[\frac{1-2m}{\rho}-2\alpha\right]\frac{dR(\rho)}{d\rho}\\ +\left[p^2 a^2 x^{2p-2}+\alpha^2+\frac{\alpha(2m-1)}{\rho}+\frac{m^2-p^2\upsilon^2}{\rho^2}\right]R(\rho)=0.\end{aligned} \tag{E.32}$$

Comparing coefficients of Eq. (E.31) and Eq. (E.32) we find the following system of equalities must hold for the generalized Bessel equation to be applicable.

$$\begin{aligned}&1-2m=3,\\ &\left(1-\gamma^2\right)=m^2-p^2\upsilon^2,\\ &2p-2=0,\\ &\left(1-\gamma^2\right)=m^2-p^2\upsilon^2,\\ &p^2a^2=\varepsilon^2,\\ &-2\alpha=0,\\ &\alpha(2m-1)=0.\end{aligned} \tag{E.33}$$

Solving for the parameters of the generalized Bessel equation gives

$$\begin{aligned} m &= -1, \\ p &= 1, \\ \upsilon &= \gamma, \\ a &= \varepsilon, \\ \alpha &= 0. \end{aligned} \tag{E.34}$$

The solution to the generalized Bessel equation is given by

$$R(\rho) = \rho^m \cdot e^{\alpha\rho}\left[C_1 \mathrm{J}_\upsilon\left(a\rho^p\right) + C_2 \mathrm{Y}_\upsilon\left(a\rho^p\right)\right]. \tag{E.35}$$

Hence, the radial function for the current density problem is given by.

$$R_r(\rho) = \frac{1}{\rho}\left[C_1 \mathrm{J}_\gamma(\varepsilon\rho) + C_2 \mathrm{Y}_\gamma(\varepsilon\rho)\right]. \tag{E.36}$$

We use the condition that the solution is finite over the region to eliminate the $C_2$ coefficients. Each term can be evaluated as the solution approaches zero. For quadrant shaped segments, $\gamma = 2, 6, 10, ...$

$$\lim_{\rho\to 0}\left[\frac{\mathrm{J}_\gamma(\varepsilon\rho)}{\rho}\right] = \frac{1}{\rho}\left(\frac{\varepsilon\rho}{2}\right)^\gamma \frac{1}{\Gamma(\gamma+1)} \to 0 \text{ for } \gamma\text{=2,6,10... .} \tag{E.37}$$

$$\lim_{\rho\to 0}\left[\frac{\mathrm{Y}_\gamma(\varepsilon\rho)}{\rho}\right] = -\frac{1}{\rho}\left(\frac{2}{\varepsilon\rho}\right)^\gamma \Gamma(\gamma) \to \infty. \tag{E.38}$$

The solution must be bounded at $\rho = 0$; therefore,

$$C_2 = 0\,. \tag{E.39}$$

The boundary condition for the radial function comes from the requirement that no current can pass the insulated boundaries of the pie-shaped segment. This means that the radial current on the cylindrical boundary must be zero and that the radial mode must be

homogeneous on the boundary. These boundary conditions result in the following eigenvalue equation

$$R_r\left(\varepsilon\right)=0\,. \tag{E.40}$$

$$\mathrm{J}_{\gamma_m}\left(\varepsilon_{k,m}\right)=0.\,. \tag{E.41}$$

The current solution gives the same radial eigenvalue equation as the magnetic field problem. Similarly, the boundary conditions on azimuthal current require that the current density into the radial faces at $\phi=0$ or $\phi_0$ also be zero. Hence, azimuthal eigenvalues are defined by

$$\begin{aligned}&\Phi_\phi\left(0\right)=\Phi_\phi\left(\gamma_m\phi_0\right)=0,\\&\sin\left(\gamma_m\phi_0\right)=0.\end{aligned} \tag{E.42}$$

This is the same eigenvalue equation for the azimuthal function as found in the magnetic field solution.

Now we turn to the radial function for the azimuthal current, $R_\phi\left(\varepsilon_{k,m}\rho\right)$. We need to evaluate the proportionality constant between $\chi^H_{k,m,p}\left(t\right)$ and $\ell_{\phi,k,m,p}\left(t\right)$ and find the function, $R_\phi\left(\varepsilon_{k,m}r\right)$, which satisfies the differential equations. We substitute the solution for the radial current mode from in Eq. (E.30) and the proportionality constant of Eq. (E.29) back into the conservation of charge equation, Eq. (E.23). We solve this equation for $R_\phi\left(\varepsilon_{k,m}r\right)$.

$$\frac{\mathcal{J}_{r,k,m,p}(t)}{\gamma_m \mathcal{J}_{\phi,k,m,p}(t)} \frac{d}{d\rho}\left[\rho R_r\left(\varepsilon_{k,m}\rho\right)\right] = -R_\phi\left(\varepsilon_{k,m}\rho\right).$$

$$\frac{\gamma_m\left(1+\frac{\chi_R r_g^2 \eta_p^2}{z_L^2 \varepsilon_{k,m}^2}\right)\mathcal{X}_{k,m,p}^M(t)}{\gamma_m \mathcal{J}_{\phi,k,m,p}(t)} \frac{d}{d\rho}\left[\rho \frac{\mathrm{J}_{\gamma_m}\left(\varepsilon_{k,m} r\right)}{\rho}\right] = -R_\phi\left(\varepsilon_{k,m}\rho\right).$$

$$\left(1+\frac{\chi_R r_g^2 \eta_p^2}{z_L^2 \varepsilon_{k,m}^2}\right)\frac{\mathcal{X}_{k,m,p}^M(t)}{\mathcal{J}_{\phi,k,m,p}(t)} \frac{d}{d\rho}\left[\mathrm{J}_{\gamma_m}\left(\varepsilon_{k,m}\rho\right)\right] = -R_\phi\left(\varepsilon_{k,m}\rho\right). \tag{E.43}$$

$$\left(1+\frac{\chi_R r_g^2 \eta_p^2}{z_L^2 \varepsilon_{k,m}^2}\right)\frac{\mathcal{X}_{k,m,p}^M(t)}{\mathcal{J}_{\phi,k,m,p}(t)}\left[-\varepsilon_{k,m}\mathrm{J}_{\gamma_m+1}\left(\varepsilon_{k,m}\rho\right)+\frac{\gamma_m \mathrm{J}_{\gamma_m}\left(\varepsilon_{k,m}\rho\right)}{\rho}\right] = -R_\phi\left(\varepsilon_{k,m}\rho\right).$$

$$\left(1+\frac{\chi_R r_g^2 \eta_p^2}{z_L^2 \varepsilon_{k,m}^2}\right)\frac{\mathcal{X}_{k,m,p}^M(t)}{\mathcal{J}_{\phi,k,m,p}(t)}\left[\varepsilon_{k,m}\mathrm{J}_{\gamma_m+1}\left(\varepsilon_{k,m}\rho\right)-\frac{\gamma_m \mathrm{J}_{\gamma_m}\left(\varepsilon_{k,m}\rho\right)}{\rho}\right] = R_\phi\left(\varepsilon_{k,m}\rho\right).$$

From this result, we deduce that only the product, $\mathcal{J}_{\phi,k,m,p}(t) R_\phi\left(\varepsilon_{k,m}\rho\right)$, is uniquely determined by the equation. The apportioning between the two factors is arbitrary. The following two factors are chosen.

$$R_\phi\left(\varepsilon_{k,m}\rho\right) = \left[\varepsilon_{k,m}\mathrm{J}_{\gamma_m+1}\left(\varepsilon_{k,m}\rho\right)-\frac{\gamma_m \mathrm{J}_{\gamma_m}\left(\varepsilon_{k,m}\rho\right)}{\rho}\right]. \tag{E.44}$$

$$\left(1+\frac{\chi_R r_g^2 \eta_p^2}{z_L^2 \varepsilon_{k,m}^2}\right)\frac{\mathcal{X}_{k,m,p}^H(t)}{\mathcal{J}_{\phi,k,m,p}(t)} = 1. \tag{E.45}$$

Equation (E.45) can be solved for the proportionality constant for the amplitude function.

$$\mathcal{J}_{\phi,k,m,p}(t) = \left(1+\frac{\chi_R r_g^2 \eta_p^2}{z_L^2 \varepsilon_{k,m}^2}\right)\mathcal{X}_{k,m,p}^M(t). \tag{E.46}$$

The solution for the current density can be written as the following series solution using the functions and constants that have been derived.

$$j_\phi(\rho,\gamma,\xi,t)=\sum_{k=1}^{kmax}\sum_{m=1}^{mmax}\sum_{p=1}^{pmax}\left\{\left(1+\frac{\chi_R r_g^2\eta_p^2}{z_L^2\varepsilon_{k,m}^2}\right)\cdot\frac{\left[\varepsilon_{k,m}\mathrm{J}_{\gamma_m+1}\left(\varepsilon_{k,m}\rho\right)-\frac{\gamma_m\mathrm{J}_{\gamma_m}\left(\varepsilon_{k,m}\rho\right)}{\rho}\right]\sin\left(\gamma_m\phi\right)\sin\left(\eta_p\xi\right)\mathcal{X}_{k,m,p}^{M}(t)}{N\left(\gamma_m\right)N\left(\varepsilon_{k,m},\gamma_m\right)N\left(\eta_p\right)}\right\}. \tag{E.47}$$

$$j_r(\rho,\gamma,\xi,t)=\sum_{k=1}^{kmax}\sum_{m=1}^{mmax}\sum_{p=1}^{pmax}\left\{\left(1+\frac{\chi_R r_g^2\eta_p^2}{z_L^2\varepsilon_{k,m}^2}\right)\cdot\frac{\gamma_m\mathrm{J}_{\gamma_m}\left(\varepsilon_{k,m}\rho\right)\cos\left(\gamma_m\phi\right)\sin\left(\eta_p\xi\right)\mathcal{X}_{k,m,p}^{M}(t)}{\rho N_r\left(\gamma_m\right)N_r\left(\varepsilon_{k,m},\gamma_m\right)N_r\left(\eta_p\right)}\right\}. \tag{E.48}$$

The current density modes can be written as dimensioned vector function as the following

$$\mathbf{f}_{k,m,p}^{M}\left(r,\phi,z\right)=\frac{T\Delta I}{r_g}\begin{bmatrix}\left(1+\frac{\chi_R r_g^2\eta_p^2}{z_L^2\varepsilon_{k,m}^2}\right)\frac{\gamma_m\mathrm{J}_{\gamma_m}\left(\frac{\varepsilon_{k,m}r}{r_g}\right)\cos\left(\gamma_m\phi\right)\sin\left(\frac{\eta_p z}{z_L}\right)}{\rho N\left(\gamma_m\right)N\left(\varepsilon_{k,m},\gamma_m\right)N\left(\eta_p\right)}\\ \left(1+\frac{\chi_R r_g^2\eta_p^2}{z_L^2\varepsilon_{k,m}^2}\right)\frac{\left[\varepsilon_{k,m}\mathrm{J}_{\gamma_m+1}\left(\frac{\varepsilon_{k,m}r}{r_g}\right)-\frac{r_g}{r}\gamma_m\mathrm{J}_{\gamma_m}\left(\frac{\varepsilon_{k,m}r}{r_g}\right)\right]\sin\left(\gamma_m\phi\right)\sin\left(\frac{\eta_p z}{z_L}\right)}{N\left(\gamma_m\right)N\left(\varepsilon_{k,m},\gamma_m\right)N\left(\eta_p\right)}\\ 0\end{bmatrix}. \tag{E.49}$$

The method of solution assuming term-by-term equality of the series is not a rigorous procedure. In this case, it can be shown by direct substitution that the modal functions in Eq. (E.47) and (E.48) are solutions to the eddy current differential equations

in Eq. (E.1) and Eq. (E.2). Hence, in this particular case, the procedure yields a solution. The substitution into the differential equation is performed using a symbolic math program as a test of the magnetic and eddy current modal functions in the following section on testing.

**Testing the Current Density and Magnetic Field Modes by Analytical Substitution**

The modal distribution for current density supplies all components of the vector and can be substituted back into the algebraic and differential equations. This process generates the corresponding modal functions for magnetic vector potential, magnetic induction, and magnetic field. Starting with any of the equations, the series of differential operations forms a closed algebraic loop returning back to the starting function. This series of operations can be used as a test to verify that the solution of the axial component of magnetic field and the current density formulae are correct. The test also generates the other modal functions which are used in other tests.

The process of substituting and differentiating is readily handled by symbolic mathematics programs such as the MATLAB Symbolic Toolbox. Given the differential equation, the Symbolic Toolbox fails to solve for the modal functions for current density. However, it can readily handle the differentiation and multiplication required for the back substitution. Thus, the algebra of this test can be done by computer which is less subject to error than the derivation by hand that found the eddy current distribution functions.

The series of operations for the analytical loop of substitutions can be collected from previously obtained results. We will write the spatial function and the amplitude function as a product. In equations not involving a time differentiation, the amplitude function cancels. From Eq. (C.10), the magnetic potential is for a mode is given by

$$\frac{\partial \mathbf{A}_{k,m,p}^{M}(r,\phi,z)\chi_{k,m,p}(t)}{\partial t} = -\frac{\mathbf{f}_{k,m,p}^{M}(r,\phi,z)\chi_{k,m,p}(t)}{\sigma}. \tag{E.50}$$

The equation for the mode function has no external current or source. Equation (C.12) gives the potential from its derivative.

$$\nabla\times\left(\boldsymbol{\mu}_{R}^{S}\right)^{-1}\left(\nabla\times\left(\mathbf{A}_{k,m,p}^{M}\chi_{k,m,p}\right)\right) = -\sigma_{R}\frac{\partial\left(\mathbf{A}_{k,m,p}^{M}\chi_{k,m,p}\right)}{\partial t}. \tag{E.51}$$

The solution to the spatial part of the differential equation is an eigenvalue problem. The solution of the magnetic field equation in Eqs (4.8) through (4.17) and its integral transform in Eqs. (D.1) through (D.25) is an application of the eigenvalue property. Applying similar steps to Eq. (E.51) gives the same eigenvalue.

$$\frac{1}{\mu_{R}\varepsilon_{k,m}^{2}}\left(1+\frac{\chi_{R}r_{g}^{2}\eta_{p}^{2}}{z_{L}^{2}\varepsilon_{k,m}^{2}}\right)\mathbf{A}_{k,m,p}^{M}\chi_{k,m,p}(t) = \sigma_{R}\mathbf{A}_{k,m,p}^{M}\frac{\partial\chi_{k,m,p}(t)}{\partial t}. \tag{E.52}$$

Solving for the potential gives

$$\mathbf{A}_{k,m,p}^{M}\chi_{k,m,p} = \frac{\sigma_{R}\mu_{R}\varepsilon_{k,m}^{2}}{\left(1+\frac{\chi_{R}r_{g}^{2}\eta_{p}^{2}}{z_{L}^{2}\varepsilon_{k,m}^{2}}\right)}\frac{\partial\left(\mathbf{A}_{k,m,p}^{M}\chi_{k,m,p}\right)}{\partial t}. \tag{E.53}$$

The magnetic induction can be obtained from the magnetic potential by applying the curl operation.

$$\begin{aligned}\mathbf{B}_{k,m,p}^{M}\chi_{k,m,p}(t) &= \nabla\times\mathbf{A}_{k,m,p}^{M}\chi_{k,m,p}(t).\\ \mathbf{B}_{k,m,p}^{M} &= \nabla\times\mathbf{A}_{k,m,p}^{M}.\end{aligned} \tag{E.54}$$

The magnetic field is obtained by the constitutive relation.

$$\mathbf{H}_{k,m,p}^{M} = \left(\boldsymbol{\mu}^{S}\right)^{-1}\mathbf{B}_{k,m,p}^{M}. \tag{E.55}$$

The analytical loop is closed by applying the curl one more time.

$$\begin{aligned} \chi_{k,m,p}\mathbf{f}_{k,m,p}^{M} &= \chi_{k,m,p}\nabla\times\mathbf{H}_{k,m,p}^{M}. \\ \mathbf{f}_{k,m,p}^{M} &= \nabla\times\mathbf{H}_{k,m,p}^{M}. \end{aligned} \tag{E.56}$$

This series of differential and algebraic operations has been programmed using the Symbolic Toolbox of MATLAB to generate vector functions for $\mathbf{A}_{k,m,p}^{M}$, $\mathbf{B}_{k,m,p}^{M}$ and $\mathbf{H}_{k,m,p}^{M}$. The following equations give the results of the symbolic processing program. The final step in Eq. (E.56) returns the original current density, $\mathbf{f}_{k,m,p}^{M}$, given in Eq. (E.49). The complete vector solutions of the magnetic potential and magnetic field are documented here for use in other parts of the dissertation.

$$\mathbf{A}_{k,m,p}^{M}\left(r,\phi,z\right)=\frac{\mu_R T\Delta l r_g}{\varepsilon_{k,m}^{2}}\begin{bmatrix} \dfrac{r_g\gamma_m \mathrm{J}_{\gamma_m}\left(\dfrac{\varepsilon_{k,m}r}{r_g}\right)\cos\left(\gamma_m\phi\right)\sin\left(\dfrac{\eta_p z}{z_L}\right)}{rN\left(\gamma_m\right)N\left(\varepsilon_{k,m},\gamma_m\right)N\left(\eta_p\right)} \\ \dfrac{\left[\begin{matrix}\varepsilon_{k,m}\mathrm{J}_{\gamma_m+1}\left(\dfrac{\varepsilon_{k,m}r}{r_g}\right) \\ -\dfrac{r_g}{r}\gamma_m\mathrm{J}_{\gamma_m}\left(\dfrac{\varepsilon_{k,m}r}{r_g}\right)\end{matrix}\right]\sin\left(\gamma_m\phi\right)\sin\left(\dfrac{\eta_p z}{z_L}\right)}{N\left(\gamma_m\right)N\left(\varepsilon_{k,m},\gamma_m\right)N\left(\eta_p\right)} \\ 0 \end{bmatrix}. \tag{E.57}$$

$$\mathbf{H}^{M}_{k,m,p}(r,\phi,z) = T\Delta I \begin{bmatrix} -\dfrac{\dfrac{r_g \chi_R \eta_p}{z_L}\left[\begin{array}{c} \varepsilon_{k,m}\mathrm{J}_{\gamma_m+1}\left(\dfrac{\varepsilon_{k,m}r}{r_g}\right) \\ -\dfrac{r_g}{r}\gamma_m \mathrm{J}_{\gamma_m}\left(\dfrac{\varepsilon_{k,m}r}{r_g}\right)\end{array}\right]\sin(\gamma_m\phi)\cos\left(\dfrac{\eta_p z}{z_L}\right)}{\varepsilon^2_{k,m}N(\gamma_m)N(\varepsilon_{k,m},\gamma_m)N(\eta_p)} \\ \dfrac{r_g^2}{r}\dfrac{\chi_R\eta_p}{z_L}\dfrac{\mathrm{J}_{\gamma_m}\left(\dfrac{\varepsilon_{k,m}r}{r_g}\right)\cos(\gamma_m\phi)\cos\left(\dfrac{\eta_p z}{z_L}\right)}{N(\gamma_m)N(\varepsilon_{k,m},\gamma_m)N(\eta_p)} \\ \dfrac{\mathrm{J}_{\gamma_m}\left(\dfrac{\varepsilon_{k,m}r}{r_g}\right)\sin(\gamma_m\phi)\sin\left(\dfrac{\eta_p z}{z_L}\right)}{N(\gamma_m)N(\varepsilon_{k,m},\gamma_m)N(\eta_p)} \end{bmatrix}. \quad (5.58)$$

**Test Calculations for the Modal Model of the Magnetic Field in the Pie-Shaped Cylinder**

The test cases for the current density solution use the FEMM infinite cylinder problem as a comparison to check the derivation and assess the order of the solution needed for control. The comparison applies the same method that was used to check the magnetic model and follows the same line of reasoning. The current distribution is evaluated using the series solution for $j_\phi(\rho,\gamma,\xi,t)$ given by Eq. (E.47) for the high and low order models. The amplitudes as a function of frequency are given by Eq. (4.79). The current density function for the modal model is evaluated with all coils energized at the midplane of the actuator. The FEMM infinite cylinder model calculates the magnetic potential (which can be interpreted as the magnetic field) by the finite element method

and then FEMM's post-processor is used to differentiate the field to get magnetic induction (which can be interpreted as current density).

Figure E.1 compares the azimuthal current density, $\underline{j}_{\phi}(\rho,\gamma,\xi,\omega)$, from the infinite pie-shaped cylinder calculated by FEMM to the series solution along a radial line. The real component is shown in the top panel and the imaginary component in the bottom panel. As in the test calculations for magnetic field, the purpose of the high order case is to verify the derivation and the programming. The low order case is plotted to assess the sufficiency of the low order case for control calculations. As in the magnetic field cases, the comparison is excellent for the high order case and sufficient for the low order case.

Additionally, the real and imaginary components can be plotted in three-dimensional plots. The real and imaginary components are more constructive than the usual amplitude and phase because of the significance of the sign of the current density in comparison to the coil current forcing the eddy current from the outside radius.

In Figure E.2, the top panel is the FEMM result for the real component of azimuthal current density. The lower two panels are the modal series solution for the high and low order cases. Figure E.3 shows the same comparison for the imaginary components. The purpose of these figures is to illustrate that the shape of all of the distributions in all six plots is very close to the same. This calculated result is the justification for using the low order model in the control calculations.

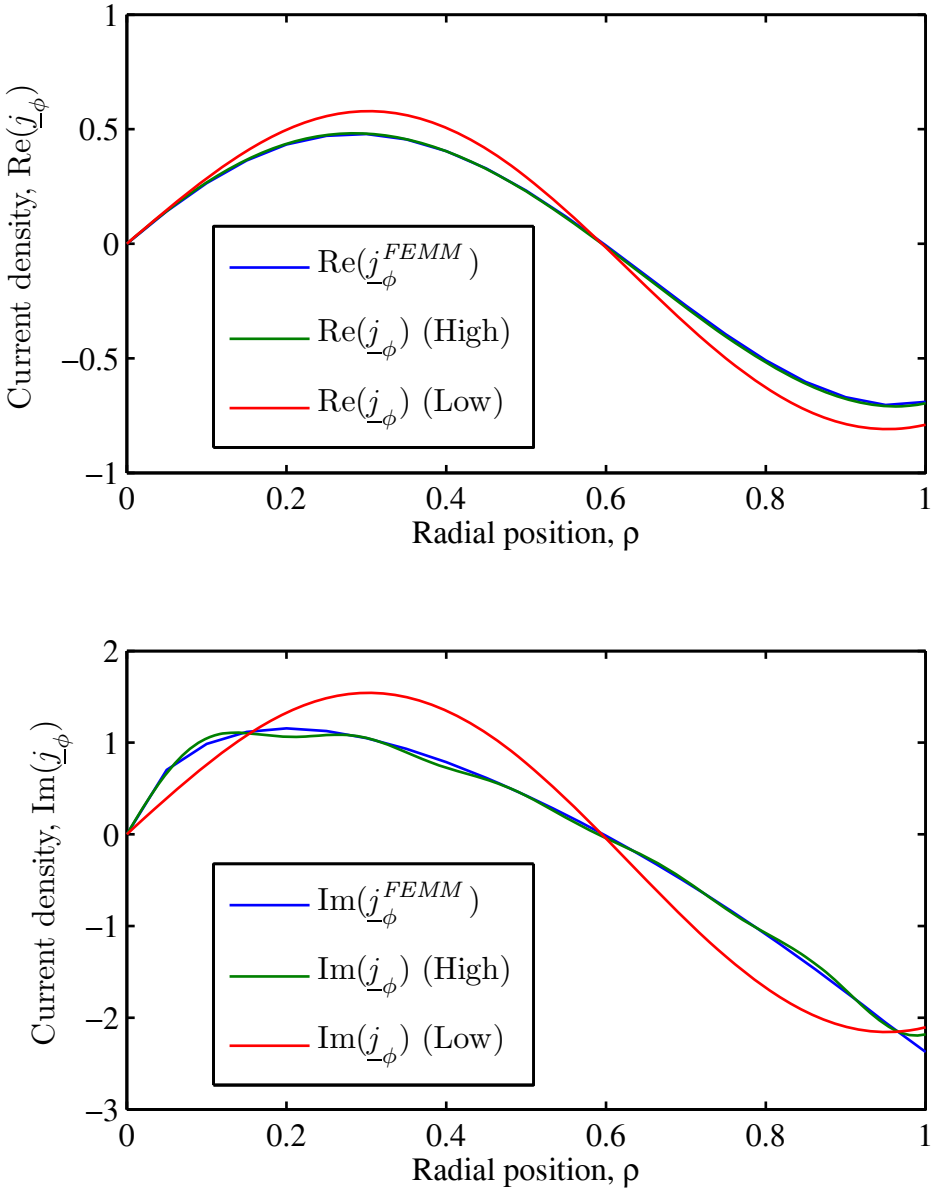


Figure E.1: Comparison of azimuthal current density calculated by the FEMM infinite cylinder model to the high and low order modal models on a radial line

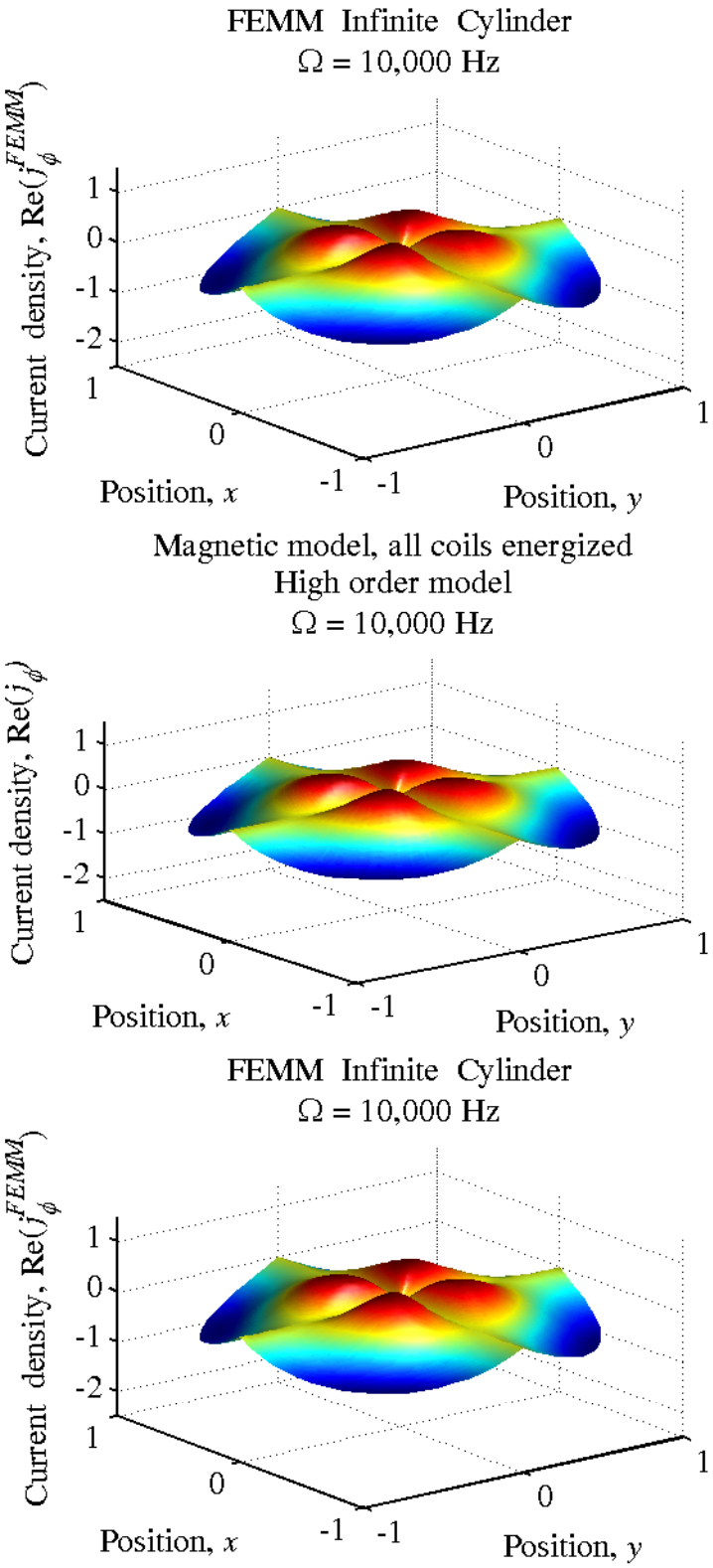


Figure E.2: Comparison of real component of azimuthal eddy current density distributions from FEMM infinite cylinder, high order model, and low order model.

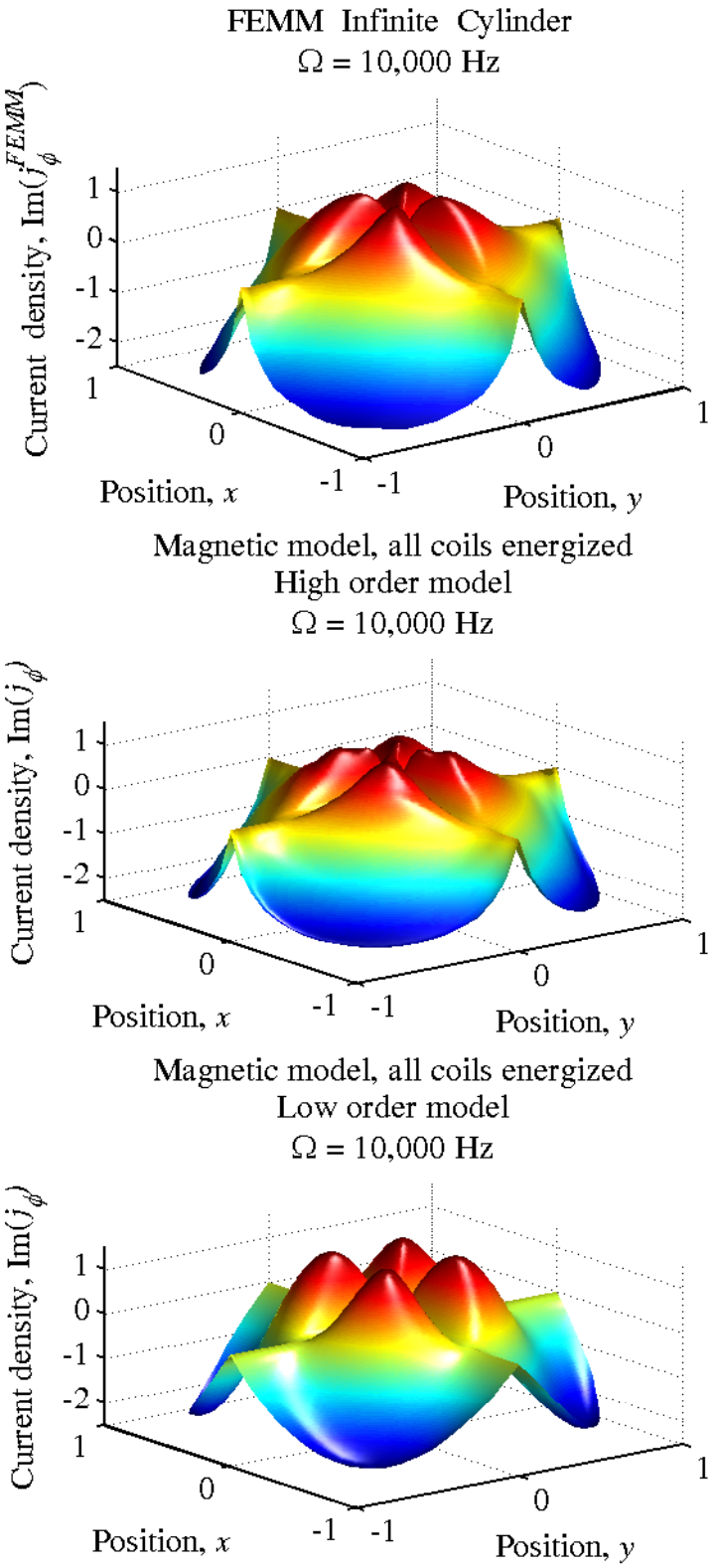


Figure E.3: Comparison of imaginary component of azimuthal eddy current density distributions from FEMM infinite cylinder, high order model, and low order model

# APPENDIX F

# INDUCTIVE COUPLING MODEL

The objective of the inductive coupling model is to find an equation in the form of Eq. (5.8) that relates the coil voltages to the coil currents, vibration modes and eddy current modes. The inductive coupling model begins with Maxwell's equations,

$$\nabla \times \mathbf{H} \approx \mathbf{J}\,, \tag{F.1}$$

$$\nabla \times \mathbf{E} = -\frac{\partial \mathbf{B}}{\partial t}, \tag{F.2}$$

$$\nabla \cdot \mathbf{B} = 0\,, \tag{F.3}$$

the linearized constitutive relation between the magnetic field from Chapter 2,

$$\mathbf{B} = \boldsymbol{\kappa}\mathbf{S} + \boldsymbol{\mu}^{\mathrm{S}}\mathbf{H}\,, \tag{F.4}$$

and Ohm's law,

$$\mathbf{J} = \sigma\mathbf{E}\,. \tag{F.5}$$

The magnetic vector potential is defined as:

$$\nabla \times \mathbf{A} = \mathbf{B}\,. \tag{F.6}$$

The derivation starts by substituting the definition of **A** from Eq. (F.6) into Eq. (F.2).

$$\nabla \times \mathbf{E} = -\frac{\partial\left(\nabla \times \mathbf{A}\right)}{\partial t}. \tag{F.7}$$

The order of operations for the time derivative and curl of **A** can be reversed.

$$\nabla \times \mathbf{E} = -\nabla \times \dot{\mathbf{A}}\,. \tag{F.8}$$

Collecting terms and applying the distributive property to the curl operation gives:

$$\nabla\times\left(\mathbf{E}+\dot{\mathbf{A}}\right)=0\,. \tag{F.9}$$

This expression can be integrated to yield,

$$\mathbf{E}+\dot{\mathbf{A}}=\nabla\mathscr{V}\,, \tag{F.10}$$

where $\mathscr{V}$ is a scalar potential function analogous to a constant of integration in scalar calculus to be determined from the boundary conditions of the problem. In this formulation, the term $\nabla\mathscr{V}$ represents a voltage gradient imposed by an external source. The use of the $\mathscr{V}$ nomenclature anticipates that this quantity is related to the coil voltage. The coil is the only region in which an external voltage gradient is imposed; so, $\nabla\mathscr{V}$ is zero everywhere except within the coil region.

Substituting the conductivity relation from Eq. (F.5) into (F.10) for the electric field intensity gives a relationship in terms of the current density, $\mathbf{J}$.

$$\frac{1}{\sigma}\mathbf{J}+\dot{\mathbf{A}}=\nabla\mathscr{V}\,. \tag{F.11}$$

Let us first consider how the voltage gradient, $\nabla\mathscr{V}$, can be integrated to yield the voltage across the coil which is termed $\mathscr{V}_j^{\,K}$ in CHAPTER 5. In the coil, the current density distribution is determined by the arrangement of insulation and conductor. The insulation of the wire forces the flow of electrons to follow a helical path. On a very fine length scale, the current density in a cross-sectional area of the coil varies with position across the insulation and conductor. At very high frequency, the current density even varies across the cross-sectional area of the conductor due to skin effects. These effects are negligible in the actuator analysis. The length scale for the variation in current

density across the coil is on the order of the diameter of the conductor. The magnetic induction effects that are important to the actuator are integral averages of the induction over the cross sectional areas of the rod and the coil which are about 100 times larger than the wire diameter. Also, the current density does not vary along the length of the wire since there is negligible capacitance in the wire and the displacement current has been neglected. Hence, from the standpoint of the magnetic induction acting on the coil, the current density can be assumed to have a uniform average value at every point in the *r-z* plane through each coil region. Let $J_\phi(t)$ represent the current density in the azimuthal direction along the direction of the helical coil and let $\dot{A}_\phi$ be the vector potential in the azimuthal direction. Thus, Eq. (F.11) can be written as a scalar equation in the azimuthal component of current density and vector potential.

$$J_\phi(t) = \sigma\left(-\dot{A}_\phi + \frac{1}{r}\frac{\partial \mathscr{V}}{\partial \phi}\right) \tag{F.12}$$

Let us now consider the physical meaning of the potential gradient. One turn of the coil conductor may be considered to be centered in an area $\Delta r_l \Delta z_k$ of the *r-z* plane. The individual turns in the coil have the same cross-sectional area. For the purposes of this discussion, the turns are numbered with *l* and *k* to indicate the position in the *r-z* plane. The differential length of an element of volume of the conductor segment is $rd\phi$. Because the insulation confines the current to the helical coil, the voltage gradient only has a component in the azimuthal direction. The voltage gradient in cylindrical components across the differential length segment is

$$\nabla \mathscr{V}_{lk} = \begin{bmatrix} 0 \\ \frac{1}{r}\frac{\partial \mathscr{V}_{lk}}{\partial \phi} \\ 0 \end{bmatrix}. \tag{F.13}$$

Integrating along one circular turn of the coil gives the voltage on that turn.

$$\begin{aligned} \int_0^{2\pi} \nabla \mathscr{V}_{l,k} \cdot \hat{\mathbf{e}}_\phi r d\phi &= \int_0^{2\pi} \begin{bmatrix} 0 \\ \frac{1}{r}\frac{\partial \mathscr{V}}{\partial \phi} \\ 0 \end{bmatrix}_{l,k} \cdot \hat{\mathbf{e}}_\phi r d\phi \\ &= \int_0^{2\pi} \frac{1}{r}\frac{\partial \mathscr{V}_{lk}}{\partial \phi} r d\phi \\ &= \int_0^{2\pi} \frac{\partial \mathscr{V}_{lk}}{\partial \phi} d\phi = \Delta \mathscr{V}_{lk}. \end{aligned} \tag{F.14}$$

where $\Delta \mathscr{V}_{lk}$ is the voltage across the (*l,k)*-th turn. Each turn is connected in series to the next, so the total voltage across the *j*-th coil is the summation of all the turns in the coil volume.

$$\sum_l \sum_k \int_0^{2\pi} \nabla \mathscr{V}_{l,k} \cdot \hat{\mathbf{e}}_\phi r d\phi = \sum_l \sum_k \Delta \mathscr{V}_{l,k} = \mathscr{V}_j^K . \tag{F.15}$$

where $\mathscr{V}_j^K$ represents the total voltage across the *j*-th coil. Now, we want to convert the summation to a volume integral. Let the number of turns per unit length in the coil be $T$, the overall length of the wire in the coil region be $z_L$, and the inner and outer radii of the coil be $r_g$ and $r_c$. All the coils in the actuator are assumed to be the same in area and number of turns. The area of one turn can be obtained in terms of overall dimensions coils by the following calculation.

$$\begin{aligned}\Delta r \Delta z &= \frac{\left(r_c - r_g\right) z_L}{T z_L} \\ &= \frac{\left(r_c - r_g\right)}{T}.\end{aligned} \tag{F.16}$$

The numerator of the first line is the area of the coil region in the *r*-*z* plane. The denominator is the total number of turns for all coils combined. The ratio is the area per turn. Multiplying the left side of (F.15) by the left side of (F.16) and the right by the right gives

$$\sum_l \sum_k \int_0^{2\pi} \nabla \mathscr{V}_{lk} \cdot \hat{\mathbf{e}}_\phi r d\phi \, \Delta r_l \, \Delta z_k = \frac{\left(r_c - r_g\right)}{T} \mathscr{V}_j^K . \tag{F.17}$$

Because the areas of the individual conductors are small and the voltage gradient varies smoothly, the double summation on the left hand side can be replaced by a double integral giving an integral over the coil volume. The smoothness assumption is valid for frequencies at which skin effects in the conductor are not important.

$$\int_{z_{j-1}}^{z_j} \int_{r_g}^{r_c} \int_0^{2\pi} \nabla \mathscr{V}(r,z) \cdot \hat{\mathbf{e}}_\phi r d\phi dr \, dz = \frac{\left(r_c - r_g\right)}{T} \mathscr{V}_j^K . \tag{F.18}$$

The reason for arranging the voltage term as a volume integral is to show that the voltage across the coil can be computed by integrating Eq.(F.12) over the coil volume. The particular volume for the *j*-th coil is indicated by adding the *j* subscript.

$$\frac{\left(r_c - r_g\right)}{T} \mathscr{V}_j^K = \int_{V_{C,j}} \frac{1}{r} \frac{\partial \mathscr{V}}{\partial \phi} dV = \int_{V_{C,j}} \left( \dot{\mathbf{A}} + \frac{\mathbf{J}}{\sigma} \right) \cdot \hat{\mathbf{e}}_\phi dV . \tag{F.19}$$

The current density in the coil and the coil's conductivity are constant over the volume so the second term in the integral on the right hand side can be performed by inspection.

$$\int_{V_{C,j}} \hat{e}_\phi \bullet \frac{\mathbf{J}}{\sigma} dV = \frac{J_{C,j}}{\sigma_C} V_{C,j} . \tag{F.20}$$

The volume of the coil, $V_{C,j}$, can be written in terms of the length and the cross sectional area of the conductor.

$$V_{C,j} = \Delta r \, \Delta z \, \ell_{wire} . \tag{F.21}$$

where $\ell_{wire}$ is the total length of the wire in the coil winding. The implication of deleting the subscripts on the right-hand-side is that the volumes of all coils are the same. The index on the left hand side is retained to indicate a particular volume's location, not the magnitude of the volume. When current density is integrated over a coil's volume, the subscript is used to indicate which coil is meant.

The current in the wire can be obtained from the definition of current density.

$$\frac{I_j^K}{\Delta r \, \Delta z} \hat{e}_\phi = \frac{T}{\left(r_c - r_g\right)} I_j^K \hat{e}_\phi = \mathbf{J}_{C,j} . \tag{F.22}$$

The integral for the current density in terms of current can be derived by substituting the definitions from Eq. (F.21) and Eq. (F.22) into Eq. (F.20).

$$\int_{V_{C,j}} \hat{e}_\phi \bullet \frac{\mathbf{J}}{\sigma_C} dV = I_j^K \frac{L_C}{\sigma_C} . \tag{F.23}$$

The resistance of the length of wire in ohms is given by:

$$\mathscr{R}_C = \frac{\ell_{wire}}{S_{wire} \sigma_C} , \tag{F.24}$$

where $S_{wire}$ is the area of one turn of the conductor within $\Delta r \, \Delta z$ and $\ell_{wire}$ is the length of the wire in the coil. Since the coil's resistance is small compared to the load resistor,

accuracy in estimating the wire resistance is not important in the model. It is sufficient to approximate the conductor area as the square area of the turn.

$$S_{wire} \approx \Delta r \Delta z = \frac{\left(r_c - r_g\right)}{T}. \tag{F.25}$$

Hence the current density integral can be written in terms of known parameters of the actuator.

$$\int_{V_{C,j}} \hat{e}_\phi \bullet \frac{\mathbf{J}_{C,j}}{\sigma_C} dV = I_j^K \frac{\mathscr{R}_C \left(r_c - r_g\right)}{T}. \tag{F.26}$$

By assumption, the coils are all identical in size and number of turns. Consequently, all coils have the same resistance. No coil subscript is added to the resistance parameter for the coil, $\mathscr{R}_C$, since all coils are the same. Solving for the voltage in Eq. (F.19) gives the following:

$$\mathscr{V}_j^K = \frac{T}{\left(r_c - r_g\right)} \int_{V_{C,j}} \hat{e}_\phi \bullet \dot{\mathbf{A}} dV + I_j^K \mathscr{R}_C. \tag{F.27}$$

This is the result needed for computing the inductance in Eq. (5.28)

# APPENDIX G

# SOLUTION OF THE INDUCTANCE COEFFICIENTS

The general form of the solution of the induced voltage is given by Eq. (5.43). This appendix provides the derivation of the formulae for each set of inductances. The solution is divided into sections corresponding to the coil-to-coil inductance, coil-to-eddy current mode inductance and the coil-to-vibration mode inductance. Each section starts with the corresponding equation from Eqs. (5.31) to (5.33) and concludes with a formula that can be evaluated numerically. The method uses the reciprocity principle so that current density distributions and FEMM potential calculations can be used to evaluate inductance integral.

## Inductance Calculations

### Inductance from coil to coil

The $L^K_{j,j'}$ coefficient represents the coupling between the *j*-th coil and the *j'*-th coil. The integration of potential over a volume is a feature built into the FEMM code so the $L^K_{j',j}$ coefficients are evaluated numerically using the tabular values computed by FEMM solution to the actuator magnetics.

$$\begin{aligned} L^K_{j,j'} &= \frac{1}{\left(\mathscr{R}_L + \mathscr{R}_C\right)\Delta I} \int_{V_{c.j'}} \mathbf{f}^K_{j'}\left(r,\phi,z\right) \bullet A^{FEMM}_j\left(r,z\right)\hat{\mathbf{e}}_\phi dV \\ &= \frac{1}{\left(\mathscr{R}_L + \mathscr{R}_C\right)\Delta I} \int_{V_{c.j'}} \frac{T\Delta I}{\left(r_c - r_g\right)}\hat{\mathbf{e}}_\phi \bullet A^{FEMM}_j\left(r,z\right)\hat{\mathbf{e}}_\phi dV \\ &= \frac{T}{\left(\mathscr{R}_L + \mathscr{R}_C\right)\left(r_c - r_g\right)} \int_{V_{c.j'}} A^{FEMM}_j\left(r,z\right) dV. \end{aligned} \tag{G.1}$$

In the following equation, the limits of the coil volume integral are explicitly stated. In the second line, the integration over $\phi$ is carried out and dimesionless variables are substituted in for the radial and axial integration.

$$\begin{aligned} L^K_{j,j'} &= \frac{T}{\left(\mathscr{R}_L + \mathscr{R}_C\right)\left(r_c - r_g\right)} \int_{z=z_{j'}}^{z_{j'+1}} \int_{\phi=0}^{2\pi} \int_{r=0}^{r_g} A_j^{FEMM}\left(r,z\right) r dr d\phi dz \\ &= \frac{2\pi T r_g^2 z_L}{\left(\mathscr{R}_L + \mathscr{R}_C\right)\left(r_c - r_g\right)} \int_{\xi=z_{j'}}^{\xi_{j'+1}} \int_{\rho=1}^{\frac{r_c}{r_g}} A_j^{FEMM}\left(r_g\rho, z_L\xi\right) \rho d\rho d\xi. \end{aligned} \tag{G.2}$$

The FEMM integration of potential is used to evaluate Eq. (G.2). The FEMM results are written to a file which can then be read by MATLAB for use by the actuator simulation model.

**Inductance from eddy current to coil**

The formula for the eddy current to coil inductance coefficient can be rewritten as the following using the equation for the FEMM case's current density distribution.

$$L^M_{j,k,m,p} = \frac{1}{\left(\mathscr{R}_L + \mathscr{R}_C\right)\Delta I} \int_{V_R} \mathbf{f}^M_{k,m,p}\left(r,\phi,z\right) \bullet A_j^{FEMM}\left(r,\phi,z\right)\hat{\mathbf{e}}_\phi dV\,. \tag{G.3}$$

The radial component of current density does not contribute to the dot product inside the integral because the FEMM potential only has an azimuthal component. The integration in three dimensions can be written out explicitly for evaluation. The azimuthal integration is over the full circle of the rod, but each pie segment is identical. The integration over one pie-segment can be multiplied by the number of segments to compute the integral. In the next line, the limits of integration are changed to $0 < \phi < \phi_0$, and a multiplier, $\frac{2\pi}{\phi_0}$, for the number of pie segments is added to the integration.

$$
\begin{aligned}
L_{j,k,m,p}^{M} &= \frac{1}{\left(\mathscr{R}_L + \mathscr{R}_C\right)\Delta I}\int_{V_R} f_{k,m,p}^{M,\phi}\left(r,\phi,z\right) A_j^{FEMM}\left(r,z\right) dV \\
&= \frac{2\pi}{\phi_0}\frac{1}{\left(\mathscr{R}_L + \mathscr{R}_C\right)\Delta I}\int_{z=0}^{z_L}\int_{r=0}^{r_g}\int_{\phi=0}^{\phi_0} f_{k,m,p}^{M,\phi}\left(r,\phi,z\right)\bullet A_j^{FEMM}\left(r,z\right) r d\phi dr dz.
\end{aligned}
\tag{G.4}
$$

The azimuthal component of eddy current can be obtained from the current density functions in Eq. (4.123).

$$
\begin{aligned}
f_{k,m,p}^{M,\phi}\left(r,\phi,z\right) &= \frac{T\Delta I}{r_g}\left(1+\frac{\chi_R r_g^2 \eta_p^2}{z_L^2 \varepsilon_{k,m}^2}\right) \\
&\cdot\frac{\left[\varepsilon_{k,m}\mathrm{J}_{\gamma_m+1}\left(\frac{\varepsilon_{k,m} r}{r_g}\right) - \frac{r_g \gamma_m \mathrm{J}_{\gamma_m}\left(\frac{\varepsilon_{k,m} r}{r_g}\right)}{r}\right]\sin\left(\gamma_m\phi\right)\sin\left(\frac{\eta_p z}{z_L}\right)}{N\left(\gamma_m\right)N\left(\varepsilon_{k,m},\gamma_m\right)N\left(\eta_p\right)}.
\end{aligned}
\tag{G.5}
$$

The azimuthal integration can be performed analytically because $A_j^{FEMM}\left(r,z\right)$ does not depend on $\phi$.

$$
\int_0^{\phi_0}\sin\left(\gamma_m\phi\right)d\phi = -\frac{\cos\left(\gamma_m\phi\right)}{\gamma_m}\bigg|_0^{\phi_0} = \frac{2}{\gamma_m}.
\tag{G.6}
$$

$$
\begin{aligned}
L_{j,k,m,p}^{M} &= \frac{4\pi}{\phi_0\gamma_m}\frac{T}{r_g\left(\mathscr{R}_L+\mathscr{R}_C\right)}\frac{\left(1+\frac{\chi_R r_g^2\eta_p^2}{z_L^2\varepsilon_{k,m}^2}\right)}{N\left(\gamma_m\right)N\left(\varepsilon_{k,m},\gamma_m\right)N\left(\eta_p\right)} \\
&\cdot\int_{z=0}^{z_L}\int_{r=0}^{r_g}\left[\varepsilon_{k,m}\mathrm{J}_{\gamma_m+1}\left(\frac{\varepsilon_{k,m} r}{r_g}\right) - \frac{r_g\gamma_m\mathrm{J}_{\gamma_m}\left(\frac{\varepsilon_{k,m} r}{r_g}\right)}{r}\right]\sin\left(\frac{\eta_p z}{z_L}\right) A_j^{FEMM}\left(r,z\right) r dr dz.
\end{aligned}
\tag{G.7}
$$

The final version of the formula is obtained by converting the integration to dimensionless variables.

$$L^{M}_{j,k,m,p} = \frac{4\pi}{\phi_0}\frac{Tr_g z_L}{\left(\mathscr{R}_L + \mathscr{R}_C\right)}\frac{\left(1+\dfrac{\chi_R r_g^2 \eta_p^2}{z_L^2 \varepsilon_{k,m}^2}\right)}{N(\gamma_m)N(\varepsilon_{k,m},\gamma_m)N(\eta_p)} \cdot \int_{\xi=0}^{1}\int_{\rho=0}^{1}\left[\frac{\varepsilon_{k,m}\rho \mathrm{J}_{\gamma_m+1}(\varepsilon_{k,m}\rho)}{\gamma_m} - \mathrm{J}_{\gamma_m}(\varepsilon_{k,m}\rho)\right]\sin(\eta_p \xi) A_j^{FEMM}(r_g\rho, z_L\xi)\, d\rho d\xi. \tag{G.8}$$

The quantity inside the integral is computed by the same numerical integration by Simpson's rule as the corresponding coupling coefficients in the magnetic field model. The FEMM calculations are performed for each coil case. The values for the vector potential are recorded in a two-dimensional grid in the *r*-*z* plane from $0 \le r \le r_g$ and $0 \le z \le z_L$. The grid spacing is $3.175\times10^{-3}$ m (0.0125 in) axially by $6.35\times10^{-5}$ m (0.0025 in) radially. This rectangular mesh size gives an array of 471 by 101 points over the radial and axial dimensions of the rod. The values of $A_j^{FEMM}(r,z)$ are written by FEMM to a file which is then transferred into MATLAB to perform the integration in Eq. (G.8).

**Inductance from vibration to coil**

The changing magnetization generated by vibration in the rod creates a time-varying magnetic field that induces a voltage in the coil. The inductance coefficients between the coil and the vibration modes can be computed by the same approach as the coupling to the eddy current modes. The magnetization must first be converted into an equivalent current density distribution to use the formulations for inductance in Eq. (5.33) and the reciprocity relation in Eq. (5.34). The definition of magnetization is the following:

$$\mathbf{B} = \boldsymbol{\mu}(\mathbf{H} + \mathbf{M}). \tag{G.9}$$

The linear constitutive relation for the magnetostrictive material is:

$$\mathbf{B} = \boldsymbol{\mu}^S \mathbf{H} + \boldsymbol{\kappa}\mathbf{S}. \tag{G.10}$$

By comparing the two, the magnetization due to the magnetostrictive effect can be found to be

$$\mathbf{M}^N = \left(\boldsymbol{\mu}^S\right)^{-1} \boldsymbol{\kappa}\mathbf{S}. \tag{G.11}$$

The superscript *N* conveys the connection of the magnetization component to the vibration model.

Ampère is credited with first recognizing that magnetization could be treated as an equivalent current density distribution [48]. Moreover, since the other terms for coil and eddy current which generate magnetic fields are in units of current density, converting the magnetization due to strain to an equivalent current density distribution puts all the magnetic effects in the same units so they can be more readily compared. The equivalent current is defined as a distribution of current density that gives the same field as the magnetized material. In the general case, the equivalent current density distribution combines a surface current and a current density distribution in the interior of the magnetized material. The surface current component in terms of the magnetization is given by

$$\mathbf{K}^N = \mathbf{M}^N \times \hat{\mathbf{e}}_n, \tag{G.12}$$

where $\mathbf{M^N}$ is the magnetization and $\hat{\mathbf{e}}_n$ is the outward normal unit vector from the surface of the magnetized material. If the magnetization varies in the interior of the magnetized material, an equivalent current density in the interior is given by

$$\mathbf{J}^N = \nabla \times \mathbf{M}^N. \tag{G.13}$$

The equivalent current for magnetization is not a real current in the sense of a free flow of electrons which produces resistive losses. The equivalent current is the net flow of the electrons traveling in bound orbits of the individual ferromagnetic atoms. The equivalent current is quite real in the sense that it gives exactly the same magnetic field and induction as the magnetized material.

The vector components of the magnetization can be written in terms of the strain by inserting the solution to the vibration model from Chapter 3 into Eq. (G.11). In the constant volume approximation in Chapter 2, the strain was approximated as uniform in the transverse direction. Hence, $\mathbf{M}^N$ is a function only of $z$ and $t$ and not $r$ and $\phi$.

$$\mathbf{M}^N(z,t) = \left(\boldsymbol{\mu}^S\right)^{-1}\boldsymbol{\kappa}\mathbf{S} = \begin{bmatrix} 0 \\ 0 \\ \dfrac{\kappa_{eff,z}}{\mu_R} \end{bmatrix} \frac{\partial \zeta_z(z,t)}{\partial z}. \tag{G.14}$$

The equivalent surface current on the cylindrical surface of the rod is given by applying the formula in Eq. (G.12). The outward normal unit vector on the cylindrical surface of the rod is $\hat{\mathbf{e}}_n = \hat{\mathbf{e}}_r$.

$$\mathbf{K}^N = \mathbf{M}^N \times \hat{\mathbf{e}}_r = \frac{\kappa_{eff,z}}{\mu_R}\frac{\partial \zeta_z}{\partial z}\hat{\mathbf{e}}_\phi. \tag{G.15}$$

As expected, only an azimuthal component of surface current remains on the rod outer surface. A similar component of surface current is present on the radial face of the pie segment. The radial term does not contribute to induction because the coil's potential function has only an azimuthal component. The dot product of a radial vector and azimuthal vector gives zero because the vectors are normal to one another.

The interpretation of the magnetization due to strain as a surface current was anticipated in the derivation of magnetic field when the conventional symbol for surface current, **K**, was used in Eq. (4.22) to designate the same group of strain components. For compactness in the subsequent derivations, the scalar tangential component of $K^N$ is used to represent the equivalent surface current. In this notation the direction of surface current flow is understood to be the azimuthal direction on the cylindrical face and radial on the radial face of the pie segment. The axial position, *z*, and time, *t*, are shown explicitly as the independent arguments of surface current to emphasize that the constant volume approximation eliminates the dependence in the transverse direction.

$$K^N(z,t) = \frac{\kappa_{eff,z}}{\mu_R} \frac{\partial \zeta_z(z,t)}{\partial z}. \tag{G.16}$$

The current density in the interior of the rod is zero by the formula of Eq. (G.13). The partial derivative terms are zero because $M_z^N(z,t)$ does not depend on *r* or $\phi$

$$\begin{aligned} \mathbf{J}^N_{interior} &= \frac{1}{r}\begin{vmatrix} \hat{e}_r & r\hat{e}_\phi & \hat{e}_z \\ \dfrac{\partial}{\partial r} & \dfrac{\partial}{\partial \phi} & \dfrac{\partial}{\partial z} \\ 0 & 0 & M_z^N(z,t) \end{vmatrix}. \\ &= 0 \end{aligned} \tag{G.17}$$

The function, $K^N$, physically represents an infinitesimally thin sheet of current on the cylindrical surface the rod whose magnitude varies axially with the strain. The units of the function are current per unit length. The surface current can be converted to a current density using the Dirac delta function. The magnitude of the surface current in amps per unit area is infinite at the surface of the rod, but zero everywhere else.

$$\mathbf{J}^N(r,z,t) = K^N(z,t)\,\delta\left(r - r_g\right)\hat{\mathbf{e}}_\phi. \tag{G.18}$$

The distribution function for the vibration model is given in Eq. (B.34).

$$\begin{aligned} K^N(z,t) &= \frac{\kappa_{eff,z}}{\mu_R} S = \frac{\kappa_{eff,z}}{\mu_R} \frac{\partial \zeta_z(z,t)}{\partial z} \\ &= \frac{\kappa_{eff,z}\kappa_{eff} T \Delta I}{\mu_R Y_{eff}^H} \left[ 2 \sum_{n=1}^{nmax} \beta_n \cos\left( \beta_n \frac{z}{z_L} \right) \chi_n^N(t) \right]. \end{aligned} \tag{G.19}$$

The leading coefficient is the scaling factor for the surface current density distribution. For compact notation, let the factor be grouped as a constant.

$$\Delta K = \frac{\kappa_{eff,z}\kappa_{eff} T \Delta I}{\mu_R Y_{eff}^H}. \tag{G.20}$$

The surface current density distribution is a linear combination of the amplitude functions and current density distributions functions.

$$\mathbf{K}^N(z,t) = \sum_{n=1}^{nmax} \mathbf{f}_n^N(z) \chi_{N,n}^H(t). \tag{G.21}$$

By comparison to Eq. (G.19), the current density distribution function for an equivalent current due to magnetization is given by the following:

$$\mathbf{f}_n^N(r,z) = 2\Delta K \beta_n \cos\left( \beta_n \frac{z}{z_L} \right) \delta(r - r_g) \hat{\mathbf{e}}_\phi. \tag{G.22}$$

The equation for the inductance between coil and vibration mode is obtained by incorporating (G.22) into Eq. (5.43).

$$\begin{aligned} L_{j,n}^N &= \frac{1}{\left( \mathscr{R}_L + \mathscr{R}_C \right) \Delta I} \int_{V_x} \mathbf{f}_n^N(r,z) \bullet A_j^{FEMM}(r,z) \hat{\mathbf{e}}_\phi dV \\ &= \frac{2\Delta K \beta_n}{\left( \mathscr{R}_L + \mathscr{R}_C \right) \Delta I} \int_{V_x} \cos\left( \beta_n \frac{z}{z_L} \right) \delta(r - r_g) A_j^{FEMM}(r,z) dV. \end{aligned} \tag{G.23}$$

The volume integral converts to a surface integral through integral properties of the Dirac delta function.

$$L_{j,n}^{N} = \frac{\Delta K 2\beta_n}{\left(\mathscr{R}_L + \mathscr{R}_C\right)\Delta I} \int_{z=0}^{z_L} \int_{\phi=0}^{2\pi} \cos\left(\beta_n \frac{z}{z_L}\right) A_j^{FEMM}\left(r_g, z\right) r_g \, d\phi \, dz \,. \tag{G.24}$$

The azimuthal integration can be carried out since the integrand does not depend on $\phi$.

$$L_{j,n}^{N} = \frac{2\pi\Delta K 2\beta_n r_g}{\left(\mathscr{R}_L + \mathscr{R}_C\right)\Delta I} \int_{z=0}^{z_L} \cos\left(\beta_n \frac{z}{z_L}\right) A_j^{FEMM}\left(r_g, z\right) dz \,. \tag{G.25}$$

Converting the variable of integration to dimensionless variables gives the final form of the coefficient. This formula can be evaluated using Simpson's rule for integration in one dimension. The spacing of the axial points for the FEMM potential is the same as in the previous case. There are 471 points spaced $3.175\times10^{-5}$ m (0.0125 in) apart.

$$L_{j,n}^{N} = \frac{4\pi r_g z_L}{\left(\mathscr{R}_L + \mathscr{R}_C\right)} \frac{\Delta K}{\Delta I} \beta_n \int_{\xi=0}^{1} \cos\left(\beta_n \xi\right) A_j^{FEMM}\left(r_g, z_L \xi\right) d\xi \,. \tag{G.26}$$

**Test Cases for the Coil Inductances Using Green's Identity**

Green's first identity for vector fields can be used to find relationships between the coefficient matrices for coils, vibration, and eddy current derived in Chapters 3, 4 and 5. The relationships serve as a test of the derivation and programming of the model. Rothwell [46] gives a form of Green's identity that is suitable for the test cases. The identity can be written as the following.

$$\int_V \left\{ \left(\nabla\times\boldsymbol{\Phi}\right)\cdot\nabla\times\boldsymbol{\Psi} - \boldsymbol{\Phi}\cdot\left[\nabla\times\left(\nabla\times\boldsymbol{\Psi}\right)\right] \right\} dV = \int_S \left[\boldsymbol{\Phi}\times\left(\nabla\times\boldsymbol{\Psi}\right)\right] dS \,. \tag{G.27}$$

The Green's identity is extraordinary in its generality. The vector fields, $\boldsymbol{\Phi}$ and $\boldsymbol{\Psi}$, in Green's identity can be any vector fields that are differentiable. The volume, *V*,

can be any volume in space and the surface, *S*, is the corresponding surface of the same volume. To create a test of the model, the fields in Eq. (G.27) may be chosen to be the potential fields due to a coil, vibration, or eddy current. Any two of the three vector potential fields may be chosen for a comparison test. Thus, relationships between $\mathbf{F}^{13}$ and $\mathbf{F}^{31}$, $\mathbf{F}^{41}$ and $\mathbf{F}^{14}$, and $\mathbf{E}^{34}$ and $\mathbf{E}^{43}$ based on Green's identity can be found.

The testing aspect of applying Green's comes from the independence in the derivations of the pairs of coefficients. One of the basic methods of computer model testing comes from solving a problem two different and independent ways and comparing the results. The value in such tests is that mistakes are not likely to be exactly the same in both derivations.

**Coil current and vibration test**

Let $\mathbf{\Phi}$ be the potential due to coil *j* calculated by FEMM. In the following formula, the coil current amplitude function is set equal to unity for the *j*-th coil, $\mathcal{I}_j^K(t)=1$, while all other coil currents are zero.

$$\mathbf{\Phi} = A_j^{FEMM}(r,z)\hat{e}_\phi . \tag{G.28}$$

$$\begin{aligned}\nabla\times\mathbf{\Phi} &= B_{r,j}^{FEMM}(r,z)\hat{e}_r + B_{z,j}^{FEMM}(r,z)\hat{e}_z \\ &= \mu_R\left[H_{r,j}^{FEMM}(r,z)\hat{e}_r + H_{z,j}^{FEMM}(r,z)\hat{e}_z\right].\end{aligned} \tag{G.29}$$

Let $\mathbf{\Psi}$ be the potential due to strain from the *n*-th vibration model. The potential itself has not been derived for strain, but the test does not need it. We only need the magnetization due to strain. From Eq. (G.14), the magnetization is given by

$$\nabla\times\boldsymbol{\Psi}=M_z^N\hat{e}_z=\begin{cases}\dfrac{k_{eff,z}}{\mu_R}\dfrac{\partial\zeta_z}{\partial z}\hat{e}_z & r<r_g \text{ and } 0<z<z_L\\ 0 & r\geq r_g \text{ or } z\leq 0 \text{ or } z\geq z_L\end{cases}. \tag{G.30}$$

By assumption of a uniform average density in the transverse plane, the magnetization only has a non-zero component in the axial direction. The second part of the condition recognizes that any material outside the rod does not produce any magnetization due strain. The magnetization is defined as zero on the boundary for convenience in evaluating the right hand side of Eq. (G.27). To get the magnetization for a single mode, we substitute in the vibration models in dimensioned units

$$\begin{aligned}\frac{k_{eff,z}}{\mu_R}\frac{\partial\zeta_z}{\partial z}\hat{e}_z&=\frac{k_{eff,z}}{\mu_R}\frac{\partial}{\partial(z_z\xi)}\left[\frac{\kappa_{eff}z_L T\Delta I}{Y_{eff}^H}x^N\right]\\&=\frac{k_{eff,z}}{\mu_R}\frac{\kappa_{eff}T\Delta I}{Y_{eff}^H}\frac{\partial x^N}{\partial\xi}\\&=\frac{k_{eff,z}}{\mu_R}\frac{\kappa_{eff}T\Delta I}{Y_{eff}^H}\frac{\partial}{\partial\xi}\left[\sum_{n'=1}^{nmax}\chi_{n'}^N(t)\frac{\sin(\beta_{n'}\xi)}{N(\beta_{n'})}\right]\\&=\frac{k_{eff,z}}{\mu_R}\frac{\kappa_{eff}T\Delta I}{Y_{eff}^H}\left[\sum_{n'=1}^{nmax}\chi_{n'}^N(t)\frac{\beta_{n'}\cos(\beta_{n'}\xi)}{N(\beta_{n'})}\right].\end{aligned} \tag{G.31}$$

Select one mode for the test case. Let $\chi_n^N(t)=1$ and $\chi_{n'}^N(t)=0$ for $n'\neq n$.

$$\nabla\times\boldsymbol{\Psi}=\begin{cases}\dfrac{k_{eff,z}}{\mu_R}\dfrac{\kappa_{eff}T\Delta I}{Y_{eff}^H}\dfrac{\beta_n\cos(\beta_n\xi)}{N(\beta_n)}\hat{e}_z & r<r_g;\ 0<z<z_L\\ 0 & r\geq r_g;\ z\leq 0 \text{ or } z\geq z_L.\end{cases} \tag{G.32}$$

The leading coefficient is defined as a grouped constant in Eq. (G.20). The normalization constant for the trigonometric function is given by $N(\beta_n)=\frac{1}{2}$. A simplified equation can be written as the following.

$$\nabla\times\boldsymbol{\Psi}=\begin{cases}2\Delta K\beta_n\cos(\beta_n\xi)\hat{e}_z & r<r_g \text{ and } 0<z<z_L\\ 0 & r\geq r_g \text{ or } z\leq 0 \text{ or } z\geq z_L\end{cases}. \tag{G.33}$$

We define the volume of integration for Green's identity as the rod volume and evaluate the right hand side of Eq. (G.32). Since $\nabla\times\boldsymbol{\Psi}$ is zero on the surface of the rod, the integral is zero.

$$\int_{S_R}\left[\boldsymbol{\Phi}\times(\nabla\times\boldsymbol{\Psi})\right]dS=\int_{S_R}\left[\boldsymbol{\Phi}\times(0)\right]dS=0. \tag{G.34}$$

The jump condition at the boundary gives a Dirac delta function when the curl is applied.

$$\nabla\times(\nabla\times\boldsymbol{\Psi})=2\Delta K\beta_n\cos(\beta_n\xi)\delta(r-r_g)\hat{e}_\phi. \tag{G.35}$$

Inserting the terms defined by Eqs. (G.33) and (G.29) on the left hand side of Green's identity and the terms defined by Eqs. (G.28) and (G.35) on the right hand side gives the following equality. On the left hand side, only the axial terms survive the dot product.

$$\begin{aligned}&\int_{V_R}\mu_R H_{z,j}^{FEMM}(r,z)2\Delta K\beta_n\cos(\beta_n\xi)\,dV\\ &\qquad=\int_{V_R}A_j^{FEMM}(r,z)\hat{e}_\phi\cdot 2\Delta K\beta_n\cos(\beta_n\xi)\delta(r-r_g)\hat{e}_\phi dV\end{aligned} \tag{G.36}$$

It is fairly easy to use the definition of magnetic potential, $\nabla\times\mathbf{A}^{FEMM}=\boldsymbol{\mu}_R\mathbf{H}^{FEMM}$, and Stokes' theorem to show that this equation holds; however, a more complete test of the model can be found by solving for a relationship between the coupling matrices. The goal is to find a relationship involving the $\mathbf{F}^{13}$ coefficients using the integral on the left and a similar expression involving the $\mathbf{F}^{31}$ coefficients from the integral on the right.

$$\int_{V_R} \mu_R H_j^{FEMM}(r,z)\hat{e}_z \cdot 2\Delta K \beta_n \cos(\beta_n \xi)\hat{e}_z dV$$
$$= 2\mu_R \Delta K \beta_n \int_{z=0}^{z_L} \cos(\beta_n \xi)\left[\int_{\phi=0}^{2\pi}\int_{r=0}^{r_g} H_j^{FEMM}(r,z) r dr d\phi\right] dz. \tag{G.37}$$

The left hand side of Eq. (G.37) is evaluated first. A series of substitutions from the derivation of the vibration model can be inserted into the expression that ultimately replace the integral with the $\mathbf{F}^{13}$ coefficient. From Eq. (B.19) of the vibration model derivation, the integral of magnetic field can be written in terms of the dimensionless, average magnetic field, $\breve{x}_{R,j}^{FEMM}(\xi)$.

$$\int_{\phi=0}^{2\pi}\int_{r=0}^{r_g} H_j^{FEMM}(r,z) r dr d\phi = \pi r_g^2 T \breve{x}_{R,j}^{FEMM}(\xi). \tag{G.38}$$

$$\int_{V_R} \mu_R H_j^{FEMM}(r,z)\hat{e}_z \cdot 2\Delta K \beta_n \cos(\beta_n \xi)\hat{e}_z dV$$
$$= 2\mu_R \Delta K \beta_n \int_{z=0}^{z_L} \pi r_g^2 T \breve{x}_{R,j}^{FEMM}\left(\frac{z}{z_L}\right) dz \tag{G.39}$$
$$= 2\pi r_g^2 z_L \mu_R \Delta K T \beta_n \int_{\xi=0}^{1} \cos(\beta_n \xi)\breve{x}_{R,j}^{FEMM}(\xi) d\xi.$$

From Eq. (B.29),

$$Q_{n,j} = \beta_n \int_{\xi=0}^{1} \cos(\beta_n \xi)\breve{x}_{R,j}^{FEMM}(\xi) d\xi. \tag{G.40}$$

From Eq. (3.41),

$$\mathbf{F}^{13} = \left[F_{n,j}^{13}\right] = \left(\frac{2\omega_1}{\pi}\right)^2 \left[Q_{n,j}\right]. \tag{G.41}$$

Combine Eqs. (G.40) and (G.41),

$$\beta_n \int_{\xi=0}^{1} \cos(\beta_n \xi)\, \breve{x}_{R,j}^{FEMM}(\xi)\, d\xi = \left(\frac{\pi}{2\omega_1}\right)^2 \mathbf{F}_{n,j}^{13} \quad . \tag{G.42}$$

Insert Eq. (G.42) into Eq. (G.39) to give the left hand side of Green's identity from Eq. (G.36) in terms of $\mathbf{F}^{13}$.

$$\begin{aligned} &\int_{V_R} \mu_R H_j^{FEMM}(r,z)\,\hat{e}_z \cdot 2\Delta K \beta_n \cos(\beta_n \xi)\,\hat{e}_z dV \\ &\qquad = 2\pi r_g^2 z_L \mu_R \Delta K T \left(\frac{\pi}{2\omega_1}\right)^2 F_{n,j}^{13}. \end{aligned} \tag{G.43}$$

The right hand side of Eq. (G.36) can be similarly transformed to give a factor proportional to $\mathbf{F}^{31}$.

$$\begin{aligned} &\int_{V_R} A_j^{FEMM}(r,z)\,\hat{e}_\phi \cdot 2\Delta K \beta_n \cos(\beta_n \xi)\,\delta(r - r_g)\,\hat{e}_\phi dV \\ &\qquad = 2\Delta K \beta_n \int_{z=0}^{z_L} \int_{\phi=0}^{2\pi} \int_{r=0}^{r_g} A_j^{FEMM}(r,z) \cos(\beta_n \xi)\,\delta(r - r_g)\, r dr d\phi dz \\ &\qquad = 4\pi \Delta K r_g z_L \beta_n \int_{\xi=0}^{1} A_j^{FEMM}(r_g, z_L \xi) \cos(\beta_n \xi)_\phi\, d\xi. \end{aligned} \tag{G.44}$$

Solve Eq. (G.26) for the term on the right hand side of Eq. (G.44).

$$4\pi r_g z_L \Delta K \beta_n \int_{\xi=0}^{1} \cos(\beta_n \xi)\, A_j^{FEMM}(r_g, z_L \xi)\, d\xi = \Delta I \left(\mathscr{R}_L + \mathscr{R}_C\right) L_{n,j}^N. \tag{G.45}$$

By Eq. (5.52), the inductance is equal to the negative of the state coefficient matrix, $F_{j,n}^{31} = -L_{j,n}^N$.

$$4\pi r_g z_L \Delta K \beta_n \int_{\xi=0}^{1} \cos(\beta_n \xi)\, A_j^{FEMM}(r_g, z_L \xi)\, d\xi = -\Delta I \left(\mathscr{R}_L + \mathscr{R}_C\right) F_{j,n}^{31}. \tag{G.46}$$

Equate the right hand sides of Eq. (G.43) and Eq. (G.46) to complete the Green's identity test equation.

$$2\pi r_g^2 z_L \mu_R \Delta K T \left(\frac{\pi}{2\omega_1}\right)^2 F_{n,j}^{13} = -\Delta I \left(\mathscr{R}_L + \mathscr{R}_C\right) F_{j,n}^{31}. \qquad \text{(G.47)}$$

This comparison is the Green's identity test for the coil and vibration models. After evaluating the coefficients, the modeling program checks them by calculating the ratio of the left hand side over the right hand side. The test gives ratios that are between 0.9994 and 1.0004. The values for two rows of coefficients, $j$=1 and 6, and $n$=1 through 10, are plotted in Figure G.1 which shows how closely the coefficients match. The differences between the coefficients stem from differences in the numerical integration of the coefficients in Eq. (G.40) and Eq. (G.45).

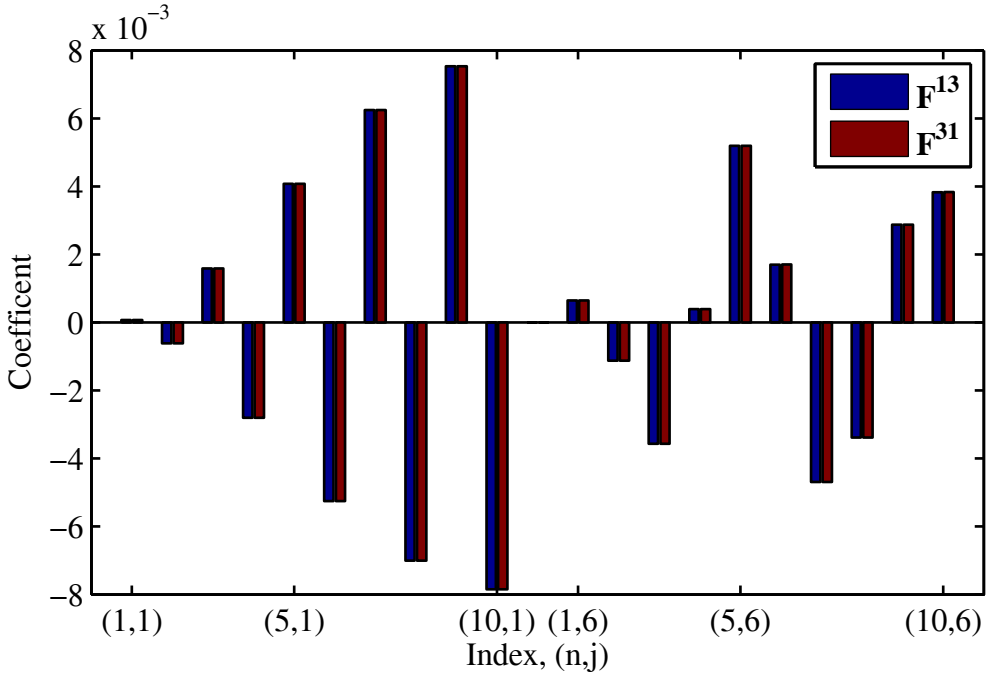


Figure G.1: Green's identity test of coefficients from vibration and coil models

**Coil current and eddy current test**

The Green's function test for coil current and eddy current finds the proportionality constant to compare the coefficients, $\mathbf{E}^{34}$ and $\mathbf{E}^{43}$. The Green's identity test for coil and eddy current coefficients is similar to the previous section; however, the situation is more complicated because fewer of the terms are exactly zero. The eddy current field has non-zero terms in all three directions and the coil's magnetic field is non-zero in radial and axial directions. Hence, the dot product in the first term in Eq. (G.27) includes both radial and axial terms. The integrand for the surface terms on the right hand side of Eq. (G.27) can be shown to be zero on the radial and cylindrical faces of the rod but it is nonzero on the end faces. While the extra terms add complexity, their values turn out to be small when evaluated. The main contribution to the integral turns out to be the axial terms in the dot product of the first term of Eq. (G.27) and the azimuthal term in the dot product in the second term.

The coil current terms remain the same as in the coil vibration problem. The $\mathbf{\Phi}$ is the potential due to coil *j* calculated by FEMM.

$$\mathbf{\Phi} = A_j^{FEMM}(r,z)\hat{e}_\phi . \tag{G.48}$$

$$\begin{aligned}\nabla\times\mathbf{\Phi} &= B_{r,j}^{FEMM}(r,z)\hat{e}_r + B_{z,j}^{FEMM}(r,z)\hat{e}_z \\ &= \mu_R\left[\frac{1}{\chi_R}H_{r,j}^{FEMM}(r,z)\hat{e}_r + H_{z,j}^{FEMM}(r,z)\hat{e}_z\right] \\ &= \boldsymbol{\mu}_R\mathbf{H}_j^{FEMM}(r,z).\end{aligned} \tag{G.49}$$

The solution for the magnetic field due to eddy current in all three directions is found in Appendix E. To select a single mode for the eddy current, let the $\chi_{k,m,p}^{M}(t) = 1$ and let all other amplitudes be zero. The (*k,m,p*)-th mode for eddy current field be

written as a vector. The mode indices are added to indicate the selected mode and the component direction.

$$\nabla\times\boldsymbol{\Psi}=\mathbf{H}_{k,m,p}^{M}=H_{r,k,m,p}^{M}\hat{e}_r+H_{\phi,k,m,p}^{M}\hat{e}_\phi+H_{z,k,m,p}^{M}\hat{e}_z \tag{G.50}$$

The modal solution for all three components of the magnetic field is given in Eq. (E.58). That solution is repeated here.

$$\mathbf{H}_{k,m,p}^{M}(r,\phi,z)=T\Delta I\begin{bmatrix} -\dfrac{\dfrac{r_g\chi_R\eta_p}{z_L}\left[\begin{array}{c}\varepsilon_{k,m}\mathrm{J}_{\gamma_m+1}\left(\dfrac{\varepsilon_{k,m}r}{r_g}\right)\\ -\dfrac{r_g}{r}\gamma_m\mathrm{J}_{\gamma_m}\left(\dfrac{\varepsilon_{k,m}r}{r_g}\right)\end{array}\right]\sin(\gamma_m\phi)\cos\left(\dfrac{\eta_p z}{z_L}\right)}{\varepsilon_{k,m}^2N(\gamma_m)N(\varepsilon_{k,m},\gamma_m)N(\eta_p)}\\ \dfrac{r_g^2}{r}\dfrac{\chi_R\eta_p}{z_L}\dfrac{\mathrm{J}_{\gamma_m}\left(\dfrac{\varepsilon_{k,m}r}{r_g}\right)\cos(\gamma_m\phi)\cos\left(\dfrac{\eta_p z}{z_L}\right)}{N(\gamma_m)N(\varepsilon_{k,m},\gamma_m)N(\eta_p)}\\ \dfrac{\mathrm{J}_{\gamma_m}\left(\dfrac{\varepsilon_{k,m}r}{r_g}\right)\sin(\gamma_m\phi)\sin\left(\dfrac{\eta_p z}{z_L}\right)}{N(\gamma_m)N(\varepsilon_{k,m},\gamma_m)N(\eta_p)}\end{bmatrix}. \tag{G.51}$$

The $\nabla\times(\nabla\times\boldsymbol{\Psi})$ term is equal to the current density distribution for a single mode.

$$\nabla\times(\nabla\times\boldsymbol{\Psi})=\nabla\times\mathbf{H}_{k,m,p}^{M}=\mathbf{f}_{k,m,p}^{M}(r,\phi,z). \tag{G.52}$$

$$\mathbf{f}^{M}_{k,m,p}\left(r,\phi,z\right)=\frac{T\Delta I}{r_g}\begin{bmatrix}\gamma_m\left(1+\dfrac{\chi_R r_g^2\eta_p^2}{z_L^2\varepsilon_{k,m}^2}\right)\dfrac{\mathrm{J}_{\gamma_m}\left(\dfrac{\varepsilon_{k,m}r}{r_g}\right)\cos\left(\gamma_m\phi\right)\sin\left(\dfrac{\eta_p z}{z_L}\right)}{\rho N_r\left(\gamma_m\right)N_r\left(\varepsilon_{k,m},\gamma_m\right)N_r\left(\eta_p\right)}\\ \left(1+\dfrac{\chi_R r_g^2\eta_p^2}{z_L^2\varepsilon_{k,m}^2}\right)\dfrac{\left[\begin{matrix}\varepsilon_{k,m}\mathrm{J}_{\gamma_m+1}\left(\dfrac{\varepsilon_{k,m}r}{r_g}\right)\\ -\dfrac{r_g}{r}\gamma_m\mathrm{J}_{\gamma_m}\left(\dfrac{\varepsilon_{k,m}r}{r_g}\right)\end{matrix}\right]\sin\left(\gamma_m\phi\right)\sin\left(\dfrac{\eta_p z}{z_L}\right)}{N\left(\gamma_m\right)N\left(\varepsilon_{k,m},\gamma_m\right)N\left(\eta_p\right)}\\ 0\end{bmatrix}. \quad \text{(G.53)}$$

The Green's identity for the coil current and eddy current test can be written compactly in terms of vector quantities.

$$\begin{aligned}&\int_{V_R}\mu_R\mathbf{H}_j^{FEMM}\left(r,z\right)\cdot\mathbf{H}^{M}_{k,m,p}dV-\int_{V_R}A_j^{FEMM}\left(r,z\right)\hat{e}_\phi\cdot\mathbf{f}^{M}_{k,m,p}\left(r,\phi,z\right)dV\\&=\int_{S_R}A_j^{FEMM}\left(r,z\right)\hat{e}_\phi\times\mathbf{H}^{M}_{k,m,p}\cdot\hat{e}_n dS.\end{aligned} \quad \text{(G.54)}$$

On the left hand side of Eq. (G.54), only the axial and radial components of the fields contribute to the integral. The azimuthal component of $\mathbf{H}_j^{FEMM}\left(r,z\right)$ is zero which eliminates that part of the dot product. We can substitute the axial and radial mode functions from Eq. (G.51) into the left hand side of Eq. (G.54). Because of the length of the expression, the radial and axial terms are separated into individual integrals.

Radial term

$$\int_{V_R} \frac{\mu_R}{\chi_R} H_{r,j}^{FEMM} H_{r,k,m,p}^{M} dV = -\frac{\mu_R r_g T \Delta I}{\varepsilon_{k,m}^2 N(\gamma_m) N(\varepsilon_{k,m}, \gamma_m) N(\eta_p)} \frac{\eta_p}{z_L} \cdot \int_{V_R} H_{r,j}^{FEMM} \left[ \varepsilon_{k,m} \mathfrak{J}_{\gamma_m+1}\left(\frac{\varepsilon_{k,m} r}{r_g}\right) - \frac{r_g}{r} \gamma_m \mathfrak{J}_{\gamma_m}\left(\frac{\varepsilon_{k,m} r}{r_g}\right) \right] \sin(\gamma_m \phi) \cos\left(\frac{\eta_p z}{z_L}\right) dV. \quad \text{(G.55)}$$

Axial term

$$\int_{V_R} \mu_R H_{z,j}^{FEMM}(r,z) H_{z,k,m,p}^{M} dV = \frac{\mu_R T \Delta I}{N(\varepsilon_{k,m}, \gamma_m) N(\gamma_m) N(\eta_p)} \cdot \int_{z=0}^{z_L} \int_{\phi=0}^{2\pi} \int_{r=0}^{r_g} H_{z,j}^{FEMM}(r,z) \sin(\gamma_m \phi) \mathfrak{J}_{\gamma_m}\left(\varepsilon_{k,m} \frac{r}{r_g}\right) \sin\left(\eta_p \frac{z}{z_L}\right) r dr d\phi dz. \quad \text{(G.56)}$$

The surface integral terms can be evaluated by substituting in the potential definitions as well.

$$\int_{S_R} A_j^{FEMM}(r,z) \hat{e}_\phi \times \mathbf{H}_{k,m,p}^{M} \cdot \hat{e}_n dS = \int_{S_R} \left[ A_j^{FEMM} H_{z,k,m,p}^{M} \hat{e}_r - A_j^{FEMM} H_{r,k,m,p}^{M} \hat{e}_z \right] \cdot \hat{e}_n dS \ . \quad \text{(G.57)}$$

The axial component of the magnetic field due to eddy current, $H_{z,k,m,p}^{M}$, is zero on all surfaces by the problem's homogeneous boundary condition. Consequently, the first term in the integrand is zero. The vectors normal to the surface are $\hat{e}_n = \hat{e}_r$ on the cylindrical surface and $\hat{e}_n = \hat{e}_\phi$ on the radial surface. Consequently, the surface integrals on those faces of the rod are zero. However, the end faces are not zero. The formula for the surface integral on the faces on the top and bottom of the rod can be written as the following.

$$\int_{S_R} A_j^{FEMM}(r,z)\hat{e}_\phi \times \mathbf{H}_{k,m,p}^{M} \cdot \hat{e}_n dS = -\int_{\phi=0}^{2\pi}\int_{r=0}^{r_g} A_j^{FEMM}(r,z_L) H_{r,k,m,p}^{M}(r,\phi,z_L) r dr d\phi + \int_{\phi=0}^{2\pi}\int_{r=0}^{r_g} A_j^{FEMM}(r,0) H_{r,k,m,p}^{M}(r,\phi,0) r dr d\phi. \quad \text{(G.58)}$$

The radial term's volume integral term from Eq. (G.55) and the surface integral terms from Eq. (G.58) are not zero but turn out to be small. The small terms are collected on the right hand side of Eq. (G.54) into a single variable for compactness in the algebra and retained until the terms are evaluated numerically. Let

$$\Delta_{l,j} = -\int_{V_R} H_{r,j}^{FEMM} H_{r,k,m,p}^{M}(r,\phi,z_L) r dr d\phi dz - \int_{\phi=0}^{2\pi}\int_{r=0}^{r_g} A_j^{FEMM}(r,z_L) H_{r,k,m,p}^{M}(r,\phi,z_L) r dr d\phi + \int_{\phi=0}^{2\pi}\int_{r=0}^{r_g} A_j^{FEMM}(r,0) H_{r,k,m,p}^{M}(r,\phi,0) r dr d\phi. \quad \text{(G.59)}$$

The axial volume integral in Eq. (G.56) is related to $\mathbf{E}^{43}$ and $\Theta_{k,m,p,j}$ from Eq. (4.88) and Eq. (D.35). Those equations give the following similar integral expression.

$$E_{l,j}^{43} = \Theta_{k,m,p,j} = \frac{1}{T}\int_{\xi=0}^{1}\int_{r=0}^{1}\int_{\phi=0}^{\phi_0} H_{R,j}^{FEMM}(r_g\rho, z_L\xi)\sin(\gamma_m\phi)\mathfrak{I}_{\gamma_m}(\varepsilon_{k,m}\rho) \cdot \sin(\eta_p\xi)\rho d\phi d\rho d\xi. \quad \text{(G.60)}$$

The next steps convert the right hand side of Eq. (G.60) to match Eq. (G.56). First, the integration limit on $\phi$ is changed from integration over an interval from $\phi = 0$ to $\phi_0$ to integration around the full circle. Because each segment is identical, we

can multiply the left hand side by the number of segments, $\frac{2\pi}{\phi_0}$, and change the limits on the integral on the right to the $\phi = 0$ to $2\pi$.

$$\frac{2\pi}{\phi_0} E_{l,j}^{43} = \frac{1}{T} \int_{\xi=0}^{1} \int_{r=0}^{1} \int_{\phi=0}^{2\pi} H_{R,j}^{FEMM}\left(r_g \rho, z_L \xi\right) \sin\left(\gamma_m \phi\right) \mathfrak{J}_{\gamma_m}\left(\varepsilon_{k,m} \rho\right) \cdot \sin\left(\eta_p \xi\right) \rho \, d\phi \, d\rho \, d\xi. \tag{G.61}$$

Now, the variables of integration, $\rho$ and $\xi$, are changed to the dimensioned variables, *r* and *z*, to match the integration in Eq. (G.56).

$$\frac{2\pi r_g^2 z_L}{\phi_0} E_{l,j}^{43} = \frac{1}{T} \int_{z=0}^{r_g} \int_{r=0}^{z_L} \int_{\phi=0}^{2\pi} H_{R,j}^{FEMM}\left(r, z\right) \sin\left(\gamma_m \phi\right) \mathfrak{J}_{\gamma_m}\left(\varepsilon_{k,m} \frac{r}{r_g}\right) \cdot \sin\left(\eta_p \frac{z}{z_L}\right) r \, d\phi \, dr \, dz. \tag{G.62}$$

To complete the transformation, both sides are multiplied by the constant

$$\frac{\mu_R T^2 \Delta I}{N\left(\varepsilon_{k,m}, \gamma_m\right) N\left(\gamma_m\right) N\left(\eta_p\right)} \tag{G.63}$$

After applying this multiplication, the right hand side of Eq. (G.62) now is equal to the left hand side of the Green's identity in Eq. (G.54).

$$\frac{2\pi r_g^2 z_L}{\phi_0} \frac{\mu_R T^2 \Delta I}{N\left(\varepsilon_{k,m}, \gamma_m\right) N\left(\gamma_m\right) N\left(\eta_p\right)} E_{l,j}^{43} = \mu_R T \Delta I \int_{z=0}^{r_g} \int_{r=0}^{z_L} \int_{\phi=0}^{2\pi} H_{R,j}^{FEMM}\left(r, z\right) \frac{\sin\left(\gamma_m \phi\right)}{N\left(\gamma_m\right)} \frac{\mathfrak{J}_{\gamma_m}\left(\varepsilon_{k,m} \frac{r}{r_g}\right)}{N\left(\varepsilon_{k,m}, \gamma_m\right)} \frac{\sin\left(\eta_p \frac{z}{z_L}\right)}{N\left(\eta_p\right)} r \, d\phi \, dr \, dz \tag{G.64}$$

The right hand side of Eq. (G.54) can be evaluated in terms of $\mathbf{E}^{34}$. From Eq. (G.3) we can determine that the right hand side of Eq. (G.54) is given by

$$\int_{V_R} A_j^{FEMM}(r,z)\hat{e}_\phi \cdot \mathbf{f}_{k,m,p}^{M}(r,\phi,z)\,dV = \Delta I\left(\mathscr{R}_L + \mathscr{R}_C\right) L_{j,k,m,p}^{M}. \tag{G.65}$$

From the state space model equations in Eq.(5.51)

$$\mathbf{E}^{34} = \left[L_{j,l}^{M}\right] = \left[L_{j,k,m,p}^{M}\right]. \tag{G.66}$$

$$\int_{V_R} A_j^{FEMM}(r,z)\hat{e}_\phi \cdot \mathbf{f}_{k,m,p}^{M}(r,\phi,z)\,dV = \Delta I\left(\mathscr{R}_L + \mathscr{R}_C\right) E_{j,l}^{34}. \tag{G.67}$$

The Green's identity for the coil current and eddy current coefficients is given by inserting Eqs. (G.59), (G.64) and (G.67) into Eq. (G.54).

$$\frac{2\pi r_g^2 z_L}{\phi_0}\frac{\mu_R T^2 \Delta I}{N\left(\varepsilon_{k,m},\gamma_m\right)N\left(\gamma_m\right)N\left(\eta_p\right)}E_{l,j}^{43} - \Delta I\left(\mathscr{R}_L + \mathscr{R}_C\right)E_{j,l}^{34} = \Delta_{l,j}. \tag{G.68}$$

All three terms in the balance can be evaluated numerically. To show representative results, Figure G.2 gives a comparison of the terms in Eq. (G.68) for the range of indices: $k = 1,2$; $m = 1,2$; $p = 1-10$; and $j = 5$. The differences between the coefficients are normalized by the maximum coefficient. The normalized differences range from -0.0086 to 0.009. The parameter, $\Delta_{l,j}$, ranges in value from $-1\times10^{-9}$ to $4\times10^{-8}$ which is five orders of magnitude smaller than the other terms in the Green's identity. Figure G.2 shows that the coefficient terms are very close. The close comparison provides reassurance that the model derivation and programming are correct.

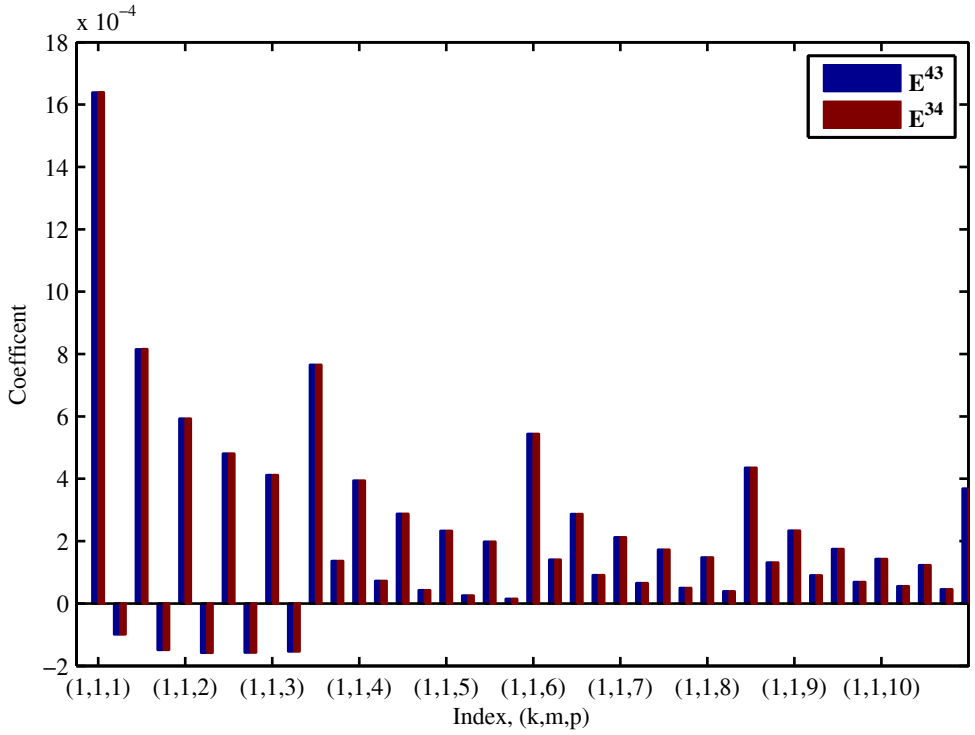


Figure G.2: Green's identity test of coefficients from magnetics and coil models, coil index, $j$=6; magnetic mode indices, $k$=1,2; $m$=1,2; $p$=1-10.

**Eddy current and vibration test**

The Green's identity test for eddy current coefficients and the vibration coefficients provides the reciprocal relationship between $\mathbf{F}^{14}$ and $\mathbf{F}^{41}$. Neither of these coefficients appears in this chapter, but the test is based on Green's identity so the calculation is included here. The coefficients for $\mathbf{F}^{14}$ and $\mathbf{F}^{41}$ both involve the same analytical integral so the test does not give a completely independent evaluation of the coefficients. Nevertheless, the comparison of the calculated model coefficients does compare the terms multiplying the integral and provides a test of the programming. We proceed by substituting the current and potential distributions into the Green's identity and identifying the coefficients as terms in the integrations.

The vibration field and current density give the $\boldsymbol{\Psi}$ terms in Green's identity. Equations (G.33) and (G.35) give the magnetic field and current density terms for the vibration model.

$$\nabla\times\boldsymbol{\Psi}=\begin{cases}2\Delta K\beta_n\cos\left(\beta_n\xi\right)\hat{e}_z & r<r_g;\ 0<z<z_L\\ 0 & r\geq r_g;\ z\leq 0 \text{ or } z\geq z_L\end{cases}. \tag{G.69}$$

In this problem, the current density on the radial face of the pie segment contributes to the integral.

$$\nabla\times\left(\nabla\times\boldsymbol{\Psi}\right)=2\Delta K\beta_n\cos\left(\beta_n\xi\right)\left[\delta\left(\phi\right)\hat{e}_r+\delta\left(r-r_g\right)\hat{e}_\phi-\delta\left(\phi-\phi_0\right)\hat{e}_r\right]. \tag{G.70}$$

The $\boldsymbol{\Phi}$ terms in the Green's identity correspond to the magnetic vector potential and magnetic induction for the eddy current density distribution.

$$\boldsymbol{\Phi}=\mathbf{A}^M_{k,m,p}\left(r,\phi,z\right). \tag{G.71}$$

$$\begin{aligned}\nabla\times\boldsymbol{\Phi}&=\mathbf{B}^M_{k,m,p}\left(r,\phi,z\right)\\ &=\boldsymbol{\mu}_R\mathbf{H}^M_{k,m,p}\left(r,\phi,z\right).\end{aligned} \tag{G.72}$$

These terms are derived in Appendix E and are given by Eq. (E.57) and (E.58).

$$\mathbf{A}^{M}_{k,m,p}\left(r,\phi,z\right)=\frac{\mu_R T\Delta I r_g}{\varepsilon_{k,m}^2}\begin{bmatrix}\dfrac{r_g\gamma_m \text{J}_{\gamma_m}\left(\dfrac{\varepsilon_{k,m}r}{r_g}\right)\cos\left(\gamma_m\phi\right)\sin\left(\dfrac{\eta_p z}{z_L}\right)}{rN\left(\gamma_m\right)N\left(\varepsilon_{k,m},\gamma_m\right)N\left(\eta_p\right)}\\ \dfrac{\begin{bmatrix}\varepsilon_{k,m}\text{J}_{\gamma_m+1}\left(\dfrac{\varepsilon_{k,m}r}{r_g}\right)\\ -\dfrac{r_g}{r}\gamma_m\text{J}_{\gamma_m}\left(\dfrac{\varepsilon_{k,m}r}{r_g}\right)\end{bmatrix}\sin\left(\gamma_m\phi\right)\sin\left(\dfrac{\eta_p z}{z_L}\right)}{N\left(\gamma_m\right)N\left(\varepsilon_{k,m},\gamma_m\right)N\left(\eta_p\right)}\\ 0\end{bmatrix}. \quad \text{(G.73)}$$

$$\mathbf{H}^{M}_{k,m,p}\left(r,\phi,z\right)=T\Delta I\begin{bmatrix}-\dfrac{\dfrac{r_g\chi_R\eta_p}{z_L}\begin{bmatrix}\varepsilon_{k,m}\text{J}_{\gamma_m+1}\left(\dfrac{\varepsilon_{k,m}r}{r_g}\right)\\ -\dfrac{r_g}{r}\gamma_m\text{J}_{\gamma_m}\left(\dfrac{\varepsilon_{k,m}r}{r_g}\right)\end{bmatrix}\sin\left(\gamma_m\phi\right)\cos\left(\dfrac{\eta_p z}{z_L}\right)}{\varepsilon_{k,m}^2N\left(\gamma_m\right)N\left(\varepsilon_{k,m},\gamma_m\right)N\left(\eta_p\right)}\\ \dfrac{r_g^2}{r}\dfrac{\chi_R\eta_p}{z_L}\dfrac{\text{J}_{\gamma_m}\left(\dfrac{\varepsilon_{k,m}r}{r_g}\right)\cos\left(\gamma_m\phi\right)\cos\left(\dfrac{\eta_p z}{z_L}\right)}{N\left(\gamma_m\right)N\left(\varepsilon_{k,m},\gamma_m\right)N\left(\eta_p\right)}\\ \dfrac{\text{J}_{\gamma_m}\left(\dfrac{\varepsilon_{k,m}r}{r_g}\right)\sin\left(\gamma_m\phi\right)\sin\left(\dfrac{\eta_p z}{z_L}\right)}{N\left(\gamma_m\right)N\left(\varepsilon_{k,m},\gamma_m\right)N\left(\eta_p\right)}\end{bmatrix} \quad \text{(G.74)}$$

The Green's identity can be simplified by eliminating the zero terms. The integrand for the surface term is zero on all faces because of either the homogeneous

boundary condition for the eddy current's magnetic field or the dot product with the normal surface vector. The first term in the Green's volume integral only has an axial term in the dot product because the vibration's field only has an axial term. The second term in the Green's volume integral only contains an azimuthal term because of the vibration's equivalent surface current density only has an azimuthal term. Hence, the Green's identity for vibration and eddy current reduces to two terms. The first term in the volume integral is given by

$$\begin{aligned}\int_V (\nabla\times\mathbf{\Phi})\cdot\nabla\times\mathbf{\Psi}dV &= \int_V \mu_R H^M_{z,k,m,p}\cdot M^N_z dV \\ &= \int_{z=0}^{r_g}\int_{r=0}^{z_L}\int_{\phi=0}^{2\pi} \frac{\mu_R T\Delta I \mathfrak{J}_{\gamma_m}\left(\frac{\varepsilon_{k,m}r}{r_g}\right)\sin(\gamma_m\phi)\sin\left(\frac{\eta_p z}{z_L}\right)}{N(\gamma_m)N(\varepsilon_{k,m},\gamma_m)N(\eta_p)} \\ &\qquad \cdot 2\Delta K\beta_n\cos\left(\frac{\beta_n z}{z_L}\right) r d\phi dr dz.\end{aligned} \tag{G.75}$$

In the next line, the integration variables are converted to dimensionless variables, the integration limit on the $\phi$ variable is converted to a single pie segment (with appropriate multiplier), and the terms are regrouped to match the terms used in the derivations of coefficients calculated elsewhere in the model.

$$\begin{aligned}\int_V (\nabla\times\mathbf{\Phi})\cdot\nabla\times\mathbf{\Psi}dV &= 2\pi r_g^2 z_L \mu_R T\Delta I\Delta K \\ &\qquad \cdot\frac{2}{\phi_0}\frac{\int_{\rho=0}^{1}\mathfrak{J}_{\gamma_m}(\varepsilon_{k,m}\rho)\rho d\rho\int_{\phi=0}^{\phi_0}\sin(\gamma_m\phi)d\phi}{N(\gamma_m)N(\varepsilon_{k,m},\gamma_m)N(\eta_p)} \\ &\qquad\qquad \cdot\beta_n\int_{\xi=0}^{1}\sin(\eta_p\xi)\cos(\beta_n\xi)d\xi.\end{aligned} \tag{G.76}$$

The azimuthal and axial integrations can be performed analytically to yield.

$$\int_V (\nabla\times\boldsymbol{\Phi})\cdot\nabla\times\boldsymbol{\Psi}dV = 2\pi r_g^2 z_L \mu_R T\Delta I\Delta K \cdot\frac{4}{\phi_0\gamma_m}\frac{\int_{\rho=0}^{1} \mathrm{J}_{\gamma_m}(\varepsilon_{k,m}\rho)\rho d\rho}{N(\gamma_m)N(\varepsilon_{k,m},\gamma_m)N(\eta_p)} \cdot\frac{\beta_n\eta_p}{(\eta_p^2-\beta_n^2)}. \tag{G.77}$$

Equation (B.16) defines the term on the middle line as $P_{k,m}$, and Eq. (3.42) defines the state space coefficient.

$$\left[\frac{\beta_n\eta_p P_{k,m}}{(\eta_p^2-\beta_n^2)}\right] = \left(\frac{\pi}{2\omega_1}\right)^2 F_{n,l}^{14}. \tag{G.78}$$

Thus, the first integral can be written in terms of $F_{n,l}^{14}$ as the following.

$$\int_V (\nabla\times\boldsymbol{\Phi})\cdot\nabla\times\boldsymbol{\Psi}dV = 2\pi r_g^2 z_L \mu_R T\Delta I\Delta K\left(\frac{\pi}{2\omega_1}\right)^2 F_{n,l}^{14}. \tag{G.79}$$

The second term in the volume integral in Green's identity in Eq. (G.27) can be written as the following. The volume integral is given by the volume of the pie segment and the multiplier for the number of segments.

$$\int_V \boldsymbol{\Phi}\cdot\left[\nabla\times(\nabla\times\boldsymbol{\Psi})\right]dV = \frac{2\pi}{\phi_0}\int_{V_{pie}} A_{r,k,m,p}^M\cdot M_z^N\delta(\phi) + A_{\phi,k,m,p}^M\cdot M_z^N\delta(r-r_g) - A_{r,k,m,p}^M\cdot M_z^N\delta(\phi-\phi_0)\,dV \tag{G.80}$$

This expression does not directly resemble the integral solved in the magnetic model for $\mathbf{F}^{41}$. It can be converted into an integral just like Eq. (G.76) to show that equality is maintained, then that formula is used to get the equivalence between $\mathbf{F}^{41}$ and $\mathbf{F}^{14}$. The first step is to recognize that, by Stoke's theorem, an integral over the transverse area on the right is the same as an integration around the perimeter of the pie

shaped segment. Let the perimeter be called $L_{pie}$. After factoring out the magnetization term which depends only on *z* from the inner integral, the path integral can be written as the following.

$$\int_V \boldsymbol{\Phi} \cdot \left[ \nabla \times \left( \nabla \times \boldsymbol{\Psi} \right) \right] dV = \frac{2\pi}{\phi_0} \int_{z=0}^{z_L} M_z^N(z) \oint_{L_{pie}} \mathbf{A}_{k,m,p}^M \cdot d\mathbf{l} dz \tag{G.81}$$

Stoke's theorem allows the perimeter integral to be replaced by a surface integral.

$$\int_V \boldsymbol{\Phi} \cdot \left[ \nabla \times \left( \nabla \times \boldsymbol{\Psi} \right) \right] dV = -\frac{2\pi}{\phi_0} \int_{z=0}^{z_L} M_z^N(z) \int_{S_{pie}} \nabla \times \mathbf{A}_{k,m,p}^M \cdot \hat{e}_z dS dz \tag{G.82}$$

The equation can be made a volume integral again over the full rod volume.

$$\int_V \boldsymbol{\Phi} \cdot \left[ \nabla \times \left( \nabla \times \boldsymbol{\Psi} \right) \right] dV = -\int_{V_R} M_z^N \hat{e}_z \cdot \nabla \times \mathbf{A}_{k,m,p}^M dV \tag{G.83}$$

The definition of magnetic potential can be used to convert the potential term into a magnetic field term. After taking the dot product, the integral is exactly the same as the first term in the Green's identity from Eq. (G.75).

$$\begin{aligned} \int_V \boldsymbol{\Phi} \cdot \left[ \nabla \times \left( \nabla \times \boldsymbol{\Psi} \right) \right] dV &= -\int_{V_R} M_z^N \hat{e}_z \cdot \boldsymbol{\mu}_R \mathbf{H}_{k,m,p}^M dS \\ &= -\int_{V_R} \mu_R M_z^N H_{z,k,m,p}^M dS \end{aligned} \tag{G.84}$$

This is reassuring, but we still want to find a relationship between the coefficients for $\mathbf{F}^{41}$ and $\mathbf{F}^{14}$. The previous formula for this integral in Eq. (G.75) can be used again to find the relationship.

$$\int_V \mu_R H^M_{z,k,m,p} M^N_z dV = \int_{z=0}^{r_g}\int_{r=0}^{z_L}\int_{\phi=0}^{2\pi} \frac{\mu_R T \Delta I \jmath_{\gamma_m}\left(\frac{\varepsilon_{k,m} r}{r_g}\right)\sin(\gamma_m\phi)\sin\left(\frac{\eta_p z}{z_L}\right)}{N(\gamma_m)N(\varepsilon_{k,m},\gamma_m)N(\eta_p)} \cdot 2\Delta K \beta_n \cos\left(\frac{\beta_n z}{z_L}\right) r d\phi dr dz. \tag{G.85}$$

The terms can be rearranged and grouped so that they can be recognized as the terms in Appendix F and Chapter 4 used in the $\mathbf{F}^{41}$ and $\mathbf{F}^{14}$ calculations.

$$\int_V \mu_R H^M_{z,k,m,p} M^N_z dV = \frac{2\pi r_g^2 z_L \mu_R T \Delta I}{\phi_0 N(\gamma_m) N(\varepsilon_{k,m},\gamma_m) N(\eta_p)} \frac{\kappa_{eff,z}\kappa_{eff} T\Delta I}{\mu_R Y^H_{eff}} \cdot \int_{\rho=0}^{1} \jmath_{\gamma_m}(\varepsilon_{k,m}\rho)\rho d\rho \int_{\phi=0}^{\phi_0} \sin(\gamma_m\phi) d\phi \cdot 2\beta_n \int_{\xi=0}^{1} \sin(\eta_p\xi)\cos(\beta_n\xi) d\xi. \tag{G.86}$$

Equation (D.42) defines the term on the middle row as $\Gamma_{k,m}$.

$$\Gamma_{k,m} = \int_{\phi=0}^{\phi_0} \sin(\gamma_m\phi) d\phi \int_{\rho=0}^{1} \jmath_{\gamma_m}(\varepsilon_{k,m}\rho)\rho d\rho. \tag{G.87}$$

The integral in the bottom line of Eq. (G.86), $\int_{\xi=0}^{1} \sin(\eta_p\xi)\cos(\beta_n\xi) d\xi$ is the integral that is in common between the $\mathbf{F}^{41}$ and $\mathbf{F}^{14}$. Equation (D.43) gives the analytical solution.

$$2\beta_n \int_{\xi=0}^{1} \sin(\eta_p\xi)\cos(\beta_n\xi) d\xi = \frac{2\beta_n\eta_p}{(\eta_p^2 - \beta_n^2)}. \tag{G.88}$$

Equation (D.45) defines the coefficient

$$\Upsilon_{k,m,p,n} = \frac{\kappa_{eff,z} d_{33}}{\mu_R} \frac{2\beta_n\eta_p\Gamma_{k,m}}{(\eta_p^2 - \beta_n^2)}. \tag{G.89}$$

The identity in the magnetostrictive properties, $d_{33} = \frac{\kappa_{eff}}{Y_{eff}^{H}}$, can be used to eliminate $d_{33}$. Substituting Eqs. (G.87), (G.88) and (G.89) into Eq. (G.86) gives a formua in terms of the model parameters and the coefficient, $\Upsilon_{k,m,p,n}$.

$$\begin{aligned}\int_V \mu_R H_{z,k,m,p}^{M} M_z^{N} dV &= \frac{2\pi r_g^2 z_L \mu_R T^2 \Delta I^2}{\phi_0 N(\gamma_m) N(\varepsilon_{k,m}, \gamma_m) N(\eta_p)} \frac{\kappa_{eff,z} \kappa_{eff}}{\mu_R Y_{eff}^{H}} \Gamma_{k,m} \frac{2\beta_n \eta_p}{(\eta_p^2 - \beta_n^2)} \\ &= \frac{2\pi r_g^2 z_L \mu_R T^2 \Delta I^2}{\phi_0 N(\gamma_m) N(\varepsilon_{k,m}, \gamma_m) N(\eta_p)} \Upsilon_{k,m,p,n}.\end{aligned} \tag{G.90}$$

From the state space coefficient definitions for the magnetic model in Eq. (4.88), this gives:

$$\int_V \mu_R H_{z,k,m,p}^{M} M_z^{N} dV = -\frac{2\pi r_g^2 z_L \mu_R T^2 \Delta I^2}{\phi_0 N(\gamma_m) N(\varepsilon_{k,m}, \gamma_m) N(\eta_p)} F_{l,n}^{41}. \tag{G.91}$$

Equating (G.79) and (G.91) and canceling like terms gives:

$$\Delta K \left( \frac{\pi}{2\omega_1} \right)^2 F_{n,l}^{14} = -\frac{T \Delta I}{\phi_0 N(\gamma_m) N(\varepsilon_{k,m}, \gamma_m) N(\eta_p)} F_{l,n}^{41}. \tag{G.92}$$

This test gives an exact match to machine accuracy. This is expected since the formulation of the coefficient matrices are computed with analytical integrals that are exactly the same.

# APPENDIX H

# TIME STEPS AND TIME HORIZON

The appropriate time step and the time horizon are functions of the dynamics of the system being controlled and can be determined from scaling analysis. The values are estimated in this section.

The prediction horizon is the time in advance of the current time over which the control response is optimized. The full duration of the transient need not be included in the predictive horizon. The usual practice in predictive control is to estimate forward to a horizon at which the effect of the next control input could just barely be detected. The horizon recedes as the solution advances so that the MPC algorithm is always acting on the reference input over fixed time interval just ahead of the current time. The horizon is chosen based on the decay time of the problem. The time decay constants of the process are the real part of the complex eigenvalues of the process model. The time decay constants are a measure of how quickly energy that is added to the system through control inputs decays away. Setting the horizon too near into the future gives suboptimal performance since future effects are not sufficiently anticipated. Setting the horizon too far ahead offers no advantage to the control and increases the computational load unnecessarily. The horizon does not need to extend beyond some (small) multiple of the longest time decay constant of the problem. For the actuator, the decay constants of the vibration modes (the negative real part of the smallest complex eigenvalue) are the longest time constants. Evaluating the eigenvalues of the full model by MATLAB produces the value $-0.46\times10^{4}$.

$$\tau = \frac{1}{-\mathrm{Re}\left[\min(\mathbf{e})\right]} = \frac{1}{0.46\times 10^{4}} = 2.17\times 10^{-4}\, s\,. \tag{H.1}$$

In the simulations, the prediction horizon is chosen to be slightly longer to show the feedforward aspect of predictive control somewhat better. The value is set to be $\tau = 2.4\times 10^{-4}\, s$. This horizon gives about two full reflections of the anticipatory wave. The number of time steps in the prediction interval from *0* to $\tau$ is given by the following formula.

$$i_H = \frac{\tau}{T_s}. \tag{H.2}$$

The time step is chosen by the frequency of the highest vibration that we wish to model. An order of magnitude faster sampling than the highest frequency (in Hz) usually gives adequate resolution of the wave form. The goal of the research is to achieve a frequency response from the actuator on the order 10,000 Hz. A rule of thumb is to set the time step at least an order of magnitude less than the period of the target frequency. To give smooth plots in the time domain for the high frequency results, the time step is chosen to be a factor of 50 less than the reference period.

$$T_s = \frac{1}{50}\cdot\frac{1}{10000} = 2\times 10^{-6}\, s\,. \tag{H.3}$$

Combining the results of Eq. (H.1) and Eq. (H.3) determines the number of time steps needed in the prediction horizon.

$$i_H = \frac{\tau}{T_s} = \frac{2.4\times 10^{-4}}{2\times 10^{-6}} = 120\,\text{steps}\,. \tag{H.4}$$

# APPENDIX I

# REDUCED ORDER MODEL FOR REAL-TIME EXPERIMENT

Even though the number of modes in the low-order actuator model derived in Chapters 3 and 4 were chosen to be as low as feasible, the control algorithm given in Chapter 6 involves too many mathematical operations to complete the calculations within the minimum time step for the data sampling on the prototype system's control computer. Model reduction can be used to eliminate unnecessary fast states and reduce the computational time for the estimator and controls even further. The model reduction technique is a quasi-steady approximation in which the derivatives of fast states are set to zero and the fast states are solved as a set of algebraic equations rather than differential equations. The method and the theory of model reduction for vibrational systems is discussed in Gawronski [22]. The method in this appendix follows Gawronski's approach.

The method for model reduction first calculates the balanced realization of the model using MATLAB's *balreal* command. The balanced realization is a linearly transformed state space system in which the transformation ensures that the controllability and observability grammians are equal. The states in the MATLAB balanced realization are arranged from slowest to fastest. Once the balanced model is obtained, the MATLAB utility for model reduction, *modred*, can be used to eliminate fast states by retaining the lower numbered states in the balanced realization and replacing the higher numbered states with a quasi-steady approximation.

The following calculation illustrates the model reduction based on the MATLAB function description. The ordered balanced realization state space model can be subdivided into the slow part and the fast part.

$$\begin{aligned}\begin{bmatrix}\dot{\mathbf{x}}_S\\ \dot{\mathbf{x}}_F\end{bmatrix}&=\begin{bmatrix}\mathbf{A}_{SS} & \mathbf{A}_{SF}\\ \mathbf{A}_{FS} & \mathbf{A}_{FF}\end{bmatrix}\begin{bmatrix}\mathbf{x}_S\\ \mathbf{x}_F\end{bmatrix}+\begin{bmatrix}\mathbf{B}_S\\ \mathbf{B}_F\end{bmatrix}\mathbf{u},\\ \mathbf{y}&=\begin{bmatrix}\mathbf{C}_S & \mathbf{C}_F\end{bmatrix}\begin{bmatrix}\mathbf{x}_S\\ \mathbf{x}_F\end{bmatrix}+\mathbf{D}\mathbf{u},\end{aligned} \tag{I.1}$$

where $\dot{\mathbf{x}}_S$ and $\dot{\mathbf{x}}_F$ are the slow and fast states respectively. Setting $\dot{\mathbf{x}}_F = 0$ in the bottom row of the state equation in Eq. (I.1) and solving for $\mathbf{x}_F$ gives the following equation.

$$\mathbf{x}_F = \left(\mathbf{A}_{FF}\right)^{-1}\mathbf{A}_{FS}\mathbf{x}_S + \left(\mathbf{A}_{FF}\right)^{-1}\mathbf{B}_F\mathbf{u}\,. \tag{I.2}$$

Inserting this result into the state equation for $\mathbf{x}_F$ in Eq. (I.1) and regrouping the $\mathbf{x}_S$ and $\mathbf{u}$ terms gives

$$\begin{aligned}\dot{\mathbf{x}}_S &= \left[\mathbf{A}_{SS} - \mathbf{A}_{SF}\left(\mathbf{A}_{FF}\right)^{-1}\mathbf{A}_{FS}\right]\mathbf{x}_S + \left[\mathbf{B}_S - \mathbf{A}_{SF}\left(\mathbf{A}_{FF}\right)^{-1}\right]\mathbf{B}_F\mathbf{u},\\ \mathbf{y} &= \left[\mathbf{C}_S - \mathbf{C}_F\left(\mathbf{A}_{FF}\right)^{-1}\mathbf{A}_{FS}\right]\mathbf{x}_S + \mathbf{D}\mathbf{u},\end{aligned} \tag{I.3}$$

In general, the reduced order model can be expected to preserve the steady state of the original problem but raise the high frequency response. The high frequency is affected because the model reduction has the effect of moving the eigenvalues of the eliminated states to $-\infty$ and shifting the remaining state in the negative direction along the real axis.

The singular values from the balance realization of the low order version of the combined vibration, magnetic and coil circuit model are plotted in Figure I.1. Small singular values correspond to states that can be eliminated by model reduction.

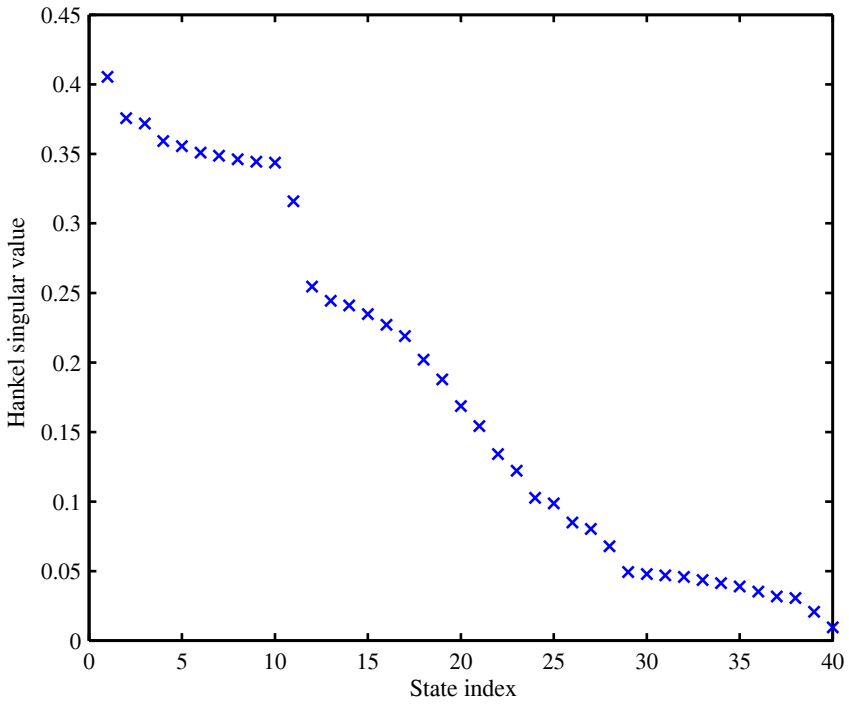


Figure I.1: Hankel Singular Values for Low Order Model

The reduction presents a problem because the singular values do not provide a distinct break point between large and small values. The only break occurs for values that are still too large to ignore. The number of states to retain is dictated by the size of the matrix calculation that can be successfully computed in the prototype system within the 70 μs time step.. Based on the singular values of the system and the available computation time, the model is reduced to the first twenty states. The effect of the reduction can be assessed by comparing the eigenvalues, and the time and frequency response of the full and reduced systems for open loop simulations. The eigenvalues for the original and reduced system models are shown in Figure I.2.

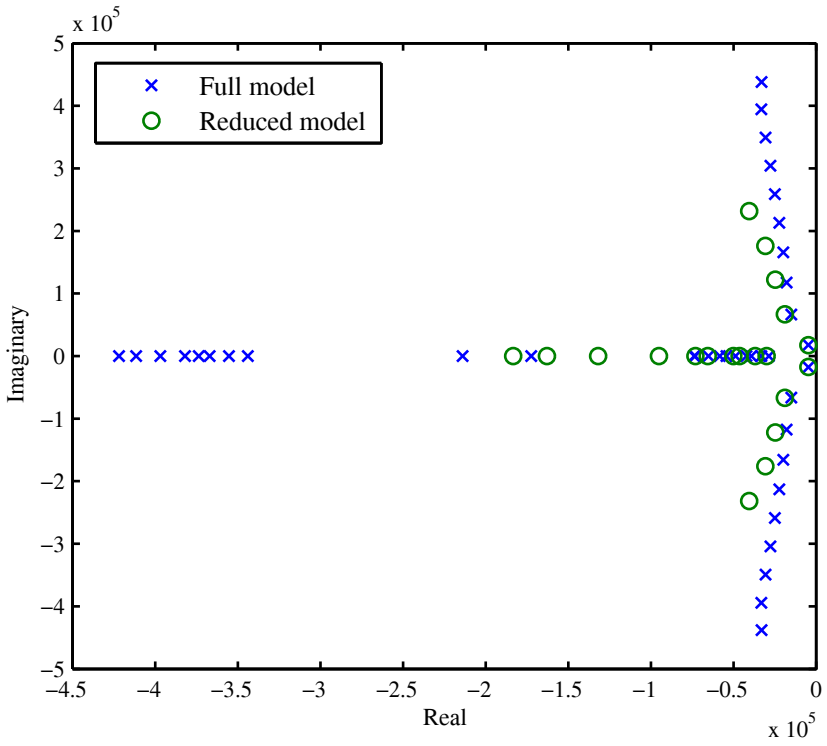


Figure I.2: Eigenvalues of full and reduced system models

The reduced system's eigenvalues have the expected shift to the left. The most important dynamic terms for the actuator are the vibration modes represented by the complex eigenvalues. The match between the full and reduced models appears satisfactory for these terms.

Open loop simulations of the reduced order system in the time and frequency domain are shown in Figure I.3 through Figure I.8. The full system model should be exactly the same as Figures 5.5, 5.6, and 5.7. The only difference between the two is that the results shown in this appendix have been balanced. The balance and original system should give the same results except for numerical deviations due to the improved numerical conditioning of the balanced model.

Figure I.3 and Figure I.4 give the response of displacement to steps in current demand. The step occurs at $t=0.7\times10^{-3}$ seconds. The plot corresponds to the Figure 5.5 in the main text.

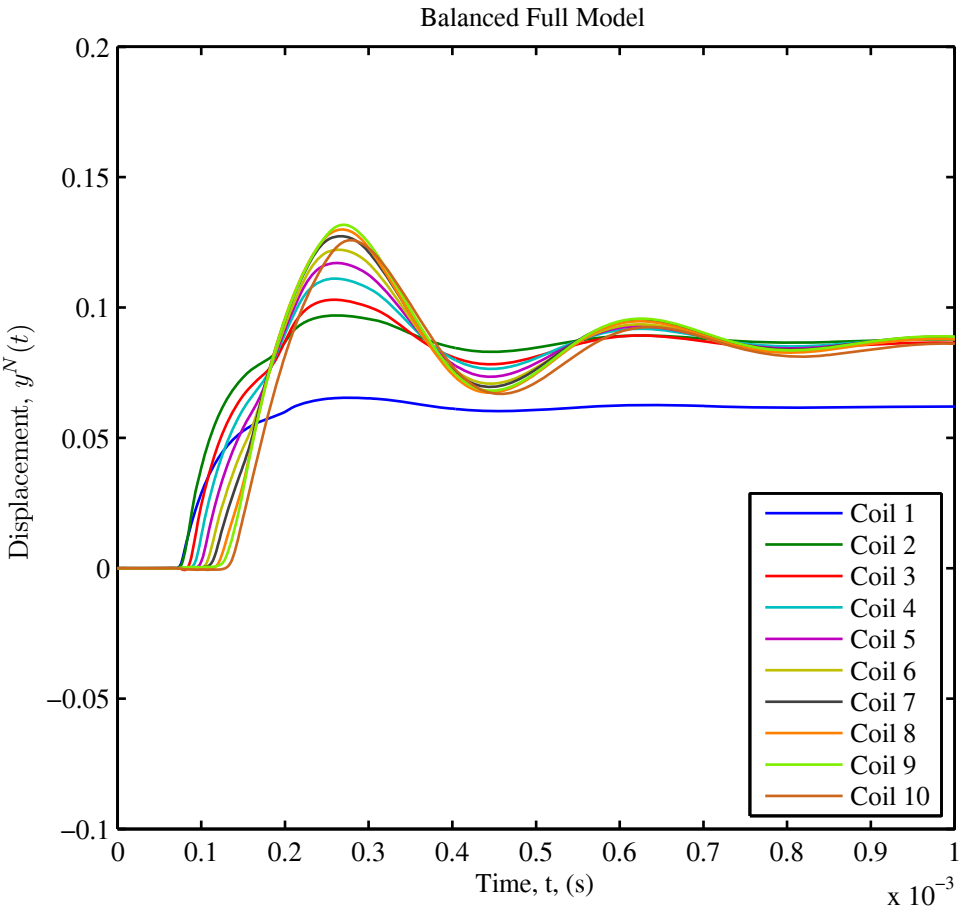


Figure I.3: Step response of displacement for balanced, full system

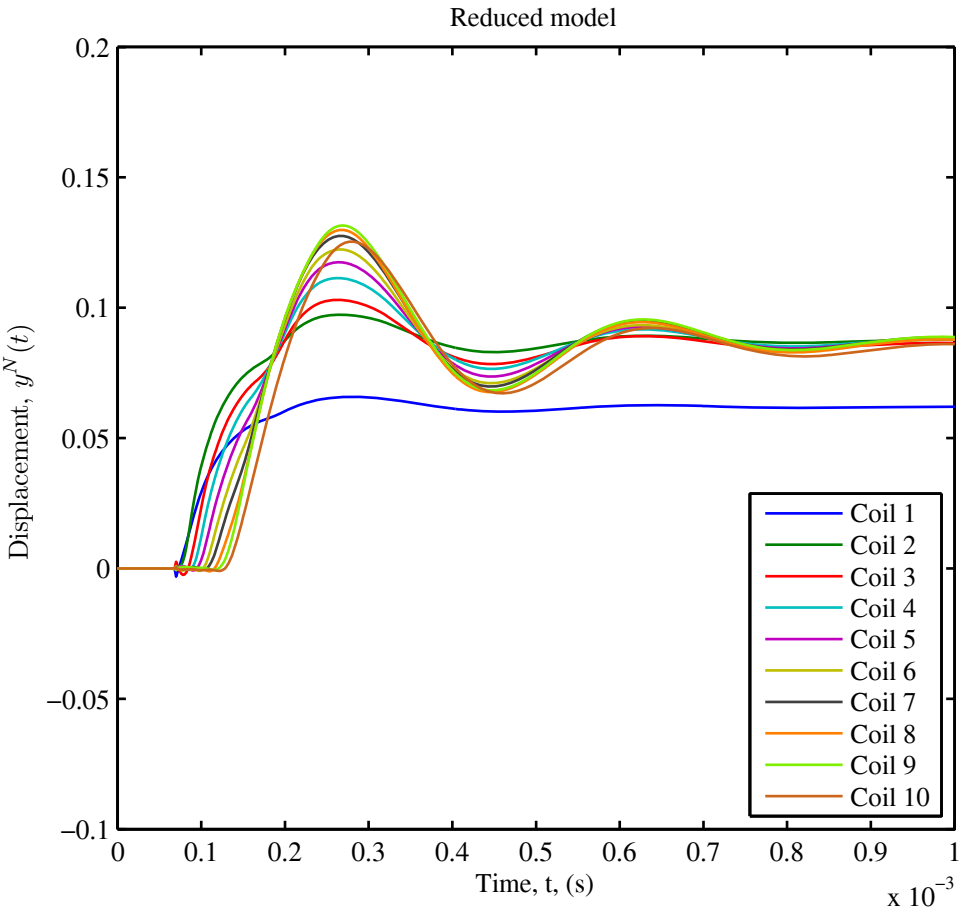


Figure I.4: Step response of displacement for reduced system

The differences between the displacement response for the full and reduced systems are not discernable. This is a good indication of that the reduction is satisfactory for the control application.

The response of all of the coil currents to a step change in the tenth coil for the balanced and then reduced models are shown in Figure I.5 and Figure K.7.

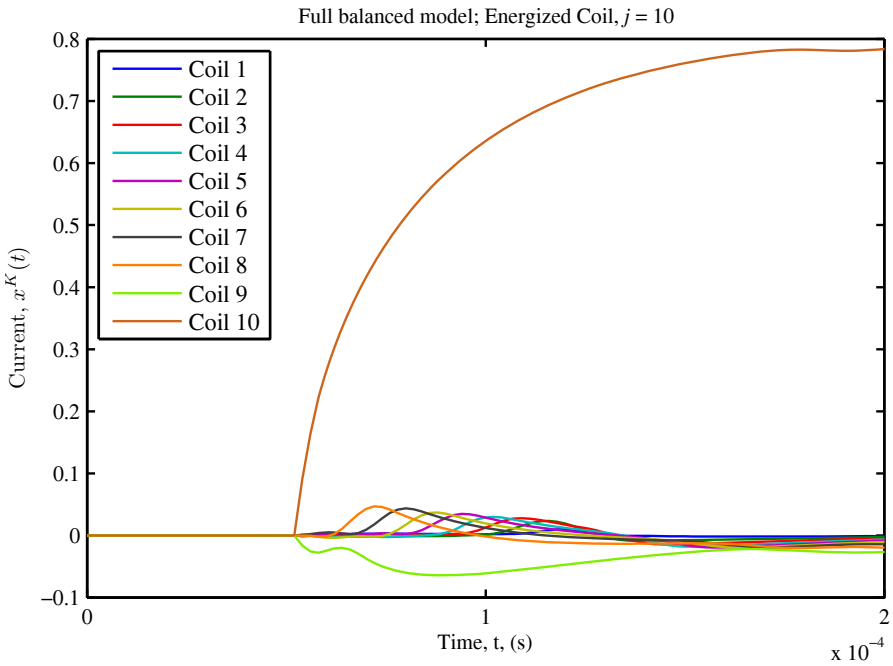


Figure I.5: Step response of coil current for full, balanced system

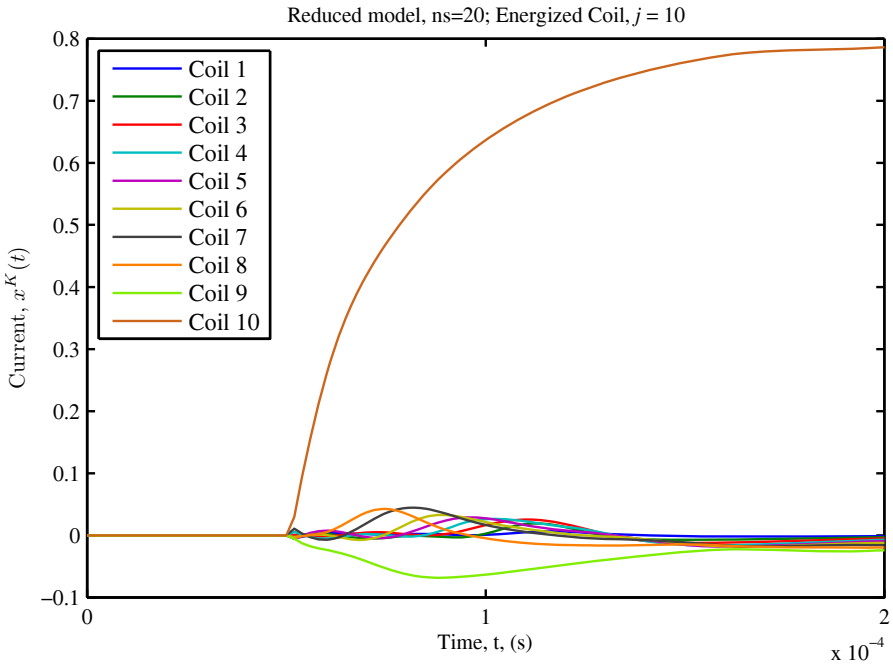


Figure I.6: Step response of coil current for reduced system

The response of the current in the energized coil, $j$=10, is essentially the same for the full and reduced models. The response of coil 9 gives a noticeably smaller bump in current as the acoustic wave passes through it. The responses other coils are very similar in shape and magnitude.

The final comparison is the frequency response of the displacement to each coil current demand. Figure I.7 and Figure I.8 give the two models. The frequency response covers the range of interest for the actuator, but does not extend to high enough frequency to show the point at which the reduced model's response diverges.

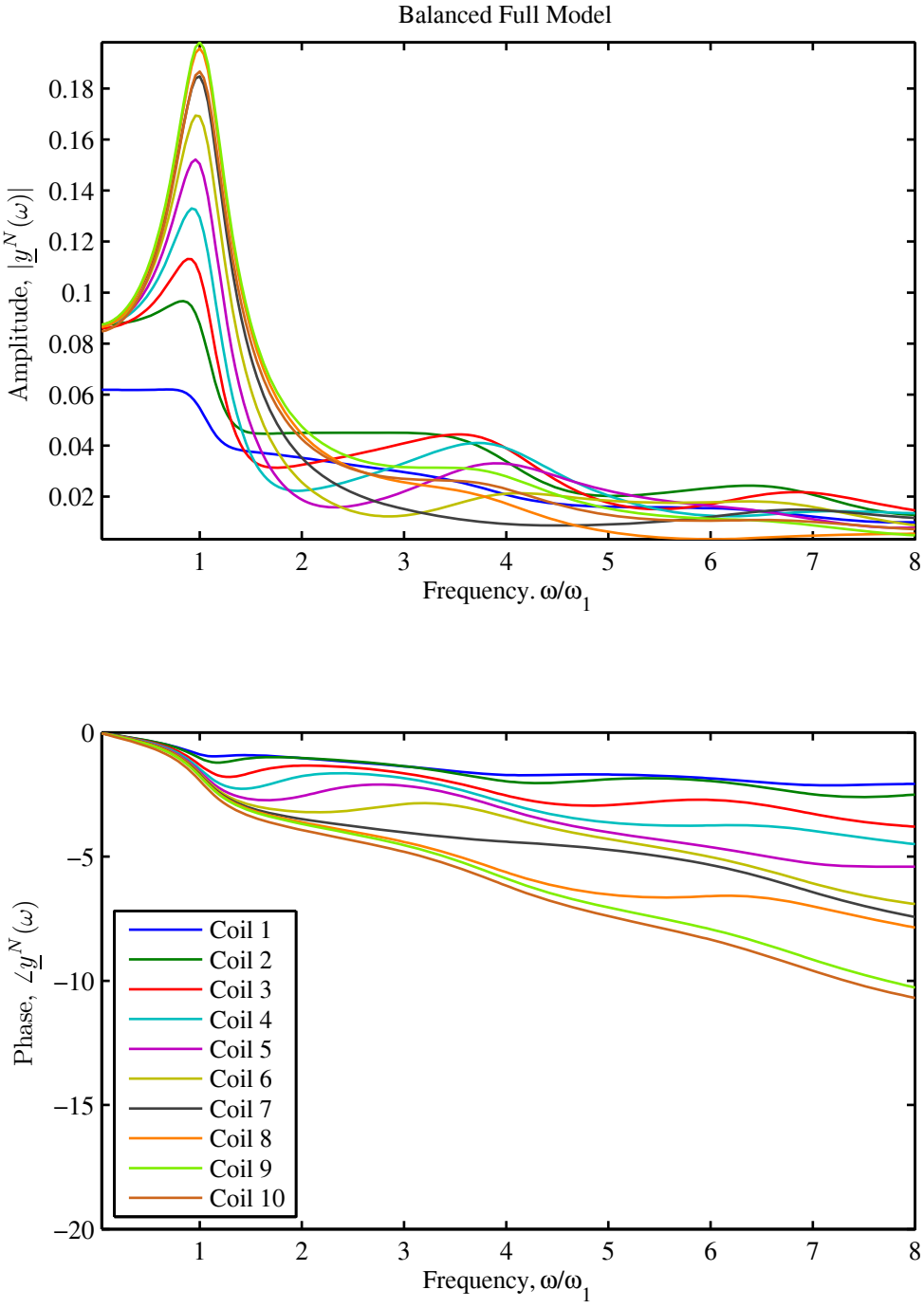


Figure I.7: Frequency response of displacement to current demand for full, balanced model

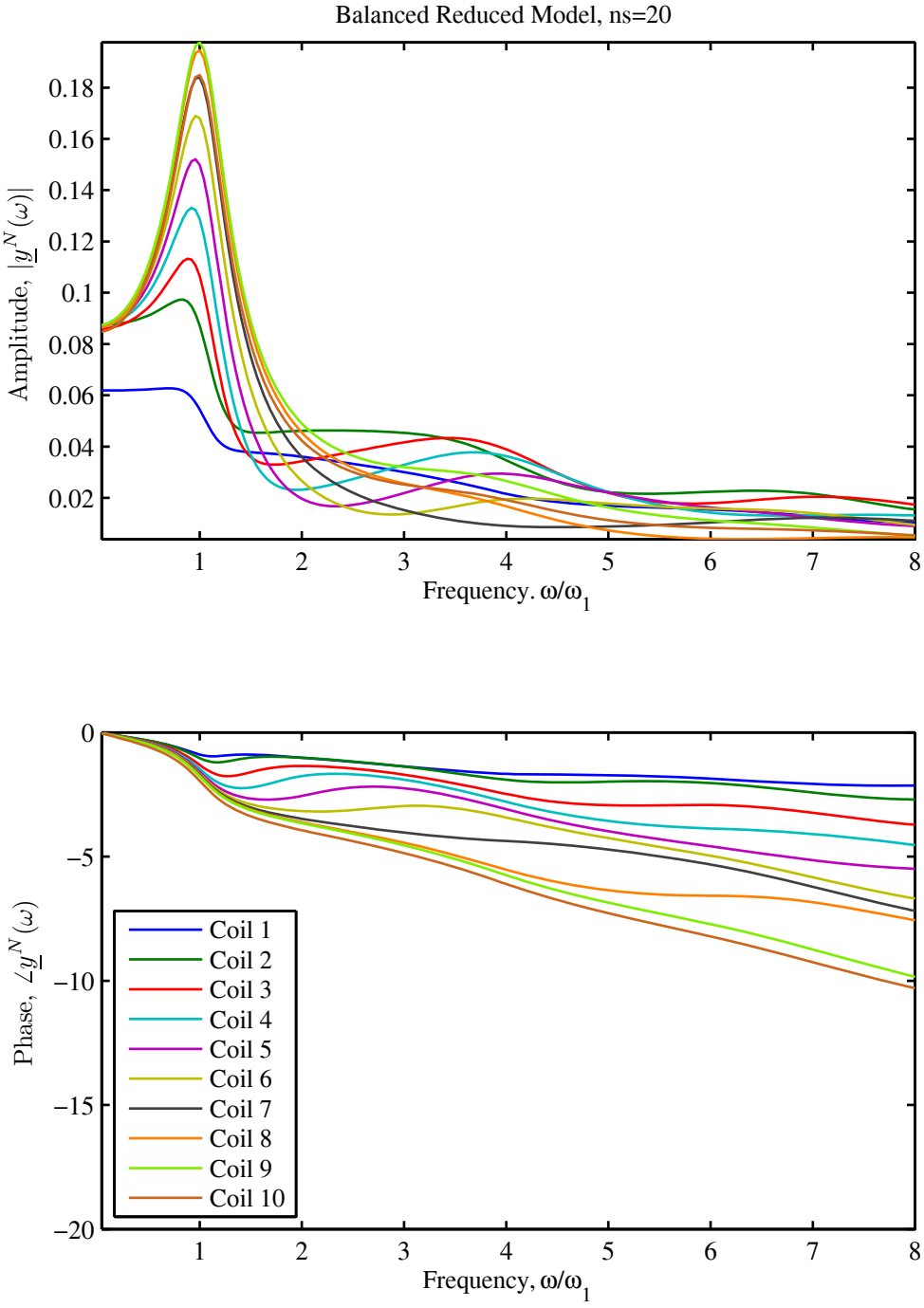


Figure I.8: Frequency response of displacement to current demand for reduced model

The overall shape of the open loop response is essentially identical between the full and reduced systems. The experimental system is operated with a much slower time step than the results in this section and Chapter 6. The slower time step results in even less effect from the mode reduction since the slower time step eliminates high frequency effects. On this basis, the development of the experimental system proceeds using the reduced system with twenty states.

# APPENDIX J

# STATE ESTIMATION AND TIME DELAY

The model predictive control law depends on the full state of the actuator at the start of the prediction interval. The experimental system cannot directly measure all the states nor can it measure them instantaneously at the current time. The time delay for a change in the control input to register with a corresponding change in the measured variables is observed experimentally to be two time steps. To compensate for the time delay, the actuator model can be used to simulate forward from the time of the measured data to the current time. This approach is a digital implementation of the Smith predictor [76].

The main purpose of this section is to document the equations and nomenclature that are used to represent the time delay with the estimation and prediction operations. We particularly want to show how the time index of the variables is used to represent measurement delay. The representation of time is handled through offsets in the time index of the variables.

A Kalman estimator is the most commonly used form of estimator and works well with predictive control. The Kalman estimator provides an optimal estimate of the system state. According to the separation principle, the MPC controller can be developed and tested using a full state feedback as if all states are measured. The estimator can be developed separately based on the state space model and the properties of the disturbance probability distribution.

The Kalman estimator problem assumes that Gaussian-distributed, random disturbances are added to the measurements and the process inputs. The optimal estimator then minimizes the difference between the actual plant state and the estimated state in the presence of the disturbances. The Kalman design produces a set of correction gains for the estimator. The Kalman estimator corrects the linear model of the plant using the error observed between the estimated values of measured variable and the actual measurements.

This section starts by restating the form of the Kalman estimator given by MATLAB documentation of the *kalman* command and gives the data and tuning choices that are needed to realize a particular Kalman estimator for the actuator. The estimator for the actuator model uses a standard MATLAB Control Toolbox routine for the Kalman estimator for discrete time systems, *kalmd*, to determine the feedback gain and innovations gain for the estimator for the model. The inputs to the calculations and discussion of the equations that are used for the estimator are given in this appendix.

The section also describes the method used to account for the time delay in the digital control experiment. Digital control systems inherently have some finite delay between the time at which a measurement is read by the digital control system and the time at which a response to that measurement is generated. The processing time consists of the time for analog to digital conversion of the measured variables, computation of the control outputs, and conversion of the control outputs from digital to analog. In the experimental control computer, these three steps are performed by separate boards in the computer. The inputs are read and converted from analog to digital values by a data acquisition board. The computations take place on the central processor of the

motherboard. Outputs are sent to a digital output board that converts the digital signals to analog and supplies a voltage signal to the amplifiers. The input, computation, and output operations form a pipeline of processing steps. Each board acts on a data value then passes the result along to the next module. The board then operates on the next value of data received. The boards operate in parallel but a data sample passes serially from one board to the next. Because the data passes through multiple devices, the total time delay for a data value to pass from input to output can be more than one time step of the control program. The system identification experiments on the actuator system indicate that the time delay for the control computer used in the experiment is two time steps ($t_{delay} = 2T_s = 140\times10^{-6}\ s$). Control stability is very sensitive to time delay. With the fairly long time step of the experimental system, an estimated time delay that is off by just one step can cause instability in the control response. The control program on the control computers is designed so that the number of steps in the delay is a parameter that can be easily changed. Experiments are conducted to verify that two time steps is the best choice for the time delay and to demonstrate stability. In reality, the number of time steps in the delay is a non-integer quantity. The implementation however approximates the delay as an integer number of time steps.

## Design of the Kalman Estimator

The most accurate way to calculate the Kalman estimator for discrete time systems involves a two step operation. However, one of the simplifications used to reduce the number of calculations in the real-time control system is to simplify the estimator to a single step. Both two step and single step estimation formulae are described in this appendix.

For the Kalman estimator, a distinction is made between the actual plant's state space model and the state space model used in the estimator. The matrices are denoted by adding a subscript *M* to the model system matrices and a *P* to the matrices representing the plant or actuator. The difference between the actual plant and the state space model could conceivably include all sources of error including unmodeled dynamics, parameter errors, and nonlinearity. In the numerical experiments that follow, different plant and model state space matrices are used to test the ability to the control system to handle linear modeling errors in the coefficient matrices and to test the effect using a reduced order model for the estimator while retaining the original, full-order plant model. The simulations include test cases in which the full-order plant model is coupled to the controller developed using the reduced order system matrices. Calibration errors in the measurements and noise in both measurements and process are programmed in the simulation cases for testing purposes.

For the purposes of the designing the estimator, the modeling equations can be written using the MATLAB notation with the time indices in parentheses rather than as subscripts as we have done in the main text. This choice of notation ties this development very closely to the source material in the MATLAB documentation.

$$\begin{aligned}\mathbf{x}(i+1) &= \mathbf{A}_M\mathbf{x}(i) + \mathbf{B}_M\mathbf{u}(i+1) + \mathbf{G}\mathbf{w}(i).\\ \mathbf{y}(i+1) &= \mathbf{C}_M\mathbf{x}(i+1) + \mathbf{D}_M\mathbf{u}(i+1) + \mathbf{H}\mathbf{w}(i+1) + \mathbf{v}(i+1).\end{aligned} \tag{J.1}$$

The coefficient matrices for the Kalman estimator are the model state matrices, $\mathbf{A}_M$, $\mathbf{B}_M$, $\mathbf{C}_M$, and $\mathbf{D}_M$, and the disturbance model matrices, **G** and **H**. The random disturbances, **w** and **v**, are zero-mean, Gaussian variables whose statistical properties are

defined by their covariance matrices. The covariance matrices of **w** and **v** are defined by the following expected values.

$$E\left[\mathbf{w}(i)\mathbf{w}^{\mathrm{T}}(i)\right]=\mathbf{Q};\ E\left[\mathbf{v}(i)\mathbf{v}^{\mathrm{T}}(i)\right]=\mathbf{R};\ E\left[\mathbf{w}(i)\mathbf{v}^{\mathrm{T}}(i)\right]=\mathbf{N}. \tag{J.2}$$

The estimator depends on a model of the disturbance which are indicated by the terms, $\mathbf{Gw}(i)$ and $\mathbf{Hw}(i+1)+\mathbf{v}(i+1)$ in Eq. (J.1). The noise covariance matrices and the matrices **G** and **H** form the input to the estimator design. The following assumptions for the disturbances varaiables are the commonly made in Kalman estimator design in the absence of better information.

$$\mathbf{G}=\mathbf{B}_{\mathbf{M}}. \tag{J.3}$$

$$\mathbf{H}=\mathbf{0}. \tag{J.4}$$

The noise covariance matrices are used as tuning parameters. The numerical values in matrices are reduced to a small number of scalar parameters to simplify the tuning process. The weight matrix for the control input disturbances, $\mathbf{R}_E$, is the identity matrix. The weight matrices for the measurements, $\mathbf{Q}_E$, consists is a diagonal with the same weight value for each current measurement and different value for the displacement measurement. The factor for the displacement measurement can be used to tune the estimator for displacement to track the measured displacement value more closely than the coil currents track their measurements. These choices reduce the number of tuning parameters to just two scalar parameters, $q_E$ and $f_D$.

$$\mathbf{R}_E=\mathbf{I}. \tag{J.5}$$

$$\mathbf{Q}_E=q_E^2\begin{bmatrix}\mathbf{I} & \mathbf{0}\\ \mathbf{0} & f_D\end{bmatrix}. \tag{J.6}$$

$$\mathbf{N} = \mathbf{0}\,. \tag{J.7}$$

Smaller values of the tuning parameters, $q_E$ and $f_D$, cause the estimator gains to be larger and cause the estimator to track the measured values more closely. The tuning parameters for the estimator are not critical. The following values for the estimator are used.

$$q_E^2 = 0.001\,. \tag{J.8}$$

$$f_D = 0.1\,. \tag{J.9}$$

The outputs for MATLAB's *kalmd* operator for the discrete time estimator are **L** which is the Kalman filter gain matrix and **M** which is the innovations gain matrix. Both gains are obtained from MATLAB by solving the discrete-time, algebraic Riccati equation.

The general form of the Kalman estimator with innovations is given in the MATLAB documentation by the following pair of equations.

$$\begin{aligned}\hat{\mathbf{x}}(i\,|\,i-1) = \mathbf{A}_\mathbf{M}\hat{\mathbf{x}}(i-1\,|\,i-2) + \mathbf{B}_\mathbf{M}\mathbf{u}\left(i-1\right)\\ +\mathbf{L}\left[\mathbf{y}_v\left(i-1\right) - \mathbf{C}_\mathbf{M}\hat{\mathbf{x}}(i-1\,|\,i-1) - \mathbf{D}_\mathbf{M}\mathbf{u}\left(i-1\right)\right].\end{aligned} \tag{J.10}$$

$$\begin{bmatrix}\hat{\mathbf{y}}\left(i\,|\,i\right)\\ \hat{\mathbf{x}}(i\,|\,i)\end{bmatrix} = \begin{bmatrix}\mathbf{C}_\mathbf{M}\left(\mathbf{I}-\mathbf{M}\mathbf{C}_\mathbf{M}\right)\\ \mathbf{I}-\mathbf{M}\mathbf{C}_\mathbf{M}\end{bmatrix}\hat{\mathbf{x}}(i\,|\,i-1) + \begin{bmatrix}\left(\mathbf{I}-\mathbf{C}_\mathbf{M}\mathbf{M}\right)\mathbf{D}_\mathbf{M} & \mathbf{C}_\mathbf{M}\mathbf{M}\\ \mathbf{M}\mathbf{D}_\mathbf{M} & \mathbf{M}\end{bmatrix}\begin{bmatrix}\mathbf{u}\left(i\right)\\ \mathbf{y}_v\left(i\right)\end{bmatrix}, \tag{J.11}$$

where $\mathbf{y}_v(i)$ is the vector of measured variables. The subscript, *v*, is added distinguish the measured variables with measurement error from their actual process variable counterparts. The Kalman estimates for the state variables and the measurements are indicated by the customary circumflex over the estimated variables. The estimation variable with two indices separated by a vertical bar is the customary notation for

estimator equations. The first index is the time index for the variable given. The second is the time index for the data on which the variable depends. The vertical bar suggests a conditional dependence. Hence, $\hat{\mathbf{x}}(i\,|\,i-1)$ is the estimate of $\hat{\mathbf{x}}$ at time $t_i$ using data up to $t_{i-1}$. Similarly, $\hat{\mathbf{x}}(i\,|\,i)$ is the current estimate based on the current data. Hence, the difference between the estimate in Eq. (J.10) and Eq. (J.11) is the time associated with measured variable and the control input. The first step, given by Eq. (J.10), is the predictor step. The second, in Eq. (J.11), is the corrector or innovations step. The first step depends on the measurements in the preceding time step. The innovations step uses the current time step data to correct the estimate with the most recent information.

The estimator can be written more compactly by combining the constant matrices.

$$\hat{\mathbf{x}}(i\,|\,i-1)=\mathbf{A}_E\hat{\mathbf{x}}(i-1\,|\,i-2)+\mathbf{B}_E\begin{bmatrix}\mathbf{u}(i-1)\\ \mathbf{y}_v(i-1)\end{bmatrix}; \tag{J.12}$$

$$\begin{bmatrix}\hat{\mathbf{y}}(i\,|\,i)\\ \hat{\mathbf{x}}(i\,|\,i)\end{bmatrix}=\mathbf{C}_E\hat{\mathbf{x}}(i\,|\,i-1)+\mathbf{D}_E\begin{bmatrix}\mathbf{u}(i)\\ \mathbf{y}_v(i)\end{bmatrix}, \tag{J.13}$$

where

$$\mathbf{A}_E=\mathbf{A}_M-\mathbf{L}\mathbf{C}_\mathbf{M};\;\; \mathbf{B}_E=\begin{bmatrix}\mathbf{B}_M-\mathbf{L}\mathbf{D}_\mathbf{M} & \mathbf{L}\end{bmatrix}; \tag{J.14}$$

$$\mathbf{C}_E=\begin{bmatrix}\mathbf{C}_\mathbf{M}\left(\mathbf{I}-\mathbf{M}\mathbf{C}_\mathbf{M}\right)\\ \mathbf{I}-\mathbf{M}\mathbf{C}_\mathbf{M}\end{bmatrix};\;\; \mathbf{D}_E=\begin{bmatrix}\left(\mathbf{I}-\mathbf{C}_\mathbf{M}\mathbf{M}\right)\mathbf{D}_\mathbf{M} & \mathbf{C}_\mathbf{M}\mathbf{M}\\ \mathbf{M}\mathbf{D}_\mathbf{M} & \mathbf{M}\end{bmatrix}. \tag{J.15}$$

Equations (J.12) and (J.13) are called the innovations form of the Kalman estimator. Normally, this form is used for estimation. However, the estimator is the part of the controls system calculation with the largest number of mathematical operations in the real time control system. To reduce the computational load, an approximate form requiring only one equation can also be used. The simpler calculation is less accurate

than the innovations form but requires fewer mathematical operations. The results for the simpler calculation are satisfactory for the actuator model. The single equation formula uses Eq. (J.12) but with the current data.

$$\hat{\mathbf{x}}(i\,|\,i) = \mathbf{A}_E \hat{\mathbf{x}}(i-1\,|\,i-1) + \mathbf{B}_E \begin{bmatrix} \mathbf{u}(i) \\ \mathbf{y}_v(i) \end{bmatrix}. \tag{J.16}$$

Numerical experiments using both forms of the estimator show little difference between them. The simpler form of Eq. (J.16) is used in the experimental system.

**Time Delay**

The equations and data given in Eqs. (J.1) through (J.9) define the estimator design. The next step is to show how the time delay is handled. The approach is simply to use the state space model to advance the Kalman estimated state from the delayed time at which the measurements are sampled to the current time. The discrete time model can be simulated forward using the estimated state as a starting value and the control inputs from the delay time to the current time that have already been calculated and sent to the actuator.

The main problem in the estimator design is to find a systematic numbering scheme which represents the time relationships clearly and accurately. The MPC design is a function of variables distributed in time both before and after the current time. The timing relationships are illustrated in Figure J.1. In the figure, $i_0$ is the current time, $i_0+1$ is the next time step at which the new control is to be calculated, $i_0-n_k$ is the time of the delayed measurements, and $i_0+i_H$ is the time of the prediction horizon. These points divide the time line into three regions. Each time interval is different with respect

to the variables that are known and those that are to be predicted. In the time interval before the measurement delay (prior to $i_0 - n_k$), the reference, **r**, controls inputs, **u**, and measurements, $\mathbf{y}_v$, are all known. In the interval from measurement delay to the current time, the reference and controls are known but measurements are not. The states are estimated in this interval. From the current time to the prediction horizon, the reference trajectory is the only variable known. The measurements and controls inputs are not known and must be predicted. The calculation of the MPC determines the control inputs over the entire prediction interval at each time step but only the control input for the next time step is actually used.

This section is concerned with advancing the Kalman estimate of the state at $i_0 - n_k$ to an estimate at the current time, $i_0$. In the numbering scheme in Figure J.1, the current measured data $y_v(i_0)$ are delayed with respect to the actual process variable $y(i_0)$ by $n_k$ time steps.

$$y_v(i_0) = y(i_0 - n_k). \tag{J.17}$$

Substituting in the time index, $i_0 - n_k$, into Eq. (J.16) and the current measured variable from Eq. (J.17) gives the Kalman estimate of the state using the most recent measurements. The value is the best Kalman estimate of the state but represents the plant from the $n_k$ steps earlier than the current state.

$$\hat{\mathbf{x}}(i_0 - n_k \mid i_0 - n_k) = \mathbf{A}_E \hat{\mathbf{x}}(i_0 - n_k - 1 \mid i_0 - n_k - 1) + \mathbf{B}_E \begin{bmatrix} \mathbf{u}(i_0 - n_k) \\ \mathbf{y}_v(i_0) \end{bmatrix}. \tag{J.18}$$

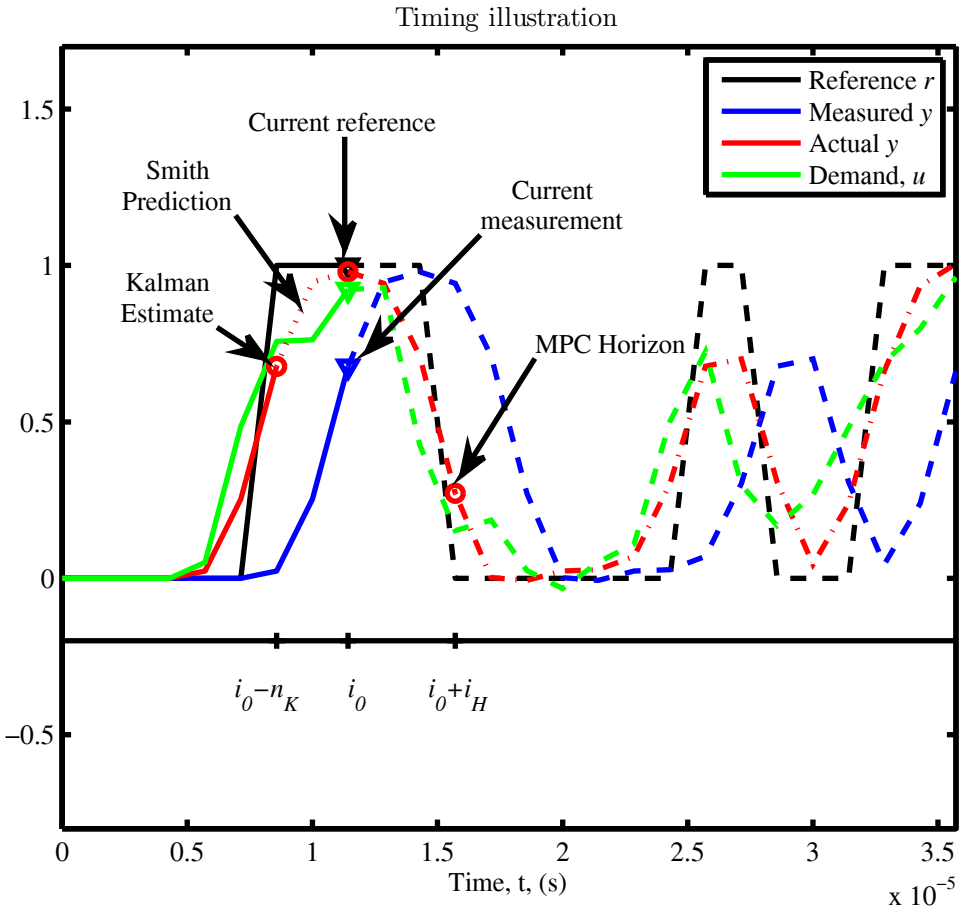


Figure J.1: Illustration of timing relationships in real-time control program

The estimated state in Eq. (J.18) at the delayed time, $i_0 - n_k$, can be advanced to $i_0$ using the control inputs from $\mathbf{u}(i_0 - n_k + 1)$ to $\mathbf{u}(i_0)$. The equations are the same as the prediction formula given in Eq. (6.40) except that the time delay, $n_k$ replaces the prediction horizon, $i_H$. The nomenclature using a double "^" is introduced to indicate an estimated and predicted variable.

$$\hat{\hat{\mathbf{x}}}(i_0 - n_k + 1 \,|\, i_0 - n_k) = \mathbf{A}_M \hat{\mathbf{x}}(i_0 - n_k \,|\, i_0 - n_k) + \mathbf{B}_M \mathbf{u}(i_0 - n_k + 1). \qquad \text{(J.19)}$$

$$\begin{aligned}\hat{\hat{\mathbf{x}}}(i-n_k+2\,|\,i_0-n_k) &= \mathbf{A}_M\hat{\hat{\mathbf{x}}}(i-n_k+1\,|\,i_0-n_k)+\mathbf{B}_M\mathbf{u}(i_0-n_k+2)\\ &= \mathbf{A}_M\left[\mathbf{A}_M\hat{\mathbf{x}}(i_0-n_k\,|\,i_0-n_k)+\mathbf{B}_M\mathbf{u}(i_0-n_k+1)\right]\\ &\quad +\mathbf{B}_M\mathbf{u}(i_0-n_k+2) \qquad \text{(J.20)}\\ &= \mathbf{A}_M^2\hat{\mathbf{x}}(i_0-n_k\,|\,i_0-n_k)+\mathbf{A}_M\mathbf{B}_M\mathbf{u}(i_0-n_k+1)\\ &\quad +\mathbf{B}_M\mathbf{u}(i_0-n_k+2).\end{aligned}$$

Following this pattern, the state at $i_0$ can be written as

$$\hat{\hat{\mathbf{x}}}(i_0\,|\,i_0-n_k)=\mathbf{A}_{\mathbf{M}}^{nk}\hat{\mathbf{x}}(i_0-n_k\,|\,i_0-n_k)+\sum_{i'=1}^{n_k}\mathbf{A}_{\mathbf{M}}^{nk-i'}\mathbf{B}_M\mathbf{u}(i-n_k+i')\,. \qquad \text{(J.21)}$$

Note that conditional time, $i_0-n_k$, indicates the time at which the measurement correction was made. Values after this time involve prediction.

To be compatible with the MPC nomenclature, Eq. (J.21) can be rewritten using the subscript notation for the time index. The conditional time variable, $_{i_0-n_k}$, can be dropped with the understanding that a predicted variable, indicated by the double "^" is conditional on the delayed measurement.

$$\hat{\hat{\mathbf{x}}}_{i_0}=\mathbf{A}_{\mathbf{M}}^{nk}\hat{\mathbf{x}}_{i_0-n_k}+\left[\mathbf{A}_{\mathbf{M}}^{nk-1}\mathbf{B}_M \quad \mathbf{A}_{\mathbf{M}}^{nk-2}\mathbf{B}_M \quad \cdots \quad \mathbf{B}_{\mathbf{M}}\right]\mathbf{u}_{i_0-n_k+1:i_0}\,. \qquad \text{(J.22)}$$

# APPENDIX K

# COMBINING THE KALMAN ESTIMATOR, SMITH PREDICTOR, AND PROPORTIONAL-INTEGRAL MPC

This appendix combines the reduced order model from 0, and the estimator and predictor equations from APPENDIX J and the proportional-integral control law from CHAPTER 6. The combined system constitutes the control algorithm for the actuator. The computations reduce to three matrix equations that can be programmed in C for the real-time control program. The main work is to rearrange the calculations to minimize the number of mathematical operations on the real-time computer.

Estimator equation, Eq. (J.16)

$$\hat{\mathbf{x}}_{i_0-n_k} = \mathbf{A}_E \hat{\mathbf{x}}_{i_0-n_k-1} + \mathbf{B}_E \begin{bmatrix} \mathbf{u}_{i_0-n_k} \\ \mathbf{y}_v(i) \end{bmatrix}. \tag{K.1}$$

Predictor equation, Eq. (J.22)

$$\hat{\hat{\mathbf{x}}}_{i_0} = \mathbf{A}_{\mathbf{M}}^{nk} \hat{\mathbf{x}}_{i_0-n_k} + \begin{bmatrix} \mathbf{A}_{\mathbf{M}}^{nk-1}\mathbf{B}_M & \mathbf{A}_{\mathbf{M}}^{nk-2}\mathbf{B}_M & \cdots & \mathbf{B}_{\mathbf{M}} \end{bmatrix} \mathbf{u}_{i_0-n_k+1:i_0}. \tag{K.2}$$

Proportional gain control law, Eq. (6.118)

$$\mathbf{u}_{i_0+1} = \mathbf{K}_{P+I} \begin{bmatrix} \mathbf{r}_{i_0+1:i_0+i_H} \\ \hat{\hat{\mathbf{x}}}_{i_0} \\ E_{i_0} \end{bmatrix}. \tag{K.3}$$

The only term that is not defined in the above equations is the integrated error. The running total equation from Eq. (6.106) could be implemented using predicted measurements as the following,

$$E_{i_0} = E_{i_0-1} + T_s\left(r_{i_0} - \hat{\hat{y}}_{i_0}\right). \tag{K.4}$$

but it is better to divide the integral into two parts, one part that depends only on the measured data and the second that depends on the predicted output over the delay interval. The advantage to the revised formula is that the predictive part of the integral is replaced every time step with updated predictions so that errors do not accumulate in the integral. This reduces the global error in the term. The derivation can begin by dividing the discrete form of the integral from Eq. (6.105) into two parts.

$$E_{i_0} = T_s\sum_{i'=0}^{i_0}\left(\mathbf{r}_{i'} - \mathbf{y}_{i'}\right). \tag{K.5}$$

$$E_{i_0} = T_s\sum_{i'=0}^{i_0-n_k}\left(\mathbf{r}_{i'} - \mathbf{y}_{v,i'+n_k}\right) + T_s\sum_{i'=i_0-n_k+1}^{i_0}\left(\mathbf{r}_{i'} - \hat{\hat{\mathbf{y}}}_{i'}\right). \tag{K.6}$$

The first term can be called, $E_{i_0-n_k}$, and can be implemented as a running total. Notice that $E_{i_0-n_k}$ does not have a "^" indicating the variable does not depend on any estimated values.

$$E_{i_0-n_k} = T_s\sum_{i'=0}^{i_0-n_k}\left(\mathbf{r}_{i'} - \mathbf{y}_{v,i'+n_k}\right) = E_{i_0-n_k-1} + T_s\left(r_{i_0-n_k} - \mathbf{y}_{v,i_0}\right). \tag{K.7}$$

The second part is calculated by substituting in the prediction formula for the output. The prediction algorithm uses the Kalman estimation of the state at $i_0 - n_k$ and the control inputs over the delay time to compute a predicted difference. This integral

depends on control inputs, $\mathbf{u}_{i_0-n_k+1:i_0}$, that have already been computed and are in the pipeline to the actuator but whose effects are not yet measured by the sensors. The equation sums the estimated values of the control error to obtain this part of the integral term. The summation operation is equivalent to a multiplication by a row vector of ones. The constant matrices can be grouped together to simplify the notation and show that the integral can be represented as a matrix multiplication operation.

$$T_s \sum_{i'=i_0-n_k+1}^{i_0} \left(\mathbf{r}_{i'} - \mathbf{y}_{i'}\right) = T_s \begin{bmatrix} 1 & 1 & \cdots & 1 \end{bmatrix} \left\{ \mathbf{r}_{i_0-n_k+1:i_0} - \begin{bmatrix} \mathbf{CA} \\ \mathbf{CA}^2 \\ \vdots \\ \mathbf{CA}^{n_k} \end{bmatrix} \hat{\mathbf{x}}_{i_0-n_k} \right.$$
$$\left. - \begin{bmatrix} \mathbf{CB}+\mathbf{D} & \mathbf{0} & \cdots & \mathbf{0} \\ \mathbf{CAB} & \mathbf{CB}+\mathbf{D} & \mathbf{0} & \vdots \\ \vdots & & \ddots & \mathbf{0} \\ \mathbf{CA}^{n_k-1}\mathbf{B} & \cdots & \mathbf{CAB} & \mathbf{CB}+\mathbf{D} \end{bmatrix} \mathbf{u}_{i_0-n_k+1:i_0} \right\}, \qquad \text{(K.8)}$$
$$= \mathbf{S}_r \mathbf{r}_{i_0-n_k+1:i_0} - \mathbf{S}_{\hat{x}} \hat{\mathbf{x}}_{i_0-n_k} - \mathbf{S}_u \mathbf{u}_{i_0-n_k+1:i_0},$$

where

$$\mathbf{S}_r = T_s \begin{bmatrix} 1 & 1 & \cdots & 1 \end{bmatrix}; \qquad \text{(K.9)}$$

$$\mathbf{S}_{\hat{x}} = T_s \begin{bmatrix} 1 & 1 & \cdots & 1 \end{bmatrix} \begin{bmatrix} \mathbf{CA} \\ \mathbf{CA}^2 \\ \vdots \\ \mathbf{CA}^{n_k} \end{bmatrix}; \qquad \text{(K.10)}$$

$$\mathbf{S}_u = T_s \begin{bmatrix} 1 & 1 & \cdots & 1 \end{bmatrix} \begin{bmatrix} \mathbf{CB}+\mathbf{D} & \mathbf{0} & \cdots & \mathbf{0} \\ \mathbf{CAB} & \mathbf{CB}+\mathbf{D} & \mathbf{0} & \vdots \\ \vdots & & \ddots & \mathbf{0} \\ \mathbf{CA}^{n_k-1}\mathbf{B} & \cdots & \mathbf{CAB} & \mathbf{CB}+\mathbf{D} \end{bmatrix}. \qquad \text{(K.11)}$$

Combining Eq. (K.7) and (K.8) gives the estimated value of the integral error at the current time.

$$\hat{\hat{E}}_{i_0} = E_{i_0-n_k} + \mathbf{S}_r \mathbf{r}_{i_0-n_k+1:i_0} - \mathbf{S}_{\hat{x}} \hat{\mathbf{x}}_{i_0-n_k} - \mathbf{S}_u \mathbf{u}_{i_0-n_k+1:i_0} . \tag{K.12}$$

The control law in Eq (K.3) can now be evaluated by including Eq. (K.7) and (K.12) in the control algorithm. However, the number of computations in the real time control program can be reduced by combining equations. First the $\mathbf{K}_{P+I}$ matrix is broken into three parts.

$$\mathbf{u}_{i_0+1} = \mathbf{K}_{P+I} \begin{bmatrix} \mathbf{r}_{i_0+1:i_0+i_H} \\ \hat{\hat{\mathbf{x}}}_{i_0} \\ E_{i_0} \end{bmatrix} = \begin{bmatrix} \mathbf{K}_r & \mathbf{K}_x & \mathbf{K}_E \end{bmatrix} \begin{bmatrix} \mathbf{r}_{i_0+1:i_0+i_H} \\ \hat{\hat{\mathbf{x}}}_{i_0} \\ E_{i_0} \end{bmatrix} . \tag{K.13}$$

Next, substitute in the definitions of the $\hat{\hat{\mathbf{x}}}_{i_0}$ and $E_{i_0}$.

$$\mathbf{u}_{i_0+1} = \begin{bmatrix} \mathbf{K}_r & \mathbf{K}_x & \mathbf{K}_E \end{bmatrix} \begin{bmatrix} \mathbf{r}_{i_0+1:i_0+i_H} \\ \mathbf{A}_{\mathbf{M}}^{nk} \hat{\mathbf{x}}_{i_0-n_k} + \begin{bmatrix} \mathbf{A}_{\mathbf{M}}^{nk-1}\mathbf{B}_M & \mathbf{A}_{\mathbf{M}}^{nk-2}\mathbf{B}_M & \cdots & \mathbf{B}_M \end{bmatrix} \mathbf{u}_{i_0-n_k+1:i_0} \\ E_{i_0-n_k} + \mathbf{S}_r \mathbf{r}_{i_0-n_k+1:i_0} - \mathbf{S}_{\hat{x}} \hat{\mathbf{x}}_{i_0-n_k} - \mathbf{S}_u \mathbf{u}_{i_0-n_k+1:i_0} \end{bmatrix} . \tag{K.14}$$

To solve the equation for a compact form, multiply the matrices and regroup terms.

$$\begin{aligned}
\mathbf{u}_{i_0+1} &= \mathbf{K}_r \mathbf{r}_{i_0+1:i_0+i_H} + \mathbf{K}_x \mathbf{A}_{\mathbf{M}}^{nk} \hat{\mathbf{x}}_{i_0-n_k} + \mathbf{K}_x \begin{bmatrix} \mathbf{A}_{\mathbf{M}}^{nk-1}\mathbf{B}_M & \mathbf{A}_{\mathbf{M}}^{nk-2}\mathbf{B}_M & \cdots & \mathbf{B}_M \end{bmatrix} \mathbf{u}_{i_0-n_k+1:i_0} \\
&\quad + \mathbf{K}_E E_{i_0-n_k} + \mathbf{K}_E \mathbf{S}_r \mathbf{r}_{i_0-n_k+1:i_0} - \mathbf{K}_E \mathbf{S}_{\hat{x}} \hat{\mathbf{x}}_{i_0-n_k} - \mathbf{K}_E \mathbf{S}_u \mathbf{u}_{i_0-n_k+1:i_0} , \\
&= \left( \mathbf{K}_r \mathbf{r}_{i_0+1:i_0+i_H} + \mathbf{K}_E \mathbf{S}_r \mathbf{r}_{i_0-n_k+1:i_0} \right) + \left( \mathbf{K}_x \mathbf{A}_{\mathbf{M}}^{nk} - \mathbf{K}_E \mathbf{S}_{\hat{x}} \right) \hat{\mathbf{x}}_{i_0-n_k} \\
&\quad + \left( \mathbf{K}_x \begin{bmatrix} \mathbf{A}_{\mathbf{M}}^{nk-1}\mathbf{B}_M & \mathbf{A}_{\mathbf{M}}^{nk-2}\mathbf{B}_M & \cdots & \mathbf{B}_M \end{bmatrix} - \mathbf{K}_E \mathbf{S}_u \right) \mathbf{u}_{i_0-n_k+1:i_0} + \mathbf{K}_E E_{i_0-n_k} , \\
&= \begin{bmatrix} \mathbf{K}_E \mathbf{S}_r & \mathbf{K}_r \end{bmatrix} \begin{bmatrix} \mathbf{r}_{i_0-n_k+1:i_0} \\ \mathbf{r}_{i_0+1:i_0+i_H} \end{bmatrix} + \left( \mathbf{K}_x \mathbf{A}_{\mathbf{M}}^{nk} - \mathbf{K}_E \mathbf{S}_{\hat{x}} \right) \hat{\mathbf{x}}_{i_0-n_k} \\
&\quad + \left( \mathbf{K}_x \begin{bmatrix} \mathbf{A}_{\mathbf{M}}^{nk-1}\mathbf{B}_M & \mathbf{A}_{\mathbf{M}}^{nk-2}\mathbf{B}_M & \cdots & \mathbf{B}_M \end{bmatrix} - \mathbf{K}_E \mathbf{S}_u \right) \mathbf{u}_{i_0-n_k+1:i_0} + \mathbf{K}_E E_{i_0-n_k} , \\
&= \begin{bmatrix} \mathbf{K}_E \mathbf{S}_r & \mathbf{K}_r \end{bmatrix} \mathbf{r}_{i_0-n_k+1:i_0+i_H} + \left( \mathbf{K}_x \mathbf{A}_{\mathbf{M}}^{nk} - \mathbf{K}_E \mathbf{S}_{\hat{x}} \right) \hat{\mathbf{x}}_{i_0-n_k} \\
&\quad + \left( \mathbf{K}_x \begin{bmatrix} \mathbf{A}_{\mathbf{M}}^{nk-1}\mathbf{B}_M & \mathbf{A}_{\mathbf{M}}^{nk-2}\mathbf{B}_M & \cdots & \mathbf{B}_M \end{bmatrix} - \mathbf{K}_E \mathbf{S}_u \right) \mathbf{u}_{i_0-n_k+1:i_0} + \mathbf{K}_E E_{i_0-n_k} .
\end{aligned} \tag{K.15}$$

For convenience, the following matrices are defined.

$$\tilde{\mathbf{K}}_r = \begin{bmatrix} \mathbf{K}_E \mathbf{S}_r & \mathbf{K}_r \end{bmatrix}; \tag{K.16}$$

$$\tilde{\mathbf{K}}_{\hat{x}} = \mathbf{K}_x \mathbf{A}_{\mathbf{M}}^{nk} - \mathbf{K}_E \mathbf{S}_{\hat{x}}; \tag{K.17}$$

$$\tilde{\mathbf{K}}_u = \mathbf{K}_x \begin{bmatrix} \mathbf{A}_{\mathbf{M}}^{nk-1} \mathbf{B}_M & \mathbf{A}_{\mathbf{M}}^{nk-2} \mathbf{B}_M & \cdots & \mathbf{B}_M \end{bmatrix} - \mathbf{K}_E \mathbf{S}_u. \tag{K.18}$$

The matrix multiplication can be reassembled in the following form.

$$\begin{aligned} \mathbf{u}_{i_0+1} &= \begin{bmatrix} \tilde{\mathbf{K}}_r & \tilde{\mathbf{K}}_{\hat{x}} & \tilde{\mathbf{K}}_u & \mathbf{K}_E \end{bmatrix} \begin{bmatrix} \mathbf{r}_{i_0+1:i_0+i_H} \\ \hat{\mathbf{x}}_{i_0-n_k} \\ \mathbf{u}_{i_0-n_k+1:i_0} \\ E_{i_0-n_k} \end{bmatrix}, \\ &= \tilde{\mathbf{K}}_{P+I} \begin{bmatrix} \mathbf{r}_{i_0+1:i_0+i_H} \\ \hat{\mathbf{x}}_{i_0-n_k} \\ \mathbf{u}_{i_0-n_k+1:i_0} \\ E_{i_0-n_k} \end{bmatrix}, \end{aligned} \tag{K.19}$$

where

$$\tilde{\mathbf{K}}_{P+I} = \begin{bmatrix} \tilde{\mathbf{K}}_r & \tilde{\mathbf{K}}_{\hat{x}} & \tilde{\mathbf{K}}_u & \mathbf{K}_E \end{bmatrix}. \tag{K.20}$$

This matrix equation combines the predictor model into the control law reducing the number of equations to be evaluated. This single matrix operation is a constant gain control law that evaluates the next set of control inputs given all the known time-dependent variables of the system. The $\tilde{\mathbf{K}}_{P+I}$ matrix in Eq. (6.118) can be evaluated for the state space model of the actuator using the equations given in this section. The response is tuned by the selection of cost function weighting factors. In the simulated results presented in this section, the same weighting factors that are used in CHAPTER 6 are also with the estimator and predictor control algorithm, $q_P = 1000$ and $q_I = 10,000$.

The control algorithm reduces to the following three equations. These equations are programmed in an iterative loop to evaluate the control input for the real actuator or the simulation of the actuator.

$$\hat{\mathbf{x}}_{i_0-n_k} = \mathbf{A}_E \hat{\mathbf{x}}_{i_0-n_k-1} + \mathbf{B}_E \begin{bmatrix} \mathbf{u}_{i_0-n_k} \\ \mathbf{y}_v(i) \end{bmatrix}; \tag{K.21}$$

$$E_{i_0-n_k} = E_{i_0-n_k-1} + T_s \left( r_{i_0-n_k} - \mathbf{y}_{v,i_0} \right); \tag{K.22}$$

$$\mathbf{u}_{i_0+1} = \tilde{\mathbf{K}}_{P+I} \begin{bmatrix} \mathbf{r}_{i_0+1:i_0+i_H} \\ \hat{\mathbf{x}}_{i_0-n_k} \\ \mathbf{u}_{i_0-n_k+1:i_0} \\ E_{i_0-n_k} \end{bmatrix}. \tag{K.23}$$

**Simulated Results using the Reduced order Predictor and Proportional-Integral MPC.**

In this section, simulated results are given for a system model which combines the MPCs with the Kalman estimator and Smith predictor. The control algorithm is applied to the low-order plant model with forty state variable described in Chapter 5. These simulations are used to test the model reduction and time delay features, to tune the control algorithm for best results using the time step of experimental system, and to predict results for the experiment.

This appendix applies the modifications in series of comparative runs so that the effect of model reduction, time step, and tuning can be seen individually. The simulated results verify the model reduction and time delay algorithms in a calculation in which the internal variables from the simulated plant are available for comparison. The closed loop model is simulated with the controls based on reduced model and compared with

simulations in which the full model is used for the control design. The model reduction is only applied to the model used for control. The plant model in both cases is the full model (full model in this section refers to the low order model from Chapter 5 in which vibration , magnetics, and coil current are represented with 40 states and best estimate parameters for the prototype system). The estimated and predicted states can be compared with their actual counterparts in the simulation model. Various combinations of results from the full and reduced system controls can be used to test the prediction, delay, and model reduction parts of the algorithm individually. The comparisons of those variables test the implementation of the estimation and time delay equations from APPENDIX K. Comparing the controls from the full and reduced system tests the approximation of model reduction on the control design.

The effect of time step size is also considered. The fastest time step that can be achieved with the experimental system is considerably slower than the time step estimated in APPENDIX H for demonstrating the advantage of the multi-coil actuation. The simulations in this section are performed at the both the fast time step needed for advantageous performance and the slower time step for the experiment. The fast time step allows the results with estimator and predictor to be compared to the results from the main text using a fast time step in which just MPC is applied without estimator and predictor. The model is programmed with time step as a parameter so that the fast and slow time step cases are exactly the same except for the time step. Because of the time step limitation of the experiment, we cannot prove the success of the actuator design performance experimentally. The goal of the experimental results is to confirm the model and theory at the available speed with the argument that, if scaled up in speed, the

predicted benefit of the multi-coil actuator would hold. The comparison of fast and slow time step results show how much the advantage of the multi-coil actuator is diminished by the time step.

The slow time step simulations are also used to tune the control algorithms for control and estimation to give the best tuning at the experimental system the time step. In general, the feedback gain must be reduced as time step increases to maintain a well-damped, smooth control response. To reduce the feedback gain of the model predictive control, the weight applied to the control error must be reduced. The weight adjustments are made by trial and error using the simulation to provide appropriate settings for gains for the experimental system. The advantages of the multi-coil design are diminished both by the time step itself and by the de-tuning of the control speed to maintain good control response.

Figure K.1 shows the reference trajectory tracking for a step change using the fast time step, ($T_s = 2\times10^{-6}$ s). The "step" is actually a fast ramp transient. The duration of the ramp is set equal to the time step of the prototype system, ($T_s = 70\times10^{-6}$ s). The plotted displacement variable is the "measured result" which includes the time delay of the experimental system, measurement delay, $\left(T_{delay} = 140\times10^{-6}\, s\right)$. The results for both the full system and model reduction are shown on the same plot. The lines track very closely which shows that the effect of model reduction on the fidelity of the results is negligible. Estimated and actual state variables are not shown in the plots, but results give indistinguishable lines. The full system and reduced system displacement lie on top of each other so that only the reduced system displacement is visible.

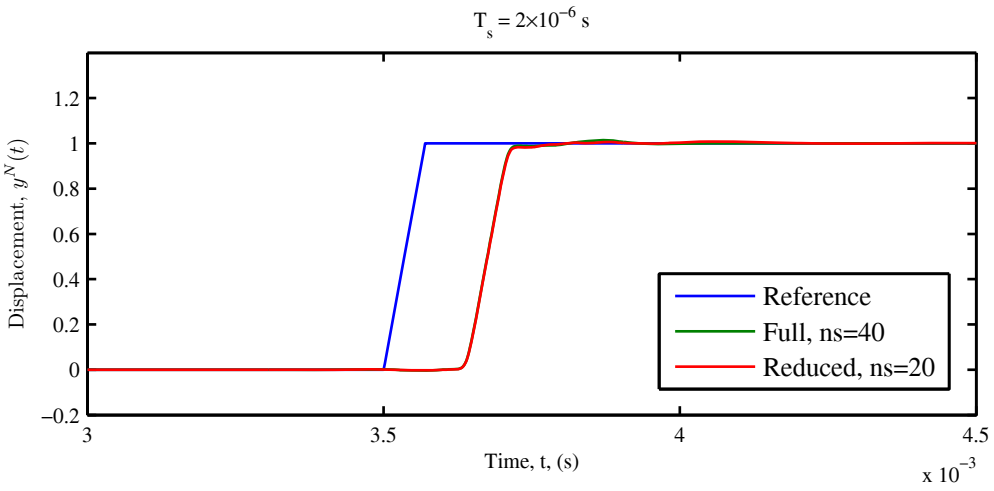


Figure K.1: Reference trajectory tracking for full system (*ns*=40) and reduced system (*ns*=20) for the fast time step, $\left(T_s = 2\times10^{-6}\ s\right)$.

Figure K.2 shows the current demands for the same transient with a comparison of the full system and reduced system. Each demand for the reduced system is shown as a dashed line of the same color as the corresponding full system demand. The lines are distinct but the reduced system is clearly an acceptable approximation.

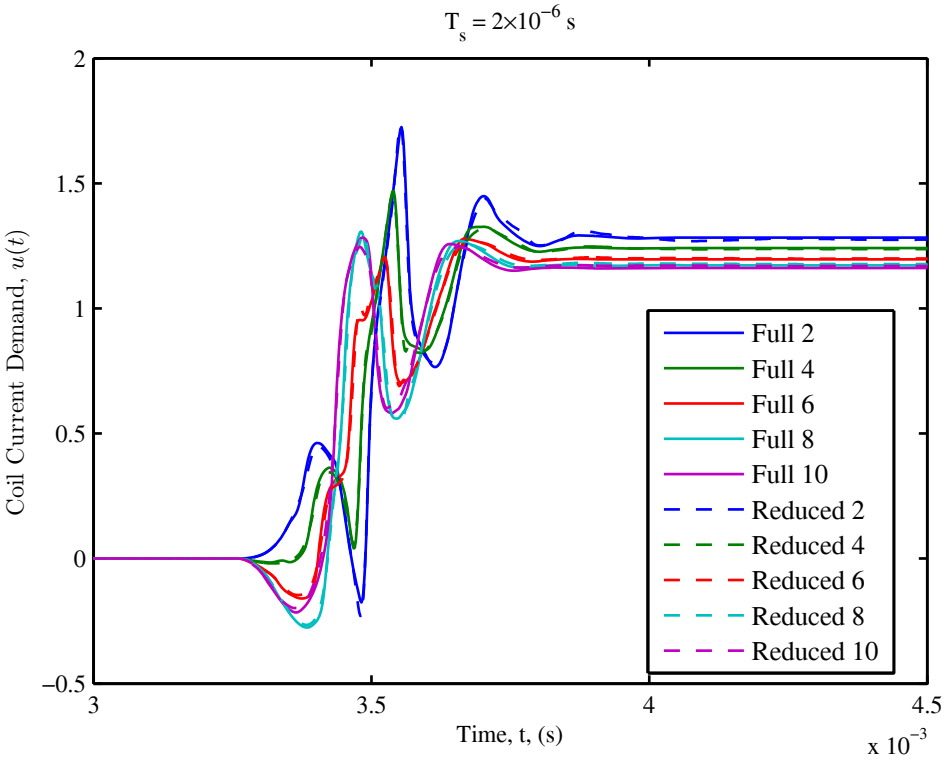


Figure K.2: Current demand for the full system (*ns*=40) and reduced system (*ns*=20) control system, $\left(T_s = 2\times10^{-6}\, s\right)$.

The same transient can be repeated with the time step for the experimental system to see the impact of time step on the control and estimation. Figure K.3 and Figure K.4 show the step transient in which the only change to the full and reduced system models is to increase the time step, $\left(T_s = 70\times10^{-6}\, s\right)$. Based on the acoustic propagation speed and the dimensions of a coil, the time step for the experimental system is at least a factor of ten slower than needed for effective use of the spatial distribution. Figure K.4 shows the control demands that are calculated by the optimization algorithm. The effect of the model predictive control is evident in the preparatory move of the coil current two steps prior to the time of the step. In Figure K.3, the displacement rises rapidly at the time of the step. The rise time for the displacement is faster than the open loop response;

however, the damping after the step is poor. The response oscillates with a long settling time. A slightly longer transient duration is shown in Figure K.3 than in Figure K.1 to show the actuator coming to rest. The feedback gain is effectively higher as step size is increased causing the feedback correction at each time step to overshoot the equilibrium giving the oscillatory response. This performance suggests that the weight matrices should be reduced to reduce the feedback gain.

Despite the poor tuning of the feedback, the full and reduced systems track closely together. This indicates that neither the model reduction nor the time step increase affects the accuracy of the estimated system response or contributes to the noisy response.

Examining the current demand plot closely shows that the coils are acting in two groups going in opposite directions. Coils 1-6 move in the same direction and coils 7-10 go in the opposite direction. This dividing line corresponds to the node in the spatial response for the second mode of the vibration model. The distribution of current demand indicates that the optimum control calculates that a high fraction of the energy should go into the second mode of the vibration model. This result of the optimization strategy gives a fast rise time but is not successful at damping the vibration after the step.

The step change is repeated a third time. In this case the weight matrices are reduced, $q_P^2 = 100$ and $q_I^2 = 2.9 \times 10^7$. This version of the control tuning gives reasonably fast rise time and moderate settling time after the step.

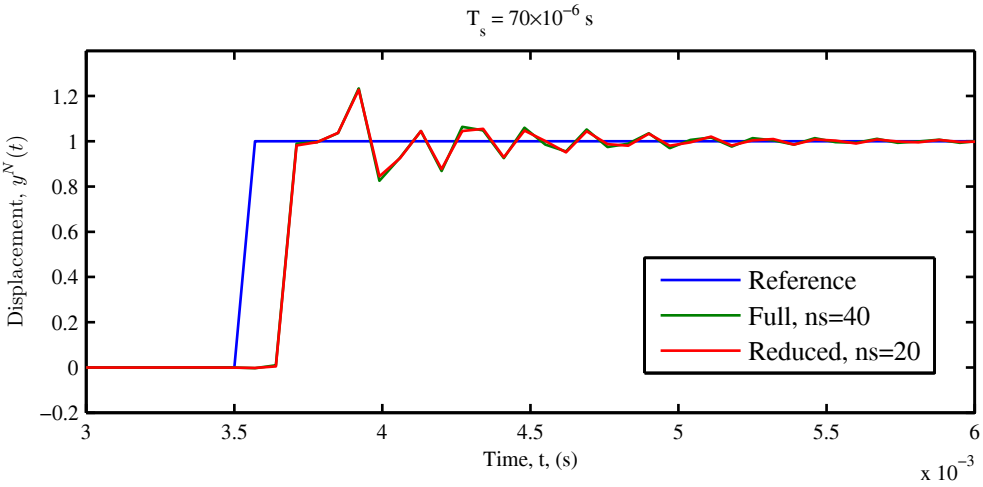


Figure K.3: Comparison of displacement for full and reduced systems at experimental time step using high weight factors $Q_P = 1000$ and $Q_I = 1\times10^{11}$

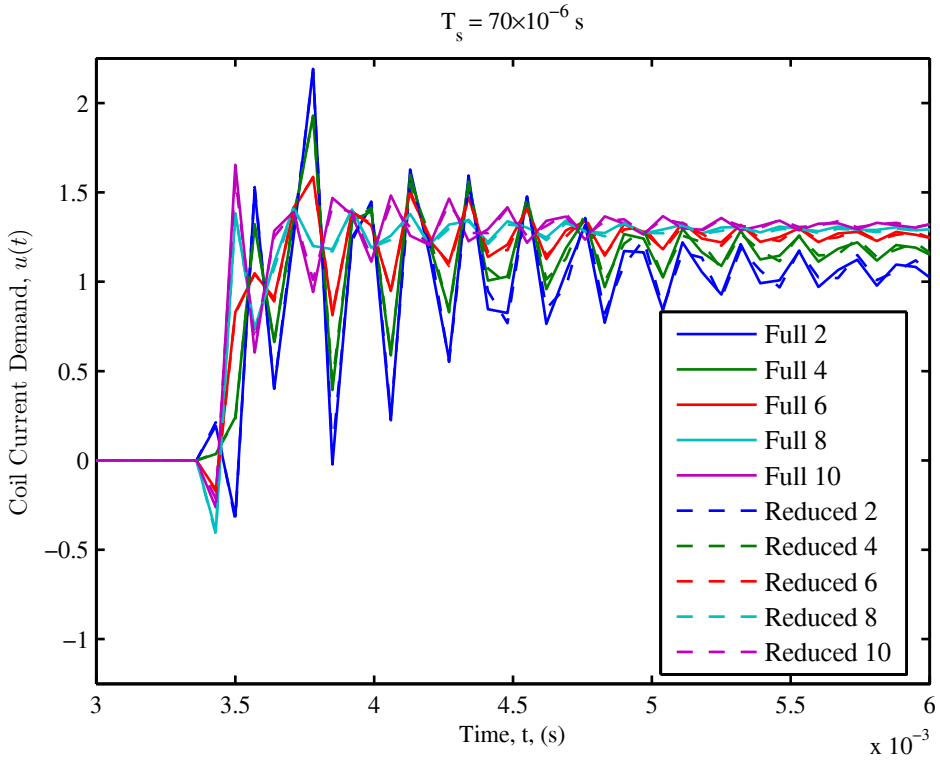


Figure K.4: Comparison of current demand for full and reduced systems at experimental time step using high weight factors $Q_P = 1000$ and $Q_I = 1\times10^{11}$

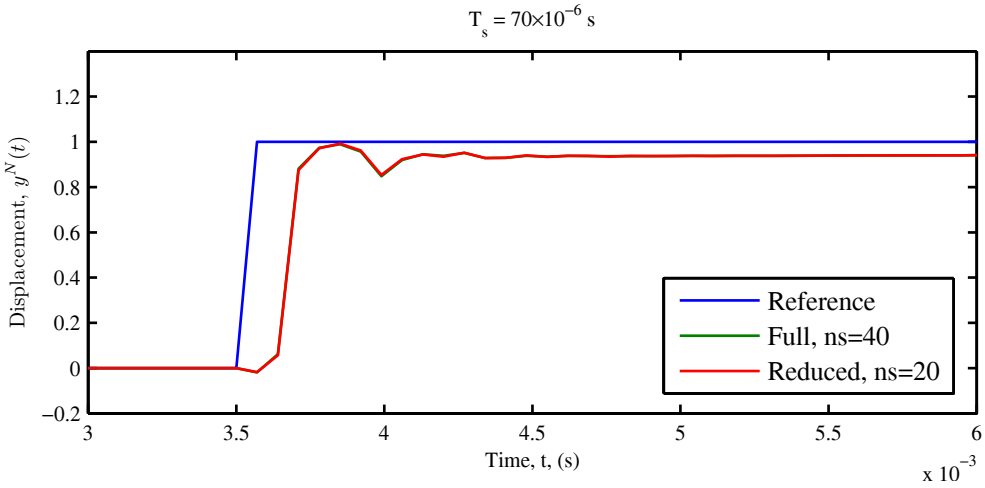


Figure K.5: Comparison of displacement for full and reduced systems at experimental time step using low weight factors $Q_P = 100$ and $Q_I = 2.9\times10^7$

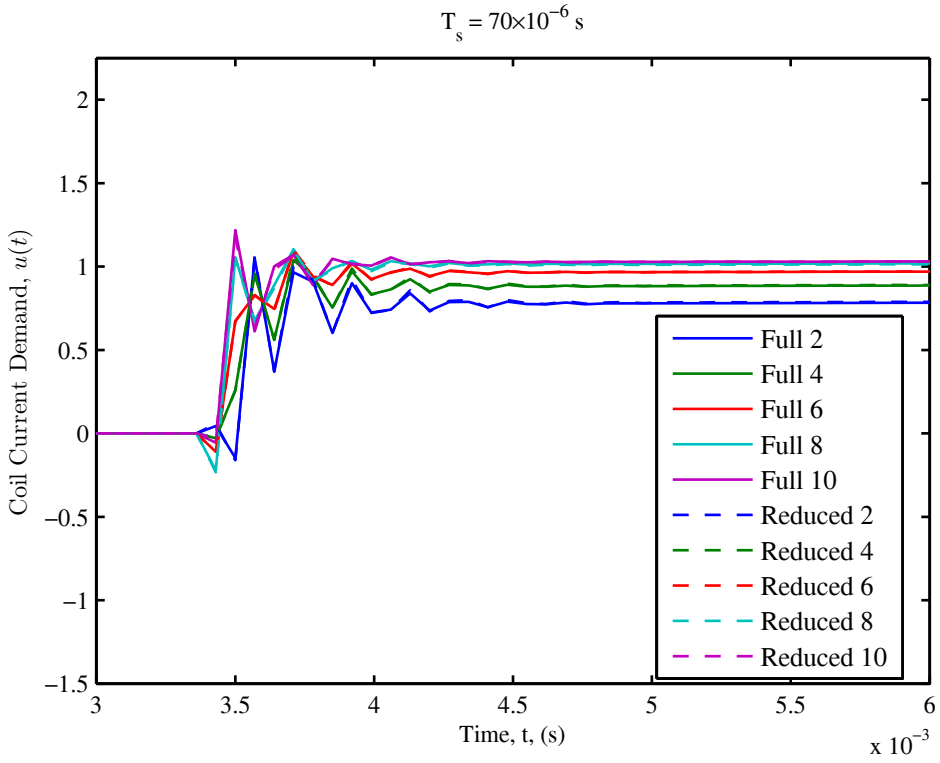


Figure K.6: Comparison of current demandt for full and reduced systems at experimental time step using low weight factors $Q_P = 100$ and $Q_I = 1\times10^{11}$

## Predicted Response for the Experimental Time Step

The benefits of the multi-coil actuator are significantly diminished by the time step of the experimental prototype. This section is a transitional section that provides predicted results at the experimental time step and weight factor settings to show how much reduction in the benefit in increased speed and reduced power to expect in the experimental results in Chapter 7. The group of three reference transients for step change, three square pulses, and swept frequency are modified to accommodate the time step. The same reference trajectories are also used to stimulate the experimental system. The range of frequency in the swept frequency case is reduced because of the sampling time. The model and prediction duplicate as closely as possible the configuration of the experimental system. The time step, prediction horizon, weight matrices, and time delay are the same values used on the experiment. The modeling matrices used in calculating the MPC matrices are slightly different than the experiment because of programming errors that were discovered after the experimental runs were completed. The effect of the errors is discussed in APPENDIX N.

The model combines the full state actuator model (40 states) with the reduced order controller (20 states) including the Kalman estimator and the Smith predictor. The amplifier gain is modified to match the experimental results in Chapter 7. A summary of the parameters in the control model design are given in Table K.1

Table K.1: MPC algorithm parameters

| Variable | Value | Units | Description |
|---|---|---|---|
| $q_P^2$ | 100 | (-) | Proportional error weight factor |
| $q_I^2$ | $2000 / T_s$ | $s^{-2}$ | Integral error weight factor[8] |
| $q_E^2$ | 0.001 | (-) | Estimator weight factor |
| $f_D$ | 0.1 | (-) | Displacement weight factor in estimator |
| $i_H$ | 3 | (-) | Prediction horizon, (number of time steps) |
| $n_K$ | 2 | (-) | Time delay (number of time steps) |
| $T_s$ | $70\times10^{-6}$ | | Time step |
| $ns_M$ | 20 | (-) | Number of states in reduced MPC model |
| $ns_P$ | 40 | (-) | Number of states in plant model |

The results in Figure K.7 through Figure K.15 show the suite of three transients. Each transient is represented by a set of three plots, the reference tracking for the displacement, the power, and the control inputs. Both open loop and closed loop results are simulated. The control inputs for the open loop transient use the reference as the demand for the coil current. The open loop results represent the response of a single coil actuator with no compensation.

The main point of the results is to show that the advantage of the multi-coil actuator is much diminished by the increase in time step. The power and tracking between the open loop and closed loop are different but there is no significant advantage to the closed loop actuator. The distribution of current plots shows that the optimum distribution is not the same as the uniform distribution but the effect on power and tracking is small. The distribution of current demand in the shape of the second mode is evident in the frequency response curves.

[8] The integral weight is only used on the portion of control error integrated over the prediction horizon. See discussion of the heading for

**Step**

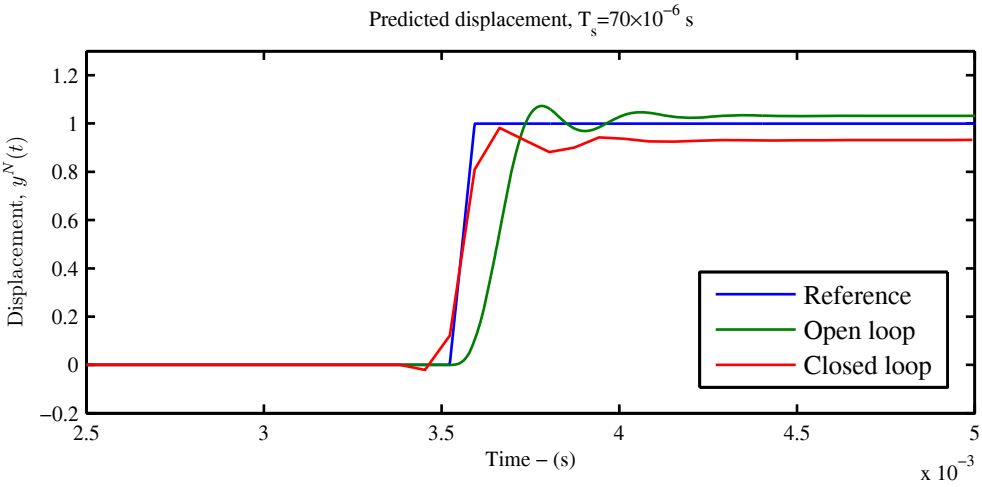


Figure K.7: Open and closed loop response of displacement on step change transient for final model

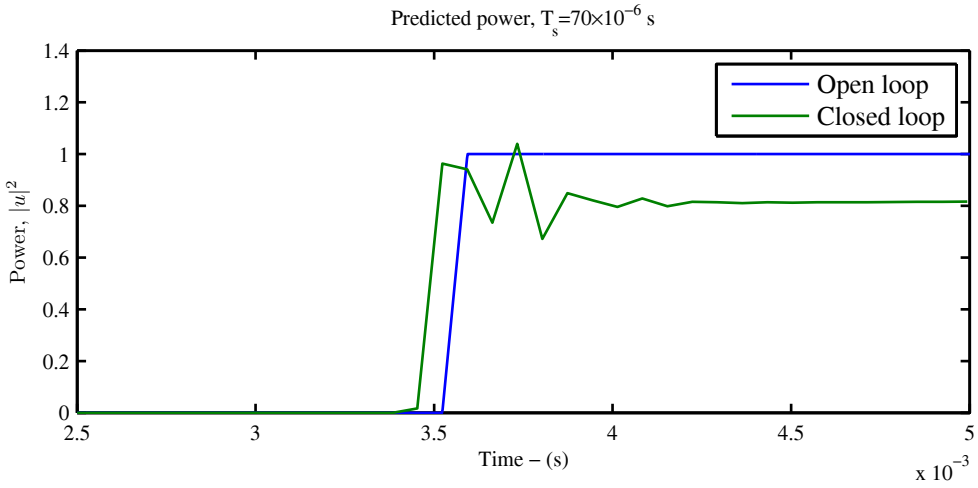


Figure K.8: Open and closed loop response of power on step change transient for final model

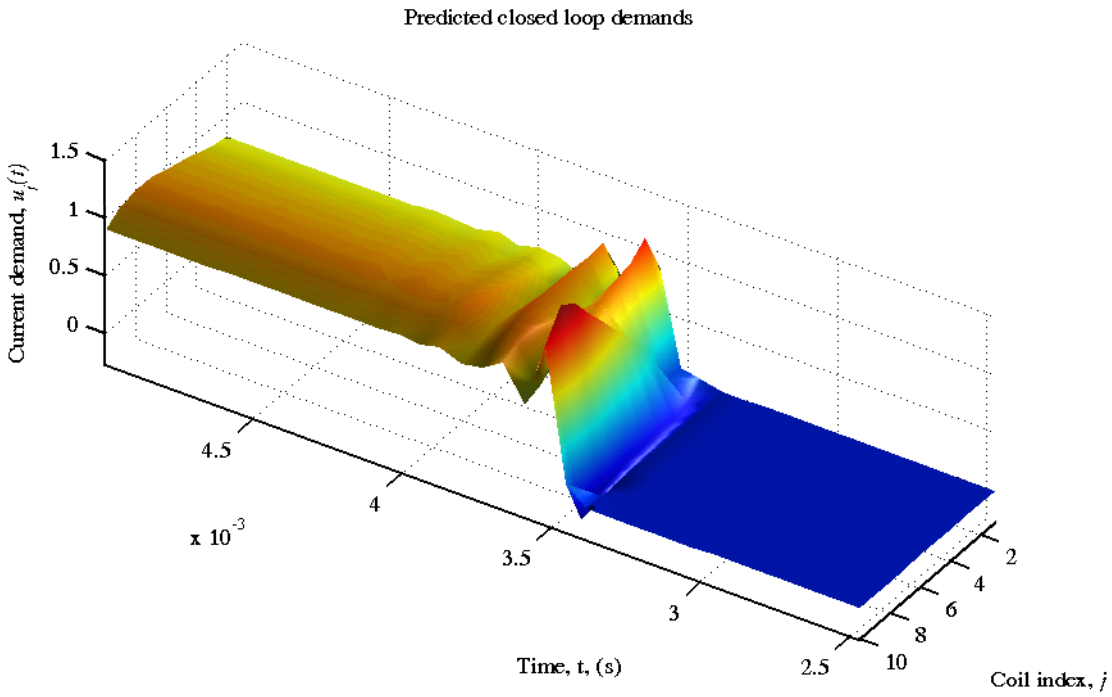


Figure K.9: Current demand versus coil index and time, closed loop, on step change transient for final model.

**Pulse**

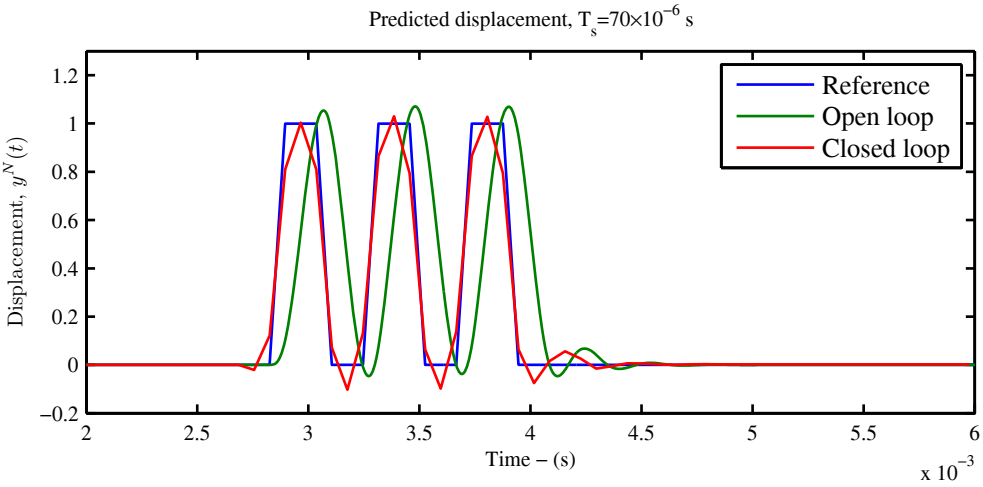


Figure K.10: Open and closed loop response of displacement on three square pulses for final model

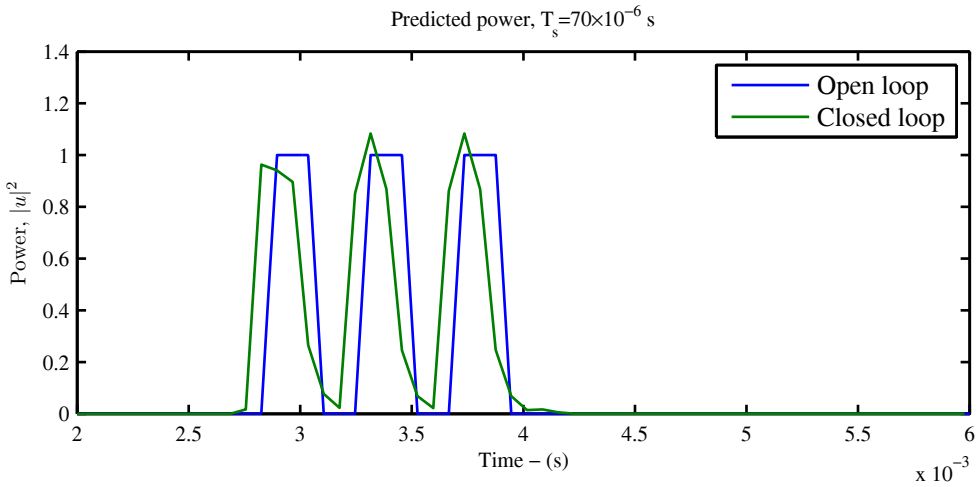


Figure K.11: Open and closed loop response of power on three square pulses for final model

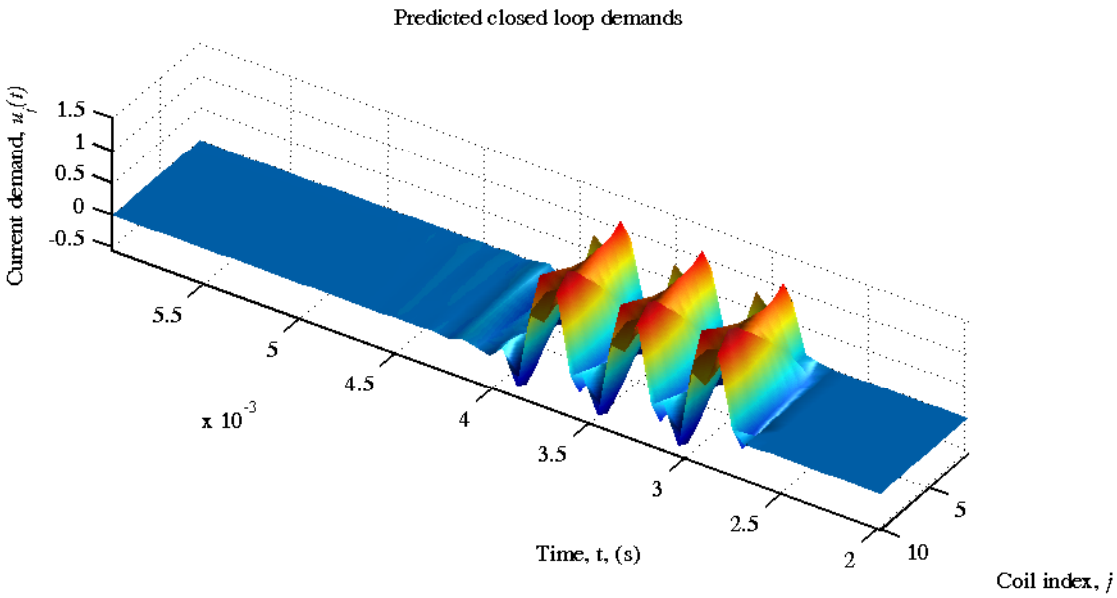


Figure K.12: Current demand versus coil index and time closed loop on three square pulses for final model

**Swept Frequency**

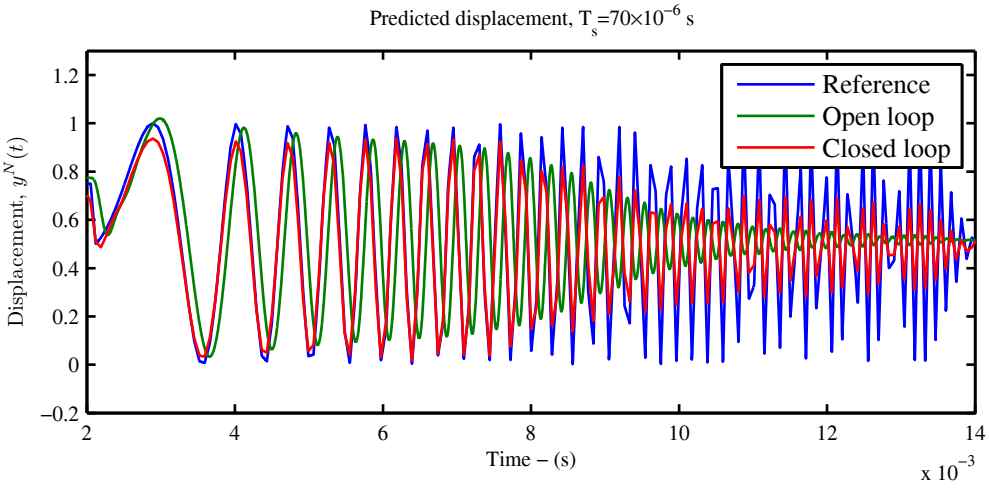


Figure K.13: Open and closed loop response of displacement on swept frequency transient for final model

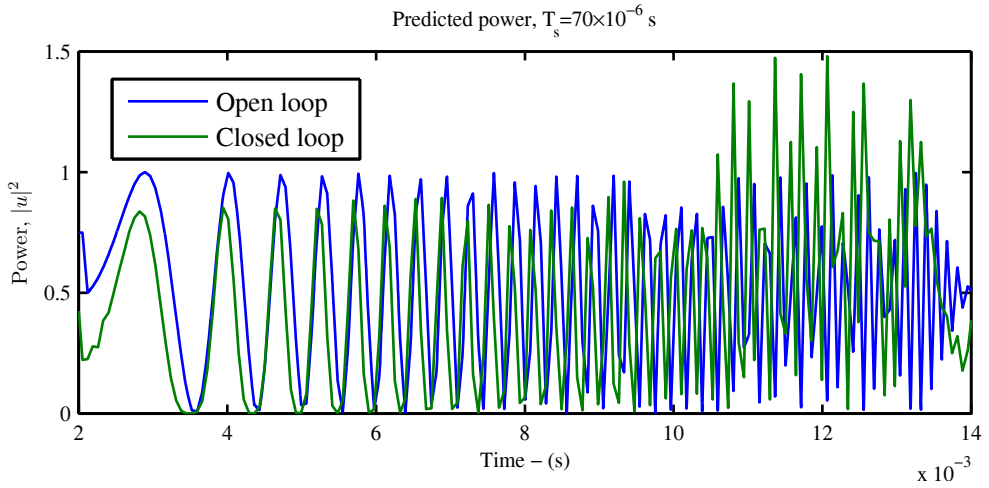


Figure K.14: Open and closed loop response of power on swept frequency transient for final model

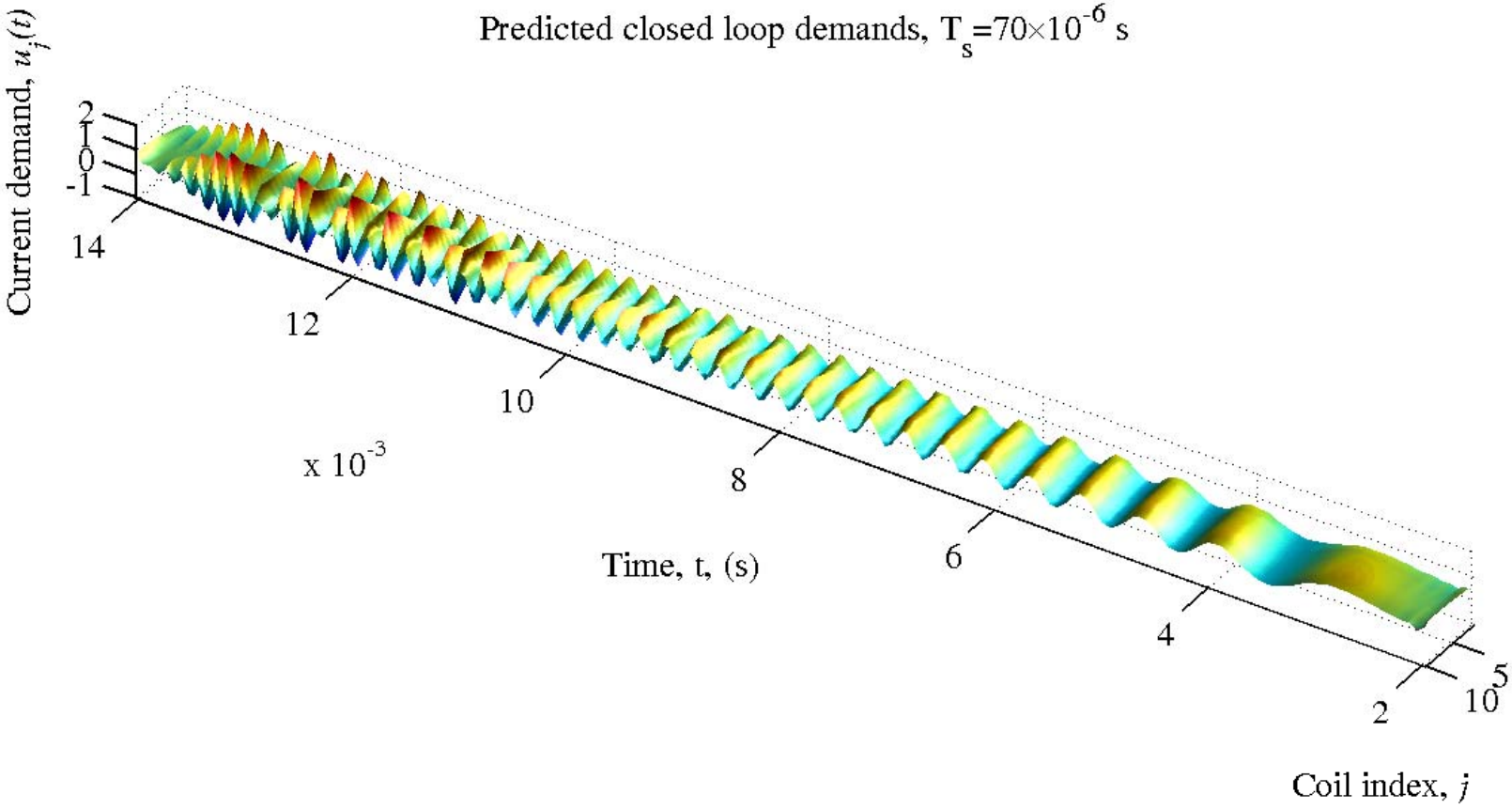


Figure K.15: Current demand versus coil index and time for close loop system on swept frequency transient for final model

# APPENDIX L

# MATHEMATICAL TREATMENT OF SENSOR DYNAMICS

## Sensor and Signal Processing Dynamics

The signal processing filter and the displacement sensor contribute dynamics to the displacement measurement that must be accounted for in the experimental data analysis. The Krohn-Hite signal processing filter is configured as a high pass filter. To illustrate the frequency dynamics of the filter, the calculated frequency response plot of a fourth order Butterworth filter with 50 Hz cut-off frequency is shown in Figure L.1.

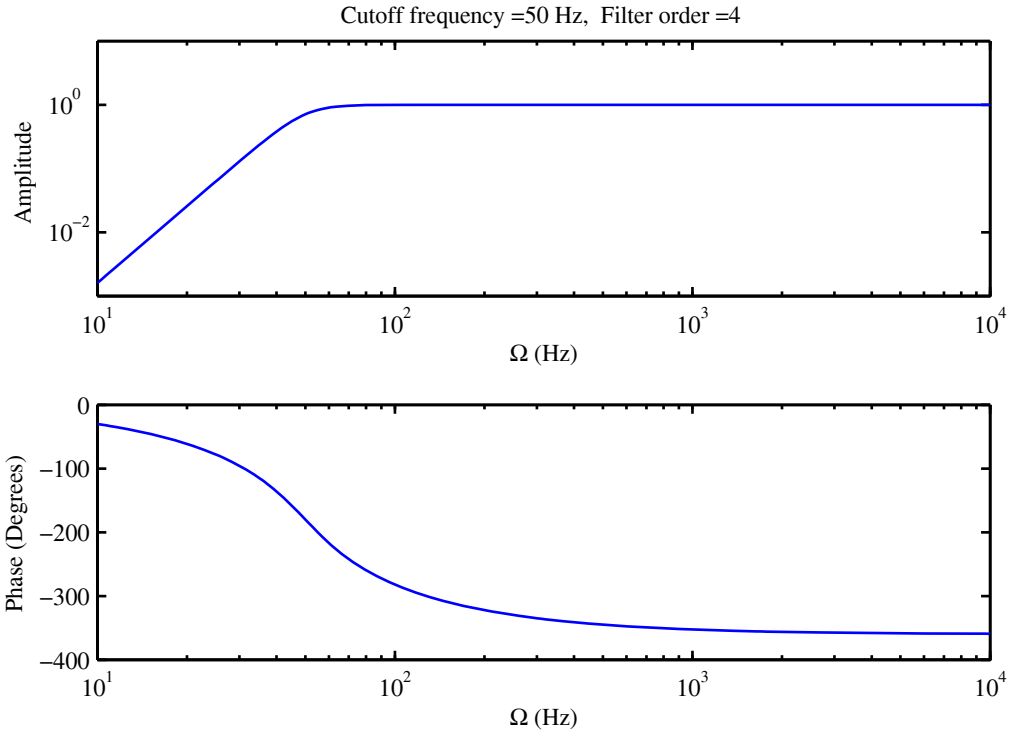


Figure L.1: Butterworth filter frequency response

In the experimental results, the frequency range of interest is from 0 to 10,000 Hz. The filter affects experimental results as the system approaches steady state.

The Philtec displacement sensor has a dynamic response as well. The sensor acts as a low pass filter. The manufacturer's data indicates that the filter's dynamic response is approximately a three pole filter with 3 dB point at 20 kHz. The sampling rates used for the experiment gives a Nyquist frequency of 7193 Hz. The filtering effect of the displacement probe can be neglected in the experiment because sampling rate is well below the filter's cut-off frequency. For experiments involving frequency content in the 20 kHz range, the displacement probe would come into play.

**Modeling of the Displacement Measurement**

The Krohn-Hite filter can be modeled using the *butter* routine from the Signal Processing Toolbox of MATLAB. The filter model can be appended to the state space model of the actuator so that the sensor dynamics are included in the control design of the experimental system. The high pass Butterworth filter is usually written mathematically as a transfer function. The formula for an *n*-th order filter is given by

$$\underline{y}^{B}(s) = G_B \frac{s^n}{s^n + a_2 s^{n-1} + \cdots + a_n s + a_{n+1}} \underline{y}^{N}(s), \qquad \text{(L.1)}$$

where $\underline{y}^{B}(s)$ is the output of the high pass filter, $\underline{y}^{N}(s)$ is the true displacement, *n* is the order of the high pass filter, and $a_x$ is the *k*-th coefficient of polynomial in the denominator of the filter's transfer function. In the numerator polynomial, all terms of the Butterworth polynomial are zero except for the first term, $s^n$. The gain of the filter approaches $G_B$ asymptotically at high frequency.

The polynomial coefficients for the Butterworth filter can be obtained from the MATLAB's *butte*r routine in which the low cutoff frequency is the input parameter. The polynomial coefficients of the transfer function can be converted into an equivalent state space form.

$$\begin{aligned} \dot{\mathbf{x}}^B &= \mathbf{A}^B \mathbf{x}^B + \mathbf{B}^B y^N; \\ y^B &= \mathbf{C}^B \mathbf{x}^B + \mathbf{D}^B y^N, \end{aligned} \tag{L.2}$$

where $\mathbf{x}^B$ is the state vector of the filter and $\mathbf{A}^B, \mathbf{B}^B, \mathbf{C}^B,$ and $\mathbf{D}^B$ are the state space system matrices equivalent to the transfer function in Eq. (L.1). Note that pass through matrix, $\mathbf{D}^B$ for the Butterworth filter is not zero.

The displacement output of the actuator model can be connected to the input of the filter. The combined system is given by the following matrices.

$$\begin{aligned} \begin{bmatrix} \dot{\mathbf{x}}^P \\ \dot{\mathbf{x}}^B \end{bmatrix} &= \begin{bmatrix} \mathbf{A}^P & \mathbf{0} \\ \mathbf{B}^B \mathbf{C}_S & \mathbf{A}^B \end{bmatrix} \begin{bmatrix} \mathbf{x}^P \\ \mathbf{x}^B \end{bmatrix} + \begin{bmatrix} \mathbf{B}^P \\ \mathbf{0} \end{bmatrix} \mathbf{u}; \\ y^B &= \begin{bmatrix} \mathbf{D}^B \mathbf{C}_S & \mathbf{C}^B \end{bmatrix} \begin{bmatrix} \mathbf{x}^P \\ \mathbf{x}^B \end{bmatrix}. \end{aligned} \tag{L.3}$$

where the actuator model is given by the state space system matrices, $\mathbf{A}^P, \mathbf{B}^P, \mathbf{C}^P,$ and $\mathbf{D}^P$. The system including the Butterworth filter model of the displacement measurement is used in the control design algorithm.

The low frequency response of the filter affects the steady state measurement of displacement. The Butterworth filter can be inverted to reconstruct the original displacement from the filtered measurement. The inverse transfer function is obtained by swapping numerator and denominator polynomials. A discrete time signal processing scheme can be created by converting the inverse of the transfer function into a state space model. The control program uses the inverse filter in post-processing to recover an

approximation to the actual displacement for display. The inverse filter output is plotted for the displacement in the experimental results.

The total gain from reference input to displacement combines the magnitude of the magnetostrictive constant, the slope of the Philtec displacement probe, and the gain of the Knohn-Hite filter. The three parameters, particularly the magnetostrictive coefficient, are subject to some variation over time and are treated as an experimentally determined parameter. The experimental results are tuned by adjusting the total measurement gain parameter so that the experimental amplitude matches the calculated results.

# APPENDIX M

# CONTROL PROGRAM OUTLINE

1. Initialization of the screen routines.
2. Initialize I/O board interface routines.
3. Read control matrices and reference trajectory from file.
4. Initialize control computations.
5. Delay process to allow all disk operations to complete.
6. Disable interrupts.
7. Set control process priority to maximum.
8. Start experiment loop.
    i. Read data values for coil current and displacement from input boards.
    ii. Convert data to normalized units.
    iii. Calculate the estimated state at the delayed time.
    iv. Get values of reference trajectory for prediction window.
    v. Calculate the control at the current time using MPC algorithm. (This step combines the MPC algorithm and the Smith predictor.)
    vi. Record measured and computed data in vector for post processing.
    vii. Send control demands to output board.
    viii. Check loop time.
        1. If time greater than final time, go to *9. Exit experiment loop.*

2. If time step is greater than max time step, restart algorithm and return to *8. Start experiment loop.*
3. If time step is between min time step and max time step, increment counter and return to *8. Start experiment loop.*
4. Otherwise, return to *viii. Check loop time.*

9. Exit experiment loop.
10. Restore normal process priority.
11. Activate disk processes.
12. Write data to disk file.
13. Check for another test case.
    i. If not last test Go to *8. Start of loop*.
    ii. Else, go to *14. Exit program.*
14. Exit program.

# APPENDIX N

# ASSESSMENT OF MODELING ERRORS IN EXPERIMENTAL ACTUATOR'S MODEL PREDICTIVE CONTROL

Several modeling errors were found in the state space model in mathematical tests conducted after the closed loop experiments were completed. The errors all involved secondary effects in the coupling coefficients of state derivative terms. The largest magnitude error was in the eddy current modeling and caused the magnetic drag to be underestimated. This error has the effect of neglecting the magnetic drag. The effect of the magnetic drag is evident in the results of the stand alone model of vibration in Figure 3.5 and the model of vibration and magnetics together in Figure 4.15.

The second largest error miscalculated the phase of voltage induced in the coils by the magnetostriction in the rod. The voltage induced in the coils by magnetostriction is a very small term at the absolute magnitude. The error caused the timing to be slightly different.

The third largest error involved the calculations using FEMM results in integrals. The FEMM results were recorded at a mesh spacing in the radial direction that was too coarse for accurate integration of the magnetics coefficients. The error was only apparent in high order radial modes of the magnetic model. Since only the first radial mode is used in the final model, this error actually caused no noticeable effect.

In Figure N.1, the control demands calculated by the corrected algorithm are compared to the demands recorded by the experimental system. The demands calculated by the experiment are the actual closed loop demands sent to the actuator. The corrected

demands are obtained in post-processing and have no effect on the experimental results. The differences between the two are evidence of the effect of the modeling errors on the control. The differences are significant, amounting to 15% near the step, but the basic character of the response is the same. The algorithm even with modeling errors achieves a degree of improvement in the cost function optimization. The overall character of the demand is similar to the corrected and the displacement response is stable but clearly suboptimal. The response of the model with error is similar to the effect of operating the actuator with a different load than considered in the design. The response indicates a degree of robustness to changes in the actuator's operating conditions.

On the other hand, the errors are significant to validation of the model. The comparison of the experimental and predicted on the PRBS transients is significantly better because of the modeling corrections.

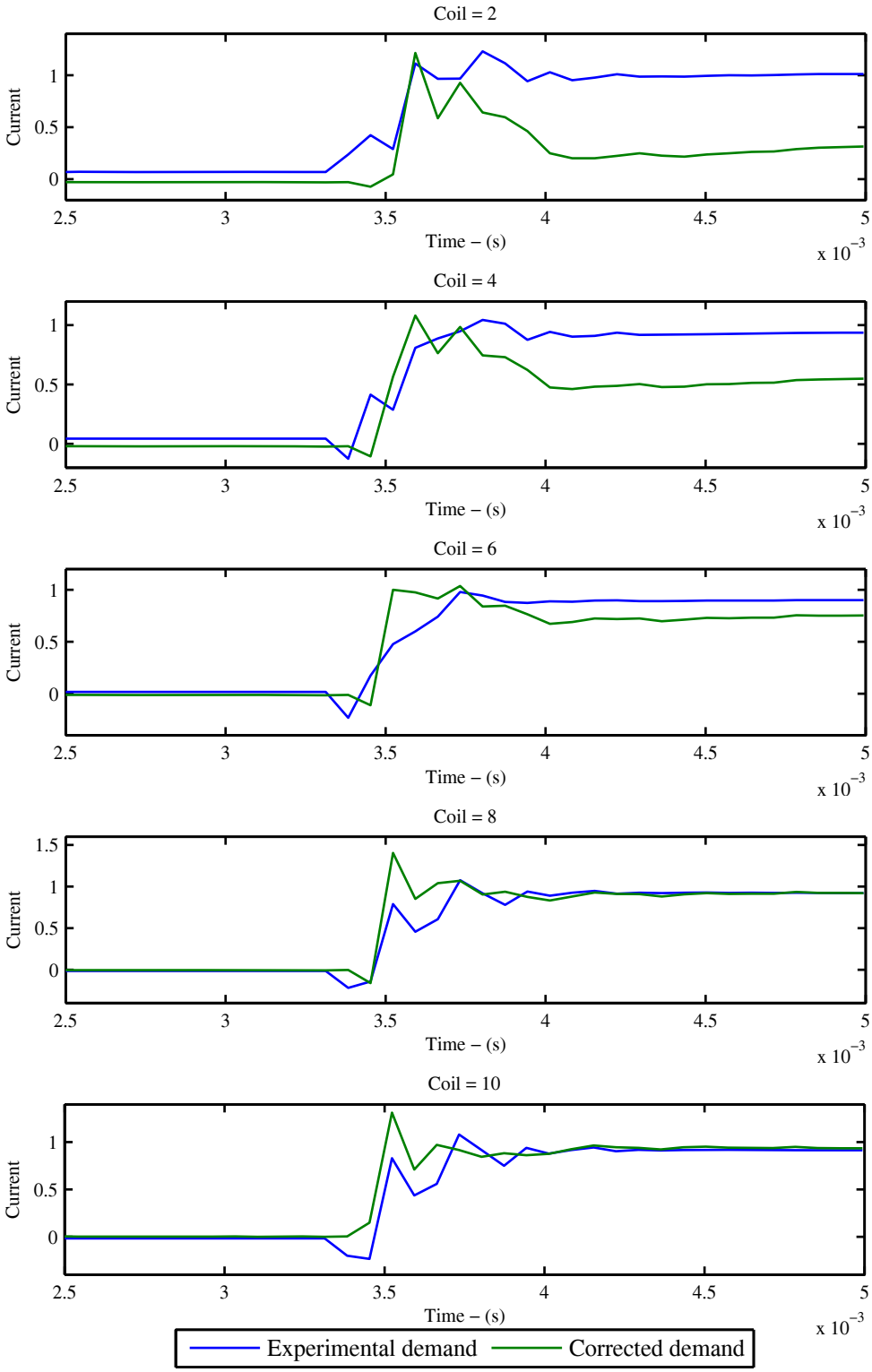


Figure N.1: Comparison of demand calculated by experiment (with model errors) and demand calculated with corrected model

# REFERENCES


1. Hansen, T.T., *Magnetostrictive materials and ultrasonics.* Chemtech, 1996: p. 56-59.

2. Clark, A.E. and H.S. Belson, *Giant Room Temperature Magnetostictions in $TbFe_2$ and Dy $Fe_2$.* Physics Review, 1972. **8**(5): p. 35-41.

3. Savage, H.T., et al., *Permeability, magnetomechanical coupling and magnetostriction in grain-oriented rare earth-iron alloys.* Physics Review, 1979. **50**(3): p. 1674-1676.

4. Savage, H.T., et al., *Permeability, magnetomechanical coupling and magnetostriction in grain-oriented rare earth-iron alloys.* Physics Review, 1972. **50**(3): p. 1674-1676.

5. Greenough, R.D., et al., *Actuation with Terfenol-D.* IEEE Transactions on Magnetics, 1991. **27**(6): p. 5346-8.

6. Fenn, R.C., et al., *Low mass, high reliability magnetostrictive reaction mass actuators.* Active Control of Vibration and Noise, ASME, 1994. **75**: p. 457-464.

7. Bryant, M.D., et al., *Active vibration control in structures using magnetostrictive Terfenol with feedback and/or neural network controllers.* Journal of Intelligent Material Systems and Structures, 1993. **4**(4): p. 465-479.

8. Dyberg, J., *Magnetostrictive Rods in Mechanical Applications*, in *The First International Conference on Giant Magnetostrictive Alloys and their Impact on Actuator and Sensor Technology*. 1986: Marbella, Spain. No. of.

9. Engdahl, G., ed. *Handbook of Giant Magnetostrictive Materials*. Academic Press Series in Electromagnetism, ed. I. Mayergoyz. 2000, Academic Press: San Diego, California.

10. Clark, A.E. and D.N. Crowder, *High temperature magnetostriction of $TbFe_2$ and $Tb_{.27}Dy_{.73}Fe_2$.* IEEE Transactions on Magnetics, 1985. **21**(5): p. 1945-1947.

11. Luenberger, D.G., *Dynamic Equations in Descriptor Form.* IEEE Transactions on Automatic Control, 1977. **22**(3): p. 312-321.

12. Maciejowski, J.M., *Predictive Control with Constraints*. 2002, Harlow, England: Pearson Educatoin.

13. Rossiter, J.A., *Model-Based Predictive Control*. Control, ed. R.H. Bishop. 2003, Boca Raton, Louisiana: CRC Press.

14. Clark, A.E., *Magnetostrictive rare earth -$Fe_2$ compounds*, in *Ferromagnetic materials*, E.P. Wohlfarth, Editor. 1980, North-Holland Publishing Company New York, New York p. 531-589.

15. Claeyssen, F., R. Bosut, and D. Boucher. *Modelling and characterization of the magnetostrictive coupling*. in *Proceedings of the International Workshop on Power Sonics and Ultrasonics*. 1991. Toulon, France.

16. Du Trémolet de Lacheisserie, E. and J. Rouchy, *La détermination de la matrice élastomagnetique et son domaine d'application dans le cas des alliages de Terfenol-D*. 1989: Le Brusc, France. No. of.

17. Lhermet, N. *ATILA V.5.1.1 User Manual-A 3D CAD Software for Piezoelectric and Magnetostrictive Structures*. 1997.

18. Claeyssen, F., *Design and construction of low-frequency sonar transducers based on rare earth-iron alloys (translated from French)*. 1989, INSA: Lyon, France. No. of.

19. Jiles, D., *Introduction to Magnetism and Magnetic Materials*. Second Edition ed. 1998, London, United Kingdom: Chapman & Hall, Inc.

20. Hughes, D.C. and J.T. Wen. *Preisach modeling and compensation for smart material hysteresis*. 1995. Bellingham, WA, USA: Society of Photo-Optical Instrumentation Engineers.

21. Halliday, D. and R. Resnick, *Physics*. Second ed. Vol. 1. 1967, New York, New York: John Wiley & Sons.

22. Gawronski, W.K., *Advanced Structural Dynamics and Active Control of Structures*. Mechanical Engineering Series, ed. F.F. Ling. 2004, New York, New York: Springer. 396.

23. Mei, C.C., *Mathematical Analysis in Engineering*. 1995, Cambridge, UK: Cambridge University Press.

24. Kinsler, L.E., et al., *Fundamentals of Acoustics*. Third ed. 1982, New York, New York: John Wiley & Sons.

25. Smith, F.D., *The magnetostriction constant for alternating magnetic fields.* Proceedings of the Physical Society of London, 1930. **42**(3): p. 181-191.

26. Courant, R. and D. Hilbert, *Methods of Mathematical Physics*. First English ed. 1953, New York, New York: John Wiley & Sons.

27. Özişik, M.N., *Heat Conduction*. Second ed. 1993, New York, New York: John Wiley & Sons.

28. Tellegren, B.D.H., *The gyrator, a new electric network component.* Philips Research Report, 1948. **3**: p. 81-101.

29. Decarpigny, J.N., et al., *In-air analysis of piezoelectric Tonpilz tranducers in a wide frequency band using a mixed finite element-plane wave method.* Journal of the Acoustical Society of America, 1985. **78**(5): p. 1499-1507.

30. Engdahl, G. and L. Svensson, *Simulation of the Magnetostrictive Performance of Terfenol-D in Mechanical Devices.* Journal of Applied Physics, 1988. **63**(8): p. 3924-3926.

31. Kvarnsjö, L. and G. Engdahl, *Nonlinear 2-D transient modeling of Terfenol-D rods.* IEEE Transactions on Magnetics, 1991. **27**(6): p. 5349-5351.

32. Hall, D.L. and A.B. Flatau, *One-Dimensional Analytical Constant Parameter Linear Electromagnetic-Magnetomechanical Models of a Cylindrical Magnetostrictive (Terfenol-D) Transducer.* Journal of Intelligent Material Systems and Structures, 1995. **6**(3): p. 315-328.

33. Smith, R.C., *A Nonlinear Physics-Based Optimal Control Method for Magnetostrictive Actuator*, I.f.C.A.i.S.a. Engineering and N.L.R. Center, Editors. 1998, National Aeronautics and Space Administration: Hampton, VA. No. of.

34. Moler, C. and J. Little. *Matlab & Simulink Student Version*. 2004; Version 7.0.1.15 (R14) Service Pack 1. Available from: www.mathworks.com.

35. Meeker, D.C. *Finite Element Method Magnetics - FEMM*. 2005; 3.4.2, Build April 15, 2005. Available from: http://femm.foster-miller.net/wiki/HomePage.

36. Pratt, J. and A.B. Flatau, *Development and analysis of a self-sensing magnetostrictive actuator design.* Journal of Intelligent Material Systems and Structures, 1995. **6**(5): p. 639-648.

37. Smith, R.C., M.J. Dapino, and S. Seelecke, *Free energy model for hysteresis in magnetostrictive transduces.* Journal of Applied Physics, 2003. **93**(1): p. 458-466.

38. Dapino, M.J., *Nonlinear and hysteretic magnetomechanical model for magnetostrictive transducers*, in *Engineering Mechanics*. 1999, Iowa State University: Ames, Iowa. No. of pages. 243.

39. Dapino, M.J., et al., *A coupled structural-magnetic strain and stress model for magnetostrictive transducers.* Journal of Intelligent Material Systems and Structures, 2000. **11**(2): p. 135-152.

40. Kvarnsjö, L. and G. Engdahl, *Examination of Eddy Current Influence on the Behavior of a Giant Magnetostrictive Functional Unit.* Journal of Applied Physics, 1990. **67**(9): p. 5010-5012.

41. Evans, P.G. and M.J. Dapino, *Fully-coupled magnetostrictive model for Galfenol alloys incorporating eddy current losses and thermal relaxation* Proceedings of SPIE, Behavior and Mechanics of Multifunctional and Composite Materials, 2008. **6929**: p. 69291W.

42. Huang, W., et al., *Dynamic strain model with eddy current effects for giant magnetostrictive transducer.* IEEE Transactions on Magnetics, 2007. **43**(4): p. 1381-1384.

43. Hall, D.L. and A.B. Flatau, *On analog feedback control for magnetostrictive transducer linearization.* Journal of Sound and Vibration, 1998. **211**(3): p. 481-494.

44. Littmarck, S. and F. Saeidi. *COMSOL Multiphysics*. 1995; COMSOL 3.4.

45. Besbes, M., z. Ren, and A. Razek, *A Generalized Finite Element Model of Magnetostriction Phenomena.* IEEE Transactions on Magnetics, 2001. **37**(5): p. 3324-3328.

46. Rothwell, E.J. and M.J. Cloud, *Electromagnetics*. Electrical Engineering Textbook Series, ed. R.C. Dorf. 2001, Boca Raton, Louisiana: CRC Press.

47. Jackson, J.D., *Classical Electrodynamics*. Third ed. 1999, New York, New York: John Wiley & Sons. 808.

48. Lorrain, P. and D.R. Corson, *Electromagnetic Fields and Waves*. Second Edition ed. 1970, San Francisco, California: W. H. Freeman and Company.

49. Stoll, R.L., *The analysis of eddy currents*. 1974, Oxford, UK: Clarendon Press.

50. Carslaw, H.S. and J.C. Jaeger, *Heat Conduction in Solids*. Second ed. 1959, New York, New York: Oxford University Press.

51. Weinberger, H.F., *A First Course in Partial Differential Equartions with Complex Variables and Transform Methods*. 1965, Waltham, MA: Blaisdell Publishing Company.

52. Dapino, M.J., et al., *A coupled magnetomechanical model for magnetostrictive transducers and its application to Villari-effect sensors.* Journal of Intelligent Material Systems and Structures, 2002. **13**(11): p. 737-747.

53. Lee, H. and Y.Y. Kim, *Wave selection using a magnetomechanical sensor.* Journal of the Acoustical Society of America, 2002. **112**(3): p. 953-960.

54. Calkins, F.T. and A.B. Flatau, *Terfenol-D Sensor Design and Optimization*. 1997, Iowa State University. No. of pages. 10.

55. Ogata, K., *System Dynamics*. Third ed. 1998, Upper Saddle River, New Jersey: Prentice-Hall.

56. Franco, S., *Design with Operational Amplifiers and Analog Integrated Circuits*. Second ed. McGraw-Hil Series in Electrical and Computer Engineering, ed. S.W. Director. 1997, New York, New York: WCB/McGraw-Hill.

57. Nagel, L.W. and D.O. Pederson, *SPICE (Simulation program with Integrated Circuit Emphasis)*. Memorandum No. ERL-M382. April 1973, University of California, Berkeley.

58. Nagel, L.W. *The Life of SPICE*. [http://www.designers-guide.org/Perspective/life-of-spice.pdf] 1996 May 12, 2006 [cited 2008 Oct. 18, 2008].

59. Goodfriend, M.J. and K.M. Shoop, *Adaptive characteristics of the magnetostrictive alloy, Terfenol-D, for active vibration control.* Journal of Intelligent Material Systems and Structures, 1992. **3**(2): p. 245-254.

60. Hiller, M.W., M.D. Bryant, and J. Umegaki, *Attenuation and transformation of vibration through active control of magnetostrictive Terfenol.* Journal of Sound and Vibration, 1989. **133**(3): p. 1-13.

61. Moon, S.-J., et al., *Structural vibration control using linear magnetostrictive actuators.* Journal of Sound and Vibration, 2007. **302**(4-5): p. 875-891.

62. Smith, R.C., C. Bouton, and R. Zrostlik. *Partial and full inverse compensation for hysteresis in smart material systems*. 2000. Piscataway, NJ, USA: Institute of Electrical and Electronics Engineers Inc.

63. Nealis, J.M. and R.C. Smith. *Robust Control of a Magnetostrictive Actuator*. 2003: The International Society for Optical Engineering.

64. Venkataraman, R. and P.S. Krishnaprasad. *Approximate inversion of hysteresis: Theory and numerical results*. in *Proceedings of the IEEE Conference on Decision and Control*. 2000: Institute of Electrical and Electronics Engineers Inc.

65. Qin, S.J. and T.A. Badgwell, *A survey of industrial model predictive control technology.* Control Engineering Practice, 2003. **11**(7): p. 733-764.

66. Magni, L. and R. Scattolini, *Tracking of non-square, nonlinear continuous time systems with piecewise constant model predictive control.* Journal of Process Control 2007. **17**: p. 631-640.

67. Shead, L.R.E., C.G. Anastassakis, and J.A. Rossiter, *Steady-state operatbility of multi-variable non-square systems: Application to model predictive control (MPC) of the Shell Heavy Oil Fractionator (SHOF)*, in *2007 Mediterranean Converence on Control and Automation*. 2007: Athens, Greece. No. of.

68. Hanagud, S., M.W. Obal, and A.J. Calise, *Optimal Vibration Control by the Use of Piezoceramic Sensors and Actuators.* Journal of Guidance, Control, and Dynamics, 1992. **15**(5): p. 1199-1206.

69. Nelson, R.D., S.F. Glover, and V.S. Rao. *Vibration suppression of smart structural systems using predictive control*. 1997. Bellingham, WA, USA: Society of Photo-Optical Instrumentation Engineers.

70. Hildebrand, F.B., *Advanced Calculus for Applications*. Second Edition ed. 1976, Englewood Cliffs, New Jersey: Prentiss-Hall, Inc. 733.

71. Neumeier, Y., Personal Communication, 2000, Excel calculation.

72. Book, W.J., *Controlled motion in an elastic world.* Journal of Dynamic Systems, Measurement and Control, Transactions of the ASME, 1993. **115**(2B): p. 252-261.

73. Kwon, D.-S. and W.J. Book, *Time-domain inverse dynamic tracking control of a single-link flexible manipulator.* Journal of Dynamic Systems, Measurement and Control, Transactions of the ASME, 1994. **116**(2): p. 193-200.

74. D'Azzo, J.J. and C.H. Houpis, *Linear Control System Analysis and Design: Conventional and Modern*. Second ed. McGraw-Hill Series in Electrical Engineering, ed. S.W. Director. 1981, New York, New York: McGraw-Hill Book Company.

75. Phillips, G.M. and P.J. Taylor, *Theory and Applications of Numerical Analysis*. 1973, New York, New York: Academic Press.

76. Grimble, M.J., *Industrial Control Systems Design*. 2001, Chichester: John Wiley & Sons, Inc.

# VITA

**Thomas L. Wilson, Jr.**

Thomas L. Wilson, Jr. was born in Huntsville, Alabama. He attended public schools in Cleveland, Tennessee where he was graduated from Cleveland High School in 1970 as class valedictorian. Mr. Wilson continued his education at the Georgia Institute of Technology where he was awarded a Bachelor of Science in Physics with highest honors in 1974 and a Master of Science in the School of Nuclear Engineering in 1976. His masters thesis, "Heat Conduction in Heat-Generating Unidirection Composites" was awarded the Monie Ferst Research Prize in 1976. Mr. Wilson joined the Babcock and Wilcox Company in Lynchburg, Virginia where he served in a number of capacities primarily in computer methods development and simulation. In 1986, Mr. Wilson moved to Oak Ridge, Tennessee to join a new project at the Oak Ridge National Laboratory on Advanced Control and Testing for nuclear power plants. While at the laboratory, Mr. Wilson developed numerous simulation models and control designs of nuclear and fossil powered electrical plants. Mr. Wilson returned to Georgia Tech in 1999 to pursue a doctorate degree.

Mr. Wilson is married and has three daughters. His other interests include endurance sports of swimming, bicycling, and running. He is an avid waterskier and woodworker.